LIBRARIES
MICHIGAN STATE UNIVERSITY
EAST LANSING, MICH 48824-1048

This is to certify that the
dissertation entitled

SEISMIC BEHAVIOR OF MOMENT RESISTING FRAMES
WITH HIGH-STRENGTH SQUARE CFT COLUMNS

presented by

ZHIHUI HUANG

has been accepted towards fulfillment
of the requirements for the

Ph.D. degree in Civil Engineering

Amit Varma
Major Professor's Signature

05/11/05
Date

MSU is an Affirmative Action/Equal Opportunity Institution

PLACE IN RETURN BOX to remove this checkout from your record.
TO AVOID FINES return on or before date due.
MAY BE RECALLED with earlier due date if requested.

DATE DUE	DATE DUE	DATE DUE

2/05 c:/CIRC/DateDue.indd-p.15

SEISMI
WIT

SEISMIC BEHAVIOR OF MOMEMT RESISTING FRAMES WITH HIGH-STRENGTH SQUARE CFT COLUMNS

VOLUME I

By

Zhihui Huang

A DISSERTATION

Submitted to
Michigan State University
in partial fulfillment of the requirements
for the degree of

DOCTOR OF PHILOSOPHY

Department of Civil and Environmental Engineering

2005

SEISMI
WI

The seismi

resisting frame

columns (CF

implemented

can effectively

used to model

connection m

of the beam-t

Six and t

CA) were des

designed to m

Code

analytically by

adaptive push

by subjecting t

Displacement

were adopted

ABSTRACT

SEISMIC BEHAVIOR OF MOMEMT RESISTING FRAMES WITH HIGH-STRENGTH SQUARE CFT COLUMNS

By

Zhihui Huang

The seismic behavior of low-rise (six-story) and medium-rise (twelve-story) moment resisting frames (MRFs) with high-strength square concrete filled steel tube (CFT) beam-columns (CFT MRFs) were investigated analytically. A special fiber-based element was implemented in DRAIN-2DX by researchers at Michigan State University. This element can effectively model the fundamental cyclic behavior of structural members. It was used to model the CFT beam-columns and steel beams of the CFT MRFs. A special connection model was developed using elements in DRAIN-2DX to model the behavior of the beam-to-column moment connections.

Six and twelve story office buildings located in a high seismic risk area (Los Angeles, CA) were designed using high strength CFT MRFs. The high strength CFT MRFs were designed to meet all the requirements of current building codes (International Building Code 2000). The seismic behavior of these high strength CFT MRFs were investigated analytically by performing static pushover analysis following FEMA 356 procedures and adaptive pushover analysis. In addition, the high strength CFT MRFs were investigated by subjecting them analytically to three sets of SAC ground motion records, including 2%, 10% and 50% probability of exceedance in 50 years. These ground motion records were adopted from those developed for the Los Angeles area as part of the SAC study.

The resul

designed to r

can meet the

FEMA 368.

strength CF

indicate that

influence on

angles are s

buckling of

Due to the s

influence th

to distinguis

When the ro

4, the seco

be neglecte

Based o

be used to d

The high st

ist, but the

fundamenta

fitted index

MSE of T

MSE, and p

The results of the analytical investigations demonstrate that high strength CFT MRFs designed to meet all the requirements of current building codes have good ductility and can meet the global and local seismic performance requirements of FEMA 350 and FEMA 368. This is an important finding because current codes limit the use of high strength CFTs in MRFs due to lack of this knowledge. The analytical results also indicate that inelastic local buckling of member section components have a small influence on the overall seismic response of high strength CFT MRFs when the roof drift angles are smaller than 1.5%. When the roof drift angle is larger than 1.5%, local buckling of steel beams controls the post-yield behavior of high strength CFT MRFs. Due to the strong column-weak beam design, local buckling of the CFTs has a smaller influence than the steel beams. In addition, the pushover analysis provides a good index to distinguish the influence zones of the higher mode and second-order P-Δ effects. When the roof displacements of the time-history analysis are larger than the design drift, Δ_d, the second-order P-Δ effects on the seismic performance of the structure should not be neglected.

Based on these analytical results, the current codes and seismic design provisions can be used to design high strength CFT MRFs for low rise or medium rise office building. The high strength CFTs can be designed using steel with 50 ksi $\leq \sigma_y \leq$ 80 ksi and $f'_c \leq$ 16 ksi, but the width-to-thickness b/t ratios must be limited to 32. The upper bound limit on fundamental period, T_{max}, set by IBC-2000 for the purposes of strength check, provides a good index to distinguish relatively rigid and flexible CFT MRFs. The flexible CFT MRF ($1 < T_1/T_{max} < 1.15$) has smaller CFT sections than the rigid ($0.9 < T_1/T_{max} < 1$) CFT MRF, and is recommended for seismic design.

I would like to
opportunity to co
thank the remaini
Bagueño. Dr. Ch
enjoyed working
engineering area
from all the mem

This research
Department of C
Michigan State U

Words cannot
throughout these
gratitude to my f

ACKNOWLEDGMENT

I would like to thank Dr. Amit Varma for his time, contribution, and giving me the opportunity to conduct this research at Michigan State University. I would also like to thank the remaining members of dissertation committee, Dr. Harichandran, Dr. Burgueño, Dr. Chatti, and Dr. Averill for their time, guidance and support. I have enjoyed working on my PhD dissertation, which was practical for the structural engineering area. The thoughtful advice, inspiration, generous help, and encouragement from all the members of my dissertation committee has made this work possible.

This research was financially supported by Michigan State University through the Department of Civil and Environmental Engineering. I would also like to thank Michigan State University for the precious opportunity of advanced study.

Words cannot express the support, guidance, and encouragement I have received throughout these years at Michigan State University. Finally, I would extend the deepest gratitude to my family for their love, support, encouragement, and understanding.

ACKNOWLEDGN

TABLE OF CONT

LIST OF TABLES

LIST OF FIGURES

CHAPTER 1 INTR
1.1 Composite
1.2 CFT Mome
1.3 Relevant Pr
1.3.1 Previ
1.3.2 Previ
1.4 High Stren
1.5 Research O
1.5.1 Resea
1.5.2 Previ
1.5.3 Resea
1.6 Dissertation

CHAPTER 2 PR
2.1 FIBER
2.1.1 Fi
2.2 FIBER-
2.2.1 Ja
2.2.2 U
2.2.3 Comp
2.3 Experime
2.3.1 Fi
2.3.2 Sp

TABLE OF CONTENTS

ACKNOWLEDGMENT iv

TABLE OF CONTENTS v

LIST OF TABLES xiii

LIST OF FIGURES xvi

CHAPTER 1 INTRODUCTION 1

1.1 Composite Structures 1

1.2 CFT Moment Resisting Frames 1

1.3 Relevant Previous Research 2

1.3.1 Previous Research on CFT Columns and Connections 2

1.3.2 Previous Research on CFT Moment Resisting Frames 3

1.4 High Strength CFT Moment Resisting Frames 4

1.5 Research Objectives, Significance and Scope 5

1.5.1 Research Goal and Research Objectives 5

1.5.2 Previous Research Significance 5

1.5.3 Research Scope 6

1.6 Dissertation Outline 6

CHAPTER 2 PREVIOUS RESEARCH AND BACKGROUND 9

2.1 FIBER ELEMENT IN DRAIN-2DX 10

2.1.1 Fiber σ–ε Relationships 12

2.2 FIBER-BASED MODELS FOR CFT BEAM-COLUMNS 15

2. 2.1 Japanese Model for CFT Beam-Columns 16

2.2.2 U.S. Model for CFT Beam-Columns 22

2.2.3 Comparison of U.S. and Japanese Models 25

2.3 Experimental and Analytical Researches on Double Split-Tee Connections .27

2.3.1 Full-scale Inelastic Cyclic Test of Split-tee Connections 28

2.3.2 Steel Beam to Steel Column T-stub Connections 29

2.3.3 Su
2.4 Experim
2.4.1 Ex
2.4.2 An
2.4.3 Su
2.5 Pushove
2.5.1 Pu
2.5
2.5
2.5.2 Ad
2.5
2.5
2.5
2.5
2.5.3 Sur
2.6 Time-Hi
2.6.1 Gr
2.6.2 Sca
2.6.3 Dy
2.6
2.6
2.6.4 Dyn
2.6
2.6.5 Sum
2.7 Summary
2.7.1 Anal
2.7.2 Anal
2.7.3 Evalu
2.7.4 Sum

2.3.3 Summary 29
2.4 Experimental and Analytical Researches on Steel Beams 30
2.4.1 Experimental Researches on Steel Beams 30
2.4.2 Analytical Model of Steel Beams 31
2.4.3 Summary 32
2.5 Pushover Analysis of Moment Resisting Frames 34
2.5.1 Pushover Analysis of Steel Moment Resisting Frames 34
2.5.1.1 Analytical Model for Postensioned Connections 34
2.5.1.2 Summary 36
2.5.2 Adaptive Spectra-Based Pushover Procedure 37
2.5.2.1 FEMA and Adaptive Pushover Spectra-Based Procedures 37
2.5.2.2. Validation of Adaptive Spectra-Based Pushover Procedure . 39
2.5.2.3 Moment Frame Structures with Stiffness Discontinuity 41
2.5.2.4 Effects of Higher Modes 42
2.5.3 Summary 42
2.6 Time-History Analysis of Moment Resisting Frames 43
2.6.1 Ground motion Time Histories for SAC Phase 2 Steel Project 44
2.6.2 Scaling of Time Histories to Target Spectra 45
2.6.3 Dynamic *P-Δ* Effects for Flexible Inelastic Steel Structures 46
2.6.3.1 Case Study 1: Los Angeles 20-Story Structure 47
2.6.3.1.1 Static Response of Model M1 47
2.6.3.1.2 Dynamic Response of Model M1 49
2.6.3.1.3 Static and Dynamic Response of Improved Models 49
2.6.3.2 Case Study 2: Seattle 3-Story Structure 52
2.6.4 Dynamic Higher Mode Effects for Flexible Steel Structures 54
2.6.4.1 Variation of the Ratio of Story Drift to Roof Drift over Height 54
2.6.5 Summary 56
2.7 Summary of Literature Review 57
2.7.1 Analytical Models for Individual Components 57
2.7.2 Analytical Models for CFT MRFs 58
2.7.3 Evaluation Methods for Seismic Performance of CFT MRFs 59
2.7.4 Summary 60

CHAPTER 3 A
R
3.1 Analy
3.1.1 I
3.1.2
3.1.3 S
3.1.4 C
3.1.5 V
3.2 Analy
3.2.1 I
3
3
3
3.2.2 V
3.2.3 S
3.3 Analy
3.3.1 I
3
3
3
3.3.2 V
3.3.3 Su
3.4 Analytic
3.4.1 De
3.4.2 M
3.4.3 Va
3.4.4 Su
CHAPTER 4 DI
4.1 Seismic I
4.1.1 Sei
4.1.2 Sei

CHAPTER 3 ANALYTICAL MODELS FOR COMPONENTS OF CFT MOMENT RESISTING FRAMES 86
3.1 Analytical Model for CFT Beam-Columns 87
3.1.1 Fiber σ–ε Relationships for CFTs 90
3.1.2 Approach for Developing Fiber σ–ε Curves in Compression 90
3.1.3 Steel Fiber σ–ε Curves in Compression 93
3.1.4 Concrete Fiber σ–ε Relationships in Compression 97
3.1.5 Validation of CFT Analytical Models 102
3.2 Analytical Model for Steel Beams 106
3.2.1 FEM Models of Steel Beams 107
3.2.1.1 Elements Used and Material Models 108
3.2.1.2 Geometric Imperfections 109
3.2.1.3 FEM-Based Effective Stress-Strain Curves 110
3.2.2 Validation of Analytical Model of Steel Beams 112
3.2.3 Summary 113
3.3 Analytical Model for Double Split-Tee Connections 113
3.3.1 FEM Models of DST Connections 114
3.3.1.1 Elements Used and Material Models 115
3.3.1.2 Simulation of Contacts and Pretension 115
3.3.1.3 FEM-Based Force-Displacement Curves of DST Connections 116
3.3.2 Validation of Analytical Model of DST Connections 116
3.3.3 Summary 117
3.4 Analytical Model for DST Connection Subassemblies 117
3.4.1 Description of Model for DST Connection Subassemblies 118
3.4.2 Modeling of CFT Beam-Columns, Steel Beams and Connections 119
3.4.3 Validation of Analytical Model for DST Connection Subassemblies 120
3.4.4 Summary 121

CHAPTER 4 DESIGN AND STATIC PUSHOVER ANALYSIS OF THE CFT MRFS 159
4.1 Seismic Design of High-Strength CFT MRFs 159
4.1.1 Seismic Design Procedures 160
4.1.2 Seismic Designs of high strength CFT MRFs 167

4.2 Model
4.3 Nonlin
4.3.1 F
4
4
4.3.2
4.3.3 S
CHAPTER 5 T
5.1 Groun
5.1.1 F
5.1.2 S
5.2 Time-I
5.2.1 C
5
5
5
5.2.2 C
5
5.2.3 C
5
5.3 Time-I
5.3.1 C
5.3.2 C
5
5.3.3 L
5
5
5.3.4 L
5
5

4.2 Model for CFT Buildings 170
4.3 Nonlinear Static Pushover Analyses 172
4.3.1 FEMA 356 NSP Procedures 173
4.3.1.1 Effects of local degradation on overall static pushover behavior 176
4.3.1.2 Earthquake Resistant Design Coefficients and Factors 180
4.3.2 Adaptive Pushover Procedures 182
4.3.3 Summary 185

CHAPTER 5 TIME-HISTORY ANALYSIS OF THE CFT MRFS 208
5.1 Ground Motion Ensemble 208
5.1.1 Response Spectra 210
5.1.2 Scale Factors of SAC Ground Motion Time-Histories 211
5.2 Time-History Analysis: Global Performance 212
5.2.1 Global Stability and Local Performance Evaluation 212
5.2.1.1 Determination of Level of Confidence 213
5.2.1.2 Global Stability and Local Performance 215
5.2.1.3 Determination of Actions and Deformation 216
5.2.2 Global Performance of Six-Story CFT MRFs 217
5.2.2.1 Confidence Levels for Global Stability 219
5.2.3 Global Performance of Twelve-Story CFT MRFs 220
5.2.3.1 Confidence Levels for Global Stability 222
5.3 Time-History Analysis: Local Performance 223
5.3.1 Confidence Levels for Connection Local Performance 223
5.3.2 Confidence Levels for Column Compression Performance 224
5.3.2.1 CFT Beam-Column Compressive Capacity 225
5.3.3 Local Performance of Six-Story CFT MRFs 228
5.3.3.1 Local Connection Performance 228
5.3.3.2 Local Column Compression Performance 229
5.3.4 Local Performance of Twelve-Story CFT MRFs 231
5.3.4.1 Local Connection Performance 231
5.3.4.2 Local Column Compression Performance 232

5.4 Time-
5.4.1
5.4.2
5.4.3
5.5 Summ
CHAPTER 6 SU
FU
6.1 Summary
6.1.1 An
6.1.2 Sel
6.1.3 Non
6.2 Conclusi
6.3 Recomme
PPENDIX: DE
A.1 T-stub Se
A.1.1 Req
A.1.2 Sele
A.1.3 T-
A.2 T-stub Cat
A.2.1 Ge

5.4 Time-History Analysis: Higher Mode and P-Δ Effects 234
5.4.1 Pushover Analysis Results: P-Δ Effects 236
5.4.2 Higher Mode and P-Δ Effects of Six-Story CFT MRF 237
5.4.2.1 Six-Story CFT MRF Subjected to SAC 2/50 ground motions 238
5.4.2.2 Six-Story CFT MRF Subjected to SAC 10/50 ground motions 240
5.4.2.3 Six-Story CFT MRF Subjected to SAC 50/50 ground motions 241
5.4.3 Higher Mode and P-Δ Effects of Twelve-Story CFT MRF 244
5.4.3.1 Twelve-Story CFT MRF Subjected to SAC 2/50 ground motions 245
5.4.3.2 Twelve -Story CFT MRF Subjected to SAC 10/50 ground motions 246
5.4.3.3 Twelve -Story CFT MRF Subjected to SAC 50/50 ground motions 247
5.5 Summary and Conclusion 249

CHAPTER 6 SUMMARY, CONCLUSIONS, AND RECOMMENDATIONS FOR FUTURE WORK 319
6.1 Summary 319
6.1.1 Analytical Models for CFT MRFs 320
6.1.2 Seismic Design and Pushover Analyses of CFT MRFs 323
6.1.3 Nonlinear Time-history Analyses of CFT MRFs 325
6.2 Conclusions 331
6.3 Recommendations for Future Work 335

APPENDIX: DESIGN OF DOUBLE SPLIT-TEE CONNECTIONS 336
A.1 T-stub Section Selection 336
A.1.1 Required Shear Strength (Flange Force) 336
A.1.2 Selection of Size and Grade for Tension Bolts 336
A.1.3 T-stub Section Selection 337
A.2 T-stub Capacity Check 343
A.2.1 Geometry for Prying Forces and Bending of T-section Flanges 343

A.2.2 Flan
A.2.3 Stem
A.2.4 Check
A.2.5 Check
A.3 Fillet Weld
A.4 Summary ..

REFERENCE.....

A.2.2 Flange Capacity Check 343
A.2.3 Stem Capacity Check 345
A.2.4 Check $t_{s,max}$ to Ensure a Balanced T-stub Failure 345
A.2.5 Check net Stem Section for Shear Capacity 346
A.3 Fillet Welds between T-Stem and Beam Flange 347
A.4 Summary 348

REFERENCE 359

Table 3.1 Idealize

Table 4.1 Dead Lo
Table 4.2 Gravity L
Table 4.3 Basic win
classific
Table 4.4 Wind loa
.....
Table 4.5 Design co
Table 4.6 Equivalen
.....
Table 4.7 Static push
design co

Table 5.1 SAC 2% in
Table 5.2 SAC 10% i
Table 5.3 SAC 50% in
Table 5.4 FEMA 350 r
Table 5.5 FEMA 350
regular SM
Table 5.6 FEMA 350 re
factor ϕ for I
connection
Table 5.7 Global perform
immediate oc

LIST OF TABLES

Table 3.1 Idealized flange and web fiber σ–ε curves of rolled shapes (A992 steel)..... 122

Table 4.1 Dead Loads of Floor 187

Table 4.2 Gravity Loads of Roof and Floor..... 187

Table 4.3 Basic wind speed, exposure category, wind importance factor and enclosure classification 187

Table 4.4 Wind loads at each floor of the six-story perimeter frames in long direction 188

Table 4.5 Design coefficients and factors for seismic-resisting system (CFT MRFs).. 188

Table 4.6 Equivalent lateral seismic force for six-story perimeter frames in long direction 188

Table 4.7 Static pushover analysis results of the six-story and twelve-story CFT MRFs: design coefficients and factors..... 189

Table 5.1 SAC 2% in 50 years time histories (Los Angles, Site Class D) 253

Table 5.2 SAC 10% in 50 years time histories (Los Angles, Site Class D) 253

Table 5.3 SAC 50% in 50 years time histories (Los Angles, Site Class D) 254

Table 5.4 FEMA 350 recommend minimum confidence levels..... 254

Table 5.5 FEMA 350 global inter-story drift angle capacity C and resistance factor ϕ for regular SMF buildings 254

Table 5.6 FEMA 350 inter-story drift angle capacity C (θ_{IO}, θ_{U}) and capacity reduction factor ϕ for Bolted Flange Plate (BFP) and Double Split Tee (DST) connections as limited by local connection response 255

Table 5.7 Global performance evaluation of flexible six-story distributed CFT MRF for immediate occupancy and collapse prevention performance levels..... 255

Table 5.8 Global
for im

Table 5.9 Local p
DS1 c

Table 5.10 Local p
limited

Table 5.11 Local p
for DS1

Table 5.12 Local p
limited b

Table 5.13 The 1st t
twelve-st

Table 5.14 Median r
displacem

Table A.1 Required t

Table A.2 Required b

Table A.3 Minimum c

Table A.4 Minimum s

Table A.5 Minimum t

Table A.6 Minimum ar

Table A.7 Minimum st
thickness of

Table A.8 Selected I-st

Table A.9 Geometries fo

Table A.10 Geometries fo

Table A.11 Design resista
plastic flange m
Piping

Table 5.8 Global performance evaluation of flexible twelve-story distributed CFT MRF for immediate occupancy and collapse prevention performance levels 256

Table 5.9 Local performance evaluation of flexible six-story distributed CFT MRF for DST connections limited by local connection response 256

Table 5.10 Local performance evaluation of flexible six-story distributed CFT MRF limited by column compressive behavior 257

Table 5.11 Local performance evaluation of flexible twelve-story distributed CFT MRF for DST connections limited by local connection response..... 257

Table 5.12 Local performance evaluation of flexible twelve-story distributed CFT MRF limited by column compressive behavior 258

Table 5.13 The 1st to 4th modes properties of the flexible ($1<T_1/T_{max}<1.15$) six-story and twelve-story distributed CFT MRFs 258

Table 5.14 Median ratios of sum of maximum story displacements to maximum roof displacement of CFT MRFs..... 259

Table A.1 Required flange forces of DST connections 350

Table A.2 Required bolt numbers of DST connections..... 350

Table A.3 Minimum distance from the bolt hole to the k-zone..... 350

Table A.4 Minimum stem thickness of T-stubs..... 351

Table A.5 Minimum flange width of T-stubs 351

Table A.6 Minimum and maximum flange thickness..... 351

Table A.7 Minimum stem thickness, required flange width and the range of flange thickness of T-stubs 352

Table A.8 Selected T-stub sections..... 352

Table A.9 Geometries for T-stub flanges 352

Table A.10 Geometries for prying forces and bending of T-section flanges..... 353

Table A.11 Design resistances per bolt of the flanges controlled by the failure modes of plastic flange mechanism and flange yielding governed by bolt fracture due to prying 353

Table A.12 Design
tension
Table A.13 Minim
Table A.14 Actual
Table A.15 Design
Table A.16 Design
and ten
Table A.17 Require
Table A.18 Design
Table A.19 Maximu
DST con
Table A.20 Design st
between T
Table A.21 Required
T-stems ar

Table A.12 Design resistances per bolt of the flanges controlled by the failure modes of tension bolt fracture without the effects of prying 353

Table A.13 Minimum design resistances of the flanges for T-stubs 354

Table A.14 Actual levels of prying in the flanges for T-stubs 354

Table A.15 Design resistances of the stems in net section fracture 354

Table A.16 Design resistances of T-stubs controlled by failure modes of net stem yielding and tension bolt fracture 355

Table A.17 Required shear strengths of DST connections 355

Table A.18 Design shear strengths of net stem sections (at k-zone) 355

Table A.19 Maximum, minimum and effective thicknesses of the fillet welds used in DST connections between T-stems and beam flanges 356

Table A.20 Design strengths per unit length of fillet welds used in DST connections between T-stems and beam flanges 356

Table A.21 Required and actual lengths of fillet welds used in DST connections between T-stems and beam flanges 356

Figure 1.1 Column
Figure 1.2 CFT M
Figure 1.3 Split-Te

Figure 2.1 DRAIN-
Figure 2.2 C-type fi
Figure 2.3 S-type fi
Figure 2.4 Cyclic be
Figure 2.5 Cyclic be
Figure 2.6 Japanese
Figure 2.7 Japanese
Figure 2.8 Japanese
(Kowalko
Figure 2.9 Japanese
Figure 2.10 Japanese
(Kowalko
Figure 2.11 Fiber dis
Figure 2.12 U.S. mode
Figure 2.13 U.S. model
Figure 2.14 U.S. model
Figure 2.15 U.S. model
(Varma et al.

LIST OF FIGURES

Figure 1.1 Columns used in composite construction 8

Figure 1.2 CFT Moment Resisting Frame 8

Figure 1.3 Split-Tee Moment Connections 8

Figure 2.1 DRAIN-2DX Fiber-based beam-column element (Prakash et al. 1993) 62

Figure 2.2 C-type fiber σ–ε relationship (Kurama et al. 1996) 62

Figure 2.3 S-type fiber σ–ε relationship monotonic behavior (Cordero et al. 2002) 62

Figure 2.4 Cyclic behavior of S-type fiber before local buckling (Cordero et al. 2002) 63

Figure 2.5 Cyclic behavior of S-type fiber after local buckling (Cordero et al. 2002) 63

Figure 2.6 Japanese model: Concrete fiber hysteretic behavior (Fujii et al. 1973) 64

Figure 2.7 Japanese model: Steel fiber hysteretic behavior (Meng et al. 1992) 64

Figure 2.8 Japanese model: Example concrete fiber σ–ε curves in compression (Kowalkowski and Varma 2003) 64

Figure 2.9 Japanese model: Steel fiber σ–ε curves in compression (Sakino et al. 2004) 65

Figure 2.10 Japanese model: Example steel fiber σ–ε curves in compression (Kowalkowski and Varma 2003) 65

Figure 2.11 Fiber discretization of CFT cross-section (Varma et al. 2001) 66

Figure 2.12 U.S. model: 3D Finite element model of CFT segment (Varma et al. 2001) 66

Figure 2.13 U.S. model: Geometric imperfection for steel tube walls (Varma et al. 2001) 66

Figure 2.14 U.S. model: Transverse and longitudinal interaction (Varma et al. 2001) 67

Figure 2.15 U.S. model: End section A of CFT model and cross-section components (Varma et al. 2001) 67

Figure 2.16 U.S
streng
Figure 2.17 U.S.
high s
Figure 2.18 Comp
f'_c=17
2003)
Figure 2.19 Comp
f'_c=16
2003)
Figure 2.20 Conne
Figure 2.21 Connec
Figure 2.22 Connec
Figure 2.23 Full-sc
compone
Figure 2.24 T-stub c
Figure 2.25 T-stub c
Figure 2.26 Spring m
Figure 2.27 Spring m
Figure 2.28 Predicted
1999)
Figure 2.29 Experime
Figure 2.30 Typical se
Figure 2.31 Experimen
Figure 2.32 Sections of
Figure 2.33 Full depth
Figure 2.34 Full depth w

Figure 2.16 U.S. model: Example effective steel fiber σ–ε curves in compression for high strength CFTs (Varma et al. 2001) 68

Figure 2.17 U.S. model: Example effective concrete fiber σ–ε curves in compression for high strength CFTs (f'_c=16ksi, σ_y=80ksi) 68

Figure 2.18 Comparisons of experimental and analytical M-ϕ responses for CFTs with f'_c=17 ksi, b/t=32, σ_y=45 ksi or 113 ksi, P/P_o=40% (Kowalkowski and Varma 2003) 69

Figure 2.19 Comparisons of experimental and analytical M-ϕ responses for CFTs with f'_c=16 ksi, b/t=32, σ_y=39 ksi or 87 ksi, P/P_o=40% (Kowalkowski and Varma 2003) 69

Figure 2.20 Connection test setup (Ricles et al., 2004) 70

Figure 2.21 Connection details, Spec. 4 and 5 (Ricles et al., 2004) 70

Figure 2.22 Connection details, Spec. 6 and 7 (Ricles et al., 2004) 71

Figure 2.23 Full-scale inelastic cyclic test of split-Tee connections: contribution of components to story drift, Spec. 6 (Peng, 2000) 71

Figure 2.24 T-stub connection test: component test frame (Swanson, 1999) 72

Figure 2.25 T-stub connection test: instrumentation scheme (Swanson, 1999) 72

Figure 2.26 Spring model for a T-stub connection (Swanson, 1999) 73

Figure 2.27 Spring model of an individual T-stub (Swanson, 1999) 73

Figure 2.28 Predicted and experimental total deformation for T-stub TA-05 (Swanson, 1999) 73

Figure 2.29 Experiment setup for 3-point flexural test specimens (Green, 2000) 74

Figure 2.30 Typical sections of flexural test specimens (Green, 2000) 74

Figure 2.31 Experiment setup for 3-point cyclic test specimens (Green, 2000) 74

Figure 2.32 Sections of cyclic test specimens (Green, 2000) 75

Figure 2.33 Full depth web imperfection for h_c/t_w=53 used in FEM model (Green, 2000) 75

Figure 2.34 Full depth web imperfection for h_c/t_w=29 used in FEM model (Green, 2000) 75

Figure 2.35 Full v
.....
Figure 2.36 FEM
flange
Figure 2.37 Analy
Spec. 3
Figure 2.38 Momer
Posttens
Figure 2.39 Fiber e
stress-st
al., 2001
Figure 2.40 Analytic
Figure 2.41 Lateral
al., 2001
Figure 2.42 Typical
Kunnath,
Figure 2.43 Inter-stor
(Gupta an
Figure 2.44 Drift prof
Kunnath, 2
Figure 2.45 Effect of
pushover n
Figure 2.46 Floor plan
Krawinkler,
Figure 2.47 Global pus
without P-D
Figure 2.48 Story pusho
Angeles (LA
Figure 2.49 Global pus
Angeles (LA
Figure 2.50 Story drift en
LA36) record (

Figure 2.35 Full width flange imperfection for $b_f/2t_f=9$ used in FEM model (Green, 2000) 76

Figure 2.36 FEM analysis results for Test Specimen 3: local buckling of compression flange and web (Green, 2000) 76

Figure 2.37 Analytical and experimental moment-average end rotation results of Test Spec. 3, using two different element type S4 and S8R5 (Green, 2000) 76

Figure 2.38 Moment connections: (a) pre-Northridge welded connection; (b) Posttensioned connection (Ricles et al., 2001) 77

Figure 2.39 Fiber element: (a) element, segments, and fibers; (b) compression-only fiber stress-strain relationship; (c) typical fiber stress-strain relationship (Ricles et al., 2001) 77

Figure 2.40 Analytical model for postensioned connection (Ricles et al., 2001) 78

Figure 2.41 Lateral load–displacement behavior of postensioned connections (Ricles et al., 2001) 78

Figure 2.42 Typical plan of prototype structure used in evaluation study (Gupta and Kunnath, 2000) 79

Figure 2.43 Inter-story drift profiles for various frames for selected ground motions (Gupta and Kunnath, 2000) 79

Figure 2.44 Drift profiles for typical structures with "soft" first story (Gupta and Kunnath, 2000) 80

Figure 2.45 Effect of number of modes on drift profile for adaptive spectra-based pushover method (Gupta and Kunnath, 2000) 80

Figure 2.46 Floor plans and elevations of 3- and 20-story buildings (Gupta and Krawinkler, 2000a) 81

Figure 2.47 Global pushover curves of 20-story building Los Angeles (LA) with and without P-Delta (Gupta and Krawinkler, 2000a) 81

Figure 2.48 Story pushover curves for lower eight sotries of 20-story structure in Los Angeles (LA) with P-Delta (Gupta and Krawinkler, 2000a) 82

Figure 2.49 Global pushover curves for various models of 20-story building in Los Angeles (LA) (Gupta and Krawinkler, 2000a) 82

Figure 2.50 Story drift envelopes for various models of 20-story building in Los Angeles, LA30 record (Gupta and Krawinkler, 2000a) 83

Figure 2.51 Story
LA36

Figure 2.52 Glob
(Gupta

Figure 2.53 Roof t
record

Figure 2.54 Plan vi
.....

Figure 2.55 Variatio
drift ang

Figure 3.1 Fiber disc

Figure 3.2 Effective
(f_c = 4ksi

Figure 3.3 Effective
(f_c = 5ksi

Figure 3.4 Effective σ
(f_c = 10ksi

Figure 3.5 Effective σ
steel tubes a

Figure 3.6 Idealized effe
CFTs (f_c = 4

Figure 3.7 Idealized effe
CFTs (f_c = 5

Figure 3.8 Idealized effe
CFTs (f_c = 10

Figure 3.9 Idealized effe
σ_y = 46ksi, b_1

Figure 3.10 Idealized effe
(σ_y = 46ksi)....

Figure 2.51 Story drift envelopes for various models of 20-story building in Los Angeles, LA36 record (Gupta and Krawinkler, 2000a) 83

Figure 2.52 Global pushover curves for various models of 3-story building in Seattle (Gupta and Krawinkler, 2000a) 84

Figure 2.53 Roof time histories for various models of 3-story building in Seattle, SE27 record (Gupta and Krawinkler, 2000a) 84

Figure 2.54 Plan views and elevations of model buildings (Gupta and Krawinkler, 2000b) 85

Figure 2.55 Variation over height of median values of ratio of story drift angle to roof drift angle of 20-story structures (Gupta and Krawinkler, 2000b) 85

Figure 3.1 Fiber discretization of CFT cross-section 123

Figure 3.2 Effective σ–ε curves for steel tube walls of conventional strength CFTs (f'_c=4ksi, σ_y=46ksi) 123

Figure 3.3 Effective σ–ε curves for steel tube walls of conventional strength CFTs (f'_c=8ksi, σ_y=46ksi) 123

Figure 3.4 Effective σ–ε curves for steel tube walls of conventional strength CFTs (f'_c=10ksi, σ_y=46ksi) 124

Figure 3.5 Effective σ–ε curves for steel tube walls of CFTs with conventional strength steel tubes and high strength concrete infills (f'_c=16ksi, σ_y=46ksi) 124

Figure 3.6 Idealized effective σ–ε curves for steel tube walls of conventional strength CFTs (f'_c=4ksi, σ_y=46ksi, b/t=24, 64) 124

Figure 3.7 Idealized effective σ–ε curves for steel tube walls of conventional strength CFTs (f'_c=8ksi, σ_y=46ksi, b/t=24, 64) 125

Figure 3.8 Idealized effective σ–ε curves for steel tube walls of conventional strength CFTs (f'_c=10ksi, σ_y=46ksi, b/t=24, 64) 125

Figure 3.9 Idealized effective σ–ε curves for high strength steel tube walls (f'_c=16ksi, σ_y=46ksi, b/t=24, 64) 125

Figure 3.10 Idealized effective σ–ε curves for conventional strength steel tube walls (σ_y=46ksi) 126

Figure 3.11 Effec
tubes a
Figure 3.12 Effec
tubes a
Figure 3.13 Effect
tubes a
Figure 3.14 Effectiv
σ_y
Figure 3.15 Idealize
σ_y
Figure 3.16 Idealize
σ_y
Figure 3.17 Idealize
σ_y
Figure 3.18 Idealize
$(f_y$
Figure 3.19 Idealize
.....
Figure 3.20 Effectiv
$(f_y$
Figure 3.21 Effectiv
$(f_y$
Figure 3.22 Effectiv
$(f_y$
Figure 3.23 Effectiv
tubes a
Figure 3.24 Effectiv
tubes a

Figure 3.11 Effective σ–ε curves for steel tube walls of CFTs with high strength steel tubes and conventional strength concrete infills (f'_c=4ksi, σ_y=80ksi)..... 126

Figure 3.12 Effective σ–ε curves for steel tube walls of CFTs with high strength steel tubes and conventional strength concrete infills (f'_c=8ksi, σ_y=80ksi)..... 126

Figure 3.13 Effective σ–ε curves for steel tube walls of CFTs with high strength steel tubes and conventional strength concrete infills (f'_c=10ksi, σ_y=80ksi)..... 127

Figure 3.14 Effective σ–ε curves for steel tube walls of high strength CFTs (f'_c=16ksi, σ_y=80ksi)..... 127

Figure 3.15 Idealized effective σ–ε curves for high strength steel tube walls (f'_c=4ksi, σ_y=80ksi, b/t=24, 64)..... 127

Figure 3.16 Idealized effective σ–ε curves for high strength steel tube walls (f'_c=8ksi, σ_y=80ksi, b/t=24, 64)..... 128

Figure 3.17 Idealized effective σ–ε curves for high strength steel tube walls (f'_c=10ksi, σ_y=80ksi, b/t=24, 64)..... 128

Figure 3.18 Idealized effective σ–ε curves for steel tube walls of high strength CFTs (f'_c=16ksi, σ_y=80ksi, b/t=24, 64)..... 128

Figure 3.19 Idealized effective σ–ε curves for high strength steel tube walls (σ_y=80ksi)..... 129

Figure 3.20 Effective σ–ε curves for concrete infills of conventional strength CFTs (f'_c=4ksi, σ_y=46ksi)..... 129

Figure 3.21 Effective σ–ε curves for concrete infills of conventional strength CFTs (f'_c=8ksi, σ_y=46ksi)..... 129

Figure 3.22 Effective σ–ε curves for concrete infills of conventional strength CFTs (f'_c=10ksi, σ_y=46ksi)..... 130

Figure 3.23 Effective σ–ε curves for concrete infills of CFTs with high strength steel tubes and conventional strength concrete infills (f'_c=4ksi, σ_y=80ksi)..... 130

Figure 3.24 Effective σ–ε curves for concrete infills of CFTs with high strength steel tubes and conventional strength concrete infills (f'_c=8ksi, σ_y=80ksi)..... 130

Figure 3.25 Effec
tubes
Figure 3.26 Norm
CFTs
Figure 3.27 Norm
CFTs
Figure 3.28 Idealiz
($f_c \leq 10k$
Figure 3.29 Effectiv
steel tub
Figure 3.30 Effectiv
σ_y 50ksi
Figure 3.31 Normali
$\sigma_y = 40ksi$
Figure 3.32 Normaliz
$\sigma_y = 50ksi$
Figure 3.33 Normaliz
Figure 3.34 Comparis
f_c=41 MP
Figure 3.35 Comparison
f_c=41 MPa
Figure 3.36 Comparison
b/t=34)
Figure 3.37 Comparison
f_c=41 MPa
Figure 3.38 Comparison
f_c=41 MPa
Figure 3.39 Comparison
b/t=23)

Figure 3.25 Effective σ–ε curves for concrete infills of CFTs with high strength steel tubes and conventional strength concrete infills (f'_c=10ksi, σ_y=80ksi)..... 131

Figure 3.26 Normalized effective σ–ε curves for concrete infills of conventional strength CFTs (f'_c=4ksi, σ_y=46ksi, b/t=24) 131

Figure 3.27 Normalized effective σ–ε curves for concrete infills of conventional strength CFTs (f'_c=4ksi, σ_y=46ksi, b/t=64) 131

Figure 3.28 Idealized effective σ–ε curves for conventional strength concrete infills ($f'_c \leq$10ksi) 132

Figure 3.29 Effective σ–ε curves for concrete infills of CFTs with conventional strength steel tubes and high strength concrete infills (f'_c=16ksi, σ_y=46ksi)..... 132

Figure 3.30 Effective σ–ε curves for concrete infills of high strength CFTs (f'_c=16ksi, σ_y=80ksi) 132

Figure 3.31 Normalized effective σ–ε curves for high strength concrete infills (f'_c=16ksi, σ_y=46ksi, b/t=24, 32, 48, 64) 133

Figure 3.32 Normalized effective σ–ε curves for high strength concrete infills (f'_c=16ksi, σ_y=80ksi, b/t=24, 32, 48 64) 133

Figure 3.33 Normalized effective σ–ε curves for concrete infills of CFTs (f'_c>10ksi) 133

Figure 3.34 Comparison of steel fiber stress-strain relationships (σ_y=262MPa, f'_c=41.1MPa, b/t=34)..... 134

Figure 3.35 Comparison of concrete fiber stress-strain relationships (σ_y=262MPa, f'_c=41.1MPa, b/t=34)..... 134

Figure 3.36 Comparison of moment-curvature relationships (σ_y=262MPa, f'_c=41.1MPa, b/t=34) 134

Figure 3.37 Comparison of steel fiber stress-strain relationships (σ_y=618MPa, f'_c=41.1MPa, b/t=23)..... 135

Figure 3.38 Comparison of concrete fiber stress-strain relationships (σ_y=618MPa, f'_c=41.1MPa, b/t=23)..... 135

Figure 3.39 Comparison of moment-curvature relationships (σ_y=618MPa, f'_c=41.1MPa, b/t=23) 135

Figure 3.40 Comp
f_c=
Figure 3.41 Comp
f_c=
Figure 3.42 Comp
h (
Figure 3.43 Compa
f_c=
Figure 3.44 Compa
f_c=
Figure 3.45 Compa
h (
Figure 3.46 Compa
f_c=
Figure 3.47 Compa
f_c=
Figure 3.48 Compa
h (
Figure 3.49 Compa
f_c=
Figure 3.50 Compa
f_c=
Figure 3.51 Compa
h (
Figure 3.52 Compa
f_c=
Figure 3.53 Compa
f_c=
Figure 3.54 Compa
h (

Figure 3.40 Comparison of steel fiber stress-strain relationships (σ_y=*835MPa*, f'_c=*77.0MPa*, *b/t=27*)..... 136

Figure 3.41 Comparison of steel fiber stress-strain relationships (σ_y=*835MPa*, f'_c=*77.0MPa*, *b/t=27*)..... 136

Figure 3.42 Comparison of moment-curvature relationships (σ_y=*835MPa*, f'_c=*77.0MPa*, *b/t=27*)..... 136

Figure 3.43 Comparison of steel fiber stress-strain relationships (σ_y=*262MPa*, f'_c=*80.3MPa*, *b/t=49*)..... 137

Figure 3.44 Comparison of concrete fiber stress-strain relationships (σ_y=*262MPa*, f'_c=*80.3MPa*, *b/t=49*)..... 137

Figure 3.45 Comparison of moment-curvature relationships (σ_y=*262MPa*, f'_c=*80.3MPa*, *b/t=49*)..... 137

Figure 3.46 Comparison of steel fiber stress-strain relationships (σ_y=*618MPa*, f'_c=*25.4MPa*, *b/t=33*)..... 138

Figure 3.47 Comparison of concrete fiber stress-strain relationships (σ_y=*618MPa*, f'_c=*25.4MPa*, *b/t=33*)..... 138

Figure 3.48 Comparison of moment-curvature relationships (σ_y=*618MPa*, f'_c=*25.4MPa*, *b/t=33*)..... 138

Figure 3.49 Comparison of steel fiber stress-strain relationships (σ_y=*835MPa*, f'_c=*25.4MPa*, *b/t=27*)..... 139

Figure 3.50 Comparison of concrete fiber stress-strain relationships (σ_y=*835MPa*, f'_c=*25.4MPa*, *b/t=27*)..... 139

Figure 3.51 Comparison of moment-curvature relationships (σ_y=*835MPa*, f'_c=*25.4MPa*, *b/t=27*)..... 139

Figure 3.52 Comparison of steel fiber stress-strain relationships (σ_y=*835MPa*, f'_c=*40.5MPa*, *b/t=41*)..... 140

Figure 3.53 Comparison of concrete fiber stress-strain relationships (σ_y=*835MPa*, f'_c=*40.5MPa*, *b/t=41*)..... 140

Figure 3.54 Comparison of moment-curvature relationships (σ_y=*835MPa*, f'_c=*40.5MPa*, *b/t=41*)..... 140

Figure 3.55 Com
f_c=41

Figure 3.56 Comp
f_c=41

Figure 3.57 Comp
b_1=5

Figure 3.58 Compa
f_c=41

Figure 3.59 Compar
f_c=41

Figure 3.60 Compari
b_1=7

Fig 3.61 FEM model
compress

Fig 3.62 Idealized str

Fig 3.63 Idealized str

Fig 3.64 Geometric in

Fig 3.65 Stress-Strain

Fig 3.66 Stress-Strain

Fig 3.67 Stress-Strain

Fig 3.68 Stress-Strain

Fig 3.69 Stress-Strain

Fig 3.70 Flange and we

Fig 3.71 Flange and we

Fig 3.72 Flange and we

Fig 3.73 Flange and we

Fig 3.74 Flange and we

Figure 3.55 Comparison of steel fiber stress-strain relationships (σ_y=*618MPa*, f'_c=*41.1MPa*, *b/t=50*) 141

Figure 3.56 Comparison of concrete fiber stress-strain relationships (σ_y=*618MPa*, f'_c=*41.1MPa*, *b/t=50*) 141

Figure 3.57 Comparison of moment-curvature relationships (σ_y=*618MPa*, f'_c=*41.1MPa*, *b/t=50*) 141

Figure 3.58 Comparison of steel fiber stress-strain relationships (σ_y=*262MPa*, f'_c=*41.1MPa*, *b/t=74*) 142

Figure 3.59 Comparison of concrete fiber stress-strain relationships (σ_y=*262MPa*, f'_c=*41.1MPa*, *b/t=74*) 142

Figure 3.60 Comparison of moment-curvature relationships (σ_y=*262MPa*, f'_c=*41.1MPa*, *b/t=74*) 142

Fig. 3.61 FEM model for determining fiber stress-strain curves of steel beam in compression 143

Fig. 3.62 Idealized stress-strain curve for A36 steel (Green's Test 11) 143

Fig. 3.63 Idealized stress-strain curve for A992 steel (Green's Test 10&12) 143

Fig. 3.64 Geometric imperfection for web of steel beam 144

Fig. 3.65 Stress-Strain Relationship of Flange Fibers (Green's Test 10) 144

Fig. 3.66 Stress-Strain Relationship of Web Fibers, Layer 1 (Green's Test 10) 144

Fig. 3.67 Stress-Strain Relationship of Web Fibers, Layer 2 (Green's Test 10) 145

Fig. 3.68 Stress-Strain Relationship of Web Fibers, Layer 3 (Green's Test 10) 145

Fig. 3.69 Stress-Strain Relationship of Web Fibers, Layer 4 (Green's Test 10) 145

Fig. 3.70 Flange and web fiber σ–ε curves for W36x135 rolled shape 146

Fig. 3.71 Flange and web fiber σ–ε curves for W33x118 rolled shape 146

Fig. 3.72 Flange and web fiber σ–ε curves for W30x108 rolled shape 146

Fig. 3.73 Flange and web fiber σ–ε curves for W27x84 rolled shape 147

Fig. 3.74 Flange and web fiber σ–ε curves for W24x62 rolled shape 147

Fig. 3.75 Ideali
Fig. 3.76 Fiber-
Fig. 3.77 Experi .....
Fig. 3.78 Experi .....
Fig. 3.79 Experi .....
Fig. 3.80 Experi .....
Fig. 3.81 Experi .....
Fig. 3.82 Experi .....
Figure 3.83 Double
Figure 3.84 FEM M
Figure 3.85 True str
(Swanson
Figure 3.86 True st
(Swanson
Figure 3.87 FEM-pre
Fig. 3.88 DRAIN-2D
Fig. 3.89 True stress-t
flange (Pen
Fig. 3.90 True stress-t
web (Peng's
Fig. 3.91 True stress-t
steel tube (Pe
Fig. 3.92 True stress-true
structural tee (

Fig. 3.75 Idealized flange and web fiber σ–ε curve for rolled shape 147

Fig. 3.76 Fiber-based Model for the Inelastic Failure Segment of Steel Beam..... 148

Fig. 3.77 Experimental and FEM analysis M-θ response (Specimen 11, Green et al 2000) 148

Fig. 3.78 Experimental and fiber analysis M-θ response (Specimen 11, Green et al 2000) 148

Fig. 3.79 Experimental and FEM analysis M-θ response (Specimen 10, Green et al 2000) 149

Fig. 3.80 Experimental and fiber analysis M-θ response (Specimen 10, Green et al 2000) 149

Fig. 3.81 Experimental and FEM analysis M-θ response (Specimen 12, Green et al 2000) 149

Fig. 3.82 Experimental and fiber analysis M-θ response (Specimen 12, Green et al 2000) 150

Figure 3.83 Double Split-Tee Moment Connections..... 150

Figure 3.84 FEM Model for DST Connection (Swanson's Test: Specimen TA-05) 151

Figure 3.85 True stress-logarithmic plastic strain relationship of T-stub base material (Swanson's Test: Specimen TA-05) 151

Figure 3.86 True stress- logarithmic plastic strain relationship of bolt material (Swanson's Test: Specimen TA-05) 152

Figure 3.87 FEM-predicted and Experimental Total Deformation for T-stub (TA-05) 152

Fig. 3.88 DRAIN-2DX Double Split-Tee connection subassembly model..... 153

Fig. 3.89 True stress-true plastic strain relationship of tensile coupon test -A36, beam flange (Peng's Specimen 5, 6 & 7) 154

Fig. 3.90 True stress-true plastic strain relationship of tensile coupon test -A36, beam web (Peng's Specimen 5, 6 & 7) 154

Fig. 3.91 True stress-true plastic strain relationship of tensile coupon test –A500, Gr. B, steel tube (Peng's Specimen 5, 6 & 7)..... 154

Fig. 3.92 True stress-true plastic strain relationship of tensile coupon test –A572, Gr. 50, structural tee (Peng's Specimen 5, 6 & 7) 155

Fig. 3.93 Stress-st

Fig. 3.94 Stress-st

Fig. 3.95 Stress-st
6 & 7)

Fig. 3.96 Stress-st
& 7)...

Fig. 3.97 Force-di
7).....

Fig. 3.98 Force-di
5, 6 &

Fig. 3.99 Comparis
respons

Fig. 3.100 Compari
respons

Fig. 3.101 Compari
respons

Figure 4.1 Typical

Figure 4.2 Structura

Figure 4.3 Structura

Figure 4.4 Typical

Figure 4.5 Design pr

Figure 4.6 Design re

Figure 4.7 Seismic R
CFT MRF

Figure 4.8 Seismic R
story CFT

Figure 4.9 Elevation

Figure 4.10 Elevation

Figure 4.11 Elevation

Fig. 3.93 Stress-strain relationship of concrete infill (Peng's Specimen 5, 6 & 7) 155

Fig. 3.94 Stress-strain relationship of steel tube (Peng's Specimen 5, 6 & 7)..... 155

Fig. 3.95 Stress-strain relationships for flange fibers of steel beams (Peng's Specimen 5, 6 & 7) 156

Fig. 3.96 Stress-strain relationships for web fibers of steel beams (Peng's Specimen 5, 6 & 7) 156

Fig. 3.97 Force-displacement relationships of T-stubs in tension (Peng's Specimen 5, 6 & 7) 156

Fig. 3.98 Force-displacement relationships of T-stubs in compression (Peng's Specimen 5, 6 & 7) 157

Fig. 3.99 Comparison of experimental and fiber analysis of lateral load-displacement response for Peng's Specimen 5 (Peng 2001)..... 157

Fig. 3.100 Comparison of experimental and fiber analysis of lateral load-displacement response for Peng's Specimen 6 (Peng 2001)..... 158

Fig. 3.101 Comparison of experimental and fiber analysis of lateral load-displacement response for Peng's Specimen 7 (Peng 2001)..... 158

Figure 4.1 Typical floor plan of prototype buildings (perimeter frames)..... 190

Figure 4.2 Structural elevation of six-story prototype building..... 190

Figure 4.3 Structural elevation of twelve-story prototype building..... 191

Figure 4.4 Typical floor plan of prototype buildings (distributed frames)..... 191

Figure 4.5 Design procedures of the prototype CFT MRFs 192

Figure 4.6 Design response spectrum for the prototype CFT MRFs..... 192

Figure 4.7 Seismic Response Coefficient-Fundamental Period Relationship for six-story CFT MRFs 193

Figure 4.8 Seismic Response Coefficient-Fundamental Period Relationship for twelve-story CFT MRFs 193

Figure 4.9 Elevation of six-story distributed CFT MRFs ($0.9<T_1/T_{max}<1$)..... 193

Figure 4.10 Elevation of six-story distributed CFT MRFs ($1<T_1/T_{max}<1.15$)..... 194

Figure 4.11 Elevation of six-story distributed CFT MRFs ($T_1/T_{max}>1.15$) 194

Figure 4.12 Elev
Figure 4.13 Elev
Figure 4.14 Elev
Figure 4.15 Elev
Figure 4.16 Elev
Figure 4.17 Streng
Figure 4.18 Streng
Figure 4.19 Model
Figure 4.20 Latera
Figure 4.21 Static
(FEMA
Figure 4.22 Static
MRFs
Figure 4.23 Static
(FEMA
Figure 4.24 Static
MRFs
Figure 4.25 Static
Figure 4.26 Static
Figure 4.27 Static
Figure 4.28 Static
MRFs
Figure 4.29 Static
Figure 4.30 Static
Figure 4.31 Static
MRFs

Figure 4.12 Elevation of six-story perimeter CFT MRF ($0.9<T_I/T_{max}<1$) 194

Figure 4.13 Elevation of twelve-story distributed CFT MRFs ($0.9<T_I/T_{max}<1$) 195

Figure 4.14 Elevation of twelve-story distributed CFT MRFs ($1<T_I/T_{max}<1.15$) 195

Figure 4.15 Elevation of twelve-story distributed CFT MRF ($T_I/T_{max}>1.15$) 196

Figure 4.16 Elevation of twelve-story perimeter CFT MRF ($T_I/T_{max}>1.15$) 196

Figure 4.17 Strength check for 1st and 2nd stories CFTs of six-story perimeter CFT MRFs 197

Figure 4.18 Strength check for *W36x135* girders 197

Figure 4.19 Model of CFT MRF 197

Figure 4.20 Lateral load patterns of six-story distributed CFT MRFs 198

Figure 4.21 Static pushover analysis results of flexible six-story distributed CFT MRFs (FEMA 356 NSP Procedures) 198

Figure 4.22 Static pushover analysis results of flexible twelve-story distributed CFT MRFs (FEMA 356 NSP Procedures) 199

Figure 4.23 Static pushover analysis results of rigid six-story perimeter CFT MRFs (FEMA 356 NSP Procedures) 199

Figure 4.24 Static pushover analysis results of six-story distributed and perimeter CFT MRFs 200

Figure 4.25 Static pushover analysis results of twelve-story distributed CFT MRFs ... 200

Figure 4.26 Static pushover analysis results of rigid six-story distributed CFT MRFs. 201

Figure 4.27 Static pushover analysis results of flexible six-story distributed CFT MRFs 201

Figure 4.28 Static pushover analysis results of highly flexible six-story distributed CFT MRFs 202

Figure 4.29 Static pushover analysis results of rigid six-story perimeter CFT MRFs .. 202

Figure 4.30 Static pushover analysis results of rigid twelve-story distributed CFT MRFs 203

Figure 4.31 Static pushover analysis results of flexible twelve-story distributed CFT MRFs 203

Figure 4.32 Stati
CFT
Figure 4.33 Ideal
MRFs
Figure 4.34 Ideali
CFT M
Figure 4.35 Adapt
MRFs.
Figure 4.36 Adapti
MRFs...
Figure 4.37 Idealiz
CFT MI
Figure 4.38 Idealize
distribut

Figure 5.1 Response
Figure 5.2 Response
1.0, 2.0 a
Figure 5.3 Response
Figure 5.4 Response
Figure 5.5 Response
Figure 5.6 Response
Figure 5.7 Response
Figure 5.8 Response
Figure 5.9 Response
Figure 5.10 Response
Figure 5.11 Response
Figure 5.12 Response
Figure 5.13 Response

Figure 4.32 Static pushover analysis results of highly flexible twelve-story distributed CFT MRFs 204

Figure 4.33 Idealized base shear-roof displacement curve of six-story perimeter CFT MRFs (positive post-yield slope) 204

Figure 4.34 Idealized base shear-roof displacement curve of flexible six-story distributed CFT MRFs (negative post-yield slope) 205

Figure 4.35 Adaptive pushover analysis results of flexible six-story distributed CFT MRFs 205

Figure 4.36 Adaptive pushover analysis results of flexible twelve-story distributed CFT MRFs 206

Figure 4.37 Idealized base shear-roof displacement curve of flexible six-story distributed CFT MRFs (adaptive pushover analysis, 3-mode) 206

Figure 4.38 Idealized base shear-roof displacement curve of flexible twelve-story distributed CFT MRFs (adaptive pushover analysis, 4-mode) 207

Figure 5.1 Response spectra of 2%, 10% and 50% exceedance in 50 years 260

Figure 5.2 Response spectra of 50% in 50 years time-history: *lwhown* (matched at 0.3, 1.0, 2.0 and 4.0 s) 260

Figure 5.3 Response spectra of 2% in 50 years time-history: *lkbjma* and *llplgpc* 260

Figure 5.4 Response spectra of 2% in 50 years time-history: *ltbtab* and *lepst04* 261

Figure 5.5 Response spectra of 2% in 50 years time-history: *lepst10* and *lepst13* 261

Figure 5.6 Response spectra of 2% in 50 years time-history: *lnrrs* and *lpvst03* 261

Figure 5.7 Response spectra of 2% in 50 years time-history: *lnrsylm* and *lpvst06* 262

Figure 5.8 Response spectra of 10% in 50 years time-history: *l40ivir* and *llnbars* 262

Figure 5.9 Response spectra of 10% in 50 years time-history: *livar05* and *livar06* 262

Figure 5.10 Response spectra of 10% in 50 years time-history: *llpgil3* and *llnyerm* 263

Figure 5.11 Response spectra of 10% in 50 years time-history: *lnrrrs* and *lnrnewh* 263

Figure 5.12 Response spectra of 10% in 50 years time-history: *lnrsylm* and *lpsdhsp* ... 263

Figure 5.13 Response spectra of 50% in 50 years time-history: *lclgil2* and *lknhsbf* 264

Figure 5.14 Resp
Figure 5.15 Resp
Figure 5.16 Resp
Figure 5.17 Resp
Figure 5.18 Inter-
Figure 5.19 Story
SAC 2
Figure 5.20 Story
SAC 2
Figure 5.21 Story
SAC 2
Figure 5.22 Maxim
distribut
Figure 5.23 Story d
SAC 10
Figure 5.24 Story dr
SAC 10
Figure 5.25 Story dr
SAC 10
Figure 5.26 Maximu
distribute
Figure 5.27 Story dr
SAC 50 5
Figure 5.28 Story dri
SAC 50 5
Figure 5.29 Story dri
SAC 50 5
Figure 5.30 Maximum
distributed
Figure 5.31 Story drift
to SAC 2 5

Figure 5.14 Response spectra of 50% in 50 years time-history: *livar06* and *llnfrti* 264

Figure 5.15 Response spectra of 50% in 50 years time-history: *lmhgil3* and *lpkcs05* .. 264

Figure 5.16 Response spectra of 50% in 50 years time-history: *lpsplma* and *lpkcs08* .. 265

Figure 5.17 Response spectra of 50% in 50 years time-history: *lsfhsbf* and *lwhdown* .. 265

Figure 5.18 Inter-story drift angle for MRFs as illustrated in FEMA 350 265

Figure 5.19 Story drift envelop of flexible six-story distributed CFT MRF subjected to SAC 2/50 time-histories: *lkbjma, lnrrrs* and *llplgpc* 266

Figure 5.20 Story drift envelop of flexible six-story distributed CFT MRF subjected to SAC 2/50 time-histories: *lnrsylm, ltbtab, lepst04* and *lepst10* 266

Figure 5.21 Story drift envelop of flexible six-story distributed CFT MRF subjected to SAC 2/50 time-histories: *lepst13, lpvst03* and *lpvst06* 266

Figure 5.22 Maximum, minimum and median story drift envelop of flexible six-story distributed CFT MRF subjected to SAC 2/50 time-histories..... 267

Figure 5.23 Story drift envelop of flexible six-story distributed CFT MRF subjected to SAC 10/50 time-histories: *l40ivir, livar05* and *livar06* 267

Figure 5.24 Story drift envelop of flexible six-story distributed CFT MRF subjected to SAC 10/50 time-histories: *llnbars, llnyerm, llpgil3* and *lnrnewh*..... 267

Figure 5.25 Story drift envelop of flexible six-story distributed CFT MRF subjected to SAC 10/50 time-histories: *lnrrrs, lnrsylm* and *lpsdhsp* 268

Figure 5.26 Maximum, minimum and median story drift envelop of flexible six-story distributed CFT MRF subjected to SAC 10/50 time-histories..... 268

Figure 5.27 Story drift envelop of flexible six-story distributed CFT MRF subjected to SAC 50/50 time-histories: *lclgil2, lknhsbf* and *livar06* 268

Figure 5.28 Story drift envelop of flexible six-story distributed CFT MRF subjected to SAC 50/50 time-histories: *lmhgil3, llnfrti, lpkcs05* and *lpkcs08* 269

Figure 5.29 Story drift envelop of flexible six-story distributed CFT MRF subjected to SAC 50/50 time-histories: *lpsplma, lsfhsbf* and *lwhdown* 269

Figure 5.30 Maximum, minimum and median story drift envelop of flexible six-story distributed CFT MRF subjected to SAC 50/50 time-histories..... 269

Figure 5.31 Story drift envelop of flexible twelve-story distributed CFT MRF subjected to SAC 2/50 time-histories: *lkbjma, lnrrrs* and *llplgpc* 270

Figure 5.32 Story
to SA

Figure 5.33 Story
to SAC

Figure 5.34 Maxir
distribu

Figure 5.35 Story
to SAC

Figure 5.36 Story d
to SAC

Figure 5.37 Story d
to SAC

Figure 5.38 Maximu
distribute

Figure 5.39 Story dri
to SAC 5

Figure 5.40 Story dri
to SAC 5

Figure 5.41 Story drift
to SAC 5

Figure 5.42 Maximum
distributed

Figure 5.43 Stress bloc

Figure 5.44 Idealized s
(Nakahara e

Figure 5.45 Interaction
bending and

Figure 5.46a Left corner
subjected to

Figure 5.46b Left corner
subjected to

Figure 5.32 Story drift envelop of flexible twelve-story distributed CFT MRF subjected to SAC 2/50 time-histories: *ltbtab, lepst04, lepst10* and *lepst13* 270

Figure 5.33 Story drift envelop of flexible twelve-story distributed CFT MRF subjected to SAC 2/50 time-histories: *lnrsylm, lpvst03* and *lpvst06* 270

Figure 5.34 Maximum, minimum and median story drift envelop of flexible twelve-story distributed CFT MRF subjected to SAC 2/50 time-histories 271

Figure 5.35 Story drift envelop of flexible twelve-story distributed CFT MRF subjected to SAC 10/50 time-histories: *l40ivir, livar05* and *livar06* 271

Figure 5.36 Story drift envelop of flexible twelve-story distributed CFT MRF subjected to SAC 10/50 time-histories: *llnbars, llnyerm, llpgil3* and *lnrnewh* 271

Figure 5.37 Story drift envelop of flexible twelve-story distributed CFT MRF subjected to SAC 10/50 time-histories: *lnrrrs, lnrsylm* and *lpsdhsp* 272

Figure 5.38 Maximum, minimum and median story drift envelop of flexible twelve-story distributed CFT MRF subjected to SAC 10/50 time-histories 272

Figure 5.39 Story drift envelop of flexible twelve-story distributed CFT MRF subjected to SAC 50/50 time-histories: *lclgil2, lknhsbf* and *livar06* 272

Figure 5.40 Story drift envelop of flexible twelve-story distributed CFT MRF subjected to SAC 50/50 time-histories: *lmhgil3, llnfrti, lpkcs05* and *lpkcs08* 273

Figure 5.41 Story drift envelop of flexible twelve-story distributed CFT MRF subjected to SAC 50/50 time-histories: *lpsplma, lsfhsbf* and *lwhdown* 273

Figure 5.42 Maximum, minimum and median story drift envelop of flexible twelve-story distributed CFT MRF subjected to SAC 50/50 time-histories 273

Figure 5.43 Stress block of MAIJ method (Sakino and Nakahara, 2000) 274

Figure 5.44 Idealized steel stress-strain curves for three different cases of CFT specimens (Nakahara et al., 1998) 274

Figure 5.45 Interaction diagram for nominal CFT beam-column strength in combined bending and axial load 274

Figure 5.46a Left corner column P-M interaction curve of flexible six-story CFT MRF subjected to SAC 2/50 time-history *lpvst03* 275

Figure 5.46b Left corner column M-Φ interaction curve of flexible six-story CFT MRF subjected to SAC 2/50 time-history *lpvst03* 275

Figure 5.47a Inte
subjec

Figure 5.47b Inte
subjec

Figure 5.48a Righ
subjec

Figure 5.48b Righ
subject

Figure 5.49a Left c
subjecte

Figure 5.49b Left c
subjecte

Figure 5.50a Interio
subjected

Figure 5.50b Interior
subjected

Figure 5.51a Right co
subjected

Figure 5.51b Right co
subjected t

Figure 5.52a Left corne
MRF subjec

Figure 5.52b Left corne
MRF subjec

Figure 5.53a Interior co
subjected to

Figure 5.53b Interior co
subjected to

Figure 5.54a Right corne
MRF subjecte

Figure 5.54b Right corne
MRF subjecte

Figure 5.47a Interior column P-M interaction curve of flexible six-story CFT MRF subjected to SAC 2/50 time-history *lpvst03* 275

Figure 5.47b Interior column M-Φ interaction curve of flexible six-story CFT MRF subjected to SAC 2/50 time-history *lpvst03* 276

Figure 5.48a Right corner column P-M interaction curve of flexible six-story CFT MRF subjected to SAC 2/50 time-history *lpvst03* 276

Figure 5.48b Right corner column M-Φ interaction curve of flexible six-story CFT MRF subjected to SAC 2/50 time-history *lpvst03* 276

Figure 5.49a Left corner column P-M interaction curve of flexible six-story CFT MRF subjected to SAC 50/50 time-history *lclgil2* 277

Figure 5.49b Left corner column M-Φ interaction curve of flexible six-story CFT MRF subjected to SAC 50/50 time-history *lclgil2* 277

Figure 5.50a Interior column P-M interaction curve of flexible six-story CFT MRF subjected to SAC 50/50 time-history *lclgil2* 277

Figure 5.50b Interior column M-Φ interaction curve of flexible six-story CFT MRF subjected to SAC 50/50 time-history *lclgil2* 278

Figure 5.51a Right corner column P-M interaction curve of flexible six-story CFT MRF subjected to SAC 50/50 time-history *lclgil2* 278

Figure 5.51b Right corner column M-Φ interaction curve of flexible six-story CFT MRF subjected to SAC 50/50 time-history *lclgil2* 278

Figure 5.52a Left corner column P-M interaction curve of flexible twelve-story CFT MRF subjected to SAC 2/50 time-history *lpvst03* 279

Figure 5.52b Left corner column M-Φ interaction curve of flexible twelve-story CFT MRF subjected to SAC 2/50 time-history *lpvst03* 279

Figure 5.53a Interior column P-M interaction curve of flexible twelve-story CFT MRF subjected to SAC 2/50 time-history *lpvst03* 279

Figure 5.53b Interior column M-Φ interaction curve of flexible twelve-story CFT MRF subjected to SAC 2/50 time-history *lpvst03* 260

Figure 5.54a Right corner column P-M interaction curve of flexible twelve-story CFT MRF subjected to SAC 2/50 time-history *lpvst03* 280

Figure 5.54b Right corner column M-Φ interaction curve of flexible twelve-story CFT MRF subjected to SAC 2/50 time-history *lpvst03* 280

Figure 5.55a Le
MR
Figure 5.55b Le
MR
Figure 5.56a Inte
subje
Figure 5.56b Inte
subje
Figure 5.57a Righ
MRF su
Figure 5.57b Right
MRF su
Figure 5.58 Story p
distribut
Figure 5.59 Story p
distribut
Figure 5.60 Story p
distribut
Figure 5.61 Story p
distribut
Figure 5.62 Story p
distribut
Figure 5.63 Story p
distribut
Figure 5.64 Story d
six-story
Interv
Figure 5.65 Static p
story dist
Figure 5.66 Static p
Bifurca
Figure 5.67 Story dr
SAC 2 5

Figure 5.55a Left corner column P-M interaction curve of flexible twelve-story CFT MRF subjected to SAC 50/50 time-history *lclgil2* 281

Figure 5.55b Left corner column M-Φ interaction curve of flexible twelve-story CFT MRF subjected to SAC 50/50 time-history *lclgil2* 281

Figure 5.56a Interior column P-M interaction curve of flexible twelve-story CFT MRF subjected to SAC 50/50 time-history *lclgil2* 281

Figure 5.56b Interior column M-Φ interaction curve of flexible twelve-story CFT MRF subjected to SAC 50/50 time-history *lclgil2* 282

Figure 5.57a Right corner column P-M interaction curve of flexible twelve-story CFT MRF subjected to SAC 50/50 time-history *lclgil2* 282

Figure 5.57b Right corner column M-Φ interaction curve of flexible twelve-story CFT MRF subjected to SAC 50/50 time-history *lclgil2* 282

Figure 5.58 Story pushover curves for lower three stories of the flexible six-story distributed CFT MRF 283

Figure 5.59 Story pushover curves for upper three stories of the flexible six-story distributed CFT MRF 283

Figure 5.60 Story pushover curves for the 1st to 3rd stories of the flexible twelve-story distributed CFT MRF 283

Figure 5.61 Story pushover curves for the 4th to 6th stories of the flexible twelve-story distributed CFT MRF 284

Figure 5.62 Story pushover curves for the 7th to 9th stories of the flexible twelve-story distributed CFT MRF 284

Figure 5.63 Story pushover curves for the 10th to 12th stories of the flexible twelve-story distributed CFT MRF 284

Figure 5.64 Story drift envelop and story drift angle to roof drift angle ratio of flexible six-story distributed CFT MRF subjected to SAC 2/50 time-histories: *lkbjma, lnrrrs* and *llplgpc* 285

Figure 5.65 Static pushover and time-history analyses (SAC 2/50, *lkbjma*) of flexible six-story distributed CFT MRF 285

Figure 5.66 Static pushover analysis and time-history analyses (SAC 2/50, *lnrrrs* and *llplgpc*) of flexible six-story distributed CFT MRF 286

Figure 5.67 Story drift envelope of flexible six-story distributed CFT MRF subjected to SAC 2/50 time-histories: *lnrsylm, ltbtab, lepst04* and *lepst10* 286

Figure 5.68 Stor
MRI
lepst

Figure 5.69 Stati
libtab

Figure 5.70 Static
lepstI

Figure 5.71 Story
SAC 2

Figure 5.72 Story
MRF

Figure 5.73 Static
lpvar05

Figure 5.74 Static p
story di

Figure 5.75 Story d
six-story
livar05 a

Figure 5.76 Static pu
livar05 a

Figure 5.77 Story dri
six-story d
linbars_lb

Figure 5.78 Static pus
six-story d

Figure 5.79 Static pus
llpgrd3 and

Figure 5.80 Story drift
six-story di
lnrcslm and

Figure 5.81 Static pusho
story distrib

Figure 5.82 Static pushov
lpdispplot fi

Figure 5.68 Story drift angle to roof drift angle ratio of flexible six-story distributed CFT MRF subjected to SAC 2/50 time-histories: *lnrsylm, ltbtab, lepst04* and *lepst10* 287

Figure 5.69 Static pushover analysis and time-history analyses (SAC 2/50, *lnrsylm* and *ltbtab*) of flexible six-story distributed CFT MRF 287

Figure 5.70 Static pushover analysis and time-history analyses (SAC 2/50, *lepst04* and *lepst10*) of flexible six-story distributed CFT MRF 288

Figure 5.71 Story drift envelop of flexible six-story distributed CFT MRF subjected to SAC 2/50 time-histories: *lepst13, lpvst03* and *lpvst06* 288

Figure 5.72 Story drift angle to roof drift angle ratio of flexible six-story distributed CFT MRF subjected to SAC 2/50 time-histories: *lepst13, lpvst03* and *lpvst06* .. 289

Figure 5.73 Static pushover analysis and time-history analyses (SAC 2/50, *lepst13* and *lpvst03*) of flexible six-story distributed CFT MRF 289

Figure 5.74 Static pushover and time-history analyses (SAC 2/50, *lpvst06*) of flexible six-story distributed CFT MRF 290

Figure 5.75 Story drift envelope and story drift angle to roof drift angle ratio of flexible six-story distributed CFT MRF subjected to SAC 10/50 time-histories: *l40ivir, livar05* and *livar06* 290

Figure 5.76 Static pushover analysis and time-history analyses (SAC 10/50, *l40ivir, livar05* and *livar06*) of flexible six-story distributed CFT MRF 291

Figure 5.77 Story drift envelope and story drift angle to roof drift angle ratio of flexible six-story distributed CFT MRF subjected to SAC 10/50 time-histories: *llnbars, llnyerm, llpgil3* and *lnrnewh* 292

Figure 5.78 Static pushover and time-history analyses (SAC 10/50, *llnbars*) of flexible six-story distributed CFT MRF 292

Figure 5.79 Static pushover analysis and time-history analyses (SAC 10/50, *llnyerm, llpgil3* and *lnrnewh*) of flexible six-story distributed CFT MRF 293

Figure 5.80 Story drift envelope and story drift angle to roof drift angle ratio of flexible six-story distributed CFT MRF subjected to SAC 10/50 time-histories: *lnrrrs, lnrsylm* and *lpsdhsp* 294

Figure 5.81 Static pushover and time-history analyses (SAC 10/50, *lnrrrs*) of flexible six-story distributed CFT MRF 294

Figure 5.82 Static pushover analysis and time-history analyses (SAC 10/50, *lnrsylm* and *lpsdhsp*) of flexible six-story distributed CFT MRF 295

Figure 5.83 Stor
SAC
Figure 5.84 Stor
MRF
Figure 5.85 Stati
livar
Figure 5.86 Stati
six-st
Figure 5.87 Story
six-sto
Imbsi
Figure 5.88 Static
Imbsi
Figure 5.89 Static p
six-story
Figure 5.90 Story d
story dis
Ishihy a
Figure 5.91 Static pu
Ishihy an
Figure 5.92 Median s
distributed
Figure 5.93 Maximum
distributed
Figure 5.94 Minimum
distributed
Figure 5.95 Story drift
twelve-story
Ibbima Inrr
Figure 5.96 Static push
twelve-story
Figure 5.97 Static pu-h
Inrrs) of flex

Figure 5.83 Story drift envelope of flexible six-story distributed CFT MRF subjected to SAC 50/50 time-histories: *lnrrrs, lnrsylm* and *lpsdhsp* 295

Figure 5.84 Story drift angle to roof drift angle ratio of flexible six-story distributed CFT MRF subjected to SAC 50/50 time-histories: *lnrrrs, lnrsylm* and *lpsdhsp*.. 296

Figure 5.85 Static pushover analysis and time-history analyses (SAC 50/50, *lclgil2* and *livar06*) of flexible six-story distributed CFT MRF 296

Figure 5.86 Static pushover and time-history analyses (SAC 50/50, *lknhsbf*) of flexible six-story distributed CFT MRF 297

Figure 5.87 Story drift envelope and story drift angle to roof drift angle ratio of flexible six-story distributed CFT MRF subjected to SAC 50/50 time-histories: *lmhgil3, llnfrti, lpkcs05* and *lpkcs08* 297

Figure 5.88 Static pushover analysis and time-history analyses (SAC 50/50, *llnfrti*, *lmhgil3* and *lpkcs05*) of flexible six-story distributed CFT MRF 298

Figure 5.89 Static pushover and time-history analyses (SAC 50/50, *lpkcs08*) of flexible six-story distributed CFT MRF 299

Figure 5.90 Story drift envelope and story drift to roof drift angle ratio of flexible six-story distributed CFT MRF subjected to SAC 50/50 time-histories: *lpsplma, lsfhsbf* and *lwhdown* 299

Figure 5.91 Static pushover analysis and time-history analyses (SAC 50/50, *lpsplma*, *lsfhsbf* and *lwhdown*) of flexible six-story distributed CFT MRF 300

Figure 5.92 Median story drift angle to roof drift angle ratio of flexible six-story distributed CFT MRF subjected to SAC time-histories 301

Figure 5.93 Maximum story drift angle to roof drift angle ratio of flexible six-story distributed CFT MRF subjected to SAC time-histories 301

Figure 5.94 Minimum story drift angle to roof drift angle ratio of flexible six-story distributed CFT MRF subjected to SAC time-histories 301

Figure 5.95 Story drift envelope and story drift angle to roof drift angle ratio of flexible twelve-story distributed CFT MRF subjected to SAC 2/50 time-histories: *lkbjma, lnrrrs* and *llplgpc* 302

Figure 5.96 Static pushover and time-history analyses (SAC 2/50, *lkbjma*) of flexible twelve-story distributed CFT MRF 302

Figure 5.97 Static pushover analysis and time-history analyses (SAC 2/50, *llplgpc* and *lnrrrs*) of flexible twelve-story distributed CFT MRF 303

Figure 5.98 Stor
to S.
Figure 5.99 Stor
CFT
lepst.
Figure 5.100 Stat
lepst
Figure 5.101 Stati
lepst.
Figure 5.102 Story
to SAC
Figure 5.103 Story
CFT M
Figure 5.104 Static
lpvst03
Figure 5.105 Static
twelve-
Figure 5.106 Story
twelve-
l40civir
Figure 5.107 Static
lvar05
Figure 5.108 Story
twelve-
linbar
Figure 5.109 Static
twelve-
Figure 5.110 Static
lpvst3
Figure 5.111 Story
twelve-
inver

Figure 5.98 Story drift envelope of flexible twelve-story distributed CFT MRF subjected to SAC 2/50 time-histories: *ltbtab, lepst04, lepst10* and *lepst13* 303

Figure 5.99 Story drift angle to roof drift angle ratio of flexible twelve-story distributed CFT MRF subjected to SAC 2/50 time-histories: *ltbtab, lepst04, lepst10* and *lepst13* 304

Figure 5.100 Static pushover analysis and time-history analyses (SAC 2/50, *ltbtab* and *lepst04*) of flexible twelve-story distributed CFT MRF 304

Figure 5.101 Static pushover analysis and time-history analyses (SAC 2/50, *lepst10* and *lepst13*) of flexible twelve-story distributed CFT MRF 305

Figure 5.102 Story drift envelope of flexible twelve-story distributed CFT MRF subjected to SAC 2/50 time-histories: *lnrsylm, lpvst03* and *lpvst06* 305

Figure 5.103 Story drift angle to roof drift angle ratio of flexible twelve-story distributed CFT MRF subjected to SAC 2/50 time-histories: *lnrsylm, lpvst03* and *lpvst06* 306

Figure 5.104 Static pushover analysis and time-history analyses (SAC 2/50, *lnrsylm* and *lpvst03*) of flexible twelve-story distributed CFT MRF 306

Figure 5.105 Static pushover and time-history analyses (SAC 2/50, *lpvst06*) of flexible twelve-story distributed CFT MRF 307

Figure 5.106 Story drift envelope and story drift angle to roof drift angle ratio of flexible twelve-story distributed CFT MRF subjected to SAC 10/50 time-histories: *l40ivir, livar05* and *livar06* 307

Figure 5.107 Static pushover analysis and time-history analyses (SAC 10/50, *l40ivir, livar05* and *livar06*) of flexible twelve-story distributed CFT MRF 308

Figure 5.108 Story drift envelope and story drift angle to roof drift angle ratio of flexible twelve-story distributed CFT MRF subjected to SAC 10/50 time-histories: *llnbars, llnyerm, llpgil3* and *lnrnewh* 309

Figure 5.109 Static pushover and time-history analyses (SAC 10/50, *llnbars*) of flexible twelve-story distributed CFT MRF 309

Figure 5.110 Static pushover analysis and time-history analyses (SAC 10/50, *llnyerm, llpgil3* and *lnrnewh*) of flexible twelve-story distributed CFT MRF 310

Figure 5.111 Story drift envelope and story drift angle to roof drift angle ratio of flexible twelve-story distributed CFT MRF subjected to SAC 10/50 time-histories: *lnrrrs, lnrsylm* and *lpsdhsp* 311

Figure 5.112 St
twel
Figure 5.113 St
of fle
Figure 5.114 St
to SA
Figure 5.115 Sto
CFI M
.....
Figure 5.116 Stati
livarin
Figure 5.117 Static
twelve-
Figure 5.118 Story
twelve-
Imbgd3
Figure 5.119 Static
Imbgd3
Figure 5.120 Static
twelve-st
Figure 5.121 Story d
MRF sub
.....
Figure 5.122 Static p
lwhdown
Figure 5.123 Median
distributed
Figure 5.124 Maximu
distributed
Figure 5.125 Minimum
distributed
Figure A.1 Geometry
Figure A.2 DST Connec

Figure 5.112 Static pushover and time-history analyses (SAC 10/50, *lnrrrs*) of flexible twelve-story distributed CFT MRF 311

Figure 5.113 Static pushover and time-history analyses (SAC 10/50, *lnrsylm* and *lpsdhsp*) of flexible twelve-story distributed CFT MRF 312

Figure 5.114 Story drift envelope of flexible twelve-story distributed CFT MRF subjected to SAC 50/50 time-histories: *lclgil2, lknhsbf* and *livar06* 312

Figure 5.115 Story drift angle to roof drift angle ratio of flexible twelve-story distributed CFT MRF subjected to SAC 50/50 time-histories: *lclgil2, lknhsbf* and *livar06* 313

Figure 5.116 Static pushover analysis and time-history analyses (SAC 50/50, *lclgil2* and *livar06*) of flexible twelve-story distributed CFT MRF 313

Figure 5.117 Static pushover and time-history analyses (SAC 50/50, *lknhsbf*) of flexible twelve-story distributed CFT MRF 314

Figure 5.118 Story drift envelope and story drift angle to roof drift angle ratio of flexible twelve-story distributed CFT MRF subjected to SAC 50/50 time-histories: *lmhgil3, llnfrti, lpkcs05* and *lpkcs08* 314

Figure 5.119 Static pushover analysis and time-history analyses (SAC 50/50, *llnfrti, lmhgil3* and *lpkcs05*) of flexible twelve-story distributed CFT MRF 315

Figure 5.120 Static pushover and time-history analyses (SAC 50/50, *lpkcs08*) of flexible twelve-story distributed CFT MRF 316

Figure 5.121 Story drift to roof drift angle ratio of flexible twelve-story distributed CFT MRF subjected to SAC 50/50 time-histories: *lpsplma, lsfhsbf* and *lwhdown* 316

Figure 5.122 Static pushover analysis and SAC 50/50 time-history (*lpsplma, lsfhbf* and *lwhdown*) of flexible twelve-story distributed CFT MRF 317

Figure 5.123 Median story drift angle to roof drift angle ratio of flexible twelve-story distributed CFT MRF subjected to SAC time-histories 318

Figure 5.124 Maximum story drift angle to roof drift angle ratio of flexible twelve-story distributed CFT MRF subjected to SAC time-histories 318

Figure 5.125 Minimum story drift angle to roof drift angle ratio of flexible twelve-story distributed CFT MRF subjected to SAC time-histories 318

Figure A.1 Geometry for prying forces and bending of T-section flanges 357

Figure A.2 DST Connection for rolled sections W36x135, W33x118 and W30x108 .. 357

Figure A.3 DST

Figure A.4 DST

Figure A.3 DST Connection for rolled sections W27x94 and W27x84 358

Figure A.4 DST Connection for rolled sections W27x94 and W27x84 358

1.1 Composite

Steel-concrete

world due to the

usually consist of

columns. Example

concrete (SRC), or

composite column

satisfying critical

economically. For

drift requirements.

weak beam design

1.2 CFT Momen

One promising

moment resisting fr

frames consists of t

and (3) moment res

significant influence

CHAPTER 1 INTRODUTION

1.1 Composite Structures

Steel-concrete composite structures are becoming increasingly popular around the world due to their structural efficiency and construction economy. Composite structures usually consist of steel moment resisting frames or braced frames with composite columns. Examples of composite columns include steel shapes encased in reinforced concrete (SRC), or concrete filled steel tube (CFT) columns, see Figure 1.1. These composite columns have additional flexural stiffness and strength, which assist in satisfying critical seismic design provisions (e.g., IBC 2000, BSSC 2001) more economically. For example, the additional flexural stiffness helps satisfy the inter-story drift requirements, and the additional flexural strength helps satisfy the strong column-weak beam design requirements more economically.

1.2 CFT Moment Resisting Frames

One promising type of composite structure for seismic-resistant design is the CFT moment resisting frame (MRF). As shown in Figure 1.2, the CFT moment resisting frames consists of three types of components: (1) square CFT columns, (2) steel beams, and (3) moment resisting beam-to-column connections. Each of these components has a significant influence on the overall seismic behavior of CFT moment resisting frames.

1.3 Relevant

1.3.1 Previou

Most previou

components of th

conducted on the

(1968), Tomii and

1997, and 1998) a

review of experim

been conducted on

et al. 2002a, b, Nak

strength steel and c

square CFT column

Significant resea

resisting beam-to-CF

Ricles et al. (1997), I

studies, the split-Tee

of the most efficient b

(Ricles et al. 1997, Pe

experimental studies th

stiffness and strength

Redundancy in CFT mo

1.3 Relevant Prior Research

1.3.1 Previous Research on CFT Columns and Connections

Most previous research has focused on the seismic behavior and design of the components of the CFT moment resisting frames. Significant research has been conducted on the behavior, analysis, and design of CFT columns, for example, Furlong (1968), Tomii and Sakino (1979a, b), Zhang and Shahrooz (1997), Hajjar et al. (1996, 1997, and 1998) among others. Hajjar et al. (2003) have presented a comprehensive review of experimental research on CFT columns. More recently, significant research has been conducted on the behavior and design of high strength square CFT columns (Varma et al. 2002a, b, Nakahara et al. 1998). These studies were motivated by the fact that high strength steel and concrete materials can be used efficiently to complement each other in square CFT columns.

Significant research has also been conducted on the development of different moment resisting beam-to-CFT column connections, for example, Alostaz and Schneider (1996), Ricles et al. (1997), Elremaily et al. (2000), Peng (2001) among others. Based on these studies, the split-Tee moment connection shown in Figure 1.3 has been identified as one of the most efficient beam-to-column connections for CFT moment resisting frames (Ricles et al. 1997, Peng 2001). These researchers have demonstrated through full-scale experimental studies that split-Tee moment connections can provide adequate cyclic joint stiffness and strength to develop the highly desirable weak beam-strong column failure mechanism in CFT moment resisting frames.

1.3.2 Previou

Research on

is quite limited.

analytical mode

reinforced concr

Foutch and Yun (

Some researc

and Ricles (1996),

behavior of CFT m

simplifying assum

components was n

connections to be

or ignored the effe

overall seismic beh

limited in scope an

Currently, there

structures with CF

conducting large-sc

moment resisting fr

conventional streng

(28 ksi). Research

to develop performan

design CFT column

1.3.2 Previous Research on CFT Moment Resisting Frames

Research on the overall seismic behavior of composite CFT moment resisting frames is quite limited. Most previous research has focused on the development of sophisticated analytical models and detailed analysis of the seismic behavior and design of steel or reinforced concrete moment resisting frames, for example, Gupta and Krawinkler (2000), Foutch and Yun (2002), Garlock et al. (2000), and Browning et al. (2001) among others.

Some researchers, for example, Hajjar et al. (1998a, b), Elremaily (2000), and Zhang and Ricles (1996), have conducted limited analytical studies to investigate the seismic behavior of CFT moment resisting frames. Most of these studies involved several simplifying assumptions, because knowledge of the behavior of the individual components was not fully developed. For example, some of these studies assumed the connections to be *rigid*, or the CFT columns to be equivalent reinforced concrete sections, or ignored the effects of local buckling of the CFT steel tubes and the steel beams on the overall seismic behavior of the frame. As a result, the conclusions from these studies are limited in scope and applicability.

Currently, there are several ongoing research on the seismic behavior of composite structures with CFT columns. For example, researchers at Lehigh University are conducting large-scale tests to experimentally investigate the seismic behavior of CFT moment resisting frames and braced frames. This study is mostly limited to frames with *conventional* strength CFT columns (steel yield stress $\sigma_y \leq 46$ ksi, and concrete strength $f'_c \leq 8$ ksi). Researchers at the University of Minnesota are conducting analytical research to develop performance-based seismic design provisions for structures with *conventional* strength CFT columns. Researchers at the University of Washington are conducting

analytical resea

strength circula

if any, have bee

1.4 High Stren

Research and

strength square C

(1) High strength

available arou

(2) These high str

in CFT colum

(3) Recent researc

beams (Green

behavior.

In spite of vari

the overall seismi

CFT columns (σ

design provisions

for composite CFT

help to overcome

analytical research to investigate the behavior of braced frames with *conventional* strength circular CFT columns. All these studies are ongoing and very preliminary results, if any, have been reported by these researchers (e.g. Fahnestock et al. 2004).

1.4 High Strength CFT Moment Resisting Frames

Research and construction interest is expanding to moment resisting frames with *high strength* square CFT columns. This growth in interest is based on the following reasons:

(1) High strength steel and concrete materials are becoming more economical and readily available around the world.

(2) These high strength materials can be combined to complement each other effectively in CFT columns (Varma et al. 2002b), and

(3) Recent research on high strength square CFT columns (Varma et al. 2002a) and steel beams (Green 2000) have established detailed knowledge regarding their cyclic behavior.

In spite of various ongoing projects, currently there is a complete lack of research on the overall seismic behavior and design of moment resisting frames with high strength CFT columns ($\sigma_y \geq 50$ ksi, and $f'_c \geq 10$ ksi). Due to this lack of research, current seismic design provisions (e.g. IBC 2000, BSSC 2001) restrict the use of high strength materials in composite CFT structures. This research project aims to develop knowledge that will help to overcome these restrictions and limitations.

1.5 Research

1.5.1 Researc

The goal of

and design of m

The researc

(1) To develop

buckling an

(2) To investig

strength squ

susceptible

(3) To evaluate

on the use o

1.5.2 Researc

The current s

high strength mat

adequate research

addressing some

design of compon

Peng (2011). There

design of moment

addressed by this re

1.5 Research Objectives, Significance and Scope

1.5.1 Research Goal and Research Objectives

The goal of this research is to advance knowledge of the seismic behavior, analysis and design of moment resisting frames with high strength square CFT columns.

The research objectives are:

(1) To develop an analytical model for investigating the effects of inelastic local buckling and degradation on the cyclic behavior of structural members and frames.

(2) To investigate the seismic behavior of moment resisting frames (MRFs) with high-strength square concrete filled steel tube (CFT) columns, which are more susceptible to inelastic local buckling and degradation effects.

(3) To evaluate current seismic design provisions for CFT MRFs, which include limits on the use of high strength materials.

1.5.2 Research Significance

The current seismic design provisions (e.g. IBC 2000, BSSC 2001) restrict the use of high strength materials ($\sigma_y \leq 50$ ksi, $f'_c \leq 10$ ksi) for CFT structures due to the lack of adequate research on their seismic behavior and design. Recent research has begun addressing some of these concerns, but has mostly focused on the seismic behavior and design of components, for example, Nakahara et al. (1998), Varma et al. (2002 a, b), and Peng (2001). There is still a need for detailed research of the *overall* seismic behavior and design of moment resisting frames with high strength CFT columns, which is being addressed by this research project.

This researc

analysis, and d

local material a

CFT steel tube.

of high strength

these studies wil

of high strength m

recommendations

components of hi

1.5.3 Researc

(1) The analy

buckling

(2) The fiber

accountin

(3) The seism

pushover

1.6 Dissertati

The remaining

follows:

- Chapter 2 p

preceded by other

This research project will develop knowledge regarding the seismic behavior, analysis, and design of *high strength* CFT moment resisting frames. The influence of local material and geometric parameters, such as the b/t ratio and the yield stress of the CFT steel tube, and the yield stress of the steel beams on the overall seismic performance of high strength CFT moment resisting frames will also be examined. The results from these studies will be used to develop recommendations for relaxing the limits on the use of high strength materials for CFT moment resisting frames. Additionally, rational recommendations will be made for limits on the local geometric parameters of the components of high strength CFT moment resisting frames.

1.5.3 Research Scope

(1) The analytical model is a fiber element capable of modeling inelastic local buckling effects through the use of specially developed fiber σ-ε curves.

(2) The fiber element is used to model CFT beam-columns and steel beams, while accounting for the effects of local buckling and degradation.

(3) The seismic behavior of CFT MRFs is investigated by conducting nonlinear static pushover and time-history analyses using DRAIN-2DX.

1.6 Dissertation Outline

The remaining chapters of this dissertation (Chapters 2 through 6) are organized as follows:

- *Chapter 2* presents the relevant experimental and analytical investigations conducted by other researchers on the seismic behavior of components of composite CFT

moment resisti

seismic behavio

- *Chapter*

for the compone

the split-Tee mo

context of the no

The developed m

MRF sub-assemb

- *Chapter 4*

12-story office b

analyses of the 6-

The effects of inc

seismic response

- *Chapter 5*

strength CFT MR

10% and 50% pro

behavior of CFT M

seismic behavior o

- *Chapter 6*

seismic behavior o

strength square CF

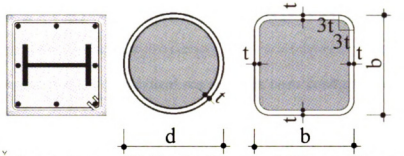
recommendations f

is presented in Ch

moment resisting frames. Chapter 2 also presents some of the relevant research on the seismic behavior of steel or reinforced concrete moment resisting frames.

- *Chapter 3* presents the development and validation of detailed analytical models for the components of CFT MRFs, namely, the CFT beam-columns, the steel beams, and the split-Tee moment connections, respectively. These models were developed within the context of the nonlinear structural analysis program DRAIN-2DX (Prakash et al. 1993). The developed models were further validated by simulating the cyclic behavior of a CFT MRF sub-assembly that was tested by Peng (2000).
- *Chapter 4* presents the seismic design of a low-rise (6 story) and a medium-rise (12-story) office building with high strength CFT MRFs. The nonlinear static pushover analyses of the 6- and 12-story high strength CFT-MRFs is also presented in Chapter 4. The effects of inelastic local buckling of the member section components on the overall seismic response of high strength CFT MRFs is also examined in Chapter 4.
- *Chapter 5* presents nonlinear time-history analyses of the 6- and 12-story high strength CFT MRFs subjected to three sets of SAC ground motion records, including 2%, 10% and 50% probability of exceedance in 50 years. To investigate the inelastic dynamic behavior of CFT MRFs. The effects of dynamic higher modes and the P-Δ effects on the seismic behavior of high strength CFT MRFs are also presented in Chapter 5.
- *Chapter 6* presents the summary and conclusions of the analytical research on the seismic behavior of low-rise and medium-rise moment resisting frames with high strength square CFTs, including the validity of the current seismic design provisions and recommendations for seismic design and analysis. Future work recommendations are also presented in Chapter 6.


(a) Str
encase
CFT
W24x
or
W24x6
T-stub, cut f
W24x1
T-stub, cut f
W24x1-6



(a) Structural steel shape encased in reinforced concrete (b) Circular Concrete filled tube (CFT) (c) Rectangular concrete filled tube (CFT)

Figure 1.1 Columns used in composite construction

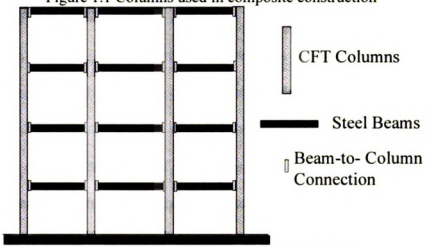


Figure 1.2 CFT Moment Resisting Frame

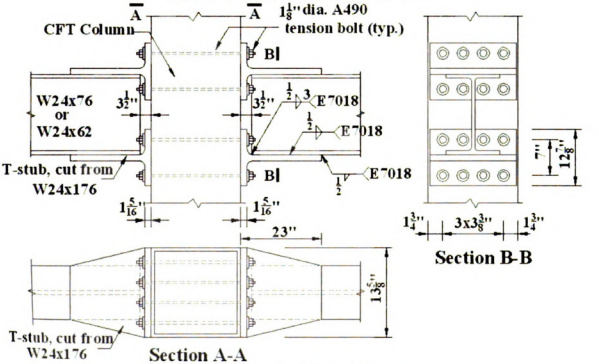


Figure 1.3 Split-Tee Moment Connection

CHAPTE

Significant

behavior, analy

namely, the CFT

Hajjar et al. (20

research on CFT

duplicated here. I

relevant to the a

Chapters 4 and 5

- Section 2.1 p

developed an

2DX. Recent

modified fibe

columns and s

- Section 2.2 p

columns by r

Earthquake R

researchers are

- Section 2.3 p

connections fo

for modeling t

experimental da

CHAPTER 2 - PRIOR RESEARCH AND BACKGROUND

Significant experimental and analytical research has been conducted on the seismic behavior, analysis, and design of the components of CFT moment resisting frames, namely, the CFT beam-columns, split-Tee moment resisting connections, and steel beams. Hajjar et al. (2003) have developed an excellent database summarizing the experimental research on CFT columns, beam-columns, and connections. Hence, this work is not duplicated here. This Chapter summarizes prior research and background that are directly relevant to the analytical models developed and validated in Chapter 3, and used in Chapters 4 and 5 for investigating the seismic behavior of high strength CFT frames.

- Section 2.1 presents the details of a fiber-based beam-column element that has been developed and implemented in the nonlinear structural analysis program DRAIN-2DX. Recent modifications to the original fiber element are also presented. This modified fiber element is used later in Chapters 3, 4, and 5 to model CFT beam-columns and steel beams. Hence, its details are presented first in Section 2.1.
- Section 2.2 presents the fiber-based analytical models developed for CFT beam-columns by researchers in U.S. and Japan as part of the U.S.-Japan Cooperative Earthquake Research Program. The modeling approaches developed by these researchers are relevant and adopted in the current work as presented in Section 3.1.
- Section 2.3 presents the results of experimental research on split-Tee moment connections for CFT moment resisting frames, and the analytical approach developed for modeling the behavior of bolted split-Tee connections for steel MRFs. The experimental data will be used to validate the analytical models for split-Tee moment

connection

- Section 2.

behavior o

presented in

developed f

- Section 2.5

steel MRFs

and adaptive

used in Chapt

- Section 2.6 p

seismic behavi

to earthquake g

steel project an

importance of

prior research.

focusing on the

2.1 FIBER ELE

DRAIN-2DX (P

be used to investigate

fiber-based beam-c

DRAIN-2DX by Pra

fiber element with a

connections in Section 3.2 later.

- Section 2.4 presents the results of experimental and analytical research of the behavior of high strength steel beams subjected to cyclic loading. The results presented in this section are used later in Section 3.3 to validate the analytical models developed for steel beams.
- Section 2.5 presents relevant research focusing on the static pushover analyses of steel MRFs with post-tensioned connections. This section also summarizes FEMA and adaptive spectra-based procedures for pushover analysis. These procedures are used in Chapter 4 to investigate the pushover behavior of high strength CFT MRFs.
- Section 2.6 presents relevant background and analytical research focusing on the seismic behavior (results of nonlinear time-history analysis) of steel MRFs subjected to earthquake ground motions. The ground motion histories developed for the SAC steel project and the methods for scaling them to target spectra are summarized. The importance of including P-Δ and higher mode effects are discussed with context to prior research. The material presented in this section is used later in Chapter 5 focusing on the seismic behavior of high strength CFT MRFs.

2.1 FIBER ELEMENT IN DRAIN-2DX

DRAIN-2DX (Prakash et al. 1993) is a nonlinear structural analysis program that can be used to investigate the nonlinear static or dynamic behavior of 2D structural frames. A 'fiber-based beam-column' element (fiber element) was developed and implemented in DRAIN-2DX by Prakash et al. (1993). This fiber element is a distributed-plasticity based finite element with a flexibility-based formulation. The mathematical formulation is

discussed in d

plane sections

bending: (2) sl

shear deformati

to uniaxial stres

A schematic

shown in this Fi

element length is

defined independ

the mid-length of

and each fiber h

relationship. The

strain-bending mo

σ-ε behavior ove

length of the segm

length of the elem

The number a

the pre-peak inela

response, the inela

largest internal for

post-peak inelastic

deformation behav

the segment is g

discussed in detail in Kurama et al. (1996). It involves the following assumptions: (1) plane sections remain plane and perpendicular to the centroidal axis before and after bending; (2) slip does not occur between the materials in the cross-section; (3) inelastic shear deformations are negligible; and (4) the materials in the cross-section are subjected to uniaxial stress-strain states.

A schematic description of the DRAIN-2DX fiber element is shown in Figure 2.1. As shown in this Figure, the length of the fiber element is defined by two end-nodes. The element length is divided into several segments, where the length of each segment can be defined independently. The behavior of each segment is represented by a slice located at the mid-length of the segment. At each slice, the cross-section is discretized into fibers and each fiber has an associated area, distance from the centroid, and uniaxial σ–ε relationship. The slice force-deformation behavior, i.e., the section axial force-axial strain-bending moment-curvature (P-ε-M-ϕ) behavior, is obtained by integrating the fiber σ–ε behavior over the cross-section. The slice flexibilities are assumed constant over the length of the segment, and the slice force-deformation responses are integrated along the length of the element to obtain its force-displacement response.

The number and distribution of segments along the length can have an influence on the pre-peak inelastic behavior of the fiber element. However, in the post-peak range of response, the inelastic deformations (failure) concentrate in the segment subjected to the largest internal forces, while the remaining segments unload elastically. As a result, the post-peak inelastic behavior of the fiber element is governed by the length and the force-deformation behavior of the failure segment. The force-deformation behavior of the failure segment is governed by the fiber discretization of the cross-section, and the fiber

σ-ε relationsh

is governed b

distribution of

segment; and (c

2.1.1 Fiber c

The main li

member behavio

and the fiber σ-

generic fiber σ-ε

'S' type fiber σ-

the behavior of c

ability to model

type σ-ε relation

The 'S' type

original 'S' type

compression. Her

Cordero et al. (2

buckling effects

recommendations

is presented later.

shown in Figure 2

explained in more d

σ–ε relationships. Thus, the behavior and consequently the accuracy of the fiber element is governed by three input parameters specified by the user: (a) the number and distribution of segments; (b) the fiber discretization of the slice cross-section in each segment; and (c) the fiber σ–ε relationships.

2.1.1 Fiber σ–ε Relationships

The main limitation of the DRAIN-2DX fiber element is that the complexities of member behavior are modeled implicitly by the fiber discretization of the cross-section and the fiber σ–ε relationships. Prakash et al. (1993) developed and implemented two generic fiber σ–ε relationships for the DRAIN-2DX fiber element. These are the 'C' and 'S' type fiber σ–ε relationships. The 'C' type σ–ε relationship was developed to model the behavior of concrete. It was further enhanced by Kurama et al. (1996) to include the ability to model the stiffness changes in concrete under cyclic loading. The modified 'C' type σ–ε relationship is shown in Figure 2.2, and explained in more detail later.

The 'S' type σ–ε relationship was developed to model the behavior of steel. The original 'S' type σ–ε relationship (Prakash et al. 1993) was symmetric in tension and compression. Hence, it could not model compression softening or local buckligng effects. Cordero et al. (2002) enhanced the 'S' type σ–ε relationship to model cyclic local buckling effects based on the recommendations of Varma et al. (2001). These recommendations were based on the cyclic behavior of high strength CFT beam-columns as presented later. The monotonic behavior of the modified 'S' type σ–ε relationship is shown in Figure 2.3, and its cyclic behavior is shown in Figures 2.4 and 2.5. These are explained in more detail below.

The fiber

(see Figures 2

based on mult

consist of three

σ-ε behavior i

cyclic loading, w

behavior.

The monoton

assigned and the

(grey dots in Figu

tension. However

the user. These li

specify up to five

the 'S' type σ-ε

σ-ε points in ten

decreasing, and (4

remain constant fo

As shown in F

behavior in compr

strain hardening or

with tension

ratios, which are c

The fiber σ–ε relationships are multilinear, i.e., composed of straight line segments, (see Figures 2.2 – 2.5) because DRAIN-2DX uses an event-to-event solution strategy based on multilinear element behavior. Both the 'C' and 'S' type fiber σ–ε relationships consist of three parts: (1) the monotonic σ–ε behavior in compression, (2) the monotonic σ–ε behavior in tension, and (3) the hysteresis rules governing the σ–ε behavior under cyclic loading, where the monotonic σ–ε curves serve as the envelopes of the cyclic σ–ε behavior.

The monotonic σ–ε curves are specified by the user. The hysteresis rules are pre-assigned and the user has little control over them. The user specifies pairs of σ–ε points (grey dots in Figures 2.2 and 2.3) to define the monotonic σ–ε curves in compression and tension. However, there are some limitations on the monotonic σ–ε curves specified by the user. These limitations are as follows: (1) for the 'C' type σ–ε curve, the user can specify up to five σ–ε points in compression and up to two σ–ε points in tension, (2) for the 'S' type σ–ε curve, the user must specify three σ–ε points in compression and two σ–ε points in tension, (3) the tangent modulus of the monotonic σ–ε curves must be decreasing, and (4) at strains beyond the last input σ–ε point, the stress is assumed to remain constant for both 'C' and 'S' type σ–ε curves.

As shown in Figure 2.2, the 'C' type fiber σ–ε relationship can model asymmetric behavior in compression and tension, post-peak softening in compression, yielding and strain hardening or strain softening in tension. Additionally, the 'C' type σ–ε relationship can model tension crack opening-and-closing behavior and stiffness changes under cyclic loading, which are controlled by the user-specified parameter β. As shown in Figure 2.2,

β equal to zer

significant stif

As shown i

in compressio

buckling, and y

σ–ε relationship

and (2) after loc

rules before loc

local buckling. T

hardening in tens

buckling on the h

shown in Figure 2

dominate and there

negligible local buc

The fiber eleme

used to model steel

et al. 2002. Kuram

element depends on

define the fiber mod

the fiber σ–ε curv

accurately modeling t

β equal to zero corresponds to no stiffness degradation, and β equal to one corresponds to significant stiffness degradation.

As shown in Figure 2.3, the 'S' type σ–ε relationship can model asymmetric behavior in compression and tension, yielding and post-peak softening in compression after local buckling, and yielding and strain hardening in tension. Under cyclic loading, the 'S' type σ–ε relationship can model two different hysteretic behaviors: (1) before local buckling, and (2) after local buckling, as shown in Figures 2.4 and 2.5, respectively. The hysteresis rules before local buckling include the effects of kinematic hardening and subsequent local buckling. The hysteresis rules after local buckling include the effects of kinematic hardening in tension and cyclic local buckling in compression. The effects of cyclic local buckling on the hysteretic behavior is controlled by the user-specified parameter α. As shown in Figure 2.5, α equal to one corresponds to the case where local buckling effects dominate and there is significant degradation. α equal to zero corresponds to the case of negligible local buckling effects and there is elastic unloading.

The fiber element along with the modified 'C' and 'S' type σ–ε relationships can be used to model steel, reinforced concrete, or steel-concrete composite members (Cordero et al. 2002, Kurama et al. 1996). As mentioned previously, the accuracy of the fiber element depends on the values of the fiber σ–ε curves and cyclic relationships used to define the fiber model of the structural member cross-section. Developing the details of the fiber σ–ε curves for particular structural members becomes the challenge for accurately modeling their behavior.

2.2 FIBER-

Several ex
subjected to d
Japan, U.K.,
summarizing th
(1999) and Gou
details of CFT sp
and failure mode

Phase V of
Composite and
on high strength
El-Remaily et al
2004). Hajjar et
the results of va
the specific de
experimental ob

The experim
to combined axi
(1) CFT beam-c
steel and con
2. Failure occur
beam-column
3. The length of

2.2 FIBER-BASED MODELS FOR CFT BEAM-COLUMNS

Several experimental and analytical studies have been conducted on CFT members subjected to different loading and boundary conditions in the U.S. and abroad (China, Japan, U.K., Australia, and Canada among others). Comprehensive databases summarizing the results of experimental studies have been compiled by Aho and Leon (1999) and Gourley et al. (2001). These databases include the geometric and material details of CFT specimens, the loading and boundary conditions, and the behavior, results, and failure mode from the experimental studies.

Phase V of the U.S.-Japan Cooperative Earthquake Research Program focused on Composite and Hybrid Structures. It included several experimental and analytical studies on high strength CFT beam-columns that were conducted in the U.S. (Varma et al. 2001, El-Remaily et al. 2002) and Japan (Sakino et al. 2004, Inai et al. 2004, and Fujimoto et al. 2004). Hajjar et al. (2003) compiled an excellent comprehensive database summarizing the results of various experimental studies on CFT members. This database summarizes the specific details of the testing approaches, material and geometric parameters, experimental observations, results, failure mode, and conclusions.

The experimental behavior, results, and failure mode of CFT beam-columns subjected to combined axial load and monotonic or cyclic flexural loading indicate that:

(1) CFT beam-columns achieve their strength and fail due to the inelastic behavior of steel and concrete materials combined with local buckling of steel tube flanges, webs.

(2) Failure occurs with the formation of an inelastic failure segment in the portion of the beam-column subjected to maximum bending moment.

(3) The length of the inelastic failure segment is approximately equal to the width (b) of

the square

(4) Local buc

occurs in ti

column unl

(5) The momer

fundamenta

From the ab

based models pr

modeling the fun

Hence, most rese

behavior of CFT

on the fiber discr

relationships (refe

development of ac

The following

2004, Inai et al. 20

steel and concrete

Cooperative Earth

Sectionally divi

Section 3.1, one of

2.2.1 Japanese M

As mentioned

to be defined comp

the square CFT.

(4) Local buckling of the steel tube flanges and webs, and crushing of the concrete infill occurs in the inelastic failure segment while the remaining portions of the CFT beam-column unload elastically.

(5) The moment-curvature (M-ϕ) response of the inelastic failure segment represents the fundamental flexural behavior of CFT beam-columns.

From the above discussion of CFT beam-column behavior and the details of the fiber-based models presented in Section 2.1, it is evident that fiber-based models are ideal for modeling the fundamental force-deformation (P-M-ϕ) behavior of CFT beam-columns. Hence, most researchers have developed fiber models for representing the fundamental behavior of CFT beam-columns. The accuracy and validity of the fiber models depends on the fiber discretization of the CFT cross-section and the steel and concrete fiber σ–ε relationships (refer Section 2.1.1). Hence, researchers have always focused on the development of accurate steel and concrete fiber σ–ε relationships for the CFT section.

The following two sub-sections 2.2.1 and 2.2.2 present the Japanese (Sakino et al. 2004, Inai et al. 2004) and the U.S. (Varma et al. 2001, 2005) approaches for developing steel and concrete fiber σ–ε curves that were developed as part of the U.S.-Japan Cooperative Earthquake Program. Both approaches are enumerated because they are fundamentally different, have unique advantages and disadvantages. As presented later in Section 3.1, one of these approaches will be adopted for the current research work.

2.2.1 Japanese Model for CFT Beam-Columns

As mentioned previously, the steel and concrete fiber σ–ε relationships for CFTs can be defined completely by specifying: (a) the monotonic σ–ε curves in tension, (b) the

monotonic σ-

behavior (wh:

al. (2004). Ina:

fiber σ-ε relati

- The steel fi

  and yield st

  concrete wa

- The hysteret

  concrete fibe

  and tension c

- The hysteret

  steel fibers. T

  reloading bra

- The steel and

  research and

  twenty-five ho

  as described be

Concrete fiber c

The concrete fi

Saiidi and Sun (1

loops. This two-pa

concrete using the u

The uncontin

monotonic σ–ε curves in compression, and (c) the hysteresis rules governing cyclic behavior (while the monotonic curves as envelopes). The Japanese researchers Sakino et al. (2004), Inai et al. (2004), and Fujimoto et al. (2004) developed the steel and concrete fiber σ–ε relationships as follows:

- The steel fiber σ–ε curves in tension were based on the material uniaxial σ–ε curves and yield stress values. The concrete fiber σ–ε behavior in tension was ignored, i.e., concrete was assumed to have zero tensile stress capacity.
- The hysteretic rule proposed by Fujii et al. (1973, see Figure 2.6) was used for the concrete fibers. This hysteretic behavior includes the effects of stiffness degradation, and tension crack opening and closing behavior, but no energy dissipation.
- The hysteretic rule proposed by Meng et al. (1992, see Figure 2.7) was used for the steel fibers. This hysteretic behavior does not account for stiffness degradation on the reloading branch due to cyclic local buckling effects.
- The steel and concrete fiber σ–ε curves in compression were developed based on past research and the experimental results for fifty-two CFT stub (short) columns and twenty-five hollow steel tube stub columns tested under concentric axial compression, as described below.

Concrete fiber σ–ε curve in compression

The concrete fiber σ–ε curves in compression are based on the σ–ε model developed Sakino and Sun (1994) for concrete confined triaxially by steel tubes and/or rectilinear hoops. This two-parameter model can determine the σ–ε behavior of triaxially confined concrete using the unconfined concrete strength (f'_c) and the lateral confining pressure (σ_{re}). The unconfined concrete strength was estimated as the cylinder compressive

strength mult

McNamara (

confining pre

hoops. They a

modulus E_c, (

confined concr

equations for E_c

Inai and Sak

infill of square

retaining the incr

for the concrete in

jacket. The confi

assumed equal to

peak ductility are

the final form of th

and endorsed by the

In Equation (1), Y is

is the normalized

strength multiplied by a scale effect factor (γ_u =1.67 $b^{-0.112}$) defined by Blanks and McNamara (1935). Sakino and Sun proposed equations for estimating the lateral confining pressure (σ_{re}) for the cases of confinement by steel jacket and/or rectilinear hoops. They also proposed equations for estimating: (a) the unconfined concrete elastic modulus E_c, (b) the unconfined concrete strain corresponding to peak stress ε_o, (c) the confined concrete strength f'_{cc}, and (d) the confined concrete peak strain ε_{co}. These equations for E_c, ε_o, f'_{cc}, and ε_{co} depend only on two parameters f'_c and σ_{re}.

Inai and Sakino (1996) modified the original Sakino and Sun model for the concrete infill of square CFT columns by *eliminating the increase* in concrete strength but *retaining the increase* in ductility due to confinement. The lateral confining pressure (σ_{re}) for the concrete infill of a CFT was assumed same as that for concrete confined by a steel jacket. The confined concrete strength and strain at peak stress (f'_{cc} and ε_{co}) were assumed equal to the unconfined values (f'_c and ε_o). The effects of confinement on post-peak ductility are defined by the lateral confining pressure σ_{re}. Equation (2.1) presents the final form of the σ–ε curve for the concrete infill of a CFT. This curve was adopted and endorsed by the Japanese researchers [Sakino et al., Inai et al., and Fujimoto et al.].

$$Y = \frac{VX + (W-1)X^2}{1 + (V-2)X + WX^2} \qquad \text{..... Equation (2.1)}$$

In Equation (1), Y is the normalized stress given by $Y = \sigma / f'_c$

X is the normalized strain given by $X = \varepsilon / \varepsilon_o$

$$V = E_c\, \varepsilon_o / f'_c \qquad \text{..... Equation (2.2)}$$

$$W = 1.50 - 0.0171\, f'_c + 2.39\sqrt{\sigma_{re}} \qquad \text{..... Equation (2.3)}$$

In Equation (

parameter W

concrete. E_c a

Figure 2.8 show

2.6. In this Figu

and b t=34, (b)

b t=52. Figure

influence on the

Steel fiber σ–ε

Inai and Sak

in compression.

modes (elastic an

was adopted and

Sakino et all, Ina

The steel fibe

parameter α given

elastic modulus of

depending on the v

$$\sigma_{re} = \frac{1}{2}\rho_h \sigma_y \left(\frac{t}{b}\right) \quad \text{..... Equation (2.4)}$$

In Equation (2.4), ρ_h is the steel volumetric ratio and σ_y is the steel yield stress. The parameter W accounts for the effects of confinement on the post-peak ductility of the concrete. E_c and ε_o can be obtained using Equations 2.5 and 2.6 (Sakino and Sun 1994).

$$E_C = 6900 + 3320\sqrt{f'_C} \quad \text{.... Equation (2.5)}$$

$$\varepsilon_{CO} = 0.94\left(f'_C\right)^{1/4} \times 10^{-3} \quad \text{..... Equation (2.6)}$$

Figure 2.8 shows some example concrete fiber σ–ε curves obtained using Equations 2.1-2.6. In this Figure, f'_c is equal to 110 MPa, and the CFT steel tubes have: (a) σ_y=87 ksi and b/t=34, (b) σ_y=96 ksi and b/t=50, (c) σ_y=39 ksi and b/t=35, and (d) σ_y=65 ksi and b/t=52. Figure 2.8 shows that both the steel tube σ_y and *b/t* ratio have significant influence on the post-peak ductility of the concrete infill of the square CFT.

Steel fiber σ–ε curve in compression

Inai and Sakino (1996) had originally proposed a σ–ε model for the CFT steel fibers in compression. Nakahara et al. (1998) enhanced this model to include additional failure modes (elastic and inelastic buckling) for high strength steel tubes. The enhanced model was adopted and endorsed for the steel tubes of CFTs by the Japanese researchers [Sakino et all, Inai et al., and Fujimoto et al. 2004]. It is described below.

The steel fiber σ–ε curves in compression depend on the normalized slenderness parameter α given by Equation (7). In this equation, σ_y and E_s are the yield stress and elastic modulus of the steel tube. The CFT steel tubes are categorized as Cases 1, 2, or 3 depending on the values of α.

When $\alpha \leq 2.3$

2.9 is recomm

buckling after

given by Equat

analysis of the

part of the U.S.

equations for loc

When 2.37

in Figure 2.9 is

local buckling at

When $\alpha \geq 4.11$,

2.9 is recommen

local buckling b

equal to $[S_y \sigma_y E$

$$\alpha = \left(\frac{b}{t}\right)^2 \frac{\sigma_y}{E_s} \qquad \text{..... Equation (2.7)}$$

When $\alpha \leq 2.37$, the steel tube is categorized as Case-1 and the σ–ε curve shown in Figure 2.9 is recommended. As shown in Figure 2.9, the Case-1 steel tube will undergo local buckling after yielding at stress equal to [S_1 σ_y] and corresponding strain equal to ε_B given by Equations 8 and 9, respectively. These equations were developed by regression analysis of the experimental results for several *hollow* steel tubes stub columns tested as part of the U.S.-Japan Program. Kato and Nishiyama (1980) had also indicated similar equations for local buckling of *hollow* steel tube walls.

$$S_1 = \frac{1}{0.698 + 0.128\,\alpha} \qquad \text{..... Equation (2.8)}$$

$$\varepsilon_B = \varepsilon_y \left(\frac{6.09}{\alpha^2} - \frac{0.801}{\alpha} + 1.10\right) \qquad \text{Equation (2.9)}$$

When $2.37 < \alpha < 4.11$, the steel tube is categorized as Case-2 and the σ–ε curve shown in Figure 2.9 is recommended. As shown in Figure 2.9, the Case-2 steel tube will undergo local buckling at yielding with stress equal to σ_y and corresponding strain ε_B equal to ε_y. When $\alpha \geq 4.11$, the steel tube is categorized as Case-3 and the σ–ε curve shown in Figure 2.9 is recommended. As shown in this Figure, the Case-3 steel tube will undergo elastic local buckling before yielding at a stress equal to [S_2 σ_y] and corresponding strain ε_B equal to [S_2 σ_y/E_s]. The value of S_2 is given by Equation (10).

$$S_2 = \frac{1}{0.698 + 0.128\,\alpha \dfrac{4.00}{6.97}} \qquad \text{..... Equation (2.10)}$$

This equ

slenderness p

buckling theor

different buck

4.00 is the pl

assumed to rep

plate-buckling

elastic local buc

As show

linearly to stress

and ε_y are given

stress. As shown

slope, i.e., the s

Equations (1

several (approx.

The developed c

concrete infill, an

experimental data

for the [σ_c, ε_c] po

relation. Signific

which is some ca

This equation was developed by modifying Equation (8) by multiplying the slenderness parameter α by 4.00/6.97. This modification is based on elastic plate buckling theory, and it considers the difference in plate edge conditions representing the different buckling modes for hollow steel tubes and CFT steel tubes. In Equation (10), 4.00 is the plate-buckling coefficient (k) for simply supported edge conditions that is assumed to represent the elastic local buckling of hollow steel tube walls, and 6.97 is the plate-buckling coefficient (k) for fixed end conditions that is assumed to represent the elastic local buckling of CFT tube walls.

As shown in Figure 2.9, for all three cases, the post-peak σ–ε curves descend linearly to stress σ_T equal to [T σ_y] and corresponding strain equal to ε_T. The values of T and ε_T are given by Equations (11) and (12) respectively, where ε_B is the strain at peak stress. As shown in Figure 2.9, after reaching [σ_T, ε_T], the σ–ε curve become flat (zero slope), i.e., the stress remains constant with increasing strain.

$$T = 1.19 - 0.21\sqrt{\alpha} \qquad \text{..... Equation (2.11)}$$

$$\varepsilon_T = \varepsilon_B + 3.59\,\varepsilon_y \qquad \text{..... Equation (2.12)}$$

Equations (11) and (12) were developed empirically using experimental results for several (approx. fifty-two) CFT stub columns tested as part of the U.S.-Japan Program. The developed concrete σ–ε curves in compression (Equation 1) were assumed for the concrete infill, and the steel σ–ε behavior in compression was back calculated from the experimental data. Equations (11) and (12) were developed by regression analysis to best fit the [σ_T, ε_T] point on the proposed steel σ–ε curves to the back calculated steel σ–ε behavior. Significant scatter was observed while performing this regression analysis, which is some cause for concern.

Figure 2.

2.12 for CFT

σ_y=39 ksi and

and Figure 2

normalized ste

steel σ-ε curve

2.2.2 U.S. Mo

The U.S. re

Program] develo

columns using th

CFT cross-section

fibers as shown

presented earlier i

section, respectivel

σ-ε curves in tens

the steel and concre

- The steel fiber

(slope=E_s), stra

(slope=0). They

nominal yield (σ

Figure 2.10 shows some example steel fiber σ–ε curves obtained using Equations 2.7-2.12 for CFT steel tubes with: (a) σ_y=87 ksi and b/t=34, (b) σ_y=96 ksi and b/t=50, (c) σ_y=39 ksi and b/t=35, and (d) σ_y=65 ksi and b/t=52. It is evident from Equations 2.7-2.12 and Figure 2.10 that the steel fiber σ–ε curves in compression depend only on the normalized slenderness parameter α. The concrete strength f'_c has no influence on the steel σ–ε curves in compression.

2.2.2 U.S. Model for CFT Beam-Columns

The U.S. researchers [Varma et al. (2001, 2005) working as part of the U.S.-Japan Program] developed and validated fiber models for high strength square CFT beam-columns using the DRAIN-2DX fiber element presented in detail in Section 2.1. The CFT cross-section was discretized into concrete fibers and steel flange, web, and corner fibers as shown in Figure 2.11. The modified 'S' and 'C' type σ–ε relationships presented earlier in Section 2.1.1 were used for steel and concrete fibers of the CFT section, respectively. These 'S' and 'C' type fiber σ–ε relationships consist of monotonic σ–ε curves in tension and compression and cyclic hysteresis rules that were defined for the steel and concrete fibers of the CFT section as follows:

- The steel fiber σ–ε curves in monotonic tension were trilinear with an elastic branch (slope=E_s), strain hardening branch (slope=0.01E_s), and ultimate plastic branch (slope=0). They were based on the measured material uniaxial σ–ε curves or the nominal yield (σ_y) and ultimate stress (σ_u) values.

- The conc
  have zero
- The cyclic
  2.1.1 and
  energy diss
- The cyclic
  Section 2.1.
  hardening an
- The steel an
  using the re
  compression

Steel and Con

The analytica
compression con
failure segment o
compressive loa
nonlinear finite
analyzed using
concrete material
between the steel
fiber σ-ε
Figure 2.12 sh
from the length

- The concrete fiber σ–ε behavior in tension was ignored, i.e., concrete was assumed to have zero tensile stress capacity. This is similar to the Japanese model.
- The cyclic hysteresis rules for the 'C' type σ–ε relationship were described in Section 2.1.1 and shown in Figure 2.3. They include the effects of cyclic stiffness degradation, energy dissipation and tension crack opening and closing behavior.
- The cyclic hysteresis rules for the 'S' type s-e relationship were also described in Section 2.1.1 and shown in Figures 2.4 and 2.5. They include the effects of kinematic hardening and cyclic local buckling.
- The steel and concrete fiber σ–ε curves in compression were developed analytically using the results of 3D finite element analysis of a CFT segment subjected to axial compression as described below.

Steel and Concrete Fiber σ–ε Curves in Compression

The analytical approach for developing the steel and concrete fiber σ–ε curves in compression consisted of three steps: (1) developing a 3D finite element model of the failure segment of the CFT beam-column, (2) analyzing the model under concentric axial compressive loading, and (3) deriving the fiber σ–ε curves from the results of the nonlinear finite element analysis. The 3D finite element models were developed and analyzed using ABAQUS (2003). They explicitly included the effects of steel and concrete material inelasticity, local buckling of the steel tube, and transverse interaction between the steel and concrete resulting in confinement of the concrete infill. Hence, the derived fiber σ–ε curves implicitly accounted for these effects.

Figure 2.12 shows the typical 3D finite element model for the CFT segment. As shown, the length of the segment was equal to the cross-section (b), which represents the

length of the

was modeled

Plane section

using four-no

isotropic multi

behavior and a

Figure 2.13 we

local buckling.

The concret

elements. The m

which is a multi

isotropic harden

was calibrated b

As shown in Fig

infill in the tran

frictionless cont

concrete infill wa

The 3D finit

procedure in AB

shortening P-Δ re

the steel and con

elements at the en

length of the inelastic failure segment (plastic hinge). Only a quarter of the cross-section was modeled because the behavior under concentric axial loading is assumed symmetric. Plane sections were assumed to remain plane at both ends. The steel tube was modeled using four-node shell elements, and the material inelasticity was modeled using an isotropic multiaxial plasticity model with Von Mises yield surface, isotropic hardening behavior and associated flow rule is used to model. Geometric imperfections shown in Figure 2.13 were introduced at the mid-height on all sides of the steel tube to initiate local buckling.

The concrete infill was modeled using six-node tetrahedral and eight-node brick elements. The material inelasticity was idealized using the 'CONCRETE' material model, which is a multiaxial plasticity model with a Drucker-Prager compression yield surface, isotropic hardening or softening behavior, and associated flow rule. This material model was calibrated by Varma et al. (2000) to account for the effects of triaxial confinement. As shown in Fig. 2.14, composite interaction between the steel tube and the concrete infill in the transverse direction was modeled by uniaxial gap-contact elements with hard frictionless contact behavior. The longitudinal bond between the steel tube and the concrete infill was modeled by rigid-plastic spring elements.

The 3D finite element model was analyzed using the modified Riks analysis procedure in ABAQUS (2003). The results from the analysis included the axial load-shortening P-Δ response of the segment, and the multiaxial state of stresses and strains in the steel and concrete elements. The longitudinal stresses in the steel and concrete elements at the end section of the segment (Section A in Figure 2.15) were used to

determine th

steel tube wa

The effec

carried divide

computed as t

curves were

compression.

compression σ-

σ-ε curve was i

The concrete in

curve for the con

Thus, the fi

results of a 3D fi

show example σ-

σ-ε curves were

CFTs with (a) σ_y

and (b) σ_y=65 ksi

local buckling of t

223 Compari

Kowalkowski a

related their va

determine the axial forces carried by the components of the cross-section, namely, the steel tube walls, corners, and concrete infill ($P_{s\text{-}w}$, $P_{s\text{-}c}$, and P_c shown in Figure 2.15).

The effective stress for each cross-section component was computed as the axial force carried divided by its cross-sectional area. The effective strain for the components was computed as the axial shortening Δ divided by the original length (b). Thus, effective σ–ε curves were developed for the steel tube walls, corners, and concrete infill in compression. The steel tube wall effective σ–ε curve was idealized and used as the compression σ–ε curve for the steel flange and web fibers. The steel tube corner effective σ–ε curve was idealized and used as the compression σ–ε curve for the steel corner fibers. The concrete infill effective σ–ε curve was idealized and used as the compression σ–ε curve for the concrete fibers.

Thus, the fiber σ–ε curves in compression were developed analytically from the results of a 3D finite element analysis of the CFT failure segment. Figures 2.16 and 2.17 show example σ–ε curves for steel and concrete fiber in compression, respectively. These σ–ε curves were obtained using the analytical approach described above for high strength CFTs with (a) σ_y=87 ksi and b/t=34, (b) σ_y=96 ksi and b/t=50, (c) σ_y=39 ksi and b/t=35, and (d) σ_y=65 ksi and b/t=52. These figures illustrate the effects of steel tube b/t ratio on local buckling of the steel tube and confinement of the concrete infill (Varma et al. 2001).

2.2.3 Comparison of U.S. and Japanese Models

Kowalkowski and Varma (2003) compared the Japanese and U.S. fiber models and evaluated their validity for high strength square CFT beam-columns. They used the

Japanese fiber n

columns tested b

the comparisons

analytical predict

σ_t=40 ksi or 87 k

results (M-ϕ) and

CFT specimens w

Kowalkowski

strength CFT bean

(Sakino et al. 2004

concrete fiber σ–ε

the same high stren

- Significant diff

by the U.S. and

- In spite of these

and Japanese an

with each other a

- Hence, both the U

the fiber σ–ε relat

- The Japanese anal

more useable to n

materials. However

- The U.S. analytical

Japanese fiber model to predict the P-M-ϕ behavior of the high strength CFT beam-columns tested by the U.S. researchers, and vice versa. For example, Figure 2.18 shows the comparisons of the experimental results (M-ϕ) and the U.S. and Japanese model analytical predictions for the U.S. high strength CFT specimens with f'_c=16 ksi, b/t=32, σ_y=40 ksi or 87 ksi, and P/P_o=40%. Figure 2.19 shows the comparisons of experimental results (M-ϕ) and the Japanese and U.S. model predictions for the Japanese high strength CFT specimens with f'_c=17 ksi, b/t=32, σ_y=45 ksi or 113 ksi, and P/P_o=40%.

Kowalkowski and Varma (2003) developed similar comparison charts for all the high strength CFT beam-columns specimens tested in the U.S. (Varma et al. 2001) and Japan (Sakino et al. 2004) as part of the U.S.-Japan Program. They also compared the steel and concrete fiber σ–ε curves predicted by the U.S. and Japanese modeling approaches for the same high strength CFTs. The results from these comparisons indicated that:

- Significant differences exist between the fiber σ–ε curves in compression developed by the U.S. and Japanese modeling approaches.
- In spite of these differences, the fundamental P-M-ϕ responses predicted by the U.S. and Japanese analytical models for high strength CFTs generally compare favorably with each other and the experimental results.
- Hence, both the U.S. and Japanese fiber models along with approaches for developing the fiber σ–ε relationships were recommended for modeling high strength CFTs.
- The Japanese analytical approach for developing fiber σ–ε curves in compression was more useable to model and analyze CFTs made from conventional or high strength materials. However, the accuracy of these fiber σ–ε curves was questionable.
- The U.S. analytical approach for developing fiber σ–ε curves in compression was

based on no

development a

They have al

materials.

2.3 Experimer Connectior

In order to tak

between the beam a

research has been c

CFT column connec

Elremaily et al. 200

Tee (DST) moment

most efficient beam-

al. 1997. Peng 2(

experimental studies

stiffness and strength

mechanism in CFT m

In the current ana

frames, for example,

1966), the connection

However, recent resear

been connection, colu

tal story drift, respectiv

based on nonlinear mechanics and more accurate. However, they require the development and analysis of a 3D finite element model for each CFT being modeled. They have also not been validated for CFTs made from conventional strength materials.

2.3 Experimental and Analytical Research of Double Split-Tee Connections

In order to take advantage of the features of a CFT MRF system, the connection between the beam and the column members must be reliable and economical. Significant research has been conducted on the development of different moment resisting beam-to-CFT column connections, for example, Alostaz and Schneider 1996, Ricles et al. 1997, Elremaily et al. 2000, Peng 2001 among others. Based on these studies, the Double Split-Tee (DST) moment connection shown in Figure 2.20 has been identified as one of the most efficient beam-to-column connections for CFT moment resisting frames (Ricles et al. 1997, Peng 2001). These researchers have demonstrated through full-scale experimental studies that split-Tee moment connections can provide adequate cyclic joint stiffness and strength to develop the highly desirable weak beam-strong column failure mechanism in CFT moment resisting frames.

In the current analytical studies on the seismic behavior of CFT moment resisting frames, for example, Hajjar et al. (1998a, b), Elremaily (2000), and Zhang and Ricles (1996), the connections between the beams and the columns are assumed to be *rigid.* However, recent research on *CFT MRFs* indicates that for a CFT subassemblage, the beam, connection, column, and panel zone contribute 83.0%, 9.7%, 7.0%, and 0.3% to total story drift, respectively (Peng, S.-W., 2001). It means that the contribution of the

connection to th

2.3.1 Full-sca

Ricles et al.

inelastic cyclic t

beams in MRFs.

adequate cyclic j

with CFT colum

comparable to th

expensive interio

advantage of the b

The test setup

specimens. Spec. 4

used fillet welds to

compared to bolting

potential for bolt-ho

been observed for t

between beam flang

panel zone contribute

and energy dissipatio

in the beams.

connection to the total story drift should not be neglected.

2.3.1 Full-scale Inelastic Cyclic Test of Split-tee Connections

Ricles et al. (Ricles et al. 1997 and 2004, Peng 2001) conducted three full-scale inelastic cyclic tests on split-tee connections for CFT column-wide flange (WF) steel beams in MRFs. The experiment results indicate that split-tee connection can provide adequate cyclic joint stiffness and strength for a weak beam-strong column MRF system with CFT columns. Connections without beam shear tabs were found to perform comparable to the connection with shear tabs. Such connections avoid the use of expensive interior diaphragms to develop the beam's flexural capacity, by taking advantage of the bearing and compressive strength of the concrete.

The test setup is shown in Fig. 2.20. Four specimens were tested. Two of these specimens, Spec. 4 and 5, were all bolted (Fig. 2.21), while the other two, Spec. 6 and 7, used fillet welds to attach the tees to the beam (Fig. 2.22). Welding tees to beam flanges, compared to bolting, resulted in more stable hysteresis, because welding eliminated the potential for bolt-hole elongation in the beam flanges and pinched hysteresis, which had been observed for the tees bolted to the beams. As shown in Fig. 2.23, without slip between beam flanges and tee stems, for Spec. 6, the beam, connection, column, and panel zone contributed 83.0%, 9.7%, 7.0%, and 0.3% to total story drift, respectively. And energy dissipation occurred primarily in the beams, since plastic hinges was formed in the beams.

2.3.2 Steel Bear

Swanson (Swa

which bolting were

stub connection tes

Fig. 2.24. The instr

Swanson also deve

spring model for a

individual T-stub is

into springs represe

stub stem stiffness.

These component sp

as a whole. The co

TA-05 is shown in

provides a good defi

this spring model is

which fillet welding

2.3.3 Summary

The split-tee conn

the beam's flexural ca

of the concrete. The

tough full-scale expe

adequate cyclic joint st

2.3.2 Steel Beam to Steel Column T-stub Connections

Swanson (Swanson, 1999) proposed a procedure to design DST connections, in which bolting were used to connect beam flanges to tee stems, based on a series of tee stub connection test. The component test frame of the T-stub connection test is shown in Fig. 2.24. The instrumentation scheme of the T-stub connection test is shown in Fig. 2.25. Swanson also developed a spring model to predict stiffness of T-stub connection. The spring model for a T-stub connection is shown in Fig. 2.26. The spring model of an individual T-stub is shown in Fig. 2.27. As shown in Fig. 2.27, the T-stub was broken into springs representing 1) the tension bolt stiffness, 2) tee stub flange stiffness, 3) tee stub stem stiffness, 4) shear bolt stiffness, 5) bearing deformation and 6) connection slip. These component springs are then assembled into a single spring representing the T-stub as a whole. The comparison of predicted and experimental total deformation for T-stub TA-05 is shown in Fig. 2.28. As shown in Fig. 2.28, the monotonic stiffness model provides a good deformation prediction for the T-stubs tested. However, the limitation of this spring model is that it's iterative and cannot be applied to the DST connections in which fillet welding were used to connect beam flanges to tee stems.

2.3.3 Summary

The split-tee connections avoid the use of expensive interior diaphragms to develop the beam's flexural capacity, by taking advantage of the bearing and compressive strength of the concrete. The researchers (Ricles et al. 1997, Peng 2001) have demonstrated through full-scale experimental studies that split-Tee moment connections can provide adequate cyclic joint stiffness and strength to develop the highly desirable weak beam-

strong column fa

sake of reliabili

connections in thi

Swanson (199

which bolting we

model proposed b

connections in wh

Therefore, a new F

for the effects of

components of the c

connections in this r

2.4 Experimental

The high-strength

(σ_y=80 ksi, and f'_c=1

show that the effects

made from high stren

buckling of high streng

the seismic behavior of

2.4.1 Experimental

Green et al. (Green

seismic and three full-

strong column failure mechanism in CFT moment resisting frames. Therefore, for the sake of reliability and economic, the split-tee connections are used as moment connections in this research.

Swanson (1999) developed a spring model to predict stiffness of T-stub connection, in which bolting were used to connect beam flanges to tee stems. However, the spring model proposed by Swanson (1999) is iterative and cannot be applied to the DST connections in which fillet welding were used to connect beam flanges to tee stems. Therefore, a new FEM-based spring model for the connections, which implicitly account for the effects of pretensioning of the bolts and contacts and interactions among components of the connections, will be developed and used to model the double split-Tee connections in this research.

2.4 Experimental and Analytical Research on Steel Beams

The high-strength CFT MRFs in this research consist with high-strength CFT column (σ_y=80 ksi, and f'_c=15 ksi) and high-strength steel beam (σ_y = 50 ksi). Current research show that, the effects of these local degradations are especially significant for members made from high strength material, due to their susceptibilities to issues such as local buckling of high strength steel (Ricles, J. M., et al., 1993). Therefore, current research on the seismic behavior of high-strength steel beam are reviewed.

2.4.1 Experimental Research on Steel Beams

Green et al. (Green et al. 2001, 2002, Green 2000) conducted nine full-scale monotonic and three full-scale inelastic cyclic tests on steel beams fabricated from high

performance steel

flexural test specir

The typical section

for 3-point cyclic

tested. The section

Based on the

criteria to higher st

addition, the yield-

influence on ductil

that a limiting va

earthquake loading

2.4.2 Analytical

FEM models of

were developed usi

imperfections of eac

models. The local v

plate, with sides a (th

deflected shape of a

clamped along the ed

along a mid-line paralle

imperfection for web an

geometric imperfection

performance steel (HSLA-80) and typical mild steel (A36). The test setup for 3-point flexural test specimens is shown in Fig. 2.29. Nine monotonic specimens were tested. The typical sections for the flexural test specimens are shown Fig. 2.30. The test setup for 3-point cyclic test specimens is shown in Fig. 2.31. Three cyclic specimens were tested. The sections for the cyclic test specimens are shown Fig. 2.32.

Based on the experimental research, the extrapolation of current US compactness criteria to higher strength steel was shown to over-estimate flexural ductility capacity. In addition, the yield-to-tensile strength ratio of the material was shown to have a significant influence on ductility and energy dissipation capacity under cyclic loading, suggesting that a limiting value should be used in order to ensure acceptable behavior under earthquake loading (Green et al. 2001).

2.4.2 Analytical Model of Steel Beams

FEM models of the inelastic behavior of the monotonic test specimens, Spec. 1 to 9, were developed using the finite element program ABAQUS. The initial geometric imperfections of each monotonic test specimens were taken into account in the FEM models. The local web imperfection has the deflected shape of a clamped rectangular plate, with sides a (the imperfection length) and b. The local flange imperfection has the deflected shape of a rectangular plate with sides a (the imperfection length) and c, clamped along the edges parallel to z, free along the edges parallel to x, and clamped along a mid-line parallel to x. Equation 2.12 and 2.13 were used to specify the geometric imperfection for web and flange, respectively, in which a_1 and b_1 are the amplitude of the geometric imperfection of web and flange, respectively (Green et al., 2002):

$\delta_{web} = a$

$\delta_{flange} = b$

For the web im

web plate, $x=0$ at n

the location of the

determined by setti

out-of-flatness limi

longitudinal or dept

For the flange i

the flange plate, x =

defines the location

is determined by set

al., 2002).

The full depth w

in Fig. 2.33 and 2.3

in FEM model is sh

model with both f

compression flange.

Specimen 3 (Green, 20

Two types of shell

ed in the FEM analy

$$\delta_{web} = a_{11}\left(1-\cos\frac{2\pi(x-x_w)}{a}\right)\left(1-\cos\frac{2\pi y}{b}\right) \tag{2.13}$$

$$\delta_{flange} = b_{11}\left(1-\cos\frac{2\pi(x-x_f)}{a}\right)\left(1-\cos\frac{2\pi z}{c}\right) \tag{2.14}$$

For the web imperfection, x and y are the longitudinal and vertical coordinates of the web plate, $x=0$ at mid-span, $y=0$ at the junction of the web and the flange, and x_w defines the location of the imperfection along the length of the web. The coefficient a_{11} is determined by setting the maximum amplitude of the imperfection to be just within the out-of-flatness limit of the AWS Structural Welding Code, which is the larger of the longitudinal or depth dimensions of the web plate divided by 150.

For the flange imperfection, x and z are the longitudinal and transverse coordinates of the flange plate, $x=0$ at mid-span, $z=0$ at the junction of the web and the flange, and x_f defines the location of the imperfection along the length of the flange. The coefficient b_{11} is determined by setting the maximum amplitude of the imperfection to $1.6mm$ (Green et al., 2002).

The full depth web imperfection for $h_c/t_w=53$ and 29 used in FEM model are shown in Fig. 2.33 and 2.34, respectively. The full width flange imperfection for $b_f/2t_f=9$ used in FEM model is shown in Fig. 2.35 (Green, 2000). As shown in Fig. 2.36, the FEM model with both flange and web imperfections captures the local buckling of compression flange, necking of the tension flange and web local buckling of Test Specimen 3 (Green, 2000).

Two types of shell elements in ABAQUS, the S8R5 and the S4 shell elements, were used in the FEM analysis. The S8R5 element is an eight-node doubly curved thin shell

element with red

strain, large-rotat

this application w

web buckling afte

(Green et al., 2002

The S8R5 ele

The S4 element i

formulated for larg

thickness changes

and has the same

Simpson's Rule m

transverse shear de

finite-strain analysis

et al., 2002). As sh

using the S4 elemen

analytical model usin

2.4.3 Summary

FEM models of t

strength steel beams w

strength steel (Green et

investigate the seismic

ion rather than monoton

element with reduced integration using five DOF per node. It's a quadrilateral small-strain, large-rotation element. It was found that the S8R5 was not appropriate for use in this application where the response of flexural members is controlled by local flange and web buckling after the flange and web have reached significant levels of inelastic strain (Green et al., 2002).

The S8R5 element was subsequently replaced with the S4 element in the models. The S4 element is a four-node, doubly curved general-purpose shell element that is formulated for large-strain analysis. It's a quadrilateral finite-strain element that includes thickness changes as a function of in-plane deformation, has six active DOF per node, and has the same default values of five integration points through the thickness and Simpson's Rule method of integration as the S8R5 element. The S4 element allows transverse shear deformation and changes in thickness to occur making it suitable for finite-strain analysis involving materials with a nonzero effective Poisson's ratio (Green et al., 2002). As shown in Fig. 2.37, the analytical moment-average end rotation results using the S4 element compares favorably well with the experimental results, while the analytical model using the S8R5 element gives a poor prediction (Green, 2000).

2.4.3 Summary

FEM models of the inelastic behavior of the monotonic test specimens of high strength steel beams were developed, accounting for the effects of local buckling of high strength steel (Green et al. 2001). However, the analytical model of steel beam used to investigate the seismic behavior of high-strength CFT MRFs should be based on cyclic tests rather than monotonic test. Therefore, a new analytical model for steel beam, which

implicitly accoun

will be developed

cyclic specimens

2.5 Pushover A

In order to use

strength CFT MRF

research on the sei

columns, existing

frames are reviewed

performance of mo

investigate the overa

2.5.1 Pushover A

2.5.1.1 Analytical

Ricles et al. (Ricl

considering stiffness

history analysis of M

strength steel strands th

Contact stresses develop

prestressing force.

resistance. Friction at th

strands run through the c

implicitly account for the effects of inelastic local buckling of beam flange and beam web, will be developed in this research and will be compared with the experimental results of cyclic specimens of Green et al. (2002).

2.5 Pushover Analysis of Moment Resisting Frames

In order to use the detailed analytical model to capture the seismic response of High-strength CFT MRFs more accurately, in addition to current experimental and analytical research on the seismic behavior of steel structures and composite structures with CFT columns, existing methods to evaluate the seismic performance of moment resisting frames are reviewed. Based on the reviews of the current methods to evaluate the seismic performance of moment resisting frames, suitable evaluation methods will be chose to investigate the overall seismic behavior of high strength CFT MRFs in this research.

2.5.1 Pushover Analysis of Steel Moment Resisting Frames

2.5.1.1 Analytical Model for Postensioned Connections

Ricles et al. (Ricles et al., 2001; Garlock et al., 2000) proposed an analytical model considering stiffness of postensioned (PT) connections for pushover analysis and time history analysis of MRFs. As shown in Fig. 2.38(b), the PT connection uses high strength steel strands that are posttensioned after bolted top and seat angles are installed. Contact stresses develop at the interface of the beam and column under the action of the posttensioning force. The prestressed contact surface provides significant moment resistance. Friction at the contact surface provides shear resistance. The posttensioning strands run through the column and are anchored outside the connection region. Shim

plates are used be

with additional ste

Elements in th

develop a model fo

Fig. 2.39(a), each

properties are con

Within a segment,

characterized by a

distance from the

relationships are m

behavior of the cr

behavior over the cr

Fig. 2.40 shows

fibers of the beam e

and B_3 in the right b

to model gap openin

angles of PT conne

analysis of the angle

slaved to master nod

degrees of freedom o

corresponding master

idealized rigid link be

relation is a function

plates are used between the end of the beam and the column face for construction fit up, with additional steel plates used to reinforce the beam flanges (Ricles et al., 2001).

Elements in the computer program DRAIN-2DX (Prakesh et al., 1993) were used to develop a model for PT connections and the associated beams and columns. As shown in Fig. 2.39(a), each fiber element is divided into a number of segments. The cross section properties are constant within a segment, but can vary from one segment to another. Within a segment, fibers model the cross section, as shown in Fig. 2.39(a). Each fiber is characterized by a uniaxial material stress-strain relationship, a cross section area, and a distance from the longitudinal reference axis of the member. The stress-strain relationships are multilinear, as shown in Figs. 2.39 (b and c). The force-deformation behavior of the cross section is determined by integration of the fiber stress-strain behavior over the cross section (Ricles et al., 2001).

Fig. 2.40 shows the model for an interior joint region with a PT connection. The fibers of the beam end segments between nodes A_M and B_S in the left beam and nodes C_M and B_S in the right beam are assigned the stress-strain relationship shown in Fig. 2.40(b) to model gap opening behavior of PT connections. Parallel springs are used to model the angles of PT connections. The properties of these springs are obtained from fiber analysis of the angles of PT connections. The nodes identified as A_S, B_S, and C_S are slaved to master nodes A_M, B_M, and C_M, respectively. The translational and rotational degrees of freedom of a slaved node are constrained to the degrees of freedom of the corresponding master node. The translation of a slaved node is constrained by a simulated rigid link between the slaved node and the master node; thus, the slaved node translation is a function of the translation and rotation of the master node as well as the

distance between

translations as ma

independent of no

placing a rotation

the spring models

Each angle in

implemented in th

behavior of the ang

in Fig. 2.40(a), eac

A_S or C_S. Elongati

the shear force in th

of the two parallel

(Ricles et al., 2001).

As shown in Fig

displacement (H-Δ)

analytical model was

details on behavior o

time history analyses

2.5.1.2 Summary

In the current analy

series, for example, H

[illegible] the connections

distance between the two nodes. Slaved node E_S is constrained to have the same translations as master node B_M; however, the rotational degree of freedom of node E_S is independent of node B_M. The flexibility of the column panel zone in shear is modeled by placing a rotational spring between nodes B_M and E_S. The moment-rotation behavior of the spring models the shear stiffness of the panel zone (Ricles et al., 2001).

Each angle in the PT connection is modeled as two parallel nonlinear springs that are implemented in the model using DRAIN-2DX truss elements. The springs model the behavior of the angle when gap opening occurs at the beam-column interface. As shown in Fig. 2.40(a), each spring is connected to the column at node D and to the beam at node A_S or C_S. Elongation or shortening of the springs results in forces that are equivalent to the shear force in the vertical leg of the angle. The combined force-deformation behavior of the two parallel bilinear springs produces a trilinear force-deformation relationship (Ricles et al., 2001).

As shown in Fig. 2.41, the model provided reasonable predictions of the lateral load-displacement (H-Δ) behavior for the test of subassemblages with PT connections. The analytical model was used for a parametric analytical study of the effects of connection details on behavior of interior connection subassemblages. It was also used for dynamic time history analyses of a six-story steel MRF with PT connections.

2.5.1.2 Summary

In the current analytical studies on the seismic behavior of CFT moment resisting frames, for example, Hajjar et al. (1998a, b), Elremaily (2000), and Zhang and Ricles (1996), the connections between the beams and the columns are assumed to be *rigid.*

However, recent

beam, connection

total story drift, re

connection to the t

model for the high

strength and stiffne

similar to the analy

by Ricles et al. (200

in this research.

2.5.2 Adaptive S

2.5.2.1 FEMA an

One major draw

performance-based d

from mid and upper s

to use the detailed ana

MRFs more accurate

investigated. Evaluati

mid and upper story m

investigate the seismic

In the non-linear st

seismic demands are co

systematically increasing

However, recent research on *CFT MRFs* indicate that, for a CFT subassemblage, the beam, connection, column, and panel zone contributed 83.0%, 9.7%, 7.0%, and 0.3% to total story drift, respectively (Peng, S.-W., 2001). It means that the contribution of the connection to the total story drift should not be neglected. Therefore, a new fiber-based model for the high-strength CFT MRF, which accounts for the combined effects of the strength and stiffness degradation of the members and connections simultaneously and is similar to the analytical model for steel MRF with postensioned connections developed by Ricles et al. (2001), will be developed and used to model the high-strength CFT MRF in this research.

2.5.2 Adaptive Spectra-Based Pushover Procedure

2.5.2.1 FEMA and Adaptive Pushover Spectra-Based Procedures

One major drawback of the previous research, in the design evaluation phase of performance-based design, is that they do not consider potential failure modes that stem from mid and upper story mechanisms caused by the influence of higher modes. In order to use the detailed analytical model to capture the seismic response of High-strength CFT MRFs more accurately, existing methods to evaluate the seismic performance are investigated. Evaluation methods that can capture potential failure modes that stem from mid and upper story mechanisms caused by the influence of higher modes are used to investigate the seismic behavior of CFT MRFs in this research.

In the non-linear static procedure (NSP), or pushover analysis in FEMA 356, the seismic demands are computed by non-linear static analysis of the structure subjected to monotonically increasing lateral forces with an invariant height-wise distribution, until a

predetermined ta

displacement are

fundamental mod

(Chopra, A. K., et a

The stiffness

yielding. Previous

approximate assum

and medium-rise str

height of the structur

For almost all

significant degrees

contributions of highe

of structural yielding

investigate the seismic

the presence of higher

based pushover proced

similar to the modal

responses are based on

2000):

(1) Compute the

motion to be

accelerations a

predetermined target displacement is reached. Both the force distribution and target displacement are based on the assumption that the response is controlled by the fundamental mode and the mode shape remains unchanged after the structure yields (Chopra, A. K., et al., 2002).

The stiffness of structural component and the overall structure are revised after yielding. Previous studies show that, using FEMA pushover procedures with theses two approximate assumptions results in satisfactory predictions of seismic demands for low- and medium-rise structures, provided the inelastic action is distributed throughout the height of the structure (Krawinkler, H., et al., 1998).

For almost all mid- and high-rise structures, high mode effects are present to significant degrees. But none of the invariant force distributions can account for the contributions of higher modes to response, or for a redistribution of inertia forces because of structural yielding (Krawinkler, H., et al., 1998). In order to use pushover analysis to investigate the seismic behavior of the moment resisting frames with reliability even in the presence of higher modes, Gupta and Kunnath (2000) proposed an adaptive spectra-based pushover procedure. The adaptive spectra-based pushover procedure used for was similar to the modal combination procedure of FEMA 356, except that the modal responses are based on the current stiffness state of the structure (Gupta and Kunnath, 2000):

(1) Compute the damped elastic response spectrum for the site-specific ground motion to be used for evaluation. This is required to obtain modal spectral accelerations at various steps.

(2) Perfor
state (1
the st
partici
(3) Compu
structu
least 9(
(4) Perform
comput
forces
member
(5) Repeat t

2.5.2.2. Validati

Five different
designed in order to
2.42) for all building
longitudinal direction
between RC beams th
consisted of four Sp
direction and six SMF
assumed throughout.
compressive strength (f

(2) Perform an eigenvalue analysis of the structural model at the current stiffness state (for the first step this will be the initial stiffness) of the structure. Using the story masses and the computed eigenvalues, determine the modal participation factors.

(3) Compute the story shear distribution by combining modal responses of the structure at the current stiffness state, including sufficient modes to capture at least 90% of the total building mass.

(4) Perform a static pushover analysis of the structure using the story forces computed in the previous step. At the end of every step, compare the member forces with their yield values. If any member has yielded, re-compute the member and global stiffness matrices and return to step 2.

(5) Repeat the process until the global drift exceeds the specified limit.

2.5.2.2. Validation of Adaptive Spectra-Based Pushover Procedure

Five different "office" buildings with heights of 4, 8, 12, 16, and 20 stories were designed in order to cover a broad range of fundamental periods. The assumed plan (Fig. 2.42) for all buildings comprised of 24-ft bays, 3 in the transverse direction and 5 in the longitudinal direction. The gravity load resisting system consisted of RC slabs spanning between RC beams that are supported on RC columns. The lateral force resisting system consisted of four Special Moment Resisting Frames (SMRFs) in the longitudinal direction and six SMRFs in the transverse direction. A story height of 12 feet was assumed throughout. All concrete was assumed normal-weight with a specified compressive strength (f_c') ranging from 4 to 6 ksi. The yield stress of all reinforcement

was assumed as (

effects were igno

strong column-we

detailed evaluation

In order to de

procedure to repr

analysis, and to sh

or modal load p

mechanisms, tradi

analysis as well as

The time histories

1997) with 10% d

hereafter) for Los A

basic SAC 10% 5

acceleration at the

important consider

(Gupta and Kunnath

Fig. 2.43 shows

MRFs respectively.

prominent were cons

Uniform correspondi

Rubber analysis usin

Scaled and uniform l

was assumed as 60 ksi. All columns were assumed fixed at the base. P-Δ and torsional effects were ignored. All buildings were designed to satisfy the drift criterion and the strong column-weak beam philosophy. A typical longitudinal frame was considered for detailed evaluation (Gupta and Kunnath, 2000).

In order to demonstrate the effectiveness of the adaptive spectra-based pushover procedure to reproduce the overall behavior predicted by a nonlinear time-history analysis, and to show the inability of traditional pushover procedures using fixed uniform or modal load patterns to capture either high mode effects or potential failure mechanisms, traditional pushover analysis and the adaptive spectra-based pushover analysis as well as the time-history analysis were performed for each prototype structure. The time histories developed as part of the SAC Phase-2 steel project (Somerville et al., 1997) with 10% probabilities of being exceeded in 50 years (referred to as 10%/50 hereafter) for Los Angeles area were utilized in the evaluation study. For each frame, the basic SAC 10%/50 records were scaled to the median (geometric mean) spectral acceleration at the fundamental frequency of the respective structure. An extremely important consideration behind this scaling was to study the effect of higher modes (Gupta and Kunnath, 2000).

Fig. 2.43 shows inter-story drift profiles for selected records for various multistory MRFs respectively. Only those drift profiles in which the effects of higher modes is most prominent were considered. The curves marked Time-history, Proposed, FEMA-273 and Uniform corresponded to the inter-story drift profiles obtained from time-history analysis, pushover analysis using the adaptive spectra-based pushover procedure, FEMA-273 load pattern, and uniform load pattern, at a roof displacement equal to that predicted by

nonlinear time-hi

period increase, i

become more pro

time-history analy

spectra-based push

Kunnath, 2000).

2.5.2.3 Moment

It is common pra

the remaining levels.

the first story level o

discontinuity. The d

However, the input gr

the modified frames.

study. Fig. 2.44 shows

the introduction of sof

compared to the same

2.44, neither the uniform

potential hinging and su

spectra-based pushover

Gupta and Kunna

nonlinear time-history analysis, respectively. As shown in Fig. 2.43, as the building period increase, i.e., as the number of stories increase, and the effect of higher modes become more pronounce, the difference between the response predicted by nonlinear time-history analysis and FEMA/uniform pushover analyses increases. The adaptive spectra-based pushover method, however, predicts response reasonably well (Gupta and Kunnath, 2000).

2.5.2.3 Moment Frame Structures with Stiffness Discontinuity

It is common practice to design structures with the first story height much taller than the remaining levels. To evaluate the potential effects of a "soft" first story, the height of the first story level of the regular frames was increased by 100% to create a stiffness discontinuity. The design of frames was not revised to incorporate the soft story. However, the input ground motions were scaled to reflect the new fundamental period of the modified frames. Only 16 and 20-story frames were considered in this phase of the study. Fig. 2.44 shows the inter-story drift profiles for a typical earthquake. As expected, the introduction of soft first story results in much higher drifts at the lowest level as compared to the same for the regular frames. In the upper levels, as evidenced in Fig. 2.44, neither the uniform load pattern nor the FEMA-modal pattern is able to predict the potential hinging and subsequent drift accumulations. It is also clear that the adaptive spectra-based pushover method captures all significant aspects of the drift profile at all levels (Gupta and Kunnath, 2000).

2.5.2.4 Effects

If higher mod
would have iden
because the spec
participation of hi
motions would be
analyses, at a roo
analysis of this fram
curves marked *1-mo*
obtained from the
modes were consider
FEMA-modal load p
nonlinear time-histor
to that for the uniform
to structures in whi
considered, the drift p
obtained for the nonli
ignoring the higher m
demands (Gupta and Ku

2.5.3 Summary

In the non-linear sta
the seismic deman

2.5.2.4 Effects of Higher Modes

If higher modes were ignored in the adaptive modal pushover procedure, each frame would have identical response for any ground motion corresponding to that frame, because the spectral acceleration at the fundamental period is identical. Due to the participation of higher modes, however, the response of a frame for different ground motions would be different. The drift profiles for a 20-story frame obtained from various analyses, at a roof displacement equal to that obtained from nonlinear time-history analysis of this frame subjected to the LA14 record, are compared in Fig. 2.45. The four curves marked *1-mode*, *2-modes*, *3-modes*, and *all-modes* correspond to the drift profiles obtained from the adaptive spectra-based pushover analysis in which one or several modes were considered in the analyses. The drift profiles obtained by using uniform and FEMA-modal load patterns were also shown for comparison with that obtained from nonlinear time-history analysis. The curve for only the fundamental mode is very similar to that for the uniform load pattern indicating that uniform load pattern may be applicable to structures in which higher modes are not significant. As additional modes are considered, the drift profiles for the adaptive modal pushover procedure approach those obtained for the nonlinear time-history analysis. The above discussion indicates that ignoring the higher modes may result in highly inaccurate estimates of deformation demands (Gupta and Kunnath, 2000).

2.5.3 Summary

In the non-linear static procedures (NSP), or pushover analysis procedures of FEMA 356, the seismic demands were computed by non-linear static analysis of the structure

subjected to m

distribution. unt

distribution and

controlled by th

structure yields (

For almost a

significant degre

contributions of h

of structural yiel

seismic response

analysis should be

procedures in this

2.6 Time-Histor

Estimation of i

moment resisting f

great damage in bo

design of CFT MRF

necessary will. bring

an individual story di

the first-order story sh

The static pushov

procedures. by pushing t

subjected to monotonically increasing lateral forces with an invariant height-wise distribution, until a predetermined target displacement is reached. Both the force distribution and target displacement are based on the assumption that, the response is controlled by the fundamental mode and the mode shape remains unchanged after the structure yields (Chopra, A. K., et al., 2002).

For almost all mid- and high-rise structures, high mode effects are present to significant degrees. But none of the invariant force distributions can account for the contributions of higher modes to response, or for a redistribution of inertia forces because of structural yielding (Krawinkler, H., et al., 1998). Hence, in order to capture the seismic response of *High-strength CFT MRFs* more accurately, adaptive pushover analysis should be performed in addition to static pushover analysis following FEMA 356 procedures in this research.

2.6 Time-History Analysis of Moment Resisting Frames

Estimation of inter-story drift demands is of great significance in seismic design of moment resisting frames, because of the exceedence of allowable limits would cause great damage in both structural and non-structural components. Another concern in the design of CFT MRFs is to avoid excessive second-order P-Δ effects, which may, but not necessary will, bring the structure close to incremental collapse. Collapse may occur if an individual story displaces sufficiently so that the second-order P-Δ effects fully offset the first-order story shear resistance and instability occurs (Gupta and Krawinkler, 2000a).

The static pushover analysis can be used to evaluate the seismic performance of the structures, by pushing the structure under a predetermined or adaptive load pattern to a

target displacem

in the design ea

displacement to

motion can be p

first mode and th

Another draw

dynamic story dr

on account of th

mode effects. P-

2000b). Hence,

more accurately,

research. The exi

reviewed. Suitabl

capture potential f

the influence of hi

in this research.

2.6.1 Ground m

The results of ti

MRFs, but also on t

motion parameters th

amplitude, frequency

the parameters of ea

target displacement, which represent the maximum demands experienced by the structure in the design earthquake, and comparing the deformation demands computed at the target displacement to available capacities. The roof displacement caused by the design ground motion can be predicted with reasonable accuracy, provided that it is controlled by the first mode and the P-Δ sensitive range is not entered (Gupta and Krawinkler, 2000b).

Another drawback of the pushover analysis is that it is difficult to predict maximum dynamic story drift demands over the height of the structure as a function of the roof drift, on account of the dependence of the relationship on a multitude of factors, e.g., higher mode effects, P-Δ effects and characteristics of ground motions (Gupta and Krawinkler, 2000b). Hence, in order to capture the seismic response of *High-strength CFT MRFs* more accurately, time history analyses are used in the design evaluation phase of this research. The existing ground motions database and time history evaluation methods are reviewed. Suitable ground motion database and time-history evaluation methods that can capture potential failure modes that stem from mid and upper story mechanics caused by the influence of higher modes are used to investigate the seismic behavior of CFT MRFs in this research.

2.6.1 Ground motion Time Histories for SAC Phase 2 Steel Project

The results of time-history analysis depend on not only on the characteristics of the MRFs, but also on the characteristic of the selected ground motion. Among the ground motion parameters that can affect the structural response, there are three key parameters: amplitude, frequency content and duration, where frequency content and duration are the main parameters of earthquakes. The seismic response of structures is very sensitive to

the frequency

Somerville

different seism

California (Zor

to provide resp

studies, and tria

are provided at

each of these thr

50% in 50 years

10% in 50 years

seismic zone 4 co

2.6.2 Scaling o

The nonlinear

ground motion an

response, which c

spectrum, an appr

realistic time histo

appropriate for th

characteristics of t

provide a statistical

ensities that are re

characteristics (Some

the frequency content and duration of different ground motions (Kramer, 1996).

Somerville et al. (1997) developed ground motions in three cities representing three different seismic zones as defined by the Uniform Building Code – Los Angeles, California (Zone 4); Seattle, Washington (Zone 3); and Boston, Massachusetts (Zone 2); to provide response spectra and time histories for use in topical investigations, case studies, and trial applications in the SAC Phase 2 Steel Project. Suites of time histories are provided at two probabilities of occurrence (2% in 50 years and 10% in 50 years) in each of these three locations for firm soil conditions. Time histories are also provided for 50% in 50 years for Los Angeles. Time histories for soft soil profiles are provided for 10% in 50 years in all three locations. Near fault time histories are also provided for seismic zone 4 conditions (Somerville et al., 1997).

2.6.2 Scaling of Time Histories to Target Spectra

The nonlinear response of structures is strongly dependent on the phasing of the input ground motion and on the detailed structure of its spectrum. Unlike the case of linear response, which can often be obtained from a single time history matched to a target spectrum, an appropriate measure of nonlinear response requires the use of multiple realistic time histories having phasing and response spectral peaks and troughs that are appropriate for the magnitude, distance, site conditions, and wave propagation characteristics of the region. The purpose of providing suites of time histories is to provide a statistical sample of this variability in phasing and spectra through a set of time histories that are realistic not only in their average properties but in their individual characteristics (Somerville et al., 1997).

The 2%, 10% and 50% probability of exceedance in 50 years correspond to the return periods of 2,475, 475 and 72 years, respectively. All the three sets of the time histories are for stiff soil sites and match (in the mean) the target response spectra defined in the 1994 NEHRP provisions, i.e., on the average, their spectral values match with a least-square error fit to the USGS mapped values at 0.3, 1.0 and 2.0 s (USGS 1996) and a predicted value at 4.0 s, for the appropriate return period. These periods (0.3, 1.0, 2.0 and 4.0 s) are selected because they cover the range of interest for the flexible steel structures. The weights used are 0.1, 0.3, 0.3 and 0.3 for periods of 0.3, 1.0, 2.0 and 4.0 seconds, respectively (Somerville et al., 1997), i.e., the scale factor, *SF*, is:

$$SF = \left(\frac{S_{target,0.3}}{S_{GM,0.3}} \right)^{0.1} \left(\frac{S_{target,1.0}}{S_{GM,1.0}} \bullet \frac{S_{target,2.0}}{S_{GM,2.0}} \bullet \frac{S_{target,4.0}}{S_{GM,4.0}} \right)^{0.3} \qquad (2.15)$$

where $S_{target,\,T}$ and $S_{GM,\,T}$ are the spectral values of the target spectrum and the ground motion spectrum being scaled, respectively, for a period equal to T in seconds.

2.6.3 Dynamic *P-Δ* Effects for Flexible Inelastic Steel Structures

Collapse prevention is a fundamental objective of earthquake resisting design. Collapse may occur if an individual story displaces sufficiently so that the second-order P-Δ effects fully offset the first-order story shear resistance and instability occurs. It is one of the major concerns in seismic design to avoid excessive second-order P-Δ effects, which may, but not necessary will, bring the structure close to incremental collapse (Gupta and Krawinkler, 2000a).

Gupta and Krawinkler (2000a) studied two structures represent a 20-story building designed for Los Angeles conditions (Seismic Zone 4), and a 3-story building designed

for Seattle conditions (Seismic Zone 3). Both designs conformed to Uniform Building Code (UBC) requirements (1994). Plane views and elevations of the two buildings were shown in Fig. 2.46. Both structures have perimeter moment frames that were designed to resist all lateral loads. The interior simple framing was designed to resist only tributary gravity effects (Gupta and Krawinkler, 2000a).

2.6.3.1 Case Study 1: Los Angeles 20-Story Structure

The values of the stability coefficient for the 20-story structure designed for Los Angeles condition is found to be <0.10 for all stories. Thus, according to present U.S. codes no special consideration needs to be given to P-Δ effects in the seismic design of this structure. The behavior of this structure under lateral loads and under specific earthquake ground motions was first using a simple centerline model of the bare moment resisting fame (model M1) and then using various improved analytical models. Inelastic behavior was permitted only at the ends of elements and was represented by bilinear moment-rotation hysteretic models with 3% strain hardening (Gupta and Krawinkler, 2000a).

2.6.3.1.1 Static Response of Model M1

The normalized base shear (base shear V over seismic weight W) versus roof drift angle (roof displacement over structure height) response for model M1, with and without P-Δ effects being considered, is shown in Fig. 2.47. The model in which P-Δ effects are not considered (model M1-NPD) has a hardening post-yield stiffness, which is maintained even at large drifts. The elastic stiffness of the model in which *P-Δ* effects are

considered (model M1) is only slightly smaller than for model M1-NPD because of the small value of θ. The post-yield global response of model M1 differs significantly from that of model M1-NPD, exhibiting a short "yield" (constant strength) plateau until a roof drift of about 0.015, followed by a rapid decrease in lateral load resistance represented by the negative slope of the curve. The structure reaches a state of zero lateral resistance at the relatively small roof drift angle of 0.04 (Gupta and Krawinkler, 2000a).

The response of the lowest eight stories of the structure, in terms of normalized story shear versus story drift angle, is shown in Fig. 2.48. The bottom five stories exhibit similar negative post-yield stiffness values, which are approximately equal to -6% of the elastic story stiffness. This implies that these stories are involved in a mechanism motion. The negative post-yield stiffness arises because of the *P-Δ* "shear", which counteracts the strain hardening that would exist without *P-Δ* effects. If the story drift in an earthquake does not exceed the value associated with the onset of negative stiffness, then stable response is expected to occur. If this limiting value is exceeded, ratcheting may occur, and the potential for dynamic instability exists (Gupta and Krawinkler, 2000a).

The story shear versus story drift response curves presented in Fig. 2.48 indicate that the bottom stories reach a state of dynamic instability (zero lateral resistance) at a story drift of about 0.14 - 0.16. Stories 6 through 8 (and stories 9 through 20) experience unloading as the structure is pushed to larger displacements (beyond 0.015 global drift), and the lateral loads applied to the structure have to be reduced to accommodate the increasing second-order *P-Δ* effects in the lower stories. Thus, as the roof displacement increases, the drift in all but the lowest five stories decreases (Gupta and Krawinkler, 2000a).

2.6.3.1.2 Dynamic Response of Model M1

The observation that the global pushover curve attains a negative stiffness at a roof drift of about 0.015 provides an indication that dynamic instability is a distinct possibility under severe ground motions. When this frame model was subjected to a set of 20 very severe ground motions (Somerville et al., 1997), potential instability problems were noted under two near-fault ground motions that have pulse-like characteristics. Dynamic instability did occur when the M1 model was subjected to the LA30 (Tabas) record, and story drift angles exceeding 0.13, which is also close to dynamic instability, were obtained when the simulated record LA36 was used as input (Gupta and Krawinkler, 2000a).

These dynamic analysis results indicate that a collapse potential exists for the analytical model M1, which is very simple representation of a complex 3D structure. If the model were representative of the structure, the analysis would point out an alarming problem since the structure was designed in accordance with recent code requirements and has considerable over-strength, the design base shear at the allowable stress design level is 0.03W, whereas the strength at the global yielding is about 0.075 W (Fig. 2.40).

2.6.3.1.3 Static and Dynamic Response of Improved Models

The bare frame centerline model M1, though commonly used in engineering analysis, is often a very approximate representation of the structural components that contribute to lateral strength and stiffness. Moreover, a centerline model is often a mediocre representation of the bare moment resisting frame. Steel moment frames with fully restrained connections consist of beams that span between column faces, columns that

extend over the clear height of a story, and panel zones that define the intersection of beams and columns and often yield in shear before beams and columns attain their bending strength. The frame analysis model that incorporates panel zones is denoted as model M2. There are many other contributions to lateral strength and stiffness, some of which can be evaluated accurately and some whose contributions can only be estimated. The following analysis models were utilized to evaluate the effects of different modeling assumptions on the dynamic response (Gupta and Krawinkler, 1999):

- M1 – basic centerline model of bare moment resisting frame
- M2 –bare moment resisting frame model incorporating panel zone strength and stiffness
- M2A –the M2 model with the best estimate of all other "dependable" contributions (gravity columns, orthogonal frame columns, shear connections, floor slabs)
- M1-NPD – the M1 model without P-Δ effects
- M1E – elastic M1 model with P-Δ effects
- M1E-NPD – elastic M1 model without P-Δ effects

Base shear versus roof drift diagrams for models M1, M2, and M2A are shown in Fig. 2.49. The more realistic bare frame model M2 shows improved behavior compared with the M1 model because maximum moments in beams and columns are computed at panel zone boundaries rather than connection centerlines, and the shear strength and stiffness of the panel zones is relatively large. Adding all "reliable" contributions to the M2 model (model M2A) increases the strength further, widens the strength plateau considerably, and increase the global drift at which dynamic instability occurs to a value of about 0.07. Proportional effects are observed in the responses of individual stories. For instance, the

story drift angle at which dynamic instability occurs increases from 0.16 for the M1 model to 0.235 for the M2A model.

A picture of the maximum story drifts in all stories and for all models subjected to the ground motion record LA30 (*Tabas*) is presented in Fig. 2.50. No results are shown for model M1 because collapse occurred. For model M2 the story drift angles in the bottom stories are as high as 0.15, which is outside the range of acceptable results. However, for the most realistic model (M2A) the story drift angles have decreased drastically, with the maximum value being 0.051. Thus, this realistic mode is far from P-Δ collapse.

Great variations in story drift patterns are evident from Fig. 2.50, depending on modeling assumptions. All inelastic models show the common pattern of large drifts in the bottom stories and small drifts in the top stories. P-Δ effects have much to do with this pattern, but the characteristics of the pulse-type ground motion are also responsible for this pattern. It is important to note that the story drift pattern changes drastically if an elastic time history analysis is performed (M1E and M1E-NPD). It must be concluded that elastic analysis is an inadequate tool for capturing P-Δ sensitive response characteristics (Gupta and Krawinkler, 2000a).

To evaluate the sensitivity of results to ground-motion variations, all analyses are repeated with the simulated ground-motion record LA36. This ground motion also exhibits clear pulse-type characteristics. The results for maximum story drifts are presented in Fig. 2.51. The patterns are mostly similar to those for the LA30 (*Tabas*) ground motion, but there are also important differences. In this case the centerline model M1 did not collapse, and the maximum story drift angles for this model are smaller than those for model M2 subjected to the Tabas record. However, not very much is gained by

using the realistic model M2A for the simulated record, and the maximum drift angles for this record are considerably larger than those for the Tabas record (0.105 versus 0.051). The conclusion is that the simulated record brings this 20-story building closer to P-Δ collapse than the Tabas record, even though the opposite conclusion would have been drawn from the centerline model M1. One reason for the small improvement from model M1 to model M2A is that for this particular record the first mode spectral displacement does not change much when the period changes from 4.0 s (for model M1) to 3.5 s (for model M2A).

2.6.3.2 Case Study 2: Seattle 3-Story Structure

The 3-story structure designed for Seattle conditions (see Fig. 2.39 for plan and elevation) also is prone to large P-Δ effects because it may attain a negative mechanism stiffness if 3% element strain hardening is assumed. The global pushover stiffness becomes negative at a global drift of about 0.020, 0.045, and 0.065 for models M1, M2, and M2A, respectively, as can be seen in Fig. 2.52. For model M2, sharing of plastification between panel zones and beams causes the negative post-yield stiffness to be reached at a much higher global drift value than that for model M1. The Seattle 3-story structural models are very flexible (first mode period for models M1 and M2 is 1.36 s), and the P-Δ effects result in a negative stiffness of about -3% once a mechanism has formed (stability coefficient is approximately 0.06).

The set of ground-motion records, which was representative of a 2% probability of being exceeded in 50 years (Somerville et al., 1997) and was used to evaluate this structure, did contain records that drive the models of the structure into the negative post-

yield stiffness region. The long strong motion duration of these records, which represent shaking in subduction zone earthquake, renders the Seattle structure susceptible to ratcheting once the range of negative stiffness is attained. A typical example is shown in Fig. 2.53.

In the M1 model, which attains a negative stiffness at a relatively small roof drift, the first significant pulse of record SE27 drives the structure far into the range of negative stiffness, no displacement recovery occurs, and the structure ratchets in one direction for the full duration of motion with each cycle causing a relatively small increase in displacement (see model M1 in Fig. 2.53). Clearly, a roof drift angle of 0.30 is only a by-product of analysis; deterioration would have occurred at much smaller roof drift angles, and the building would have collapsed in a P-Δ mode if the analytical model were indeed a realistic representation of the complete system.

As Fig. 2.53 shows, significant improvement in drift response is obtained when the M2 model is used in the analysis rather than the M1 model. Going one step further, a well-contained roof drift response is obtained when the M2A model is employed, due to the somewhat larger structure strength and the much larger drift at which a negative stiffness forms. The M2A model is not driven into the range of negative stiffness by this ground motion record.

These results clearly show the P-Δ dilemma. Small differences in structural or ground-motion characteristics can result in large differences in responses. This indicates great sensitivity to P-Δ effects. For this reason, every effort should be made to avoid P-Δ sensitive situations (Gupta and Krawinkler, 2000a).

2.6.4 Dynamic Higher Mode Effects for Flexible Steel Structures

In order to estimate the seismic drift demands for frame structures, Gupta and Krawinkler (2000b) investigated three structures of various heights (3, 9, and 20 stories) which are located in three regions of different seismicity (Los Angeles, Seattle, and Boston). The designs comply with applicable 1994 U.S. code requirements for gravity, wind, and seismic design. The plan views and elevations of the structures are shown in Fig. 2.54. Following typical U.S. practice, only the perimeter frames are moment resisting. The interior system, consisting of beams connected with shear tabs to columns, is designed as a gravity load resisting system only.

The response of the structures was evaluated for sets of ground motions representative of the following three hazard levels (Somerville et al., 1997): 2% probability of exceedance in 50 years (denoted as 2/50), 10% probability of exceedance in 50 years (denoted as 10/50), and 50% probability of exceedance in 50 years (denoted as 50/50, for Los Angeles only) (Gupta and Krawinkler, 2000b).

2.6.4.1 Variation of the Ratio of Story Drift to Roof Drift over Height

The distribution of story drifts over the height of the structure, and therefore the relationship between story drifts and roof drifts, is strongly dependent on the ground motion and structure characteristics. The median values of the ratios of maximum story drift angle to roof drift angle for individual stories are presented in Fig. 2.55 for the 20-story structures in the three locations. The values are shown for the 10/50 and 2/50 sets of ground motions. The following patters can be identified:

(1) With few exceptions, the distribution and values are similar for the 10/50 and 2/50

sets of ground motions, indicating little sensitivity to severity of the records. The notable exception is the LA 20-story structure, for which the data for the 2/50 set of ground motions shows a migration of large drift demands to the bottom of the structure. Two reasons can be quoted for this migration, one being the P-Δ effects which are larger for the more severe ground motions, and the other being the pulse-like nature of the 2/50 records.

(2) The Boston structures exhibit very large ratios of story drift angle to roof drift angle near the top of the structure, demonstrating the great importance of higher mode effects generated by the Boston ground motions.

(3) For all nine structures the ratios are larger than 1.0 for most or all stories, and in many cases much larger than 1.0. This implies that the maximum story drift angle is larger than the maximum roof drift angle in almost all stories. The reason is that maximum story drifts do not occur simultaneously in all stories. Thus, the sum of maximum story displacements is always larger than the maximum roof displacement. If the pushover analysis is to capture all maximum story drifts over the height of the structure, then the target displacement should be amplified by the ratio of the sum of maximum story displacements to maximum roof displacement.

The distribution of story drifts over the height of the structure depends on configuration, design decisions, and on the ground motion characteristics. The sensitivity to ground motion characteristics can be evaluated only through time history analysis, which may lead to consistent but ground motion dependent patterns that potentially can be generalized. The sensitivity to the design decision can possibly be evaluated from a

static pushover analysis.

In conclusion, an estimation of story drift demands over the height of the structure as a function of the roof drift is difficult to accomplish on account of the dependence of the relationship on a multitude of factors. These factors include, among others, relative strength and stiffness of the stories, higher mode and *P-Δ* effects, and characteristics of the ground motions. The pushover analysis procedure will provide good prediction for low-rise structures and will provide much insight into structural behavior in many other cases. For instance, it is very useful in assessing the importance of *P-Δ* effects by providing good estimates of the drift demand associated with the onset of negative stiffness. However, it is not a good means for predicting drift demands in structures subjected to ground motions that cause significant higher mode effects (Gupta and Krawinkler, 2000b).

2.6.5 Summary

The pushover analysis procedure will provide good prediction for low-rise steel structures and will provide much insight into structural behavior in many other cases. For instance, it is very useful in assessing the importance of *P-Δ* effects by providing good estimates of the drift demand associated with the onset of negative stiffness. However, it is not a good means for predicting drift demands in structures subjected to ground motions that cause significant higher mode effects (Gupta and Krawinkler, 2000b). Currently there is a lack of knowledge of the second-order P-Δ effects on the seismic performance of CFT MRFs. Therefore, the influence of higher mode effects and P-Δ effects on the seismic performance of CFT MRFs will be investigated in this research by

comparing the results of the pushover and time-history analyses.

This research is intended to evaluate the seismic performance of *High-strength CFT MRFs*, but not intended to conduct a statistical study of the seismic response of *High-strength CFT MRFs* to ground motion of varying characteristics. Therefore, the MRFs in this research will be subjected to three sets of SAC ground motion records for Los Angeles (Somerville et al., 1997), including 2%, 10% and 50% probability of exceedance in 50 years (return periods of 2,475, 475 and 72 years, respectively), to investigate the inelastic dynamic behavior of the MRFs.

2.7 Summary of Literature Review

Current seismic design provisions (BSSC 2001) restrict the use of high strength materials ($\sigma_y \geq 80$ ksi, and $f'_c \geq 10$ ksi) in composite CFT structures. In order to develop knowledge that will help to overcome these restrictions and limitations, current experimental and analytical research on the seismic behavior of steel structures and composite structures with CFT columns, as well as the seismic behavior of the components of these steel structures and composite structures, and the existing methods to evaluate the seismic performance of moment resisting frames were reviewed.

2.7.1 Analytical Models for Individual Components

For the analytical models of the individual structural components of CFT MRFs, the FEM model (US model) for CFT beam-column developed by Varma et al. (2001), which implicitly accounts for the effects of local buckling, concrete confinement and crushing, and transverse interaction between the steel and concrete, is selected to model the CFT

beam-column in this research, other than the Japanese empirical model (Sakino and Nakahara, 2000). For the analytical model of steel beam, a new analytical model for steel beam, which implicitly account for the effects of inelastic local buckling of beam flange and beam web, will be developed and compared with the experimental results of cyclic specimens of Green et al. (2002) in this research, other than the FEM models of the inelastic behavior of the monotonic test specimens developed by Green et al. (2001). For the analytical model of double split-tee connections, a new FEM-based spring model for the connections, which implicitly account for the effects of pretensioning of the bolts and contacts and interactions among components of the connections, will be developed and compared with the experimental results of Swanson (1999) in this research, other than the spring model developed by Swanson (1999), which is iterative and cannot be applied to the DST connections in which fillet welding were used to connect beam flanges to tee stems.

2.7.2 Analytical Models for CFT MRFs

For the analytical model of CFT MRFs, recent research on *CFT MRFs* indicate that, for a CFT subassemblage, the beam, connection, column, and panel zone contributed 83.0%, 9.7%, 7.0%, and 0.3% to total story drift, respectively (Peng, S.-W., 2001). It means that the contribution of the connection to the total story drift should not be neglected. Therefore, a new fiber-based model for the high-strength CFT MRF, which accounts for the combined effects of the strength and stiffness degradation of the members and connections simultaneously and is similar to the analytical model for steel MRF with postensioned connections developed by Ricles et al. (2001), will be developed

and used to model the high-strength CFT MRF in this research, other than the models used in the current analytical studies on the seismic behavior of CFT moment resisting frames, e.g., Hajjar et al. (1998a, b), Elremaily (2000), and Zhang and Ricles (1996), in which the connections between the beams and the columns are assumed to be *rigid.*

2.7.3 Evaluation Methods for Seismic Performance of CFT MRFs

In the pushover analysis procedures of FEMA 356, the seismic demands are computed by non-linear static analysis of the structure subjected to monotonically increasing lateral forces with an invariant height-wise distribution, until a predetermined target displacement is reached. For almost all mid- and high-rise structures, high mode effects are present to significant degrees. But none of the invariant force distributions in the pushover analysis procedures of FEMA 356 can account for the contributions of higher modes to response, or for a redistribution of inertia forces because of structural yielding (Krawinkler, H., et al., 1998). Hence, in order to capture the seismic response of *High-strength CFT MRFs* more accurately, adaptive pushover analysis should be performed in addition to static pushover analysis following FEMA 356 procedures in this research.

The pushover analysis procedure is not a good means for predicting drift demands in structures subjected to ground motions that cause significant higher mode effects (Gupta and Krawinkler, 2000b). Therefore, influence of higher mode effects and P-Δ effects on the seismic performance of CFT MRFs will be investigated in this research by comparing the results of the pushover and time-history analyses, in which CFT MRFs will be subjected to three sets of SAC ground motion records for Los Angeles (Somerville et al.,

1997), including 2%, 10% and 50% probability of exceedance in 50 years, respectively, to investigate the inelastic dynamic behavior of CFT MRFs.

2.7.4 Summary

Current experimental and analytical research on the seismic behavior of steel structures and composite structures with CFT columns, as well as the seismic behavior of the components of these steel structures and composite structures, and the existing methods to evaluate the seismic performance of moment resisting frames were reviewed. For the analytical models of the individual structural components of CFT MRFs, the FEM model for CFT beam-column developed by Varma et al. (2001) is selected to model the CFT beam-column in this research. For the analytical model of steel beam, a new analytical model for steel beam, which implicitly account for the effects of inelastic local buckling of beam flange and beam web, will be developed and compared with the experimental results of cyclic specimens of Green et al. (2002) in this research. For the analytical model of double split-tee connections, a new FEM-based spring model for the connections, which implicitly account for the effects of pretensioning of the bolts and contacts and interactions among components of the connections, will be developed and compared with the experimental results of Swanson (1999) in this research.

For the analytical model of CFT MRFs, a new fiber-based model for the high-strength CFT MRF, which accounts for the combined effects of the strength and stiffness degradation of the members and connections simultaneously, will be developed and used to model the high-strength CFT MRF in this research, other than the models used in the

current analytical studies on the seismic behavior of CFT MRF, in which the connections between the beams and the columns are assumed to be *rigid.*

For the evaluation methods of seismic behavior of CFT MRFs, adaptive pushover analysis as well as static pushover analysis following FEMA 356 procedures will be used in this research. In addition, the influence of higher mode effects and P-Δ effects on the seismic performance of CFT MRFs will be investigated in this research by comparing the results of the pushover and time-history analyses, in which CFT MRFs will be subjected to three sets of SAC ground motion records for Los Angeles (Somerville et al., 1997), including 2%, 10% and 50% probability of exceedance in 50 years, respectively, to investigate the inelastic dynamic behavior of CFT MRFs.

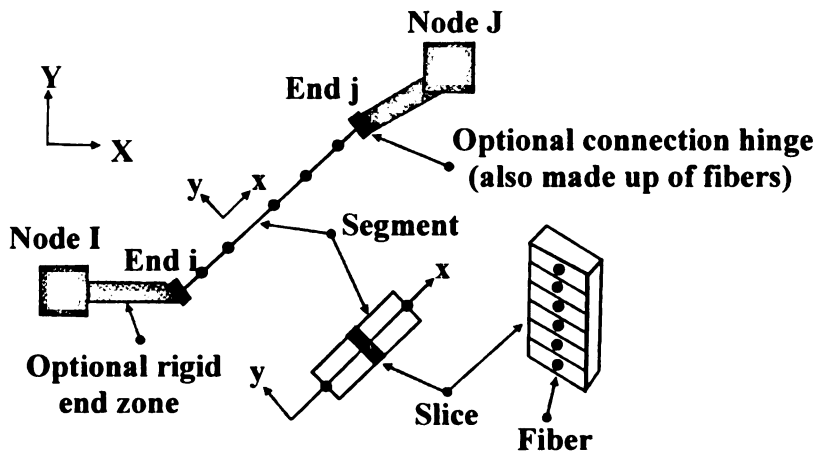


Figure 2.1 DRAIN-2DX Fiber-based beam-column element (Prakash et al. 1993)

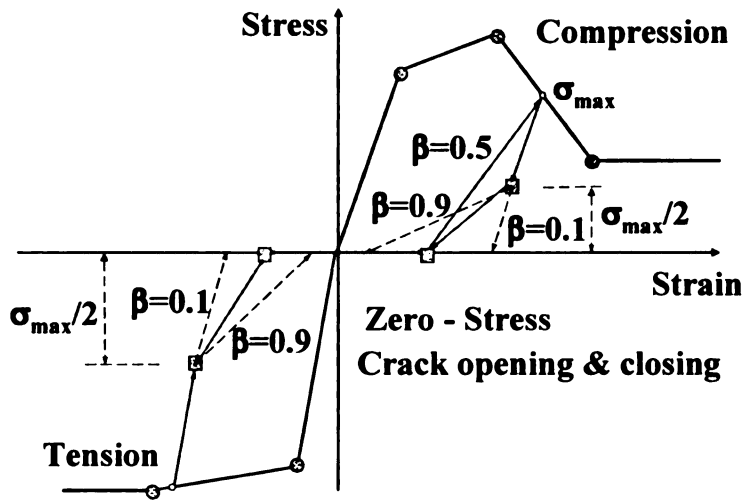


Figure 2.2 C-type fiber σ–ε relationship (Kurama et al. 1996)

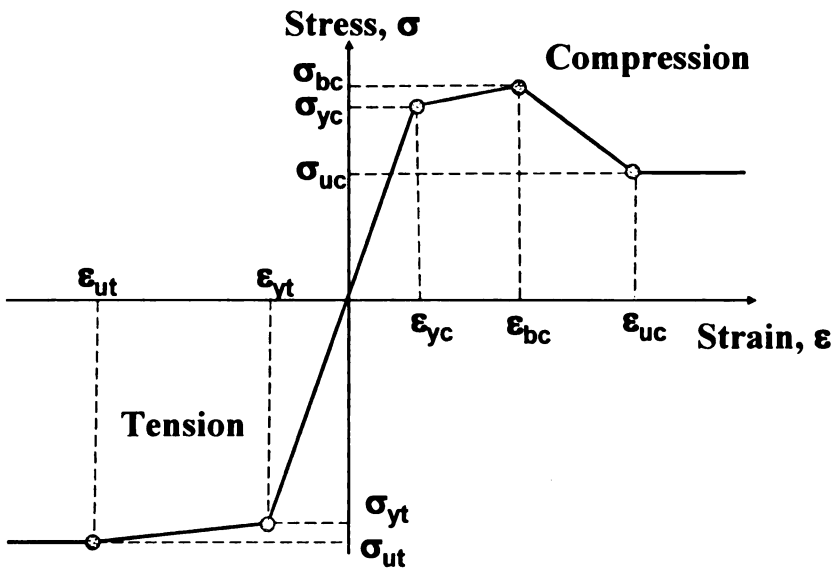


Figure 2.3 S-type fiber σ–ε relationship monotonic behavior (Cordero et al. 2002)

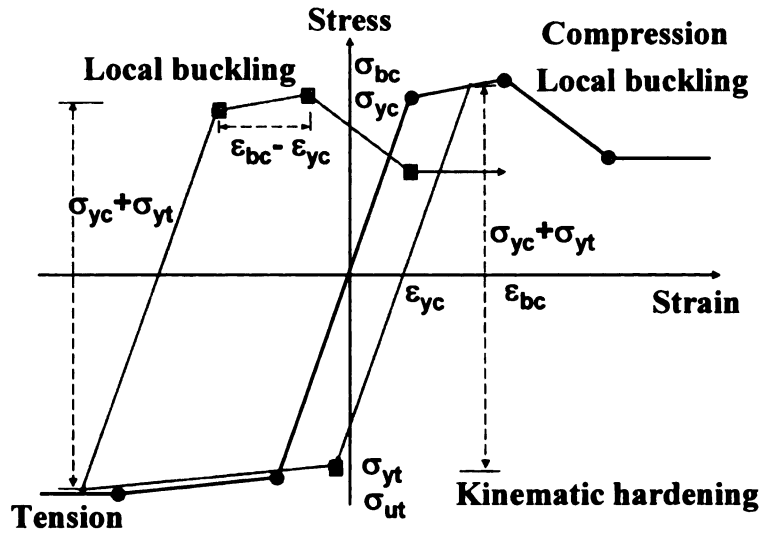


Figure 2.4 Cyclic behavior of S-type fiber before local buckling (Cordero et al. 2002)

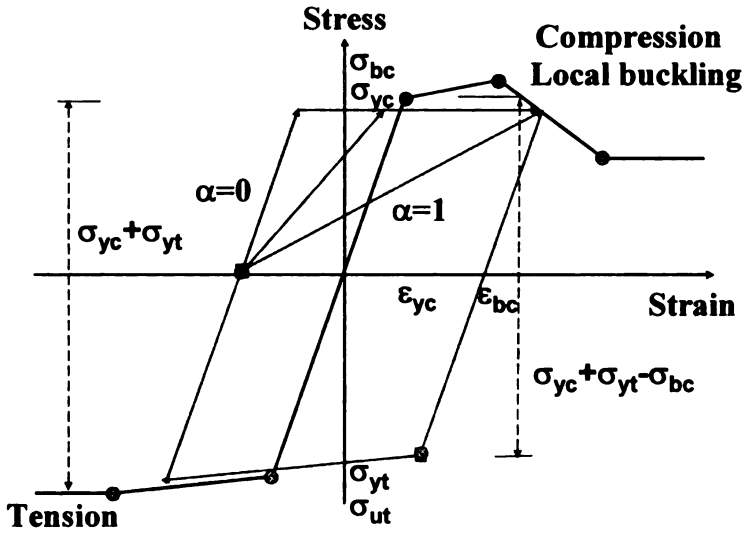


Figure 2.5 Cyclic behavior of S-type fiber after local buckling (Cordero et al. 2002).

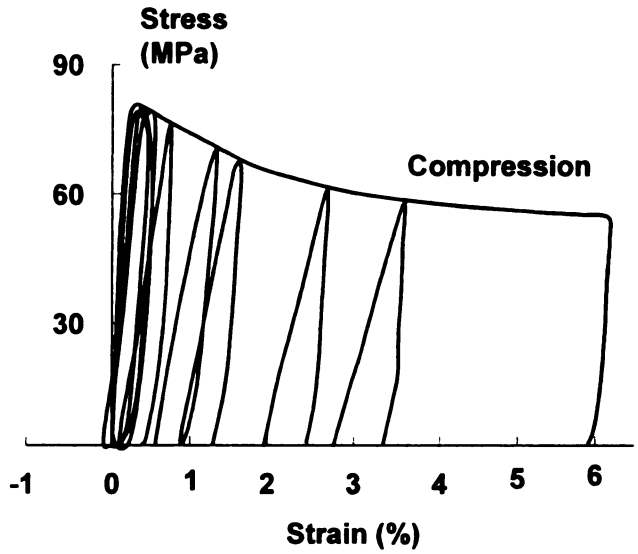


Figure 2.6 Japanese model: Concrete fiber hysteretic behavior (Fujii et al. 1973)

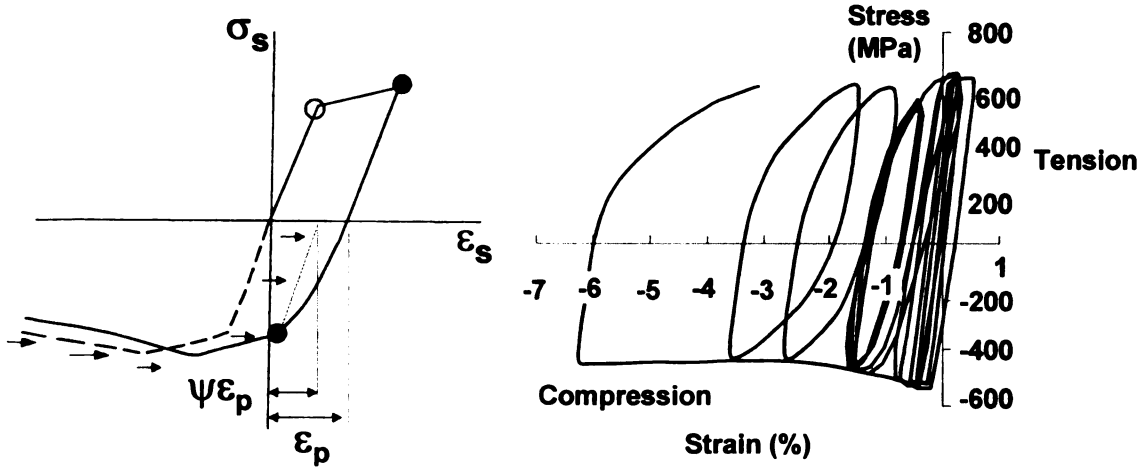


Figure 2.7 Japanese model: Steel fiber hysteretic behavior (Meng et al. 1992)

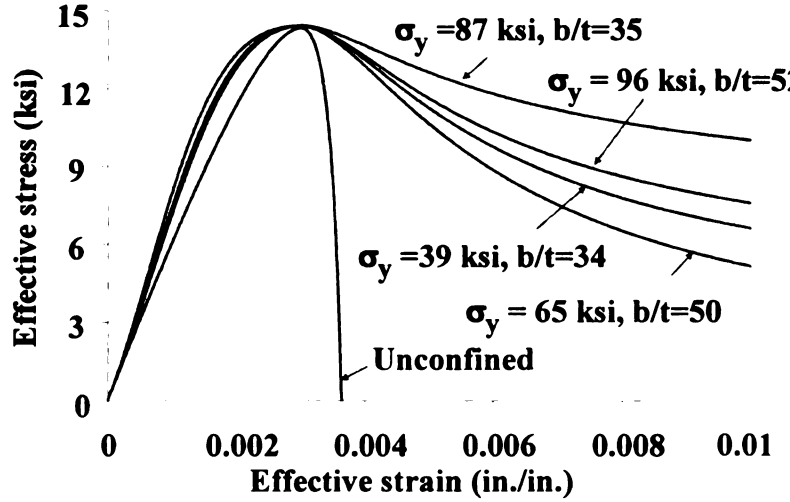


Figure 2.8 Japanese model: Example concrete fiber σ–ε curves in compression (Kowalkowski and Varma 2003)

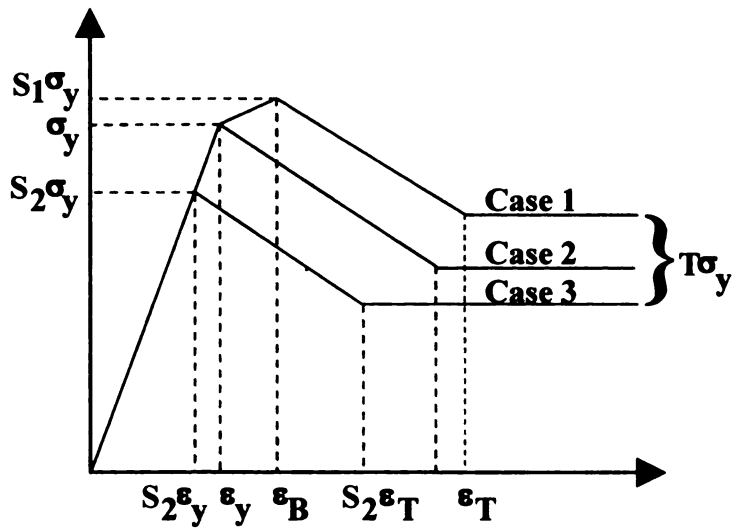


Figure 2.9 Japanese model: Steel fiber σ–ε curves in compression (Sakino et al. 2004)

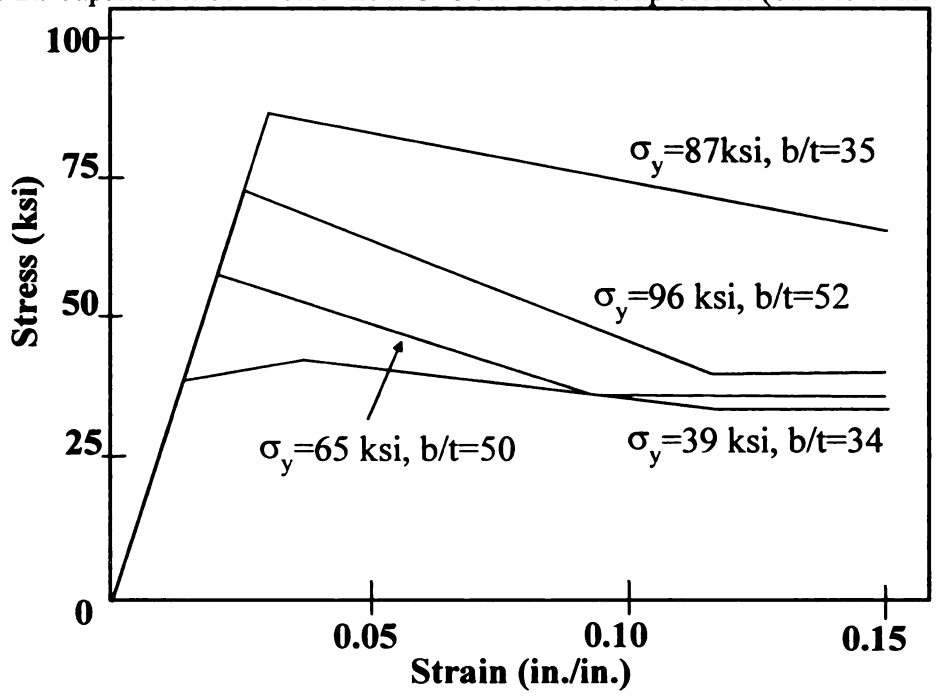


Figure 2.10 Japanese model: Example steel fiber σ–ε curves in compression (Kowalkowski and Varma 2003)

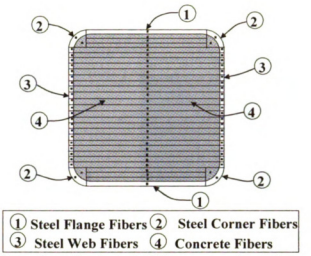


Figure 2.11 Fiber discretization of CFT cross-section (Varma et al. 2001)

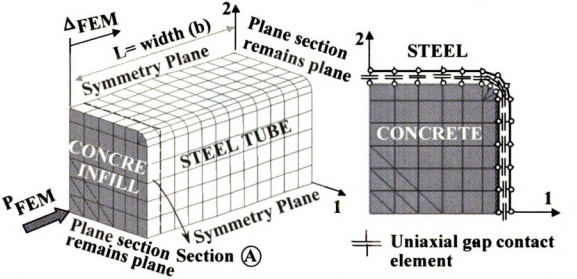


Figure 2.12 U.S. model: 3D Finite element model of CFT segment (Varma et al. 2001)

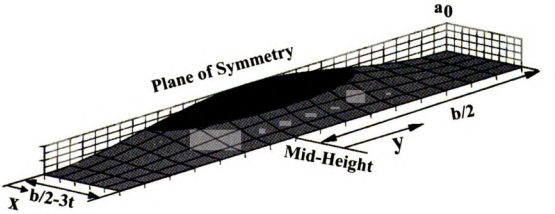
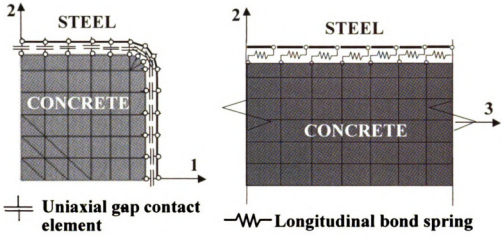


Figure 2.13 U.S. model: Geometric imperfection for steel tube walls (Varma et al. 2001)



(a) Transverse interaction (b) Longitudinal interaction

Figure 2.14 U.S. model: Transverse and longitudinal interaction (Varma et al. 2001)

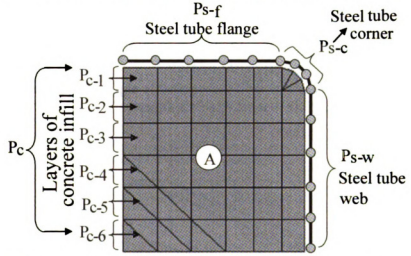


Figure 2.15 U.S. model: End section A of CFT model and cross-section components (Varma et al. 2001).

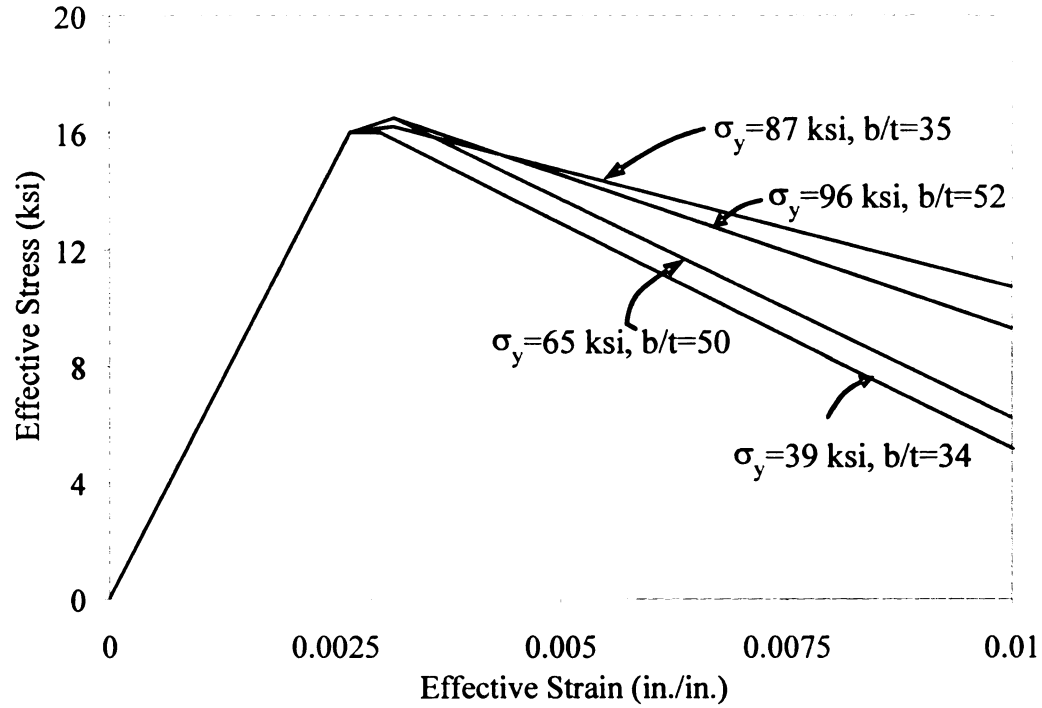


Figure 2.16 U.S. model: Example effective steel fiber σ–ε curves in compression for high strength CFTs (Varma et al. 2001)

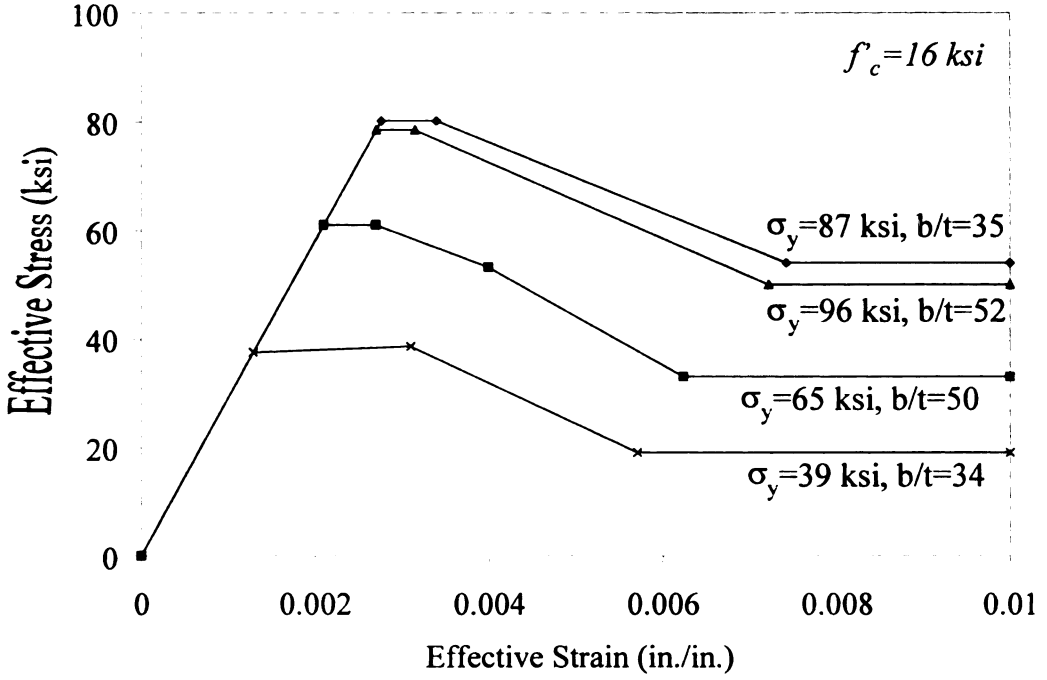


Figure 2.17 U.S. model: Example effective concrete fiber σ–ε curves in compression for high strength CFTs (f'_c=16ksi)

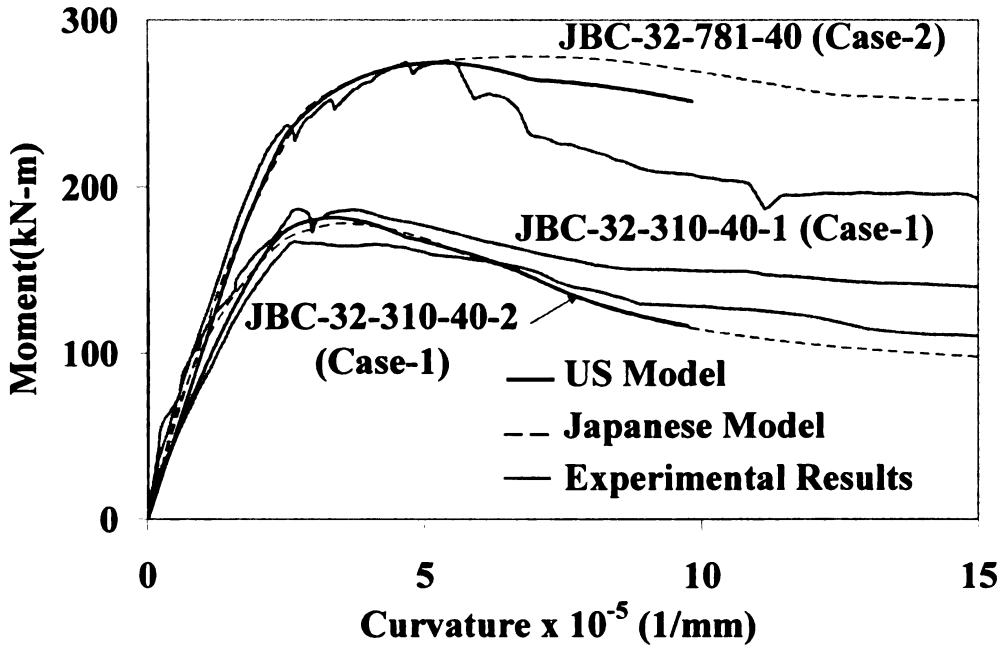


Figure 2.18 Comparisons of experimental and analytical M-ϕ responses for CFTs with f'_c=17 ksi, b/t=32, σ_y=45 ksi or 113 ksi, P/P_0=40% (Kowalkowski and Varma 2003)

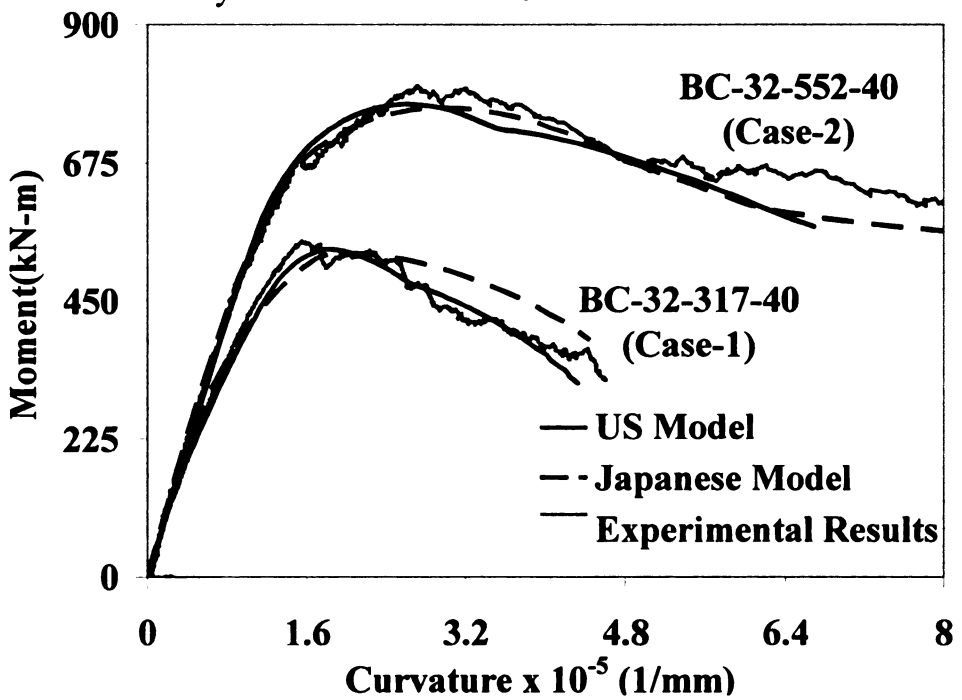


Figure 2.19 Comparisons of experimental and analytical M-ϕ responses for CFTs with f'_c=16 ksi, b/t=32, σ_y=39 ksi or 87 ksi, P/P_0=40% (Kowalkowski and Varma 2003)

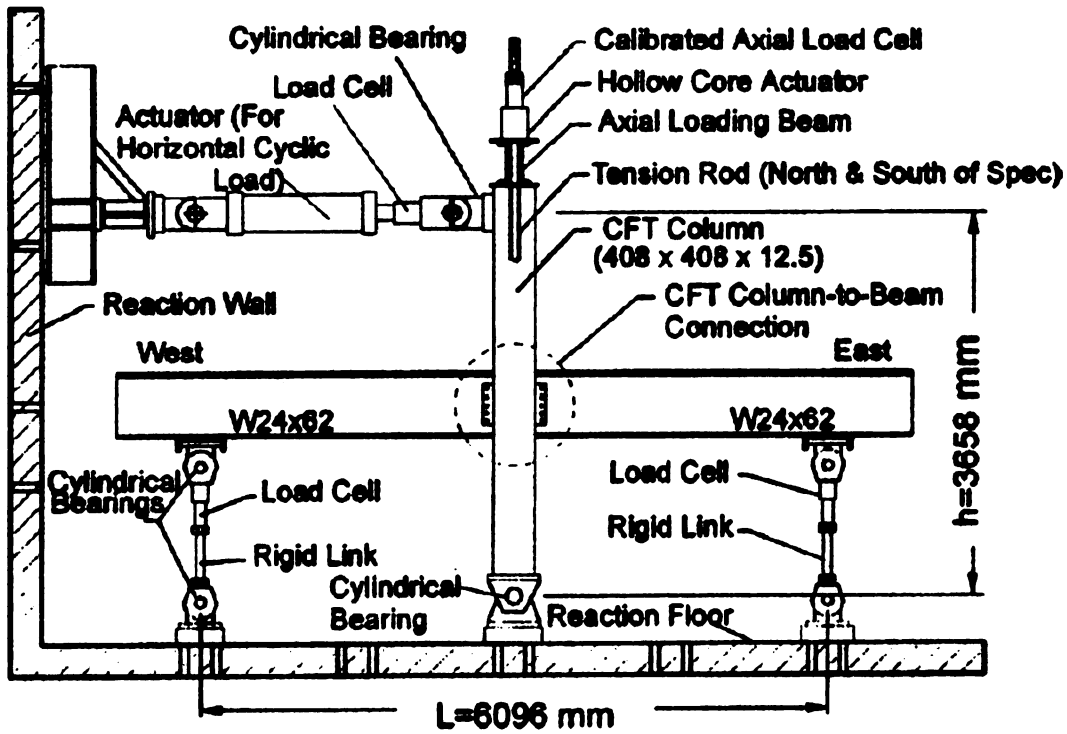


Figure 2.20 Connection test setup (Ricles et al., 2004)

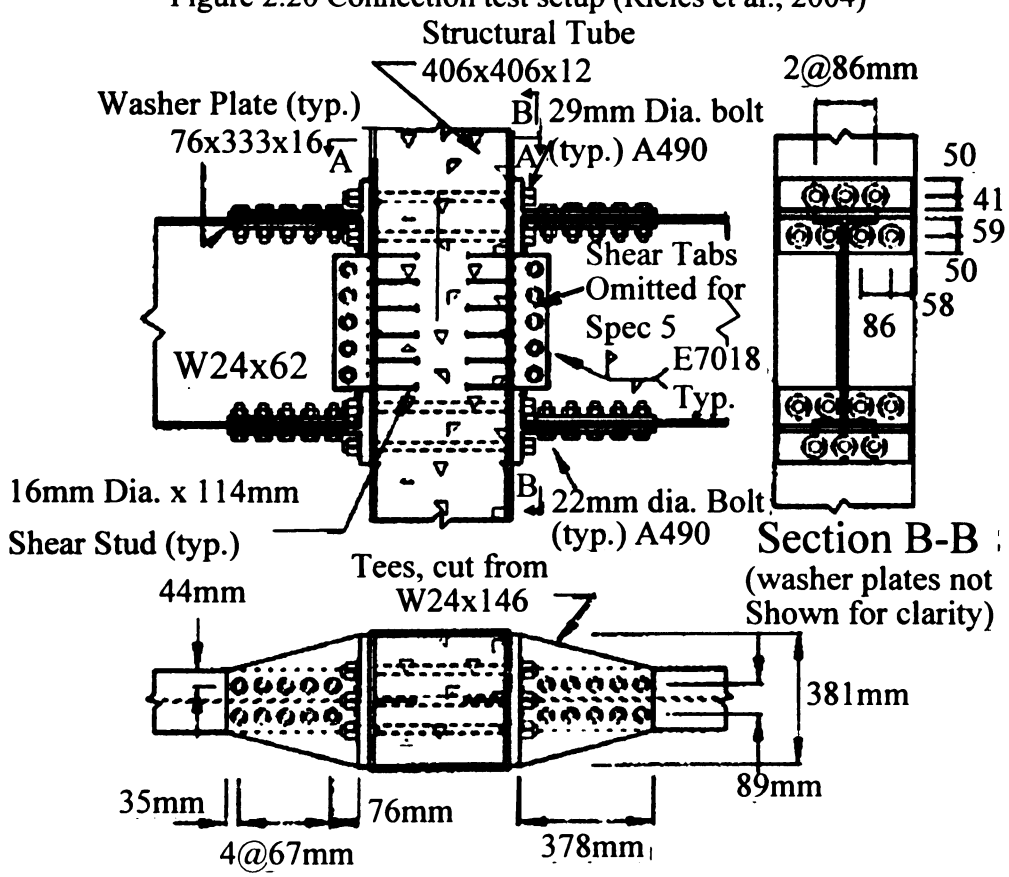


Figure 2.21 Connection details, Spec. 4 and 5 (Ricles et al., 2004)

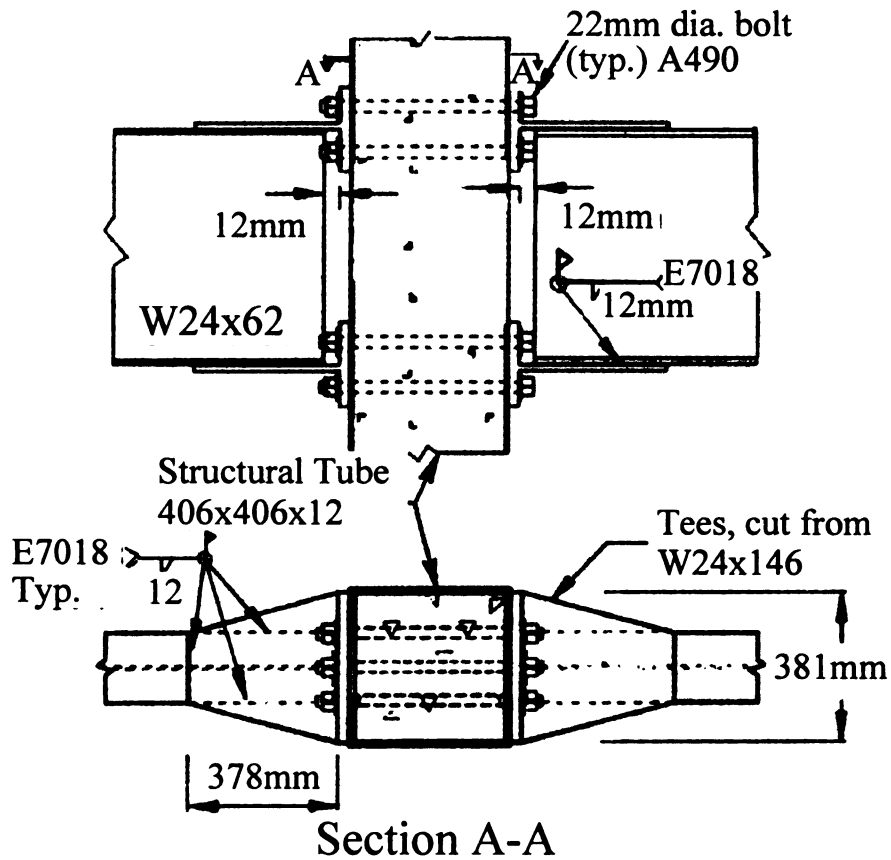


Figure 2.22 Connection details, Spec. 6 and 7 (Ricles et al., 2004)

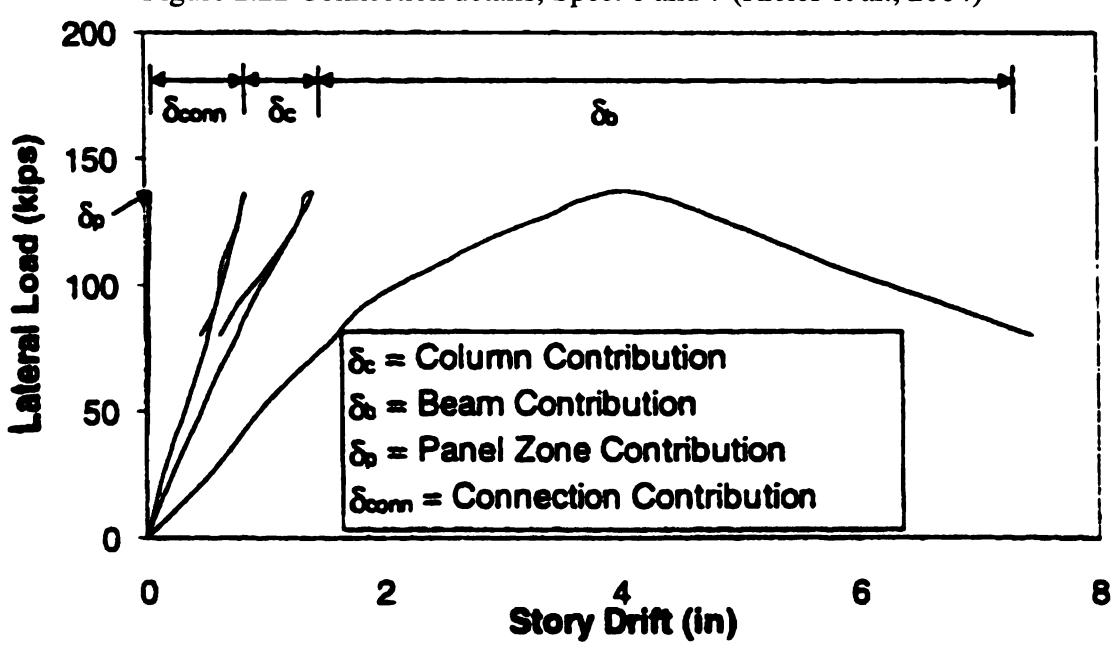


Figure 2.23 Full-scale inelastic cyclic test of split-Tee connections: contribution of components to story drift, Spec. 6 (Peng, 2000)

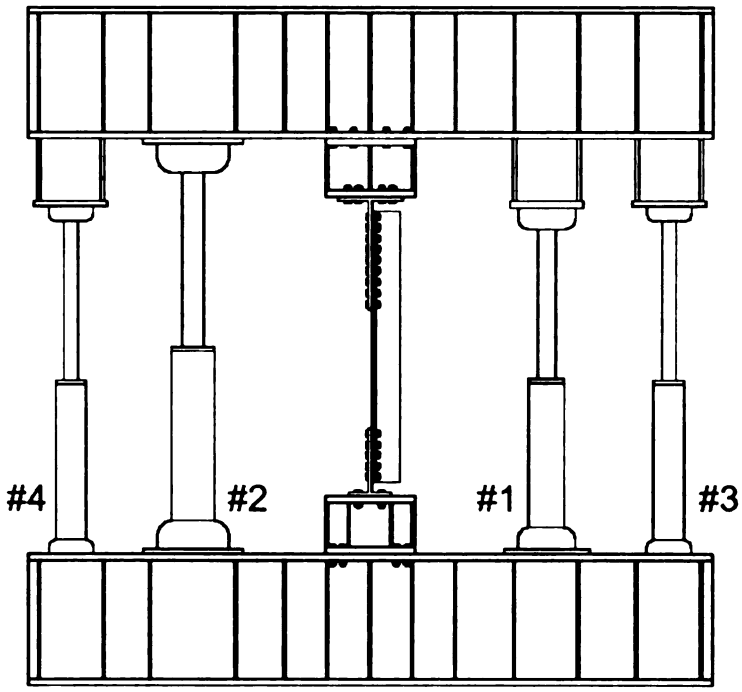


Figure 2.24 T-stub connection test: component test frame (Swanson, 1999)

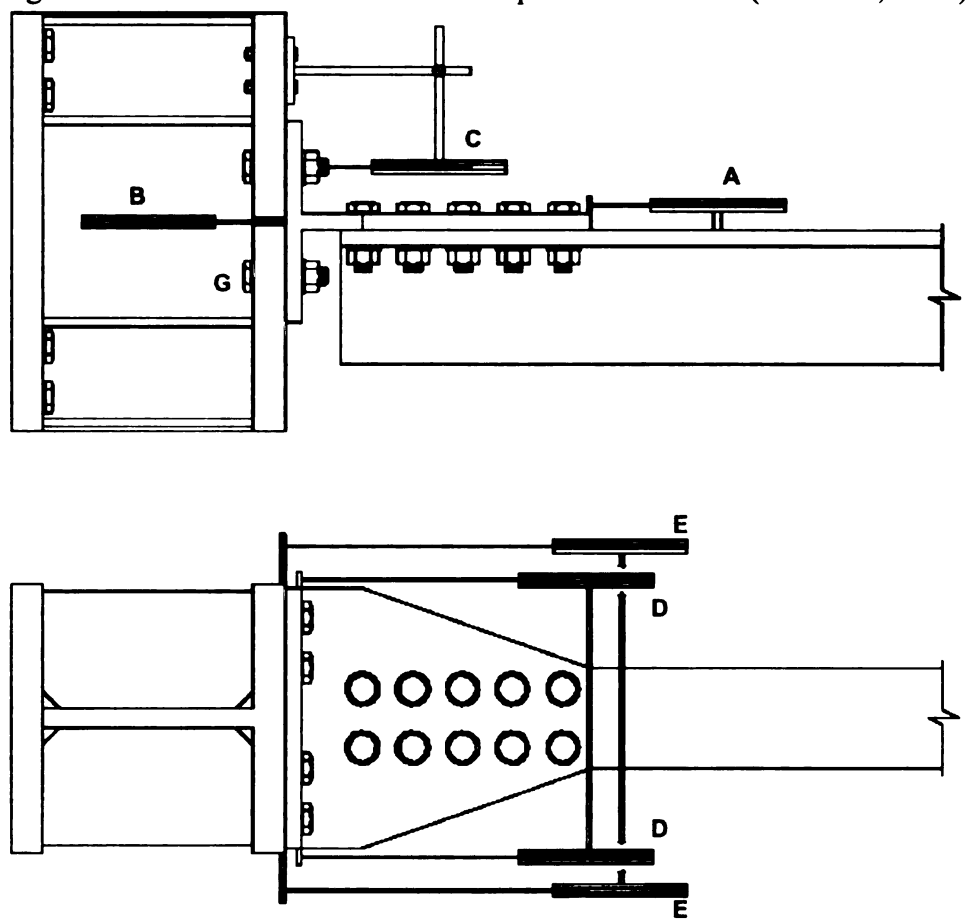


Figure 2.25 T-stub connection test: instrumentation scheme (Swanson, 1999)

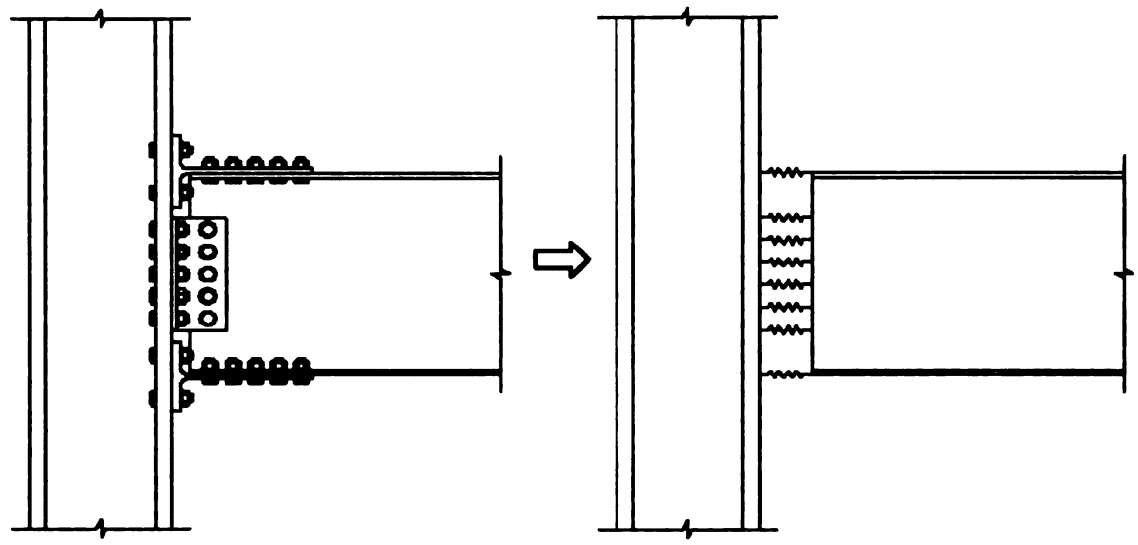


Figure 2.26 Spring model for a T-stub connection (Swanson, 1999)

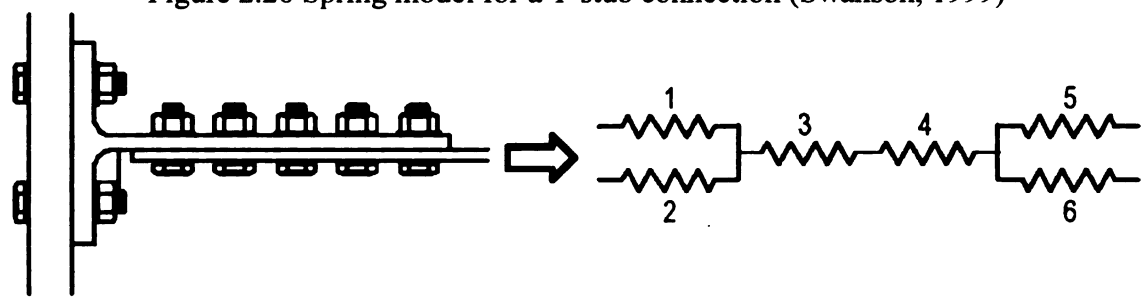


Figure 2.27 Spring model of an individual T-stub (Swanson, 1999)

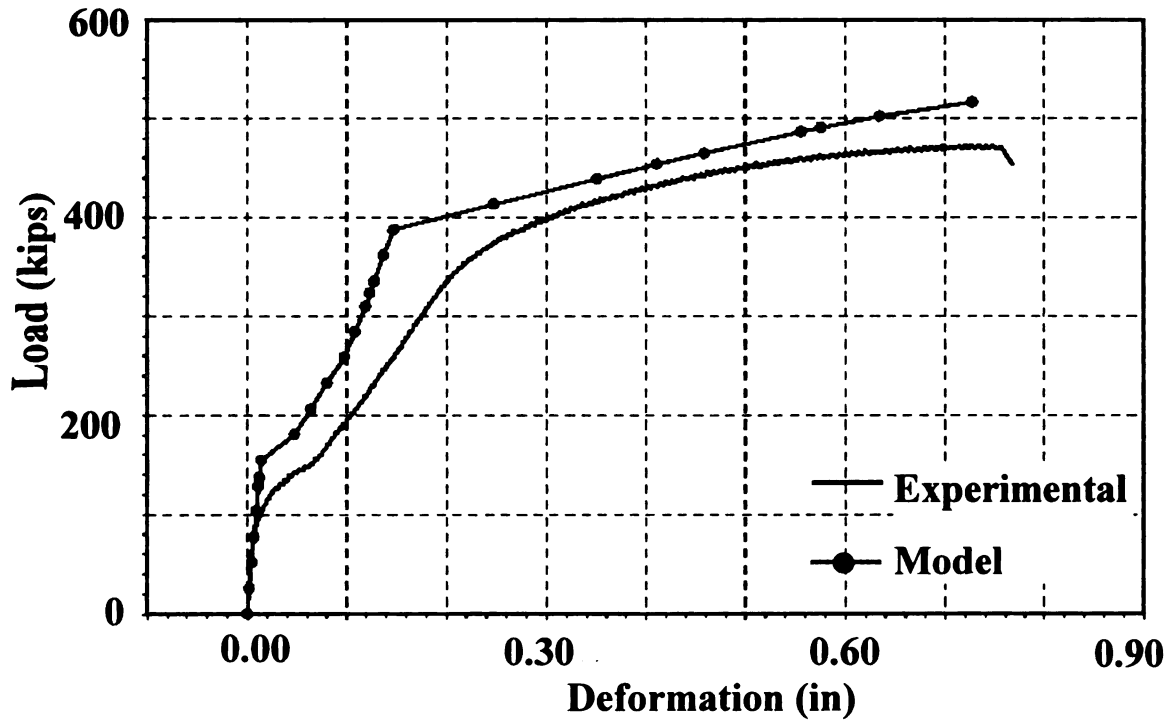


Figure 2.28 Predicted and experimental total deformation for T-stub TA-05 (Swanson, 1999)

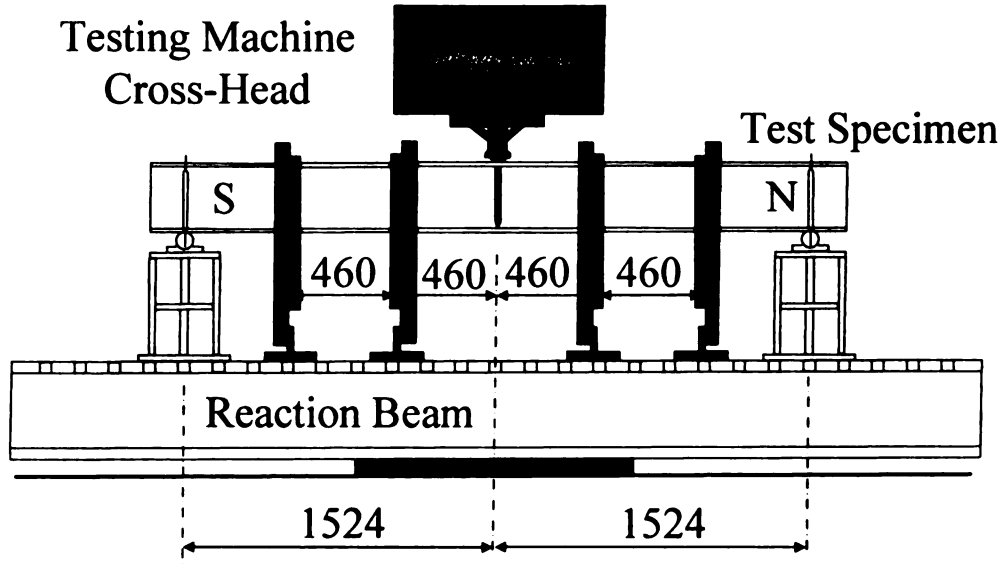


Figure 2.29 Experiment setup for 3-point flexural test specimens (Green, 2000)

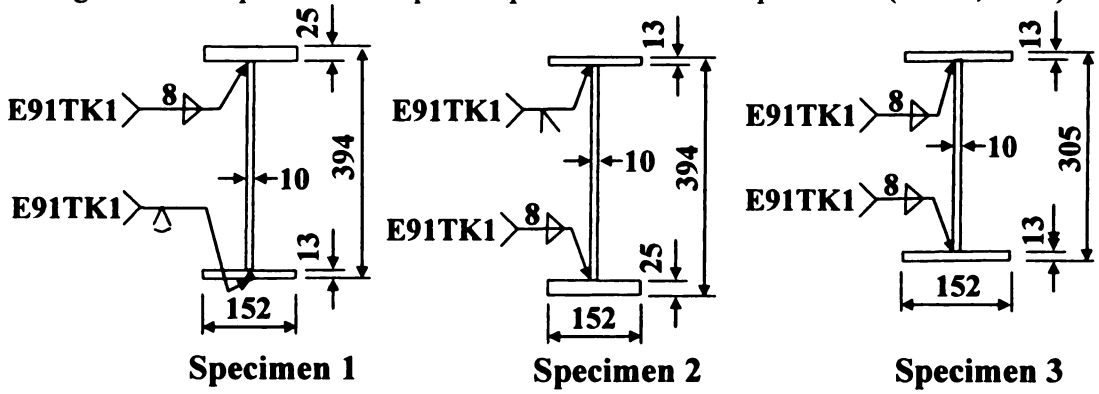


Figure 2.30 Typical sections of flexural test specimens (Green, 2000)

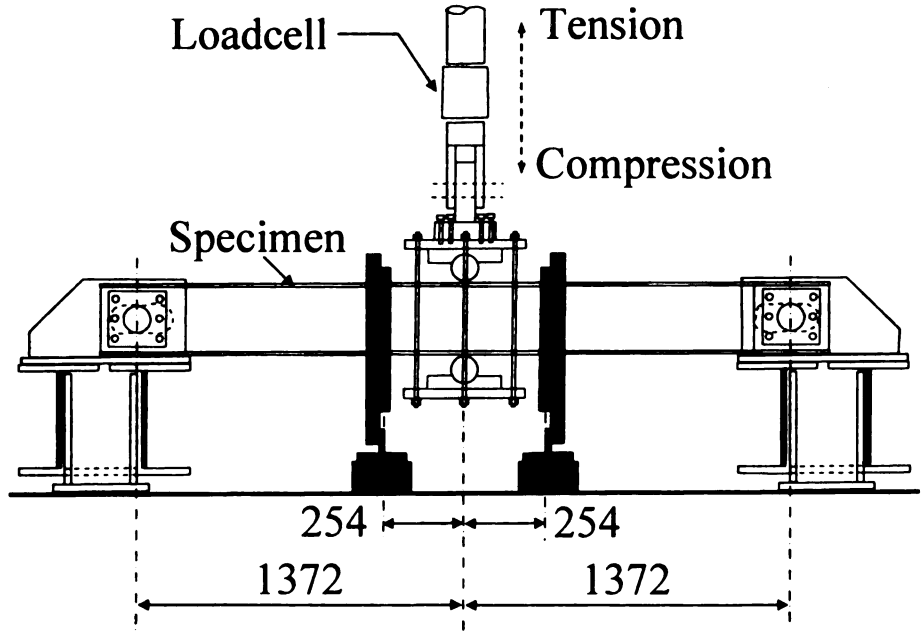


Figure 2.31 Experiment setup for 3-point cyclic test specimens (Green, 2000)

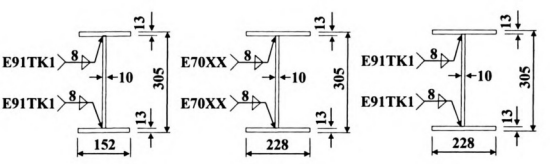


Figure 2.32 Sections of cyclic test specimens (Green, 2000)

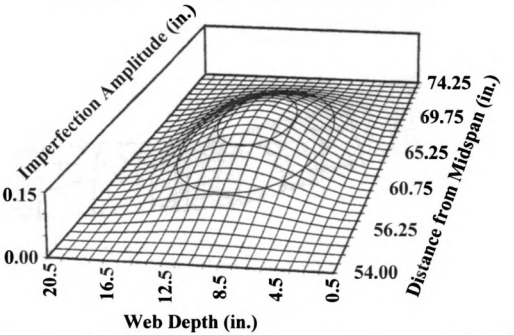


Figure 2.33 Full depth web imperfection for $h_c/t_w=53$ used in FEM model (Green, 2000)

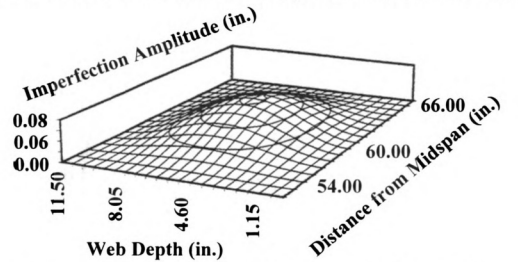


Figure 2.34 Full depth web imperfection for $h_c/t_w=29$ used in FEM model (Green, 2000)

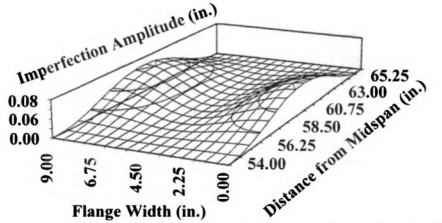


Figure 2.35 Full width flange imperfection for $b_f/2t_f=9$ used in FEM model (Green, 2000)

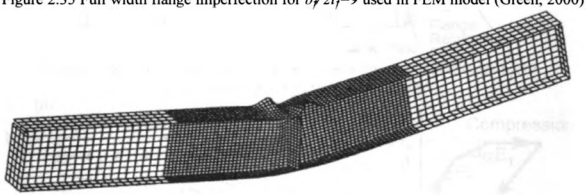


Figure 2.36 FEM analysis results for Test Specimen 3: local buckling of compression flange and web (Green, 2000)

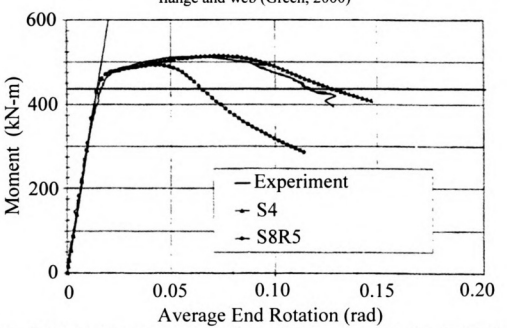


Figure 2.37 Analytical and experimental moment-average end rotation results of Test Spec. 3, using two different element type S4 and S8R5 (Green, 2000)

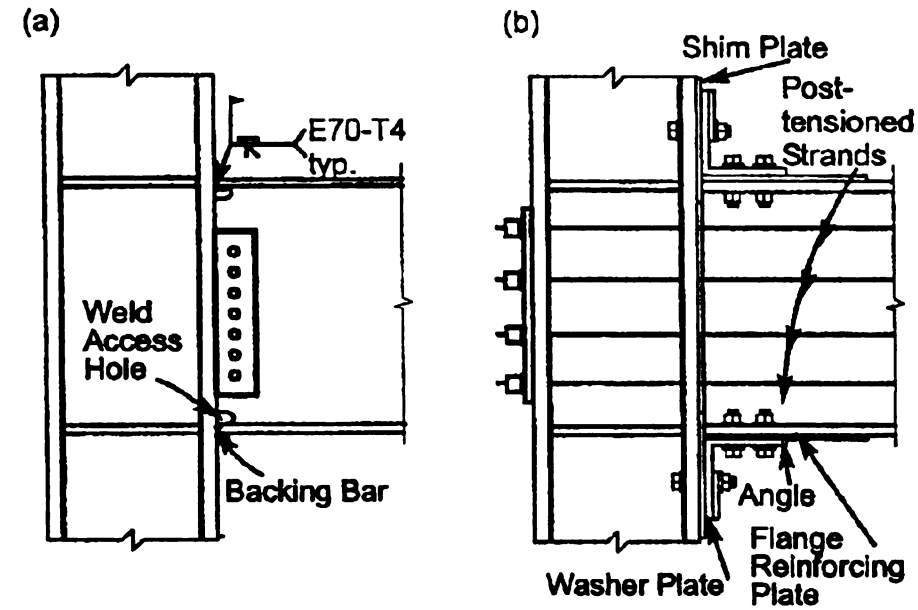


Figure 2.38 Moment connections: (a) pre-Northridge welded connection; (b) Posttensioned connection (Ricles et al., 2001)

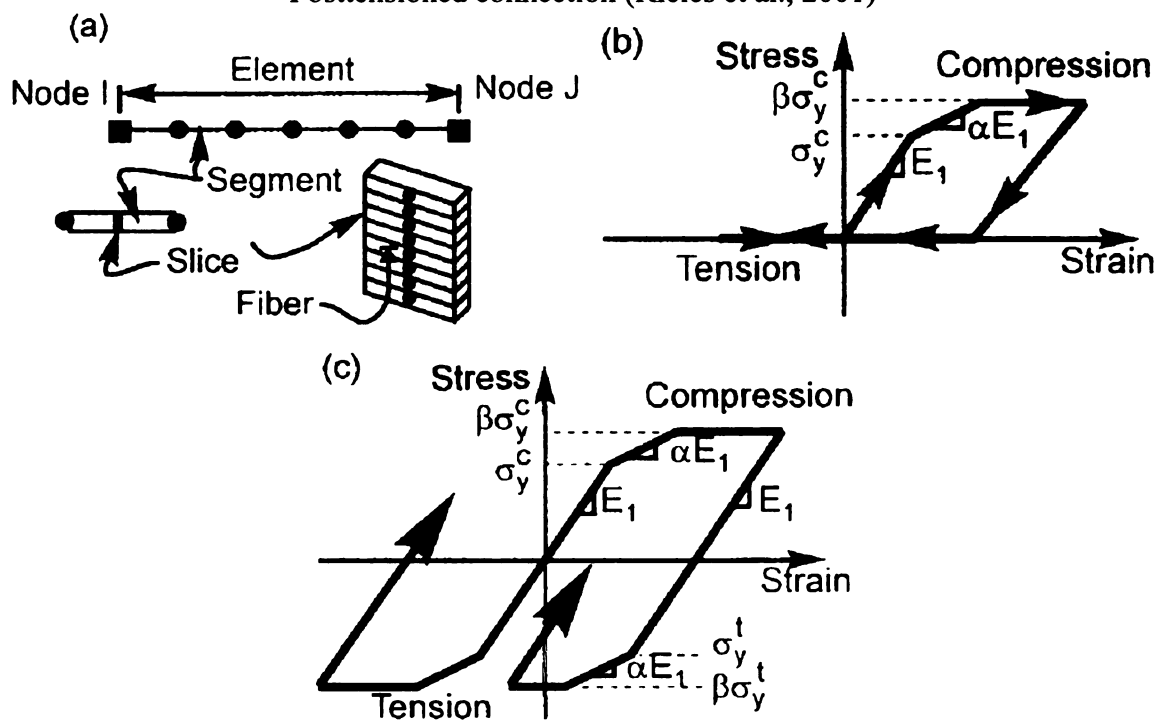


Figure 2.39 Fiber element: (a) element, segments, and fibers; (b) compression-only fiber stress-strain relationship; (c) typical fiber stress-strain relationship (Ricles et al., 2001)

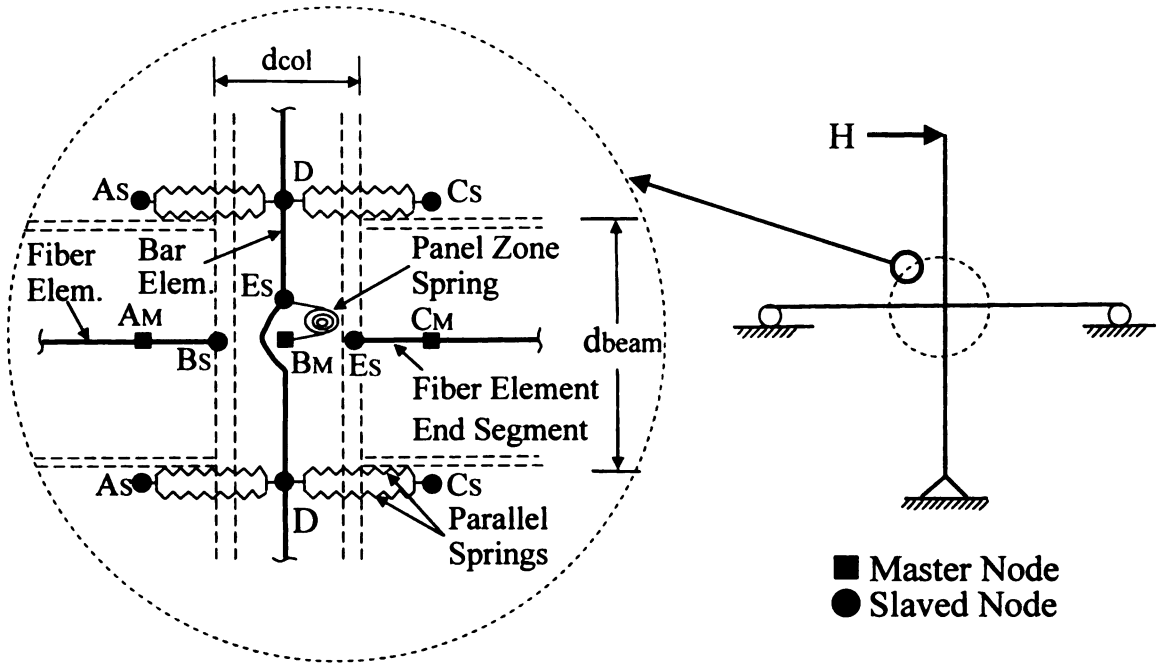


Figure 2.40 Analytical model for postensioned connection (Ricles et al., 2001)

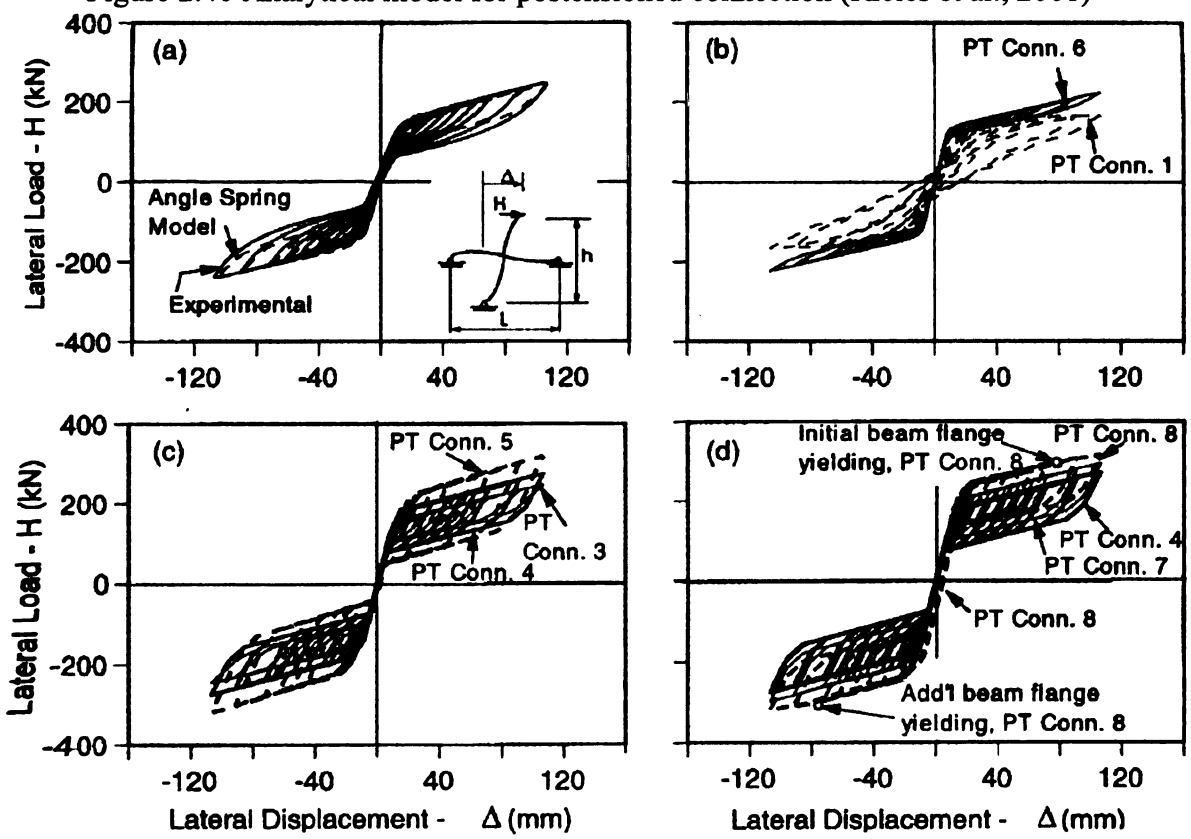


Figure 2.41 Lateral load–displacement behavior of postensioned connections (Ricles et al., 2001)

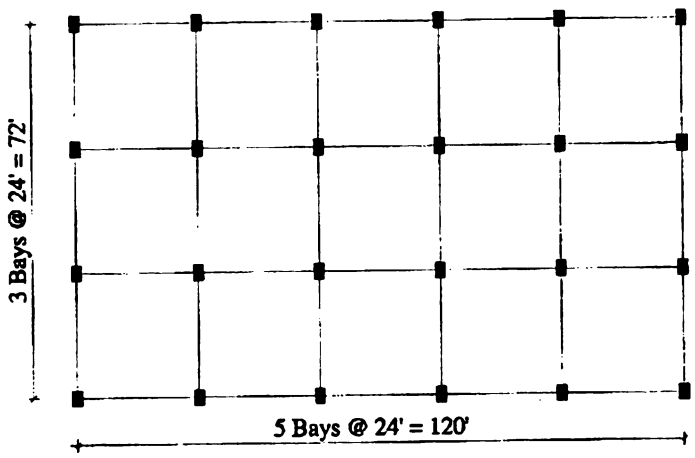


Figure 2.42 Typical plan of prototype structure used in evaluation study (Gupta and Kunnath, 2000)

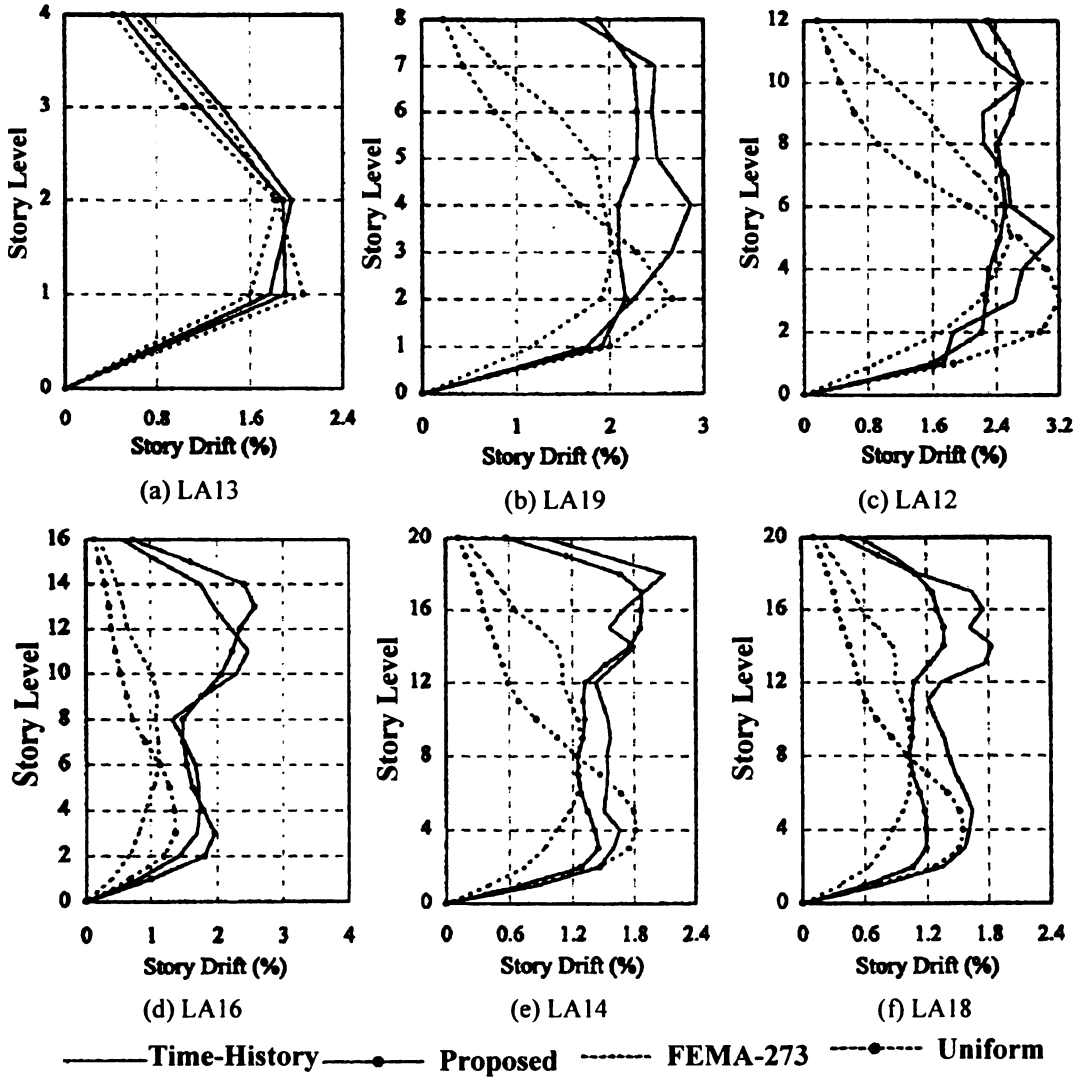


Figure 2.43 Inter-story drift profiles for various frames for selected ground motions (Gupta and Kunnath, 2000)

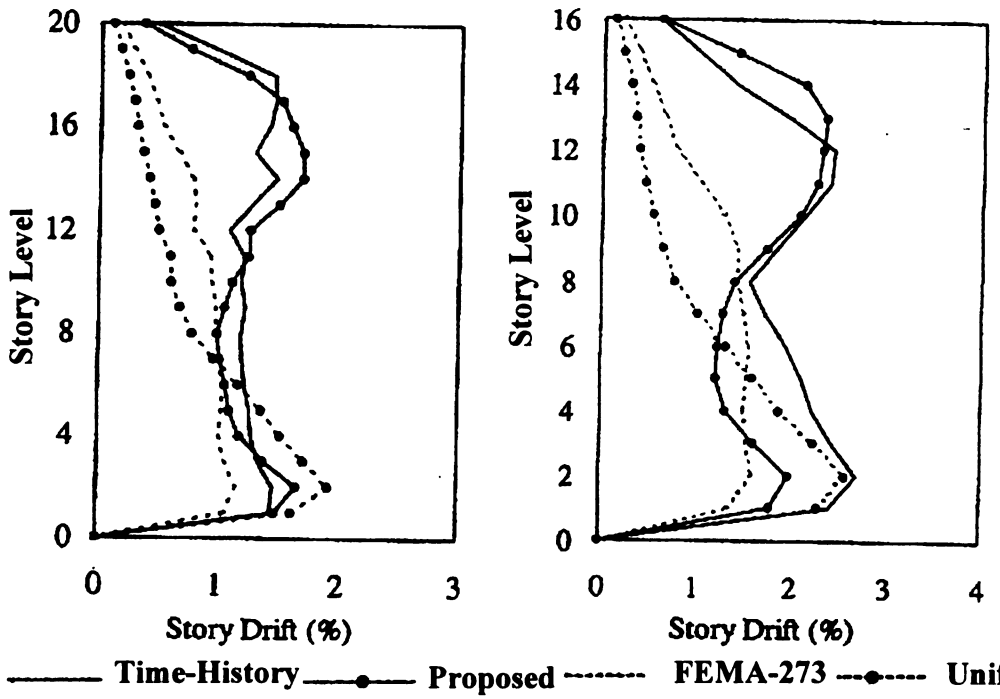


Figure 2.44 Drift profiles for typical structures with "soft" first story (Gupta and Kunnath, 2000)

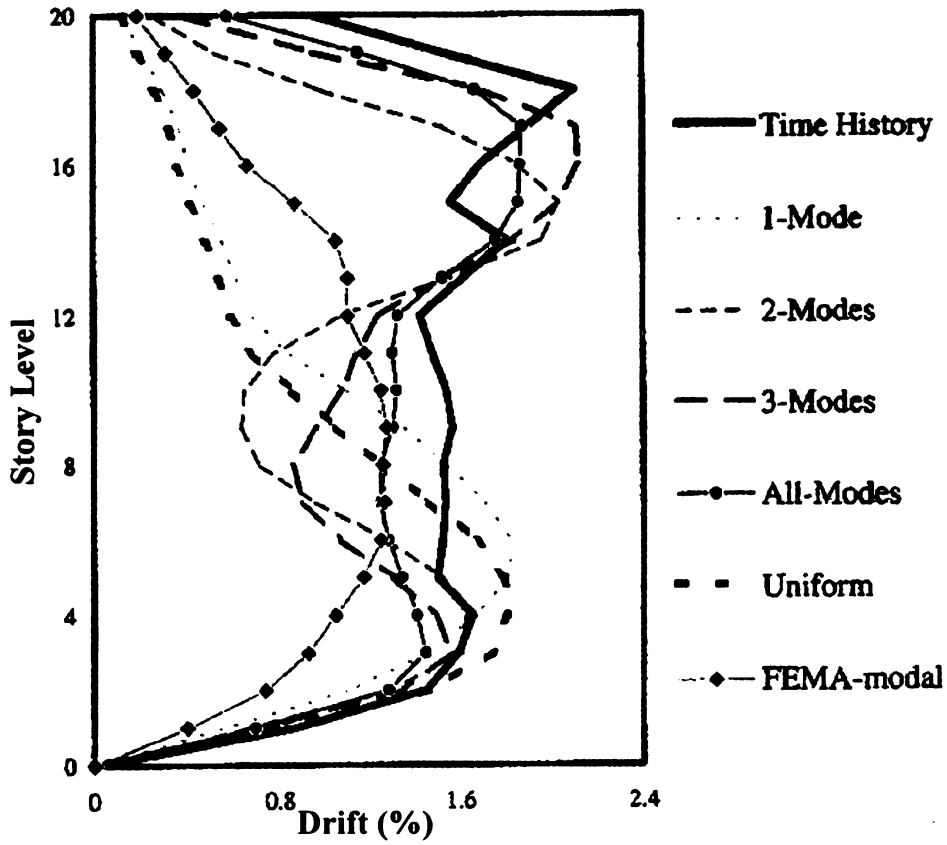


Figure 2.45 Effect of number of modes on drift profile for adaptive spectra-based pushover method (Gupta and Kunnath, 2000)

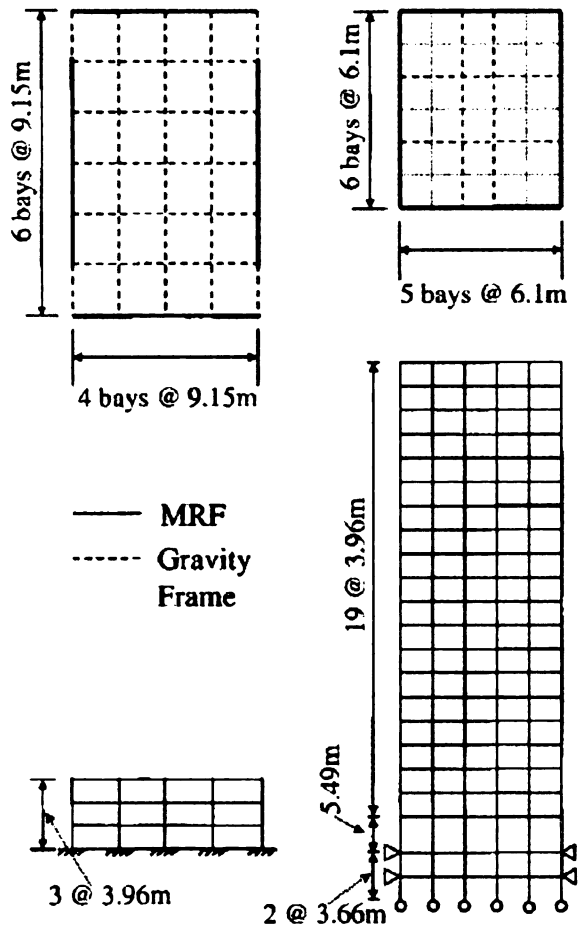


Figure 2.46 Floor plans and elevations of 3- and 20-story buildings (Gupta and Krawinkler, 2000a)

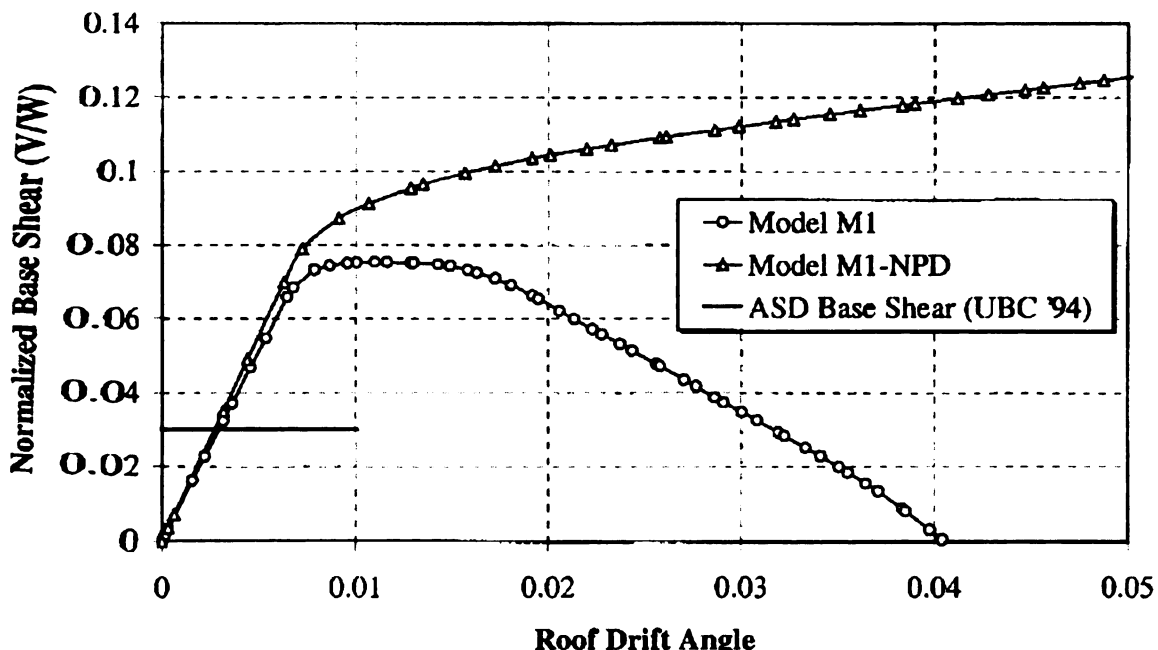


Figure 2.47 Global pushover curves of 20-story building Los Angeles (LA) with and without P-Delta (Gupta and Krawinkler, 2000a)

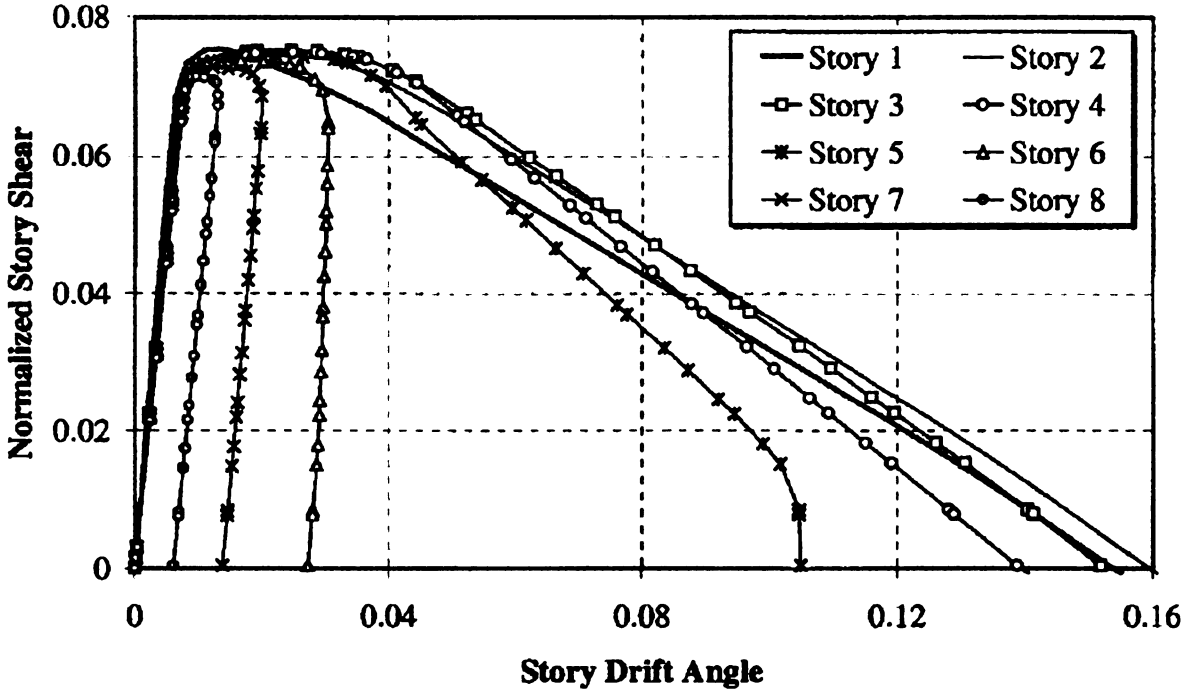


Figure 2.48 Story pushover curves for lower eight stories of 20-story structure in Los Angeles (LA) with P-Delta (Gupta and Krawinkler, 2000a)

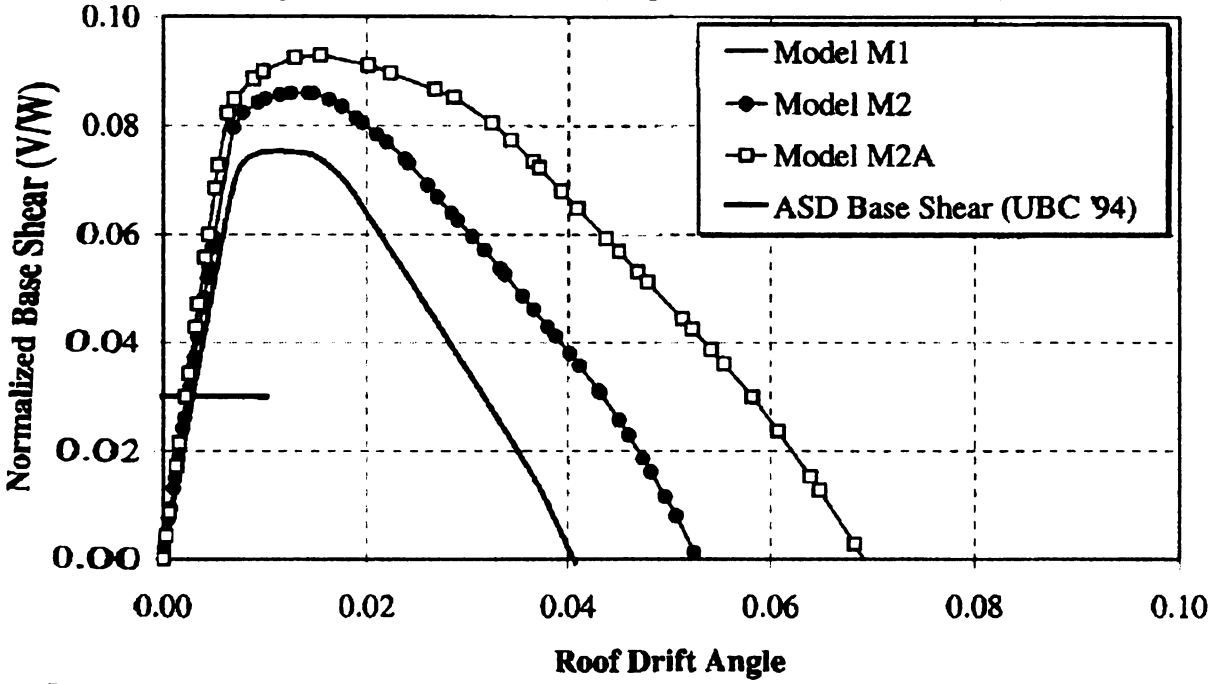


Figure 2.49 Global pushover curves for various models of 20-story building in Los Angeles (LA) (Gupta and Krawinkler, 2000a)

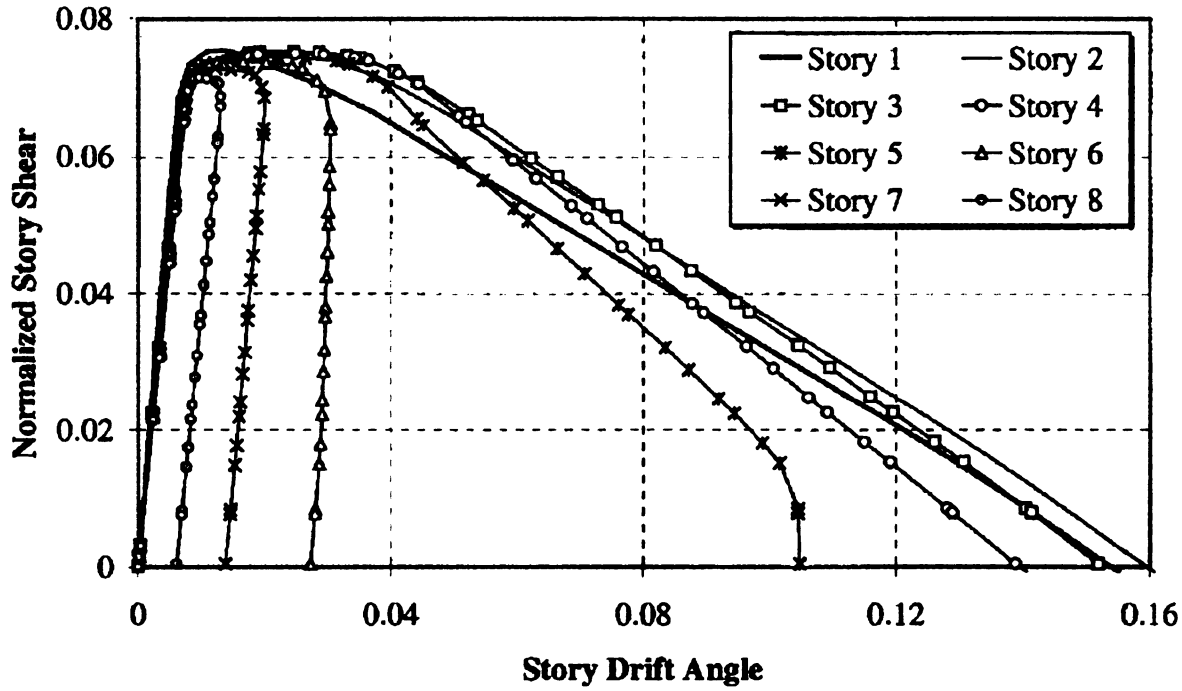


Figure 2.50 Story drift envelopes for various models of 20-story building in Los Angeles, LA30 record (Gupta and Krawinkler, 2000a)

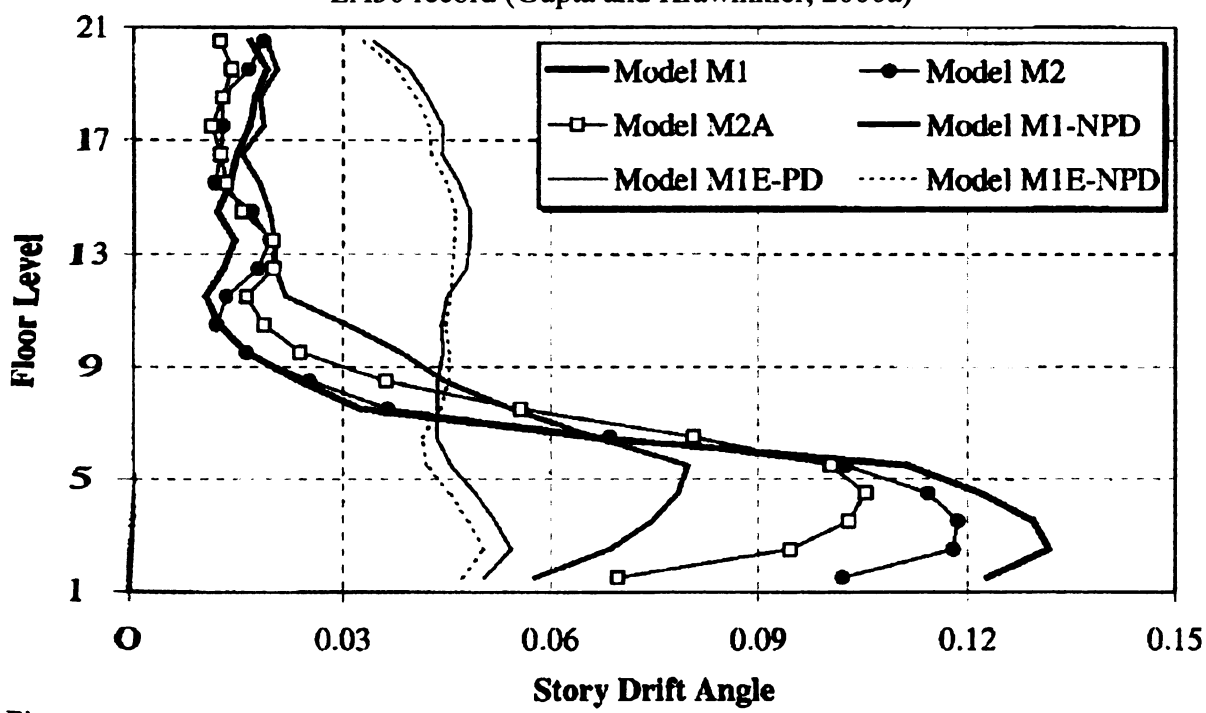


Figure 2.51 Story drift envelopes for various models of 20-story building in Los Angeles, LA36 record (Gupta and Krawinkler, 2000a)

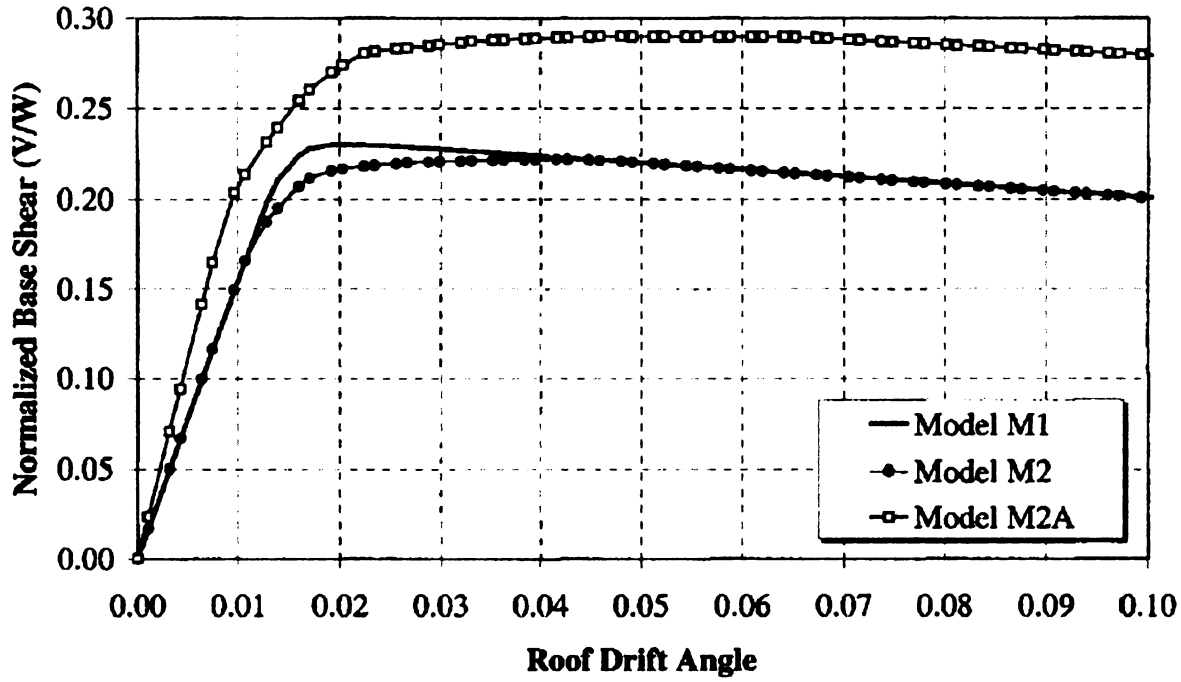


Figure 2.52 Global pushover curves for various models of 3-story building in Seattle (Gupta and Krawinkler, 2000a)

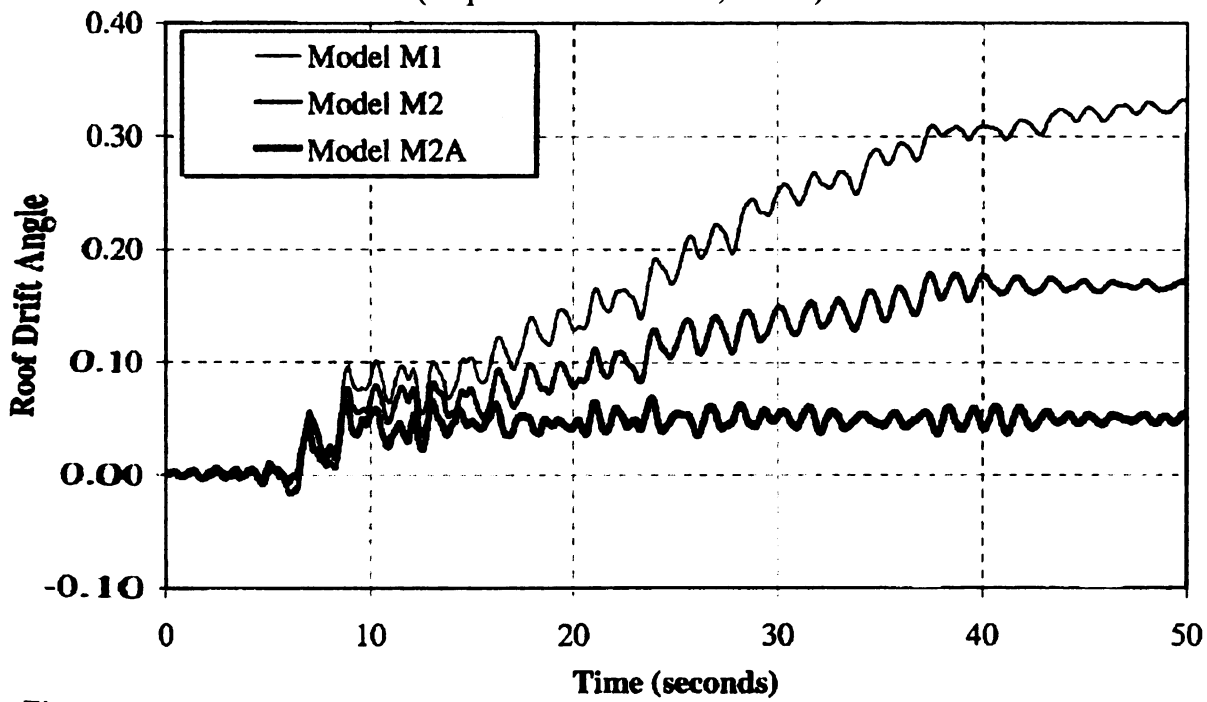


Figure 2.53 Roof time histories for various models of 3-story building in Seattle, SE27 record (Gupta and Krawinkler, 2000a)

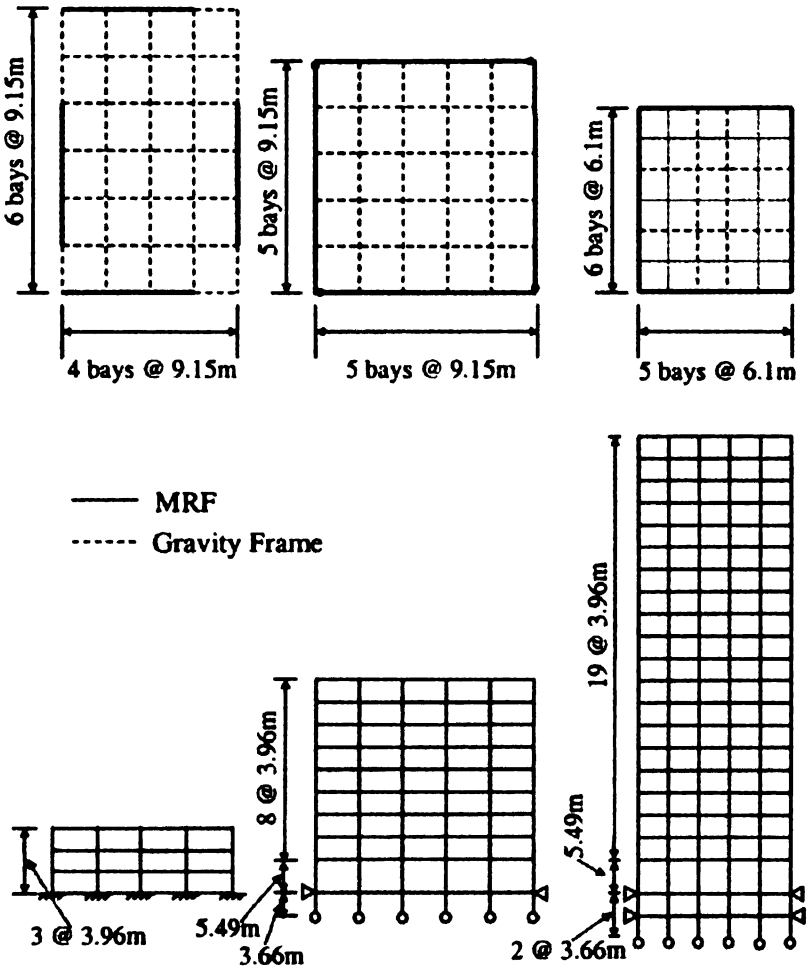


Figure 2.54 Plan views and elevations of model buildings (Gupta and Krawinkler, 2000b)

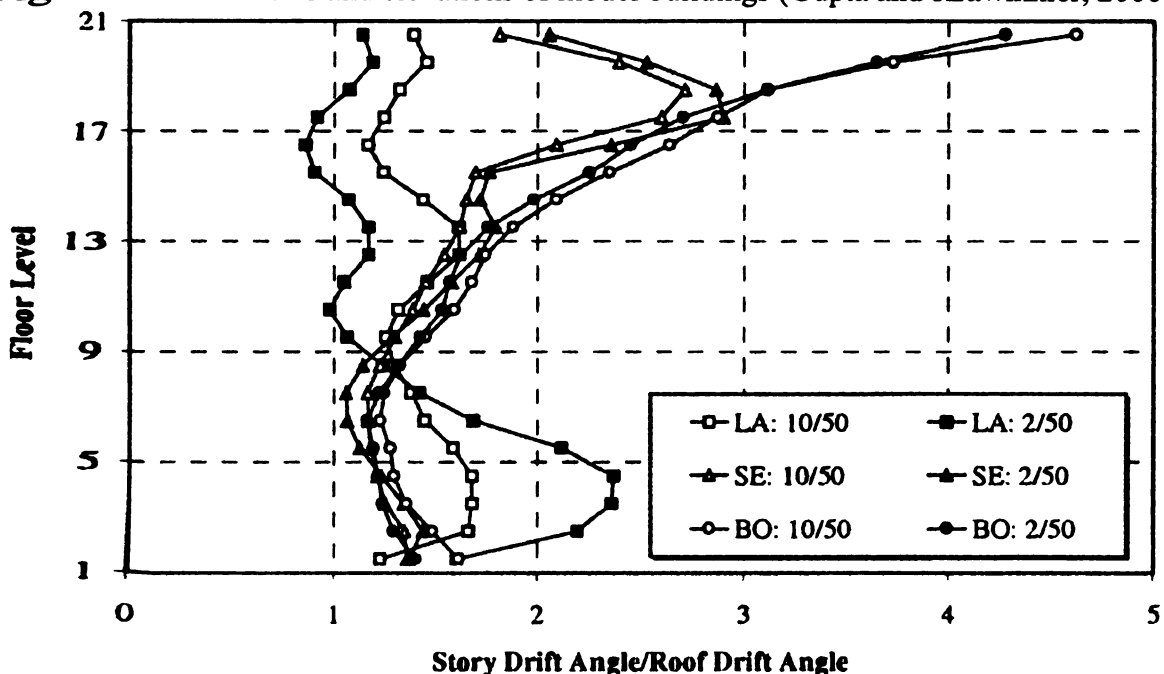


Figure 2.55 Variation over height of median values of ratio of story drift angle to roof drift angle of 20-story structures (Gupta and Krawinkler, 2000b)

CHAPTER 3 ANALYTICAL MODELS FOR COMPONENTS OF CFT MOMENT RESISTING FRAMES

This chapter presents the development and validation of analytical models for the major structural components of high strength CFT moment resisting frames, i.e., the CFT beam-columns, steel beams, and double split-Tee beam-to-column moment connections. The modified fiber element in DRAIN-2DX is used to model the CFT beam-columns and steel beams. The connection finite elements in DRAIN-2DX (Prakash et al. 1993) are used to model the double split-Tee moment connections. The governing input parameters for the models, i.e., the fiber σ–ε relationships for the fiber elements, and the spring force-deformation relations for the connection elements are developed using the results of rigorous 3D finite element analyses of the components (beam-columns, beams, and connections) and their experimental behavior. The developed analytical models for the components are validated using existing experimental data presented earlier in Chapter 2 (Sections 2.2-2.5).

- Section 3.1 presents the development and validation of the fiber element models for CFT beam-columns made from conventional or high strength materials.
- Section 3.2 presents the development and validation of the fiber element models for conventional strength steel beams.
- Section 3.3 presents the development and validation of the connection element models for double split-Tee moment connections.
- Finally, section 3.4 validates the developed component models for predicting the experimental behavior of CFT moment resisting frame *sub-systems* tested by Peng

(2000) at Lehigh University.

3.1 Analytical Model for CFT Beam-Columns

The modified fiber element in DRAIN-2DX will be used to model the CFT beam-columns of the moment resisting frames. The details of this fiber element were presented earlier in Section 2.1. As presented, the fiber element was developed by Prakash et al. (1993), and modified by Kurama et al. (1997) and Cordero et al. (2002) to model more accurately the behavior of reinforced concrete, steel, and steel-concrete composite members. Two fiber σ–ε relationships have been implemented in DRAIN-2DX for use with this fiber element. These are the 'S' and 'C' type fiber σ–ε relationships that were developed for modeling the behavior of steel and concrete fibers by Cordero et al. (2002) and Kurama et al. (1997), respectively. The 'S' and 'C' type fiber σ–ε relationships were presented in detail in Section 2.1.1. As presented, they consist of monotonic σ–ε curves in tension and compression and pre-assigned hysteresis rules for cyclic behavior.

The fundamental input parameters for the fiber element are: (a) the number and distribution of segments along the length, (b) the fiber discretization of the CFT cross-section, and (c) the values of the σ–ε relationships for the fibers modeling the cross-section. Figure 3.1 shows the fiber discretization of the CFT cross-section that will be used in this research. As shown, the CFT cross-section will be discretized into concrete fibers, and steel flange, web, and corner fibers. The 'S' type σ–ε relationship will be used for the steel fibers and the 'C' type σ–ε relationship will be used for the concrete fibers. As explained in Section 2.1.1., the values of the monotonic σ–ε curves in tension and compression are required to define completely the σ–ε relationships. The hysteresis rules defining the cyclic behavior of the 'S' and 'C' type σ–ε relationships are pre-assigned,

and the monotonic σ–ε curves serve as envelopes of the cyclic behavior.

Section 2.2 presented two approaches for developing the monotonic σ–ε curves for the steel and concrete fibers of CFT beam-columns. The first approach was developed and validated by Japanese researchers [Sakino et al. (2004), Inai et al. (2004), and Fujimoto et al. (2004)] and presented in detail in Section 2.2.1. According to this approach, the monotonic σ–ε curves for the steel fibers in tension can be developed based on the nominal or measured steel material properties (yield and ultimate stress). The monotonic σ–ε behavior of the concrete fibers in tension can be ignored, i.e., the concrete fibers can be assumed to have zero tensile stress capacity. The monotonic σ–ε curves for the steel and concrete fibers in compression can be developed using a series of equations 2.1-2.12 developed empirically by the Japanese researchers using regression analysis and the experimental results for several (at least 52) CFT stub column and (at least 25) hollow steel tube stub column tests.

The second approach was developed and validated by U.S. researchers (Varma et al. 2005) and presented in detail in Section 2.2.2. According to this approach, the monotonic σ–ε curves for the steel fibers can be trilinear and based on the nominal or measured steel material properties (yield and ultimate stress). The monotonic σ–ε behavior of the concrete fibers in tension can be ignored. The monotonic σ–ε curves for the steel and concrete fibers in compression can be developed using the results of a 3D finite element analysis of a corresponding CFT segment subjected to pure axial compression loading. The details regarding the development and analysis of the 3D finite element model of the CFT segment using ABAQUS (2003) were presented in detail in Section 2.1.1.

Thus, the two approaches (Japanese and U.S.) differed primarily regarding the development of the steel and concrete fiber σ–ε curves in compression. The Japanese approach consisting of equations 2.1-2.12 is more general and has been validated for CFT beam-columns made from conventional or high strength materials. The U.S. approach is more specific and currently validated only for CFTs made from high strength materials.

Section 2.2.3 presented the results of additional studies conducted by Kowalkowski and Varma (2003) to further compare and evaluate the validity of the fiber σ–ε curves developed by the two approaches. They used to Japanese fiber σ–ε curves to predict the behavior of high strength CFT specimens tested in the U.S., and vice versa. They also compared the steel and concrete fiber σ–ε curves in compression developed by the two approaches for the same CFT specimens. The results indicated significant differences between the steel and concrete fiber σ–ε curves developed by the two approaches for the same CFT specimen. However, the CFT specimen behavior predicted by fiber models using either the U.S. or the Japanese fiber σ–ε curves compared favorably with experimental results and with each other.

According to Kowalkowski and Varma (2003), the fiber σ–ε curves developed by the Japanese approach (equations 2.1-2.12) include several assumptions, simplifications, and calibration with experimental results. Their accuracy is somewhat questionable. However, they can be used easily for CFTs made from conventional or high strength materials. The fiber σ–ε curves developed by the U.S. approach are based in nonlinear mechanics and obtained analytically from the results of 3D finite element analysis, which enhances their credibility. However, they require the development and analysis of 3D finite element models, and are currently limited to CFTs made from high strength materials.

3.1.1 Fiber σ–ε Relationships for CFTs

Based on the recommendations of Kowalkowski and Varma (2003), and the discussions presented above and in section 2.2, the U.S. approach for developing fiber σ–ε curves in compression will be used in this research. The U.S. researchers (Varma et al. 2005) validated this approach only for high strength square CFTs with ($\sigma_y \geq 80$ ksi, and $f'_c \geq 10$ ksi). Hence, the following sub-sections will: (a) extend and validate this analytical approach for CFTs made from conventional or high strength materials, and (b) develop general parametric forms for the fiber σ–ε curves in compression that can be used with a wide range of material (σ_y and f'_c) and geometric (width-to-thickness b/t) parameters without resorting to rigorous 3D finite element analysis.

3.1.2 Approach for Developing Fiber σ–ε Curves in Compression

The analytical approach for developing the steel and concrete fiber σ–ε curves in compression was developed by Varma et al. (2001) and presented in detail in Varma et al. (2005) and Section 2.2.2 of this dissertation. It consists of three steps: (1) developing a 3D finite element model of the failure segment of the CFT beam-column, (2) analyzing the model under pure axial compressive loading, and (3) deriving the fiber σ–ε curves from the results of the nonlinear finite element analysis.

The 3D finite element models are developed and analyzed using ABAQUS (2003). They explicitly include the effects of steel and concrete material inelasticity, local buckling of the steel tube, and transverse interaction between the steel and concrete resulting in confinement of the concrete infill. Hence, the derived fiber σ–ε curves also implicitly account for the effects. The details of the 3D finite element models, nonlinear

analyses, and the development of fiber σ–ε curves from the results of the analyses were presented in Section 2.2.2 and Varma et al. (2005). Hence, they are only summarized briefly in this section.

Figure 2.12 (in Chapter 2) shows the 3D finite element model of the CFT failure segment. As shown, the length of the finite element model was equal to the width (b) of the CFT cross-section, which represents the length of the inelastic failure segment. The CFT segment was analyzed for concentric axial loading, so symmetry of behavior is assumed, and only one-fourth of the CFT cross-section is modeled. Plane sections were constrained to remain plane at the axially loaded and supported ends.

The steel tube was modeled using four node 'S4' shell elements. The elastic behavior of the steel elements was idealized by an isotropic multiaxial elasticity model, which is defined by the elastic modulus (E_s) and Poisson's ratio (ν_s). The inelastic behavior of the steel elements was idealized by a multiaxial plasticity model with a Von Mises yield surface, isotropic hardening behavior, and associated flow rule. The uniaxial σ–ε curve of the steel material is required to define this multiaxial plasticity model. This σ–ε curve was specified based on nominal steel material properties (yield and ultimate stress). Geometric imperfections shown in Figure 2.13 were introduced at the mid-height on all sides of the steel tube to stimulate local buckling. Equation 3.1 was used to specify the geometric impefections, in which a_o is the amplitude that can be taken as wall thickness (t) divided by 10.

$$\delta = \frac{a_0}{4}\left(1+\cos\frac{\pi x}{b/2-3t}\right)\left(1+\cos\frac{\pi y}{b/3}\right) \qquad (3.1)$$

The concrete infill was modeled using six-node 'C3D6' tetrahedral and eight-node 'C3D8' solid elements. The elastic behavior of the concrete elements was idealized by an isotropic multiaxial elasticity model, which is defined by specifying the elastic modulus (E_c) and Poisson's ratio (ν_c) of the concrete material. The inelastic behavior in compression was idealized by the 'CONCRETE' material model, which is a multiaxial plasticity model with a Drucker-Prager compression yield surface, isotropic hardening or softening behavior, and the associated flow rule. Varma et al. (2001) developed the details for calibrating the 'CONCRETE' model to account for the effects of confinement on strength and ductility. This calibrated model was used for the elements modeling the concrete infill of the CFT. The uniaxial σ–ε curve of the concrete in compression was required to define completely the 'CONCRETE' material model. Popovic's empirical σ–ε model was used for conventional strength concrete with f'_c < 10 ksi, and the idealized uniaxial σ–ε model proposed by Varma et al. (2001) was used for high strength concrete with $f'_c \geq 10$ ksi.

As shown in Figure 2.14, the composite interactions between the steel tube and the concrete infill in the transverse and longitudinal directions were modeled. The transverse interaction was modeled using uniaxial gap-contact elements. The gap-contact elements connect corresponding nodes of the steel tube and the concrete infill. These elements have a hard frictionless contact behavior and are closed (in contact) at the beginning of the analyses. The longitudinal interaction was modeled using spring elements. These elements also connect corresponding nodes of the steel tube and the concrete infill. The spring elements act in the longitudinal direction and offer resistance to slip (relative motion). A rigid-plastic force-slip behavior is used for the spring elements. The yield

force is equal to the contact area multiplied by the bond strength (τ_{bond}). τ_{bond} was estimated using the empirical equations proposed by Roeder et al. (1998) or Parsley et al. (2000), whichever was applicable.

The 3D finite element models were analyzed for concentric axial loading using the Riks arc analysis option in ABAQUS (2003). The results from the finite element analyses included the axial force-displacement (P_{FEM}-Δ_{FEM}) response for the CFT segment and the states of stresses and strains in all the steel and concrete elements. The longitudinal stresses in the steel and concrete elements at the end section of the segment (Section A in Figure 2.15) were used to determine the axial forces carried by the steel tube (P_s) and the concrete infill (P_c shown in Figure 2.15).

Effective σ–ε curves were developed for the steel tube and the concrete infill, where the effective stress was calculated as the axial force carried by the steel tube or concrete infill (P_s or P_c) divided by the corresponding cross-sectional area, and the effective strain was calculated as the axial displacement (Δ_{FEM}) of the CFT segment divided by its original length. The effective σ–ε curves for the steel tube and the concrete infill were idealized multi-linearly and used as the steel and concrete fiber σ–ε curves in compression for the CFT fiber model.

3.1.3 Steel Fiber σ–ε Curves in Compression

Several 3D finite element models were developed and analyzed for CFT segments. The results from the finite element analyses were used to develop steel and concrete fiber σ–ε curves in compression presented in this and the following sub-section. The finite element models were developed and analyzed for CFT segments made from: (a) either

A500 Grade-B (σ_y=46 ksi) or A500 Grade-80 (σ_y=80 ksi) steel tubes, with (b) width-to-thickness (b/t) ratios equal to 24, 32, 48, or 64, and (c) filled with concrete with compressive strength equal to 4, 8, 10, or 16 ksi. A total of thirty-two (32) finite element models were developed and analyzed.

Fiber σ–ε Curves for Conventional Strength Steel Tube Walls

Figures 3.2 to 3.5 present the effective σ–ε curves for the steel tube walls of CFTs made from conventional strength A500 Grade-B (σ_y=46 ksi) steel. These Figures indicate that the steel tubes develop and sustain the yield stress σ_y before softening due to combined local buckling and biaxial stress effects, which is similar to the observations of Varma et al. (2001, 2005). These Figures also indicate that increasing the width-to-thickness (b/t) ratio of the steel tube or the compressive strength f'_c of the concrete infill results in more significant post-peak softening of the steel tube walls due to the increased local buckling and biaxial stress effects.

These effective σ–ε curves were idealized to develop fiber σ–ε curves that can be used with the DRAIN-2DX fiber element. Figures 3.6 to 3.9 present the multilinear idealizations of the effective σ–ε curves for the steel tube walls of CFTs with σ_y=46 ksi, f'_c=4, 8, 10, 16 ksi and b/t=24, 64, respectively. As shown in these figures, the multilinear idealizations are very similar in their general form and nature. Figure 3.10 shows the general form of the multilinear σ–ε curve that can be used for the steel fibers of CFTs made from A500 Grade-B (σ_y=46 ksi) steel tube. As shown in Figure 3.10, the idealized σ–ε curve consists of four branches, (a) elastic with slope equal to E_s, (b) elastic-plastic with slope equal to zero, (c) post-peak softening with negative slope, and (d) post-peak plastic with slope equal to zero.

The parameters required to completely define the idealized σ–ε curve are the elastic modulus E_s, the yield stress σ_y, the strain at the onset of softening ε_p, the post-peak plastic stress σ_T, and the strain at the onset of post-peak plastic stress ε_T. Of these parameters, E_s and σ_y are equal to 29000 ksi and 46 ksi, respectively. Multiple regression analysis was performed to define the parameters ε_p, σ_T, and ε_T as functions of the steel yield stress σ_y, the concrete strength f'_c, and the steel tube b/t ratio. The results of the multiple regression analysis are given by Equations 3.2, 3.3, and 3.4.

$$\varepsilon_P = \left(0.651 + 3.43\frac{f'_c}{\sigma_y} + \frac{0.162}{\alpha_s} - \frac{0.067}{\alpha_s^2} \right) \varepsilon_y \tag{3.2}$$

$$\sigma_T = \left(0.625 - 0.452\frac{f'_c}{\sigma_y} + \frac{0.199}{\alpha_s} - \frac{0.097}{\alpha_s^2} \right) \sigma_y \tag{3.3}$$

$$\varepsilon_T = \begin{cases} \left(3.40 - 2.88\dfrac{f'_c}{\sigma_y} + \dfrac{2.45}{\alpha_s} - \dfrac{1.09}{\alpha_s^2} \right) \varepsilon_y & (f'_c < 10ksi) \\ \left(2.67 + 0.383\dfrac{f'_c}{\sigma_y} + \dfrac{2.79}{\alpha_s} - \dfrac{1.52}{\alpha_s^2} \right) \varepsilon_y & (f'_c \geq 10ksi) \end{cases} \tag{3.4}$$

Where, $\sqrt{\alpha_s} = (b/t)\sqrt{\sigma_y / E}$ is the normalized depth-to-thickness ratio of the steel tube and E_s=Young's modulus of steel. These equations can be used to obtain the parameters and define the idealized σ–ε curves for the steel fibers of CFTs made from A500 Grade-B (σ_y=46 ksi) steel with b/t ratios between 24 and 64 and f'_c between 4 and 16 ksi.

Fiber σ–ε Curves for High Strength Steel Tube Walls

Figures 3.11 to 3.14 present the effective σ–ε curves for the steel tube walls of CFTs made from high strength A500 Grade-80 (σ_y=80 ksi) steel. These figures indicate for

most cases the high strength steel tubes develop the yield stress σ_y before softening due to the combined effects of local buckling and biaxial stress. These figures also indicate that increasing the width-to-thickness (b/t) ratio of the high strength steel tube or the strength f'_c of the concrete infill results in more significant post-peak softening of the steel tube walls due to increased local buckling and biaxial stress effects. In some cases the steel tubes did not reach the yield stress σ_y before undergoing softening.

These effective σ–ε curves were idealized to develop fiber σ–ε curves that can be used with the DRAIN-2DX fiber element. Figures 3.15 to 3.18 present the multilinear idealizations of the effective σ–ε curves for the steel tube walls of CFTs with σ_y=80 ksi, f'_c=4, 8, 10, 16 ksi and b/t=24, 64, respectively. As shown in these figures, the multilinear idealizations are very similar in their general form and nature. Figure 3.19 shows the general form of the multilinear σ–ε curve that can be used for the steel fibers of CFTs made from A500 Grade-80 (σ_y=80 ksi) steel tube. As shown in Figure 3.19, the idealized σ–ε curve consists of three branches and can be defined by specifying the values of four parameters: (a) the strain at onset of softening ε_P (b) the elastic modulus E_s, (c) the post-peak plastic stress σ_T, and (d) the strain at onset of post-peak plastic stress ε_T. The first branch is linear elastic with slope equal to E_s. The steel buckles inelastically at stress equal to σ_P when $\varepsilon_P < \varepsilon_y$, or at the yield stress σ_y when $\varepsilon_p \geq \varepsilon_y$. The steel undergoes post-yield softening in the second branch until it reaches the post-peak plastic stress of σ_T at the strain of ε_T. The stress remains constant in the third branch for all strain $\varepsilon \geq \varepsilon_T$.

The parameters required to completely define the idealized σ–ε curve are the elastic modulus E_s, the strain corresponding to the peak stress εp, the post-peak plastic stress σ_T,

and the strain at the onset of post-peak plastic stress ε_T. Of these parameters, E_s is equal to 29000 ksi. Multiple regression analyses were performed to define the parameters ε_p, σ_T, and ε_T as functions of the steel yield stress σ_y, the concrete strength f'_c, and the steel tube *b/t* ratio. The results of the multiple regression analysis are given by Equations 3.5, 3.6, and 3.7.

$$\varepsilon_P = \left(0.797 + 0.393\frac{f'_c}{\sigma_y} + \frac{0.515}{\alpha_s} - \frac{0.528}{\alpha_s^2}\right)\varepsilon_y \tag{3.5}$$

$$\sigma_T = \left(0.616 - 0.093\frac{f'_c}{\sigma_y} + \frac{0.245}{\alpha_s} - \frac{0.195}{\alpha_s^2}\right)\sigma_y \tag{3.6}$$

$$\varepsilon_T = \begin{cases} \left(2.99 - 10.5\frac{f'_c}{\sigma_y} + \frac{3.65}{\alpha_s} - \frac{1.91}{\alpha_s^2}\right)\varepsilon_y & (f'_c < 10ksi) \\ \left(2.12 - 1.33\frac{f'_c}{\sigma_y} + \frac{3.53}{\alpha_s} - \frac{2.98}{\alpha_s^2}\right)\varepsilon_y & (f'_c \geq 10ksi) \end{cases} \tag{3.7}$$

These equations can be used to obtain the parameters and define the idealized σ–ε curves for the steel fibers of CFTs made from A500 Grade-80 (σ_y=80 ksi) steel with *b/t* ratios between 24 and 64 and f'_c between 4 and 16 ksi.

3.1.4 Concrete Fiber σ–ε Relationships in Compression

Fiber σ–ε curves for Conventional Strength Concrete Infills ($f'_c \leq 10ksi$)

Figures 3.20 to 3.22 present the effective σ–ε curves for the concrete infills of CFTs made from A500 Grade-B (σ_y=46 ksi) steel tubes with b/t ratios of 24, 32, 48, or 64, and concrete strength f'_c equal to 4, 8, and 10 ksi, respectively. Similarly, Figures 3.23 to 3.25 show the effective σ–ε curves for the concrete infills of CFTs made from A500-Grade 80

(σ_y=80 ksi) steel tubes with b/t ratios of 24, 32, 48, or 64, and concrete strength f'_c equal to 4, 8, and 10 ksi, respectively. These figures indicate that confinement increases the effective strength and ductility of the concrete infill. Increasing the yield stress of the steel tube from 46 to 80 ksi or decreasing the steel tube b/t ratio results in better confinement of the concrete infill.

The effective σ–ε curves for the concrete infills with $f'_c \leq 10$ ksi (i.e., Figures 3.20 to 3.25) were normalized with respect to their peak stress (f'_{cc}) and strain (ε'_{cc}) values. The normalized curves were similar in general form and nature. For example, Figures 3.26 and 3.27 show the normalized effective σ–ε curves for the concrete infills of CFTs with σ_y=46 ksi, f'_c = 4 ksi, and b/t = 24 or 64. Figure 3.28 shows the general form of the normalized effective σ–ε curve. As shown in Figure 3.28, the normalized σ–ε consists of an ascending branch and a post-peak softening branch. The ascending branch of the normalized effective σ–ε curve (strain $\varepsilon_c/\varepsilon'_{cc} \leq 1$) can be described using the empirical σ–ε model proposed by Mander et al. (1988). Equation 3.8 summarizes this σ–ε model for the ascending branch.

$$\frac{f_c}{f'_{cc}} = \frac{\varepsilon_c}{\varepsilon'_{cc}} \cdot \frac{n}{n-1+\left(\varepsilon_c/\varepsilon'_{cc}\right)^n} \tag{3.8}$$

Where,

$$n = \frac{E_c}{E_c - f'_{cc}/\varepsilon'_{cc}} \tag{3.9}$$

f'_{cc} is the compressive strength of confined concrete, ε'_{cc} is the compressive strain at which this peak compressive stress would be reached, E_c is the initial tangent stiffness of the unconfined concrete and n is determined using Equation (3.9). The post-peak descending branch can be modeled as a straight line with negative stiffness equal to k.

The σ–ε behavior of the descending branch ($\varepsilon_c/\varepsilon'_{cc}>1$) can be defined using Equation 3.10.

$$\frac{f_c}{f'_{cc}} = k\left(\frac{\varepsilon_c}{\varepsilon'_{cc}} - 1\right) + 1 \tag{3.10}$$

The normalized effective σ–ε curve in Figure 3.28 can be defined completely by specifying the values of f'_{cc}, ε'_{cc}, and k. Multiple regression analyses were performed to define the value of these parameters as functions of σ_y, f'_c, and the b/t ratio. The results of the multiple regression analyses are given in Equations 3.11 to 3.14.

$$f'_{cc} = \begin{cases} \left(2.10 - 1.14\dfrac{f'_c}{\sigma_y} - 1.98\sqrt{\lambda_t} + 1.29\lambda_t - \dfrac{0.034}{\lambda_t} - \dfrac{0.002}{\lambda_t^2}\right) f'_c & (\sigma_y \le 46ksi) \\ \left(38.7 - 1.95\dfrac{f'_c}{\sigma_y} - 41.8\sqrt{\lambda_t} + 13.6\lambda_t - \dfrac{11.0}{\lambda_t} + \dfrac{1.84}{\lambda_t^2}\right) f'_c & (\sigma_y > 46ksi, \dfrac{f'_c}{\sigma_y} > 0.05) \\ \left(3.22 - 3.28\sqrt{\lambda_t} + 1.47\lambda_t\right) f'_c & (\sigma_y > 46ksi, \dfrac{f'_c}{\sigma_y} \le 0.05) \end{cases} \tag{3.11}$$

$$\varepsilon'_{cc} = \begin{cases} \left(\begin{array}{l} -1.55 + .004\dfrac{f'_{cc}}{f'_c} - 1.92\sqrt{\lambda_t} + 2.07\lambda_t - 0.472\lambda_t^2 + 0.060\lambda_t^3 \\ -\dfrac{1.49}{\lambda_t} + \dfrac{0.133}{\lambda_t^2} - \dfrac{0.008}{\lambda_t^3} + \dfrac{3.182}{\sqrt{\lambda_t}} \end{array}\right) \varepsilon'_c & (\sigma_y \le 46ksi) \\ \left(\begin{array}{l} -570.8 + 7.82\dfrac{f'_{cc}}{f'_c} + 810.6\sqrt{\lambda_t} - 382.1\lambda_t \\ +31.8\lambda_t^2 + \dfrac{119.5}{\lambda_t} - \dfrac{16.4}{\lambda_t^2} \end{array}\right) \varepsilon'_c & (\sigma_y > 46ksi, \dfrac{f'_c}{\sigma_y} > 0.05) \\ \left(421.0 - 130.3\dfrac{f'_{cc}}{f'_c} - 430.1\sqrt{\lambda_t} + 195.4\lambda_t\right) \varepsilon'_c & (\sigma_y > 46ksi, \dfrac{f'_c}{\sigma_y} \le 0.05) \end{cases} \tag{3.12}$$

$$k = \begin{cases} 294.0 - 224.0\sqrt{\lambda_t} + 73.1\lambda_t - 3.70\lambda_t^2 + \dfrac{52.6}{\lambda_t} - \dfrac{1.91}{\lambda_t^2} - \dfrac{190.2}{\sqrt{\lambda_t}} & (\sigma_y \le 46ksi) \\ -101.5 + 61.8\sqrt{\lambda_t} - 16.3\lambda_t + 0.553\lambda_t^2 - \dfrac{30.0}{\lambda_t} + \dfrac{1.88}{\lambda_t^2} + \dfrac{83.5}{\sqrt{\lambda_t}} & (\sigma_y > 46ksi) \end{cases} \quad (3.13)$$

where $$\lambda_t = \frac{\sigma_y A_s}{f_c' A_c} = \frac{\sigma_y}{f_c'} \bullet \frac{4(b/t-1)}{(b/t-2)^2} \quad (3.14)$$

λ_t is the referred as the confinement index for the CFT. Thus, Equations 3.8 and 3.10 can be used to define the normalized σ–ε curve for concrete infills with $f'_c \le 10$ ksi, and Equations 3.11 to 3.13 can be used to obtain the values of the parameters f'_{cc}, ε'_{cc}, and k required to completely define the normalized σ–ε curve for CFTs with σ_y = 46 or 80 ksi, b/t ratios between 24 and 64, and f'_c between 4 and 10 ksi.

Fiber σ–ε Curves for High Strength Concrete Infills

Figures 3.29 shows the effective σ–ε curves for the concrete infills of CFTs made from A500 Grade-B (σ_y=46 ksi) steel tubes with b/t ratios of 24, 32, 48, or 64, and concrete strength f'_c equal to 16 ksi. Similarly, Figures 3.30 shows the effective σ–ε curves for the concrete infills of CFTs made from A500 Grade-80 (σ_y=80 ksi) steel tubes with b/t ratios of 24, 32, 48, and 64, and concrete strength f'_c equal to 16 ksi. These figures indicate that confinement increases the ductility of the high strength concrete infill but does not have a significant influence on its strength. Increasing the yield stress of the steel tube from 46 to 80 ksi or decreasing the steel tube b/t ratio results in better confinement of the concrete infill.

The effective σ–ε curves for the concrete infills with f'_c = 16 ksi (i.e., Figures 3.29 and 3.30) were normalized with respect to their peak stress and strain values. These normalized σ–ε curves are shown in Figures 3.31 and 3.32. These normalized σ–ε curves

are similar in form and nature. Figure 3.33 shows the general form of the normalized effective σ–ε curve for high strength concrete infills. As shown in Figure 3.33, the normalized σ–ε consists of three branches that can be defined completely by specifying the values of three parameters: (a) the modulus of elasticity E_c, (b) the peak stress f'_c, (c) the strain at onset of softening (ε_{uc}), and (d) the post-peak softening slope k. The first branch is linear elastic with slope equal to $E_c=f'_c/\varepsilon'_c$. The second branch is perfectly plastic with constant stress (f'_c). The third branch begins when the strain reaches ε_{uc} and has a constant negative (softening) slope equal to $-k$.

The normalized effective σ–ε curve in Figure 3.33 can be defined completely by specifying the values of E_c, f'_c, ε_{uc}, and k. The values of E_c and f'_c can be taken based on the high strength concrete material properties. ε_{uc} can be estimated using Equation 3.14, which was developed by Collins and Porasz (1989) for estimating the peak strain of unconfined high strength concrete.

$$\varepsilon_{uc} = (f'_c + 17)/ E_c \qquad (3.14)$$

Multiple regression analyses were performed to develop Equation 3.15 defining the post-peak softening slope k as a function of σ_y, f'_c, and the b/t ratio.

$$k = \begin{cases} -1.46 + 2.88\sqrt{\lambda_t} - 1.42\lambda_t & (\sigma_y \le 46ksi) \\ -0.99 + 1.25\sqrt{\lambda_t} - 0.278\lambda_t & (\sigma_y > 46ksi) \end{cases} \qquad (3.15)$$

The normalized σ–ε curve shown in Figure 3.33 can be used for the high strength concrete infills (f'_c>10 ksi) of CFTs. The parameters used to define the curve can be obtained using Equations 3.14 and 3.15.

3.1.5 Validation of CFT Analytical Models

The validity of the fiber element and the steel and concrete fiber σ–ε relationships was evaluated by using them to predict the moment-curvature (M-ϕ) responses of CFT beam-column specimens tested by several researchers as part of the U.S.-Japan Cooperative Earthquake Research Program, and reported by Fujimoto et al. (2004). Fiber-based models were developed to model the inelastic failure segments of the CFT beam-column specimens. The steel and concrete fiber σ–ε relationships were developed as described in Sections 3.1.2 to 3.1.4. These σ–ε models implicitly accounted for the effects of local buckling, concrete confinement and crushing, and transverse interaction between the steel and concrete. The results from the fiber analyses were compared to the experimental and analytical moment-curvature (M-ϕ) responses reported by Fujimoto et al. (2004). Additionally, the developed fiber σ–ε curves were compared with the fiber σ–ε curves developed and used by Fujimoto et al. (2004) for the analytically predicting the M-ϕ behavior of the tested specimens.

Figures 3.34 to 3.60 present the comparisons of the analytical and experimental results for several square CFT beam-columns made from conventional or high strength materials and with b/t ratios ranging from 23 to 74. A set of three figures is shown for each CFT.

- Figures 3.34 to 3.36 pertain to CFTs with σ_y=262 MPa, f'_c=41.1 MPa, and b/t=34.
- Figures 3.37 to 3.39 are for CFTs with σ_y=618 MPa, f'_c=41.1 MPa, and b/t=23.
- Figures 3.40 to 3.42 are for CFTs with σ_y=835 MPa, f'_c=77.0 MPa, and b/t=27.
- Figures 3.43 to 3.45 are for CFTs with σ_y=262 MPa, f'_c=80.3 MPa, and b/t=49.

- Figures 3.46 to 3.48 are for CFTs with σ_y=618 MPa, f'_c=25.4 MPa, and b/t=33.
- Figures 3.49 to 3.51 are for CFTs with σ_y=835 MPa, f'_c=25.4 MPa, and b/t=27.
- Figures 3.52 to 3.54 are for CFTs with σ_y=835 MPa, f'_c=40.5 MPa, and b/t=41.
- Figures 3.55 to 3.57 are for CFTs with σ_y=618 MPa, f'_c=41.1 MPa, and b/t=50.
- Figures 3.58 to 3.60 are for CFTs with σ_y=262 MPa, f'_c=41.1 MPa, and b/t=74.

The first figure in each set of three figures compares the concrete fiber σ–ε curves in compression developed as part of this research (U.S.) with the corresponding fiber σ–ε curves developed using the (Japanese) empirical models reported by Fujimoto et al. The second figure compares the U.S. and Japanese steel fiber σ–ε curves for the CFT. The third figure compares the M-ϕ responses predicted using the U.S. fiber models and σ–ε curves and the Japanese fiber models and σ–ε curves with the experimental M-ϕ responses.

Comparison of Concrete Fiber σ–ε Curves

The scale factor for compressive strength used by Fujimoto et al. (2004) makes the Japanese σ–ε curves have a smaller peak stress than U.S. concrete fiber σ–ε curves. For conventional strength concrete ($f'_c \leq$10ksi), the U.S. concrete fiber σ–ε model indicates that confinement has greater influence on both the peak strength and post-peak ductility (Figs. 3.35, 3.38, 3.47, and 3.53) for b/t<48, and smaller influence for b/t≥48 (Figs. 3.56 and 3.59). The Japanese concrete fiber σ–ε model indicates that confinement does not have influence on the peak strength. The post-peak slopes of the US model and the Japanese model are comparable to each other for b/t<48 (Figs. 3.35, 3.38, 3.47, and 3.53).

For b/t≥48, the Japanese σ–ε model has a better post-peak ductility than the US σ–ε model (Figs. 3.56 and 3.59).

For high strength concrete (f'_c>10ksi), both the US and Japanese concrete fiber σ–ε models indicate that confinement has no influence on the peak strength (Figs. 3.41 and 3.44). The post-peak slopes of the US model and the Japanese model are comparable to each other for b/t>48 (Figs. 3.44). For b/t≤48, the Japanese model has a better post-peak ductility than the US model (Figs. 3.41).

Comparison of Steel σ–ε Curves

In Japanese design practice, the b/t ratio of steel tubes is classified into three ranks depending on the expected deformation capacity of the plastic hinge formed in the hollow steel tubes. According to AIJ (1981), the ductility factors of rank FA and FC are 4 and 1, respectively, and rank FD steel tubes buckle elastically. The comparison of the US and Japanese σ–ε curves for the steel fibers are therefore grouped by these three ranks (rank FA, FC and FD).

Rank FA. For rank FA, both the US model and the Japanese steel σ–ε models show that local buckling after yielding and have a similar post-peak slope (Fig. 3.34) for conventional strength steel, but the Japanese model has a greater peak stress and delayed local buckling than the US model. For high strength steel tube with conventional strength concrete infill (Fig. 3.37), the US σ–ε model shows that steel tube yields slightly lower than the yield stress due to the biaxial effect, while the Japanese σ–ε model still predicts local buckling after yielding. Again, both the US model and Japanese steel σ–ε models have a similar post-peak slope for high strength steel tube with conventional strength concrete infill of rank FA (Fig. 3.37).

Rank FC.

3.40 and

stress, but

strength st

σ–ε model

yielding at

peak slope

FC (Figs. 3.

Rank FD.

FD (Figs. 3

before yield

the Japanes

with conver

that local bu

The Japanes

Comparis

The fiber

were subject

specimens. F

ϕ responses

experimental

Fujimoto et al.

responses pred

Rank FC. For high strength steel tube with high strength concrete infill of rank FC (Figs. 3.40 and 3.43), both the US and Japanese steel σ–ε models show yielding at the yield stress, but the Japanese model has a greater post-peak slope than the US model. For high strength steel tube with conventional strength concrete infill (Figs. 3.46 and 3.49), the US σ–ε model shows that local buckling before yielding, while the Japanese still predicts yielding at the yield stress. Both the US model and Japanese model have a similar post-peak slope for high strength steel tube with conventional strength concrete infill of rank FC (Figs. 3.46 and 3.49).

Rank FD. For high strength steel tube with conventional strength concrete infill of rank FD (Figs. 3.52 and 3.55), both the US and Japanese σ–ε models show local buckling before yielding. The US σ–ε model has a higher peak stress than the Japanese model, but the Japanese model has a greater post-peak slope. For conventional strength steel tube with conventional strength concrete infill and b/t>64 (Fig. 3.58), the US model shows that local buckling after yielding, while the Japanese predicts buckling before yielding. The Japanese model has a greater post-peak slope than the US model (Fig. 3.58).

Comparison of M–ϕ Responses

The fiber-based models for the failure segments of the CFT beam-column specimens were subjected to the same loading history as the failure segments of the corresponding specimens. Figures 3.36, 3.39, 3,42, 3.45, 3.48, 3.51, 3.54, 3.57, and 3.60 compare the *M*-ϕ responses predicted using the developed fiber model and σ–ε curves with the experimental *M*-ϕ responses, and also with the analytical *M*-ϕ responses predicted by Fujimoto et al. (2004) using the Japanese fiber model. These comparisons shows the *M*-ϕ responses predicted using the developed fiber model compare favorably with the

experimen

exception

h_t=74 (Fig

FEM analy

σ-ε curves

3.2 ANAL

Recent

split-Tee co

9.7%, 7.0%

that, the eff

from high s

of high stre

Obviously,

MRFs cons

accurately, t

and connect

The exp

with double

ends of the c

by local flang

inelastic failu

length of the

experimental and analytical M-ϕ responses reported by Fujimoto et al. (2004). An exception is for case of b/t=74 (Figure 3.60). The reason for the over prediction for b/t=74 (Figures 3.58 to 3.60) is that all the US fiber σ–ε curves were developed from FEM analysis for CFTs with $b/t \leq 64$. When the b/t ratio is larger than 64, the developed σ–ε curves for CFTs may not suitable to use in that case.

3.2 ANALYTICAL MODEL FOR STEEL BEAMS

Recent research on *CFT MRFs* indicate that, for a CFT subassemblage with double split-Tee connection, the beam, connection, column, and panel zone contributed 83.0%, 9.7%, 7.0%, and 0.3% to total story drift, respectively (Peng, 2001). Other research show that, the effects of these local degradations are especially significant for members made from high strength material, due to their susceptibilities to issues such as local buckling of high strength steel (Ricles et al., 1993) and crushing of high strength concrete, etc. Obviously, in order to evaluate the seismic response of *High-strength CFT MRFs* (CFT MRFs consisting of high-strength CFT column and high-strength steel beam) more accurately, the combined effects of the strength and stiffness degradation of the members and connections should be considered simultaneously.

The experimental studies indicate that the steel beams of the CFT subassemblages with double split-Tee connections developed full plastic flexural hinges in the beams at ends of the connection, where the pronounced flange and web yielding occurred followed by local flange and web buckling (Peng, 2001). Failure occurs with the formation of an inelastic failure segment in the portion of the beams subjected to maximum forces. The length of the failure segment is approximately equal to the depth (d_b) of the beam cross-

section. In

failure seg

The D

elastic and

segment w

located in t

inelastic be

steel beam

cross-sectio

The fibe

implicitly ac

steel flange a

buckling. Bas

can be used f

3.2.1 FEM

The stress-

from three-di

As a result, th

for the effects

Three-dime

steel beams we

Fig. 3.61). Sy

section. Inelastic deformations including local buckling of the steel flange and web in the failure segment while the remaining portions of the length unload elastically.

The DRAIN-2DX fiber element can be used with several segments to model the elastic and pre-peak inelastic behavior of steel beams before failure. Additionally, a fiber segment with length equal to the depth (d_b) of the steel beam cross-section must be located in the anticipated region of maximum forces to appropriately model the post-peak inelastic behavior of the failure segment. Figure 3.85 shows fiber discretization of the steel beam cross-section at the slice locations. As shown in Figure 3.87, the steel beam cross-section is discretized into steel flange, and web fibers.

The fiber σ–ε relationships govern the accuracy of the fiber element and must implicitly account for the complexities of the cyclic behavior for the steel beams, i.e., the steel flange and web fiber σ–ε relationships must account for the effects of inelastic local buckling. Based on previous discussion, the 'S' type σ-ε relationship (Cordero et al. 2002) can be used for the steel flange and web fibers.

3.2.1 FEM Models of Steel Beams

The stress-strain curves for the steel fibers of steel beam in compression were derived from three-dimensional nonlinear finite element analyses of the beam failure segments. As a result, the finite element model (FEM)-based stress-strain curves implicitly account for the effects of inelastic flange and web buckling.

Three-dimensional finite element models for the failure segment (plastic hinge) of steel beams were developed and analyzed under pure flexural loading using ABAQUS (Fig. 3.61). Symmetry was considered and one half of the specimen cross-section was

modeled.

The FEM

The result

steel beam

steel flange

3.2.1.1 El

The stee

of the steel

yield surface

Idealized S

The ideal

of the flexura

idealized stre

specifying the

the yield stres

ultimate strai

second branch

(σ), respectiv

plateau with a

hardening (ε=

modeled. Plane sections were enforced to remain plane at the loaded and supported ends. The FEM analyses included local buckling of the flanges and web of the steel beams. The results from the FEM analyses included the moment-rotation (M-θ) responses of the steel beam failure segments and the complex state of multiaxial stresses and strains in the steel flange and web of the FEM models for the steel beams.

3.2.1.1 Elements Used and Material Models

The steel beam was modeled using four-node shell elements. The inelastic behavior of the steel elements was idealized by a multiaxial plasticity model with a von Mises yield surface, isotropic hardening behavior and associated flow rule.

Idealized Stress-Strain Curves for Steel

The idealized stress-strain curve was used to model the measured stress-strain curve of the flexural test specimens tested by Green et al (2000). As shown in Figure 3.62, the idealized stress-strain curve consists of four branches that could be completely defined by specifying the values of six parameters: the elastic modulus (E), the static yield stress (σ_s), the yield stress (σ_y), the strain at onset of hardening (ε_{sh}), the ultimate stress (σ_u), and the ultimate strain (ε_u). The first branch is linear elastic with modulus equal to E. The second branch links the two points represent the static yield stress (σ_s) and the yield stress (σ_y), respectively. The third branch begins with the onset of yielding ($\varepsilon=\varepsilon_y$) and is a yield plateau with a constant stress equal to σ_y, the fourth branch begins at the onset of strain hardening ($\varepsilon=\varepsilon_{sh}$) and follows the power-hardening rule given in Equation 3.16.

When $\varepsilon \geq$

Simila

seismic ar

3.63, the

values of fi

of hardenin

linear elasti

yielding (ε=

begins at th

given in Ec

σ_1=50ksi, σ_2

Peng's CFT

relationships

and 3.63) we

3.2.1.2 Geo

Geometri

the steel bear

were based o

recommended

web and flan

imperfection o

When $\varepsilon \geq \varepsilon_{sh}$: $\sigma = \sigma_u - (\sigma_u - \sigma_y)\left(\frac{\varepsilon_u - \varepsilon}{\varepsilon_u - \varepsilon_{sh}}\right)^3$ (3.16)

Similar stress-strain curve with three branches was used to model A992 steel in the seismic analysis of moment resisting frames with CFT columns. As shown in Figure 3.63, the idealized stress-strain curve could be completely defined by specifying the values of five parameters: the elastic modulus (E), the yield stress (σ_y), the strain at onset of hardening (ε_{sh}), the ultimate stress (σ_u), and the ultimate strain (ε_u). The first branch is linear elastic with modulus equal to E. The second branch begins with the onset of yielding ($\varepsilon=\varepsilon_y$) and is a yield plateau with a constant stress equal to σ_y, the third branch begins at the onset of strain hardening ($\varepsilon=\varepsilon_{sh}$) and follows the power-hardening rule given in Equation 3.16. In order to make a conservative prediction, $E=29000ksi$, $\sigma_y=50ksi$, $\sigma_u=65ksi$, $\varepsilon_{sh}=11\varepsilon_y$, and $\varepsilon_u=81\varepsilon_y$ was used for A992 steel. For validation of Peng's CFT connection subassembly test (Peng, 2001), the true stress-plastic strain relationships of tension coupon tests for A36 steel beam flange and beam web (Fig. 3.62 and 3.63) were used.

3.2.1.2 Geometric Imperfections

Geometric imperfections were introduced at the mid-height of the flanges and web of the steel beams to stimulate local buckling. The shapes of the geometric imperfections were based on the recommendations of Green et al. (2002). Equation (3.17) and (3.18) recommended by were Green et al. (2002) used to specify the geometric imperfection for web and flange, respectively, in which a_1 and b_1 are the amplitude of the geometric imperfection of web and flange, respectively (fig. 3.64):

δ

The im

and web o

for the flan

3.2.1.3 FE

The cyc

cyclic axial

namely, the

of the failur

section is

correspondir

divided by it

sum of the

force carried

sectional are

flanges and

curves are us

As shown

10 of Green's

stress) steel in

$$\delta_{web} = a_1/4\left(1+\cos 2\pi x/d_b\right)\left(1+\cos 2\pi y/d_b\right) \quad (3.17)$$

$$\delta_{flange} = b_1/4\left(1+\cos 2\pi x/d_b\right)\left(1+\cos 2\pi z/b_f\right) \quad (3.18)$$

The imperfection amplitudes used in this study are the nominal *b/t* ratios of the flange and web of the steel beams. Maximum imperfection amplitudes of *b/t/1000* were used for the flange and web of the steel beams.

3.2.1.3 FEM-Based Effective Stress-Strain Curves

The cyclic finite element analyses for failure segment of steel beam provided the cyclic axial normal stress distribution of the components of the steel beam cross-section, namely, the steel beam flanges and web layers 1-4 identified in Figure 3.61(b), at the end of the failure segment. The effective stress for the components of steel beam cross-section is defined as the axial force divided by the cross-sectional area. The corresponding effective strain is defined as the longitudinal shortening of the component divided by its original length. The axial force carried by a component is calculated as the sum of the axial forces carried by the corresponding end-section elements. The axial force carried by an element is calculated as its longitudinal stress multiplied by its cross-sectional area. Thus, effective stress-strain curves are developed for the steel beam flanges and web layers 1-4. Multilinear idealizations of these effective stress-strain curves are used as the corresponding fiber σ–ε curves in compression.

As shown in Figures 3.65 to 3.69, the effective stress-strain curves for Test Specimen 10 of Green's experiment (Green et al. 2002) for high strength HSLA-80 (80 ksi yield stress) steel indicate that, local buckling web layer 1 reduce the post-peak stress capacity

below σ_y, while the local buckling influence on flange and web layers 2, 3 and 4 is not so remarkable.

Figs 3.70 to 3.74 show the fiber σ–ε curves in compression developed for the flange and web layers (1-4) of W36x135, W33x118 W30x108, W27 x84 and W24x62 rolled steel shapes made from ASTM A992 (50 ksi yield stress) material. These fiber σ–ε curves illustrate the detrimental effects of inelastic flange and web local buckling.

The idealized effective stress-strain curve for rolled shape (Fig 3.75) consists of four branches and can be completely defined by specifying the values of six parameters: the elastic stress (σ_1), the elastic strain (ε_1), the peak stress (σ_2), the strain at the onset of unloading (ε_2), the residual stress (σ_3), and the strain at the onset of constant stress (ε_3). The first branch is linear elastic with slope equal to $E = \sigma_1/\varepsilon_1$. The second branch links the two points represent the elastic stress (σ_1) and the peak stress (σ_2), respectively. The third branch begins when the strain reaches ε_2 and decreases to a stable stress, σ_3, at the strain ε_3. The fourth branch is a residual plateau and the compressive stress is assumed to reach stability after $\varepsilon \geq \varepsilon_3$. The values of the six parameters, σ_1, ε_1, σ_2, ε_2, σ_3, ε_3, for the idealized flange and web fiber σ–ε curves of rolled shapes made with A992 steel are summarized in Table 3.1. The fiber σ–ε curves developed were used to model steel beams made with A992 steel in the seismic analysis of moment resisting frames with CFT columns.

3.2.2 V

The v

curves fo

rotation (

ksi yield

Fiber-base

steel beam

used only

segment.

The u

steel bear

curves of

strain beh

in an appr

The

were subj

cyclic stee

responses

are shown

M-ϕ respon

are shown

M-ϕ respon

are shown i

3.2.2 Validation of Analytical Model of Steel Beams

The validity of the fiber element and this analytical approach for developing fiber σ–ε curves for steel beams was evaluated by using them to predict the cyclic moment-end rotation (M-θ) response of one A36 (36 ksi yield stress) steel beam and two HSLA-80 (80 ksi yield stress) steel beams tested under cyclic flexural loading by Green et al. (2002). Fiber-based model were developed to model the inelastic failure segments of the cyclic steel beam specimens. As shown in Fig. 3.76, the fiber-based steel beam element was used only one segment, and therefore only one slice, to model the inelastic failure segment. The length of the failure segment was identical to the depth of the steel beam.

The uniaxial stress-strain curves that were developed from cyclic FEM analysis of steel beam (Figs 3.65 to 3.69) were used as the envelopes of the cyclic stress-strain curves of steel beam in compression for the fiber-based models. The hysteretic stress-strain behavior implicitly accounts for the effects of kinematic hardening, local buckling in an approximate manner.

The fiber-based models for the failure segments of the cyclic steel beam specimens were subjected to the same loading history as the failure segments of the corresponding cyclic steel beam specimens. The cyclic FEM analysis and fiber analysis results for M-ϕ responses of Green's experiment for conventional strength A36 steel, Test specimen 11, are shown in Figs 3.77 and 3.78. The cyclic FEM analysis and fiber analysis results for M-ϕ responses of Green's experiment for high strength HSLA-80 steel, Test specimen 10, are shown in Figs 3.79 and 3.80. The cyclic FEM analysis and fiber analysis results for M-ϕ responses of Green's experiment for high strength HSLA-80 steel, Test specimen 12, are shown in Figs 3.81 and 3.82.

The

beam spe

results. F

web local

3.2.3 Sur

A fiber

finite elem

for the effi

model we

specimens

beams in c

the cyclic

Green et a

in this rese

3.3 Analy

Signific

resisting be

Ricles et a

studies, the

identified a

resisting fra

The results from both the FEM analysis and the fiber analysis of the cyclic steel beam specimen for the three specimens all compared favorably with the experimental results. Figs 3.77 to 3.82 also illustrated the importance of modeling inelastic flange and web local buckling effects while predicting the cyclic M-θ response of steel beams.

3.2.3 Summary

A fiber-base model for the steel beam was developed from the results of nonlinear 3D finite element analyses. This FEM-based fiber model for steel beams implicitly account for the effects of inelastic local buckling of beam flange and beam web. Fiber-based model were developed to model the inelastic failure segments of the steel beam specimens. The σ–ε curves developed were used as the stress-strain curves of steel beams in compression for the fiber-based model. The results from the fiber analysis of the cyclic steel beam specimens compared favorably with the experimental results of Green et al. (2002). Therefore, the fiber-base model was used to model the steel beams in this research.

3.3 Analytical Model for Double Split-Tee Connections

Significant research has also been conducted on the development of different moment resisting beam-to-CFT column connections, for example, Alostaz and Schneider 1996, Ricles et al. 1997, Elremaily et al. 2000, Peng 2001 among others. Based on these studies, the Double Split-Tee (DST) moment connection shown in Figure 3.83 has been identified as one of the most efficient beam-to-column connections for CFT moment resisting frames (Ricles et al. 1997, Peng 2001). These researchers have demonstrated

through

adequate

strong co

The I

split-Tee

the spring

the connec

of pretensi

connection

3.3.1 FE

The str

from three

As a result

for the effe

Three-d

and analyz

Symmetry

Plane sectio

included pr

contacting a

The results f

the DST conn

through full-scale experimental studies that split-Tee moment connections can provide adequate cyclic joint stiffness and strength to develop the highly desirable weak beam-strong column failure mechanism in CFT moment resisting frames.

The DRAIN-2DX spring element can be used to model inelastic behavior of double split-Tee connections before failure. The spring $P-\Delta$ relationships govern the accuracy of the spring element and must implicitly account for the complexities of the behavior for the connections. For example, the spring $P-\Delta$ relationships must account for the effects of pretensioning of the bolts and contacts and interactions among components of the connections.

3.3.1 FEM Model of DST Connections

The stress-strain curves for the steel fibers of steel beam in compression were derived from three-dimensional nonlinear finite element analyses of the beam failure segments. As a result, the finite element model (FEM)-based stress-strain curves implicitly account for the effects of inelastic flange and web buckling.

Three-dimensional finite element models for the DST connections were developed and analyzed under tensile and compressive loading using ABAQUS (Fig. 3.84). Symmetry was considered and one half of the specimen cross-section was modeled. Plane sections were enforced to remain plane at the loaded ends. The FEM analyses included pretensioning of the tension bolts as well as shear bolts (if applicable), the contacting and sliding between the flanges of the T-sections and the flanges of columns. The results from the FEM analyses included the force-displacement ($P-\Delta$) responses of the DST connections under tension and compression loadings.

3.3.1.1

The h

modeled

was idea

hardening

The m

include th

A572-50 s

3.3.1.2 S

Contac

"Surfaces"

either the

between th

slip betwe

in order to

pretension

connection

applicable)

applied at th

The pre

connections

members cau

3.3.1.1 Elements Used and Material Models

The beam, column, T-stub, tension bolts and shear bolts of the DST connection were modeled using eight-node brick elements. The inelastic behavior of the steel elements was idealized by a multiaxial plasticity model with a von Mises yield surface, isotropic hardening behavior and associated flow rule.

The mechanical properties of monotonic test specimens given by Swanson (1999) include the true stress-logarithmic plastic strain relationships of tension coupon tests for A572-50 structural Tee and A490 bolts (Figs. 3.85 and 3.86).

3.3.1.2 Simulation of Contacts and Pretension

Contacts and interactions among components were simulated by the option call "Surfaces" provided in ABAQUS. Small-Sliding Surface was used at the face between either the bolt head or nut and the base metal. Finite-sliding was used for the interface between the flange of T-stubs and either column or beam flange due to potentially large slip between them. It was also used for interface between bolt shank and the base metal, in order to prevent the bolt from penetrating into the metal and permit application of the pretension. The friction coefficient for all interactions was 0.33. Analysis of DST connection was divided into two steps: First, all the tension bolts and shear bolts (if applicable) were pretensioned. Second, monotonic tensile or compressive load were applied at the beam end.

The pretension of the bolts and friction are critical parameters in the bolted connections. The forces are transferred through friction due to clamping between the members caused by the pretensioning of the bolts. The pretension of the tension bolts as

well as shear bolts, if applicable, were simulated by the option call "predefined fields" provided in ABAQUS. A temperature difference between the temperature field in one of the bolt heads was defined for the bolts, so that the bolts contracted and clamped the parts of the connection. The temperature drop was chosen so that the pretension met the requirements of minimum bolt pretension for pretensioned joints (*Specification for Structural Joints Using ASTM A325 or A490 Bolts, 2000,* Table 8.1).

3.3.1.3 FEM-Based Force-Displacement Curves of DST Connections

The monotonic finite element analyses of DST connection provided the force-displacement ($P-\Delta$) responses of the DST connections under tension and compression loadings. The force-displacement relationships developed are used as the corresponding $P-\Delta$ curves for the nonlinear springs, which are used to model the DST connections in DRAIN2DX.

3.3.2 Validation of Analytical Model of DST Connections

The validity of the analytical approach for developing force-displacement ($P-\Delta$) responses of the DST connections was evaluated by using them to predict the DST connection Specimen TA-05 under monotonic loading by Swanson et al. (1999). FEM model was developed to model the DST connection specimen TA-05. As shown in Fig. 3.87, the result of 3D brick element model was compared favorably well with Swanson's experimental result of split-tee connections.

3.3.3 Sum

A spring

nonlinear 3

implicitly

interactions

the double

Swanson e

double spl

No ge

connectior

sections th

Second, fa

and the ar

DST conn

bolts are

double sp

connectior

3.4 Analy

Full sca

moment res

experimenta

provide adeq

3.3.3 Summary

A spring model for the double split-Tee connection was developed from the results of nonlinear 3D finite element analyses. This FEM-based spring model for the connections implicitly account for the effects of pretensioning of the bolts and contacts and interactions among components of the connections. The results from the FEM analysis of the double split-Tee connection compared favorably with the experimental results of Swanson et al. (1999). Therefore, the FEM-base spring model was used to model the double split-Tee connections in this research.

No general formula for the force-displacement (P–Δ) responses of the DST connections is recommended. The reasons are as follow: First, there are several T-sections that can be selected for the double split-Tee connection of a specific steel beam; Second, for a selected T-section, there are several options for the diameter, the number and the arrangement of the tension bolts, while the force-displacement response of the DST connection varies if the diameter, the number and the arrangement of the tension bolts are different. Therefore, FEM analysis should be conducted for each different double split-Tee connection to develop the force-displacement (P–Δ) responses of the connection.

3.4 Analytical Model for DST Connection Subassemblies

Full scale inelastic cyclic tests on the Double Split-Tee (DST) connection for CFT moment resisting frames had been conducted (Ricles et al. 1997, Peng 2001). These experimental results of DST connection subassemblies show that the connections can provide adequate cyclic strength and stiffness to enable full plastic hinges to develop in

the beams of CFT moment resisting frames.

The DRAIN-2DX fiber element and spring element can be used to model inelastic behavior of DST connection subassemblies. The developed FEM-based fiber models for CFT beam-columns and steel beams are used to model the CFT beam-columns and the steel beams of the DST connection subassemblies, respectively. The developed spring models for DST connections are used to model the DST connections of the subassemblies. The developed models for the CFT beam-columns, the steel beams and the DST connections implicitly account for the complexities of the behaviors for the components such as local buckling of the steel tubes and steel beams, cracking and confinement of concrete infills of CFTs, pretensioning of the bolts and contacts and interactions among components of the connections, etc.

3.4.1 Description of Model for DST Connection Subassemblies

The DST connection subassembly modeled by the element and spring element of DRAIN2DX is shown in Fig 3.88. Recent research on *CFT MRFs* indicate that, for a CFT subassembly with DST connection, the beam, connection, column, and panel zone contributed 83.0%, 9.7%, 7.0%, and 0.3% to the total story drift, respectively (Peng, 2001). The contribution of panel zone to the total story drift of the CFT subassembly with DST connection is only 0.3%. In addition, the strong column-weak beam and strong panel zone-weak column design philosophy requires that the panel zone must fail only after the beam and column are all fail. Therefore, the developed FEM-based models for the CFT beam-columns are used for the panel zone instead of a detail model specially developed for the panel zone.

As show

slaved node.

and 5 are us

to account f

3.4.2 Mo

As sho

fiber elem

results of

model as

and 12) r

location

beam.

Elem

strain rel

and 7 ar

frame. N

(nodes 1

through t

the top a

column to

Eleme

the force-d

As shown in Fig 3.88, each node defined by a number is either a master node, a slaved node, or a standard node as described in the legend of Fig 3.88. Slaved nodes 3 and 5 are used to account for the column depth. Slaved nodes 13, 14, 15 and 16 are used to account for the beam depth.

3.4.2 Modeling of CFT Beam-Columns, Steel Beams and Connections

As shown in Fig 3.88, the CFT beam-columns are modeled by Element group 1 with fiber elements, in which the stress-strain relationship of the fiber is developed from the results of FEM analysis. Element group 2 models the panel zone with FEM-based fiber model as the CFT beam-columns. The top and bottom nodes in the subassembly (nodes 9 and 12) represent the story mid-height of the frame. Nodes 10 and 11 are placed at the location where the T-stubs are bolted to the column, at the top and bottom flange of the beam.

Element group 3 is used to model the beam with fiber elements, in which the stress-strain relationship of the fiber is developed from the results of FEM analysis. Nodes 1 and 7 are placed at the roller supports, which represent the mid-point of a bay in the frame. Master nodes 2 and 6 are placed at the same location as the tips of the T-stubs (nodes 13 to 16), so that the end moments of the beams are transferred to the columns through the tensile and compressive forces of the top and bottom springs, which represent the top and bottom Tees, respectively. Nodes 3 and 5 are placed at the edges of the column to account for the column depth.

Element group 4 is used to model the DST connection with spring elements, in which the force-displacement relationship of the spring is developed from the results of FEM

analysis. Sl

respectively.

3.4.3 Vali

The v

evaluated b

7 under cy

fillet weld

bolted to

pensioned

The

structural

based fib

and steel

and web

beams (F

tension a

connectio

Ana

Specimen

beams, ar

Fig 3.10

experime

analysis. Slaved nodes 13, 14 and 15, 16 are placed at the tips of the bottom and top Tees, respectively, to account for the beam depth.

3.4.3 Validation of Analytical Model for DST Connection Subassemblies

The validity of the analytical model for the DST connection subassemblies was evaluated by using them to predict the DST connection subassemblies Specimen 5, 6 and 7 under cyclic loading by Peng (2001). The T-stub stems of Specimens 6 and 7 were fillet welded to the flange of steel beams, while the T-stub stem of Specimen 5 was bolted to the flange of steel beams. The tension bolts of Specimen 6 were fully pensioned while the pretension force of Specimen 7 is 40% of Specimen 6.

The true stress-strain relationships of beam flanges, beam webs, steel tube and structural tees are shown in Figs 3.89 to 3.92, respectively. Using the developed FEM-based fiber model for CFT beam-columns, the stress-strain relationships of concrete infill and steel tube are obtained (Figs 3.93 and 3.94). The stress-strain relationships for flange and web fibers of steel beams are obtained from the FEM-based fiber model for steel beams (Figs 3.95 and 3.96). And the force-displacement relationships of the T-stubs in tension and in compression are obtained from the FEM-based spring model of DST connections (Figs 3.97 and 3.98).

Analytical models were developed to model the DST connection subassemblies Specimen 5, 6 and 7, using the FEM-based fiber models for CFT beam-columns and steel beams, and the FEM-based spring model for DST connections. As shown in Fig. 3.99 to Fig 3.101, the results of fiber analysis were compared favorably well with Peng's experimental results of DST connection subassembly Specimens 5, 6 and 7 (Peng, 2001).

3.4.4 Summary

Analytical model for DST connection subassemblies was developed in DRAIN2DX, using the FEM-based fiber models for CFT beam-columns and steel beams, and the FEM-based spring model for DST connections. The FEM-based fiber model for CFTs implicitly account for the effects of local buckling, concrete confinement and crushing, and transverse interaction between the steel and concrete. The FEM-based fiber model for steel beams implicitly account for the effects of inelastic local buckling of beam flange and beam web. The FEM-based spring model for the connections implicitly account for the effects of pretensioning of the bolts and contacts and interactions among components of the connections. The results of fiber analysis were compared favorably well with Peng's experimental results of DST connection subassembly Specimens (Peng, 2001). Therefore, the analytical model is used to model CFT MRFs in this research.

Table 3.1 Id

Section
W24x62
W27x84
W30x10
W33x1
W36x1

Table 3.1 Idealized flange and web fiber σ–ε curves of rolled shapes (A992 steel)

Section	Fiber		σ_1/σ_y	$\varepsilon_1/\varepsilon_y$	σ_2/σ_y	$\varepsilon_2/\varepsilon_y$	σ_3/σ_y	$\varepsilon_3/\varepsilon_y$
W24x62	Flange		*1*	*1*	*1.1444*	*1.6332*	*0.4344*	*48.4722*
	Web	Layer 1	*0.86*	*0.86*	*0.9382*	*2.6721*	*0.2402*	*63.4068*
		Layer 2	*1*	*1*	*1.1154*	*1.2120*	*0.3466*	*61.1267*
		Layer 3	*1*	*1*	*1.1312*	*3.2133*	*0.4044*	*59.1856*
		Layer 4	*1*	*1*	*1.2670*	*3.5051*	*0.7692*	*56.0746*
W27x84	Flange		*1*	*1*	*1.2418*	*2.9882*	*0.5756*	*70.4231*
	Web	Layer 1	*0.73*	*0.73*	*0.8642*	*1.7168*	*0.22*	*66.1923*
		Layer 2	*1*	*1*	*1.0444*	*1.4104*	*0.3394*	*61.8033*
		Layer 3	*1*	*1*	*1.1094*	*1.3400*	*0.41*	*64.5218*
		Layer 4	*1*	*1*	*1.1512*	*1.6274*	*0.7086*	*68.4560*
W30x108	Flange		*1*	*1*	*1.322*	*1.6496*	*0.6018*	*75.5614*
	Web	Layer 1	*0.73*	*0.73*	*0.8694*	*1.5977*	*0.237*	*68.0968*
		Layer 2	*1*	*1*	*1.0468*	*1.3119*	*0.3268*	*61.1917*
		Layer 3	*1*	*1*	*1.118*	*1.1497*	*0.3428*	*64.1667*
		Layer 4	*1*	*1*	*1.153*	*1.4830*	*0.5988*	*70.3656*
W33x118	Flange		*1*	*1*	*1.2404*	*1.5111*	*0.4436*	*76.0392*
	Web	Layer 1	*0.73*	*0.73*	*0.86*	*1.8876*	*0.2122*	*75.6595*
		Layer 2	*1*	*1*	*1.0156*	*1.5961*	*0.2772*	*82.1252*
		Layer 3	*1*	*1*	*1.0604*	*1.7998*	*0.2978*	*85.6445*
		Layer 4	*1*	*1*	*1.1264*	*2.0737*	*0.5362*	*85.6173*
W36x135	Flange		*1*	*1*	*1.2404*	*1.5111*	*0.4966*	*71.7398*
	Web	Layer 1	*0.73*	*0.73*	*0.862*	*1.7320*	*0.2054*	*70.6061*
		Layer 2	*1*	*1*	*1.018*	*1.4559*	*0.2632*	*81.0416*
		Layer 3	*1*	*1*	*1.0932*	*1.1813*	*0.3328*	*86.9172*
		Layer 4	*1*	*1*	*1.139*	*1.4012*	*0.5114*	*87.4519*

Stress (ksi)

Figure 3.2

Stress (ksi)

Figure 3.3

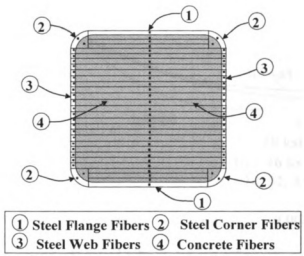


Figure 3.1 Fiber discretization of CFT cross-section

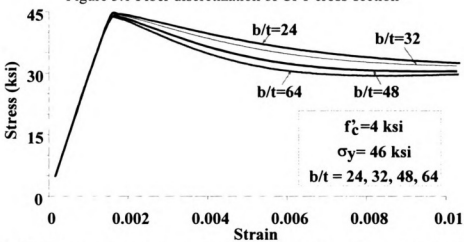


Figure 3.2 Effective σ–ε curves for steel tube walls of CFTs with σ_y=46ksi and f'_c=4ksi

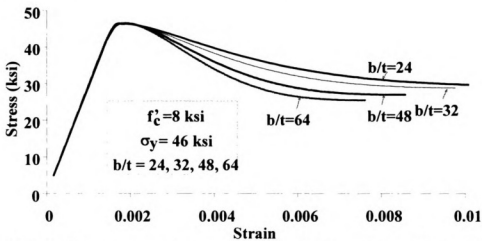


Figure 3.3 Effective σ–ε curves for steel tube walls of CFTs with σ_y=46ksi and f'_c=8ksi

Figure 3.4 F

Figure 3.5

Figure 3.6

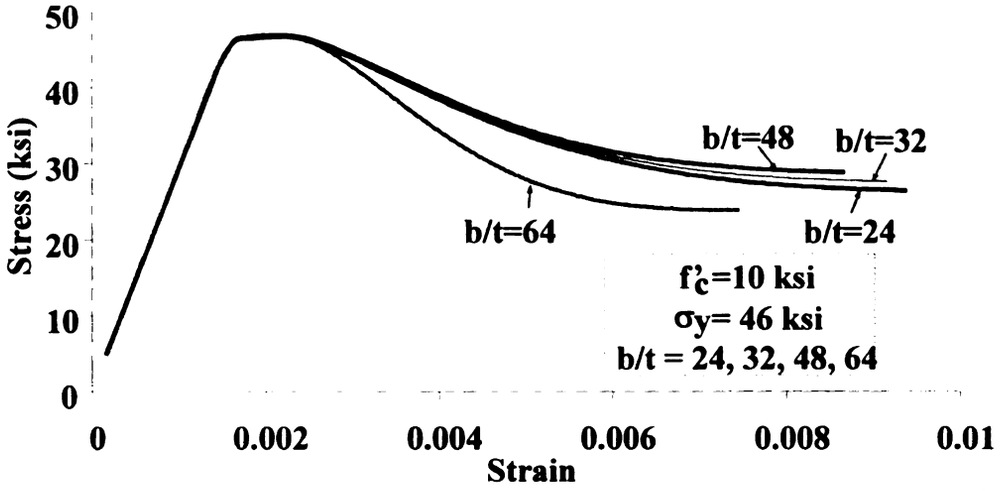


Figure 3.4 Effective σ–ε curves for steel tube walls of CFTs with σ_y=46ksi and f_c'=10ksi

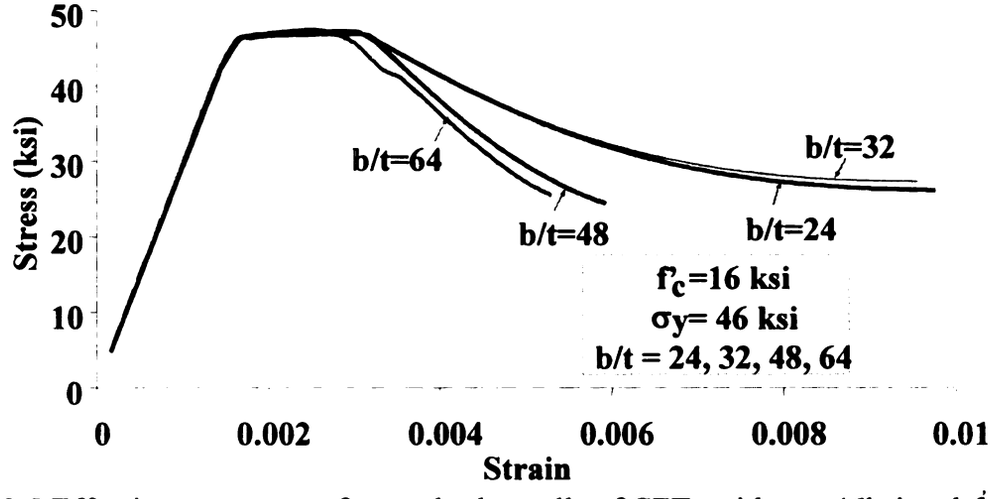


Figure 3.5 Effective σ–ε curves for steel tube walls of CFTs with σ_y=46ksi and f_c'=16ksi

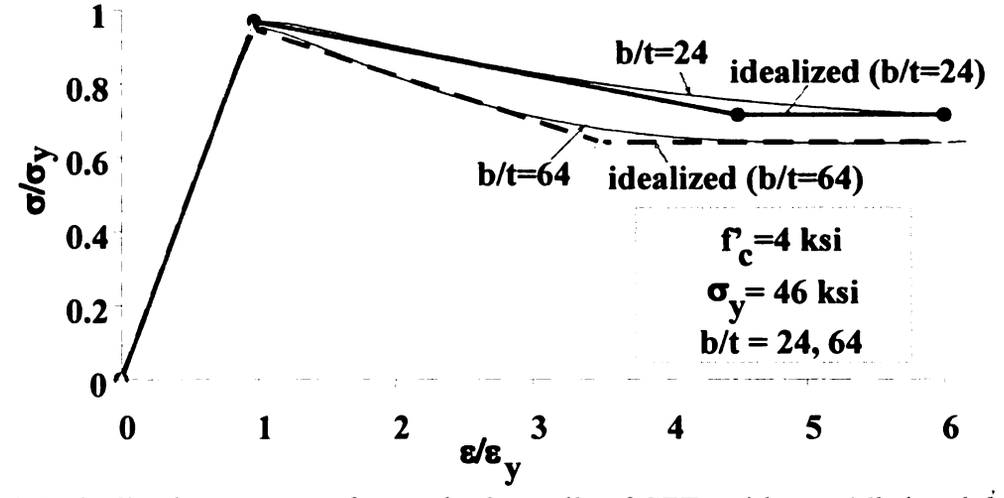


Figure 3.6 Idealized σ–ε curves for steel tube walls of CFTs with σ_y=46ksi and f_c'=4ksi

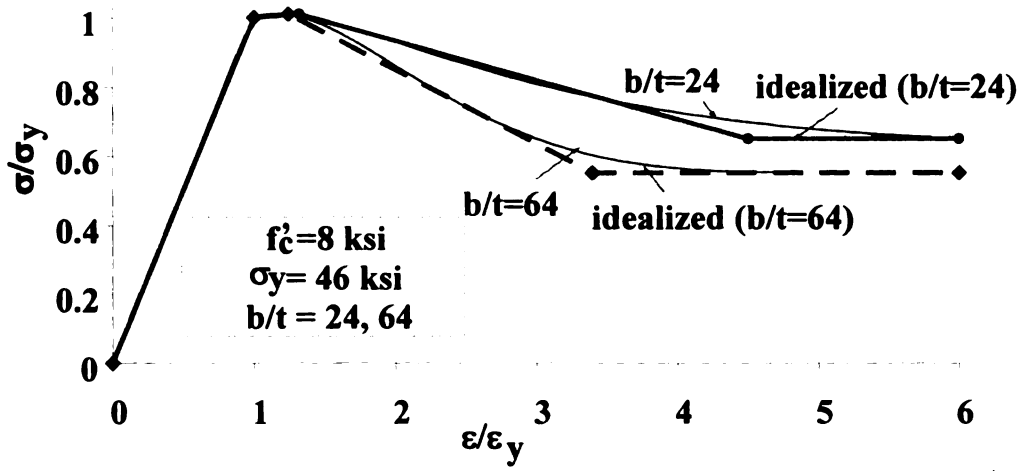


Figure 3.7 Idealized σ–ε curves for steel tube walls of CFTs with σ_y=46ksi and f_c'=8ksi

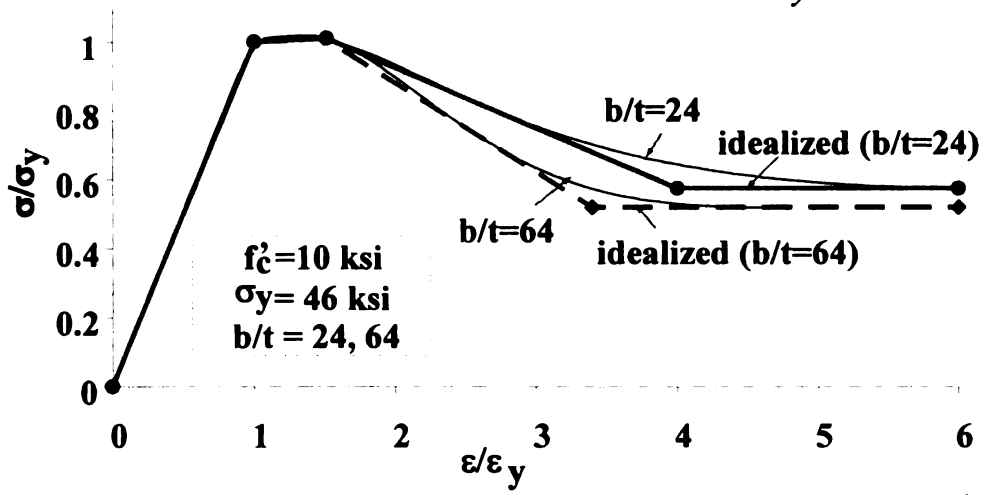


Figure 3.8 Idealized σ–ε curves for steel tube walls of CFTs with σ_y=46ksi and f_c'=10ksi

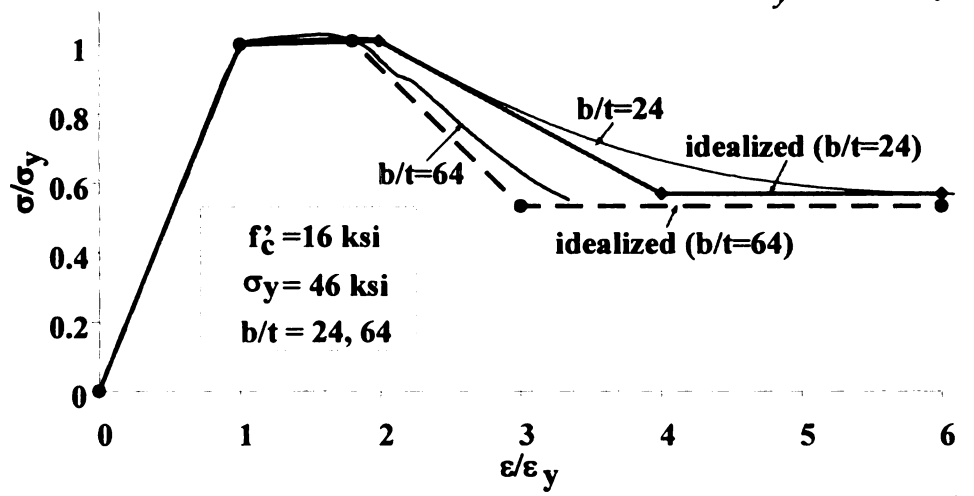


Figure 3.9 Idealized σ–ε curves for steel tube walls of CFTs with σ_y=46ksi and f_c'=16ksi

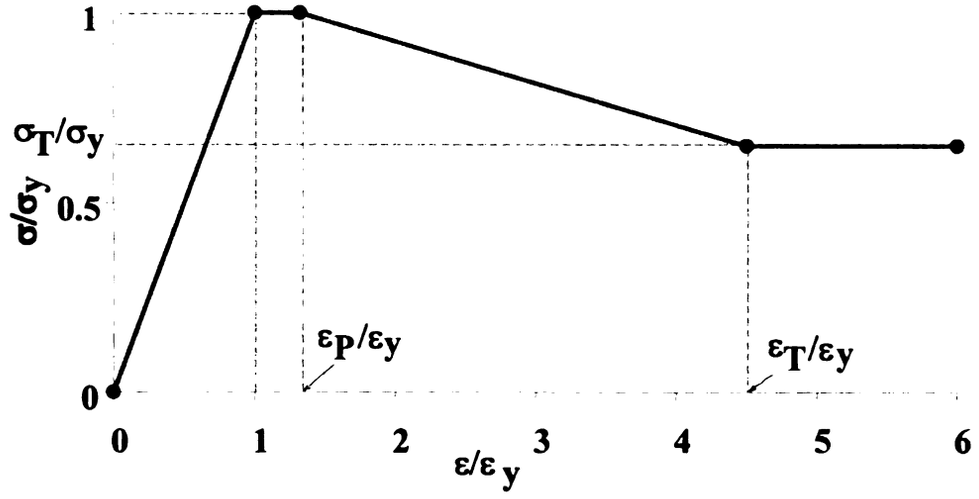


Figure 3.10 Idealized σ–ε curve for steel tube walls of CFTs with σ_y=*46ksi*

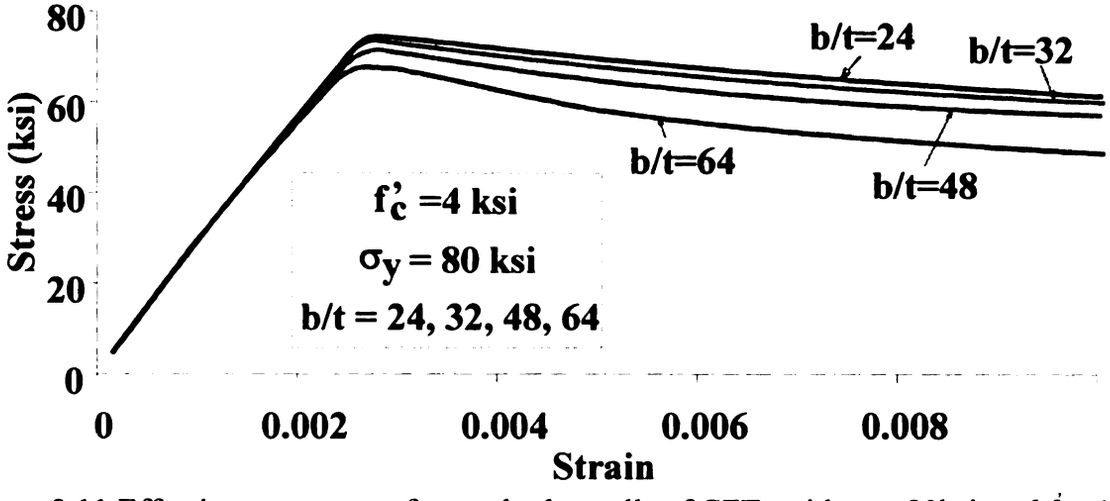


Figure 3.11 Effective σ–ε curves for steel tube walls of CFTs with σ_y=80ksi *and* $f_c^{'}$=4ksi

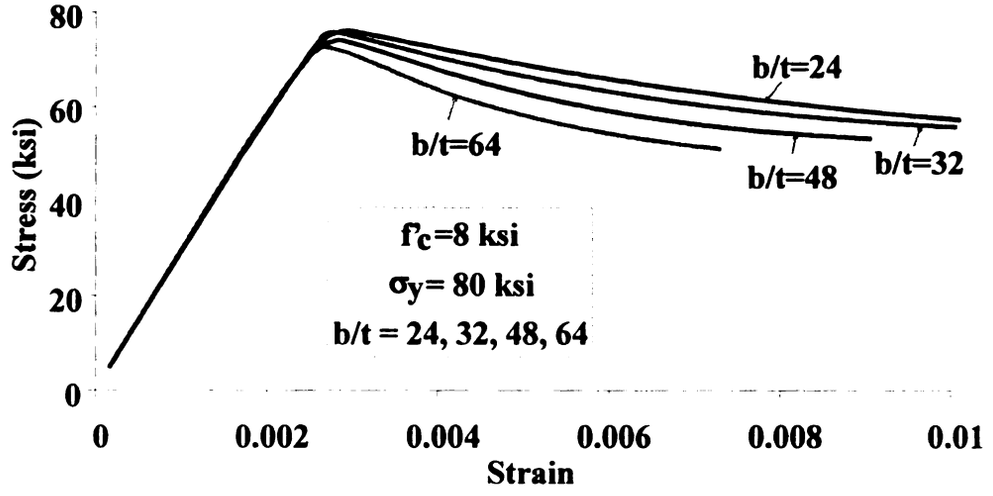


Figure 3.12 Effective σ–ε curves for steel tube walls of CFTs with σ_y=80ksi *and* $f_c^{'}$=8ksi

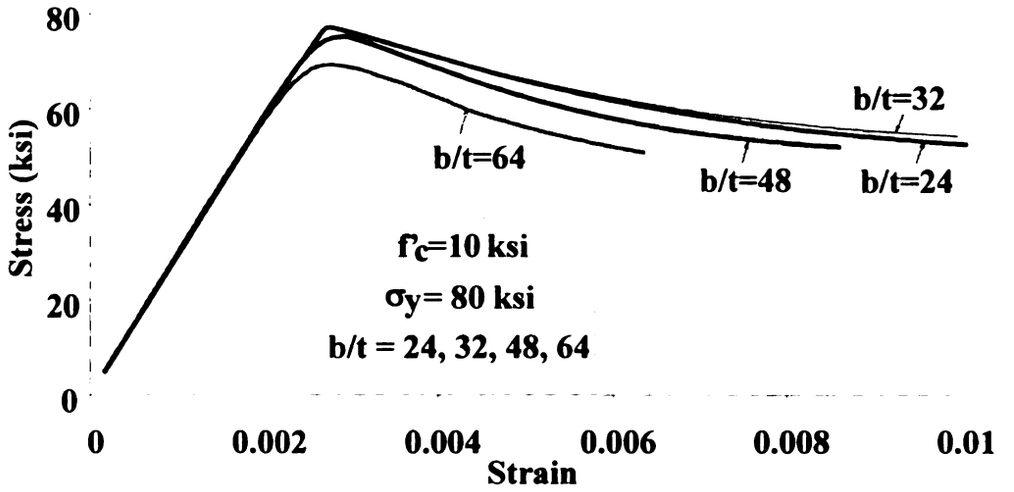


Figure 3.13 Effective σ–ε curves for steel tube walls of CFTs with σ_y=80ksi *and* $f_c^{'}$=10ksi

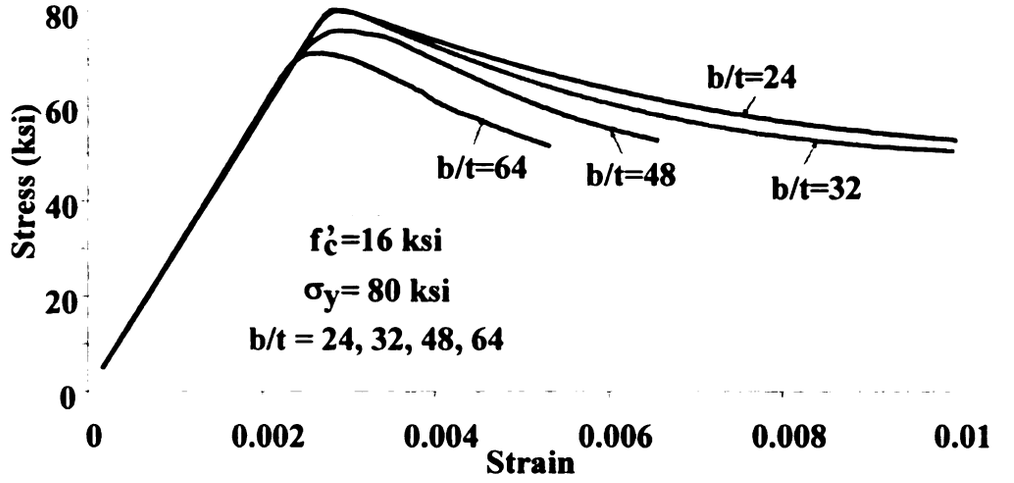


Figure 3.14 Effective σ–ε curves for steel tube walls of CFTs with σ_y=80ksi *and* $f_c^{'}$=16ksi

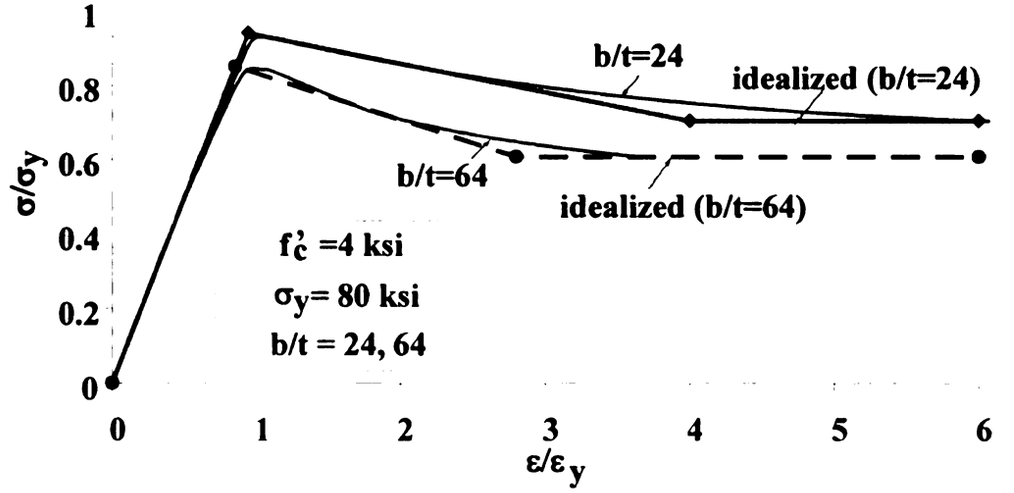


Figure 3.15 Idealized σ–ε curves for steel tube walls of CFTs with σ_y=80ksi *and* $f_c^{'}$=4ksi

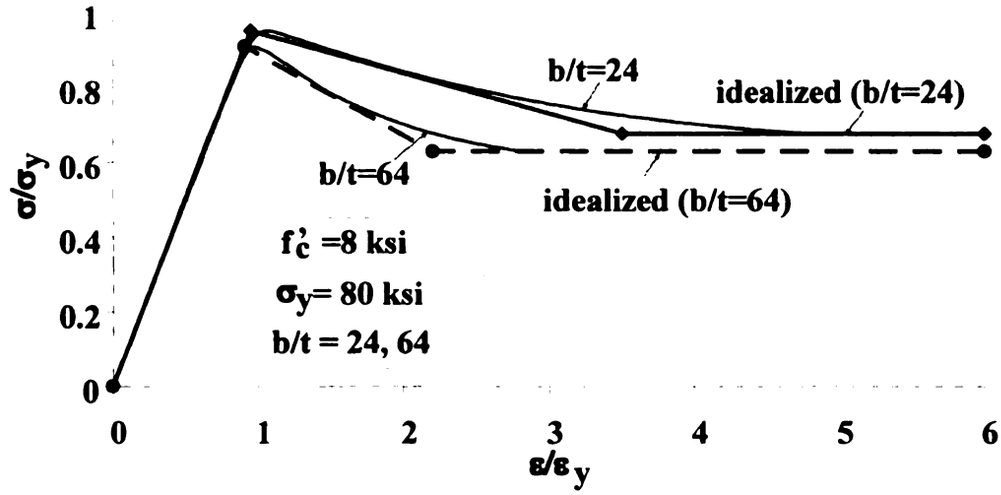


Figure 3.16 Idealized σ–ε curves for steel tube walls of CFTs with σ_y=80ksi *and* $f_c^{'}$=8ksi

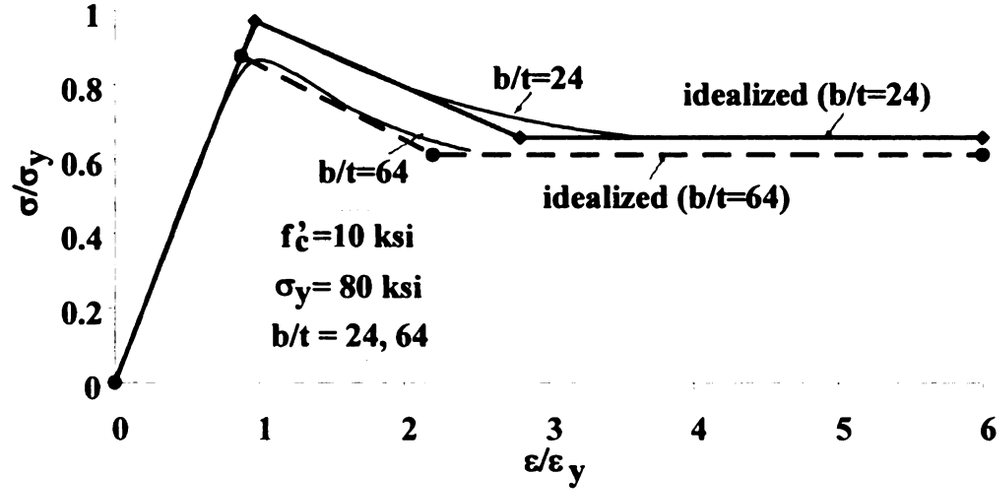


Figure 3.17 Idealized σ–ε curves for steel tube walls of CFTs with σ_y=80ksi *and* $f_c^{'}$=10ksi

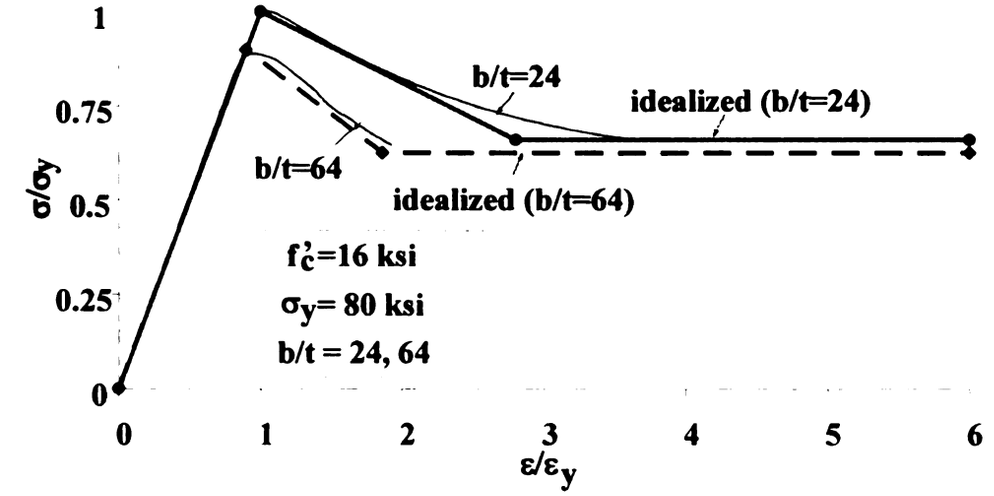


Figure 3.18 Idealized σ–ε curves for steel tube walls of CFTs with σ_y=80ksi *and* $f_c^{'}$=16ksi

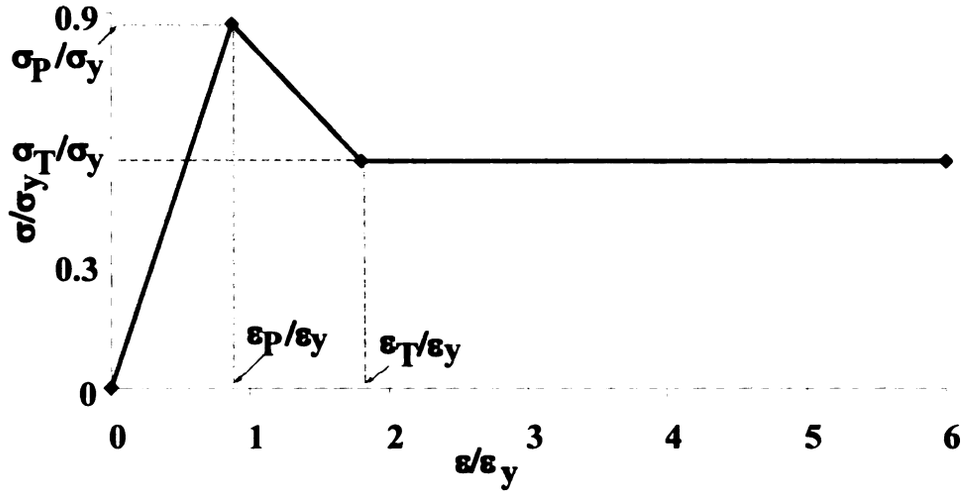


Figure 3.19 Idealized effective σ–ε curves for steel tube walls of CFTs with σ_y=*80ksi*

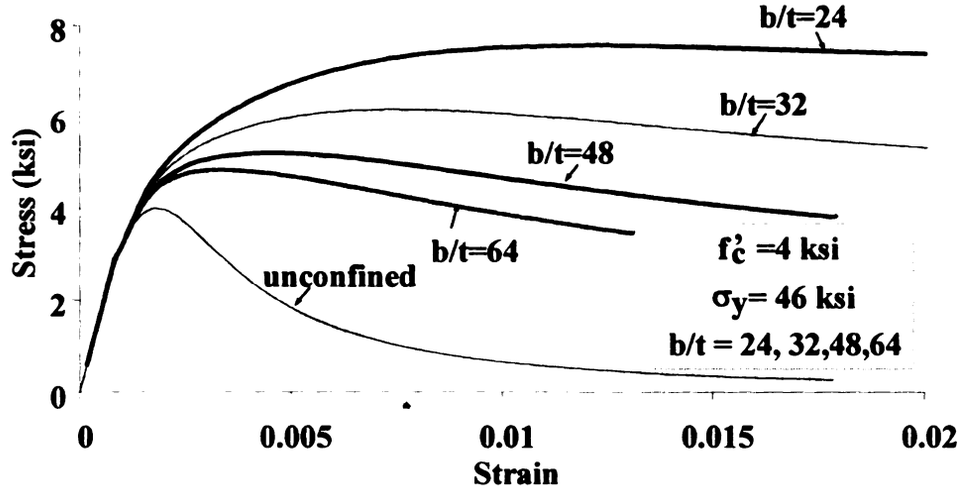


Figure 3.20 Effective σ–ε curves for concrete infills of CFTs with f'_c=*4ksi* and σ_y=*46ksi*

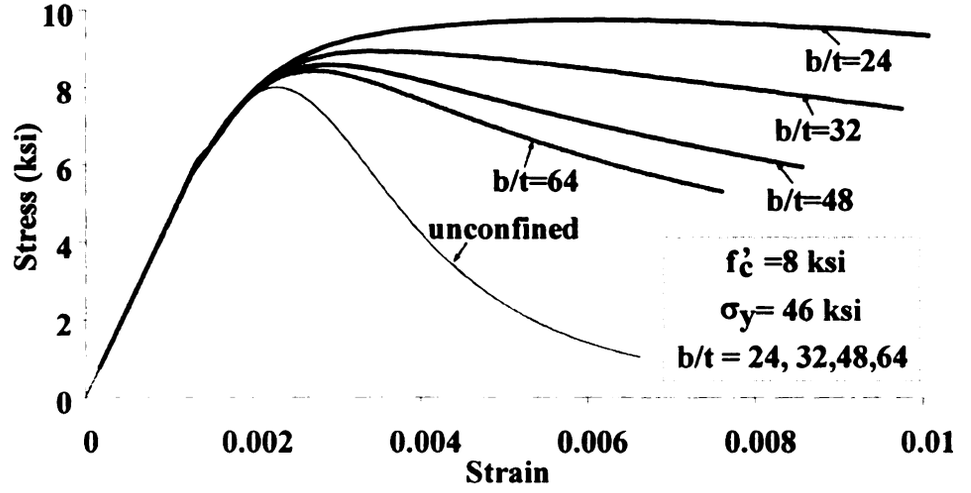


Figure 3.21 Effective σ–ε curves for concrete infill of CFTs with f'_c=*8ksi*, σ_y=46ksi

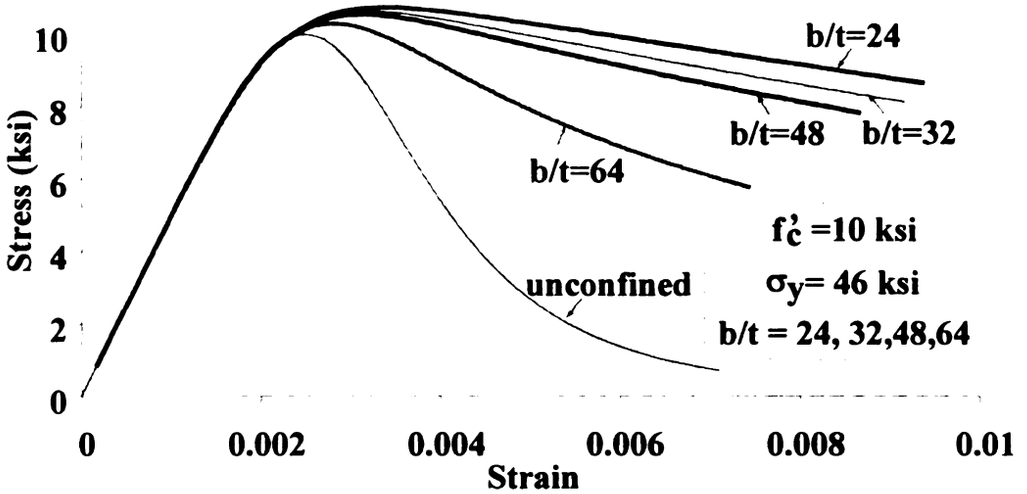


Figure 3.22 Effective σ–ε curves for concrete infills of CFTs with f'_c=*10ksi* and σ_y=46ksi

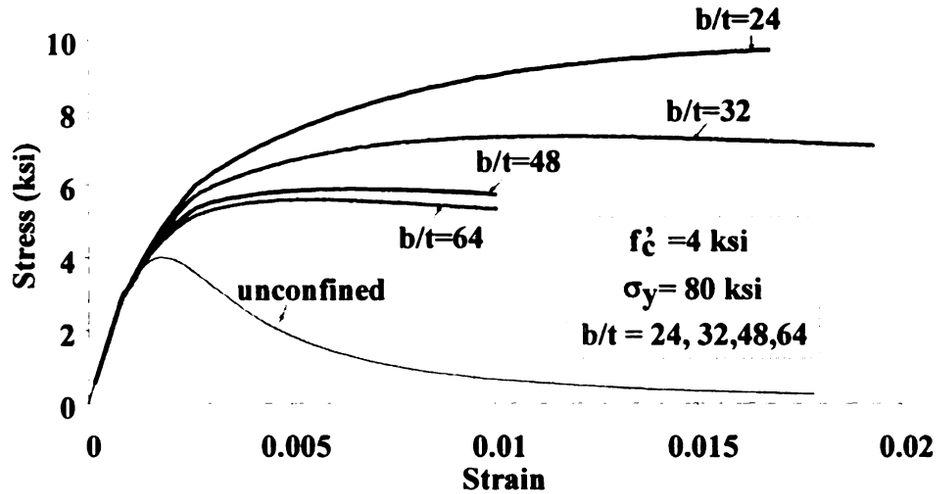


Figure 3.23 Effective σ–ε curves for concrete infills of CFTs with f'_c=*4ksi* and σ_y=*80ksi*

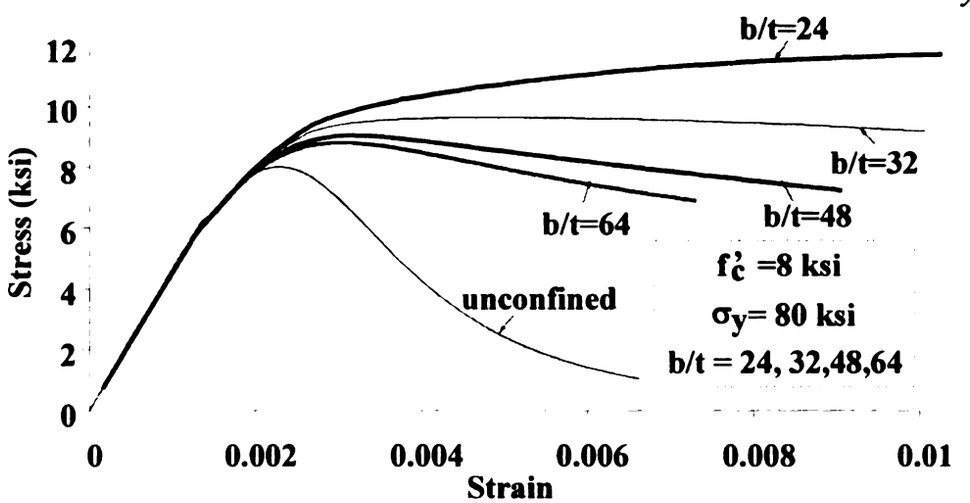


Figure 3.24 Effective σ–ε curves for concrete infills of CFTs with f'_c=8ksi and σ_y=80ksi

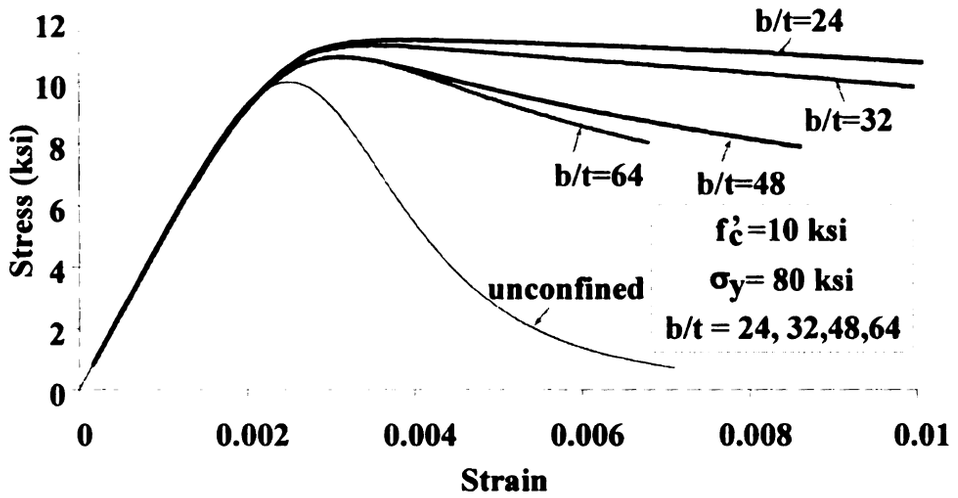


Figure 3.25 Effective σ–ε curves for concrete infills of CFTs with $f_c^{'}$=10ksi and σ_y=80ksi

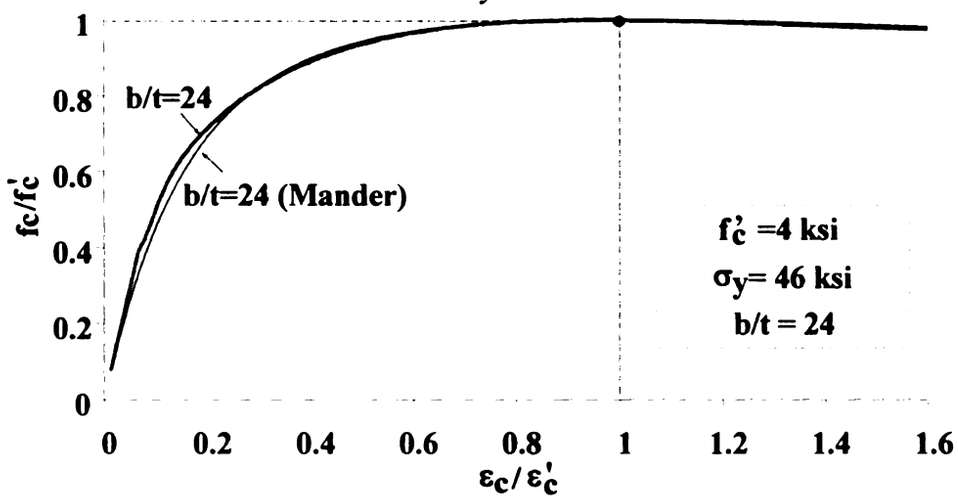


Figure 3.26 Normalized σ–ε curves for concrete infills of CFTs with $f_c^{'}$=4ksi and σ_y=46ksi, b/t=24

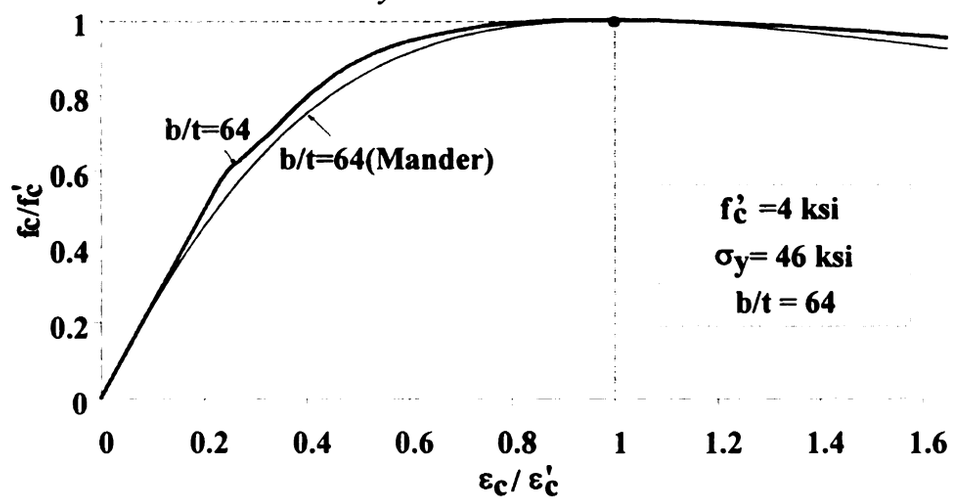


Figure 3.27 Normalized σ–ε curves for concrete infills of CFTs with $f_c^{'}$=4ksi and σ_y=46ksi, b/t=64

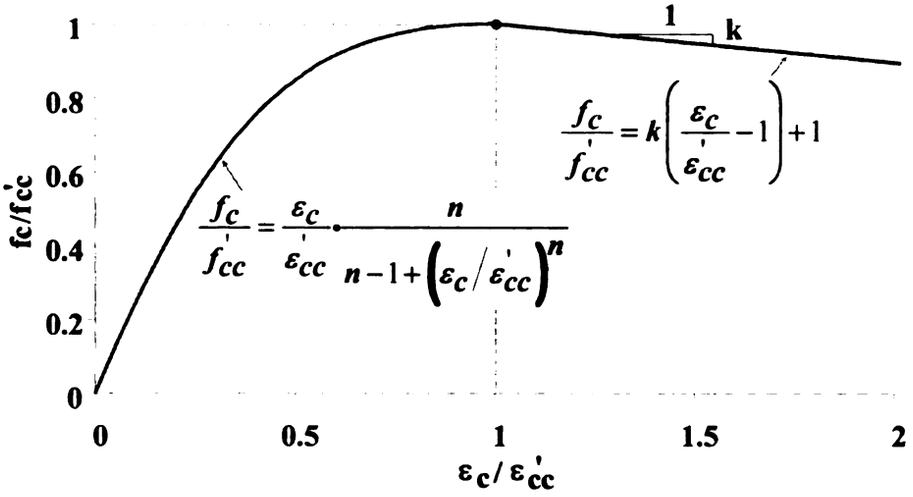


Figure 3.28 Idealized σ–ε curve for concrete infills of CFTs with $f'_c \leq 10ksi$

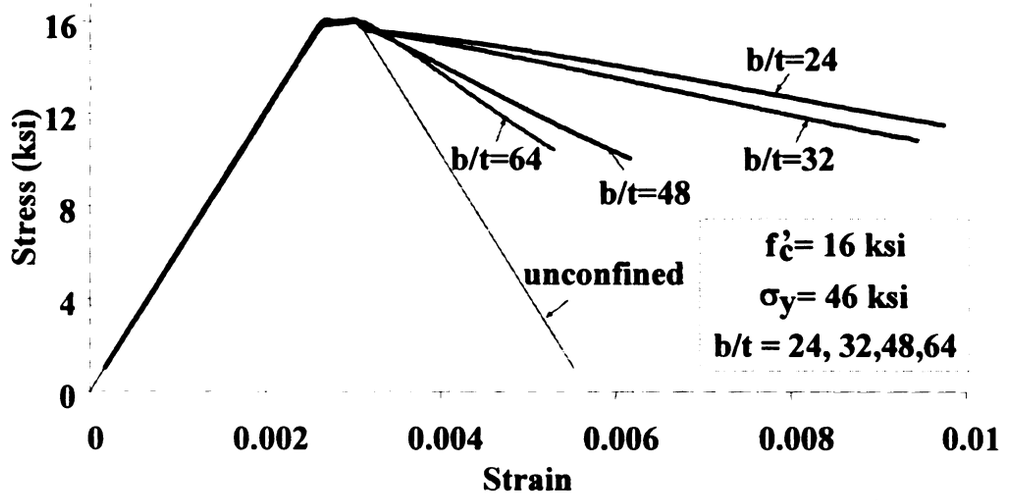


Figure 3.29 Effective σ–ε curves for concrete infills of CFTs with f'_c=16ksi and σ_y=46ksi

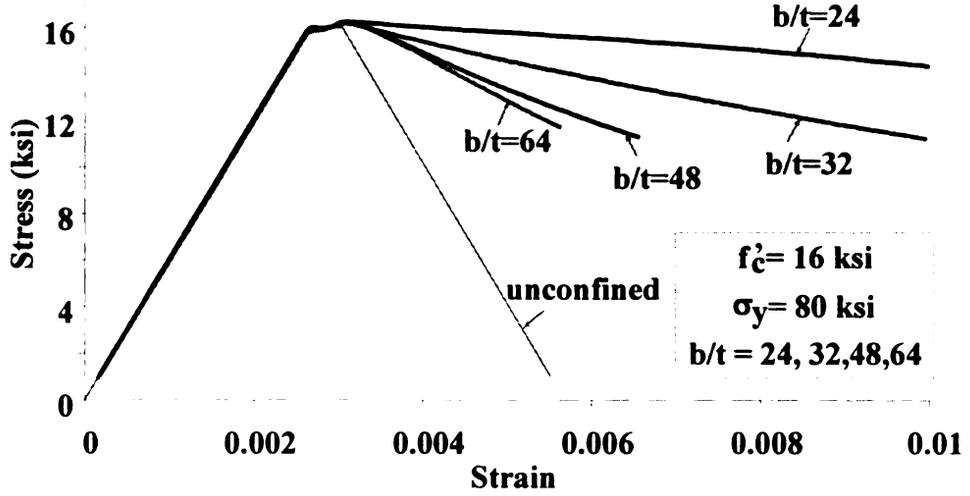


Figure 3.30 Effective σ–ε curves for concrete infills of CFTs with f'_c=16ksi and σ_y=80ksi

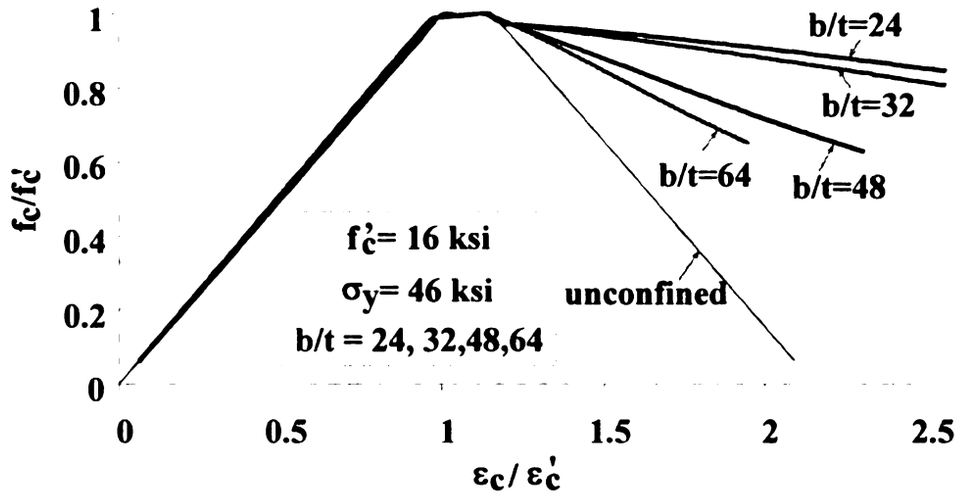


Figure 3.31 Normalized σ–ε curves for concrete infills of CFts with f'_c=16ksi and σ_y=46ksi.

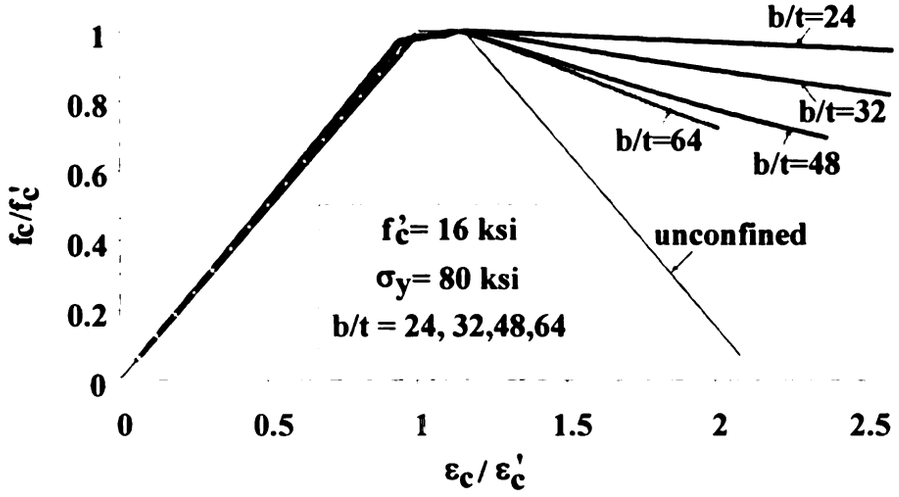


Figure 3.32 Normalized σ–ε curves for concrete infills of CFTs with f'_c=16ksi and σ_y=80ksi

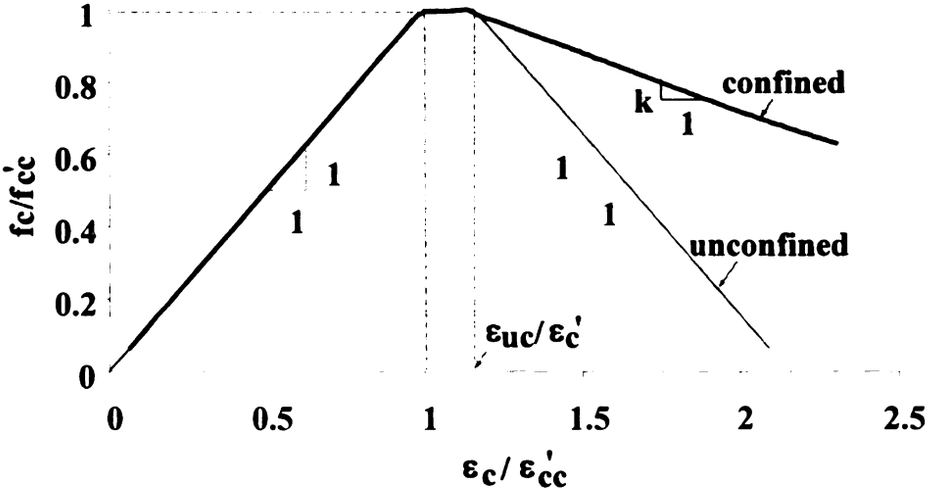


Figure 3.33 Normalized effective σ–ε curves for concrete infills of CFTs with f'_c>10ksi

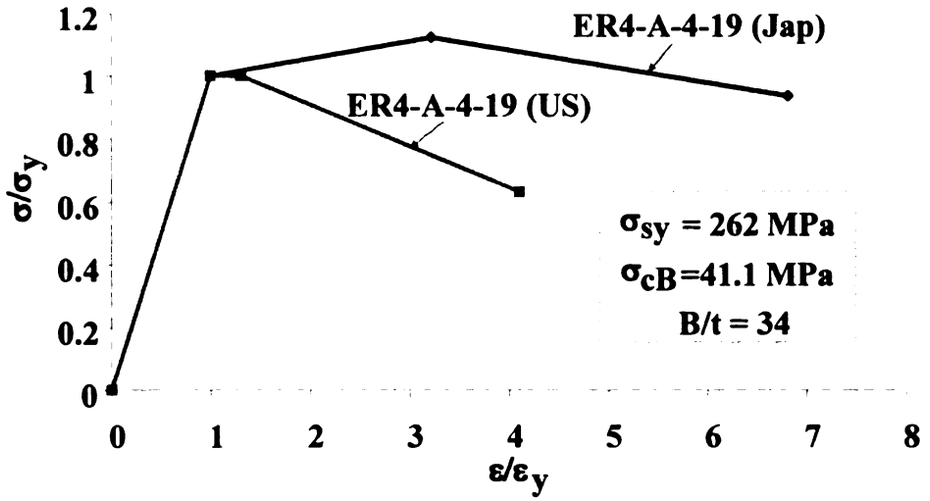


Figure 3.34 Normalized steel fiber σ–ε curve in compression for CFT specimen with σ_y=262MPa, f'_c=41.1MPa, b/t=34

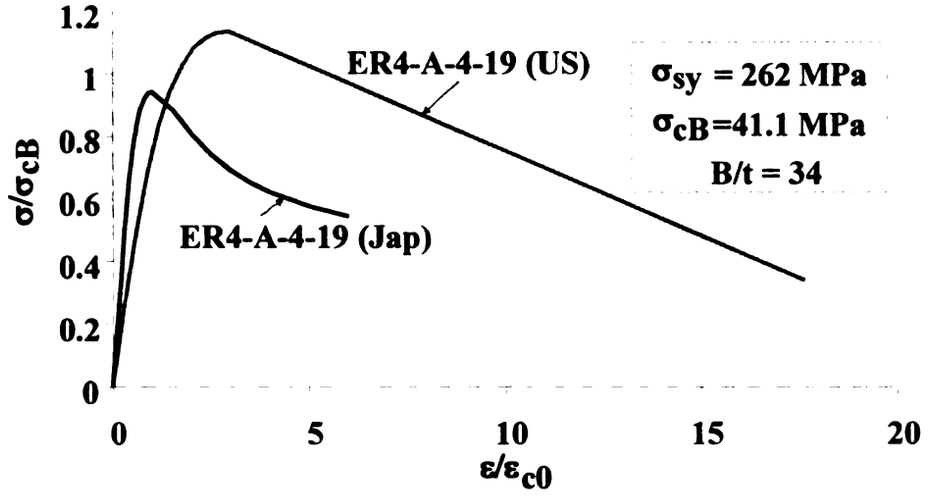


Figure 3.35 Normalized concrete fiber σ–ε curve in compression for CFT specimen with σ_y=262MPa, f'_c=41.1MPa, b/t=34

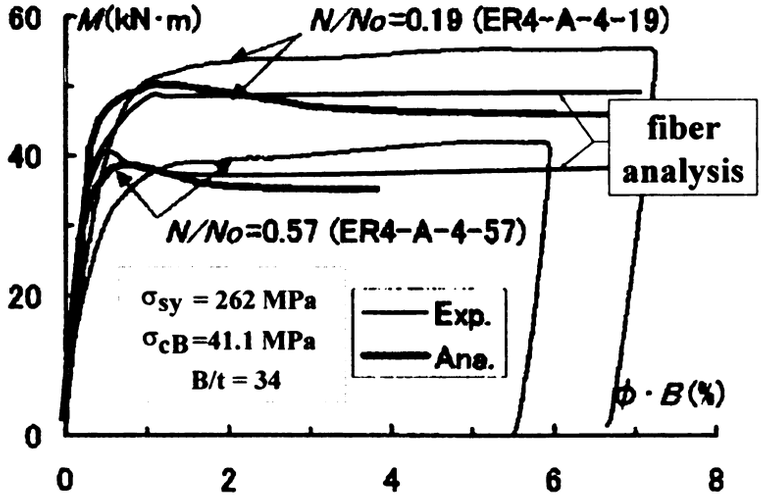


Figure 3.36 Comparison of experimental and analytical M-ϕ curves for CFT specimen with σ_y=262MPa, f'_c=41.1MPa, b/t=34

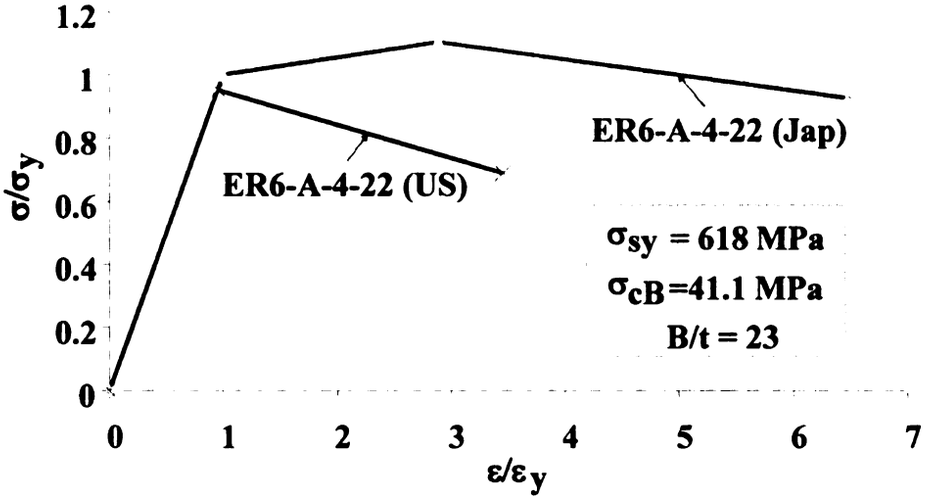


Figure 3.37 Normalized steel fiber σ–ε curve in compression for CFT specimen with σ_y=618MPa, f'_c=41.1MPa, b/t=23

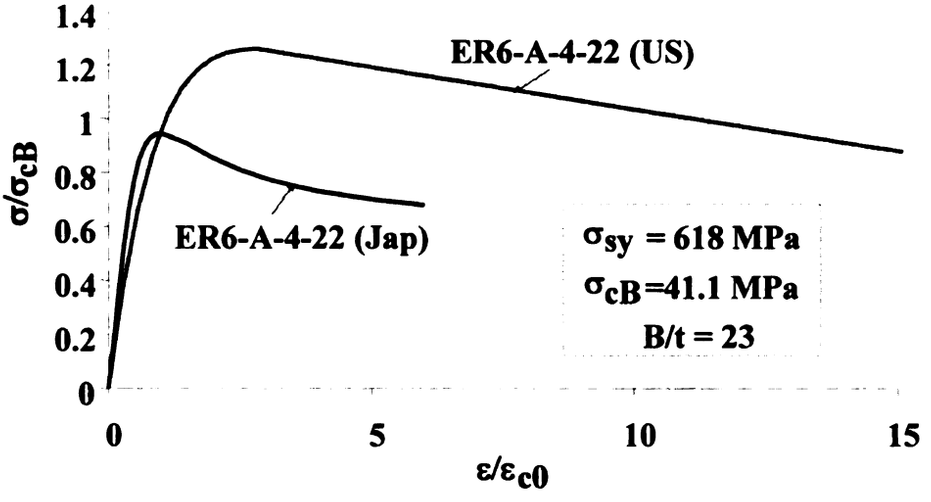


Figure 3.38 Normalized concrete fiber σ–ε curve in compression for CFT specimen with σ_y=618MPa, f'_c=41.1MPa, b/t=23

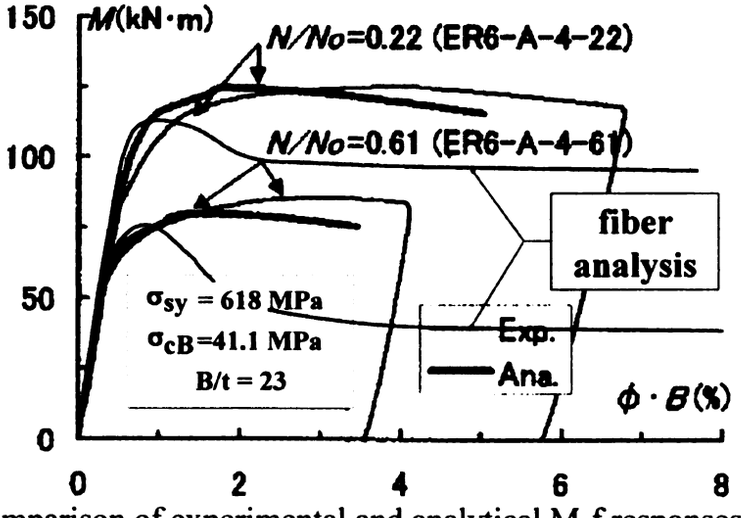


Figure 3.39 Comparison of experimental and analytical M-f responses for CFTs with σ_y=618MPa, f'_c=41.1MPa, b/t=23

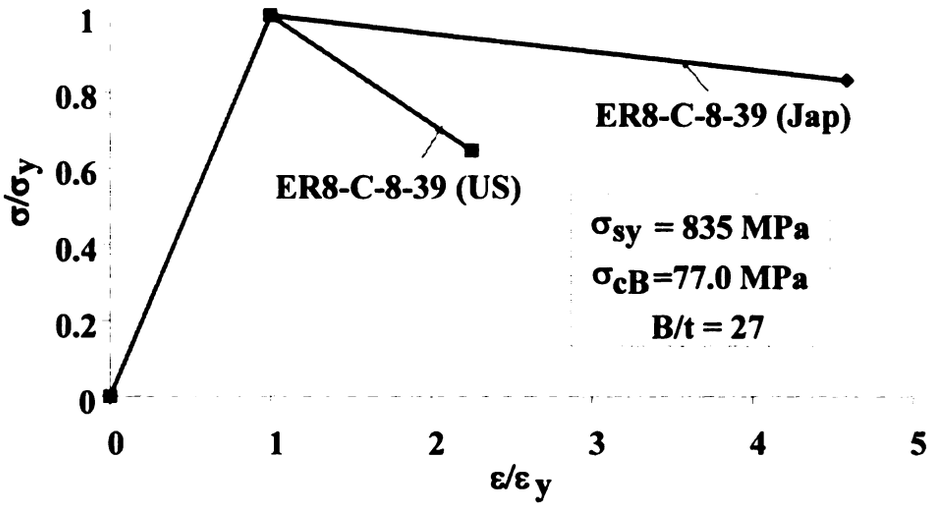


Figure 3.40 Normalized steel fiber σ–ε curve in compression for CFT specimen with σ_y=835MPa, f'_c=77.0MPa, b/t=27

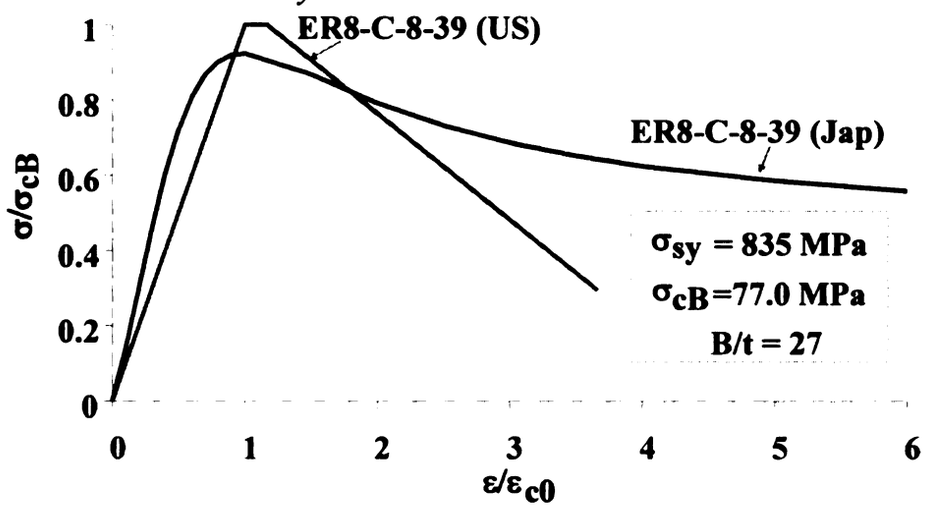


Figure 3.41 Normalized concrete fiber σ–ε curve in compression for CFT specimen with σ_y=835MPa, f'_c=77.0MPa, b/t=27

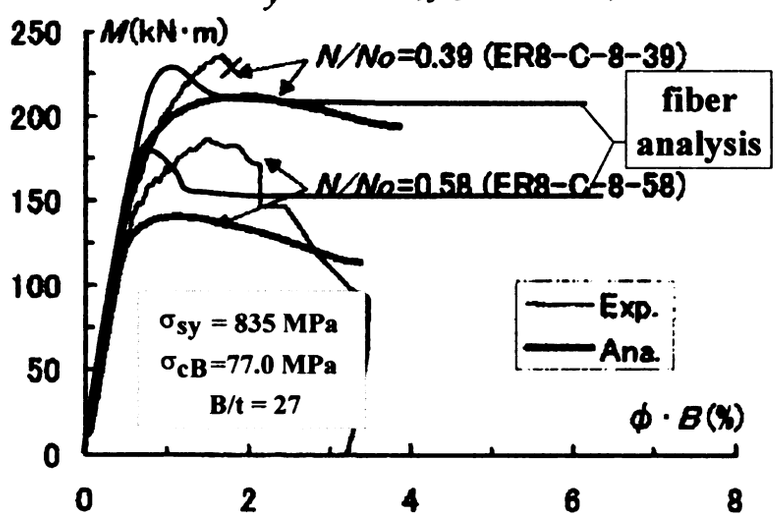


Figure 3.42 Comparison of experimental and analytical M-ϕ responses for CFTs with σ_y=835MPa, f'_c=77.0MPa, b/t=27

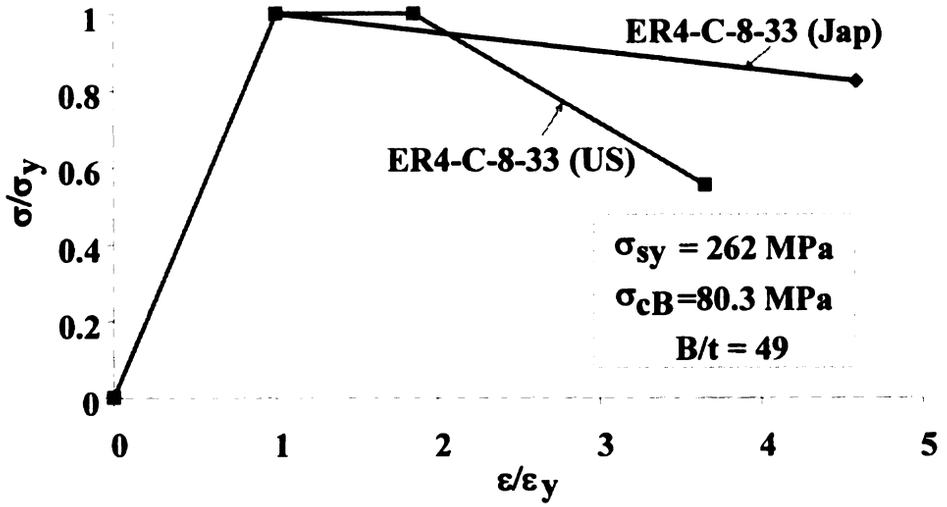


Figure 3.43 Normalized steel fiber σ–ε curve in compression for CFT specimen with σ_y=262MPa, f'_c=80.3MPa, b/t=49

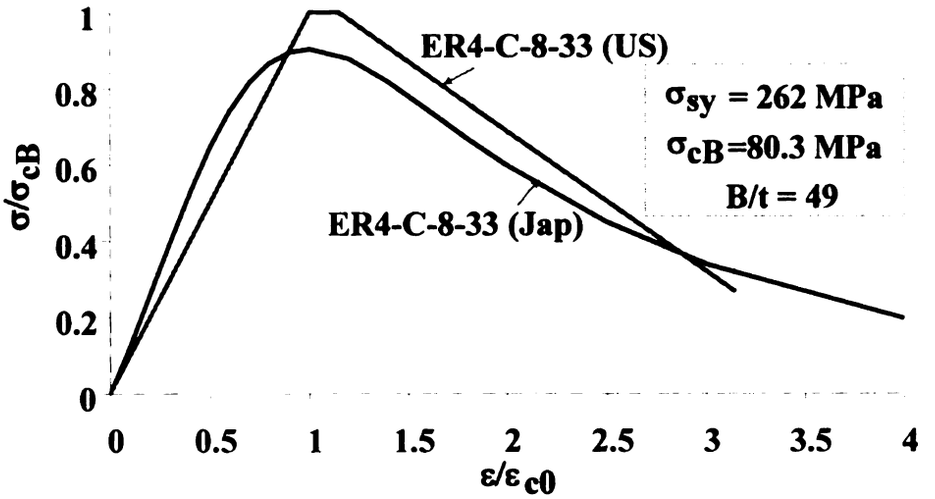


Figure 3.44 Normalized concrete fiber σ–ε curve in compression for CFT specimen with σ_y=262MPa, f'_c=80.3MPa, b/t=49

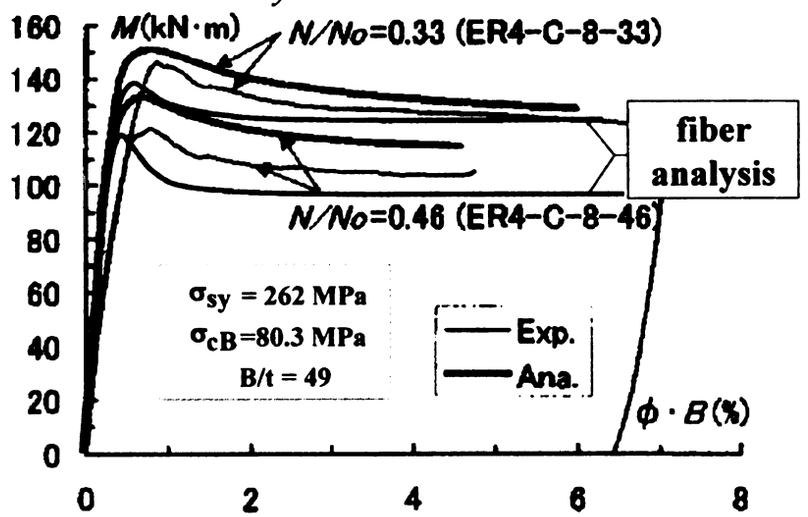


Figure 3.45 Comparison of experimental and analytical M-ϕ responses for CFTs with σ_y=262MPa, f'_c=80.3MPa, b/t=49

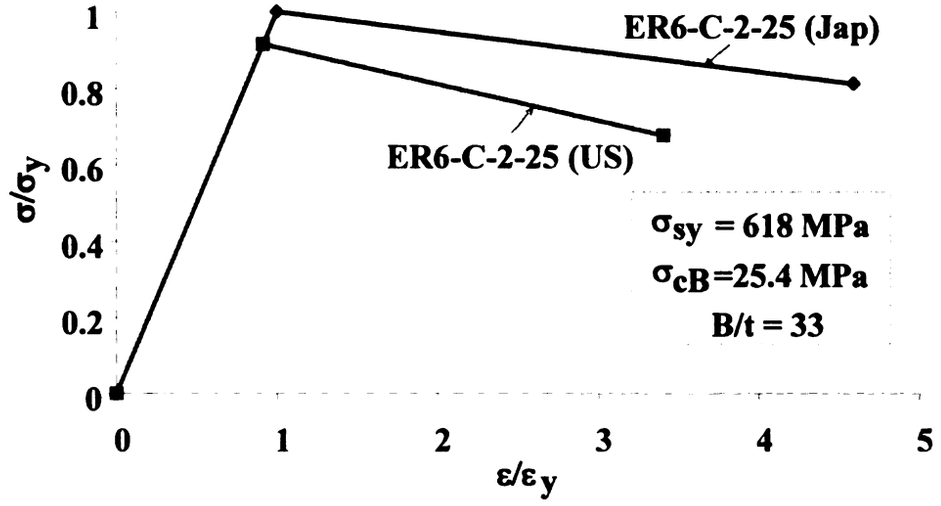


Figure 3.46 Normalized steel fiber σ–ε curve in compression for CFT specimen with σ_y=618MPa, f'_c=25.4MPa, b/t=33

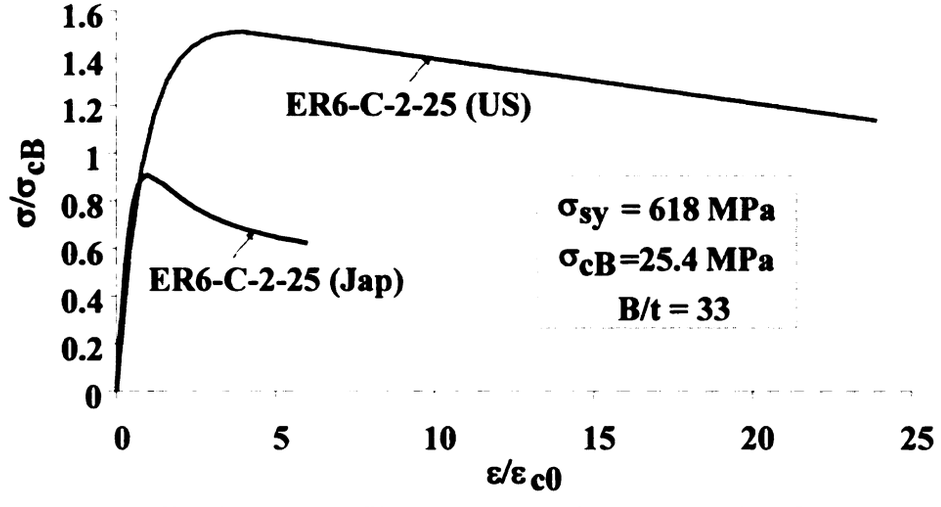


Figure 3.47 Normalized concrete fiber σ–ε curve in compression for CFT specimen with σ_y=618MPa, f'_c=25.4MPa, b/t=33

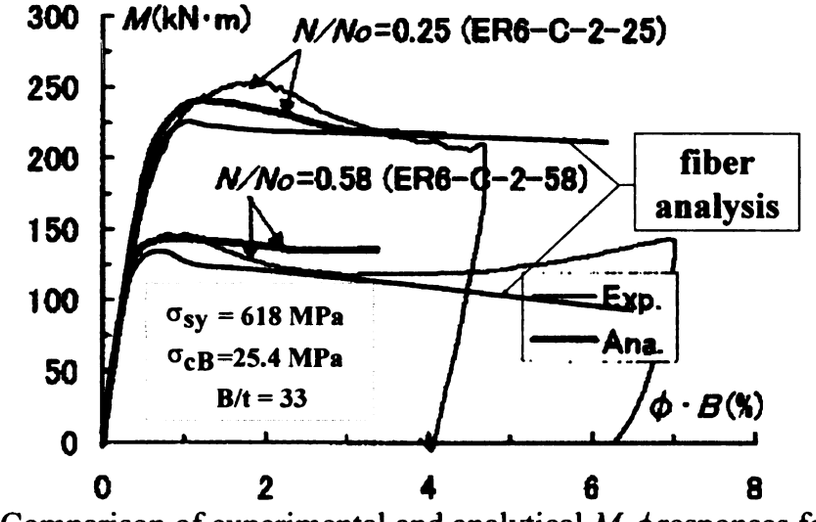


Figure 3.48 Comparison of experimental and analytical M-ϕ responses for CFTs with σ_y=618MPa, f'_c=25.4MPa, b/t=33

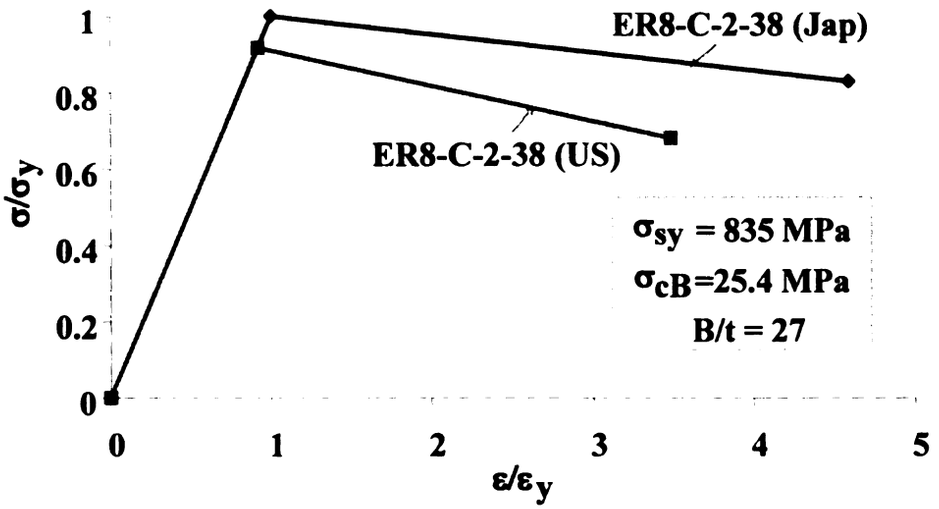


Figure 3.49 Normalized steel fiber σ–ε curve in compression for CFT specimen with σ_y=835MPa, f'_c=25.4MPa, b/t=27

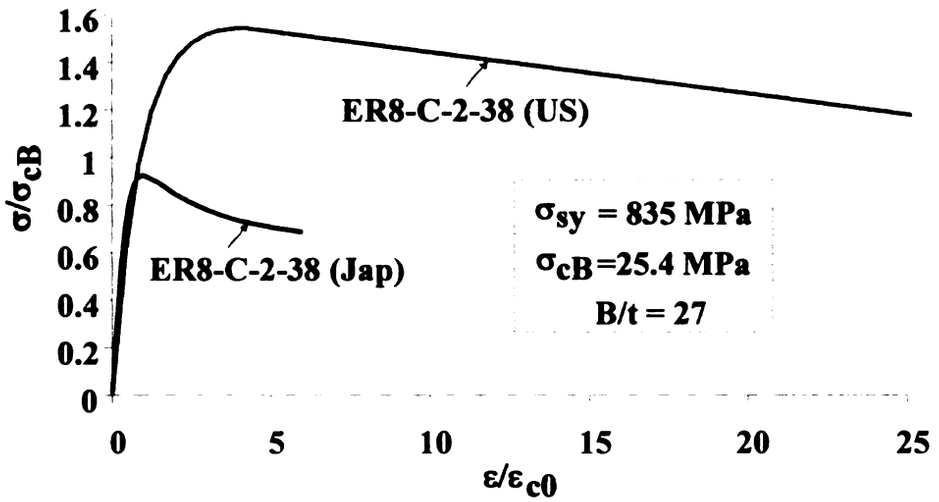


Figure 3.50 Normalized concrete fiber σ–ε curve in compression for CFT specimen with σ_y=835MPa, f'_c=25.4MPa, b/t=27

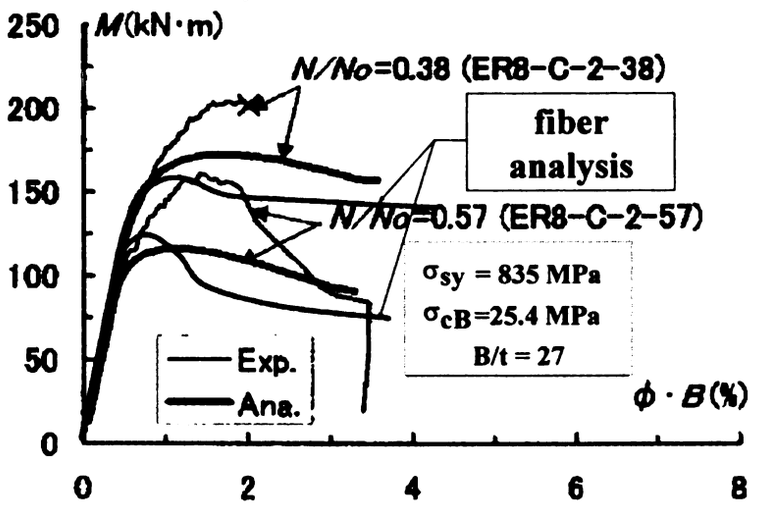


Figure 3.51 Comparison of experimental and analytical M-ϕ responses for CFTs with σ_y=835MPa, f'_c=25.4MPa, b/t=27

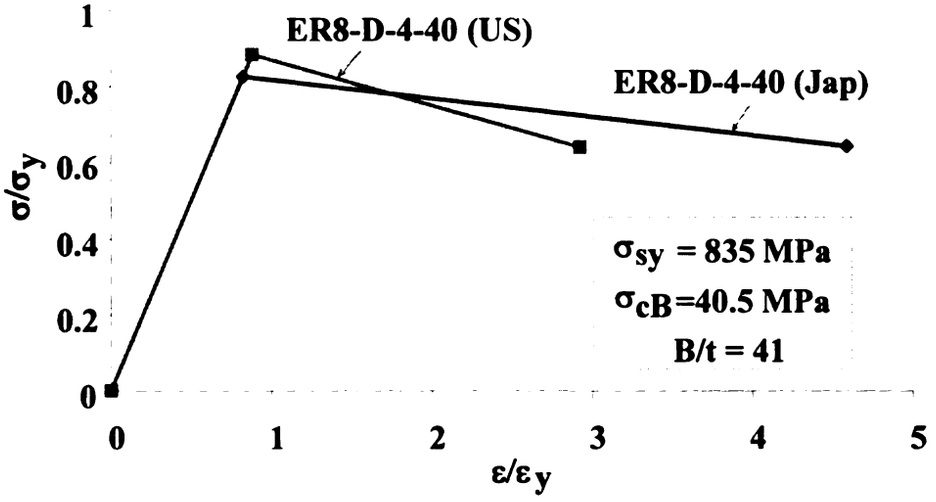


Figure 3.52 Normalized steel fiber σ–ε curve in compression for CFT specimen with σ_y=835MPa, f'_c=40.5MPa, b/t=41

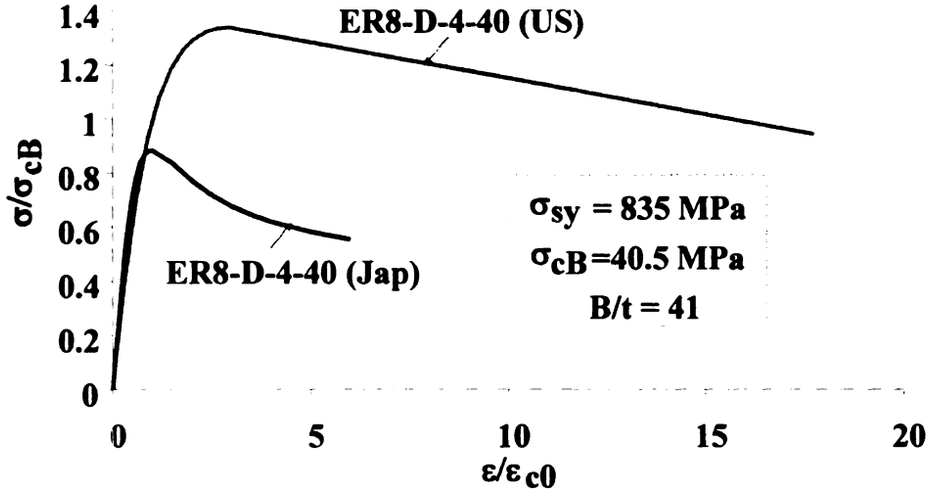


Figure 3.53 Normalized concrete fiber σ–ε curve in compression for CFT specimen with σ_y=835MPa, f'_c=40.5MPa, b/t=41

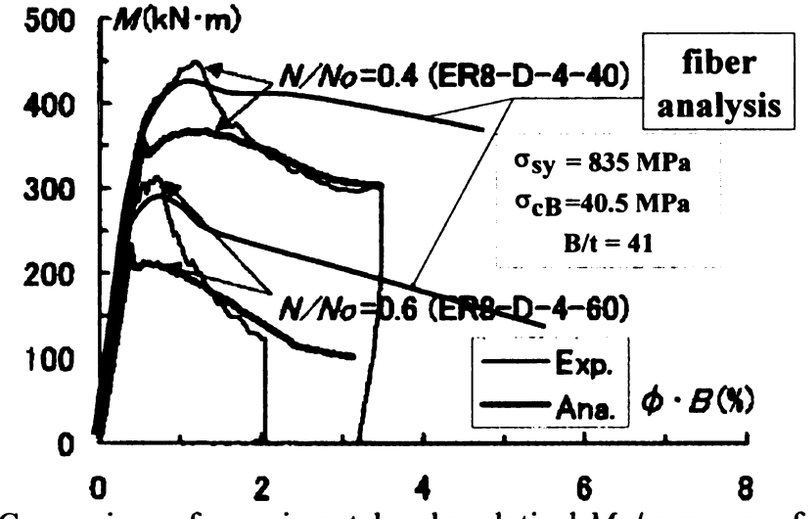


Figure 3.54 Comparison of experimental and analytical M-ϕ responses for CFTs with σ_y=835MPa, f'_c=40.5MPa, b/t=41

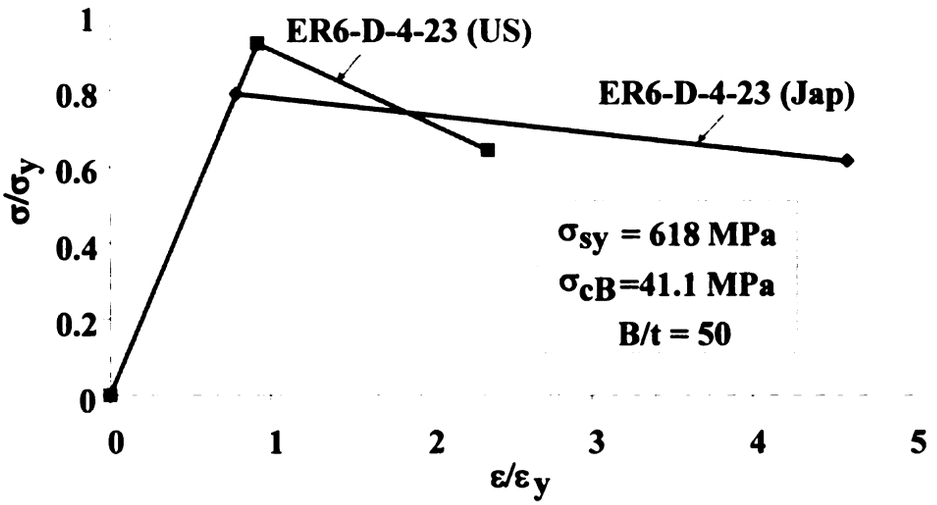


Figure 3.55 Normalized steel fiber σ–ε curve in compression for CFT specimen with σ_y=618MPa, f'_c=41.1MPa, b/t=50

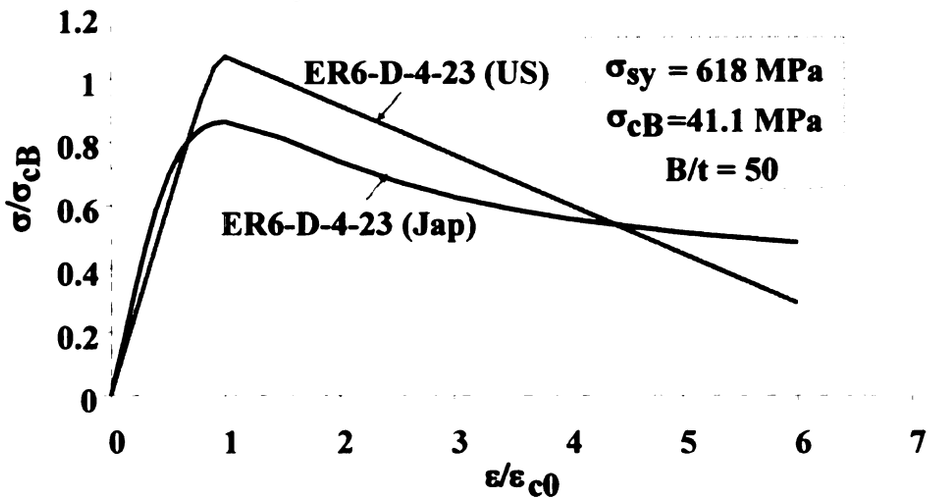


Figure 3.56 Normalized concrete fiber σ–ε curve in compression for CFT specimen with σ_y=618MPa, f'_c=41.1MPa, b/t=50

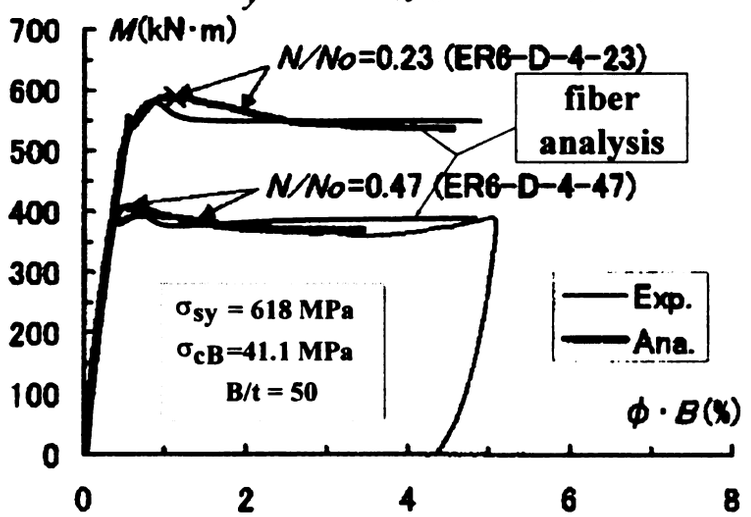


Figure 3.57 Comparison of experimental and analytical M-ϕ responses for CFTs with σ_y=618MPa, f'_c=41.1MPa, b/t=50

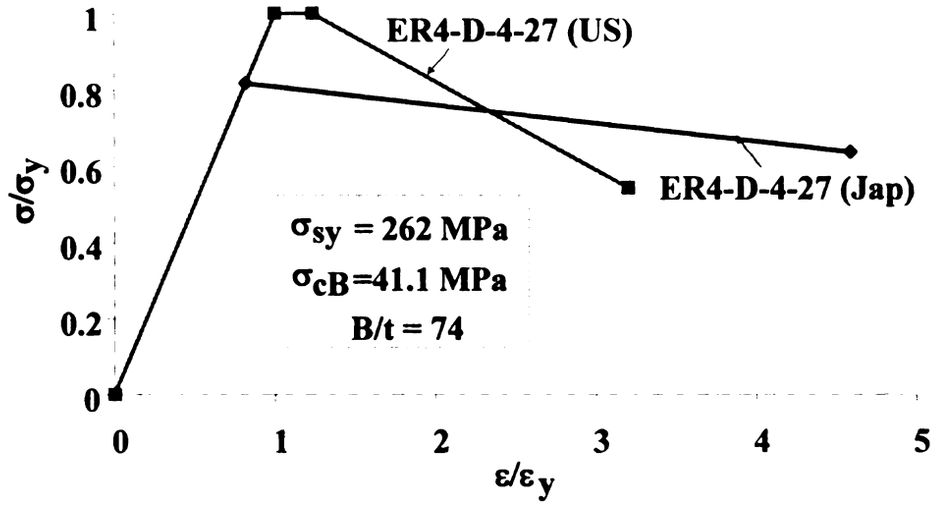


Figure 3.58 Normalized steel fiber σ–ε curve in compression for CFT specimen with σ_y=262MPa, f'_c=41.1MPa, b/t=74

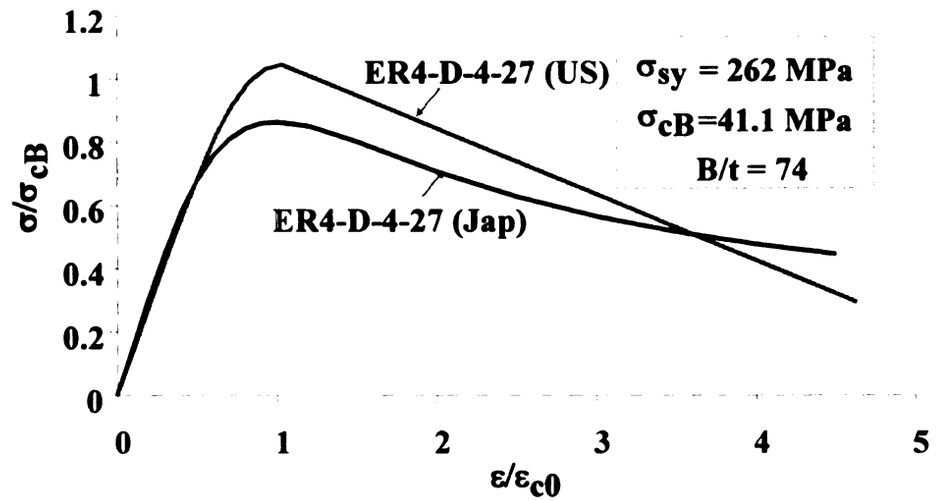


Figure 3.59 Normalized concrete fiber σ–ε curve in compression for CFT specimen with σ_y=262MPa, f'_c=41.1MPa, b/t=74

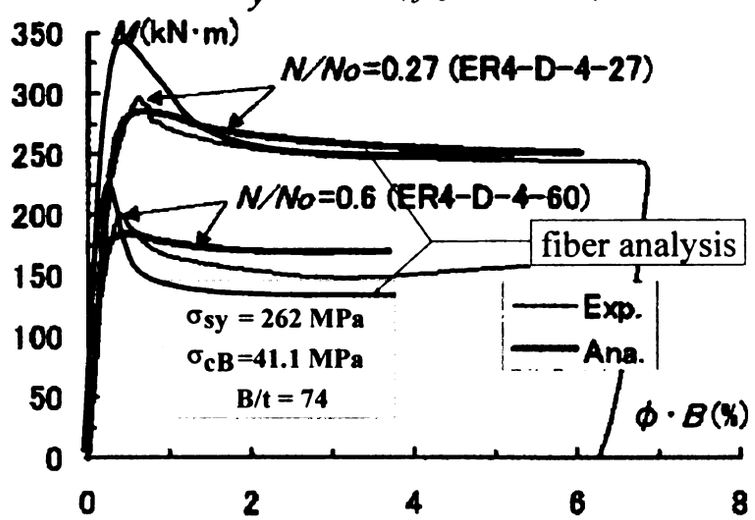


Figure 3.60 Comparison of experimental and analytical M-ϕ responses for CFTs with σ_y=262MPa, f'_c=41.1MPa, b/t=74

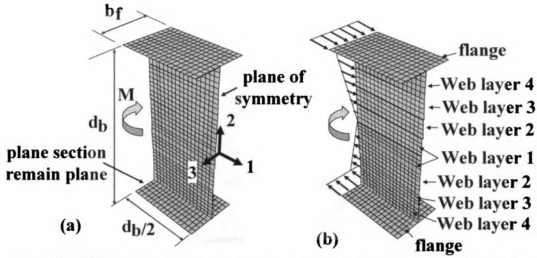


Fig. 3.61 FEM model for determining fiber stress-strain curves of steel beam in compression

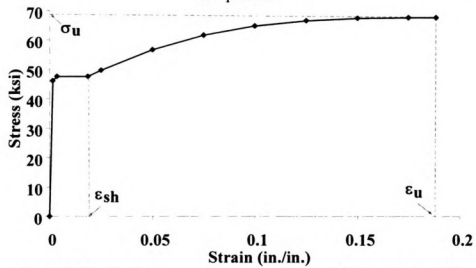


Fig. 3.62 Idealized stress-strain curve for A36 steel (Green's Test 11)

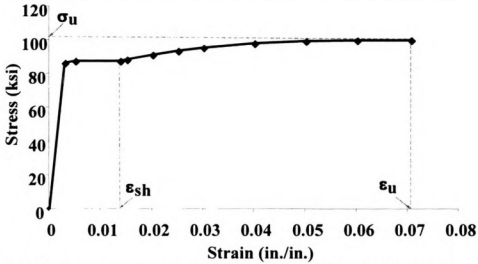


Fig. 3.63 Idealized stress-strain curve for HSLA-80 steel (Green's Test 10&12)

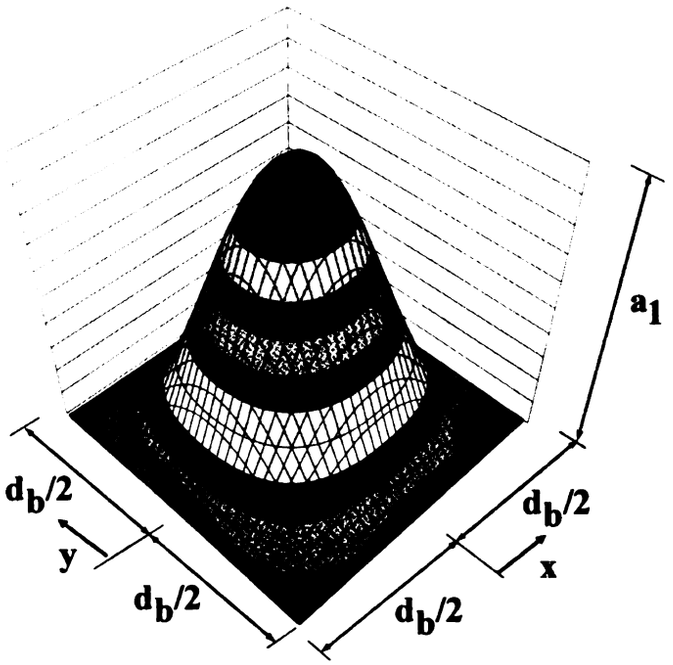


Fig. 3.64 Geometric imperfection for web of steel beam

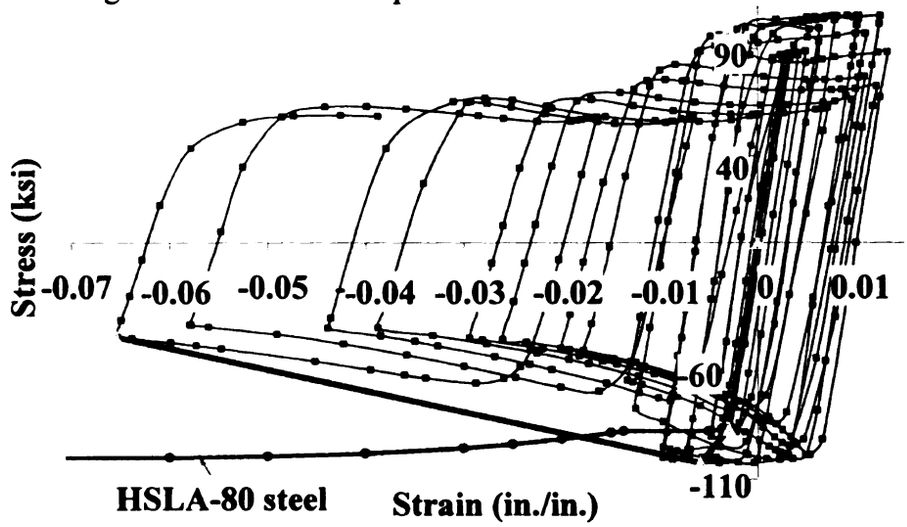


Fig. 3.65 Stress-Strain Relationship of Flange Fibers (Green's Test 10)

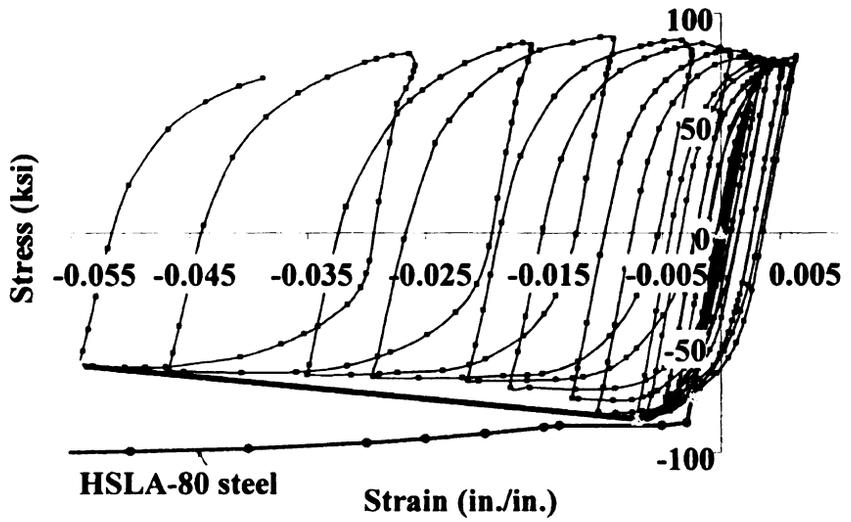


Fig. 3.66 Stress-Strain Relationship of Web Fibers, Layer 1 (Green's Test 10)

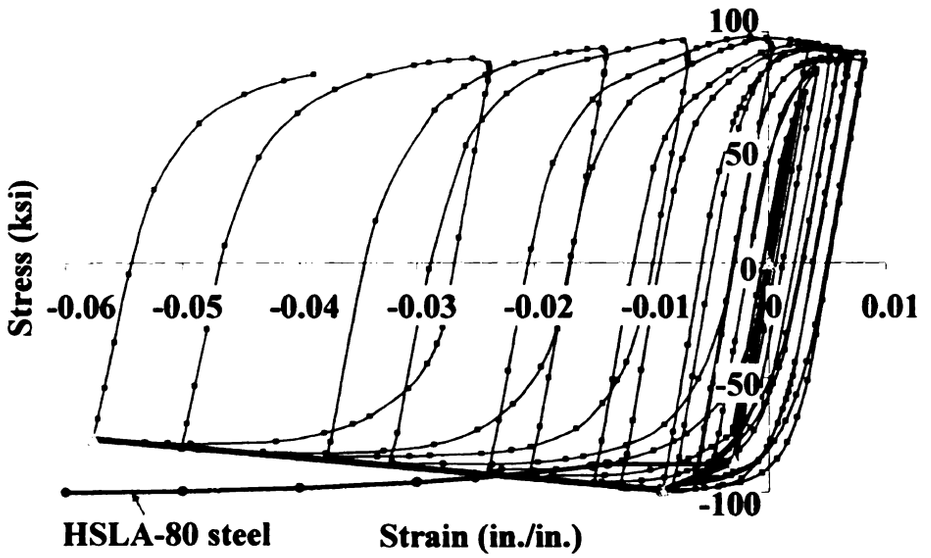


Fig. 3.67 Stress-Strain Relationship of Web Fibers, Layer 2 (Green's Test 10)

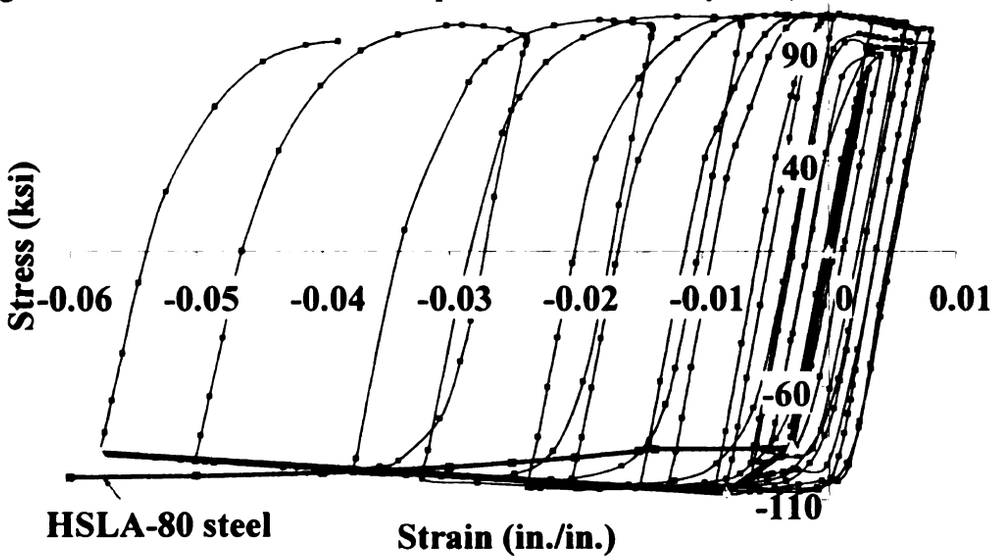


Fig. 3.68 Stress-Strain Relationship of Web Fibers, Layer 3 (Green's Test 10)

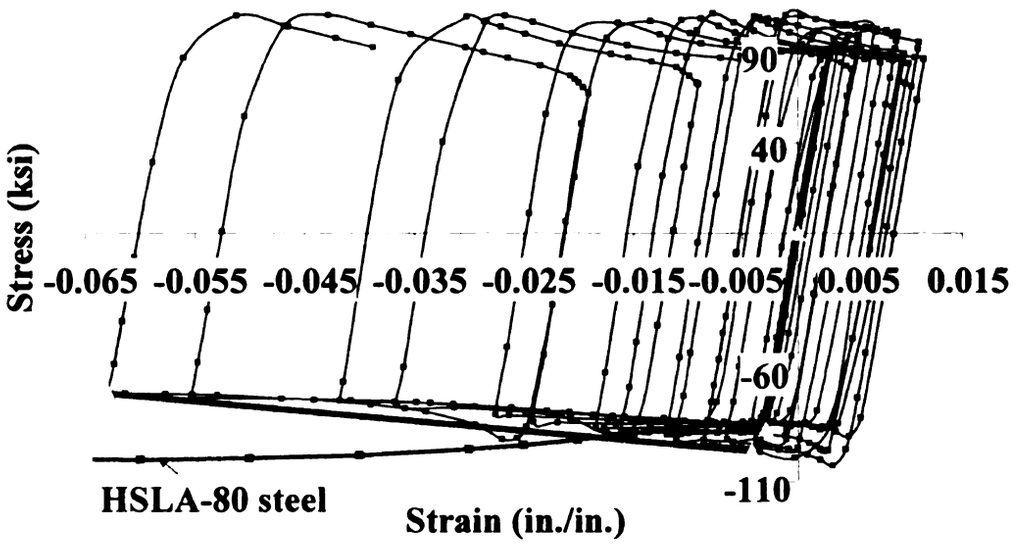


Fig. 3.69 Stress-Strain Relationship of Web Fibers, Layer 4 (Green's Test 10)

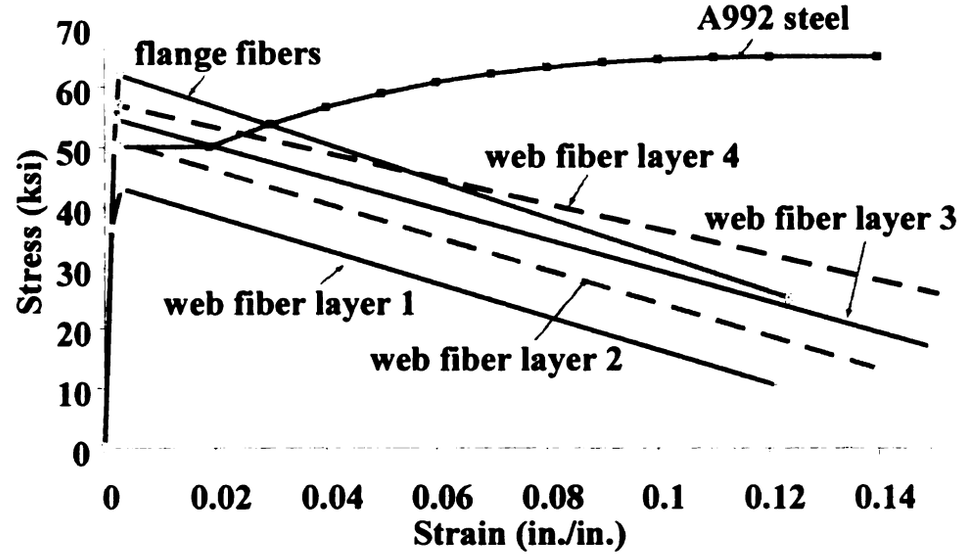


Fig. 3.70 Flange and web fiber σ–ε curves for W36x135 rolled shape

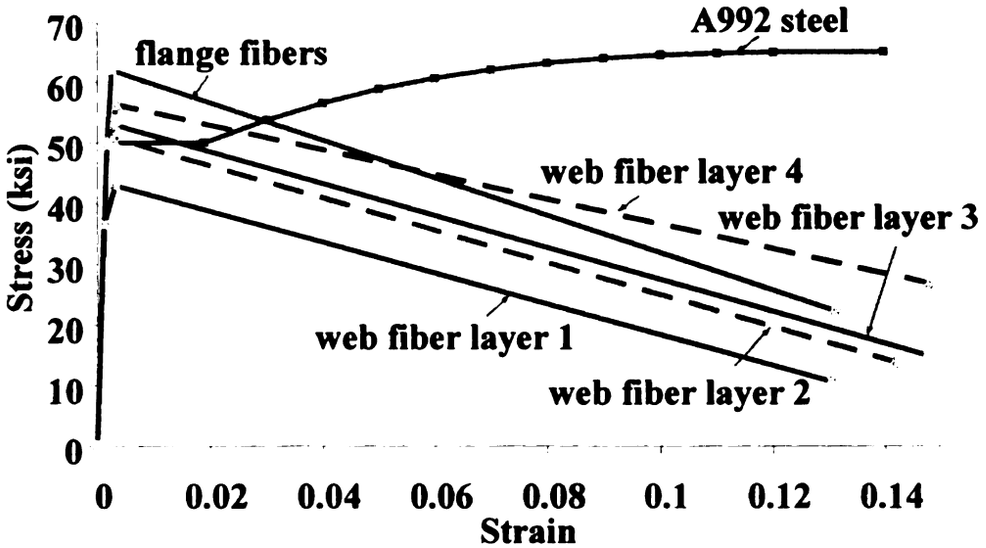


Fig. 3.71 Flange and web fiber σ–ε curves for W33x118 rolled shape

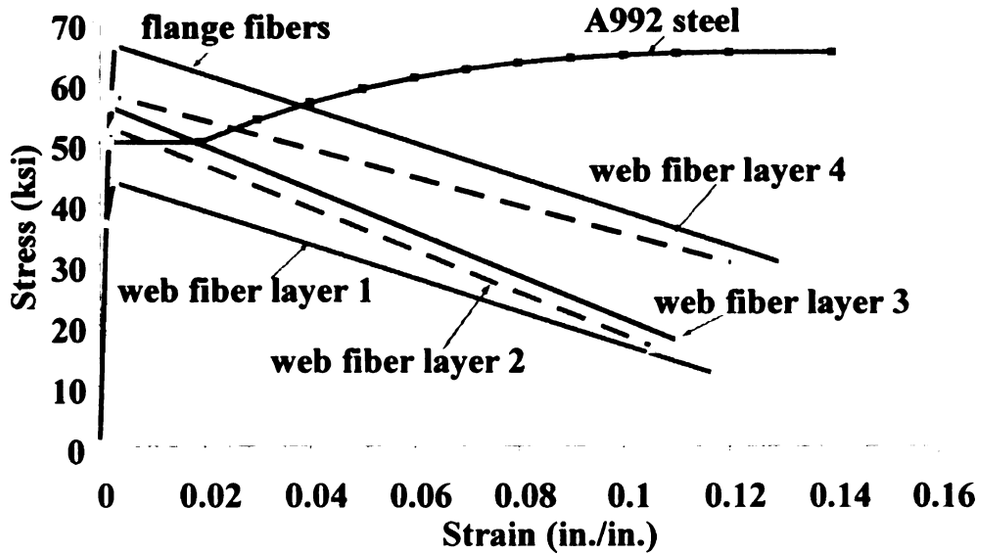


Fig. 3.72 Flange and web fiber σ–ε curves for W30x108 rolled shape

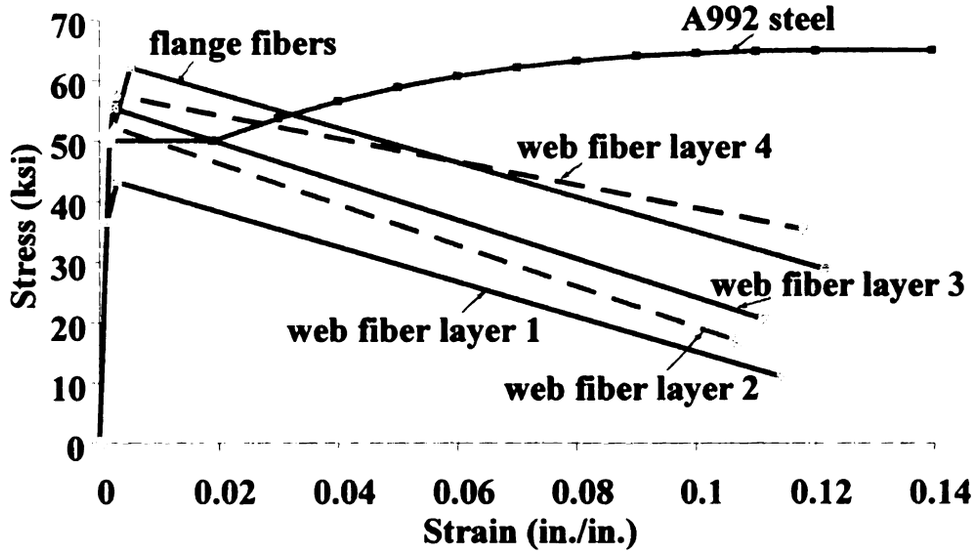


Fig. 3.73 Flange and web fiber σ–ε curves for W27x84 rolled shape

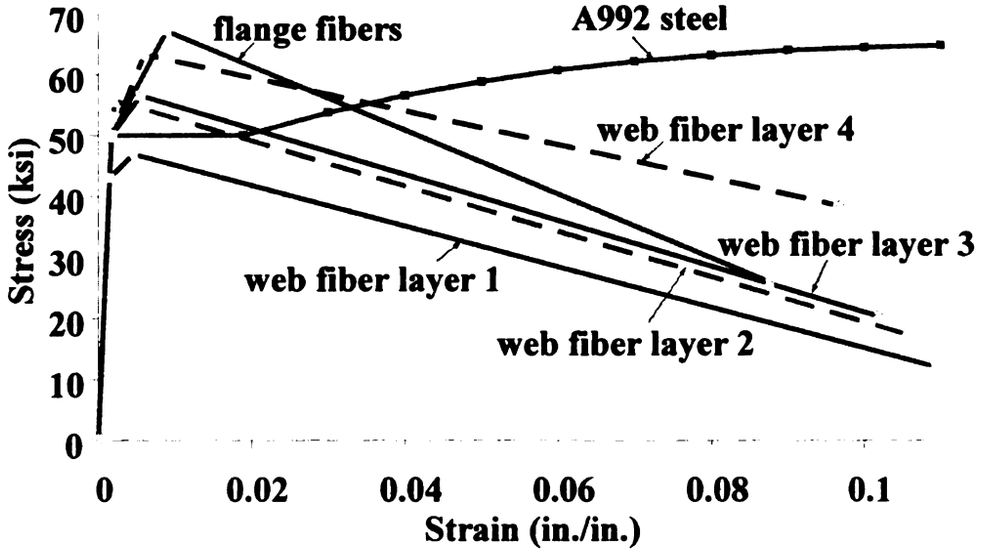


Fig. 3.74 Flange and web fiber σ–ε curves for W24x62 rolled shape

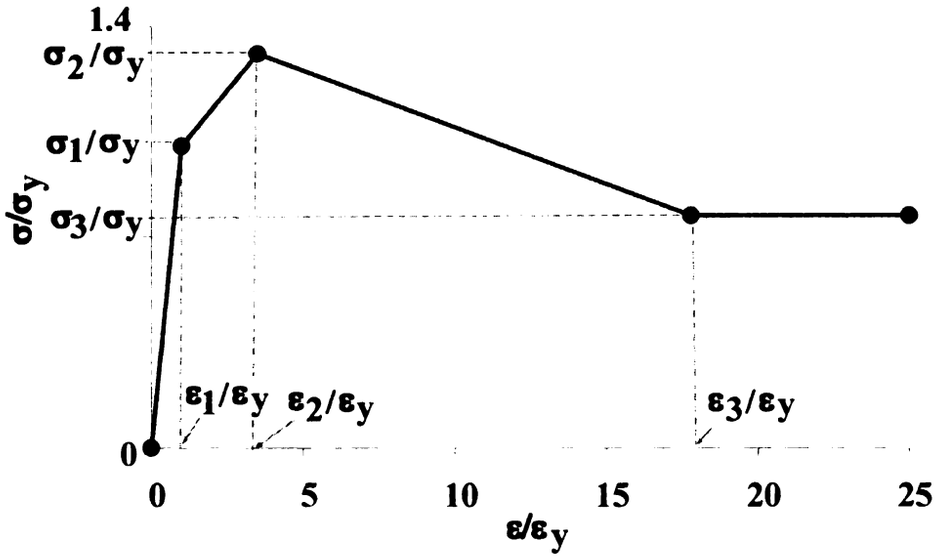


Fig. 3.75 Idealized flange and web fiber σ–ε curve for rolled shape

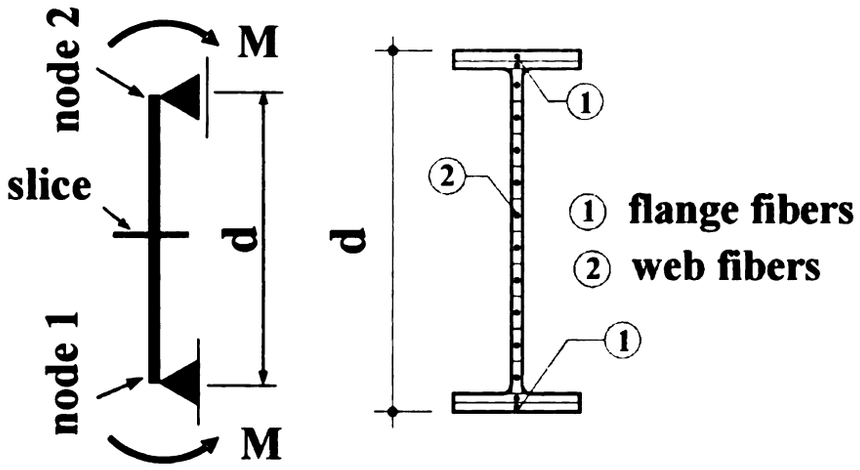


Fig. 3.76 Fiber-based Model for the Inelastic Failure Segment of Steel Beam

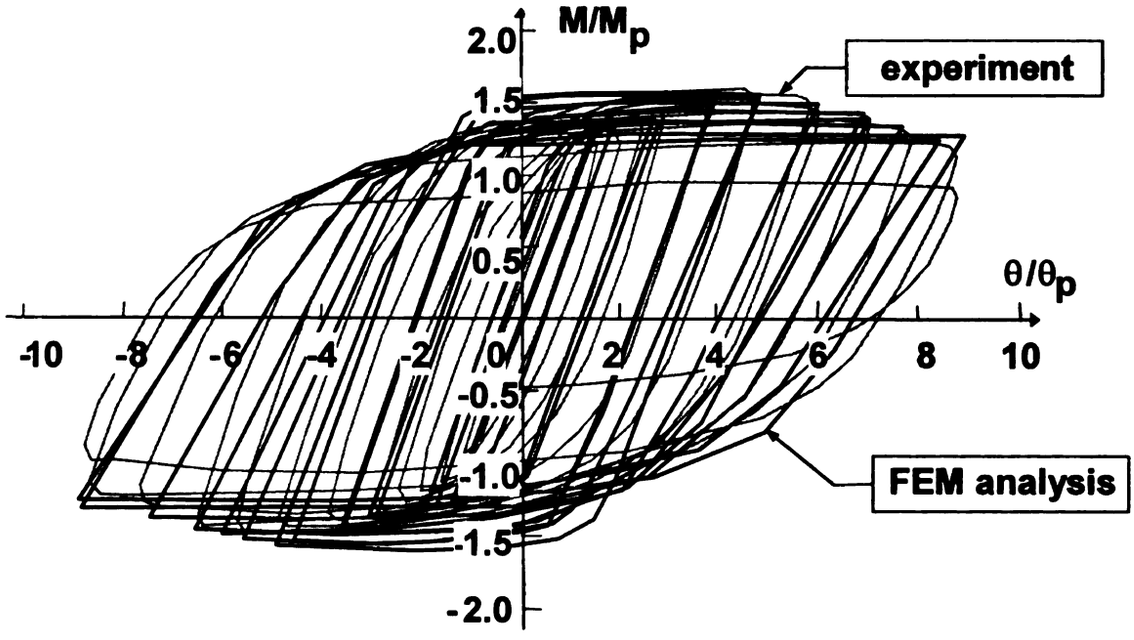


Fig. 3.77 Experimental and FEM analysis M-θ response (Specimen 11, Green et al 2000)

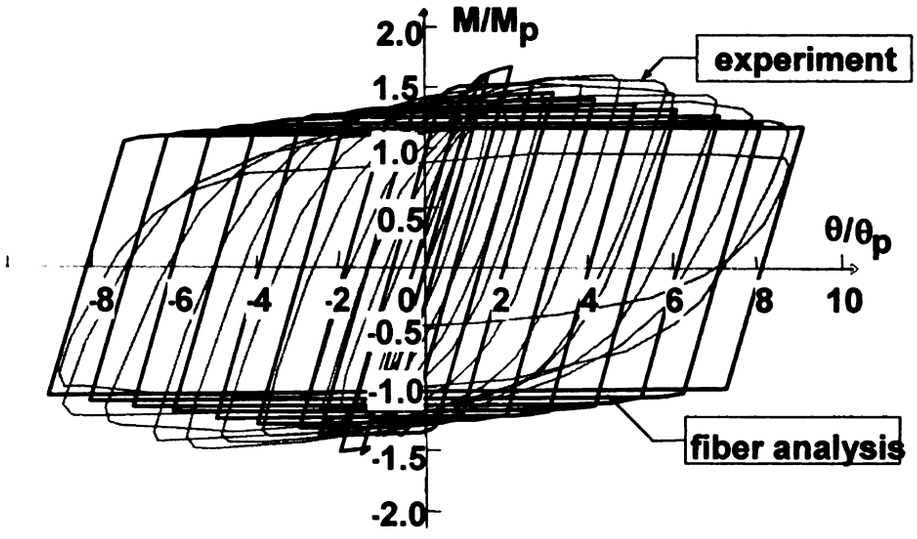


Fig. 3.78 Experimental and fiber analysis M-θ response (Specimen 11, Green et al 2000)

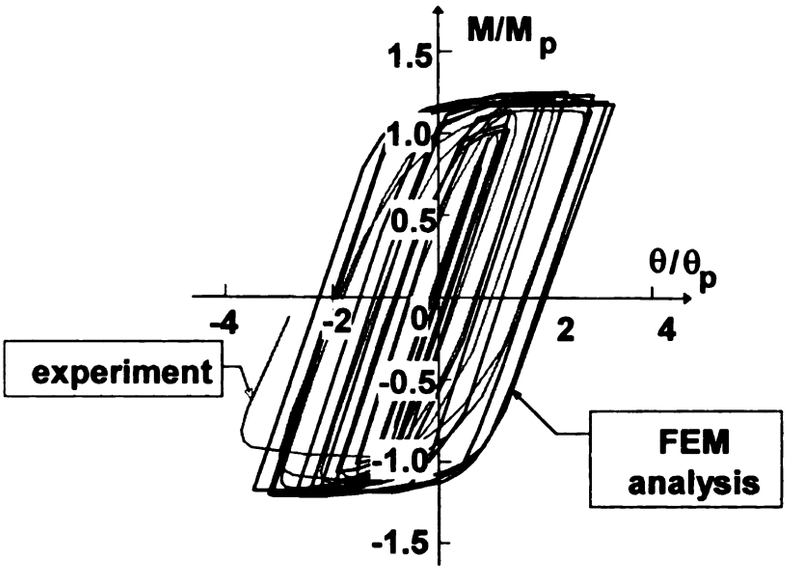


Fig. 3.79 Experimental and FEM analysis M-θ response (Specimen 10, Green et al 2000)

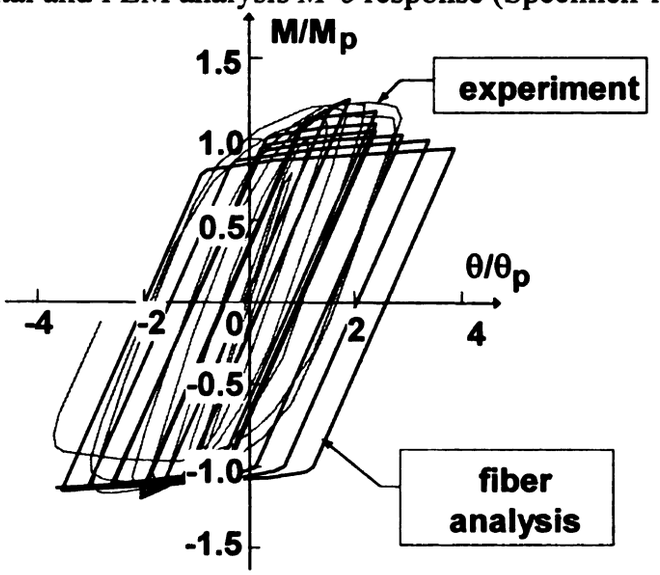


Fig. 3.80 Experimental and fiber analysis M-θ response (Specimen 10, Green et al 2000)

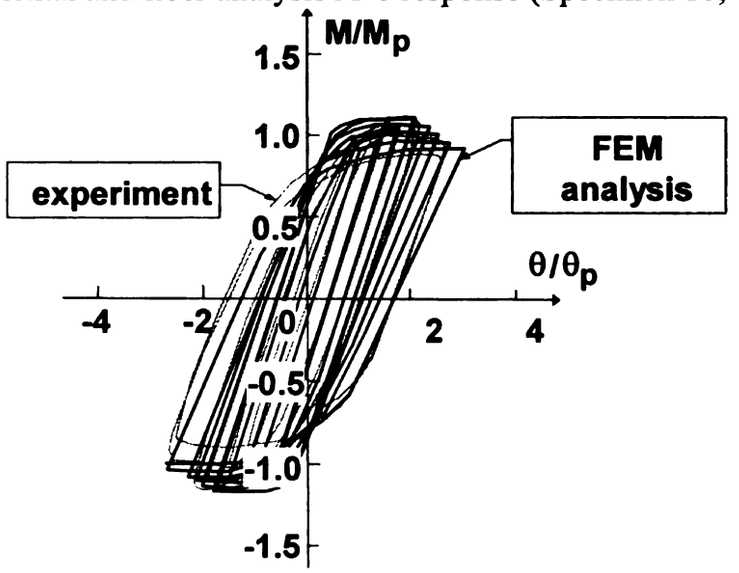


Fig. 3.81 Experimental and FEM analysis M-θ response (Specimen 12, Green et al 2000)

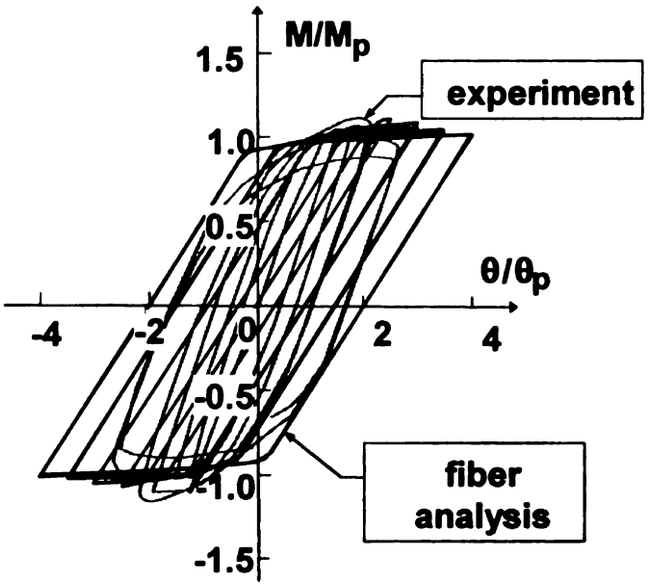


Fig. 3.82 Experimental and fiber analysis M-θ response (Specimen 12, Green et al 2000)

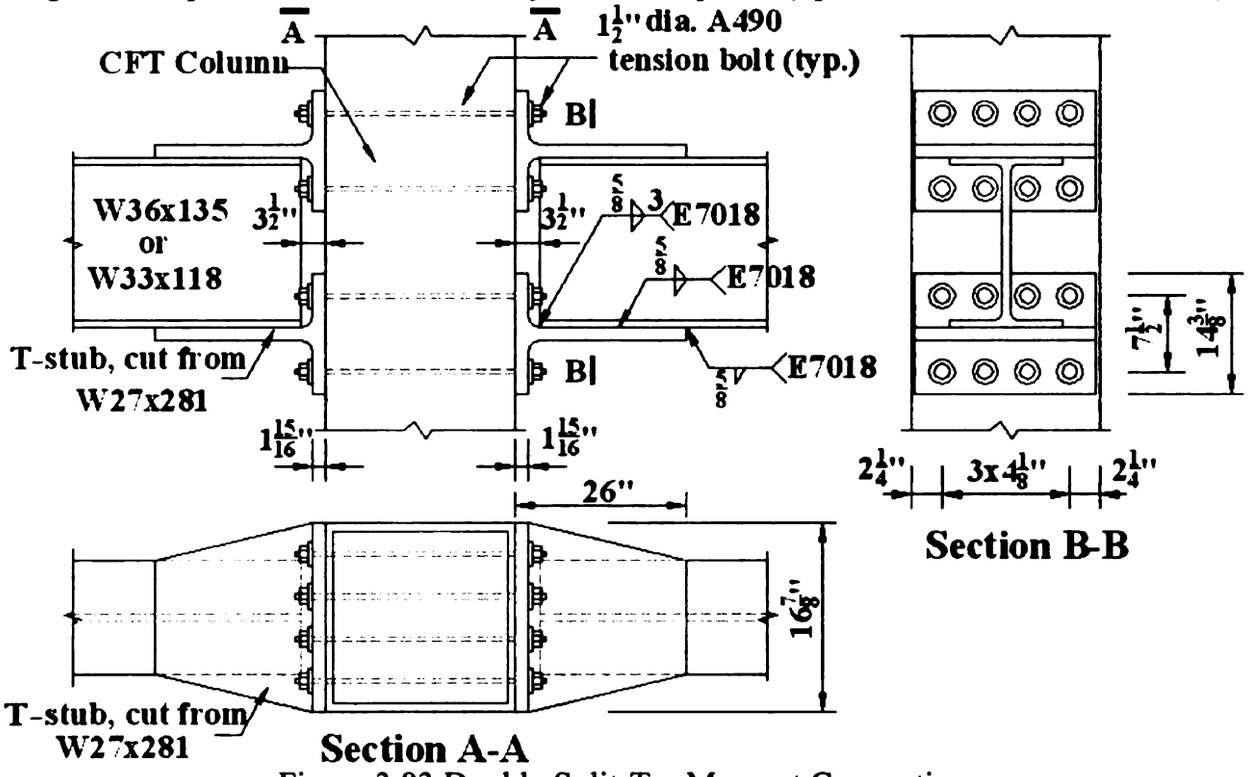


Figure 3.83 Double Split-Tee Moment Connection

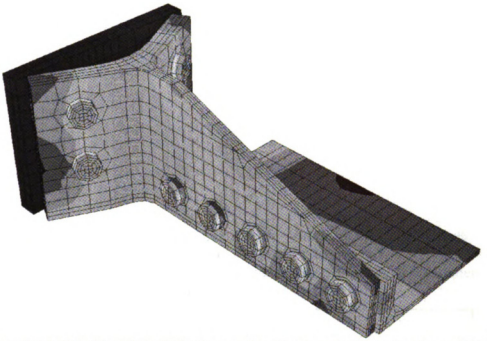


Figure 3.84 FEM Model for DST Connection (Swanson's Test: Specimen TA-05)

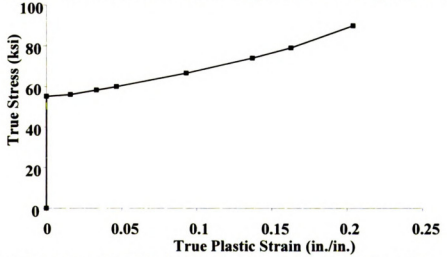


Figure 3.85 True stress-logarithmic plastic strain relationship of T-stub base material (Swanson's Test: Specimen TA-05)

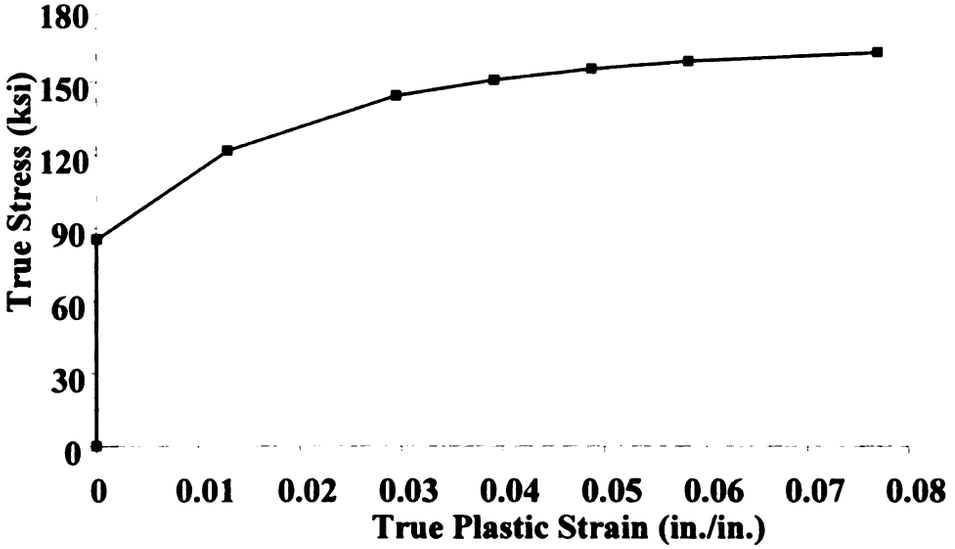


Figure 3.86 True stress- logarithmic plastic strain relationship of bolt material (Swanson's Test: Specimen TA-05)

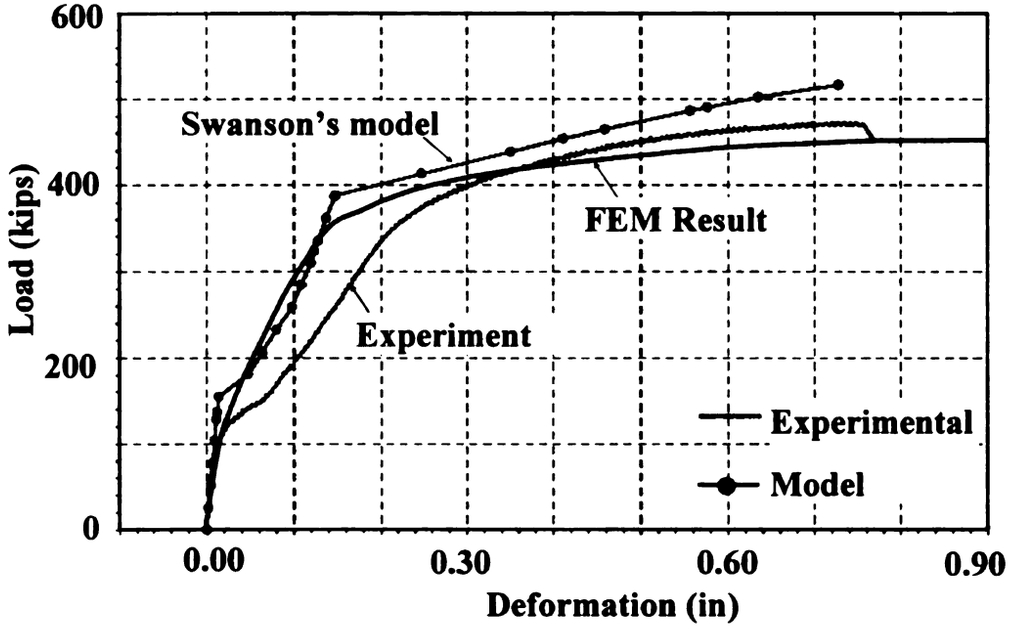


Figure 3.87 FEM-predicted and Experimental Total Deformation for T-stub (TA-05)

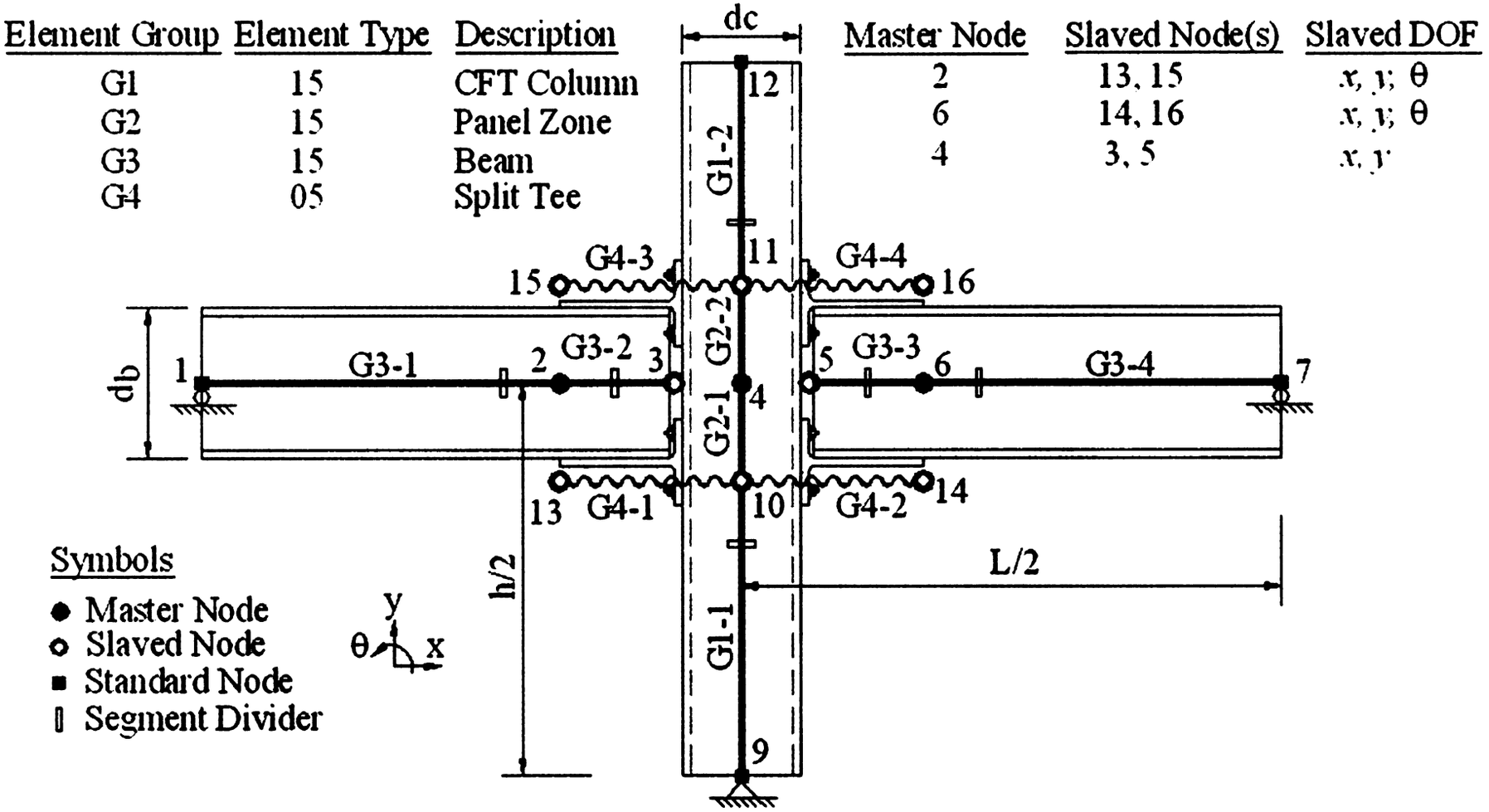


Figure 3.88 *DRAIN-2DX* Double Split-Tee connection subassembly model

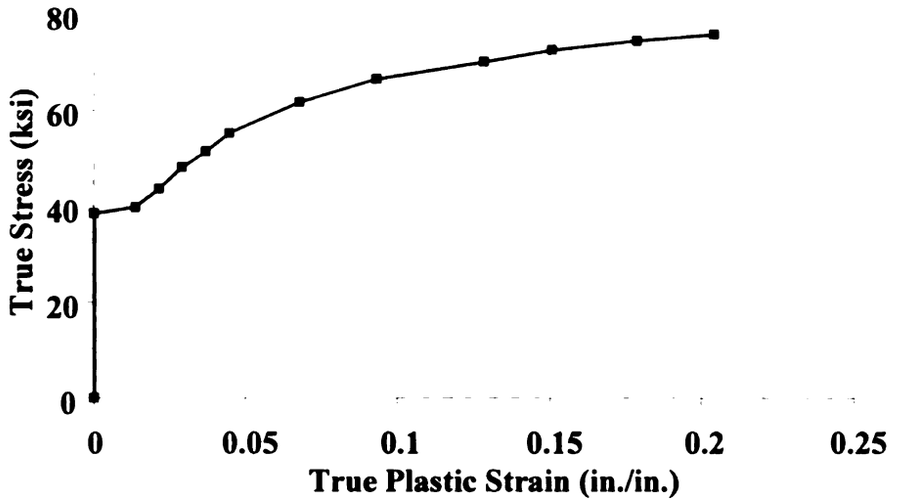


Fig. 3.89 True stress-true plastic strain relationship of tensile coupon test -A36, beam flange (Peng's Specimen 5, 6 & 7)

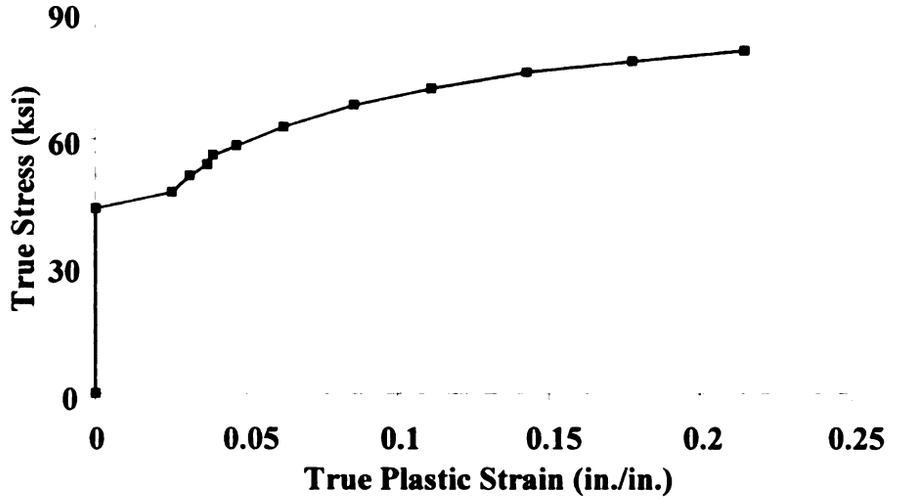


Fig. 3.90 True stress-true plastic strain relationship of tensile coupon test -A36, beam web (Peng's Specimen 5, 6 & 7)

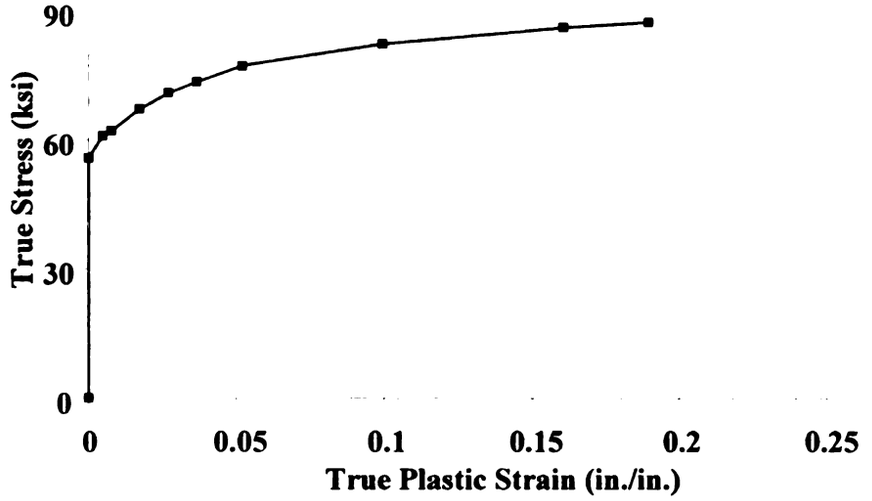


Fig. 3.91 True stress-true plastic strain relationship of tensile coupon test –A500, Gr. B, steel tube (Peng's Specimen 5, 6 & 7)

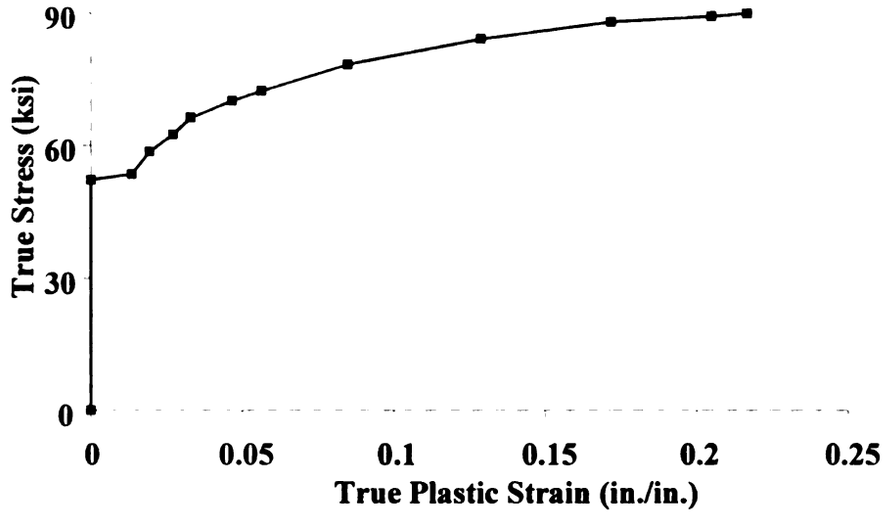


Fig. 3.92 True stress-true plastic strain relationship of tensile coupon test –A572, Gr. 50, structural tee (Peng's Specimen 5, 6 & 7)

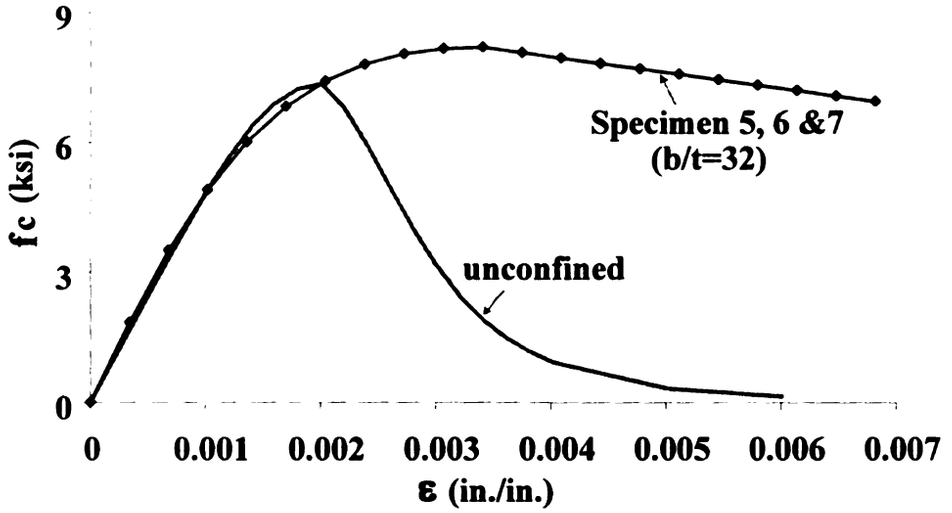


Fig. 3.93 Stress-strain relationship of concrete infill (Peng's Specimen 5, 6 & 7)

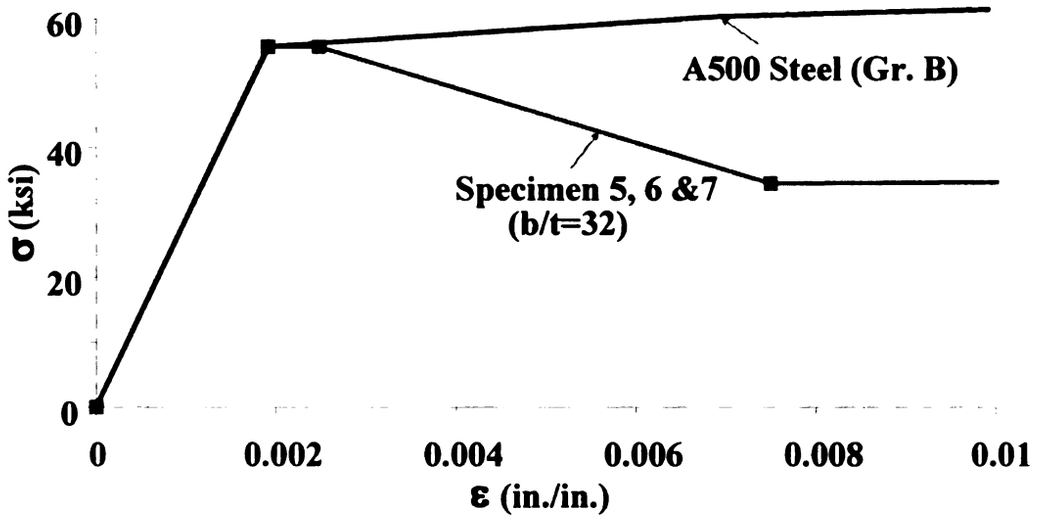


Fig. 3.94 Stress-strain relationship of steel tube (Peng's Specimen 5, 6 & 7)

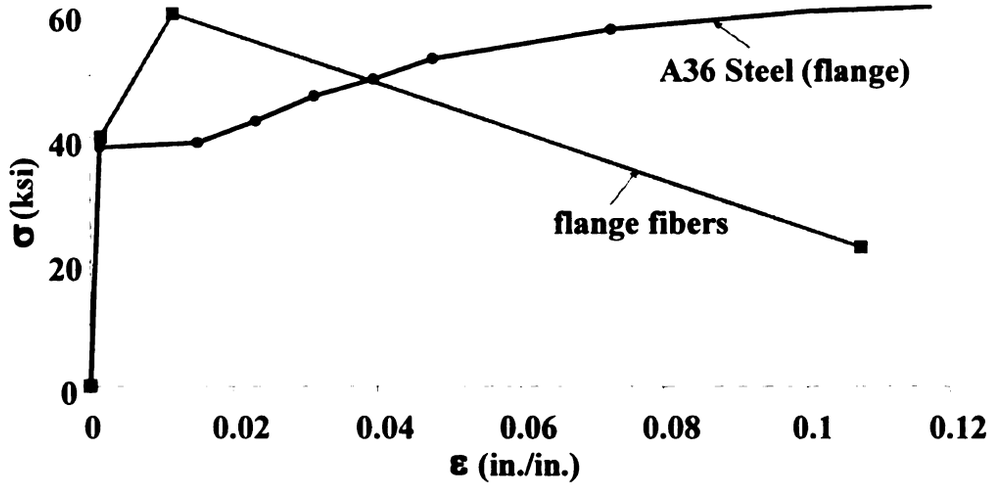


Fig. 3.95 Stress-strain relationships for flange fibers of steel beams (Peng's Specimen 5, 6 & 7)

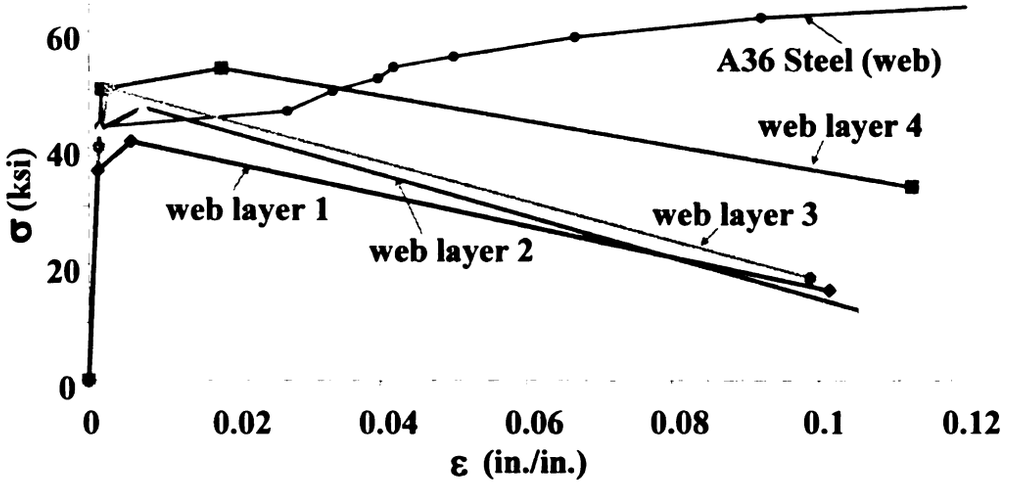


Fig. 3.96 Stress-strain relationships for web fibers of steel beams (Peng's Specimen 5, 6 & 7)

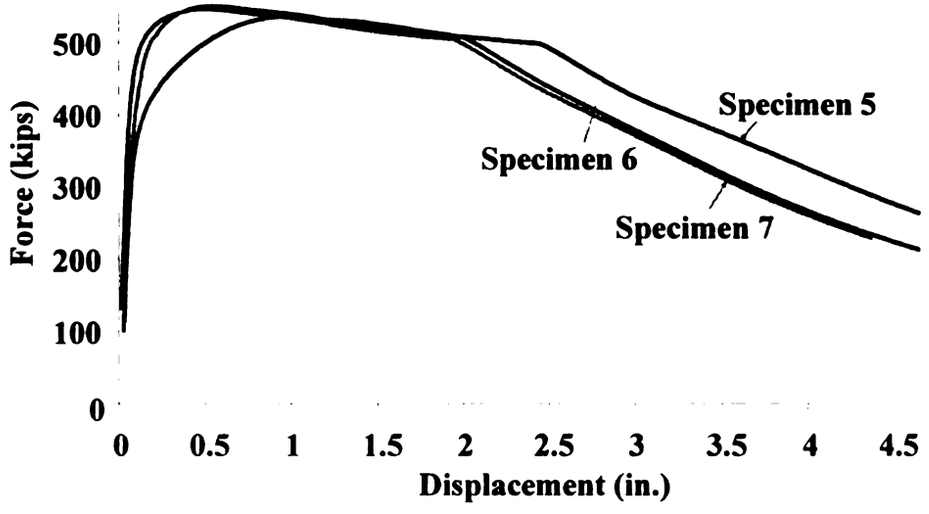


Fig. 3.97 Force-displacement relationships of T-stubs in tension (Peng's Specimen 5, 6 & 7)

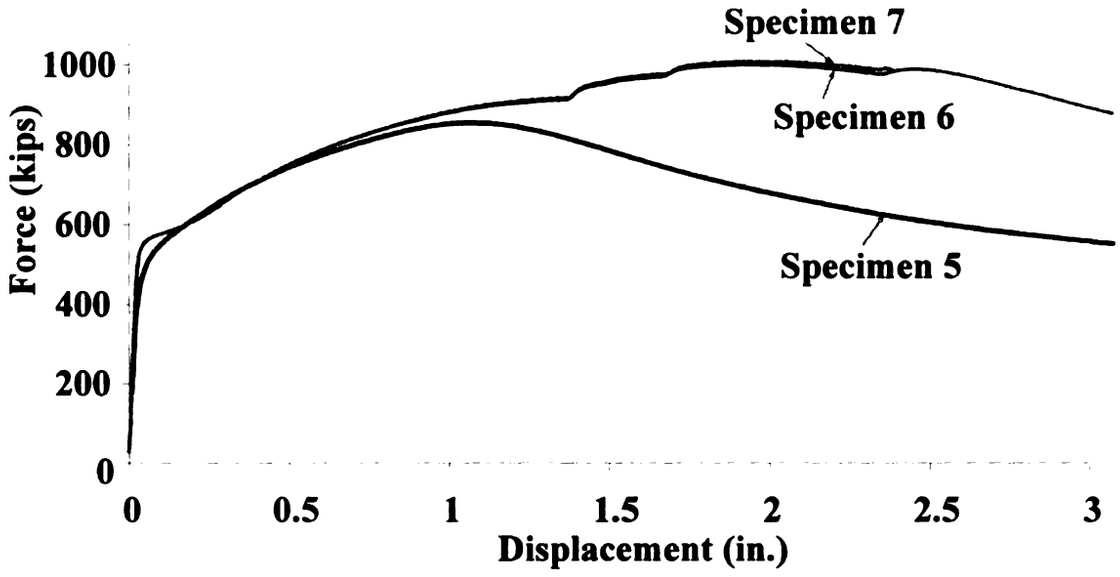


Fig. 3.98 Force-displacement relationships of T-stubs in compression (Peng's Specimen 5, 6 & 7)

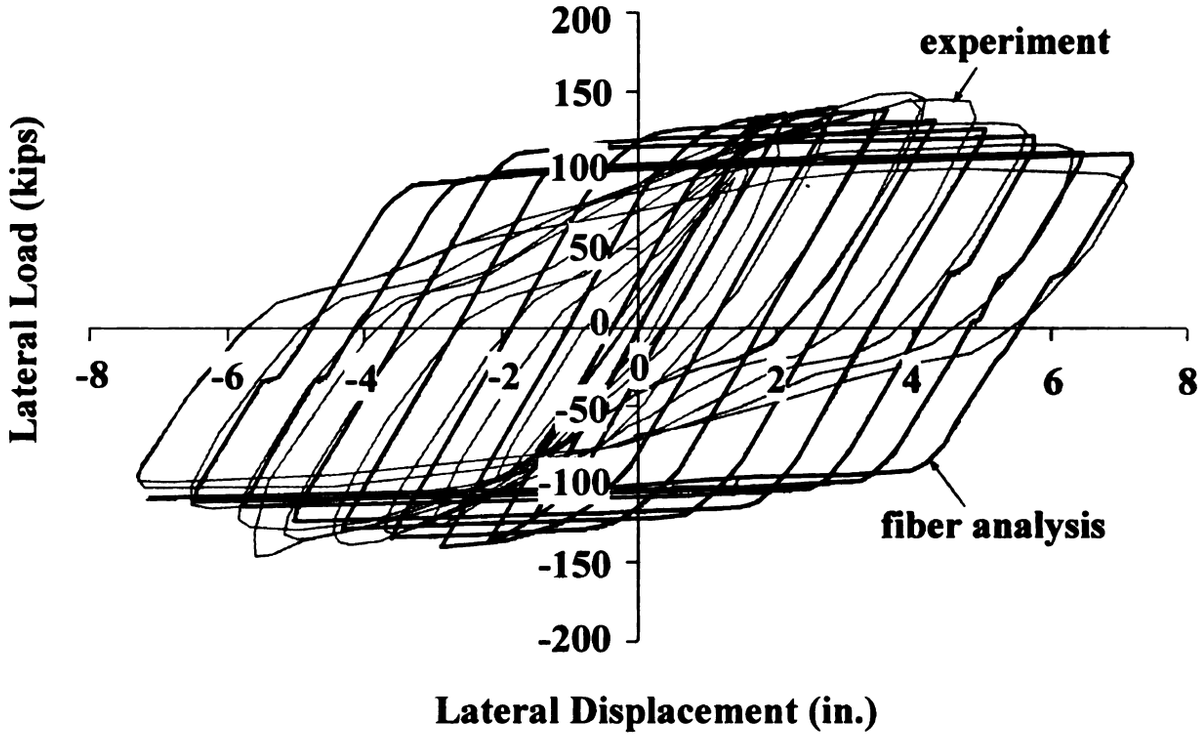


Fig. 3.99 Comparison of experimental and fiber analysis of lateral load-displacement response for Peng's Specimen 5 (Peng 2001)

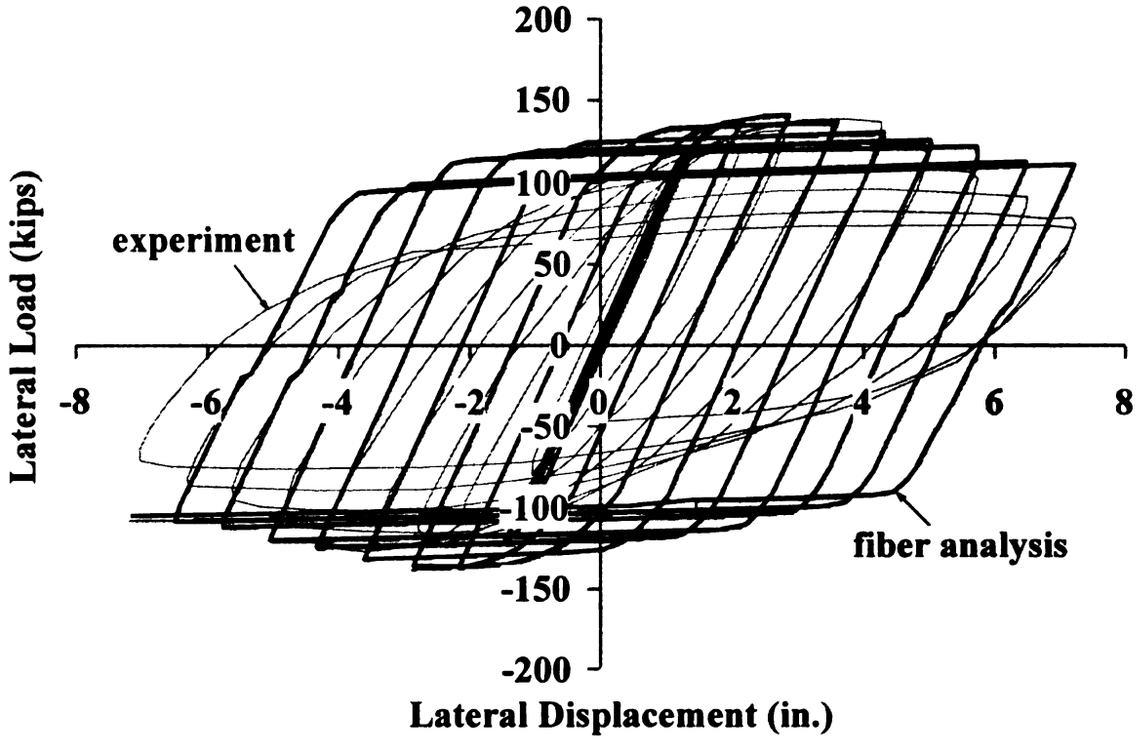


Fig. 3.100 Comparison of experimental and fiber analysis of lateral load-displacement response for Peng's Specimen 6 (Peng 2001)

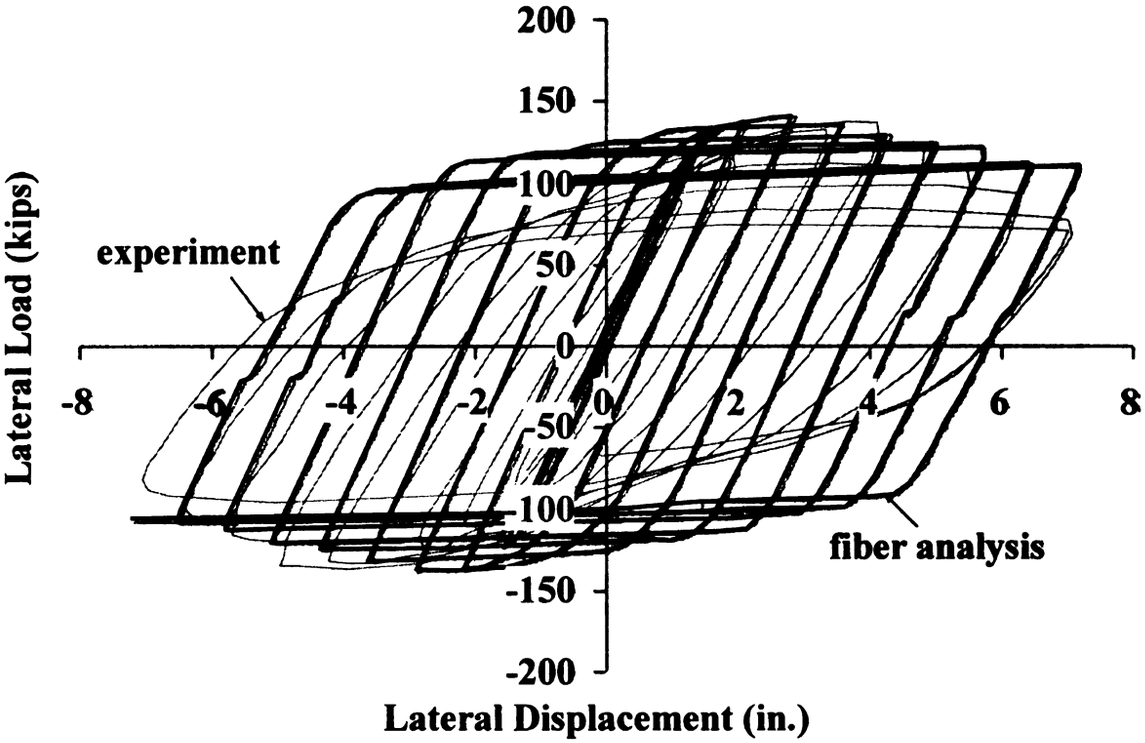


Fig. 3.101 Comparison of experimental and fiber analysis of lateral load-displacement response for Peng's Specimen 7 (Peng 2001)

CHAPTER 4 DESIGN AND STATIC PUSHOVER ANALYSIS OF THE CFT MRFS

Section 4.1 presents the seismic design of high strength CFT moment resisting frames (MRFs) for low-rise (6-story) and high-rise (12-story) building structures located in a high seismic risk region (Los Angeles, CA). Section 4.2 summarizes the analytical models used to conduct nonlinear static pushover analysis of high strength CFT MRFs. These models are developed based on the analytical models presented in detail in Chapter 3.0. Section 4.3 presents the results of the nonlinear static pushover analyses of the high strength CFT MRFs designed for the 6- and 12-story building structures. Sub-section 4.3.1 focuses on the results of the pushover analyses conducted according to the FEMA 356 NSP procedures, and sub-section 4.3.2 presents the results of pushover analyses conducted per adaptive pushover procedures developed by Gupta et al. (2000).

4.1 Seismic Design of High Strength CFT MRFs

A low-rise 6-story office building and a high-rise 12-story office building were designed using high strength CFT MRFs. The office buildings are located in Los Angeles, CA (Latitude 34°3'N, Longitude 118°15'W) with *stiff* soil profile and site class *D*. Two structural floor plans were considered for each building. Figure 4.1 shows the first floor plan, which consists of *perimeter* moment resisting frames and interior gravity frames. The structural elevations of the 6-story and the 12-story building in the east-west direction are shown in Figures 4.2 and 4.3, respectively. High strength CFT MRFs are used as the perimeter MRFs to provide lateral stiffness, strength, and ductility for design-level seismic loads. As shown in Figure 4.1, the perimeter MRFs in the east-west

direction are pin connected to the corner columns A1, A7, F1, and F7 to prevent their biaxial bending.

Figure 4.4 shows the second floor plan, which consists of distributed moment resisting frames MRFs in the east-west direction and braced frames in the north-south direction. The structural elevations are same as those shown in Figures 4.2 and 4.3. High strength CFT MRFs are *used* as the distributed MRFs in the east-west direction to provide lateral stiffness, strength, and ductility. CFT braced frames are used in the north-south direction to provide lateral stiffness, strength, and ductility. Figure 4.5 shows an example structural elevation of the CFT braced frames for the 12-story office building.

The high strength CFT MRFs (perimeter MRFs for floor plan 1 and distributed MRFs for floor plan 2) for the 6-story and 12-story office buildings were designed to meet the requirements of the current building codes (IBC 2000) and FEMA 368. The structural members and connections of the MRFs were designed using the applicable steel and concrete design specimens (AISC 1999, ACI 2003) as presented in the following sub-sections. The CFT braced frames of floor plan 2 were not the focus of this research, hence their design and analysis are included in this or following chapters.

4.1.1 Seismic Design Procedure

The seismic design procedure for high strength CFT MRFs is summarized in Figure 4.5. As shown in this Figure, the first step is to estimate the gravity and wind loads acting on the structure. These are used to design the floor beams and girders. The designed members are used to estimate the effective seismic weight. The design response spectrum for the structure is calculated, and used along with the seismic weight to calculate the

equivalent lateral forces for seismic design. Second-order elastic analysis is conducted for all factored load combinations to estimate the member forces for design. The strength check, inter-story drift check, and strong column-weak beam check are performed. If all the code requirements are met, then the design is complete. Otherwise, the member sizes are increased and the analysis is conducted again, and is followed by various checks. The seismic design of the 6- and 12-story high strength CFT MRFs is explained in more detail below in this section:

Step 1 - Gravity and wind loads

Table 4.1 summarizes the dead loads for the floor systems. As shown in Table 4.1, the total dead load including the weights of various attachments is equal to 90 psf. Table 4.2 summarizes the gravity loads, i.e., the dead loads and live loads for the roof and floor systems. The design live load is assumed to be 100 psf (office rooms for computer use – IBC 2000), but it can be reduced for design as permitted by IBC 2000. Table 4.2 also includes the partition loads, which are also needed for estimating the effective seismic weight. The gravity loads for designing the high strength CFT frames are calculated using the floor dead loads and reduced live loads multiplied by the appropriate tributary areas. The design wind loads are calculated using the procedures outlined in IBC 2000. Table 4.3 summarizes the basic wind speed, exposure category, wind importance factor and enclosure classification for Los Angeles, CA, which is the location of the structure. The unfactored wind load acting on each story of the 6-story perimeter MRFs in the east-west direction are provided in Table 4.4. Similar calculations were performed and tables developed for the 12-story and the distributed MRFs.

Step 2 – Floor beams and girders

The floor beams were designed as simply supported beams subjected to uniformly distributed loading. The design loads for the floor beams were obtained by combining the factored dead loads and reduced live loads: $w_u=1.2w_D+1.6w_L$, where w_u, w_D and w_L are design load, dead load and reduced live load (as permitted by IBC 2000), respectively. The AISC-LRFD (1999) specifications and manual were used to select wide flange sections that satisfy the stiffness and strength requirements for floor beams. The girders in the lower-level stories (1st and 2nd stories in the 6-story MRF) were assumed to behave as simply supported beams after a severe earthquake. The girders in the intermediate stories (3rd and 4th stories in the 6-story MRF) were assumed to behave as pin supported at one end (exterior joint) and fixed at the other end after a severe earthquake. The girders in the top stories (5th and 6th stories in the 6-story MRF) were assumed to be fixed at both ends after a severe earthquake. These assumptions were based on the results of preliminary time-history analysis, which indicated that the girders of lower-level stories undergo large inelastic deformations, while the girders of the higher-level stories undergo small or no inelastic deformations. The girder sections are usually increased later to meet the inter-story drift requirements of IBC 2000, Table 1617.3.

Step 3 – Seismic Weight

The effective seismic weight of each story was calculated by adding the dead loads and the partition loads for each story (floor) and multiplying it by the appropriate tributary area. No other live loads are considered in the calculation of effective seismic weight. This is also according to IBC (2000) recommendations.

Step 4 – Design Response Spectrum

The design response spectrum was developed according to the procedures outlined in IBC (2000). The design coefficients and factors for the seismic-resisting systems are given in Table 4.5. The step-by-step procedure for developing the design response spectrum is outlined below:

- The maximum spectral response accelerations S_S and S_1 for fundamental periods of 0.2 and 1.0 seconds, respectively, were determined using maps 5 and 6 of FEMA 368 (2003). The values of S_S and S_1 for structures located in Los Angeles (34°3' N, 118°15'W) with 5% critical damping ratio and site class *B* were found to be equal to 1.50 *g* and 0.60 *g*, respectively, where g is the gravitational acceleration.
- The 6 and 12-story office buildings are located in site class *D*. Hence, S_S and S_1 were adjusted to account for the change in site class from *B* to *D*. The site adjustment coefficients F_a and F_v for site class D with $S_S \geq 1.25$ g and $S_1 \geq 0.5$ g are equal to 1.0 and 1.5, respectively (IBC 2000; Table 1615.1.2). The adjusted maximum spectral response accelerations S_{MS} and S_{M1} are equal to F_a x S_S and F_v x S_1, i.e., 1.50 *g* and 0.90 *g* respectively.
- The design spectral response accelerations at short periods S_{DS} and at 1 second period S_{D1} were calculated as 0.667 x S_{MS} and 0.667 x S_{M1}, respectively (IBC 2000, Section 1615.1.3). The resulting values of S_{DS} and S_{D1} are equal to 1.00 *g* and 0.60 *g*, respectively.
- Figure 4.6 shows the design response spectrum developed according to IBC (2000). In Figure 4.6, where S_a is the design spectral response acceleration as the function of the structure fundamental period *T*. Additionally:

$$T_0 = 0.2\frac{S_{D1}}{S_{DS}} = 0.2 \times \frac{0.60g}{1.00g} = 0.12 \ \ Sec.$$
$$T_S = \frac{S_{D1}}{S_{DS}} = \frac{0.60g}{1.00g} = 0.60 \ \ Sec. \tag{4.1}$$

$$S_a = \begin{cases} 0.6\dfrac{T}{T_0}S_{DS} + 0.4S_{DS} & T \le T_0 = 0.12s \\ S_{DS} & T_0 = 0.12s \le T \le T_S = 0.60s \\ \dfrac{S_{D1}}{T} & T \ge T_S = 0.60s \end{cases} \tag{4.2}$$

Step 5 – Equivalent Lateral Force

The high strength CFT MRFs belong to seismic design category (IBC 2000, Table 1616.3). The seismic base shear is calculated Equation 4.3, where W is the effective seismic weight supported by the frame, and C_S is the seismic response coefficient that can be calculated using Equation 4.4, but must satisfy the limits defined by Equations 4.5 and 4.6 (Section 1617.4.1.1). In these equations R is the response modification factor given by IBC (2000) to be equal to *8* for special composite moment resisting frames. I_E is related to the importance of the structure and is equal to 1.25 for CFT MRFs.

$$V = C_S W \tag{4.3}$$

$$C_S = \frac{S_{DS}}{R/I_E} \tag{4.4}$$

$$0.044\, S_{DS} I_E \le C_S \le \frac{S_{D1}}{[R/I_E]T} \tag{4.5}$$

$$\text{If } S_1 \ge 0.60 \text{ g, then } C_S \ge \frac{0.5\, S_1}{R/I_E} \tag{4.6}$$

Figures 4.7 and 4.8 show the seismic response coefficient – fundamental period (C_S - T) relationships for the 6-story and 12-story high strength CFT MRFs. The fundamental

periods T_S, T_g, and T_{max} are also indicated in these Figures. T_S and T_g are the fundamental periods marking substantial changes in the equations for calculating C_S. T_{max} is the upper limit for the computed fundamental period of the structure. It is calculated as $T_{max} = T_a C_u$, where C_u is a coefficient and T_a is the approximate fundamental period calculated using Equation 4.7 (IBC 2000, Section 1617.4.2). In Equation 4.7, C_T is the building period coefficient and h_n is the height above the base to the highest level of the building

$$T_a = C_T (h_n)^{3/4} \tag{4.7}$$

The upper bound limit of T_{max} is imposed on the computed period when calculating the maximum base shear (V) for designing and conducting the strength check. This upper bound limit is released when calculating the base shear for checking the interstory drift requirements of IBC (Section 1617.3). The seismic base shear (V) is distributed as equivalent lateral forces (Q_E) over the height of the building according to the seismic weights (w_i) of the individual stories. For example, Table 4.6 gives the equivalent lateral seismic forces for the 6-story perimeter MRFs in the east-west direction.

Steps 6 - Second Order Elastic Analysis

Second-order elastic analyses were conducted for various loading combinations (IBC 2000, Section 1605.2.1) to determine the maximum internal forces and interstory deflections (δ_x at story x) of the high strength CFT MRFs. The second-order elastic analyses were conducted using DRAIN-2DX (Prakash et al. 1993) while using fiber elements were used to model the steel beams and CFTs. The seismic load combinations given by Equations 4.7 and 4.8 govern the design by producing maximum internal forces and interstory drifts in the high strength CFT MRFs.

$$1.2\,D + 1.0\,E + f_l\,L, \tag{4.7}$$

$$0.9\,D + 1.0\,E \tag{4.8}$$

In Equations 4.7 and 4.8, D, L, and E are the dead, live, and earthquake loads, and f_1=0.5.

For Equation 4.7, $$E = \rho\,Q_E + 0.2\,S_{DS}\,D \tag{4.9 a}$$

For Equation 4.8, $$E = \rho\,Q_E - 0.2\,S_{DS}\,D \tag{4.9 b}$$

In these equations, Q_E is the equivalent lateral force obtained as described in *Step 5*. ρ is the redundancy coefficient = 1.25 for structures with special moment resisting frames (IBC 2000, Section 1617.2.2). Equations 4.7 and 4.8 simplify to 4.10 and 4.11, which are the governing loading combinations for the seismic design of high strength CFT MRFs.

$$1.4\,D + 1.25\,Q_E + 0.5\,L \tag{4.10}$$

$$0.7\,D + 1.25\,Q_E \tag{4.11}$$

Second-order elastic analyses are conducted for these governing loading combinations to determine: (a) the maximum internal forces in the structural members, and (b) the maximum interstory drifts. The equivalent lateral forces (Q_E) used to determine the maximum internal forces are calculated as shown in *Step 5* while limiting the computed fundamental period T_1 to T_{max}. This limit on the computed period T_1 is usually released when determining Q_E used for estimating the maximum interstory drifts.

Step 7, 8 - Strength and Stiffness Design Checks

The maximum internal forces and interstory drifts from *Step 6* are required to perform the following strength and stiffness design checks. All the structural members of the high strength CFT MRFs, i.e., the steel beams and the CFT beam-columns are designed to have greater factored resistance (strength) than the maximum internal forces determined from the second order analyses in *Step-6*. Additionally, the strong column – weak beam design philosophy is implemented by designing the columns to be stronger than the

beams connected to them, i.e., the factored flexural resistance of the beam-columns are greater than the factored flexural resistance of the beams connected to them.

The structural members of the high strength CFT MRFs are also designed so that the maximum interstory drift determined from the second order analyses in *Step 6* is less than the interstory drift limits defined by IBC 2000 (Table 1617.3). These interstory drift limits (δ_x) are determined using Equation 4.12 given by IBC 2000 (Section 1617.4.6).

$$\delta_x = C_d \, \delta_{xe} / I_E \tag{4.12}$$

In Equation 4.12, C_d is the displacement amplification factor given by IBC (2000) to be equal to *5.5* for special composite MRFs. δ_{xe} is the interstory drift from the second order elastic analyses for the two seismic loading combinations (Eq. 4.10, 4.11).

The interstory drift requirements usually govern the seismic design of the high strength CFT MRFs. The steel beam sizes have to be increased considerably to increase the lateral stiffness of the frame and satisfy the interstory drift limit of Equation 4.12. The CFT beam-column sizes have to be increased correspondingly to maintain the strong column – weak beam design philosophy. Thus, the interstory drift requirements govern the overall seismic design of the high strength CFT MRFs.

4.1.2 Seismic Designs of high strength CFT MRFs

Seismic structures are usually designed to achieve fundamental periods T_1 less than the upper limit T_{max}. However, the use of high strength materials becomes more efficient when the structures are designed with *smaller* member cross-sections, resulting in reduced lateral stiffness and greater fundamental periods. The effects of lateral stiffness

(or flexibility) on the seismic design and behavior of high strength CFT MRFs were investigated analytically. Three seismic designs were developed and investigated analytically for both the 6-story and 12-story distributed MRFs. These are as follows:

- The first design achieved fundamental period $0.9 \leq T_1 \leq 1.0$ and is referred as rigid. The computed period T_1 was used to calculate the earthquake lateral forces Q_E for conducting the strength and interstory drift checks.
- The second design achieved $T_1 > T_{max}$. The computed period was limited to T_{max} when calculating Q_E for conducting the strength check. This limit was released and the computed period T_1 was used to calculate Q_E for the interstory drift check. The resulting design had $T_1/T_{max} > 1.15$ and is referred as highly flexible.
- The third design also achieved $T_1 > T_{max}$, but the computed period T_1 was limited to T_{max} when calculating Q_E for the interstory drift check. The resulting design had $1.0 < T_1/T_{max} \leq 1.15$ and is referred as flexible.

The 6- and 12-story perimeter MRFs were designed to be rigid, i.e., $0.9 \leq T_1 \leq 1.0$. However, only the 6-story perimeter MRF was investigated analytically for reasons that are explained later.

All of these frames were designed according to the procedure presented in Section 4.1.1. The rigid, flexible, and highly flexible designs for the 6-story distributed high strength CFT MRFs are shown in Figures 4.9, 4.10, and 4.11, respectively. The steel beams for the high strength CFT MRFs were made from A992 steel (50 ksi yield stress). The CFT beam-columns were made from high strength materials (80 ksi yield stress steel tubes filled with 16 ksi compressive strength concrete). Comparing the designs in Figures 4.9, 4.10, and 4.11, it is evident that the CFT column sizes increase significantly

as the design changes from highly flexible to flexible to rigid. The rigid design of the 6-story perimeter MRF is shown in Figure 4.12. Comparing Figure 4.12 with Figures 4.9, 4.10, and 4.11 indicates that the CFT column sizes for the perimeter MRF are much larger than the CFT columns for the distributed MRFs.

The rigid, flexible, and highly flexible designs of the 12-story distributed high strength CFT MRFs are shown in Figures 4.13, 4.14, and 4.15, respectively. These designs also use A992 steel beams and high strength CFT beam-columns. As evident from these figures, the CFT size reduce significantly as the design changes from rigid, to flexible, to highly flexible. Figure 4.16 shows the highly flexible design ($T_1/T_{max} > 1.15$) for the 12-story perimeter MRF. As shown in Figure 4.16, the CFT column sizes for the highly flexible design of the 12-story perimeter MRFs are too large (78 in. square CFTs at the base) and not practical. The flexible or rigid designs for the 12-story perimeter MRFs will require even larger CFT columns, making them impractical. Hence, the 12-story perimeter MRFs were not included in further studies of the seismic behavior.

As mentioned earlier, the seismic design of the high strength CFT MRFs is governed by the interstory drift check. For example, Figures 4.17 and 4.18 present the results of strength checks of the high strength CFT beam-columns and steel beams of the 6-story perimeter MRFs, respectively. Figure 4.17 shows the strength check for the 1st and 2nd story high strength CFT beam-columns. The P-M interaction curve of the high strength CFTs is calculated using the modified-AIJ approach, which was developed by Sakino and Nakahara (2000) and further validated by Varma et al. (2004). The basic load combinations considered are: 1) 1.4 D, 2) 0.9 D + 1.0 E, 3) 0.9 D + 1.6 W, 4) 1.2 D + 1.0 E + 0.5 L, 5) 1.2 D + 1.6 L + 0.5 L_r, 6) 1.2 D + 1.6 L_r + 0.5 L, 7) 1.2 D + 1.6 L_r + 0.8 W,

and 8) 1.2 D + 1.6 W + 0.5 L + 0.5 L_r. As shown in Figure 4.17, the factored load effects are much lower than the P-M capacity (resistance) of the CFT beam-columns. Similarly, Figure 4.18 shows the strength check for the W36x135 girders of the 6-story perimeter CFT MRFs. The basic load combinations are the same as those considered in Figure 4.17. As shown in Figure 4.18, the factored load effects are much lower than the moment capacity (M_y=1829 k-ft) of the W36x135 steel beams. Similar strength checks were conducted for the CFT beam-columns and steel beams of all the 6- and 12-story high strength CFT MRFs. In all cases, the factored load effects are much lower than the factored resistance of the individual members. This indicates that the interstory drift requirements under seismic loads (δ_x < 1.5%) govern the design of the high strength CFT MRFs and the sizes of the steel beams and CFT beam-columns.

4.2 Model for CFT Buildings

The model of CFT MRFs used to analysis the seismic behaviors of CFT MRFs are shown in Fig. 4.19. As shown in Fig. 4.19, the horizontal translations of the slaved nodes in each story are slaved to the master node in the same story. A dummy column connected to the CFT MRF is used to account for the second order P-Δ effects. The CFT columns, steel beams and connections are modeled as shown in Fig. 3.97.

CFT Columns, Steel Beams and Connections

The CFT columns, steel beams and connections in the CFT MRF are modeled the same as those in the DST connection subassembly. As shown in Figure 3.97, the columns are divided into several elements to account for the beam depth. The beams are divided into several elements to account for the length of the sterms of DST connections. In

modeling DST connections, slaved nodes are placed at the tips of the bottom and top Tees, respectively, to account for the beam depth.

Dummy Column and P-Δ Effects

The second order *P-Δ* effects of CFT MRFs are modeled by a dummy column connected to the CFT MRF (Fig. 4.19). As shown in Fig. 4.19, the horizontal translations of the slaved nodes in each story of the dummy column are slaved to the master node in the same story of CFT MRFs. The dummy column carries the sum of the gravity loads carried by the columns in the same story of the CFT MRF. Inelastic truss bar elements are used to model the dummy column.

Gravity Loads

The gravity loads applied to the CFT MRF and the dummy column are: (1) the dead loads of floor listed in Table 4.2; (2) 25% of the live loads required by *IBC 2000* listed in Table 4.2, all the live loads can be reduced as permitted by *IBC 2000*. All the gravity loads are unfactored.

Building Mass

For the perimeter moment resisting frames, masses corresponding to half of the effective seismic weights (dead loads plus partition loads listed in Table 4.2 per *IBC 2000*) of the buildings are lumped at the nodes of the perimeter frames. For distributed moment resisting frames, masses corresponding to the effective seismic weights of the buildings tributary to the distributed moment resisting frames are lumped at the nodes of the distributed moment resisting frames.

Viscous Damping

In *DRAIN2DX*, the viscous damping is proportional to the nodal masses and element stiffness as shown in Equation 4.9. [C] is the viscous damping matrix, [M] is the lumped mass matrix, [K] is the element stiffness matrix, α and β and are the mass and stiffness matrix damping factors, respectively. Using the orthogonality condition between two modes of vibration (the 1st and 2nd modes), α and β can be determined using Equation (4.10). In this equation ξ_1 and ξ_2 are the critical damping ratios for the 1st and 2nd modes, and ω_1 and ω_2 are the frequency for the 1st 2nd and modes. Assume both modes have the same damping ratio $\xi=0.05$, which is reasonable based on experimental data. Note that in current version of *DRAIN2DX*, the damper stiffness matrix of the element [K] is set equal to the initial element stiffness.

$$[C]=\alpha[M]+\beta[K] \qquad (4.9)$$

$$\begin{Bmatrix}\alpha\\ \beta\end{Bmatrix}=\frac{2\omega_1\omega_2}{\omega_1^2-\omega_2^2}\begin{bmatrix}\omega_1 & -\omega_2\\ -1/\omega_1 & 1/\omega_2\end{bmatrix}\begin{Bmatrix}\xi_1\\ \xi_2\end{Bmatrix} \qquad (4.10)$$

$$\alpha=\xi\frac{2\omega_1\omega_2}{\omega_1+\omega_2} \qquad \beta=\xi\frac{2}{\omega_1+\omega_2} \qquad (4.11)$$

4.3 Nonlinear Static Pushover Analyses

The seismic behavior of high strength CFT MRFs were investigated by conducting: (a) nonlinear static pushover analyses, and (b) nonlinear time-history analysis of the designed 6-story and 12-story high strength CFT MRFs. These nonlinear inelastic analyses were conducted using DRAIN-2DX (Prakash et al. 1993) and the models summarized in Section 4.2. The nonlinear static pushover analyses were conducted using

two procedures for reasons explained later. These include: (1) the nonlinear static pushover procedures of FEMA 356 (ASCE 2000), and (2) the adaptive spectra-based nonlinear static pushover procedures of Gupta et al. (2000). The nonlinear time-history analyses were conducted for the scaled SAC earthquake ground motions for Los Angeles developed by Somerville et al. (1997). The results of the nonlinear static pushover analyses are presented in this Section, and the results of the time-history analyses are presented in Chapter 5.0.

4.3.1 FEMA 356 NSP Procedures

The lateral force patterns used to conduct the nonlinear static pushover analysis according to FEMA 356 procedures are based on the effective modal mass for the 1st fundamental mode of the structure. If the effective modal mass for the 1st mode is greater than 75% of the total mass then *four* lateral load patterns can be used to conduct the static pushover analyses. These include: (1) a vertical distribution proportional to the 1st mode shape in the lateral direction, (2) a vertical distribution proportional to the equivalent lateral forces calculated for design Q_E, (3) a vertical distribution proportional to the story shear distribution calculated by modal analysis, and (4) a uniform distribution consisting of lateral forces proportional to the total mass at each level. These lateral load patterns are shown graphically in Figures 4.20 (a-d), where they are identified as 1st mode shape, equivalent lateral force, modal analysis, and uniform distribution, respectively. If the effective modal mass for the first mode is less than 75% of the total mass then only two lateral load patterns can be used to conduct the static pushover analyses. These are: (1) the vertical distribution proportional to the story shear distribution calculated by modal

analysis, and (2) the uniform distribution consisting of lateral forces proportional to the total mass at each level shown graphically in Figures 4.20 (c) and (d), respectively.

The effective modal mass for the 1st fundamental mode of the 6-story and 12-story distributed CFT MRFs are greater than 75% of the total mass. Therefore, all four lateral load patterns were used to investigate their static pushover behavior. Figures 4.21 and 4.22 present the results of nonlinear static pushover analyses using all four lateral load patterns for the flexible designs ($1.0 < T_1/T_{maz} < 1.15$) of the 6-story (see Fig. 4.10) and 12-story (see Fig. 4.14) distributed CFT MRFs, respectively. These Figures also include the normalized design seismic base shear (V_s/W) for comparison. Figures 4.21 and 4.22 indicate that the lateral load pattern proportional to the equivalent lateral forces for design Q_E results in the lowest normalized base shear – roof drift angle response for the distributed CFT MRFs. Hence, further studies of distributed CFT MRFs focused on static pushover analyses using lateral load patterns proportional to the equivalent lateral forces for design.

The effective modal mass for the 1st fundamental mode of the 6-story perimeter CFT MRF is equal to 61% of the total mass (which is less than 75% of the total mass). Therefore, two lateral load patterns (modal analysis and uniform distribution in Fig. 4.20) were used to investigate their static pushover behavior. Figure 4.23 presents the results of nonlinear static pushover analyses for the rigid design ($0.9<T_1/T_{maz}< 1.0$) of the 6-story (see Fig. 4.9) perimeter CFT MRF. This Figure indicates that the lateral load pattern proportional to the story shear distribution calculated by modal analysis results in the lowest normalized base shear – roof drift angle response for the perimeter CFT MRF. Hence, further studies of the 6-story perimeter CFT MRF focused on static pushover

analyses using this lateral load pattern.

The results from the nonlinear static pushover analyses of the 6-story CFT MRFs are summarized and compared in Figure 4.24. This figure includes:

- The results of nonlinear static pushover analyses of the rigid, flexible, and highly flexible designs of the 6-story distributed CFT MRFs. These analyses are conducted using the lateral load pattern proportional to the equivalent lateral forces for design.
- The results of the nonlinear static pushover analyses of the rigid designs of the 6-story perimeter CFT MRF. This analysis was conducted using the lateral load pattern proportional to the story-shear distribution from modal analysis.
- The normalized seismic design shear (V_s/W) for the 6-story CFT MRFs.

It is evident from Figure 4.24 that all the designs result in significant over strength as compared to the design base shear (V_s/W). The rigid design for the 6-story distributed CFT MRF has the highest normalized base shear-roof drift angle response. As the design changes from rigid to flexible to highly flexible: (a) the peak normalized base shear decreases, and (b) the post-peak normalized base shear-roof drift angle response become increasingly negative. The rigid design for the 6-story perimeter MRF has approximately the same normalized base shear capacity as the highly flexible design for the distributed MRF, but it has more ductile post-peak behavior.

The results from the nonlinear static pushover analyses of the 12-story distributed CFT MRFs are summarized and compared in Figure 4.25. This figure includes the results of nonlinear static pushover analyses of the rigid, flexible, and highly flexible designs of the 12-story distributed CFT MRFs. These analyses are conducted using the lateral load pattern proportional to the equivalent lateral forces for design. The figure also includes

the normalized seismic design shear (V_s/W) for the 6-story CFT MRFs. As mentioned previously, the 12-story perimeter CFT MRF was not analyzed due to the impractical CFT column sizes it required to meet the interstory drift requirements. It is evident from Figure 4.25 that all designs result in significant over strength as compared to the design base shear (V_s/W). The rigid design has the highest normalized base shear-roof drift angle response. As the design changes from rigid to flexible to highly flexible, the post-peak normalized base shear-roof drift angle response becomes increasingly negative (non-ductile). The peak normalized base shears (V_s/W) are comparable for the rigid, flexible, and highly flexible design.

4.3.1.1 Effects of local degradation on overall static pushover behavior

A major issue with high strength CFT MRFs is the local degradation of members (steel beams, CFT beam-columns, and beam-to-column connections) and its potential influence on the overall static pushover behavior of the frame. The CFT beam-columns undergo post-peak degradation after achieving peak strength due to the: (a) degradation of the high strength concrete in compression, and (b) local buckling of the high strength steel tube walls in compression. The steel beams undergo post-peak degradation after reaching M_p due to the local buckling of the flanges and webs.

The effects of these local degradations on the overall frame behavior was evaluated by conducting the following static pushover analyses and comparing the results:

(1) Analysis with no local degradation in the steel beam or CFT beam-column. The steel beam and CFT beam-columns fiber elements were specified with non-degrading concrete and steel fiber σ–ε relationships.

(2) Analysis with post-peak degradation of the concrete of the CFT beam-column only. The steel beam and CFT beam-column fiber elements were specified with non-degrading steel fiber σ–ε, and post-peak degrading concrete fiber σ–ε relationships.

(3) Analysis with post-peak degradation of the concrete in the CFT beam-column and local buckling of the steel beam flanges and webs only. The steel beam fiber element was specified with degrading steel fiber σ–ε, and the CFT beam-column fiber element was specified with post-peak degrading concrete fiber σ–ε relationships.

(4) Analysis with post-peak degradation of the concrete and local buckling of the CFT steel tube walls only. The steel beam fiber element is specified with non-degrading steel fiber σ–ε, and the CFT fiber element is specified with post-peak degrading concrete and steel fiber σ–ε relationships.

(5) Analysis with post-peak degradation of the concrete and local buckling of the CFT steel tube wall, and local buckling of the steel beams flanges and webs. The steel beam fiber element is specified with degrading steel fiber σ–ε, and the CFT fiber element is specified with degrading concrete and steel fibers σ–ε relationships.

These analyses were conducted for the rigid, flexible, and highly flexible designs of the 6-story and 12-story high strength CFT MRFs. The results were compared to evaluate the effects and relative influence of the local degradations.

6-Story CFT MRFs

The results of the static pushover analyses (1-5 above) for the rigid, flexible, and highly flexible designs of the 6-story distributed CFT MRFs are presented in Figures 4.26, 4.27, and 4.28, respectively. The analyses were conducted according to FEMA 356 procedures using lateral load distributions proportional to the equivalent lateral force Q_E

for design. The results from these analyses are as follows:

- Figure 4.26 indicates that local degradation does not have a significant influence on the overall static pushover behavior of the rigid design for the 6-story distributed CFT MRF. Local buckling of the steel beams combined with local buckling of the CFT beam-columns has the most influence on the post-peak normalized base shear - roof drift angle, and results in slightly negative $V_s/W - \Delta/h$ response.
- Figure 4.27 shows that local degradation has moderate influence on the the overall static pushover behavior of the flexible design for the 6-story distributed CFT MRF. Local buckling of the steel beams combined with CFT beam-columns has the most influence on the post-peak normalized $V_s/W - \Delta/h$ response.
- Figure 4.28 shows that local degradation has a significant influence on the overall static pushover behavior of the highly flexible design for the 6-story distributed CFT MRF. Local buckling of the CFT steel tubes has the most significant influence on the peak normalized base shear (V_s/W) capacity and the post-peak $V_s/W - \Delta/h$ response.

The results of the static pushover analyses for the rigid design of the 6-story perimeter CFT MRF are shown in Figure 4.29. This Figure indicates that local degradation does not have a significant influence on the overall static pushover behavior of the 6-story perimeter CFT MRF. Local buckling of the steel beams combined with local buckling of the CFT beam-columns reduces the normalized base shear capacity (V_s/W) and the post-peak $V_s/W - \Delta/h$ response very slightly.

12-Story CFT MRFs

The results of the static pushover analyses for the rigid, flexible, and highly flexible designs of the 12-story distributed CFT MRFs are presented in Figures 4.30, 4.31, and

4.32, respectively. The analyses were also conducted using lateral load distributions proportional to the equivalent lateral force Q_E for design. The results are as follows:

- Figure 4.30 indicates that local degradation has a moderate influence on the overall static pushover behavior of the rigid design for the 12-story distributed CFT MRF. Local buckling of the steel beams has the most significant influence on the overall frame behavior. It reduces the peak normalized base shear (V_s/W) slightly and results in a negative post-peak $V_s/W - \Delta/h$ response.
- Figure 4.31 indicates that local degradation has a similar (moderate) influence on the overall static pushover behavior of the flexible design for the 12-story distributed CFT MRF. Local buckling of the steel beams again has the most significant influence on the overall frame behavior. It reduces the peak normalized base shear (V_s/W) slightly and results in a negative post-peak $V_s/W - \Delta/h$ response.
- Figure 4.32 indicates that local degradation has a significant influence on the overall static pushover behavior of the highly flexible design for the 12-story distributed CFT MRF. Local buckling of the steel beams has the most significant influence and results in a significantly negative post-peak $V_s/W - \Delta/h$ response.

Figures 4.30, 4.31, and 4.32 indicate that for the 12-story distributed CFT MRFs, local buckling of the steel beams has the most significant influence on the overall static pushover behavior as compared to the other sources of local degradation (concrete degradation or CFT local buckling). The highly flexible design has the most negative post-peak $V_s/W - \Delta/h$ response.

4.3.1.2 Earthquake Resistant Design Coefficients and Factors

The results from the static pushover analyses were used to calculate the earthquake resistant design coefficients and factors for the 6- and 12-story high strength CFT MRFs. These include: (a) the over strength factor Ω_0, (b) the displacement amplification factor C_d, and (c) the displacement ductility ratio μ. The seismic designs of the 6- and 12-story high strength CFT MRFs are evaluated by comparing the calculated coefficients and factors with the values recommended by IBC (2000) for special composite moment resisting frames.

The base shear-roof displacement (V_s -Δ) responses from the static pushover analyses are idealized as shown in Figure 4.33 and 4.34. Figures 4.33 and 4.34 show the bilinear idealizations of the V_s -Δ responses with positive and negative post-peak stiffness, respectively. These idealizations are developed using an iterative graphical procedure that approximately balances the area above and below the curve. In Figures 4.33 and 4.34:

- V_s is the design base shear, and Δ_s is the roof displacement corresponding to V_s,
- V_y is the base shear corresponding to the idealized yield strength of the structure,
- K_i is the initial stiffness of the building,
- K_e is the secant stiffness corresponding to 0.6 V_y,
- Δ_y is the yield displacement calculated as V_y/K_e,
- Δ_d is the roof displacement when the allowable interstory drift 1.5% is achieved,
- V_d is the structure base shear corresponding to Δ_d,
- Δ_t is the target displacement for the analysis calculated according to FEMA 356,
- V_t is the base shear corresponding to Δ_t, and
- αK_e is the idealized post-yield stiffness calculated as $(V_t\text{-}V_y)/(\Delta_t\text{-}\Delta_y)$

The idealized V_s-Δ responses are used to calculate the coefficients and factors as follows:

- The deflection amplification factor C_d is calculated as the ratio of the roof displacement (Δ_d) at the onset of allowable inter-story drift (1.5%) to the roof displacement (Δ_s) at the design base shear.
- The system over-strength factor Ω_0 is calculated as the ratio of the base shear (V_d) at the onset of allowable inter-story drift to the design base shear (V_s).
- The displacement ductility ratio μ is calculated as the ratio of target displacement (Δ_t) to the yield displacement (Δ_y).

Table 4.7 provides the calculated values of the displacement amplification factors (C_d), system over-strength factors (Ω_0), and displacement ductility ratios (μ) for the rigid, flexible, and highly flexible designs of the 6-story and 12-story distributed CFT MRFs. The IBC (2000) specifies minimum requirements of $\Omega_0 \geq 3$ and $C_d \geq 5.5$ for special composite moment resisting frames. The values in Table 4.7 indicate that:

1) The rigid and flexible designs for the 6-story CFT MRF satisfy the IBC (2000) requirements and have significant displacement ductility ($\mu > 4$).
2) The highly flexible design for the 6-story distributed CFT MRF does not satisfy the C_d requirement and has poor ductility (μ=2.44).
3) The rigid, flexible, and highly flexible designs for the 12-story distributed CFT MRF satisfy the IBC requirements.
4) The rigid and flexible designs for the 12-story CFT MRF have excellent ductility ($\mu >$ 5), while the highly flexible design has much lower ductility (μ=2.78).

5) The rigid and flexible designs for the 6-story CFT MRF have significant over-strength factor (Ω_0=6.2 for flexible, and Ω_0=7.41 for rigid design), which indicates some over-design.

6) The over-strength factors for the rigid, flexible, and highly flexible designs for the 12-story CFT MRF vary from 5.88 – 5.38, and thus are comparable.

4.3.2 Adaptive Pushover Procedures

The FEMA 356 static pushover analysis procedures involve the use of invariant lateral load patterns, i.e., the lateral load patterns used to conduct the pushover analyses do not change as the structure undergoes inelasticity and yielding. These invariant force distributions cannot adequately account for: (a) the contributions of the higher modes to dynamic response, and (b) the redistribution of inertia forces due to structural yielding (Krawinkler et al. 1998). Hence the adaptive static pushover analyses procedures recommended by Gupta et al. (2000) were used to investigate the behavior of the designed high strength CFT MRFs with relevant higher mode effects.

The adaptive static pushover analyses were conducted for the designs of the 6-story and 12-story high strength CFT MRFs with effective modal mass for the 1st mode < 75% of the total mass. These included:

(a) The rigid design for the 6-story perimeter MRF with effective modal masses for the 1st – 4th modes equal to 61%, 19.6%, 9.5%, and 3.6% of the total mass, respectively.

(b) The flexible design of the 6-story distributed MRF with effective modal masses for the 1st – 4th modes equal to 81.5%, 10.9%, 4.5%, and 1.8%, respectively.

(c) The flexible design of the 12-story distributed MRF with effective modal masses for the $1^{st} - 4^{th}$ modes equal to 75.3%, 12.7%, 5.1%, and 2.8%, respectively.

The adaptive static pushover procedure used for this study is similar to the modal combination procedure of FEMA 356, except that the modal responses are based on the current stiffness state of the structure (Gupta et al. 2000). It consists of following steps:

Step 1) Compute the damped elastic response spectrum for the site-specific ground motion to be used for evaluation. This is used to obtain modal spectral accelerations at various steps.

Step 2) Perform an eigenvalue analysis of the structural model at the current stiffness state of the structure (for the first step this will be the initial stiffness). Determine the modal participation factors using the story masses and the eigenvalues.

Step 3) Compute the story shear distribution by combining modal responses of the structure at the current stiffness state, including sufficient modes to capture at least 90% of the total building mass.

Step 4) Perform a static pushover analysis of the structure using the story forces computed in the previous step. At the end of every step, compare the member forces with their yield values. If any member has yielded, re-compute the member and global stiffness matrices and return to Step 2.

Step 5) Repeat the process until the global drift exceeds the specified or target limit.

- The adaptive pushover analysis results for the flexible ($1<T_1/T_{max}<1.15$) six-story distributed CFT MRFs are shown in Fig. 4.35. The 3-mode and 4-mode adaptive pushover analysis results are very close to the "*modal analysis*" result of FEMA 356

procedures due to the fact that the effective modal mass for 1st mode is larger than 80% of the total mass.

- The adaptive pushover analysis results for the flexible twelve-story distributed CFT MRFs are shown in Fig. 4.36. The 3-mode and 4-mode adaptive pushover analysis results obviously predict small displacement ductility than the FEMA 356 procedures due to the fact that the effective modal mass for 1st mode is just slightly larger than 75% of the total mass.
- Adaptive pushover analyses are performed for the flexible ($1<T_1/T_{max}<1.15$) six-story and twelve-story distributed CFT MRFs, as well as the six-story perimeter CFT MRFs. The base shear-roof displacement curves are idealized in accordance with FEMA 356 to calculate the design coefficients and factors for CFT MRFs. The nonlinear force-displacement relationship is replaced with an idealized bi-linear curve (Figs. 4.37 and 4.38).
- Table 4.7 shows the deflection amplification factors (C_d), system over-strength factors (Ω_0) and displacement ductility ratios (μ) obtained for the six-story and twelve-story CFT MRFs from adaptive pushover analysis. All the six-story and twelve-story CFT MRFs satisfy $\Omega_0 \geq 3$, $C_d \geq 5.5$ set by *IBC 2000* for *special composite moment frames*. The flexible ($1<T_1/T_{max}<1.15$) six-story and twelve-story distributed CFT MRFs and the six-story perimeter CFT MRFs ($0.9<T_1/T_{max}<1$) have good ductility ($\mu>4$). Therefore, the flexible CFT MRFs could be used despite of their negative post-yield stiffness.

For the flexible ($1<T_1/T_{max}<1.15$) twelve-story distributed CFT MRFs, the adaptive analysis predicts smaller displacement ductility ratios (μ), which is about 90% of that

predicted by the static pushover analysis following FEMA 356 procedures. While for the flexible ($1<T_1/T_{max}<1.15$) six-story distributed CFT MRFs and the six-story perimeter CFT MRFs ($0.9<T_1/T_{max}<1$), the adaptive analysis predicts smaller displacement ductility ratios (μ), which is about 95% of that predicted by the static pushover analysis following FEMA 356 procedures. In addition, for the flexible six-story distributed CFT MRFs, the six-story perimeter CFT MRFs and the flexible twelve-story distributed CFT MRFs, the adaptive pushover analysis predicts larger deflection amplification factors (C_d), which is about 105% of that predicted by the static pushover analysis following FEMA 356 procedures. Therefore, high mode effects on the seismic behavior of CFT MRFs should not be neglected, and adaptive pushover analysis should be performed in addition to static pushover analysis following FEMA 356 procedures.

4.3.3 Summary

The seismic behavior of the six-story and twelve-story CFT MRFs was analytically investigated by performing static pushover analysis following FEMA 356 procedures and adaptive pushover analysis. The developed FEM-based fiber models for the CFT beam-columns and the steel beams, and the spring model for DST connections were used to model CFT MRFs. The pushover analysis results indicate that, when the roof drift angle (roof displacement/building height) is less than a upper bond limit, incorporating the effects of inelastic local buckling of the steel tubes and steel beams and the effects of confinement of concrete infills of CFTs has a small influence on the overall seismic response of the six-story and twelve-story CFT MRFs. This upper bond limit on the roof

drift angle is 1.5% for the rigid ($0.9<T_1/T_{max}<1$) and the flexible ($1<T_1/T_{max}<1.15$) CFT MRFs, 1.0% for the highly flexible ($T_1/T_{max}>1.15$) CFT MRFs, respectively.

For the highly flexible CFT MRFs, when the roof drift angle is larger than 1.0%, local buckling of CFT columns control the post-yield behavior of the MRFs, local buckling of beam has a small influence. For the flexible and the rigid CFT MRFs, when the roof drift angle is larger than 1.5%, local buckling of steel beams controls the post-yield behavior, local buckling of the CFTs has a smaller influence than the steel beams.

For the flexible twelve-story distributed CFT MRFs, the adaptive analysis predicts smaller displacement ductility ratios (μ), which is about 90% of that predicted by the static pushover analysis following FEMA 356 procedures. In addition, for the flexible six-story distributed CFT MRFs, the six-story perimeter CFT MRFs and the flexible twelve-story distributed CFT MRFs, the adaptive pushover analysis predicts larger deflection amplification factors (C_d), which is about 105% of that predicted by the static pushover analysis following FEMA 356 procedures. Therefore, high mode effects on the seismic behavior of CFT MRFs should not be neglected, and adaptive pushover analysis should be performed in addition to static pushover analysis following FEMA 356 procedures.

Table 4.1 Dead Loads of Floor

	Description	Equivalent uniform load (psf)
slab	3 ½" on 2", lightweight concrete	43
metal deck	18 gage metal deck	3
ceiling		5
finish	carpet	2
Mechanical/electrical		10
fireproofing		2
curtain wall	25 psf on vertical projection	10
steel structure	Floor beams, girders, etc.	15
Total		90

Table 4.2 Gravity Loads of Roof and Floor

	Description	Equivalent uniform load (psf)
Roof	Dead load	90
	Live load (promenade, IBC 2000, Sec. 1607.11.2.2)	60
Floor	Dead load	90
	Live load (computer use, IBC 2000, Table 1607.1)	100
	Partition load (only use for effective seismic weight, when Live load >80psf, IBC 2000, Sec. 1607.5 and Sec. 1617.4.1)	20

Table 4.3 Basic wind speed, exposure category, wind importance factor and enclosure classification

	Description
Base wind speed	V=85mph (IBC 2000, Fig 1609)
Exposure category	Exposure B (IBC 2000, Sec. 1609.4, urban area)
Wind load importance factor	I_w=1.15 (IBC 2000, Table 1604.5, Category II, Building where more than 300 people congregate in one area)
Enclosure classification	Enclosed (ASCE 7-98, Sec. 6.5.9 & Sec. 6.2)

Table 4.4 Wind loads at each floor of the six-story perimeter frames in long direction

Floor	Wind loads acted on windward walls (kips)	Wind loads acted on leeward walls (kips)
6	*13.610*	*3.092*
5	*26.418*	*5.728*
4	*25.214*	*5.044*
3	*23.785*	*4.231*
2	*21.990*	*3.210*
1	*22.327*	*2.240*

Table 4.5 Design coefficients and factors for seismic-resisting system (CFT MRFs)

	Description
Soil Profile	*Stiff soil profile*
Site Class	*D* (IBC 2000, Table 1615.1.1)
Response modification coefficient	*R=8* (IBC 2000, Table 1617.6, 3.H. special composite moment frames)
Deflection amplification factor	C_d*=5.5* (IBC 2000, Table 1617.6, 3.H. special composite moment frames)
Seismic importance Factor	I_E*=1.25* (IBC 2000, Table 1604.5, Category II, Building where more than 300 people congregate in one area)

Table 4.6 Equivalent lateral seismic force for six-story perimeter frames in long direction

Floor Number	Story Shear (kips)	
	For Strength Check	For Story Drift Determination
6	*278.535*	*278.535*
5	*288.284*	*288.284*
4	*226.581*	*226.581*
3	*166.303*	*166.303*
2	*108.478*	*108.478*
1	*55.377*	*55.377*

Table 4.7 Static pushover analysis results of the six-story and twelve-story CFT MRFs: design coefficients and factors

Pushover Procedures			Equivalent Lateral Force	Modal Analysis	Adaptive (3-mode)	Adaptive (4-mode)
Six-Story Distributed MRFs	Highly flexible	C_d	*5.31*	/	/	/
		Ω_0	*4.74*	/	/	/
		μ	*2.44*	/	/	/
	Flexible	C_d	*7.05*	/	*7.59*	*7.59*
		Ω_0	*6.20*	/	*6.59*	*6.63*
		μ	*4.33*	/	*4.24*	*4.30*
	Rigid	C_d	*8.74*	/	/	/
		Ω_0	*7.41*	/	/	/
		μ	*4.27*	/	/	/
Six-Story Perimeter MRFs	Rigid	C_d	/	*7.07*	*8.13*	*8.21*
		Ω_0	/	*4.44*	*5.11*	*5.11*
		μ	/	*6.22*	*6.13*	*6.14*
Twelve-Story Distributed MRFs	Highly flexible	C_d	*6.21*	/	/	/
		Ω_0	*5.38*	/	/	/
		μ	*2.78*	/	/	/
	Flexible	C_d	*7.20*	/	*7.52*	*7.75*
		Ω_0	*5.69*	/	*5.68*	*5.75*
		μ	*5.18*	/	*4.62*	*4.68*
	Rigid	C_d	*7.42*	/	/	/
		Ω_0	*5.88*	/	/	/
		μ	*5.16*	/	/	/

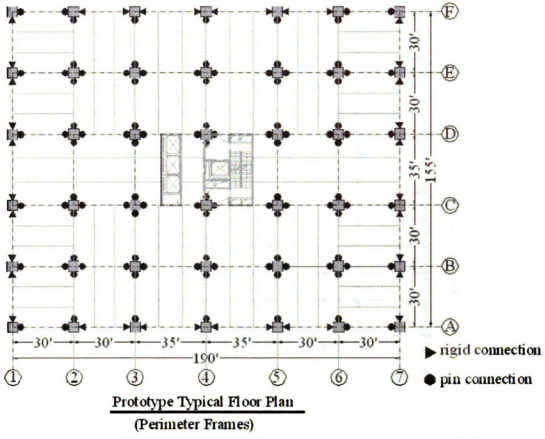


Figure 4.1 Typical floor plan of prototype buildings (perimeter frames)

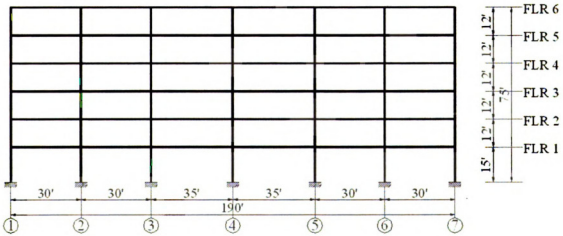


Figure 4.2 Structural elevation of six-story prototype building

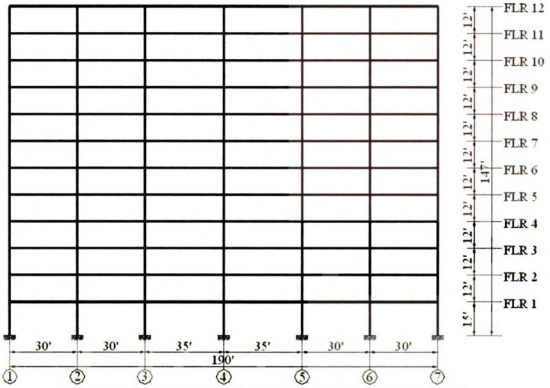


Figure 4.3 Structural elevation of twelve-story prototype building

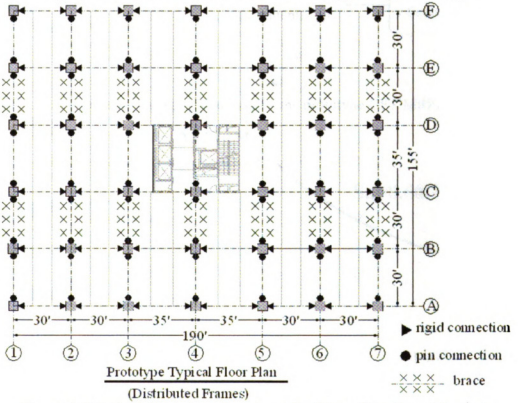


Figure 4.4 Typical floor plan of prototype buildings (distributed frames)

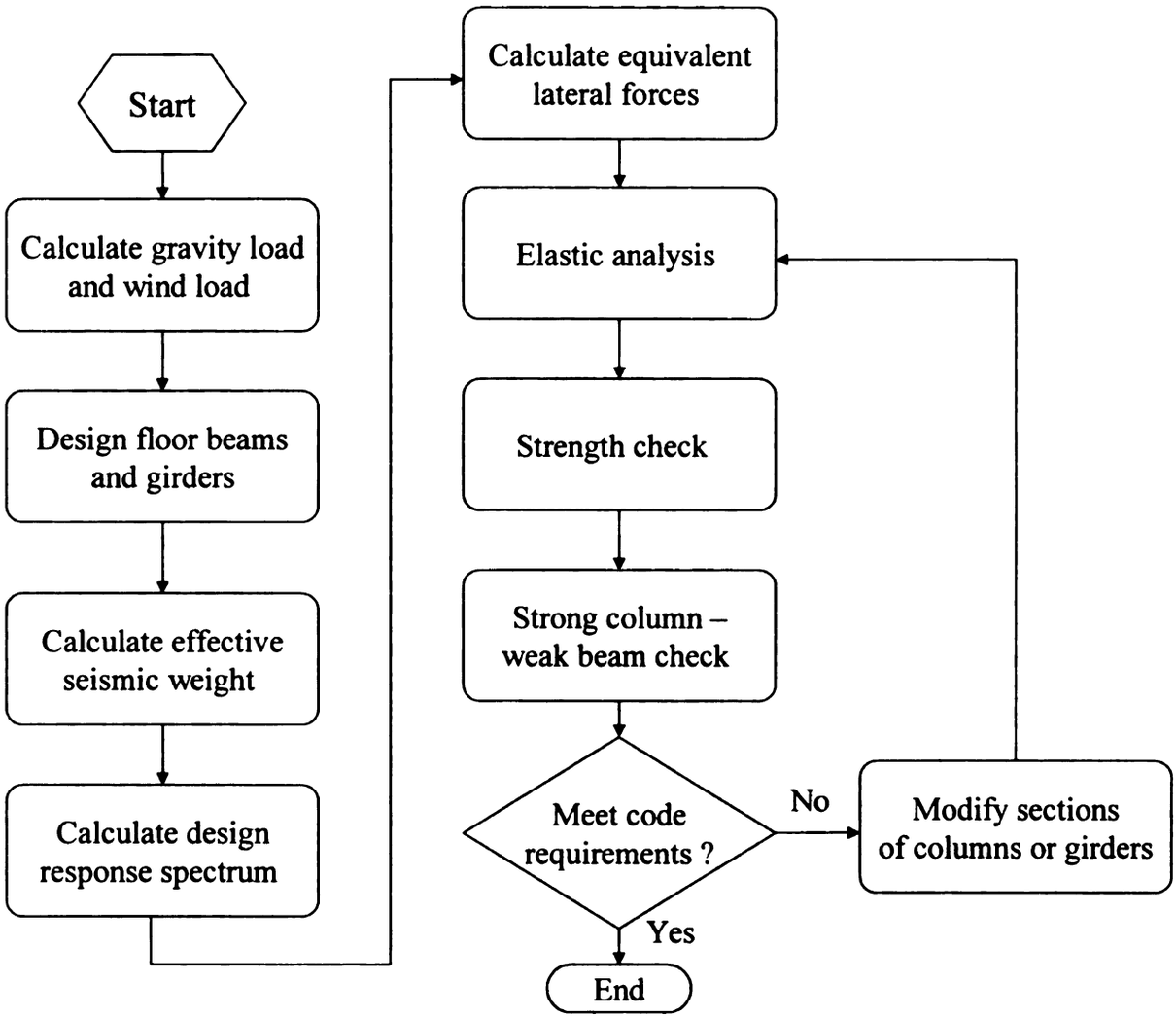


Figure 4.5 Design procedures of the prototype CFT MRFs

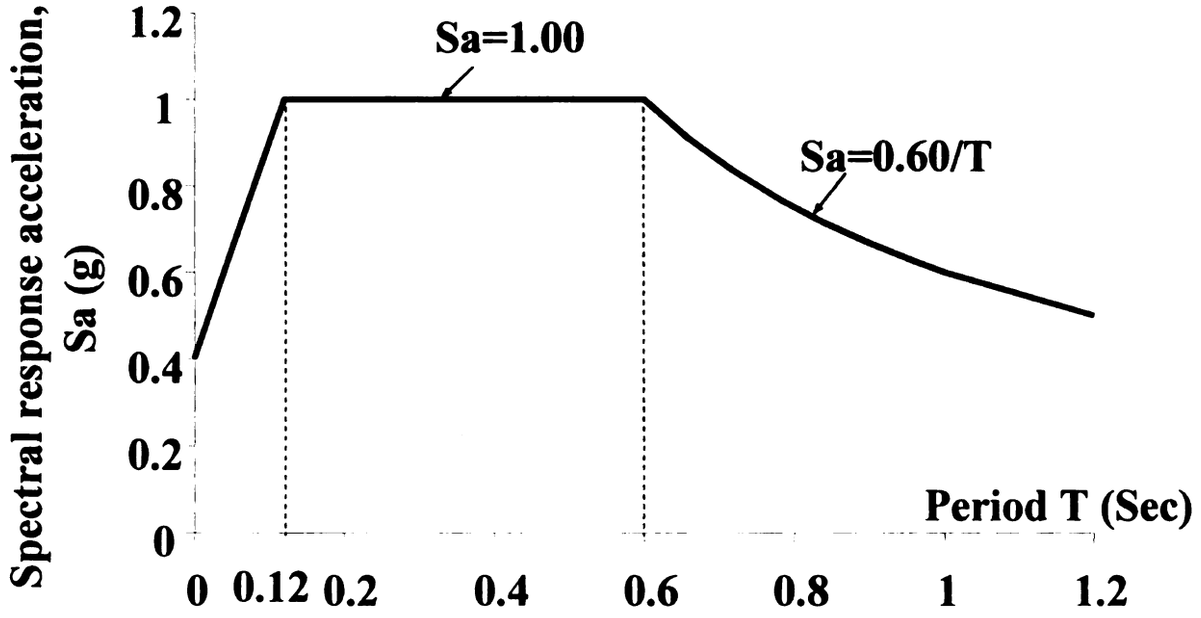


Figure 4.6 Design response spectrum for the prototype CFT MRFs

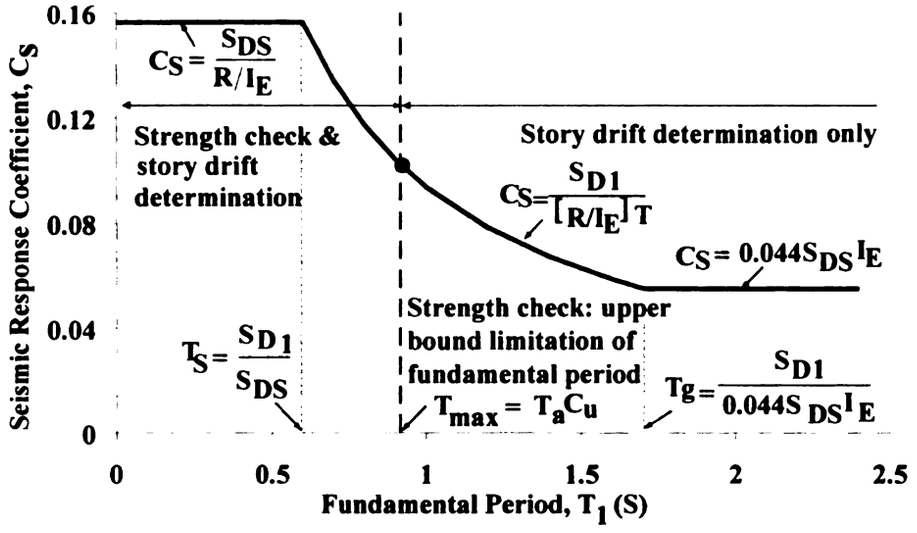


Figure 4.7 Seismic Response Coefficient-Fundamental Period Relationship for six-story CFT MRFs

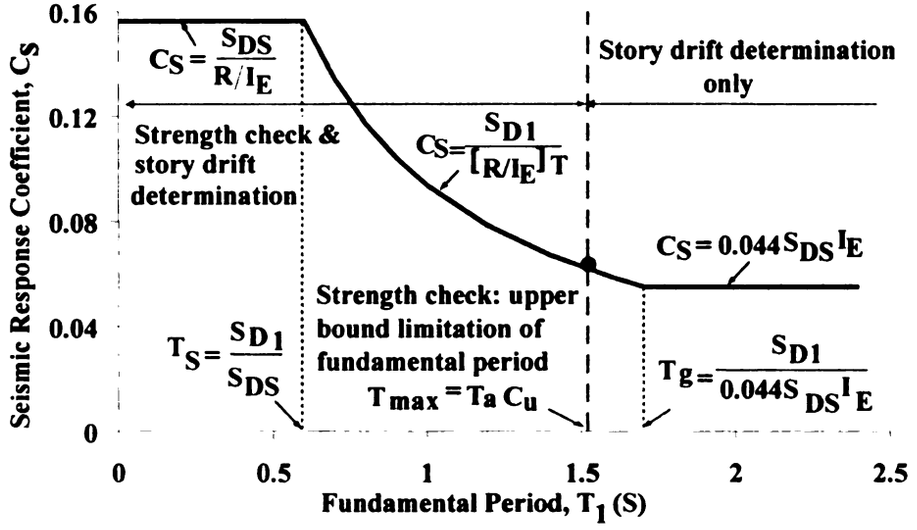


Figure 4.8 Seismic Response Coefficient-Fundamental Period Relationship for twelve-story CFT MRFs

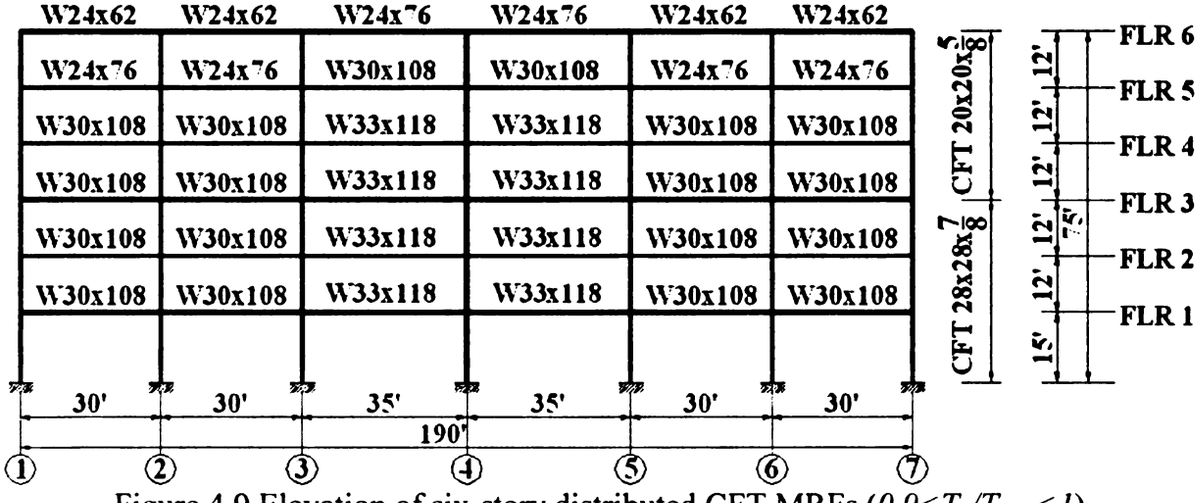


Figure 4.9 Elevation of six-story distributed CFT MRFs ($0.9<T_1/T_{max}<1$)

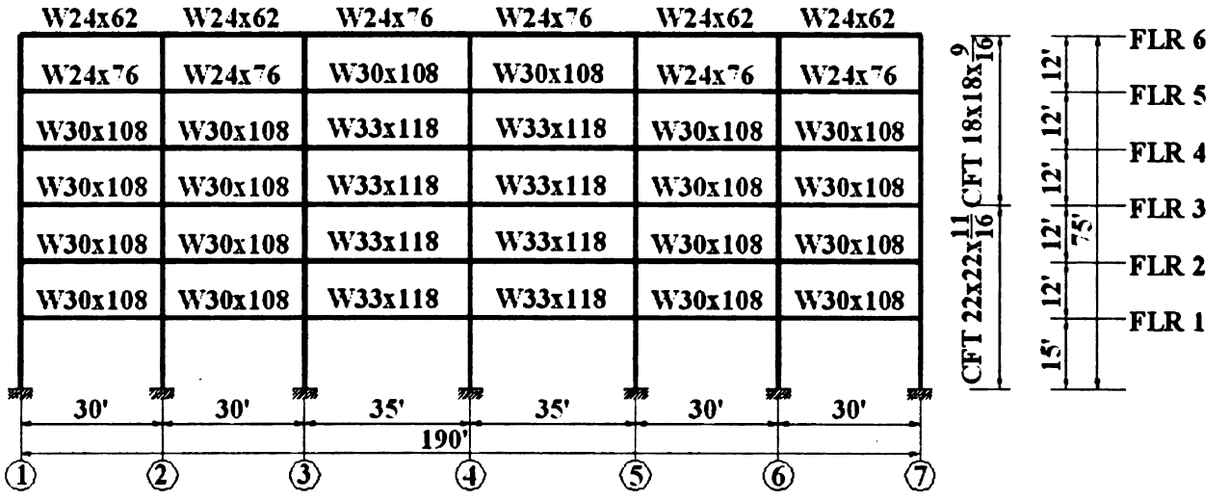


Figure 4.10 Elevation of six-story distributed CFT MRFs ($1<T_1/T_{max}<1.15$)

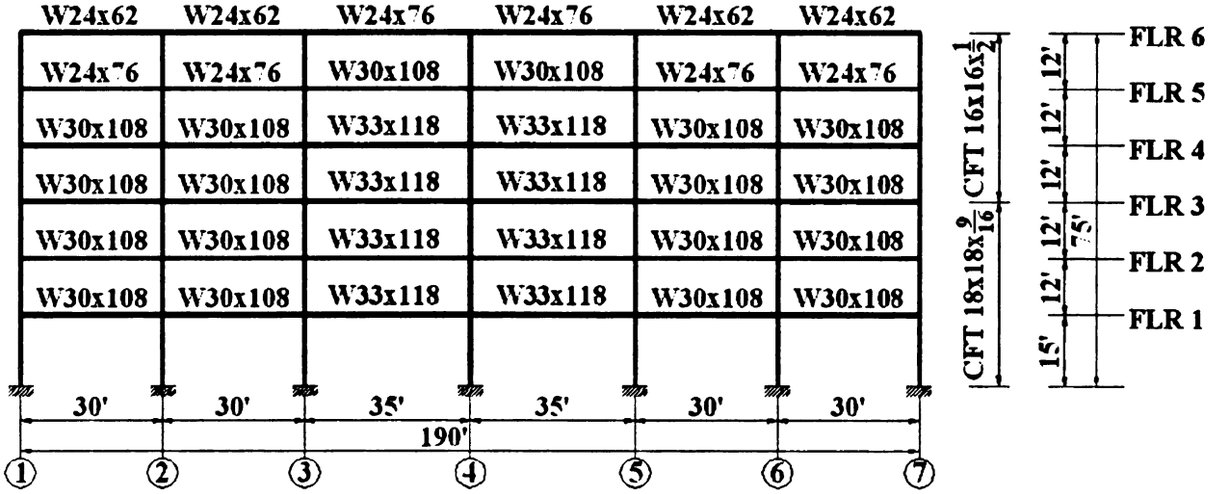


Figure 4.11 Elevation of six-story distributed CFT MRFs ($T_1/T_{max}>1.15$)

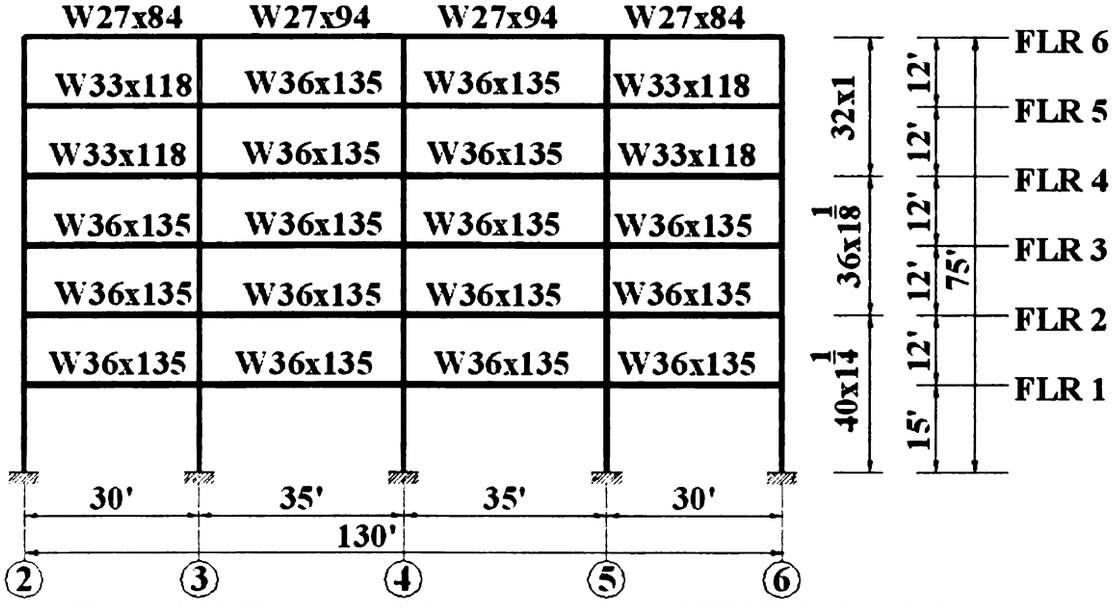


Figure 4.12 Elevation of six-story perimeter CFT MRF ($0.9<T_1/T_{max}<1$)

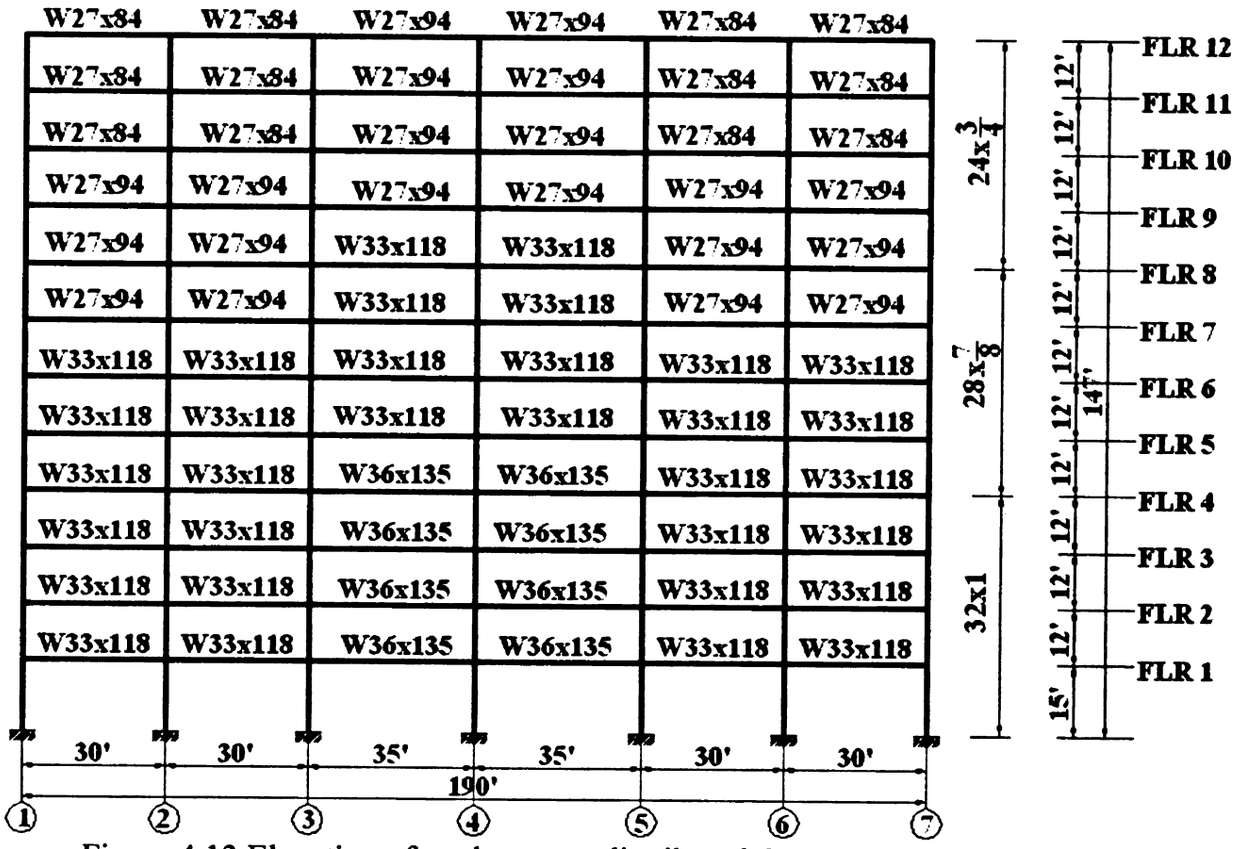


Figure 4.13 Elevation of twelve-story distributed CFT MRFs ($0.9<T_1/T_{max}<1$)

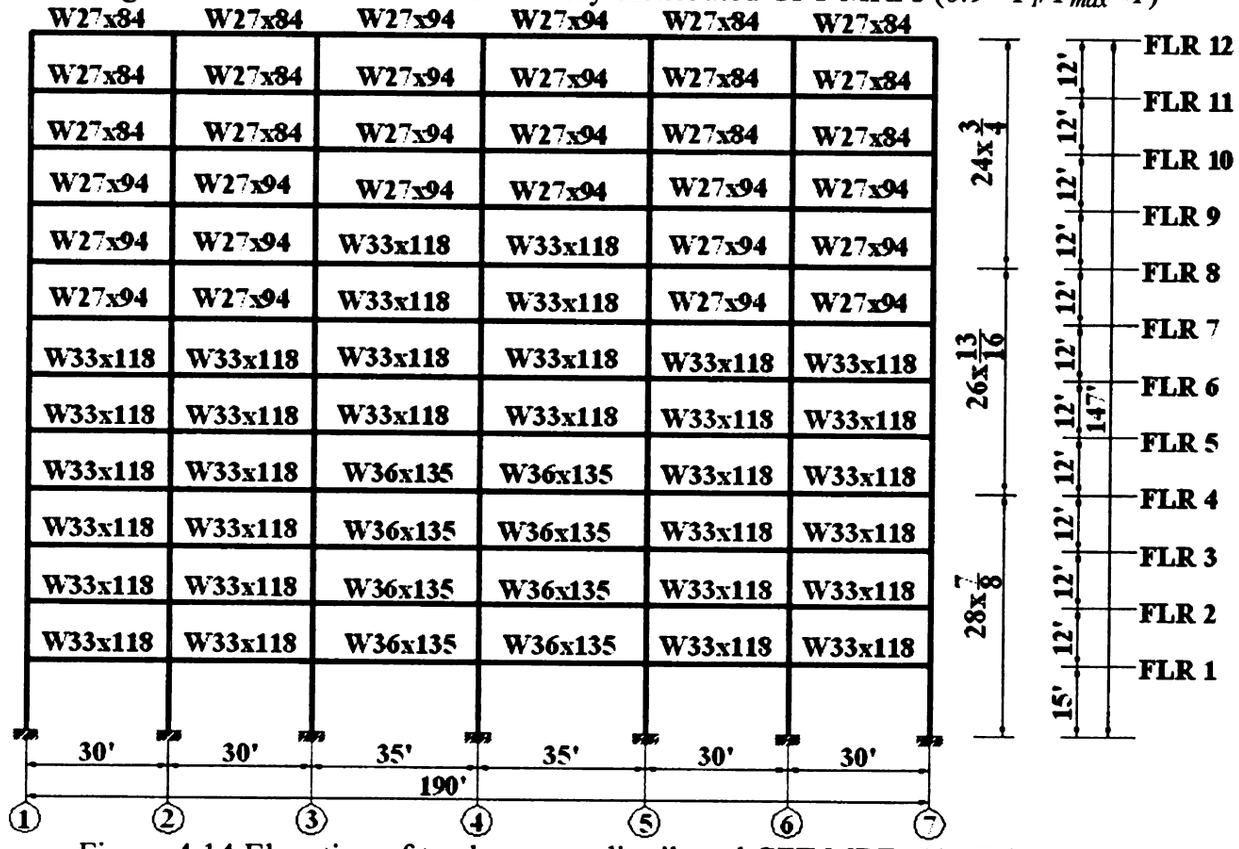


Figure 4.14 Elevation of twelve-story distributed CFT MRFs ($1<T_1/T_{max}<1.15$)

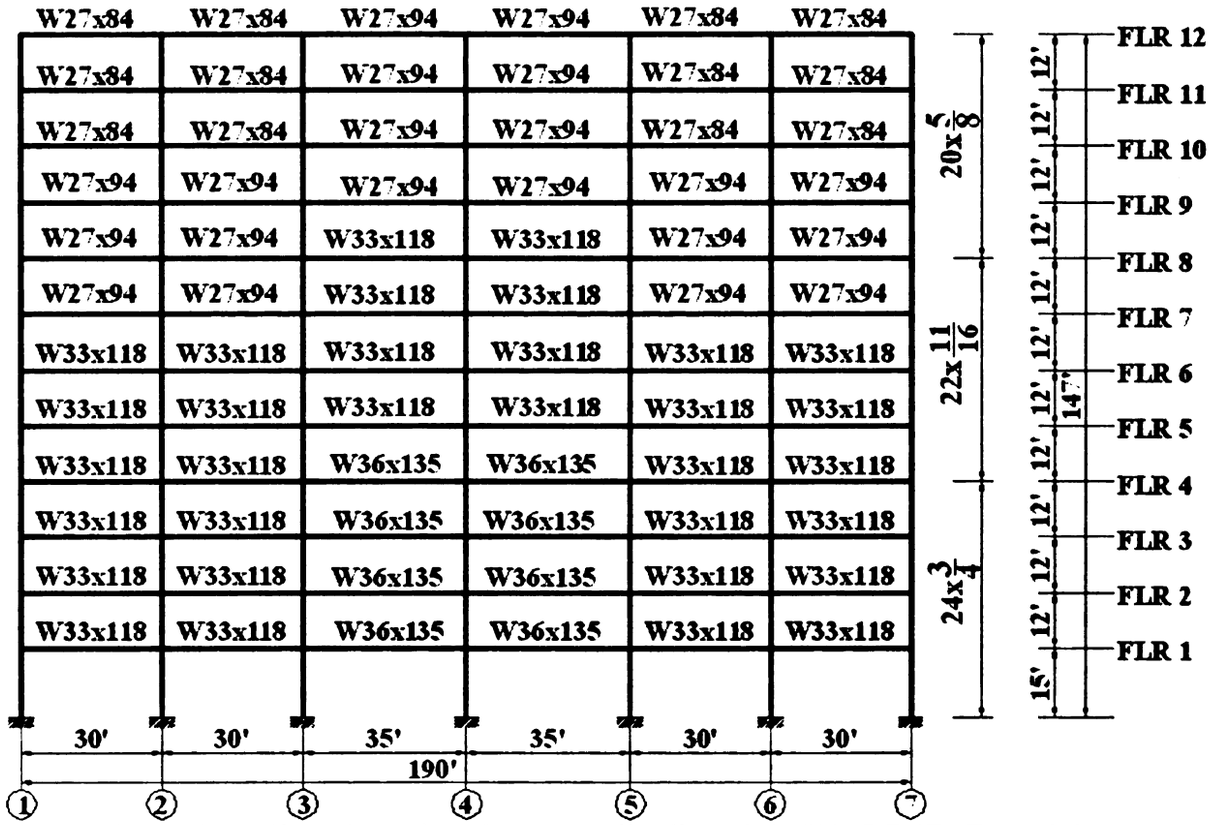


Figure 4.15 Elevation of twelve-story distributed CFT MRF ($T_I/T_{max}>1.15$)

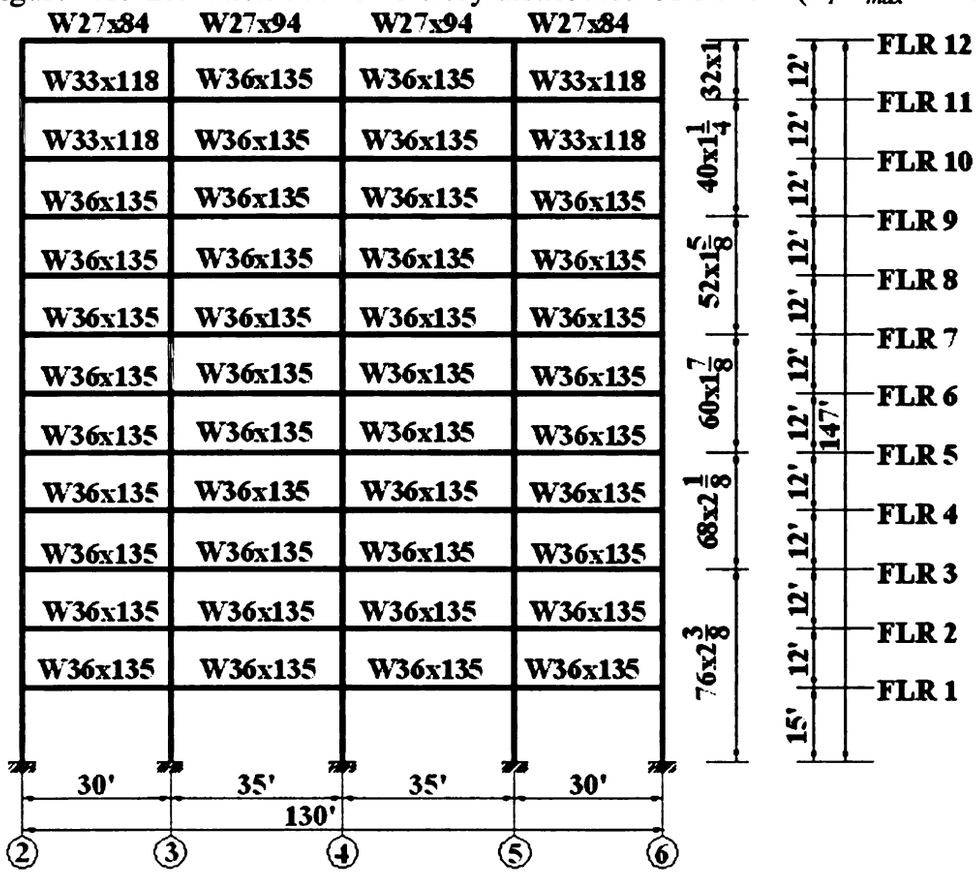


Figure 4.16 Elevation of twelve-story perimeter CFT MRF ($T_I/T_{max}>1.15$)

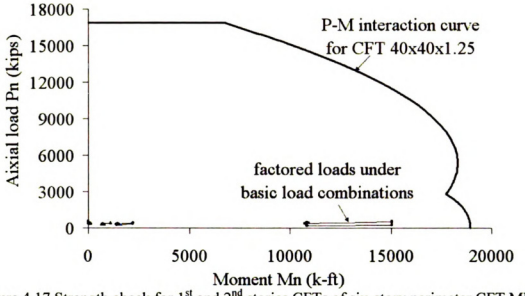


Figure 4.17 Strength check for 1st and 2nd stories CFTs of six-story perimeter CFT MRF

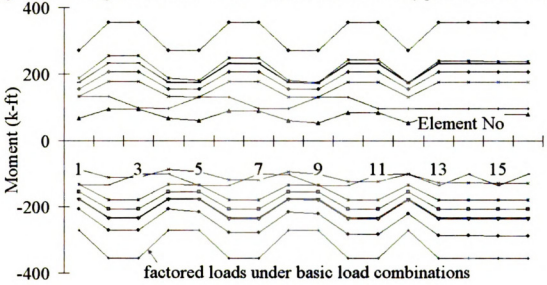


Figure 4.18 Strength check for *W36x135* girders

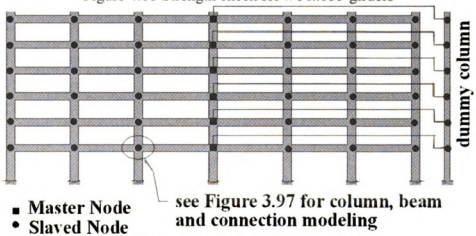


Figure 4.19 Model of CFT MRF

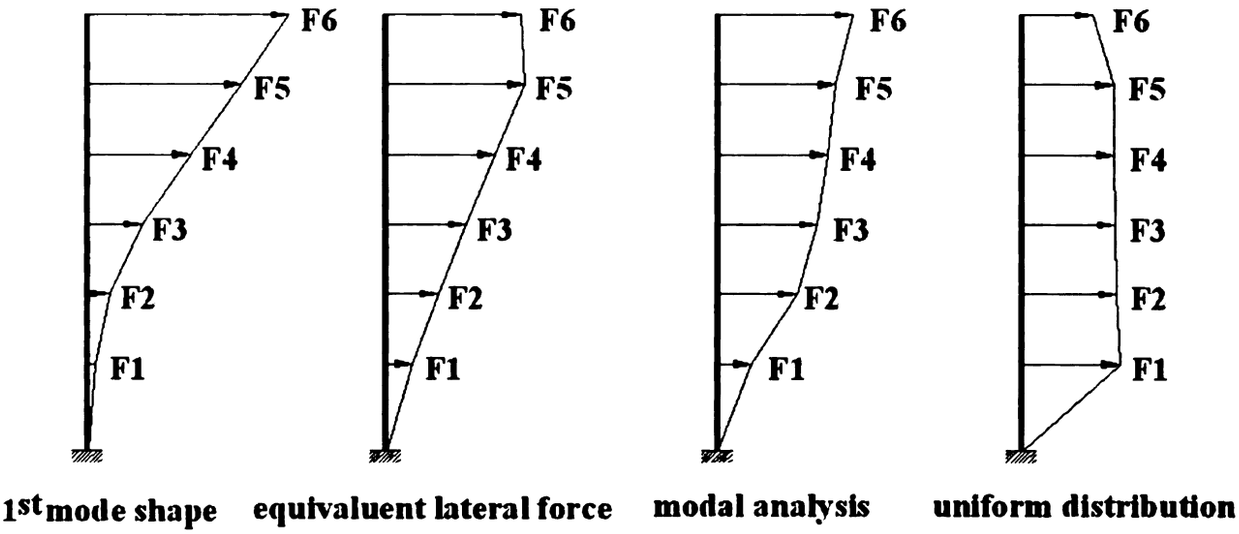


Figure 4.20 Lateral load patterns of six-story distributed CFT MRFs

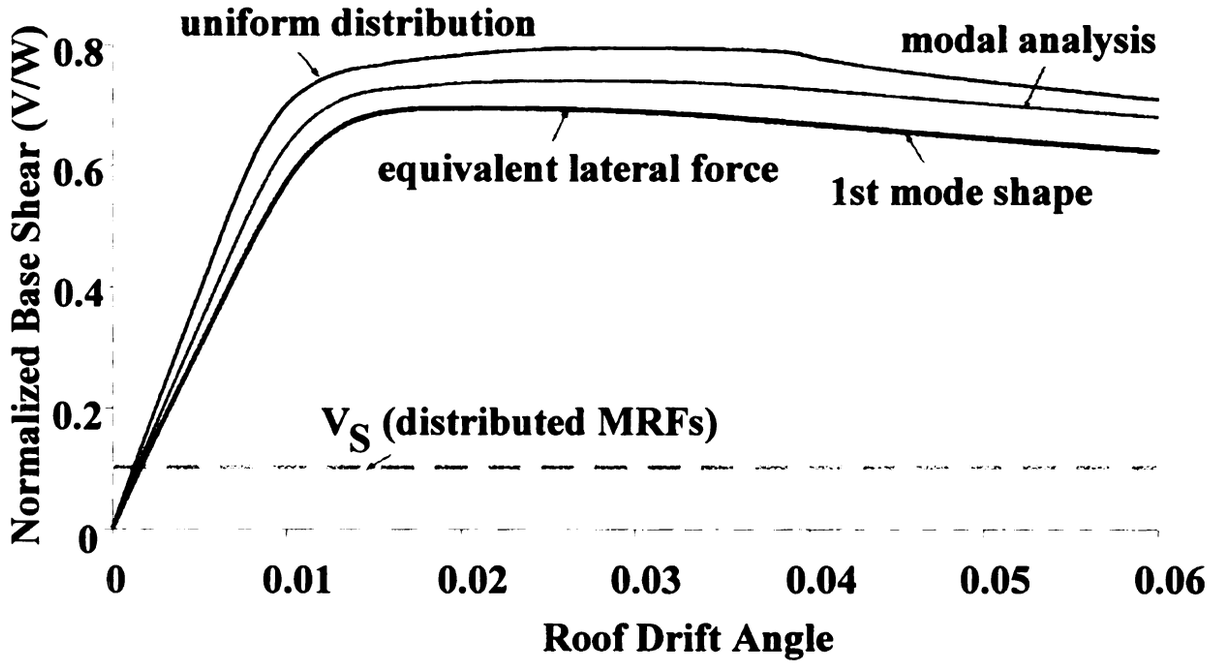


Figure 4.21 Static pushover analysis results of flexible six-story distributed CFT MRFs (FEMA 356 NSP Procedures)

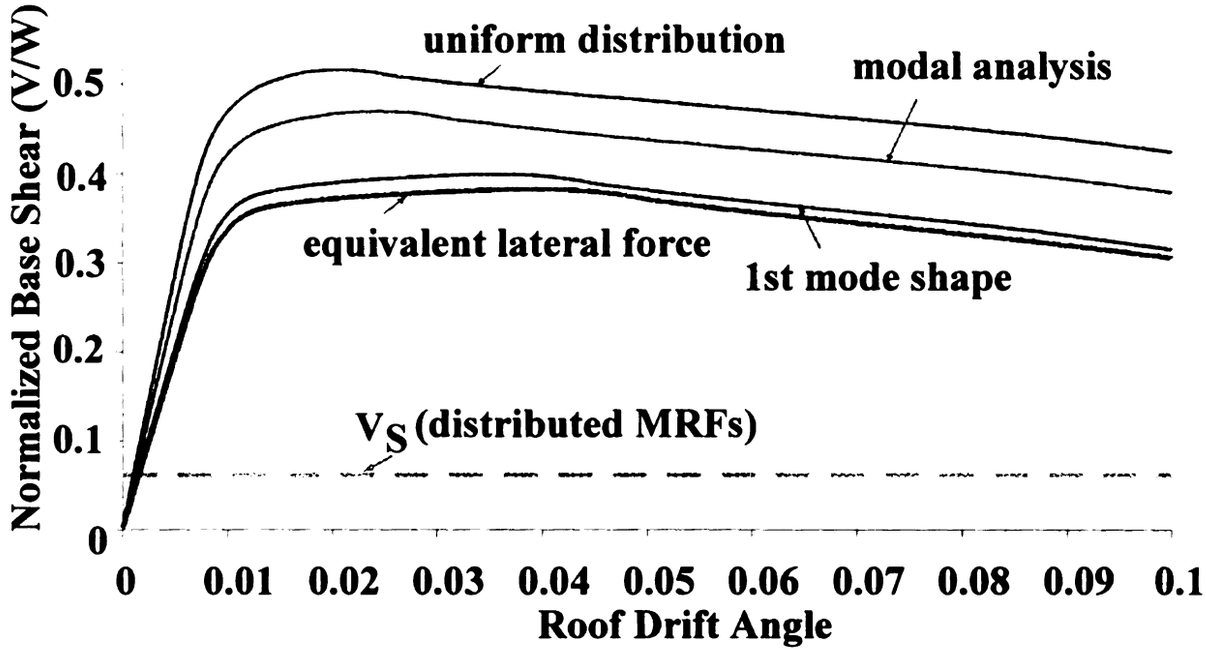


Figure 4.22 Static pushover analysis results of flexible twelve-story distributed CFT MRFs (FEMA 356 NSP Procedures)

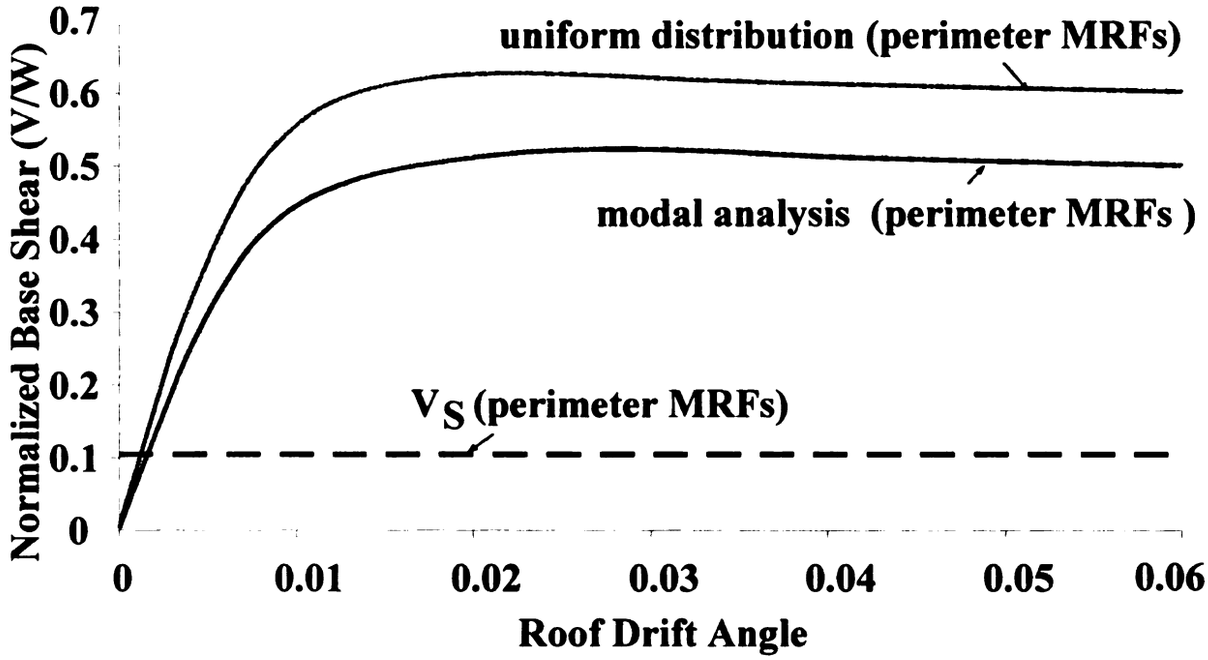


Figure 4.23 Static pushover analysis results of rigid six-story perimeter CFT MRFs (FEMA 356 NSP Procedures)

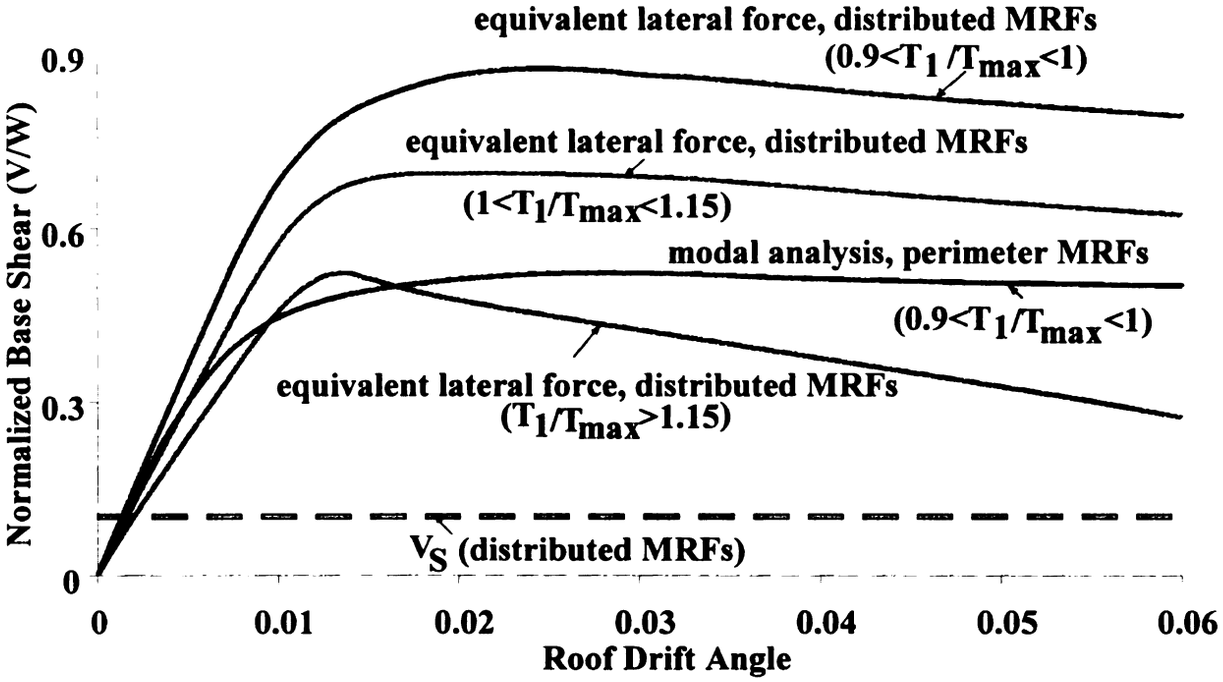


Figure 4.24 Static pushover analysis results of six-story distributed and perimeter CFT MRFs

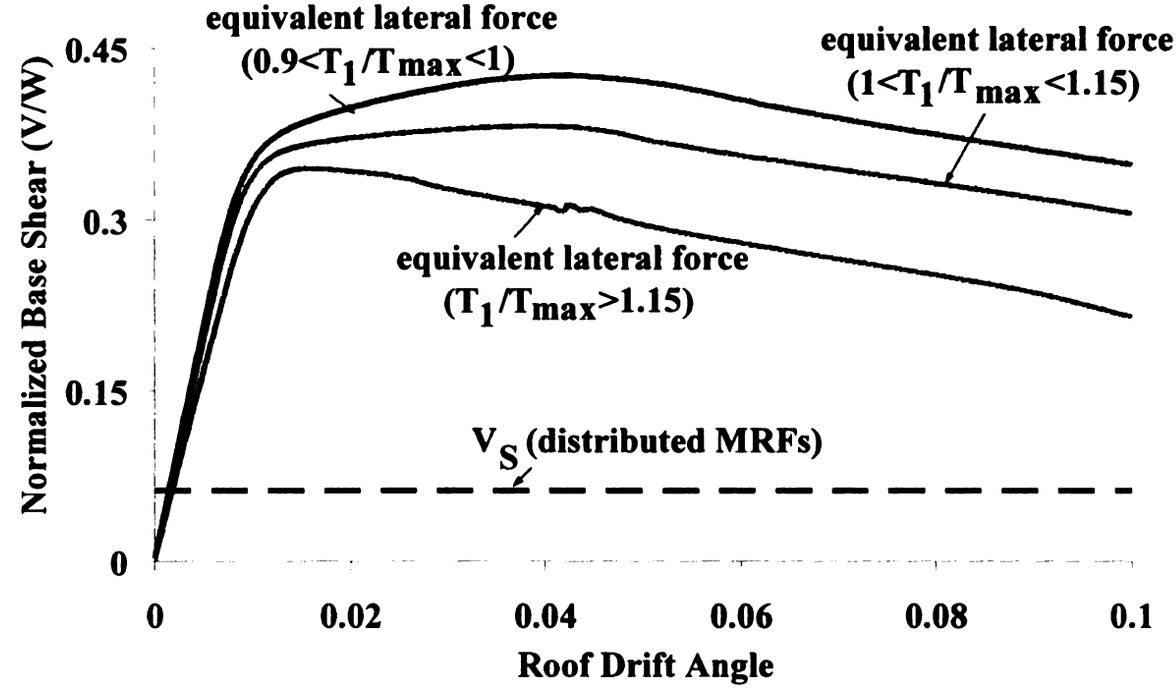


Figure 4.25 Static pushover analysis results of twelve-story distributed CFT MRFs

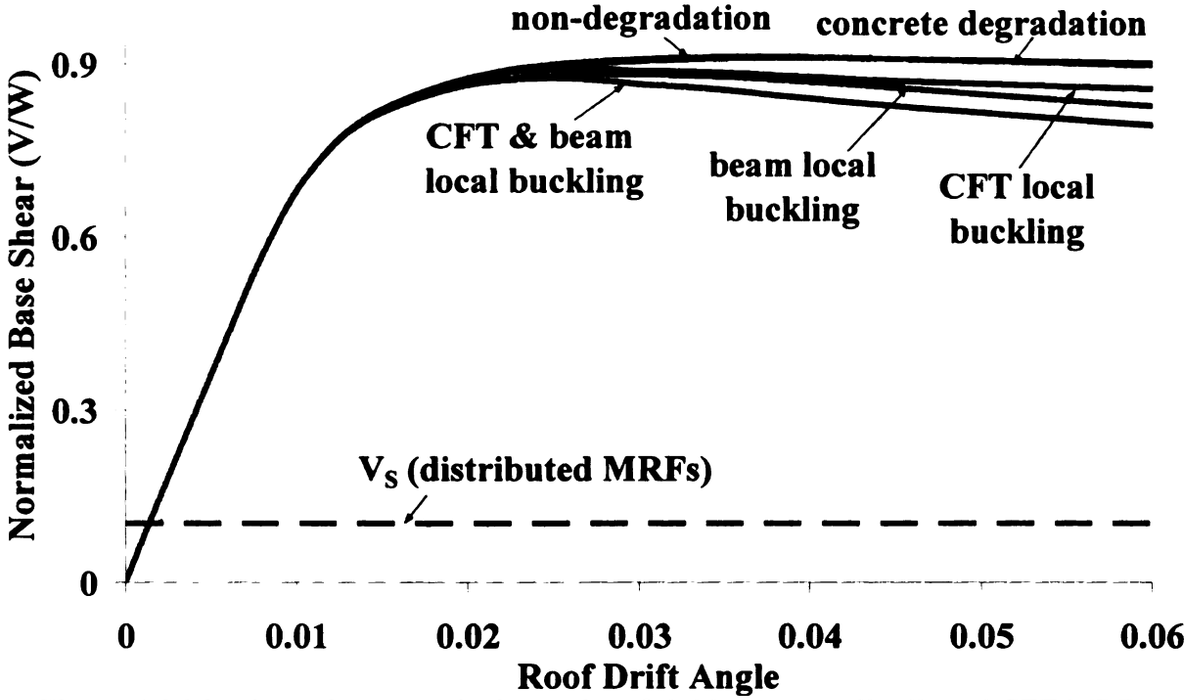


Figure 4.26 Static pushover analysis results of rigid six-story distributed CFT MRFs

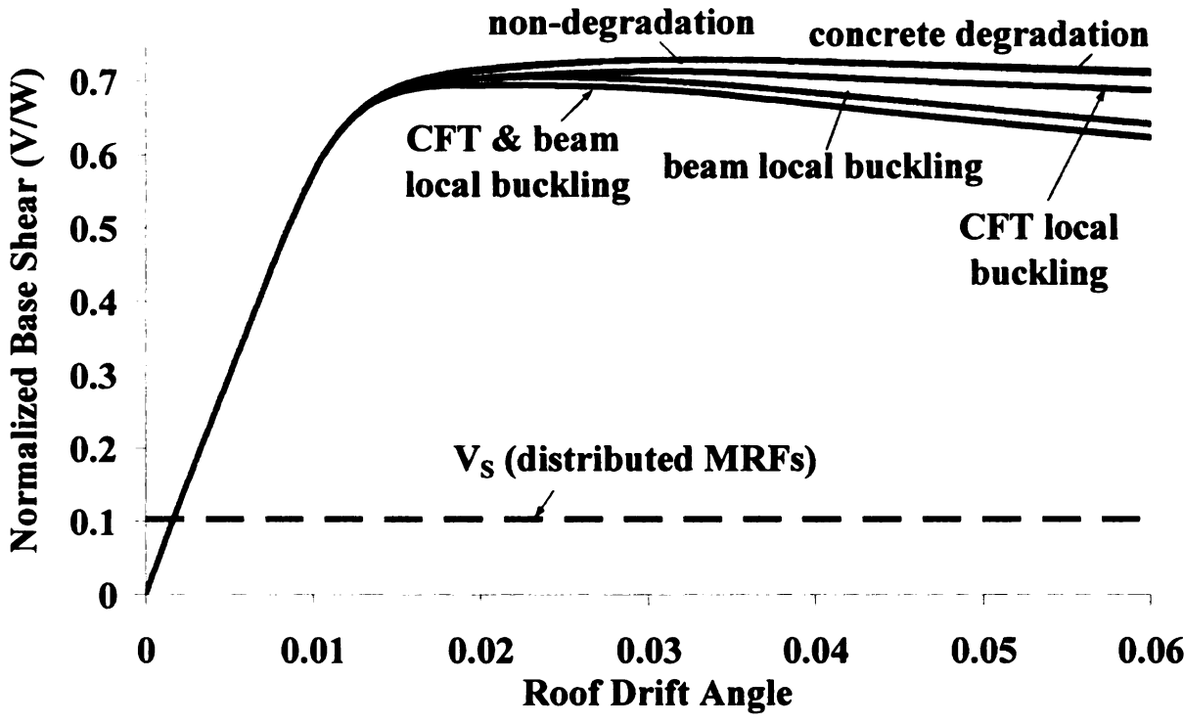


Figure 4.27 Static pushover analysis results of flexible six-story distributed CFT MRFs

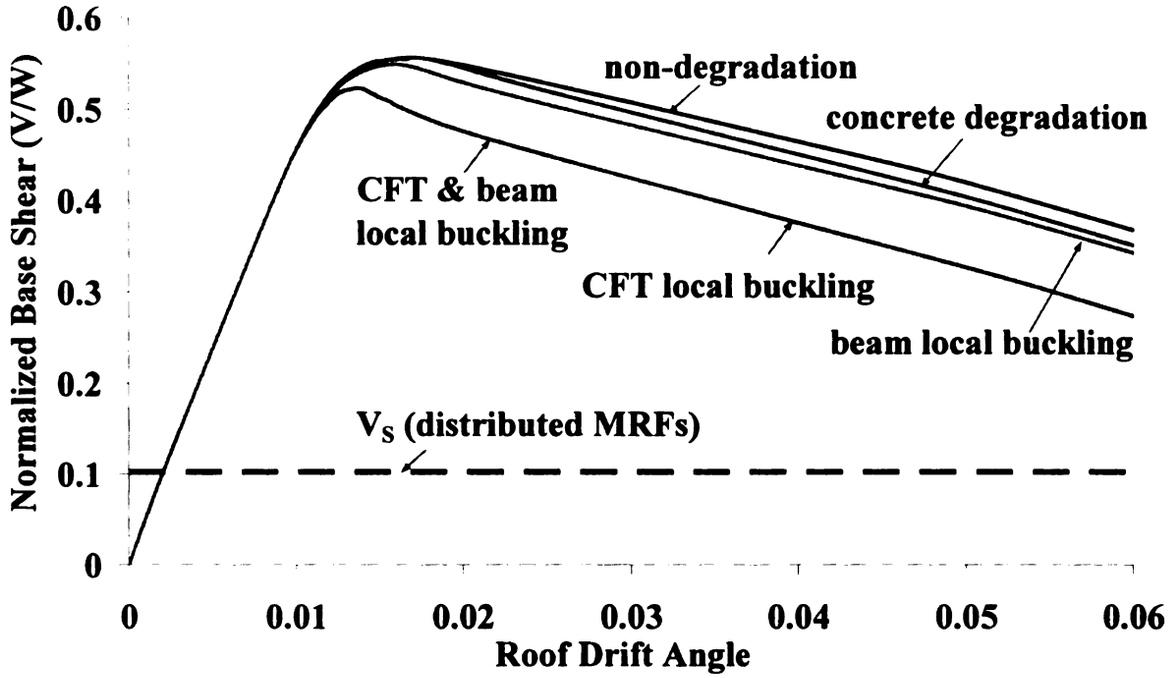


Figure 4.28 Static pushover analysis results of highly flexible six-story distributed CFT MRFs

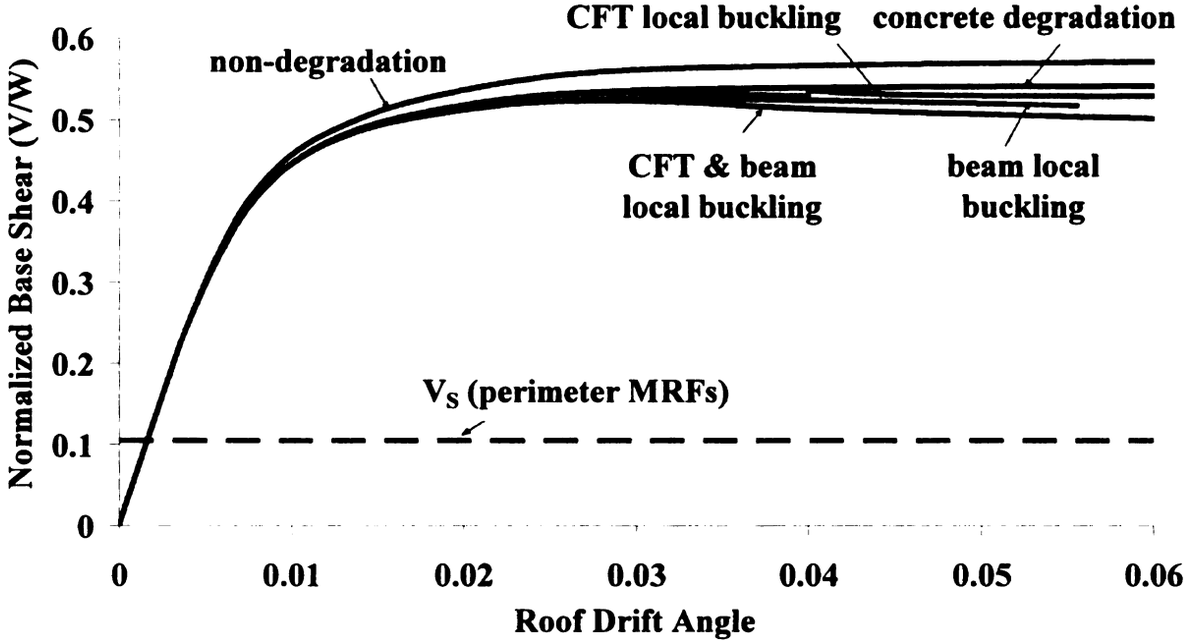


Figure 4.29 Static pushover analysis results of rigid six-story perimeter CFT MRFs

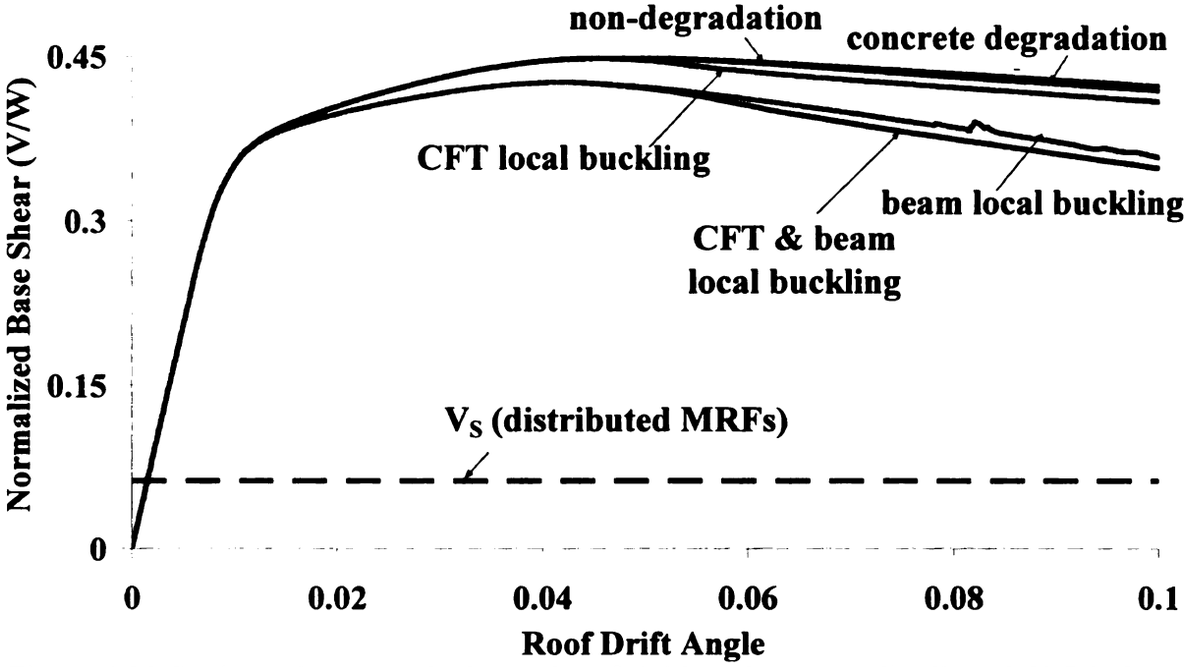


Figure 4.30 Static pushover analysis results of rigid twelve-story distributed CFT MRFs

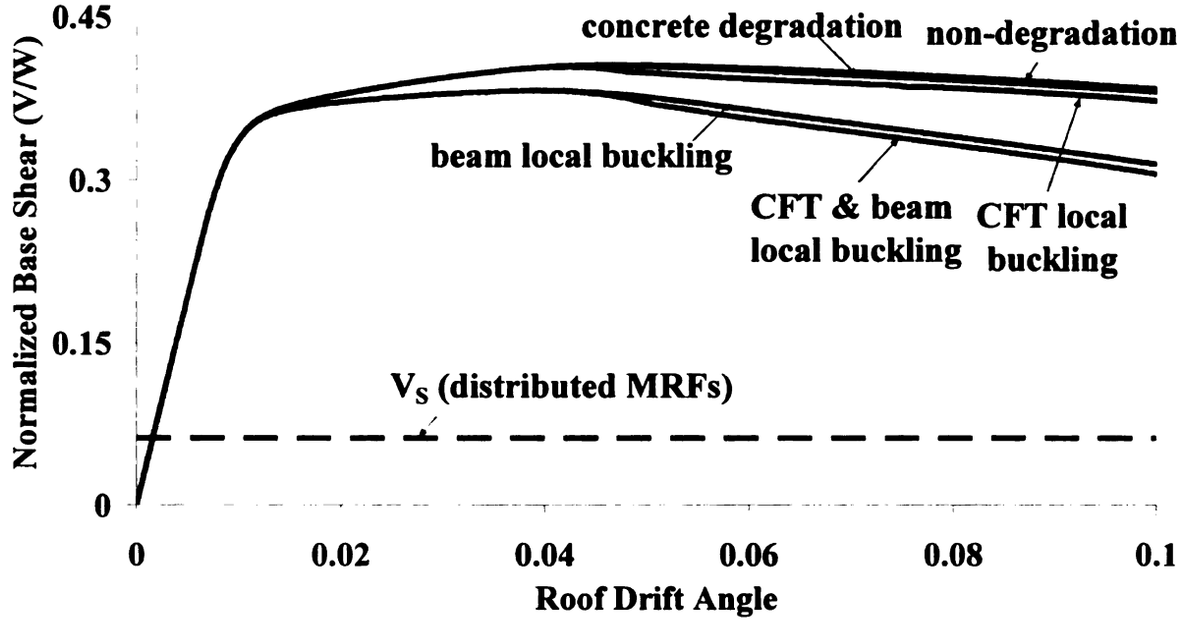


Figure 4.31 Static pushover analysis results of flexible twelve-story distributed CFT MRFs

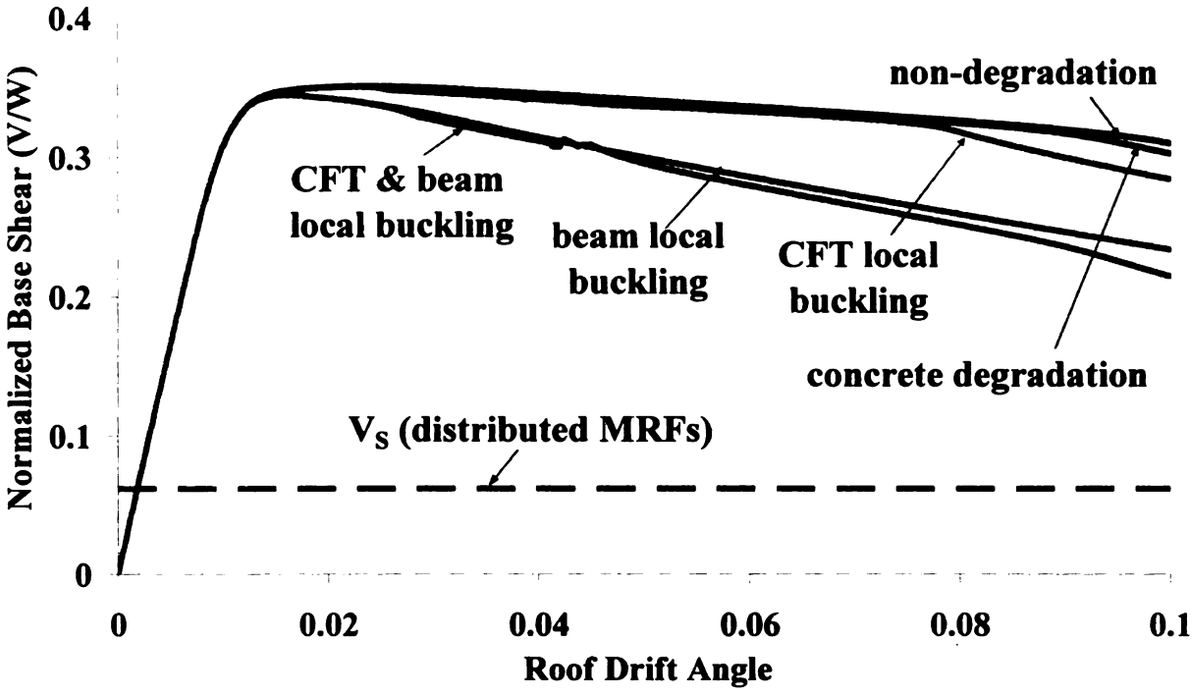


Figure 4.32 Static pushover analysis results of highly flexible twelve-story distributed CFT MRFs

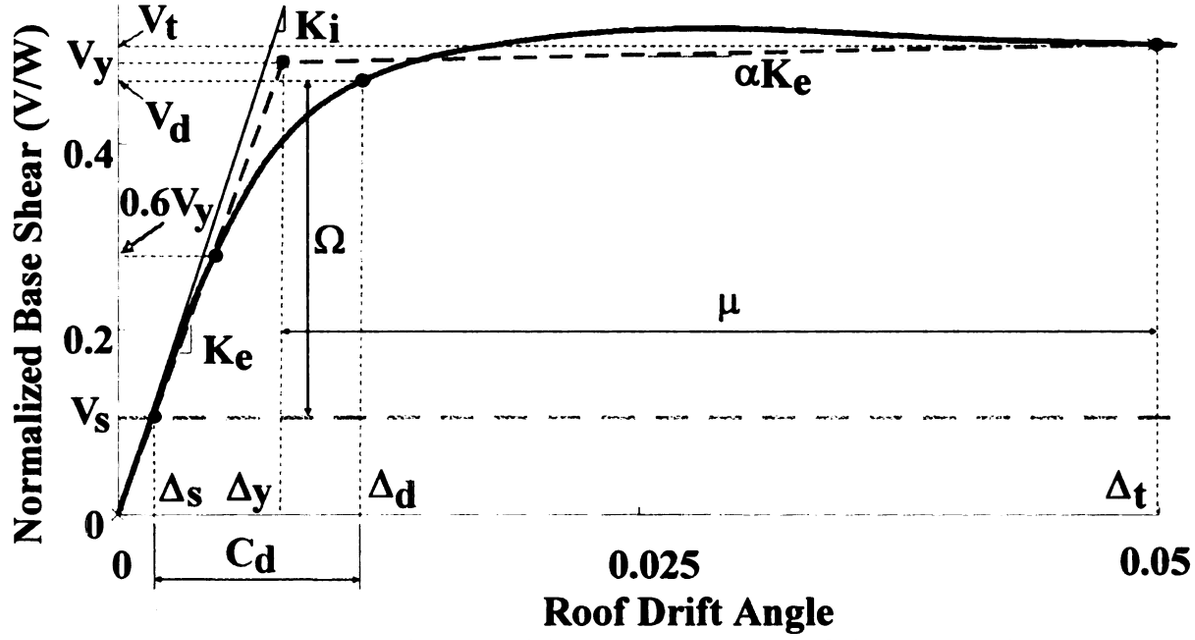


Figure 4.33 Idealized base shear-roof displacement curve of six-story perimeter CFT MRFs (positive post-yield slope)

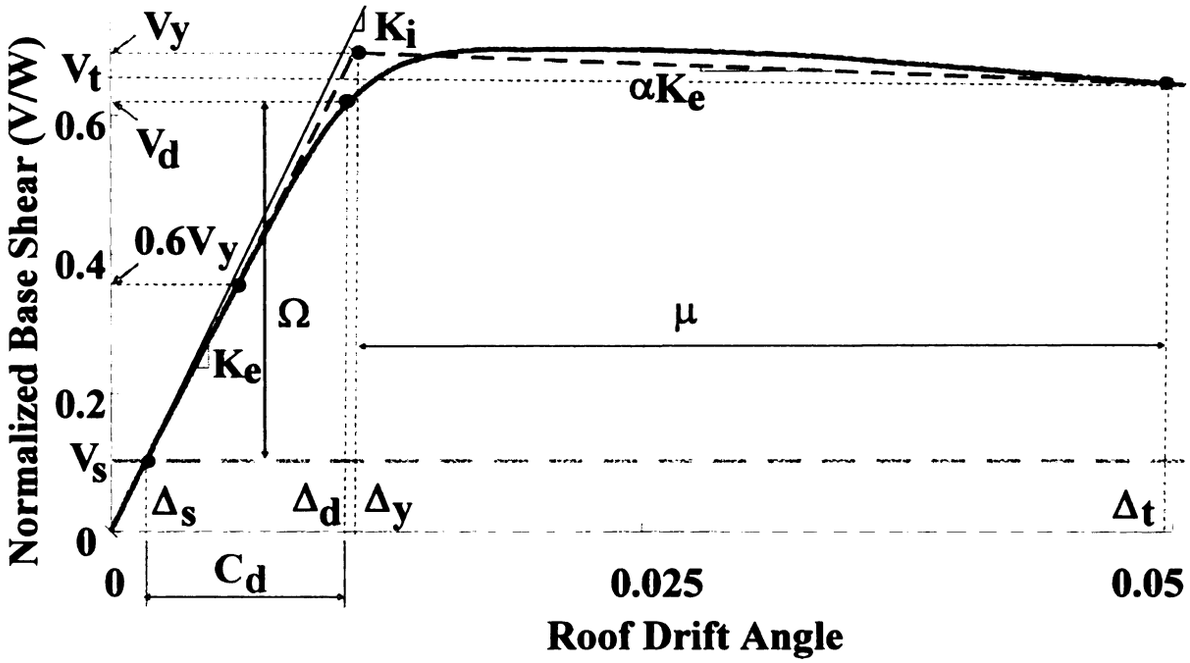


Figure 4.34 Idealized base shear-roof displacement curve of flexible six-story distributed CFT MRFs (negative post-yield slope)

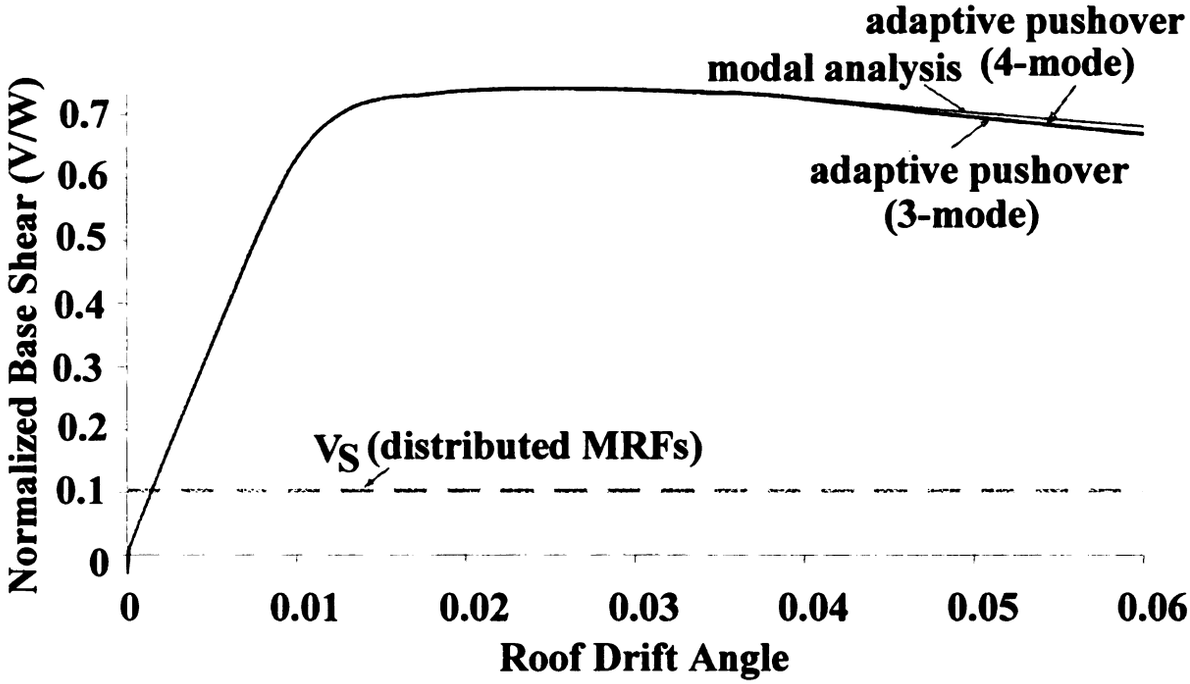


Figure 4.35 Adaptive pushover analysis results of flexible six-story distributed CFT MRFs

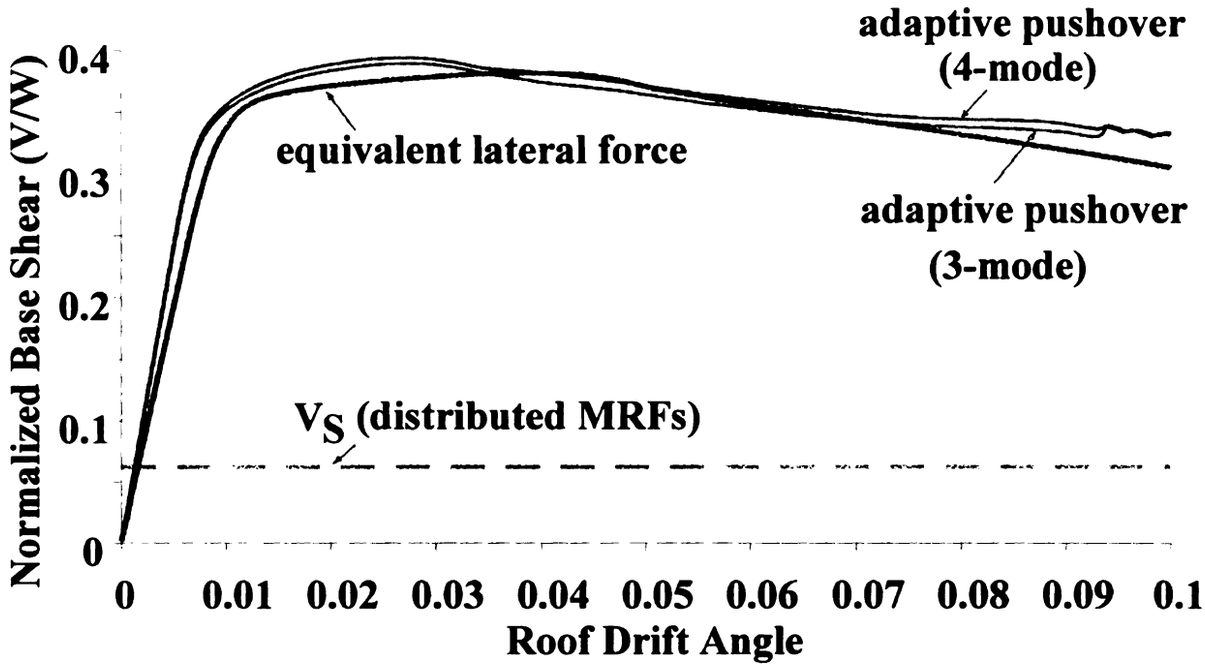


Figure 4.36 Adaptive pushover analysis results of flexible twelve-story distributed CFT MRFs

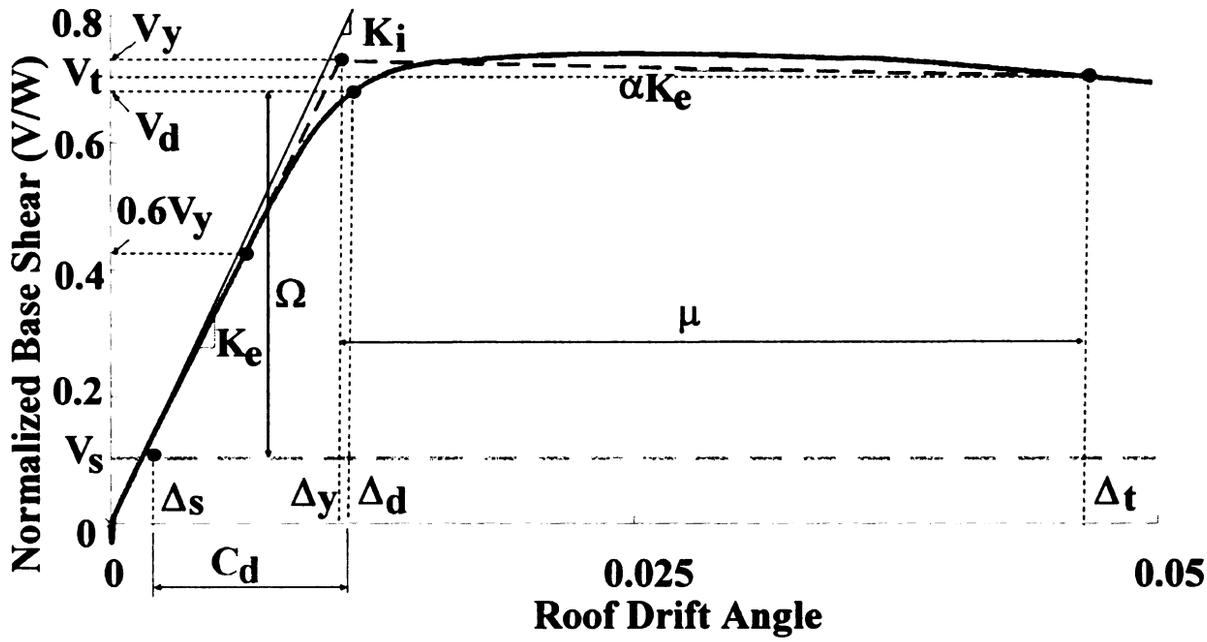


Figure 4.37 Idealized base shear-roof displacement curve of flexible six-story distributed CFT MRFs (adaptive pushover analysis, 3-mode)

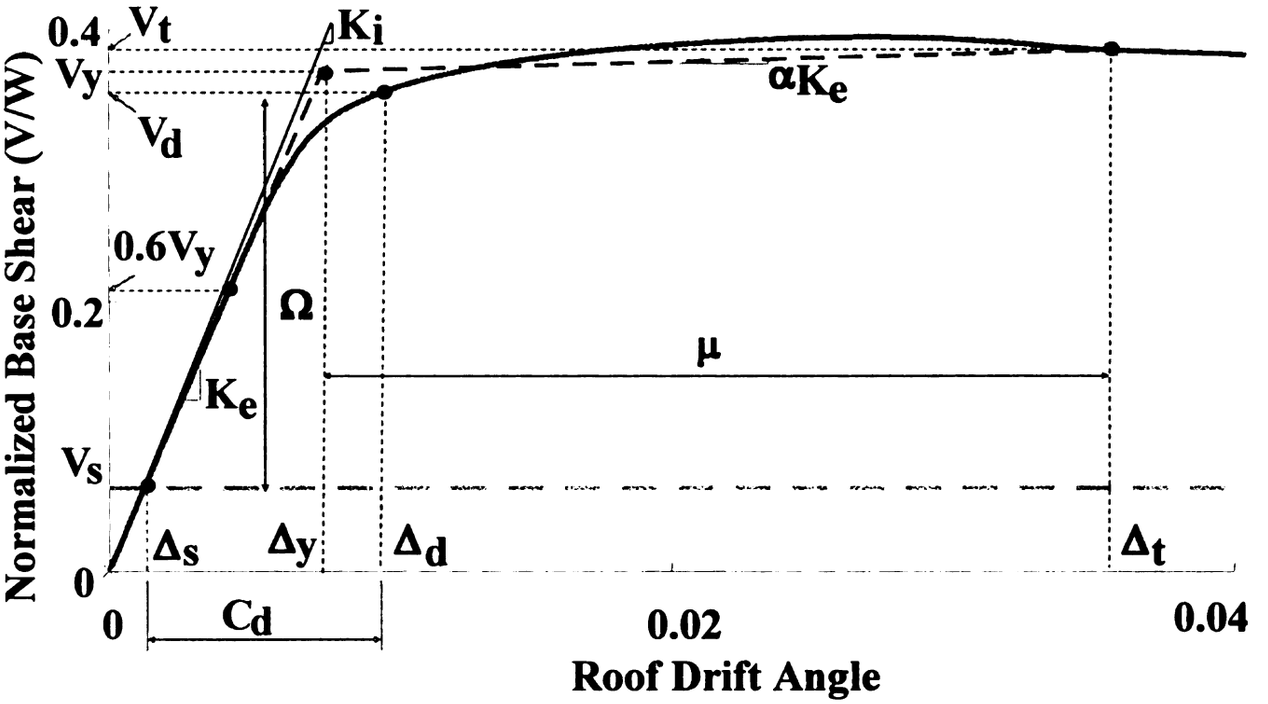
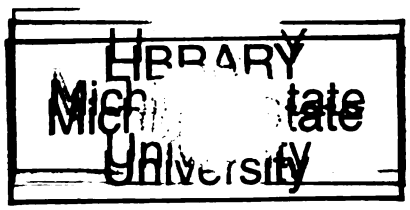


Figure 4.38 Idealized base shear-roof displacement curve of flexible twelve-story distributed CFT MRFs (adaptive pushover analysis, 4-mode)

MICHIGAN STATE UNIVERSITY LIBRARIES
3 1293 02736 0829

138
656
THS
6319245



PLACE IN RETURN BOX to remove this checkout from your record.
TO AVOID FINES return on or before date due.
MAY BE RECALLED with earlier due date if requested.

DATE DUE	DATE DUE	DATE DUE

2/05 c:/CIRC/DateDue.indd-p.15

SEISMIC BEHAVIOR OF MOMEMT RESISTING FRAMES WITH HIGH-STRENGTH SQUARE CFT COLUMNS

VOLUME II

By

Zhihui Huang

A DISSERTATION

Submitted to
Michigan State University
in partial fulfillment of the requirements
for the degree of

DOCTOR OF PHILOSOPHY

Department of Civil and Environmental Engineering

2005

CHAPTER 5 TIME-HISTORY ANALYSIS OF THE CFT MRFS

Higher mode effects are present to significant degrees for almost all mid-to-high rise structures. For example, the effective modal masses for the 1st to 4th modes of the six-story perimeter CFT MRF are 61%, 19.6%, 9.5%, and 3.6%, respectively; the effective modal masses for the 1st to 4th modes of the flexible ($1<T_1/T_{max}<1.15$) six-story distributed CFT MRF are 81.5%, 10.9%, 4.5%, and 1.8%, respectively; the effective modal masses for the 1st to 4th modes of the flexible ($1<T_1/T_{max}<1.15$) twelve-story distributed CFT MRF are 75.3%, 12.7%, 5.1%, and 2.8%, respectively. But none of the invariant force distributions of the static pushover analysis can account for the contributions of higher modes to response, or for a redistribution of inertia forces because of structural yielding (Krawinkler et al., 1998). In order to capture the seismic response of *High-strength CFT MRFs* more accurately, in addition to FEMA pushover procedures and adaptive pushover procedures, time history analyses are used in the design evaluation phase of this research.

5.1 Ground Motion Ensemble

The results of time-history analyses depend on not only on the characteristics of the MRFs, but also on the characteristic of the selected ground motion. Among the ground motion parameters that can affect the structural response, there are three key parameters: amplitude, frequency content and duration, where frequency content and duration are the main parameters of earthquakes. The seismic response of structures is very sensitive to the frequency content and duration of different ground motions (Kramer, 1996).

This research is intended to evaluate the seismic performance of *High-strength CFT MRFs*, but not intended to conduct a statistical study of the seismic response of *High-strength CFT MRFs* to ground motion of varying characteristics. Therefore, the MRFs in this research will be subjected to three sets of SAC ground motion records for Los Angeles (Somerville et al., 1997), including 2%, 10% and 50% probability of exceedance in 50 years (return periods of 2,475, 475 and 72 years, respectively), to investigate the inelastic dynamic behavior of the MRFs. The 2% in 50 years time histories (denoted as 2/50) consist with five natural ground motions and five simulated ground motions (Table 5.1). The 10% and 50% in 50 years time histories (denoted as 10/50 and 50/50, for respectively) all consist with ten natural ground motions (Tables 5.2 and 5.3). Each record consists with two horizontal components: strike normal and strike parallel components. Due to the fact that the strike parallel component always has a smaller spectral value than the strike normal component, only the strike normal component of each record is used in the time-history analysis of CFT MRFs.

All the three sets of the time histories are for stiff soil sites and match (in the mean) the target response spectra defined in the 1994 NEHRP provisions (Somerville et al., 1997), i.e., on the average, their spectral values match with a least-square error fit to the USGS mapped values at 0.3, 1.0 and 2.0 s (USGS 1996) and a predicted value at 4.0 s, for the appropriate return period. These periods (0.3, 1.0, 2.0 and 4.0 s) are selected because they cover the range of interest for the flexible steel structures.

5.1.1 Response Spectra

The design response spectrum (10% exceedance in 50 years) was already obtained per procedures of *IBC 2000* in Chapter 4.1 as:

$$S_a = \begin{cases} 0.6\dfrac{T}{T_0}S_{DS} + 0.4S_{DS} & T \le T_0 = 0.12s \\ S_{DS} & T_0 = 0.12s \le T \le T_S = 0.60s \\ \dfrac{S_{D1}}{T} & T \ge T_S = 0.60s \end{cases} \qquad (5.1)$$

where S_{DS}=*1.00g* and S_{D1}=*0.60g*. Similarly, per procedures of IBC 2000 Sec. 1615.2, the maximum considered response spectrum (2% exceedance in 50 years) can be obtained as:

$$S_a = \begin{cases} 1.5Fa & T \le T_S = 0.60s \\ 0.6F_v/T & T \ge T_S = 0.60s \end{cases} \qquad (5.2)$$

where F_a=*1.00g* and F_v=*1.50g*. In addition, the 50% in 50 years response spectrum (50% exceedance in 50 years) can be obtained by divided the design response spectrum (10% exceedance in 50 years) by 1.5:

$$S_a = \begin{cases} 0.4\dfrac{T}{T_0}S_{DS} + \dfrac{4}{15}S_{DS} & T \le T_0 = 0.12s \\ 2S_{DS}/3 & T_0 = 0.12s \le T \le T_S = 0.60s \\ \dfrac{2S_{D1}}{3T} & T \ge T_S = 0.60s \end{cases} \qquad (5.3)$$

where S_{DS}=*1.00g* and S_{D1}=*0.60g*. The response spectra of 2%, 10% and 50% exceedance in 50 years, i.e., the maximum considered response spectrum, design response spectrum and 50% in 50 years response spectrum, are shown in Fig. 5.1.

5.1.2 Scale Factors of SAC Ground Motion Time-Histories

The original SAC ground motion time-histories which match with a least-square error fit to the USGS mapped values at 0.3, 1.0, 2.0 and 4.0 s may not suitable for the low-rise and medium-rise CFT MRFs, which have fundamental periods range from around 1.0 s to 2.0 s. As shown in Fig. 5.2, one of the original 50% in 50 years time-history, *lwhdown*, has a spectral value significantly higher than the maximum considered response spectrum (2% exceedance in 50 years). Therefore, all the original SAC ground motion records are rescaled so that their spectral values match with a least-square error fit to the response spectra at 0.3, 1.0, 1.5 and 2.0 s, i.e., 1.5 s is used instead of 4.0 s in the original SAC ground motion records. The scaling procedure is followed Somerville's recommendation (Somerville et al., 1997). The weights used are 0.1, 0.3, 0.3 and 0.3 for periods of 0.3, 1.0, 1.5 and 2.0 seconds, respectively, i.e., the scale factor, *SF*, is:

$$SF = \left(\frac{S_{target,0.3}}{S_{GM,0.3}} \right)^{0.1} \left(\frac{S_{target,1.0}}{S_{GM,1.0}} \bullet \frac{S_{target,1.5}}{S_{GM,1.5}} \bullet \frac{S_{target,2.0}}{S_{GM,2.0}} \right)^{0.3} \qquad (5.4)$$

where $S_{target,\,T}$ and $S_{GM,\,T}$ are the spectral values of the target spectrum and the ground motion spectrum being scaled, respectively, for a period equal to T in seconds. The resulting scale factors applied to the time-histories of the 2/50, 10/50 and 50/50 SAC ground motion records used in this study are listed in Tables 5.1, 5.2 and 5.3, respectively. The rescaled response spectra of the 2/50, 10/50 and 50/50 SAC ground motion records used in this study are shown in Figs. 5.3 to 5.7, 5.8 to 5.12 and 5.8 to 5.12, along with the maximum considered response spectrum (2% exceedance in 50 years), the design response sepctrum (10% exceedance in 50 years) and the 50% in 50 years response spectrum (50% exceedance in 50 years), respectively. The 1st to 4th mode periods of the

flexible ($1<T_1/T_{max}<1.15$) twelve-story distributed CFT MRF are also marked in the pseudo-acceleration response spectra.

5.2 Time-History Analysis: Global Performance

5.2.1 Global Stability and Local Performance Evaluation

Consistent with the FEMA 356 "Prestandard and Commentary for the Seismic Rehabilitation of Buildings" (ASCE, 2000), three performance levels, ***Immediate Occupancy*** (IO), ***Life Safety*** (LS) and ***Collapse Prevention*** (CP), are considered for the three sets of SAC ground motions. The ***Immediate Occupancy*** (IO) level, defined as the post-earthquake damage state that remains safe to occupy, essentially retains the pre-earthquake design strength and stiffness of the structure, should be achieved for CFT MRFs subjected to SAC 50/50 time-histories (50% exceedance in 50 years). The ***Life Safety*** (LS) level, defined as the post-earthquake damage state that includes damage to structural components but retains a margin against onset of partial or total collapse, should be achieved for CFT MRFs subjected to SAC 10/50 time-histories (10% exceedance in 50 years). The ***Collapse Prevention*** (CP) level, defined as the post-earthquake damage state that includes damage to structural components such that the structure continues to support gravity loads but retains margin against collapse, should be achieved for CFT MRFs subjected to SAC 2/50 time-histories (2% exceedance in 50 years).

In order to evaluate the performance of CFT MRFs subjected to the 2/50 and 50/50 SAC ground motion time-histories, the global behavior limited by inter-story drift and the local performances including the local connection behavior limited by local connection

response and column compression behavior are used to predict the confidence levels for the ***Immediate Occupancy*** (IO) level under SAC 50/50 ground motions and the ***Collapse Prevention*** (CP) level SAC 2/50 ground motions, per evaluation procedures of FEMA 350 "Recommended Seismic Design Criteria for New Steel Moment-Frame Buildings" (SAC, 2000). Due to the fact that no factor and confidence level are recommended by FEMA 350 for the ***Life Safety*** (LS) level, for CFT MRFs subjected to the 10/50 SAC ground motion time-histories, only the global performance, i.e., the global behavior limited by inter-story drift, is evaluated according to the deflection and drift limits set by FEMA 368 "NEHRP Recommended Provisions for Seismic Regulations for New Buildings and Other Structures" (BSSC, 2001). No local behavior of CFT MRFs subjected to the 10/50 SAC ground motion time-histories will be evaluated.

5.2.1.1 Determination of Level of Confidence

The acceptability of the seismic performance for CFT MRFs subjected to SAC 2/50 and 50/50 time-histories are evaluated by determining a level of confidence in the building's ability to meet the desired performance objectives. The confidence level is determined through evaluation of the factored-demand-to-capacity ratio given by:

$$\lambda = \frac{\gamma\gamma_a D}{\phi C} \qquad (5.5)$$

where:

C = capacity of the structure, as indicated in FEMA 350 for global inter-story drift demand, local inter-story drift demand of pre-qualified *Special Moment Frame* (SMF) connections, and column compressive demand, respectively;

D = calculated demand for the structure, obtained from structural analysis;

γ = a demand variability factor that accounts for the variability inherent in the prediction of demand related to assumptions made in structural modeling and prediction of the character of ground shaking, as indicated in FEMA 350 for global inter-story drift demand, local inter-story drift demand of pre-qualified SMF connections, and column compressive demand, respectively;

γ_a = an analysis uncertainty factor that accounts for bias and uncertainty, inherent in the specific analytical procedure used to estimate demand as a function of ground shaking intensity, as indicated in FEMA 350 for global inter-story drift demand, local inter-story drift demand of pre-qualified SMF connections, and column compressive demand, respectively;

ϕ = a resistance factor that accounts for the uncertainty and variability, inherent in the prediction of structural capacity as a function of ground shaking intensity, as indicated in FEMA 350 for global inter-story drift demand, local inter-story drift demand of pre-qualified SMF connections, and column compressive demand, respectively; and

λ= a confidence index parameter from which a level of confidence can be obtained, as indicated in FEMA 350 for global inter-story drift demand, local inter-story drift demand of pre-qualified SMF connections, and column compressive demand, respectively.

FEMA 350 also defines an uncertainty parameter β_{UT} associated with the evaluation of global inter-story drift capacity, local inter-story drift capacity of pre-qualified SMF connections, and column compressive capacity, respectively. These uncertainties are related to the building's configuration, the structural framing system (*Ordinary Moment*

Frame or *Special Moment Frame*), the type of analytical procedure employed and the performance level being evaluated. The level of confidence associated with various values of the factored-demand-to-capacity ratio λ calculated using Equation 5.5, for various values of the uncertainty parameter β_{UT} is already indicated in a table in FEMA 350. Linear interpolation between the values give in the table may be used for values of factored-demand-to-capacity ratio λ and uncertainty β_{UT} intermediate to those tabulated.

5.2.1.2 Global Stability and Local Performance

The recommended minimum levels of confidence by FEMA 350 for the ***Immediate Occupancy*** (IO) performance level and the ***Collapse Prevention*** (CP) performance level are listed in Table 5.4. Table 5.4 provides recommended minimum levels of confidence for each of the potential controlling behavior modes, i.e., global stability, local connection capacity, column buckling failure, for the ***Immediate Occupancy*** (IO) and ***Collapse Prevention*** (CP) levels, respectively.

In addition to global stability evaluation, FEMA 350 also uses inter-story drift angle (Fig. 5.18) to evaluate the local performance of connections. For frames with partially restrained connections, or frames exhibit plasticity at the connections, the inter-story drift angle, reduced for the effects of axial column elongation, is a better measure of the total imposed rotation on all elements of the connection, including panel zones and connection elements, and is used as the basis of the recommended criteria in FEMA 350. The local inter-story drift angle capacities given by FEMA 350 were determined from cyclic tests of full-size connection subassemblies. The local ***Immediate Occupancy*** (IO) level capacity is defined as the inter-story drift angle at which any one of the following

behaviors occurs:

(1) onset of local flange buckling of beams;

(2) degradation of moment-resisting capacity of the assembly to a value below the nominal moment-resisting capacity; or

(3) initiation of fracture of bolts, welds, or base metal that results in significant strength degradation of the assembly.

The local ***Collapse Prevention*** (CP) level capacity is defined as the inter-story drift angle at which the connection completely fails, characterized by an inability of the connection to maintain integrity of beam-to-column connection under gravity loading. The global inter-story drift angle capacities of Special Moment Frames (SMF) given by FEMA 350 (SAC 2000) for the ***Immediate Occupancy*** (IO) and ***Collapse Prevention*** (CP) levels are listed in Table 5.5, in which the reduced capacity is the product of the resistance factor, ϕ, and the capacity values, C. The inter-story drift angle capacities given by FEMA 350 (SAC 2000) for Bolted Flange Plate (BFP) and Double Split Tee (DST) connections as limited by local connection response are listed in Table 5.6.

5.2.1.3 Determination of Actions and Deformation

According to FEMA 368 (BSSC, 2001), the response quantities shall be computed as follows:

1. If at less seven ground motions are analyzed, the median value of each of the response quantity (e.g., inter-story drift demand, or column axial demand) computed from the suite of analyses may be use as the demand.
2. If less than seven ground motions are analyzed, each response quantity shall be

taken as the maximum value obtained from any of the analyses.

The three sets of SAC ground motion records for Los Angeles (Somerville et al., 1997) used in this study, including 2%, 10% and 50% probability of exceedance in 50 years, all consist with ten ground motions, respectively. Therefore, the median value of each of the response quantity (e.g., inter-story drift demand, or column axial demand) may be use as the demand. Due to the fact that the maximum inter-story drifts for both the flexible ($1<T_1/T_{max}<1.15$) six-story and twelve-story distributed CFT MRFs subjected to SAC 2/50, 10/50 and 50/50 time-histories are less than 3%, 1.5% and 1%, respectively, in addition to the median values, the maximum values of the inter-story drift angles obtained from any of the analyses will also be evaluated, and the maximum values of the column axial demand will be used instead of the median values for the reason of simplification.

5.2.2 Global Performance of Six-Story CFT MRFs

The inter-story drift envelop of the flexible ($1<T_1/T_{max}<1.15$) six-story distributed CFT MRF subjected to SAC 2/50, 10/50 and 50/50 time-histories are shown in Figs. 5.19 to 5.21, Figs. 5.23 to 5.25 and Figs. 5.27 to 5.29, respectively. The maximum, minimum and median story drift envelop of the flexible six-story distributed CFT MRF subjected to SAC 2/50, 10/50 and 50/50 time-histories are shown in Figs. 5.22, 5.26 and 5.30, respectively. As shown in Figs. 5.19 to 5.22, the inter-story drift envelopes of most of the SAC 2/50 ground motions have the same trend as the maximum, minimum and median inter-story drift envelops, i.e., the maximum inter-story drifts take place at the 2nd story and the inter-story drifts reduce as the height increase. It means that the first mode

dominates the global performance of flexible six-story distributed CFT MRF subjected to the SAC 2/50 ground motions.

While for the flexible six-story distributed CFT MRF subjected to the SAC 10/50 ground motions, the first mode has less influence on the global performance of CFT MRFs. As shown in Figs. 5.23 to 5.26, for two of the SAC 10/50 time-histories, *llpgil3* and *lpsdhsp*, the maximum inter-story drifts take place at the 5th story and the inter-story drifts reduce as the height decrease. In addition, the influence of the higher mode effects on the distribution of inter-story drifts over height is more obvious for the maximum, minimum and median inter-story drift envelops (Fig. 5.26). Similarly, as shown in Figs. 5.27 to 5.30, the maximum inter-story drifts of most of the SAC 50/50 ground motions take place at the 4th or 5th story, and the higher mode effects have great influence on the distribution of inter-story drifts over height for the maximum, minimum and median inter-story drift envelops of the SAC 50/50 ground motions (Fig. 5.30).

The effective modal masses for the 1st to 4th modes of the flexible ($1<T_1/T_{max}<1.15$) six-story distributed CFT MRF are 81.5%, 10.9%, 4.5%, and 1.8%, respectively. According to FEMA 356, this six-story CFT MRF has more than 75% of the total mass participating in the 1st mode and can be categorized as a fundamental mode dominated structure. If nonlinear static pushover analysis is used to evaluate the seismic performance of this CFT MRFs, a vertical distribution proportion to the shape of the 1st mode and a vertical distribution proportion to the equivalent lateral forces can be used. However, from the different distribution of inter-story drifts over height of the same flexible six-story CFT MRF subjected to the SAC 2/50, 10/50 and 50/50 time-histories, it

can be seen that the sensitivity of the higher mode effects on the inter-story drift patterns to ground motion characteristics can be evaluated only through time history analysis.

As shown in Fig. 5.26, for the case in which at less seven ground motions are analyzed, the median value instead of the maximum value, of the response quantity can be used as the demand, the time-history analysis can lead to distribution of inter-story drifts over height which is greatly different from the distribution of a fundamental mode dominated structure. Therefore, in order to capture the seismic response of six-story CFT MRFs more accurately, in addition to the pushover analysis, time history analysis should be used in the design evaluation.

5.2.2.1 Confidence Levels for Global Stability

For the flexible six-story distributed CFT MRF subjected to SAC 2/50 and 50/50 time-histories, the global performance for the ***Immediate Occupancy*** (IO) and ***Collapse Prevention*** (CP) performance levels, corresponding to hazard level of 2% and 50% probability of exceedance in 50 years, respectively, are evaluated per FEMA 350 procedures. As shown in Table 5.7, for both the maximum values and the median value of the inter-story drift angles obtained from the analyses, the confidence levels for the global stability of the flexible six-story CFT MRFs are larger than 50% and 90% for the immediate occupancy and collapse prevention performance levels, respectively, as required by FEMA 350.

For the flexible six-story distributed CFT MRF subjected to SAC 10/50 time-histories, the global performance for the ***Life Safety*** (LS) performance level, corresponding to hazard level of 10% probability of exceedance in 50 years, is evaluated according to the

deflection and drift limits set by FEMA 368. The maximum inter-story drift angle and the maximum of the median value for each of the inter-story drift angles obtained from the analyses are 1.44% and 1.09%, respectively, which are all less than 1.5%, the drift limit specified in FEMA 368. Therefore, the global performance of the flexible six-story CFT MRF for the ***Immediate Occupancy*** (IO), ***Life Safety*** (LS) and ***Collapse Prevention*** (CP) performance levels all meet the requirements of FEMA 350 and FEMA 368.

5.2.3 Global Performance of Twelve-Story CFT MRFs

The inter-story drift envelop of the flexible ($1<T_1/T_{max}<1.15$) twelve-story distributed CFT MRF subjected to SAC 2/50, 10/50 and 50/50 time-histories are shown in Figs. 5.31 to 5.33, Figs. 5.35 to 5.37 and Figs. 5.39 to 5.41, respectively. The maximum, minimum and median story drift envelop of the flexible six-story distributed CFT MRF subjected to SAC 2/50, 10/50 and 50/50 time-histories are shown in Figs. 5.34, 5.38 and 5.42, respectively. As shown in Figs. 5.31 to 5.34, the higher mode effects have great influence on the distribution of inter-story drifts over height of the flexible twelve-story CFT MRF subjected to the SAC 2/50 ground motions, e.g., the maximum inter-story drifts of all the ten SAC 2/50 ground motions take place at the 5^{th} to 9^{th} stories and the inter-story drifts in the middle stories are greater than those in the lower and upper stories. It means that the higher mode effects dominate the global performance of flexible twelve-story distributed CFT MRF subjected to the SAC 2/50 ground motions.

The higher mode effects also dominate the global performance of flexible twelve-story distributed CFT MRF subjected to the SAC 10/50 ground motions. As shown in Figs. 5.35 to 5.38, similar to the case in six-story CFT MRF, the two SAC 10/50 time-

histories, *llpgil3* and *lpsdhsp*, have the most complicate distribution of inter-story drifts over height. For the twelve-story CFT MRF, higher mode effects make the distribution of inter-story drifts over height for the two ground motions become a saddle shape; while for the six-story CFT MRFs, higher mode effects only make the distribution of inter-story drifts over height for the two ground motions become a more complex shape, a bell shape. It means that higher mode effects have a greater influence on the twelve-story CFT MRF than the six-story CFT MRF.

Similarly, as shown in Figs. 5.39 to 5.42, higher mode effects make the maximum inter-story drifts of most of the SAC 50/50 ground motions take place at the upper stories (the 9^{th} to 11^{th} stories), while for most of the SAC 2/50 ground motions, the maximum inter-story drifts take place at the middle stories (the 5^{th} to 9^{th} stories). Obviously, for the twelve-story CFT MRF, higher mode effects have a greater influence on the 50/50 ground motions than the SAC 2/50 ground motions. It means that the influence of higher mode effects on the seismic behavior of CFT MRFs depend greatly on the frequency content rather than the intensity of the ground motion.

The effective modal masses for the 1^{st} to 4^{th} modes of the flexible ($1<T_1/T_{max}<1.15$) twelve-story distributed CFT MRF are 75.3%, 12.7%, 5.1%, and 2.8%, respectively. According to FEMA 356, this twelve-story CFT MRF has more than 75% of the total mass participating in the 1^{st} mode and can be categorized as a fundamental mode dominated structure. If nonlinear static pushover analysis is used to evaluate the seismic performance of this CFT MRFs, a vertical distribution proportion to the shape of the 1^{st} mode and a vertical distribution proportion to the equivalent lateral forces can be used. However, from the different distribution of inter-story drifts over height of the same

flexible six-story CFT MRF subjected to the SAC 2/50, 10/50 and 50/50 time-histories, it can be seen that the sensitivity of the higher mode effects on the inter-story drift patterns to ground motion characteristics can be evaluated only through time history analysis. Therefore, in order to capture the seismic response of *High-strength CFT MRFs* more accurately, in addition to the pushover analysis, time history analysis should be used in the design evaluation.

5.2.3.1 Confidence Levels for Global Stability

For the flexible twelve-story distributed CFT MRF subjected to SAC 2/50 and 50/50 time-histories, the global performance for the ***Immediate Occupancy*** (IO) and ***Collapse Prevention*** (CP) performance levels, corresponding to hazard level of 2% and 50% probability of exceedance in 50 years, respectively, are evaluated per FEMA 350 procedures. As shown in Table 5.8, for both the maximum values and the median value of the inter-story drift angles obtained from the analyses, the confidence levels for the global stability of the flexible twelve-story CFT MRFs are larger than 50% and 90% for the immediate occupancy and collapse prevention performance levels, respectively, as required by FEMA 350.

For the flexible twelve-story distributed CFT MRF subjected to SAC 10/50 time-histories, the global performance for the ***Life Safety*** (LS) performance level, corresponding to hazard level of 10% probability of exceedance in 50 years, is evaluated according to the deflection and drift limits set by FEMA 368. The maximum inter-story drift angle and the maximum of the median value for each of the inter-story drift angles obtained from the analyses are 1.03% and 0.85%, respectively, which are all less than

1.5%, the drift limit specified in FEMA 368. Therefore, the global performance of the flexible twelve-story CFT MRF for the ***Immediate Occupancy*** (IO), ***Life Safety*** (LS) and ***Collapse Prevention*** (CP) performance levels all meet the requirements of FEMA 350 and FEMA 368.

5.3 Time-History Analysis: Local Performance

5.3.1 Confidence Levels for Connection Local Performance

The local connection performance of the flexible six-story distributed CFT MRF subjected to SAC 2/50 and 50/50 time-histories, corresponding to the ***Immediate Occupancy*** (IO) and ***Collapse Prevention*** (CP) performance levels, respectively, are evaluated per FEMA 350 procedures. In addition to global stability evaluation, FEMA 350 also uses inter-story drift angle (Fig. 5.18) to evaluate the local performance of connections. This is because the inter-story drift angle, (1) seems to be stable with regard to prediction of frame performance, (2) is closely related to plastic rotation angle, (3) is less ambiguous with regard to definition, and (4) is a quantity that is easily determined from the results if standard frame analyses using either linear or nonlinear methods.

As shown in Table 5.9, for both the maximum values and the median value of the inter-story drift angles obtained from the analyses, the confidence levels for the local connection performance of the flexible six-story CFT MRFs are larger than 50% and 50% for the immediate occupancy and collapse prevention performance levels, respectively, as required by FEMA 350.

Due to the fact that no factor and confidence level are recommended by FEMA 350 for the ***Life Safety*** (LS) level, for CFT MRFs subjected to the 10/50 SAC ground motion

time-histories, only the global performance, i.e., the global behavior limited by inter-story drift, is evaluated according to the deflection and drift limits set by FEMA 368 "NEHRP Recommended Provisions for Seismic Regulations for New Buildings and Other Structures" (BSSC, 2001). No local behavior of CFT MRFs subjected to the 10/50 SAC ground motion time-histories will be evaluated.

5.3.2 Confidence Levels for Column Compression Performance

The local column compression performance of the flexible six-story distributed CFT MRF subjected to SAC 2/50 and 50/50 time-histories, corresponding to the ***Immediate Occupancy*** (IO) and ***Collapse Prevention*** (CP) performance levels, respectively, are evaluated per FEMA 350 procedures. The factored column compressive demand shall be determined for each column as the quantity $\gamma\gamma_a D$, where:

D = the compressive axial load on the column determined as the sum of the Dead Load, 25% of the unreduced Live Load, and the Seismic Demand. Seismic demand shall be determined by either of the following four analysis methods:

Linear: The axial demands may be those predicted by a linear static or linear dynamic analysis, conducted in accordance with FEMA 350.

Plastic: The axial demands may be based on plastic analysis, as indicated in FEMA 350.

Nonlinear Static: The axial demands may be based on the computed forces from a nonlinear static analysis, at the target displacement, in accordance with FEMA 350.

Nonlinear Dynamic: The axial demands may be based on the computed design forces from a nonlinear dynamic analysis, in accordance with FEMA 350.

γ = Demand variability factor, taken as having the constant value 1.05.

γ_a = Analysis uncertainty factor, for nonlinear dynamic analysis procedure, it is given by:

$$\gamma_a = e^{1.4\beta^2} \qquad (5.6)$$

And for nonlinear dynamic analysis procedure, the uncertainty coefficient β_{UT} shall be taken as:

$$\beta_{UT} = \sqrt{0.0225 + \beta^2} \qquad (5.7)$$

where β may be taken as the coefficient of variation (COV) of the axial load values determined from the suite of nonlinear analysis.

5.3.2.1 CFT Beam-Column Compressive Capacity

Factored compressive capacity of each column to resist compressive axial loads, shall be determined as the product of the resistance factor ϕ and the nominal axial strength C. For the purposes of this evaluation, the effective length coefficient k shall be taken as having a value of 1.0 and the resistance factor ϕ shall be assigned a value of 0.95. The axial strength C of the CFT beam-column is determined in accordance with MAIJ method (Sakino and Nakahara, 2000). According to MAIJ, the normalized depth to thickness ratio is:

$$\alpha = (b/t)^2 (\sigma_y / E_s) \qquad (5.8)$$

where:

b, t = the width and the thickness of the CFT beam-column, respectively;

σ_y = the yield stress of the steel tube for the CFT beam-column;

E_S = the elastic modulus of the steel tube for the CFT beam-column.

The stress block of MAIJ method is shown in Fig. 5.53. The compressive stress of the steel tube in compression is decreased by a factor S, which is used to incorporate the effects of local buckling in compression zone before yielding. The $\sigma-\varepsilon$ curves of the steel tube are divided into three distinct cases. Case 1, Case 2 and Case 3 represent specimens with small, medium and high b/t ratios, respectively. The idealized steel stress-strain curves for three different cases of CFT specimens (Nakahara et al., 1998) are shown in Fig. 5.54. A specimen with $\alpha \leq 2.37$ is classified as a Case 1 specimen, where the steel tube fails by mean of local buckling at a stress capacity greater than the yield stress. For a Case 1 specimen, the yield stress is multiplied by the factor S, to estimate the stress capacity of steel tube:

$$S = \frac{1}{0.698 + 0.128\alpha} \qquad (5.9)$$

where α is the normalized depth to thickness ratio.

A specimen with $2.37 < \alpha < 4.11$ is classified as a Case 2 specimen, where the steel tube is expected to fail at a stress capacity close to the measured yield strength and yield strain. For a Case 2 specimen, $S=1$. A specimen with $\alpha \geq 4.11$ is classified as a Case 3 specimen, where the steel tube fails by mean of local buckling at a stress capacity less than the yield

stress. For a Case 3 specimen, the yield stress is multiplied by the factor S_2, to estimate the stress capacity or buckling stress of steel tube:

$$S_2 = \frac{1}{0.698 + 0.128\alpha \dfrac{4.00}{6.97}} \qquad (5.10)$$

where α is the normalized depth to thickness ratio.

The Case 2 specimens are used in this study, i.e., $S=1$. As shown in Fig. 5.43, from the equilibrium of axial forces, the nominal axial strength for CFT beam-column, P_n, can be expressed as:

$$P_n = \gamma_u f_c' \times k_1 x_n \times B_c + \sigma_y (b + 2x_n)t - \sigma_y \left[b + 2(B_c - x_n)\right]t \qquad (5.11)$$

where:

$\gamma_u = 1.67b^{-0.112}$, factor of scale effect, for simplification, a value of 0.85 can be used;

$\sigma_c = \gamma_u f_c'$, equivalent compressive stress, expressed in MPa;

$k_1 = 0.831 - 0.076(\sigma_c / 41.2) \geq 0.65$;

$k_2 = 0.429 - 0.010(\sigma_c / 41.2)$;

$B_c = b - 2t$, outside width of steel tube.

Then the distance x_n can be expressed as:

$$x_n = \left(P_n + 2\sigma_y B_c t\right) \Big/ \left(k_1 \gamma_u f_c' B_c + 4\sigma_y t\right) \qquad (5.12)$$

From the equilibrium of moment about the neutral axis, the nominal flexural strength for CFT beam-column, M_n, can be expressed as:

$$M_n = k_1 \left(\frac{B_c}{2} - k_2 x_n\right) x_n \gamma_u f_c' B_c + \sigma_y bt(b - t) + 2\sigma_y t x_n (B_c - x_n) \qquad (5.13)$$

A further limitation on column strength is imposed by ACI 318-99 in order to allow

for accidental eccentricities of loading, for columns with very small or zero calculated eccentricities:

$$P_n \leq 0.85P_0 \qquad (5.14)$$

where P_0 is the nominal strength of axially loaded column with zero eccentricity.

Using Equations 5.11 to 5.14, the interaction diagram for nominal CFT beam-column strength in combined bending and axial load can be obtained. The P-M interaction curve of CFT 22x22x0.6875 is shown in Fig. 5.45, along with the P-M diagram of CFT beam-column at the hinge location of the flexible six-story CFT MRF subjected the SAC 2/50 time-history, *lpvst03*. As shown in Fig. 5.45, for a given maximum axial force, P_{max}, obtained from a time-history analysis of the CFT MRF, the nominal axial strength, P_n, can be determined according to the corresponding moment, M_n, using the P-M interaction curve of CFT beam-column.

5.3.3 Local Performance of Six-Story CFT MRFs

5.3.3.1 Local Connection Performance

For the flexible six-story distributed CFT MRF subjected to SAC 2/50 and 50/50 time-histories, the local connection performance for the ***Immediate Occupancy*** (IO) and ***Collapse Prevention*** (CP) performance levels, corresponding to hazard level of 2% and 50% probability of exceedance in 50 years, respectively, are evaluated per FEMA 350 procedures. As shown in Table 5.9, for both the maximum value and the median value of the inter-story drift angles obtained from the analyses, the confidence levels for the local connection performance of the flexible twelve-story CFT MRFs are larger than 50% and

50%, for the immediate occupancy and collapse prevention performance levels, respectively, as required by FEMA 350.

Due to the fact that no factor and confidence level are recommended by FEMA 350 for the ***Life Safety*** (LS) level, for CFT MRFs subjected to the 10/50 SAC ground motion time-histories, only the global performance, i.e., the global behavior limited by inter-story drift, is evaluated according to the deflection and drift limits set by FEMA. No local behavior of CFT MRFs subjected to the 10/50 SAC ground motion time-histories will be evaluated.

5.3.3.2 Local Column Compression Performance

The local column compression performance of the flexible six-story distributed CFT MRF subjected to SAC 2/50 and 50/50 time-histories, corresponding to the ***Immediate Occupancy*** (IO) and ***Collapse Prevention*** (CP) performance levels, respectively, are evaluated per FEMA 350 procedures. The axial strength C of the CFT beam-column is determined in accordance with MAIJ method (Sakino and Nakahara, 2000). The P-M interaction curves of the left corner, interior and right corner columns of the flexible six-story CFT MRF subjected to SAC 2/50 time-history, *lpvst03,* are shown in Figs. 5.46a, 5.47a and 5.48a, respectively. The P-M interaction curves of the left corner, interior and right corner columns of the flexible six-story CFT MRF subjected to SAC 50/50 time-history, *lclgil2,* are shown in Figs. 5.49a, 5.50a and 5.51a, respectively. For a given maximum axial force, P_{max}, obtained from a time-history analysis of the CFT MRF, the nominal axial strength, P_n, can be determined according to the corresponding moment, M_n, using the P-M interaction curve of CFT beam-column, as presented in Chapter 5.3.2.

As shown in Table 5.10, for both the maximum value and the median value of the axial forces obtained from the analyses, the confidence levels for the local column compression performance of the flexible six-story CFT MRFs are larger than 50% and 90%, for the immediate occupancy and collapse prevention performance levels, respectively, as required by FEMA 350. Therefore, the global performance of the flexible six-story CFT MRF limited by inter-story drift, as well as the local connection performance and the local column compression performance for the ***Immediate Occupancy*** (IO) and ***Collapse Prevention*** (CP) performance levels meet the requirements of FEMA 350. In addition, the global performance of the flexible six-story CFT MRF limited by inter-story drift for the ***Life Safety*** (LS) performance level also meet the requirement of FEMA 368.

This evaluation procedure for the local column compression performance is also compared with the experiment results of CFT beam-columns (Varma, 2000). The normalized M-Φ interaction curves of the left corner, interior and right corner columns of the flexible six-story CFT MRF subjected to SAC 2/50 time-history, *lpvst03,* are shown in Figs. 5.46b, 5.47b and 5.48b, respectively, along with the experiment result of CFT beam-columns (Varma, 2000). The normalized M-Φ interaction curves of the left corner, interior and right corner columns of the flexible six-story CFT MRF subjected to SAC 50/50 time-history, *lclgil2,* are shown in Figs. 5.49b, 5.50b and 5.51b, respectively, along with the experiment result of CFT beam-columns (Varma, 2000). The experimental result was obtained from cyclic test of a CFT beam-column specimen CBC-32-80-20 with high-strength steel (σ_y=*80ksi*), high-strength concrete (f_c'=*16ksi*), nominal *b/t* ratio of *32*, and subjected to an axial level of $0.20P_0$ (P_0 is the axial load capacity of CFT).

The axial load level, the material properties and the nominal b/t ratio of the specimen CBC-32-80-20 are very similar to the high-strength CFT columns used in this research. As shown in Figs. 5.46b, 5.47b and 5.48b, local buckling of the steel tube flange (Point F) takes place in the CFT beam-columns of the six-story CFT MRF subjected to SAC 2/50 ground motions, while the CFT beam-columns fail when local buckling of the steel tube corner (Point H) takes place. Therefore, no failure takes place in the CFT beam-columns of the six-story CFT MRF subjected to SAC 2/50 ground motions, just the same as predicted by the confidence levels for the local column compression performance of the flexible six-story CFT MRFs, per FEMA 350 procedures.

5.3.4 Local Performance of Twelve-Story CFT MRFs

5.3.4.1 Local Connection Performance

For the flexible twelve-story distributed CFT MRF subjected to SAC 2/50 and 50/50 time-histories, the local connection performance for the ***Immediate Occupancy*** (IO) and ***Collapse Prevention*** (CP) performance levels, corresponding to hazard level of 2% and 50% probability of exceedance in 50 years, respectively, are evaluated per FEMA 350 procedures. As shown in Table 5.11, for both the maximum value and the median value of the inter-story drift angles obtained from the analyses, the confidence levels for the local connection performance of the flexible twelve-story CFT MRFs are larger than 50% and 50%, respectively, for the immediate occupancy performance level as required by FEMA 350.

For the collapse prevention performance level, the confidence level for the local connection performance obtained from the maximum value of inter-story drift angles is

less than 50%, while the confidence level for the local connection performance obtained from the median value of inter-story drift angles is larger than 50%. Since the SAC 2/50 and 50/50 ground motion records used in this study both consist with ten ground motions, which is larger than seven ground motions, according to FEMA 350, the median value of each of the response quantity may be use as the demand. The confidence level obtained from median values may be used as the expected confidence levels. Therefore, the local connection performances of the flexible twelve-story CFT MRT for both the immediate occupancy and collapse prevention performance levels have already met the requirements of FEMA 350.

Due to the fact that no factor and confidence level are recommended by FEMA 350 for the ***Life Safety*** (LS) level, for CFT MRFs subjected to the 10/50 SAC ground motion time-histories, only the global performance, i.e., the global behavior limited by inter-story drift, is evaluated according to the deflection and drift limits set by FEMA. No local behavior of CFT MRFs subjected to the 10/50 SAC ground motion time-histories will be evaluated.

5.3.4.2 Local Column Compression Performance

The local column compression performance of the flexible twelve-story distributed CFT MRF subjected to SAC 2/50 and 50/50 time-histories, corresponding to the ***Immediate Occupancy*** (IO) and ***Collapse Prevention*** (CP) performance levels, respectively, are evaluated per FEMA 350 procedures. The axial strength C of the CFT beam-column is determined in accordance with MAIJ method (Sakino and Nakahara, 2000). The P-M interaction curves of the left corner, interior and right corner columns of

the flexible twelve-story CFT MRF subjected to SAC 2/50 time-history, *lpvst03,* are shown in Figs. 5.52a, 5.53a and 5.54a, respectively. The P-M interaction curves of the left corner, interior and right corner columns of the flexible twelve-story CFT MRF subjected to SAC 50/50 time-history, *lclgil2,* are shown in Figs. 5.55a, 5.56a and 5.57a, respectively. For a given maximum axial force, P_{max}, obtained from a time-history analysis of the CFT MRF, the nominal axial strength, P_n, can be determined according to the corresponding moment, M_n, using the P-M interaction curve of CFT beam-column, as presented in Chapter 5.3.2.

As shown in Table 5.12, for both the maximum value and the median value of the axial forces obtained from the analyses, the confidence levels for the local column compression performance of the flexible twelve-story CFT MRFs are larger than 50% and 90%, for the immediate occupancy and collapse prevention performance levels, respectively, as required by FEMA 350. Therefore, the global performance of the flexible twelve-story CFT MRF limited by inter-story drift, as well as the local connection performance and the local column compression performance for the ***Immediate Occupancy*** (IO) and ***Collapse Prevention*** (CP) performance levels meet the requirements of FEMA 350. In addition, the global performance of the flexible twelve-story CFT MRF limited by inter-story drift for the ***Life Safety*** (LS) performance level also meet the requirement of FEMA 368.

This evaluation procedure for the local column compression performance is also compared with the experiment results of CFT beam-columns (Varma, 2000). The normalized M-Φ interaction curves of the left corner, interior and right corner columns of the flexible twelve-story CFT MRF subjected to SAC 2/50 time-history, *lpvst03,* are

shown in Figs. 5.52b, 5.53b and 5.54b, respectively, along with the experiment result of CFT beam-columns (Varma, 2000). The normalized M-Φ interaction curves of the left corner, interior and right corner columns of the flexible twelve-story CFT MRF subjected to SAC 50/50 time-history, *lclgil2,* are shown in Figs. 5.55b, 5.56b and 5.57b, respectively, along with the experiment result of CFT beam-columns (Varma, 2000). The experimental result was obtained from cyclic test of a CFT beam-column specimen CBC-32-80-20 with high-strength steel (σ_y=*80ksi*), high-strength concrete (f_c'=*16ksi*), nominal *b/t* ratio of *32*, and subjected to an axial level of $0.20P_0$ (P_0 is the axial load capacity of CFT). The axial load level, the material properties and the nominal b/t ratio of the specimen CBC-32-80-20 are very similar to the high-strength CFT columns used in this research. As shown in Figs. 5.52b, 5.53b and 5.54b, initial crushing of concrete (Point E) other than local buckling of the steel tube (Point F) takes place in the CFT beam-columns of the twelve-story CFT MRF subjected to SAC 2/50 ground motions, while the CFT beam-columns fail when local buckling of the steel tube corner (Point H) takes place. Therefore, no failure takes place in the CFT beam-columns of the twelve-story CFT MRF subjected to SAC 2/50 ground motions, just the same as predicted by the confidence levels for the local column compression performance of the flexible twelve-story CFT MRFs, per FEMA 350 procedures.

5.4 Time-History Analysis: Higher Mode and P-Δ Effects

Estimation of inter-story drift demands is of great significance in seismic design of moment resisting frames, because of the exceedence of allowable limits would cause great damage in both structural and non-structural components. Another concern in the

design of CFT MRFs is to avoid excessive second-order P-Δ effects, which may, but not necessary will, bring the structure close to incremental collapse. Collapse may occur if an individual story displaces sufficiently so that the second-order P-Δ effects fully offset the first-order story shear resistance and instability occurs (Gupta and Krawinkler, 2000a).

The static pushover analysis can be used to evaluate the seismic performance of the structures, by pushing the structure under a predetermined or adaptive load pattern to a target displacement, which represent the maximum demands experienced by the structure in the design earthquake, and comparing the deformation demands computed at the target displacement to available capacities. The roof displacement caused by the design ground motion can be predicted with reasonable accuracy, provided that it is controlled by the first mode and the P-Δ sensitive range is not entered (Gupta and Krawinkler, 2000b).

Another drawback of the pushover analysis is that it is difficult to predict maximum dynamic story drift demands over the height of the structure as a function of the roof drift, on account of the dependence of the relationship on a multitude of factors, e.g., higher mode effects, P-Δ effects and characteristics of ground motions (Gupta and Krawinkler, 2000b).

As presented in Chapter 5.2, higher mode effects on the distribution of inter-story drifts over height for flexible distributed CFT MRFs cannot be neglected, especially for the flexible distributed twelve-story CFT MRF. However, currently there is a lack of knowledge of the second-order P-Δ effects on the seismic performance of CFT MRFs. The influence of higher mode effects and P-Δ effects on the seismic performance of CFT MRFs will be investigated in this section by comparing the results of the pushover and time-history analyses.

5.4.1 Pushover Analysis Results: P-Δ Effects

As shown in Figs. 5.58 to 5.60, the post-yield response of the pushover analysis results for the flexible six-story CFT MRF exhibits a short "yield" (constant strength) plateau until a roof drift angle of about 0.025, followed by a rapid decrease in lateral load resistance represented by the negative slope of the curve. The bottom three stories exhibit similar negative post-yield stiffness values, which are higher than the post-yield stiffness of the global (roof) drift angle. The 4^{th} story has a negative post-yield stiffness very close to that of the global (roof) drift angle. As the structure is pushed to larger displacements beyond 0.025 global drift, which is also the global (roof) drift at which the slope of the global push over curve clearly becomes negative, the top two stories experience unloading, and the lateral loads applied to the structure have to be reduced to accommodate the increasing second-order P-Δ effects in the lower stories. Thus, as the roof displacement increases, the story drifts in the top two stories decrease. Therefore, sudden amplification of story drift in lower stories of this six-story CFT MRF is due to the second-order P-Δ effects, while the occurrence of such amplification in upper stories is attributed to higher mode effects.

For the flexible twelve-story CFT MRF, as shown in Figs. 5.61 to 5.63, the post-yield response of the pushover analysis results exhibits a relatively long "yield" (constant strength) plateau until a roof drift angle of about 0.042, followed by a rapid decrease in lateral load resistance represented by the negative slope of the curve. The lower six stories exhibit similar negative post-yield stiffness values, which are also close to the post-yield stiffness of the global (roof) drift angle. The 7^{th} to 10^{th} stories have negative post-yield stiffness slightly higher that of the global (roof) drift angle. As the structure is

pushed to larger displacements beyond 0.042 global drift, which is also the global (roof) drift at which the slope clearly becomes negative, the top two stories, especially the 12th story, exhibit negative post-yield stiffness values, which are much higher than the post-yield stiffness of the global (roof) drift angle. As the global (roof) drift angle approaches close to 0.078, the top two stories experience unloading, and the lateral loads applied to the structure have to be reduced to accommodate the increasing second-order P-Δ effects in the lower stories. Thus, as the roof displacement increases, the story drifts in the top two stories decrease. Therefore, sudden amplification of story drift in lower stories of this twelve-story CFT MRF is due to the second-order P-Δ effects, while the occurrence of such amplification in upper stories is attributed to higher mode effects.

5.4.2 Higher Mode and P-Δ Effects of Six-Story CFT MRF

The 1st to 4th modes properties of the flexible ($1<T_1/T_{max}<1.15$) six-story and twelve-story distributed CFT MRFs are shown in Table 5.13. As shown in Table 5.13, the effective modal masses for the 1st to 4th modes of the flexible ($1<T_1/T_{max}<1.15$) six-story distributed CFT MRF are 81.5%, 10.9%, 4.5%, and 1.8%, respectively. According to FEMA 356, this six-story CFT MRF has more than 75% of the total mass participating in the 1st mode and can be categorized as a fundamental mode dominated structure. However, the results of time-history analysis and pushover analysis show that higher mode effects and P-Δ effects on the seismic performance of the fundamental mode dominated six-story CFT MRFs should not be neglected.

The story drift envelop, variation of story drift angle to roof drift angle over height of structure, as well as the normalized base shear-roof drift angle relationships obtained

from both the pushover and time-history analyses of the flexible six-story CFT MRF subjected to SAC 2/50, 10/50 and 50/50 time-histories are shown in Figs. 5.64 to 5.74 Figs. 5.75 to 5.82, and Figs. 5.83 to 5.91, respectively. The story drift envelops, the variation of story drift to roof drift over the height, as well as the normalized base shear-roof drift angle relationships obtained from both the pushover and time-history analyses, provide much insight into the higher mode effects and the second-order P-Δ effects on the seismic behavior of CFT MRFs.

5.4.2.1 Six-Story CFT MRF Subjected to SAC 2/50 ground motions

As shown in Figs. 5.64 to 5.74, only two of the SAC 2/50 ground motions, *ltbtab* and *lepst10*, demonstrate the higher mode effects on the distribution inter-story drift demands over the height. As shown in Figs. 5.69 and 5.70, it is due to the fact that the roof displacements of these two time-histories are less than the design drift, Δ_d, at which the maximum inter-story drift angle reaches the design limit in pushover analysis (1.5% for the case of CFT MRFs) and beyond which the second-order P-Δ effects on the seismic performance of the structure cannot be neglected.

While for the other eight time-histories of the SAC 2/50 ground motions, the global (roof) drift angles have either entered the "yield" (constant strength) plateau, at which the second-order P-Δ effects on the seismic performance of the structure becomes significant, or at less larger than the design drift, Δ_d, e.g., in the case of the 2/50 time-history, *llpglc*. Since the maximum roof drift angle of the other eight time-histories of the SAC 2/50 ground motions is about 0.018, which is less than 0.025, at which the slope of the global push over curve clearly becomes negative, the second-order P-Δ effects have not fully

offset the first-order story shear resistance and dynamic instability is considered an unlikely event. However, the second-order P-Δ effects control the seismic performance of the flexible six-story distributed CFT MRF subjected to these eight time-histories of the SAC 2/50 ground motions, and the maximum story drifts occur in the 2nd story for all these eight 2/50 ground motions.

The shapes of the variation of story drift angle to roof drift angle over height and the normalized base shear-roof drift angle relationships obtained from time-history analysis also provide helpful information to distinguish the higher mode effects and P-Δ effects on the seismic performance of the six-story CFT MRFs. As shown in Figs. 5.64 to 5.74, for the higher mode effects dominated cases, both the story drift angle to roof drift angle over height and the normalized base shear-roof drift angle relationships obtained from time-history analysis have more complicate shapes than those of the P-Δ effects dominated cases. In the P-Δ effects dominated cases, the maximum ratios of story drift to roof drift all occur at the 2nd story, and the ratios approximately linearly decrease to the minimum ratios at the 6th story. The backbone curves of the normalized base shear-roof drift angle curves obtained from time-history analysis in the P-Δ effects dominated cases all approximately coincide with the pushover analysis results.

On the contrary, in those higher mode effects dominated cases, the shapes for the ratios of story drift to roof drift over height become more complex saddle shapes, in which the ratios at the 2nd and the 4th stories both achieve local peak values. In addition, the backbone curves of the normalized base shear-roof drift angle curves obtained from time-history analysis in the higher mode effects dominated cases may not coincide with the pushover analysis results, or even vibrate around the pushover curves.

5.4.2.2 Six-Story CFT MRF Subjected to SAC 10/50 ground motions

As shown in Figs. 5.75 to 5.82, for the SAC 10/50 ground motions, only two time-histories, *livar05* and *lnrrrs*, demonstrate the influence of P-Δ effects on the distribution inter-story drift demands over the height. It is due to the fact that the roof displacements of these two time-histories are larger than the design drift, Δ_d, at which the maximum inter-story drift angle reaches the design limit in pushover analysis (1.5% for the case of CFT MRFs) and beyond which the second-order P-Δ effects on the seismic performance of the structure cannot be neglected. For these two time-histories, the maximum story drifts occur at the 2nd story, and the story drifts monotonically decrease to the minimum ratios at the 6th story.

While for the other eight time-histories of the SAC 10/50 ground motions, the global (roof) drift angles are all less than the design drift, Δ_d, below which the second-order P-Δ effects on the seismic performance of the structure could be neglected. The higher mode effects control the seismic performance of the flexible six-story distributed CFT MRF subjected to these eight time-histories of the SAC 10/50 ground motions. For these eight time-histories, almost all the maximum story drifts occur at the 4th or 5th stories for these 10/50 ground motions. The only two exceptions are the time-histories, *l40ivir* and *livar06*, in which the maximum story drifts occur at the 2nd story in the negative direction only, yet still with relative large story drifts in the 3rd and the 4th stories, which are close to the maximum story drifts occur at the 2nd story.

As in the cases of SAC 2/50 ground motions, for the higher mode effects dominated cases, both the story drift angle to roof drift angle over height and the normalized base shear-roof drift angle relationships obtained from time-history analysis have more

complicate shapes than those of the P-Δ effects dominated cases. In the P-Δ effects dominated cases, the maximum ratios of story drift to roof drift all occur at the 2nd story and the ratios monotonically decrease to the minimum ratios at the 6th story. The backbone curves of the normalized base shear-roof drift angle curves obtained from time-history analysis in the P-Δ effects dominated cases all approximately coincide with the pushover analysis results.

On the contrary, in the higher mode effects dominated cases, the shapes for the ratios of story drift to roof drift over height become very complex zigzag shapes, in which the ratios at the 2nd and the 4th stories both achieve local peak values, and the values at the 5th story is larger than or close to that at the 3rd story. The shapes for the ratios of story drift to roof drift of the time-history, *lpsdhsp*, even exhibit a large ratio at the 5th story, demonstrating the great importance of higher mode effects generated by this ground motion. In addition, the backbone curves of the normalized base shear-roof drift angle curves obtained from time-history analysis in the higher mode effects dominated cases may not coincide with the pushover analysis results, or even vibrate around the pushover curves.

5.4.2.3 Six-Story CFT MRF Subjected to SAC 50/50 ground motions

As shown in Figs. 5.83 to 5.91, for the SAC 50/50 ground motions, the higher mode effects control the seismic performance of the flexible six-story distributed CFT MRF. It is due to the fact that the roof displacements under these ground motions are all less than the design drift, Δ_d, below which the second-order P-Δ effects on the seismic performance of the structure could be neglected and higher mode effects may control the seismic

performance of the structure. Almost all the maximum story drifts occur at the 4th or 5th stories for these 50/50 ground motions. The only two exceptions are the time-histories, *lclgil2* and *livar06*, in which the maximum story drifts occur at the 2nd story, yet still with relative large story drifts in the 4th and the 5th stories, which are close to the maximum story drifts occur at the 2nd story.

As in the cases of SAC 10/50 ground motions, for the higher mode effects dominated cases, both the story drift angle to roof drift angle over height and the normalized base shear-roof drift angle relationships obtained from time-history analysis have more complicate shapes than those of the P-Δ effects dominated cases. The shapes for the ratios of story drift to roof drift over height become very complex zigzag shapes, in which the ratios at the 2nd and the 4th or the 5th stories both achieve local peak values. The shapes for the ratios of story drift to roof drift of the time-history, *lpkcs05*, even exhibit a very large ratio at the 5th story, demonstrating the great importance of higher mode effects generated by this ground motion. In addition, the backbone curves of the normalized base shear-roof drift angle curves obtained from time-history analysis in the higher mode effects dominated cases may not coincide with the pushover analysis results, or even vibrate around the pushover curves.

The median, maximum and minimum values of the ratios of story drift to roof drift for the flexible six-story distributed CFT MRF subjected to the SAC 2/50, 10/50 and 50/50 ground motions are presented in Figs. 5.92, 5.93 and 5.94, respectively. The median values of the ratios of story drift to roof drift represent the influence of higher mode and P-Δ effects on the distribution of inter-story drift over height. As shown in Fig. 5.92, the 2/50 ground motions exhibit great influence of the P-Δ effects, with the

maximum values of the ratios of story drift to roof drift occur at the 2nd story and monotonically decrease to the minimum values at the 6th story.

While the 10/50 and 50/50 ground motions all exhibit the influence of the higher mode effects. The shapes of the story drift to roof drift ratios over the building height become very complex zigzag shapes, in which the ratios at the 2nd and the 4th stories both achieve local peak values, and the values at the 5th story is larger than or close to that at the 3rd story. The influence of the higher mode effects for the 50/50 ground motions is greater than that for the 10/50 ground motions, which is demonstrated by the fact that the shapes of the variation of the story drift to roof drift ratios are similar, but the ratios of the 50/50 ground motions are all larger than the corresponding values of the 10/50 ground motions.

As shown in Figs. 5.92, 5.93 and 5.94, the story drift to roof drift ratios are larger than 1.0 for most stories. The reason is that the maximum inter-story drifts do not occur simultaneously in all stories. Therefore, the sum of the maximum story displacements is always larger than the maximum roof displacement. If pushover analysis is used to capture all maximum story drifts over height of CFT MRFs, the target displacement should be amplified by the median ratios of the sum of maximum story displacements to maximum roof displacement, as listed in Table 5.14.

Another observation from the story drift to roof drift ratios over the building height of the flexible six-story CFT MRF subjected to SAC 2/50, 10/50 and 50/50 time-histories is that, for a first mode dominated low-rise CFT MRF with effective modal masses for the 1st mode larger than 80%, the distribution of the story drift to roof drift ratios over the building height is sensitive to the severity of the records. For example, for the same time-

history, *lnrrrs*, the maximum ratios of story drift to roof drift in both the 2/50 and 10/50 hazard levels occur at the 2nd story, the ratios in the 2/50 hazard level approximately linearly decrease to the minimum ratios at the 6th story, while the ratio in the 10/50 hazard level monotonically decrease to the minimum ratios at the 6th story, with the value at the 4th story close to that at the 3rd story. It is different from the observation for a 20-story steel structure subjected to the same ground motion records (Gupta and Krawinkler, 2000b), in which the distribution and values of the story drift to roof drift ratios over the building height for the 2/50 and 10/50 sets of ground motions are similar, indicating little sensitivity to the severity of the records.

5.4.3 Higher Mode Effects and P-Δ Effects of Twelve-Story CFT MRF

As shown in Table 5.13, the effective modal masses for the 1st to 4th modes of the flexible ($1<T_1/T_{max}<1.15$) twelve-story distributed CFT MRF are 75.3%, 12.7%, 5.1%, and 2.8%, respectively. According to FEMA 356, this twelve-story CFT MRF has more than 75% of the total mass participating in the 1st mode and can be categorized as a fundamental mode dominated structure. However, the results of time-history analysis and pushover analysis show that higher mode effects and P-Δ effects on the seismic performance of the fundamental mode dominated twelve-story CFT MRFs should not be neglected.

The story drift envelop, variation of story drift angle to roof drift angle over height of structure, as well as the normalized base shear-roof drift angle relationships obtained from both the pushover and time-history analyses of the flexible twelve-story CFT MRF subjected to SAC 2/50, 10/50 and 50/50 time-histories are shown in Figs. 5.95 to 5.105,

Figs. 5.106 to 5.113, and Figs. 5.114 to 5.122, respectively. The story drift envelops, the variation of story drift to roof drift over the height, as well as the normalized base shear-roof drift angle relationships obtained from both the pushover and time-history analyses, provide much insight into the higher mode effects and the second-order P-Δ effects on the seismic behavior of CFT MRFs.

5.4.3.1 Twelve-Story CFT MRF Subjected to SAC 2/50 ground motions

As shown in Figs. 5.95 to 5.105, the higher mode effects control the seismic performance of the flexible twelve-story distributed CFT MRF subjected to the SAC 2/50 ground motions. It is due to the fact that the effective modal masses for the 1st mode of this twelve-story CFT MRF is 75.3%, which is slightly larger than 75% but less than 80%, below which the higher mode effects on the seismic performance of CFT MRF should not be neglected, according to the pushover analysis and time history analysis results of this study. In addition, for the case in which the roof displacements of the time-history analysis are larger than the design drift, Δ_d, the second-order P-Δ effects on the seismic performance of the structure cannot be neglected. Especially for the cases in which the global (roof) drift angles have entered the "yield" (constant strength) plateau, the second-order P-Δ effects on the seismic performance of the structure becomes significant, yet the higher mode effects still control the seismic performance of this CFT MRF in this case. Since the maximum roof drift angle of the SAC 2/50 ground motions is about 0.019, which is less than 0.042, at which the slope of the global push over curve clearly becomes negative, the second-order P-Δ effects have not fully offset the first-order story shear resistance and dynamic instability is considered an unlikely event.

As shown in Figs. 5.95 to 5.105, for the cases in which roof displacements are less than the design drift, Δ_d, the higher mode effects on the seismic performance of this CFT MRF become significant, and the shapes of the story drift to roof drift ratios become bell shapes, with the maximum ratio of story drift to roof drift occur at the 9th story. The backbone curves of the normalized base shear-roof drift angle curves obtained from time-history analysis in the higher mode effects dominated cases intensively vibrate around the pushover curves.

For the cases in which roof displacements are larger than the design drift, Δ_d, but haven't entered the "yield" (constant strength) plateau, the second-order P-Δ effects on the seismic performance of the structure cannot be neglected. For example, for the time-history "*llplgpc*", the maximum ratios of story drift to roof drift shifts from the 9th story to the 7th story in the positive direction, and the shape of these ratios becomes a saddle shape in the negative direction, in which the ratios at the 3rd and the 9th stories both achieve local peak values.

For the cases in which roof displacements have entered the "yield" (constant strength) plateau, the second-order P-Δ effects becomes significant, yet the higher mode effects still control the seismic performance. For example, for the time-histories *lepst13*, *lpvst03* and *lpvst06*, the maximum ratios of story drift to roof drift all shift from the 9th story to the 5th story.

5.4.3.2 Twelve-Story CFT MRF Subjected to SAC 10/50 ground motions

As shown in Figs. 5.106 to 5.113, for the SAC 10/50 ground motions, the higher mode effects control the seismic performance of the flexible twelve-story distributed CFT MRF. It is due to the fact that the roof displacements of these time-histories are all less

than the design drift, Δ_d, below which the second-order P-Δ effects on the seismic performance of the structure could be neglected. Almost all the maximum story drifts occur at the 9th or 10th stories for these 10/50 ground motions. The only exception is the time-history "*lnrsylm*", in which the maximum story drifts occur at the 7th story in the negative direction, yet still with relative large local peak story drifts in the 3rd and the 9th stories, which are close to the maximum story drifts occur at the 7th story.

5.4.3.3 Twelve-Story CFT MRF Subjected to SAC 50/50 ground motions

As shown in Figs. 5.114 to 5.122, for the SAC 50/50 ground motions, the higher mode effects control the seismic performance of the flexible twelve-story distributed CFT MRF. It is due to the fact that the roof displacements under these ground motions are all less than the design drift, Δ_d, below which the second-order P-Δ effects on the seismic performance of the structure could be neglected and higher mode effects may control the seismic performance of the structure. Almost all the maximum story drifts occur at the 9th or 10th stories for these 50/50 ground motions. The three exceptions are the time-histories, *lclgil2, lknhsbf* and *lpkcs05*. For the time-history "*lclgil2*", the maximum story drifts occur at the 7th story in the negative direction, yet still with relative large story drifts in the 9th story, which is close to the maximum story drifts occur at the 7th story. The ratios of story drift to roof drift of the two time-histories, *lknhsbf* and *lpkcs05*, exhibit a very large ratio at the 11th story, demonstrating the great importance of higher mode effects generated by this ground motion, which is similar to the case in which the flexible six-story distributed CFT MRF subjected to the time-history "*lpkcs05*".

The median, maximum and minimum values of the ratios of story drift to roof drift for the flexible twelve-story distributed CFT MRF subjected to the SAC 2/50, 10/50 and

50/50 ground motions are presented in Figs. 5.123, 5.124 and 5.125, respectively. The median values of the ratios of story drift to roof drift represent the influence of higher mode and P-Δ effects on the distribution of inter-story drift over height. As shown in Fig. 5.123, the seismic performance of this twelve-story CFT MRF subjected to the 2/50 ground motions is controlled by the higher mode effects, yet still influenced by the P-Δ effects, with the maximum values of the ratios of story drift to roof drift occur at the 7^{th} story and achieves a local peak value at the 9^{th} story, which is close to the maximum value at the 7^{th} story.

The influence of the higher mode effects for the 50/50 ground motions is greater than that for the 10/50 ground motions, which is demonstrated by the fact that the shapes of the variation of the story drift to roof drift ratios are similar, but the ratios of the 50/50 ground motions in the upper six stories, i.e., the 7^{th} to the 12^{th} stories, are all larger than the corresponding values of the 10/50 ground motions. In addition, for the 10/50 sets, the maximum value of the ratios for the story drift to roof drift occurs at the 10^{th} story. While for the 50/50 sets, the maximum value of the story drift to roof drift ratios occurs at the 11^{th} story, demonstrating the great importance of higher mode effects. . In addition, the backbone curves of the normalized base shear-roof drift angle curves obtained from time-history analysis of the flexible twelve-story distributed CFT MRF subjected to the SAC 2/50, 10/50 and 50/50 ground motions are not coincide with the pushover analysis results, and even vibrate around the pushover curves in many cases.

As shown in Figs. 5.123, 5.124 and 5.125, the story drift to roof drift ratios are larger than 1.0 for most stories. The reason is that the maximum inter-story drifts do not occur simultaneously in all stories. Therefore, the sum of the maximum story displacements is

always larger than the maximum roof displacement. If pushover analysis is used to capture all maximum story drifts over height of CFT MRFs, the target displacement should be amplified by the median ratios of the sum of maximum story displacements to maximum roof displacement, as listed in Table 5.14.

Another observation from the story drift to roof drift ratios over the building height of the flexible twelve-story CFT MRF subjected to SAC 2/50, 10/50 and 50/50 time-histories is that, for a higher mode effects dominated medium-rise CFT MRF with effective modal masses for the 1st mode less than 80%, the distribution of the story drift to roof drift ratios over the building height indicate little sensitivity to the severity of the records. For example, for the same time-history, *lnrrrs*, the distribution and values of the ratios of story drift to roof drift in both the 2/50 and 10/50 hazard levels are similar. It is the same as the observation for a 20-story steel structure subjected to the same ground motion records (Gupta and Krawinkler, 2000b).

5.5 Summary and Conclusion

The global and local seismic performances of the six-story and twelve-story CFT MRFs were evaluated by following FEMA 350 procedures to determine a level of confidence in the building's ability to meet the desired performance objectives, based on the time-history results of the six-story and twelve-story CFT MRF subjected to SAC 2/50, 10/50 and 50/50 ground motions. The global performance of the flexible ($1<T_1/T_{max}<1.15$) six-story and twelve-story distributed CFT MRF limited by inter-story drift, as well as the local connection performance and the local column compression performance for the ***Immediate Occupancy*** (IO) and ***Collapse Prevention*** (CP) performance levels meets the requirements of FEMA 350. In addition, the global

performance of the flexible six-story and twelve-story CFT MRF limited by inter-story drift for the ***Life Safety*** (LS) performance level also meets the requirement of FEMA 368.

The story drift envelop, variation of story drift angle to roof drift angle over height of structure, in combination with the normalized base shear-roof drift angle relationships obtained from both the pushover and time-history analyses of the flexible six-story CFT MRF subjected to SAC 2/50, 10/50 and 50/50 ground motions were used to provide insight into higher mode and second-order P-Δ effects on the global seismic performance of the six-story and twelve-story CFT MRFs. The normalized base shear-roof drift angle relationships obtained from the pushover analysis provide good indices to distinguish the influence zones of the higher mode and second-order P-Δ effects. For the cases in which the roof displacements of the time-history analysis are larger than the design drift, Δ_d, the second-order P-Δ effects on the seismic performance of the structure should not be neglected. Especially for the cases in which the global (roof) drift angles have entered the "yield" (constant strength) plateau, the second-order P-Δ effects on the seismic performance of the structure becomes significant.

The roof displacements of the time-history analysis for the six-story and twelve-story CFT MRF subjected to the SAC 2/50 ground motions are all larger than the design drift, Δ_d, and in some cases have even entered the "yield" (constant strength) plateau. With more than 80% of the total mass participating in the 1st mode, the seismic performance of the six-story CFT MRF subjected to the 2/50 ground motions is controlled by P-Δ effects. While with less than 80% of the total mass participating in the 1st mode, the seismic performance of the twelve-story CFT MRF subjected to the 2/50 ground motions is controlled by higher mode effects, yet still influenced by P-Δ effects. Since the

maximum roof drift angles of the six-story and twelve-story CFT MRFs subjected to the SAC 2/50 ground motions are all less than the roof drift angle at which the slope of the global push over curve clearly becomes negative, the second-order P-Δ effects have not fully offset the first-order story shear resistance and dynamic instability is considered an unlikely event.

Almost all the roof displacements of the time-history analysis for the six-story and twelve-story CFT MRF subjected to the SAC 10/50 and 50/50 ground motions, except for the cases in which the six-story CFT MRF subjected to the two 10/50 ground motions, *livar05* and *lnrrrs*, are all less than the design drift, Δ_d. Except for the cases in which the six-story CFT MRF subjected to the two 10/50 ground motions, the seismic performances of the six-story and twelve-story CFT MRFs subjected to the 10/50 and 50/50 ground motions are all controlled by the higher mode effects. For the cases in which the six-story CFT MRF subjected to the two 10/50 ground motions, P-Δ effects control the seismic performance of the six-story CFT MRF.

For a structure with a negative post-yield stiffness for the simplified pushover curve, which is simplified per FEMA 356 bilinear simplification procedure, it is usually considered to be a structure prone to dynamic instability. One important finding based on the pushover and time-history analyses results is that, the desired global and local performance objectives of such a structure could still be met, providing that the maximum roof drift angle has entered the relatively short "yield" (constant strength) plateau of the actual pushover curve, but is less than the roof drift angle at which the slope of the actual pushover curve clearly becomes negative. The second-order P-Δ effects do not fully offset the first-order story shear resistance and dynamic instability is

considered an unlikely event in this case. For example, the flexible six-story distributed CFT MRF has a negative post-yield stiffness for the simplified pushover curve. It still meets all the desired global and local performance objectives since the maximum roof drift angle has entered the relatively short "yield" (constant strength) plateau of the actual pushover curve, but is less than the roof drift angle at which the slope of the actual pushover curve clearly becomes negative.

For the six-story and twelve-story CFT MRFs subjected to the SAC 2/50, 10/50 and 50/50 ground motions, the story drift to roof drift ratios are larger than 1.0 for most stories. The sum of the maximum story displacements is always larger than the maximum roof displacement. If pushover analysis is used to capture all maximum story drifts over height of CFT MRFs, the target displacement should be amplified by the median ratios of the sum of maximum story displacements to maximum roof displacement, as listed in Table 5.14.

Another observation from the story drift to roof drift ratios over the building height of the flexible six-story and twelve-story CFT MRFs subjected to SAC 2/50, 10/50 and 50/50 time-histories is that, for a first mode dominated low-rise CFT MRF with effective modal masses for the 1st mode larger than 80%, the distribution of the story drift to roof drift ratios over the building height is sensitive to the severity of the records. While for a higher mode effects dominated medium-rise CFT MRF with effective modal masses for the 1st mode less than 80%, the distribution of the story drift to roof drift ratios over the building height indicate little sensitivity to the severity of the records, which is the same as the observation for a 20-story steel structure subjected to the same ground motion records (Gupta and Krawinkler, 2000b).

Table 5.1 SAC 2% in 50 years time histories (Los Angles, Site Class D)

Earthquake	M_w	Stn	R-km	Scale	Filename	Comments
1995 Kobe	6.9	jma	3.4	0.46	lkbjma	Japan, thin alluvium
1989 Loma Prieta	7.0	lgpc	3.5	0.53	llplgpc	
1994 Northridge	6.7	rrs	7.5	0.59	lnrrs	
1994 Northridge	6.7	sylm	6.4	0.97	lnrsylm	
1974 Tabas	7.4	tab	1.2	0.99	ltbtab	Iran
Elysian Park 1	7.1	st04	17.5	0.62	lepst04	simulation
Elysian Park 2	7.1	st10	10.7	0.67	lepst10	simulation
Elysian Park 3	7.1	st13	11.2	0.62	lepst13	simulation
Palos Verdes 1	7.1	st03	1.5	0.55	lpvst03	simulation
Palos Verdes 2	7.1	st06	1.5	0.68	lpvst06	simulation

Table 5.2 SAC 10% in 50 years time histories (Los Angles, Site Class D)

Earthquake	M_w	Stn	R-km	Scale	Filename	Comments
1940 Imperial Valley	6.9	ivir	10	1.94	l40ivir	
1979 Imperial Valley	6.5	ar05	4.1	1.17	livar05	
1979 Imperial Valley	6.5	ar06	1.2	1.09	livar06	
1992 Landers	7.3	bars	36	2.92	llnbars	
1992 Landers	7.3	yerm	25	1.31	llnyerm	
1989 Loma Prieta	7.0	gil3	12.4	1.38	llpgil3	
1994 Northridge	6.7	newh	6.7	0.49	lnrnewh	
1994 Northridge	6.7	rrs	7.5	0.39	lnrrrs	
1994 Northridge	6.7	sylm	6.4	0.64	lnrsylm	
1986 N.Palm Springs	6.0	dhsp	6.7	1.80	lpsdhsp	

Table 5.3 SAC 50% in 50 years time histories (Los Angles, Site Class D)

Earthquake	M_w	Stn	R-km	Scale	Filename	Comments
1979 Coyote Lake	5.7	gil2	8.8	1.57	lclgil2	Gilroy 2
1979 Imperial Valley	6.5	ar06	1.2	0.82	livar06	Array 6
1952 Kern	7.7	hsbf	107	3.70	lknhsbf	Hollywood Storage FF
1992 Landers	7.3	frti	64	3.84	llnfrti	Fort Irwin
1984 Morgan Hill	6.2	gil3	15	2.35	lmhgil3	Gilroy 3
1966 Parkfield	6.1	cs05	3.7	1.98	lpkcs05	Cholame 5W
1966 Parkfield	6.1	cs08	8.0	3.06	lpkcs08	Cholame 8W
1986 N.Palm Springs	6.0	plma	9.6	2.50	lpsplma	Palm Springs Airport
1971 San Fernando	6.5	hsbf	10	1.78	lsfhsbf	Hollywood Storage FF
1987 Whittier	6.0	down	17	1.35	lwhdown	Downey

Table 5.4 FEMA 350 recommend minimum confidence levels

Behavior	Performance level	
	Immediate Occupancy	Collapse Prevention
Global behavior limited by inter-story drift	50%	90%
Local connection behavior limited by inter-story drift	50%	50%
Column compression behavior	50%	90%

Table 5.5 FEMA 350 global inter-story drift angle capacity C and resistance factor ϕ for regular SMF buildings

Building Height	Performance level			
	Immediate Occupancy		Collapse Prevention	
	C	ϕ	C	ϕ
Low rise (3 stories or less)	*0.02*	*1.0*	*0.10*	*0.90*
Mid rise (4-12 stories)	*0.02*	*1.0*	*0.10*	*0.85*
High rise (>12 stories)	*0.02*	*1.0*	*0.085*	*0.75*

Table 5.6 FEMA 350 inter-story drift angle capacity C (θ_{IO}, θ_U) and capacity reduction factor ϕ for Bolted Flange Plate (BFP) and Double Split Tee (DST) connections as limited by local connection response

Connection Type	Immediate Occupancy		Collapse Prevention	
	θ_{IO}	ϕ	θ_U	ϕ
BFP	*0.15*	*0.9*	*0.10-0.001d_b*	*0.9*
DST	*0.15*	*0.9*	*0.14-0.0032d_b*	*0.9*

Note: d_b is the beam depth, inches.

Table 5.7 Global performance evaluation of flexible six-story distributed CFT MRF for immediate occupancy and collapse prevention performance levels

Performance level			Immediate Occupancy	Collapse Prevention
Capacity	C		*0.02*	*0.10*
	ϕ		*1.0*	*0.85*
Demand	D	*Max.*[1]	*0.0093744*	*0.0273227*
		Median[2]	*0.0070592*	*0.0161339*
	γ_a		*1.02*	*1.06*
	γ		*1.4*	*1.2*
Uncertainty coefficient β_{UT}			*0.20*	*0.4*
Factored-demand-to-capacity ratio λ	*Max.*[1]		*0.6693*	*0.4089*
	Median[2]		*0.5040*	*0.2414*
Confidence level of λ, given β_{UT}	*Max.*[1]		*99%>50%, OK*	*99%>90%, OK*
	Median[2]		*99%>50%, OK*	*99%>90%, OK*

Note: 1. *Max.* = the maximum values of the inter-story drift angles obtained from any of the analyses;

2. *Median* = the maximum of the median value for each of the inter-story drift angles obtained from the analyses.

Table 5.8 Global performance evaluation of flexible twelve-story distributed CFT MRF for immediate occupancy and collapse prevention performance levels

Performance level			Immediate Occupancy	Collapse Prevention
Capacity	C		*0.02*	*0.10*
	ϕ		*1.0*	*0.85*
Demand	D	*Max.*[1]	*0.0076547*	*0.0298313*
		Median[2]	*0.0042218*	*0.0151943*
	γ_a		*1.02*	*1.06*
	γ		*1.4*	*1.2*
Uncertainty coefficient β_{UT}			*0.20*	*0.4*
Factored-demand-to-capacity ratio λ	*Max.*[1]		*0.5465*	*0.4464*
	Median[2]		*0.30144*	*0.2274*
Confidence level of λ, given β_{UT}	*Max.*[1]		*99%>50%, OK*	*99%>90%, OK*
	Median[2]		*99%>50%, OK*	*99%>90%, OK*

Note: 1. *Max.* = the maximum values of the inter-story drift angles obtained from any of the analyses;
2. *Median* = the maximum of the median value for each of the inter-story drift angles obtained from the analyses.

Table 5.9 Local performance evaluation of flexible six-story distributed CFT MRF for DST connections limited by local connection response

Performance level			Immediate Occupancy	Collapse Prevention
Capacity	C		*0.015*	*0.14-0.0032x33*
	ϕ		*0.9*	*0.9*
Demand	D	*Max.*[1]	*0.0093744*	*0.0273227*
		Median[2]	*0.0070592*	*0.0161339*
	γ_a		*1.02*	*1.06*
	γ		*1.4*	*1.2*
Uncertainty coefficient β_{UT}			*0.25*	*0.30*
Factored-demand-to-capacity ratio λ	*Max.*[1]		*0.9916*	*1.1226*
	Median[2]		*0.7467*	*0.6629*
Confidence level of λ, given β_{UT}	*Max.*[1]		*66.1%>50%, OK*	*52.2%>50%, OK*
	Median[2]		*93.8%>50%, OK*	*96.1%>50%, OK*

Note: 1. *Max.* = the maximum values of the inter-story drift angles obtained from any of the analyses;
2. *Median* = the maximum of the median value for each of the inter-story drift angles obtained from the analyses.

Table 5.10 Local performance evaluation of flexible six-story distributed CFT MRF limited by column compressive behavior

Performance level			Immediate Occupancy	Collapse Prevention
Capacity	C	*Max.*[1]	*6918.9*	*4102.2*
		Median[2]	*6787.0*	*4213.5*
	ϕ		*0.95*	*0.95*
Demand	D	*Max.*[1]	*732.6*	*1125.0*
		Median[2]	*703.6*	*754.0*
	γ_a		*1.01*	*1.06*
	γ		*1.05*	*1.05*
Uncertainty coefficient β_{UT}			*0.17*	*0.26*
Factored-demand-to-capacity ratio λ	*Max.*[1]		*0.1182*	*0.3214*
	Median[2]		*0.1157*	*0.2213*
Confidence level of λ, given β_{UT}	*Max.*[1]		*99%>50%, OK*	*99%>90%, OK*
	Median[2]		*99%>50%, OK*	*99%>90%, OK*

Note: 1. *Max.* = the maximum values of the column compressive force obtained from any of the analyses;
2. *Median* = the maximum of the median value for each of the column compressive force obtained from the analyses.

Table 5.11 Local performance evaluation of flexible twelve-story distributed CFT MRF for DST connections limited by local connection response

Performance level			Immediate Occupancy	Collapse Prevention
Capacity	C		*0.015*	*0.14-0.0032x36*
	ϕ		*0.9*	*0.9*
Demand	D	*Max.*[1]	*0.0076547*	*0.0298313*
		Median[2]	*0.0042218*	*0.0151943*
	γ_a		*1.02*	*1.06*
	γ		*1.4*	*1.2*
Uncertainty coefficient β_{UT}			*0.25*	*0.30*
Factored-demand-to-capacity ratio λ	*Max.*[1]		*0.8097*	*1.7000*
	Median[2]		*0.4466*	*0.8659*
Confidence level of λ, given β_{UT}	*Max.*[1]		*89.5%>50%, OK*	*10%<50%, NOT OK*
	Median[2]		*99%>50%, OK*	*82.2%>50%, OK*

Note: 1. *Max.* = the maximum values of the inter-story drift angles obtained from any of the analyses;
2. *Median* = the maximum of the median value for each of the inter-story drift angles obtained from the analyses.

Table 5.12 Local performance evaluation of flexible twelve-story distributed CFT MRF limited by column compressive behavior

Performance level			Immediate Occupancy	Collapse Prevention
Capacity	C	*Max.*[1]	*15572.4*	*12901.1*
		Median[2]	*15572.4*	*15572.4*
	ϕ		*0.95*	*0.95*
Demand	D	*Max.*[1]	*1483.0*	*2428.0*
		Median[2]	*1390.0*	*1530.0*
	γ_a		*1.01*	*1.07*
	γ		*1.05*	*1.05*
Uncertainty coefficient β_{UT}			*0.15*	*0.26*
Factored-demand-to-capacity ratio λ	*Max.*[1]		*0.1063*	*0.2226*
	Median[2]		*0.0996*	*0.1162*
Confidence level of λ, given β_{UT}	*Max.*[1]		*99%>50%, OK*	*99%>90%, OK*
	Median[2]		*99%>50%, OK*	*99%>90%, OK*

Note: 1. *Max.* = the maximum values of the column compressive force obtained from any of the analyses;
2. *Median* = the maximum of the median value for each of the column compressive force obtained from the analyses.

Table 5.13 The 1st to 4th modes properties of the flexible ($1<T_1/T_{max}<1.15$) six-story and twelve-story distributed CFT MRFs

Mode		Six-Story	Twelve-Story
1st	Period (s)	*1.0246*	*1.6990*
	Effective modal mass (%)	*81.5%*	*75.3%*
2nd	Period (s)	*0.35912*	*0.60927*
	Effective modal mass (%)	*10.9%*	*12.7%*
3rd	Period (s)	*0.20033*	*0.33158*
	Effective modal mass (%)	*4.5%*	*5.1%*
4th	Period (s)	*0.12901*	*0.21189*
	Effective modal mass (%)	*1.8%*	*2.8%*
Upper bound limitation on T_1	T_{max} (s)	*0.91748*	*1.51981*
	T_1/T_{max}	*1.117*	*1.118*

Note: 1. T_{max} = the upper bound limitation on computed fundamental period, T_1, in seconds, of the building set in IBC 2000, Sec. 1617.3, for the purpose of calculating equivalent lateral forces.

Table 5.14 Median ratios of sum of maximum story displacements to maximum roof displacement of CFT MRFs

Hazard level	Six-story	Twelve-story
50/50 set	*1.10*	*1.22*
10/50 set	*1.06*	*1.14*
2/50 set	*1.04*	*1.13*

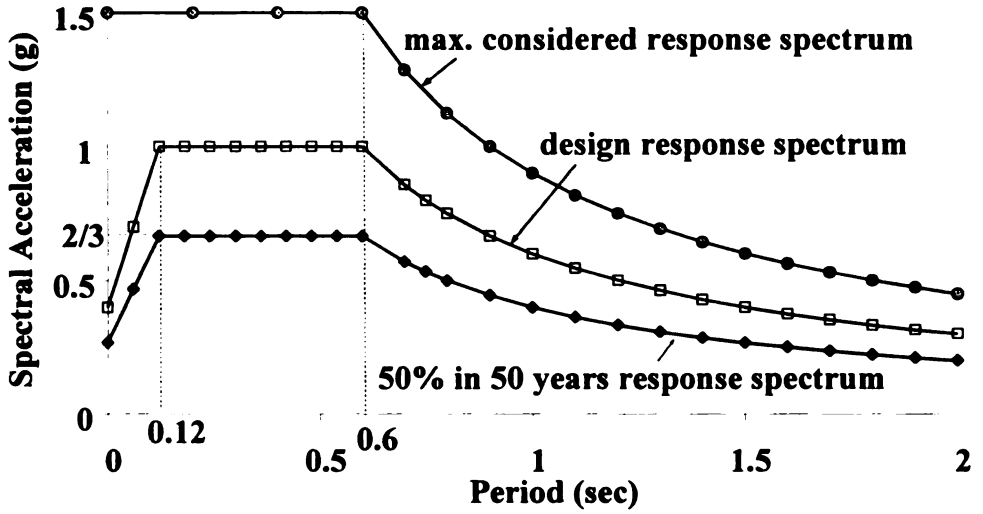


Figure 5.1 Response spectra of 2%, 10% and 50% exceedance in 50 years

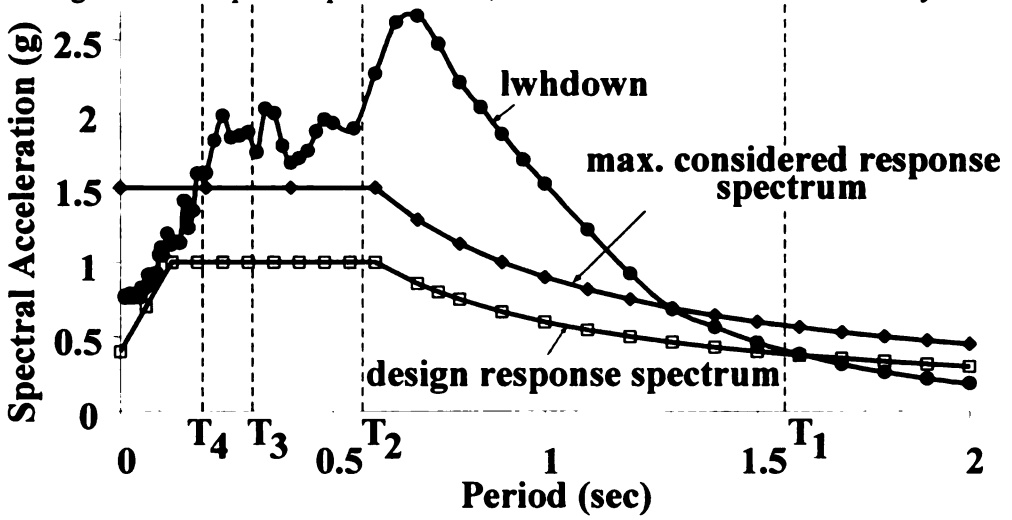


Figure 5.2 Response spectra of 50% in 50 years time-history: *lwhown* (matched at 0.3, 1.0, 2.0 and 4.0 s)

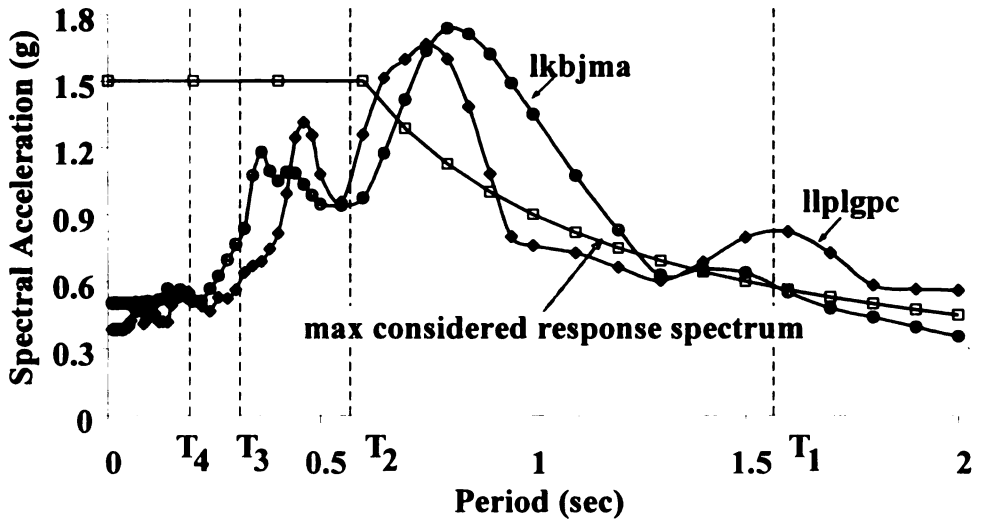


Figure 5.3 Response spectra of 2% in 50 years time-history: *lkbjma* and *llplgpc*

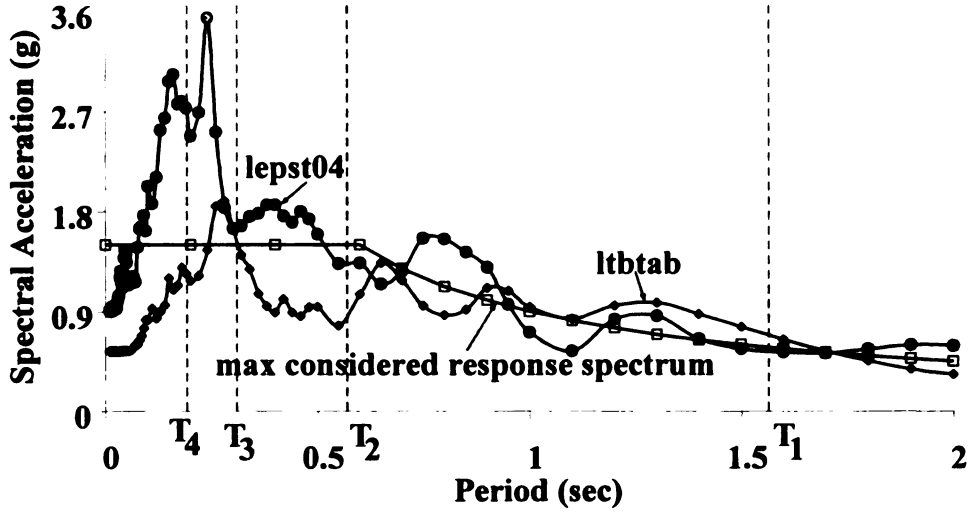


Figure 5.4 Response spectra of 2% in 50 years time-history: *ltbtab* and *lepst04*

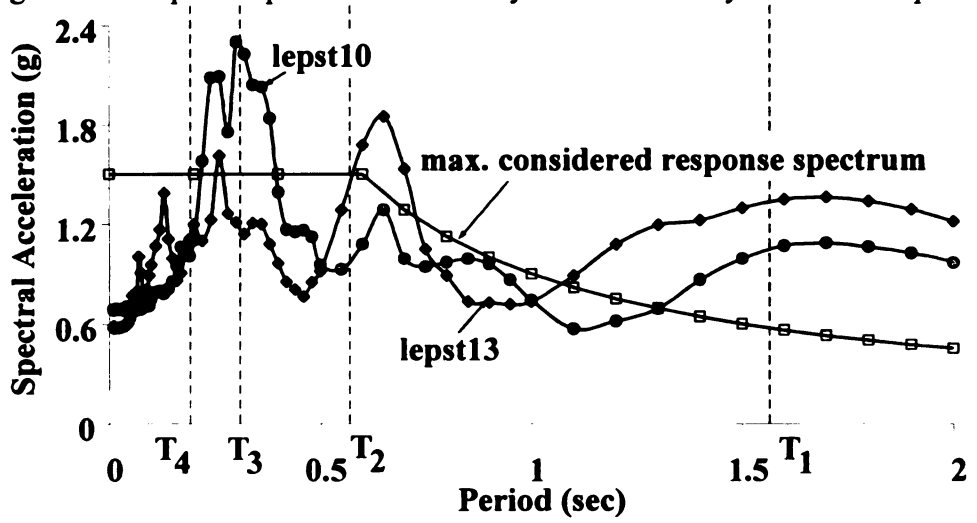


Figure 5.5 Response spectra of 2% in 50 years time-history: *lepst10* and *lepst13*

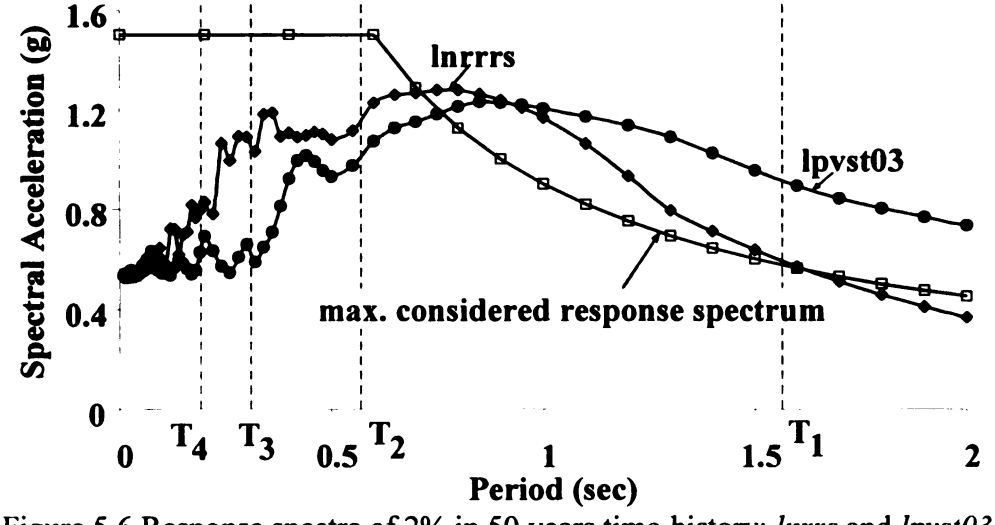


Figure 5.6 Response spectra of 2% in 50 years time-history: *lnrrs* and *lpvst03*

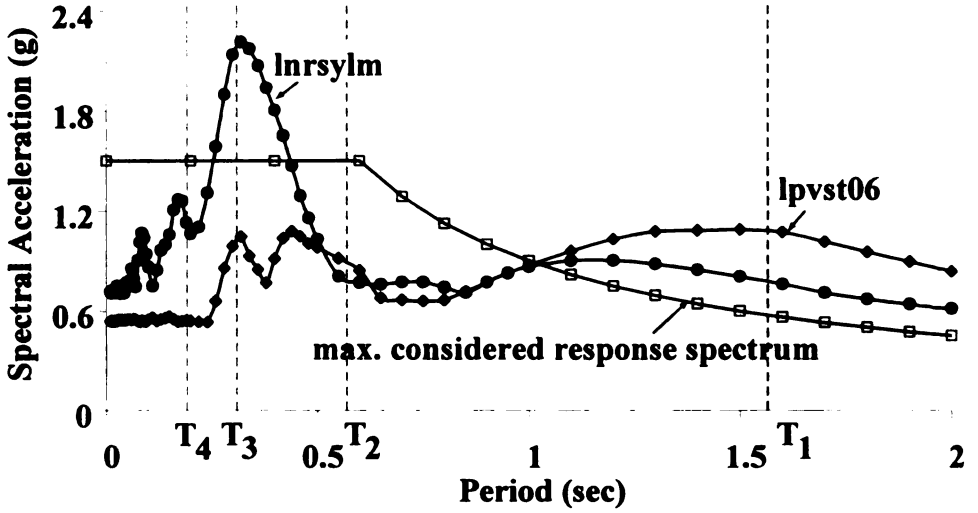


Figure 5.7 Response spectra of 2% in 50 years time-history: *lnrsylm* and *lpvst06*

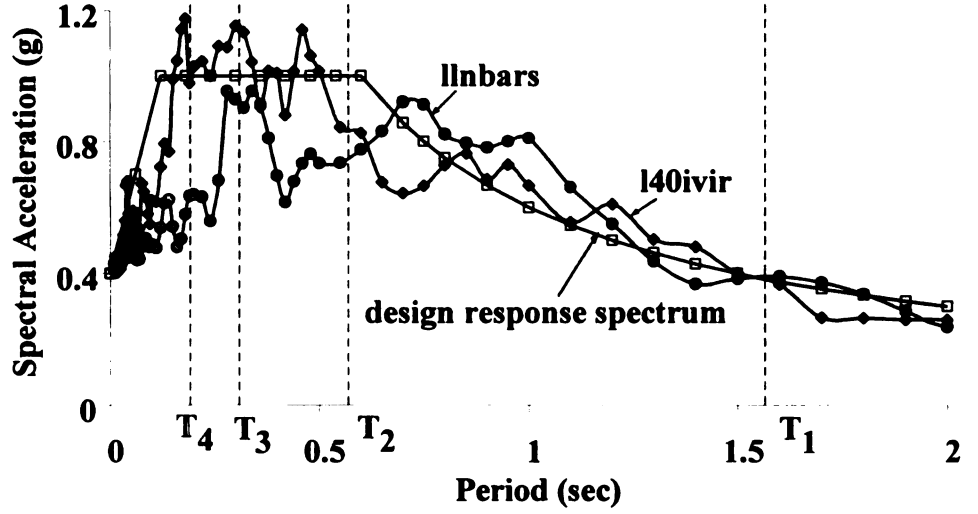


Figure 5.8 Response spectra of 10% in 50 years time-history: *l40ivir* and *llnbars*

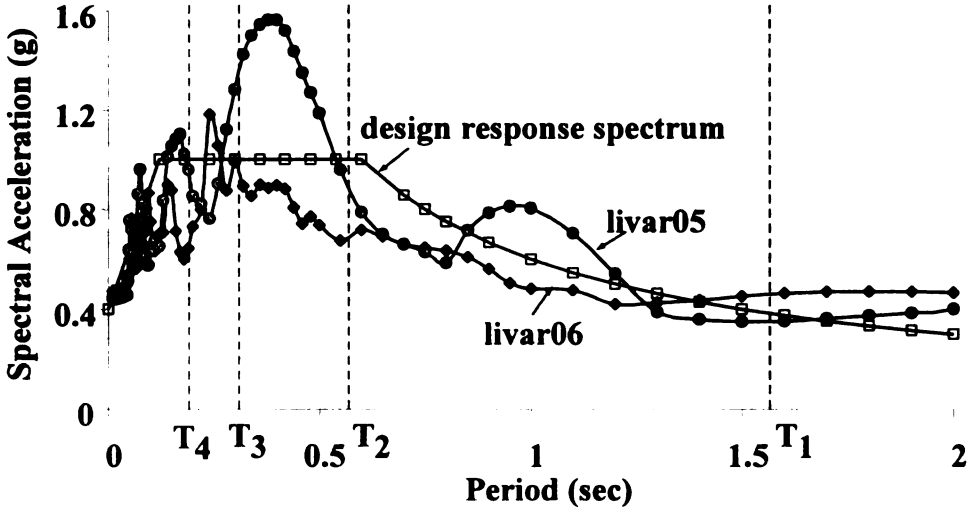


Figure 5.9 Response spectra of 10% in 50 years time-history: *livar05* and *livar06*

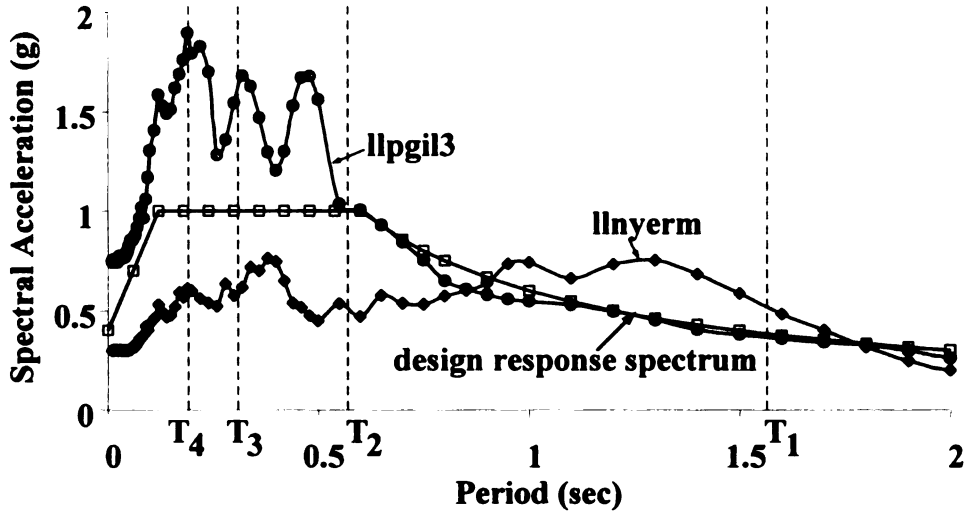


Figure 5.10 Response spectra of 10% in 50 years time-history: *llpgil3* and *llnyerm*

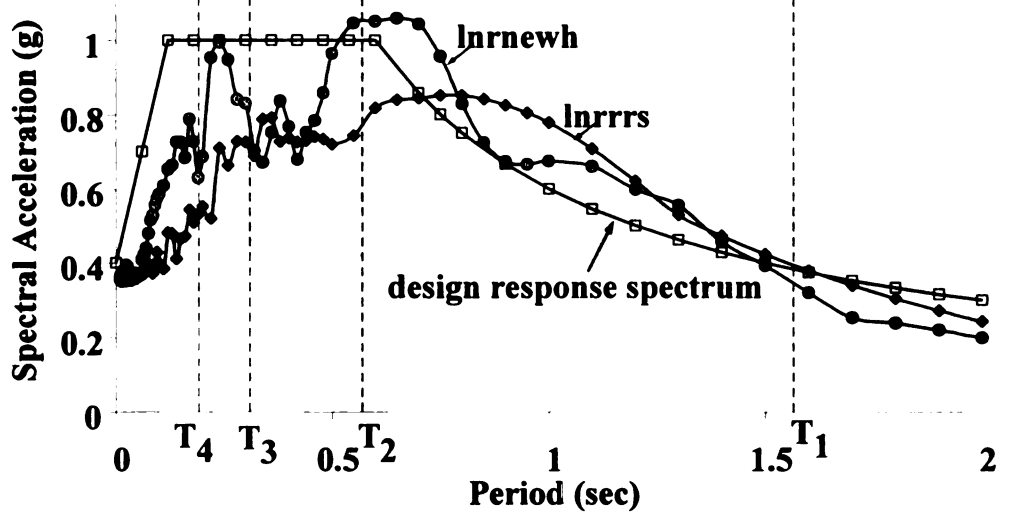


Figure 5.11 Response spectra of 10% in 50 years time-history: *lnrrrs* and *lnrnewh*

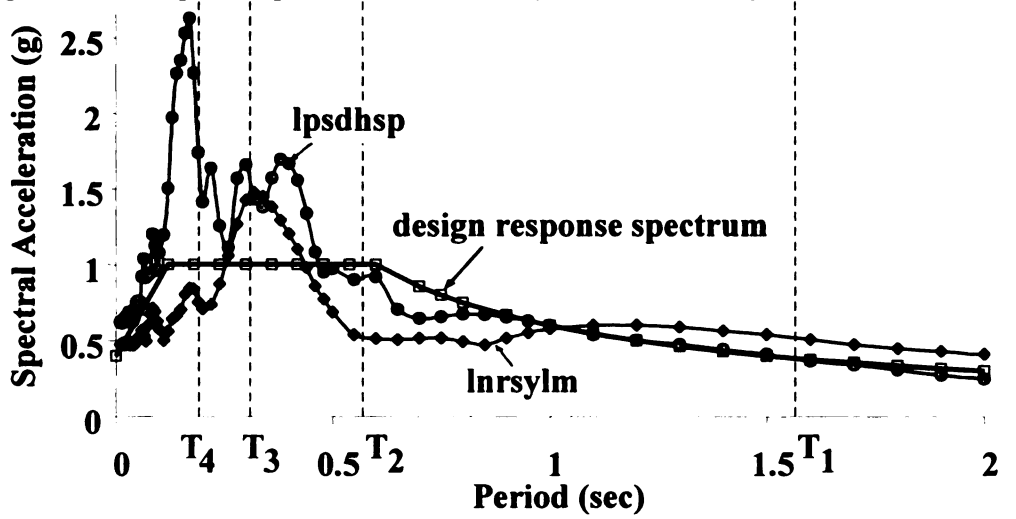


Figure 5.12 Response spectra of 10% in 50 years time-history: *lnrsylm* and *lpsdhsp*

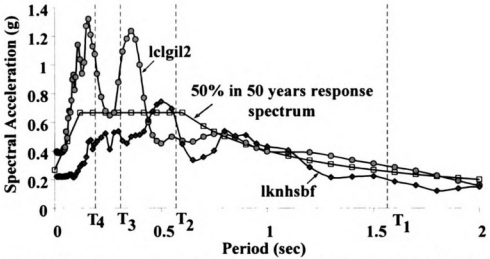


Figure 5.13 Response spectra of 50% in 50 years time-history: *lclgil2* and *lknhsbf*

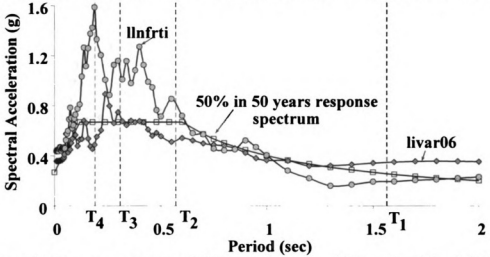


Figure 5.14 Response spectra of 50% in 50 years time-history: *livar06* and *llnfrti*

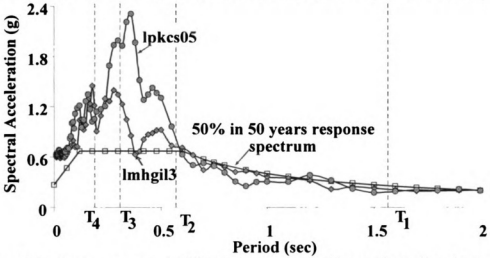


Figure 5.15 Response spectra of 50% in 50 years time-history: *lmhgil3* and *lpkcs05*

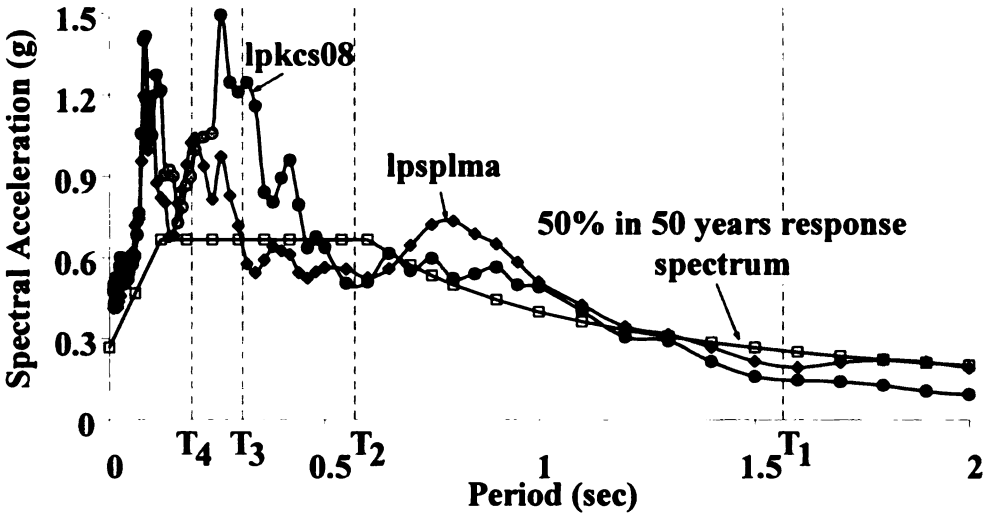


Figure 5.16 Response spectra of 50% in 50 years time-history: *lpsplma* and *lpkcs08*

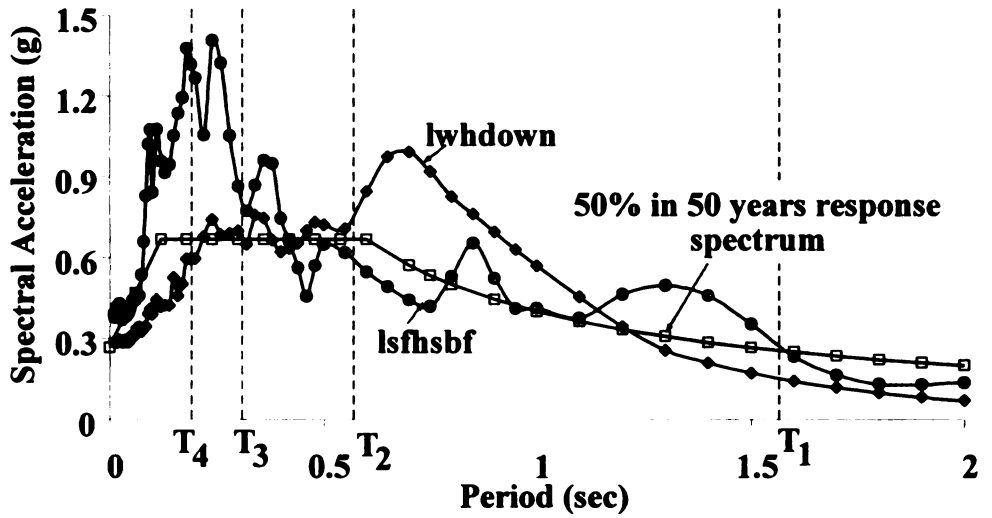


Figure 5.17 Response spectra of 50% in 50 years time-history: *lsfhsbf* and *lwhdown*

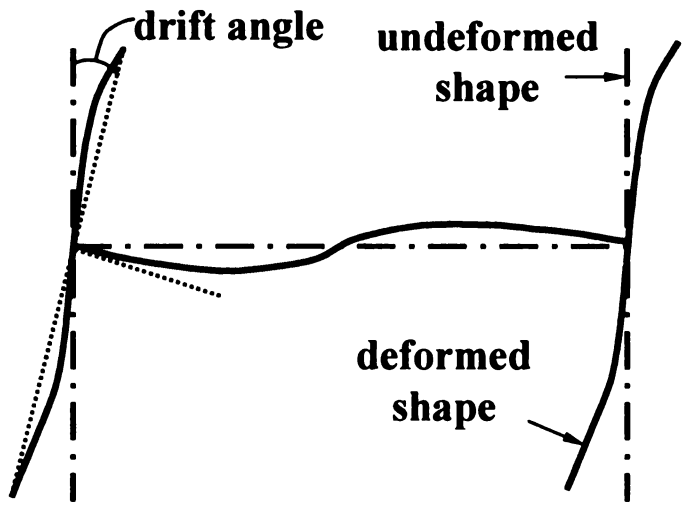


Figure 5.18 Inter-story drift angle for MRFs as illustrated in FEMA 350

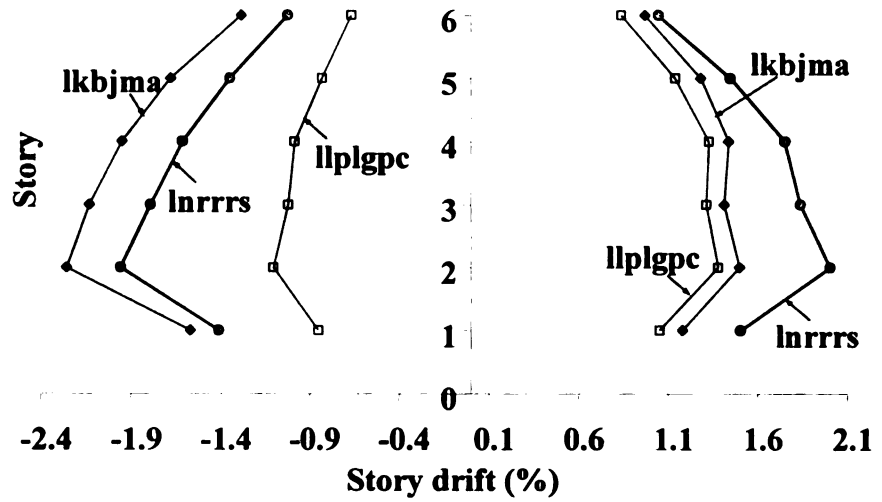


Figure 5.19 Story drift envelop of flexible six-story distributed CFT MRF subjected to SAC 2/50 time-histories: *lkbjma, lnrrrs* and *llplgpc*

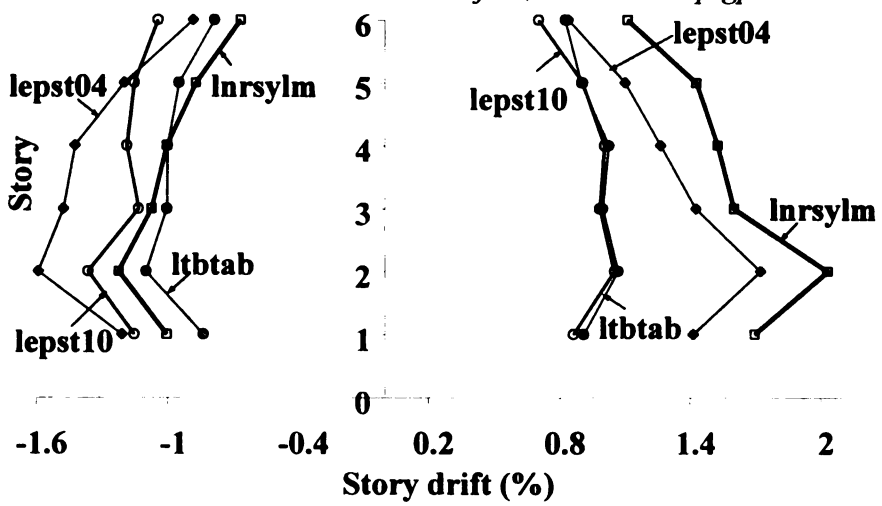


Figure 5.20 Story drift envelop of flexible six-story distributed CFT MRF subjected to SAC 2/50 time-histories: *lnrsylm, ltbtab, lepst04* and *lepst10*

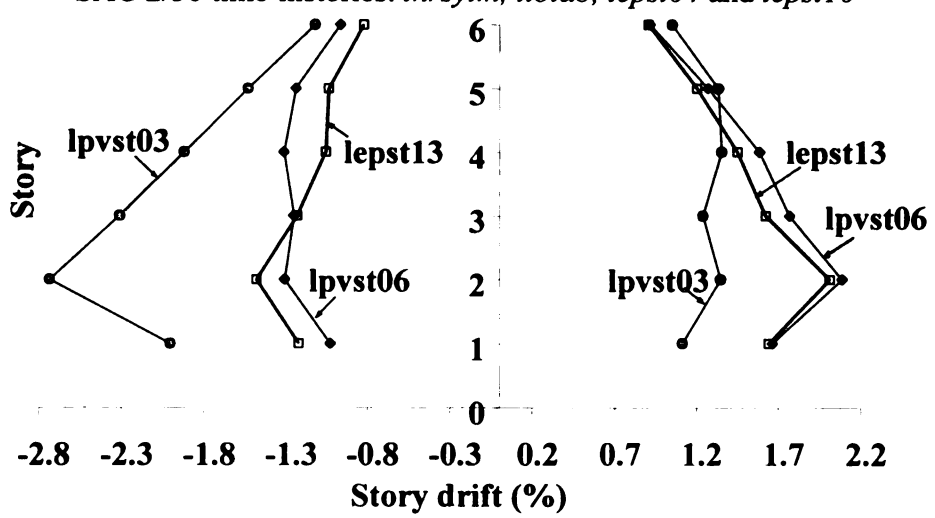


Figure 5.21 Story drift envelop of flexible six-story distributed CFT MRF subjected to SAC 2/50 time-histories: *lepst13, lpvst03* and *lpvst06*

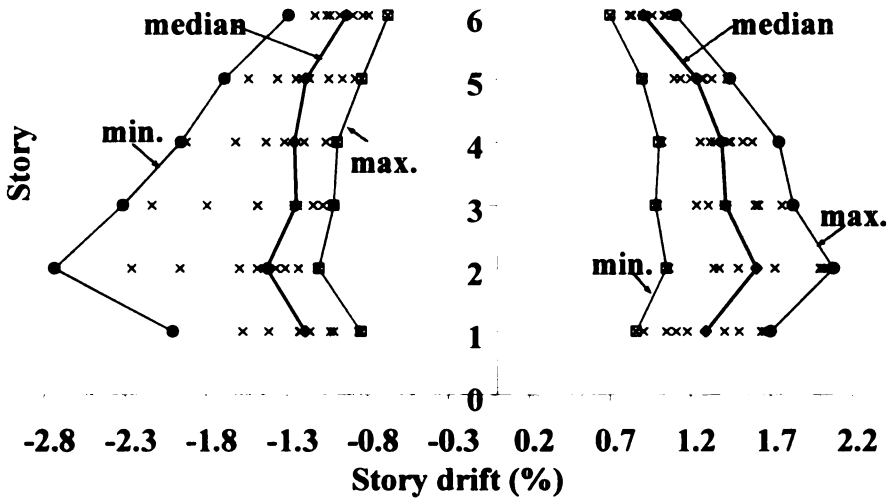


Figure 5.22 Maximum, minimum and median story drift envelop of flexible six-story distributed CFT MRF subjected to SAC 2/50 time-histories

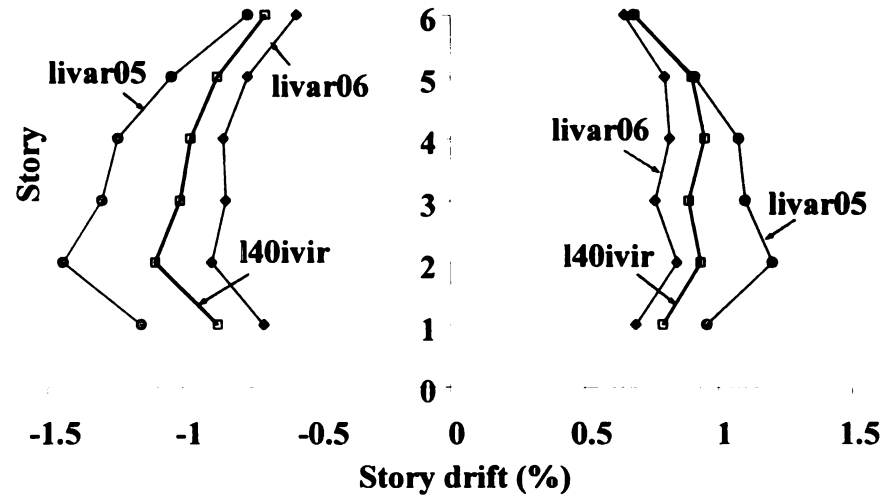


Figure 5.23 Story drift envelop of flexible six-story distributed CFT MRF subjected to SAC 10/50 time-histories: *l40ivir*, *livar05* and *livar06*

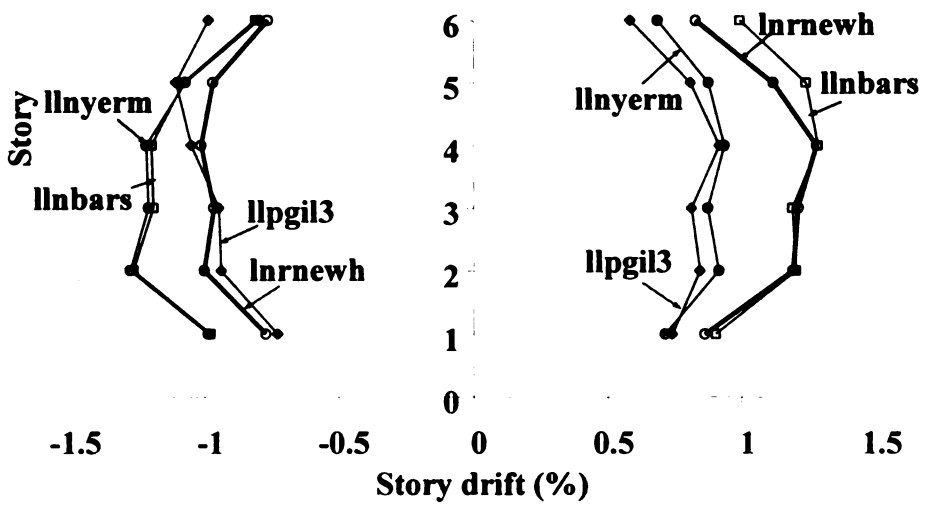


Figure 5.24 Story drift envelop of flexible six-story distributed CFT MRF subjected to SAC 10/50 time-histories: *llnbars*, *llnyerm*, *llpgil3* and *lnrnewh*

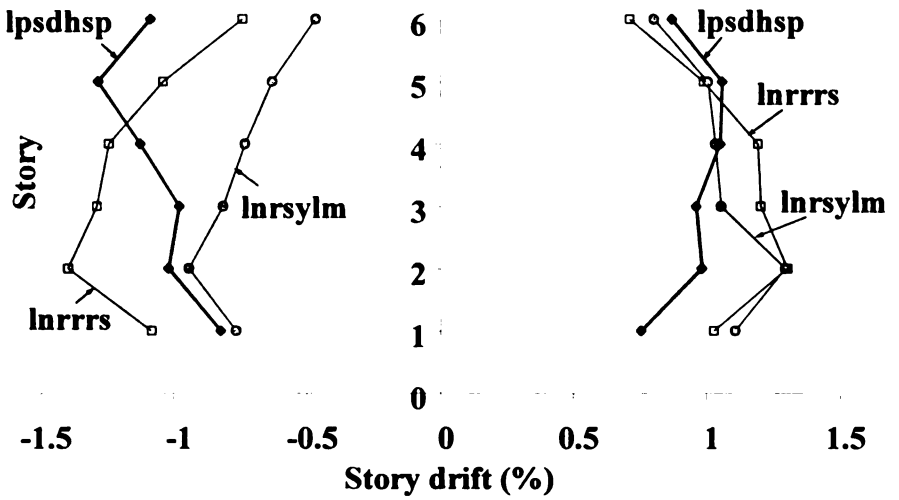


Figure 5.25 Story drift envelop of flexible six-story distributed CFT MRF subjected to SAC 10/50 time-histories: *lnrrrs, lnrsylm* and *lpsdhsp*

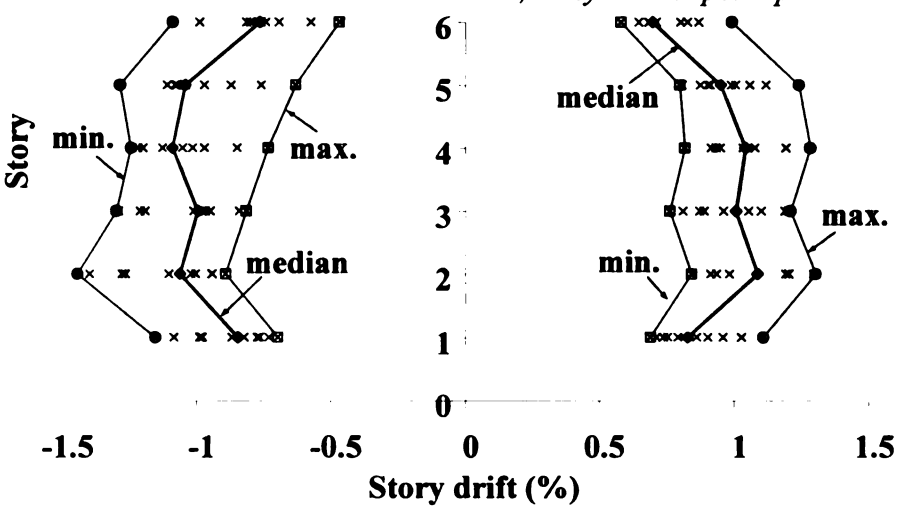


Figure 5.26 Maximum, minimum and median story drift envelop of flexible six-story distributed CFT MRF subjected to SAC 10/50 time-histories

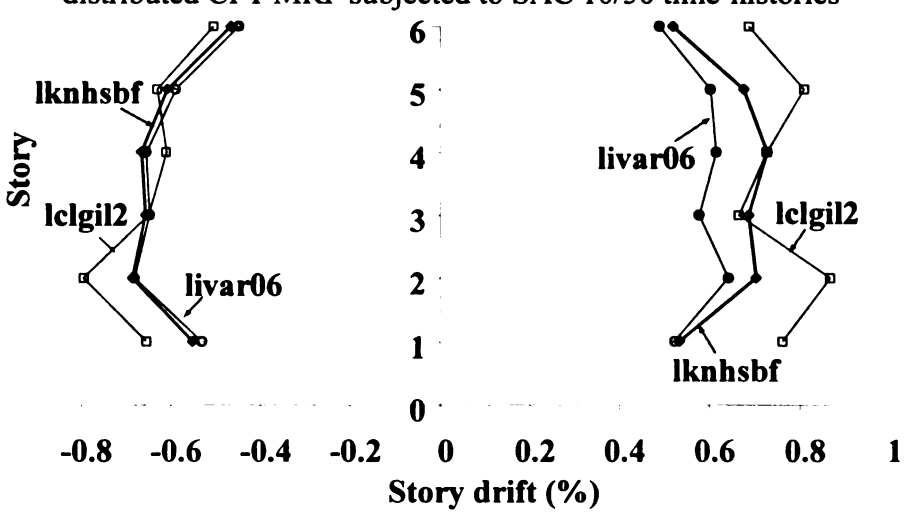


Figure 5.27 Story drift envelop of flexible six-story distributed CFT MRF subjected to SAC 50/50 time-histories: *lclgil2, lknhsbf* and *livar06*

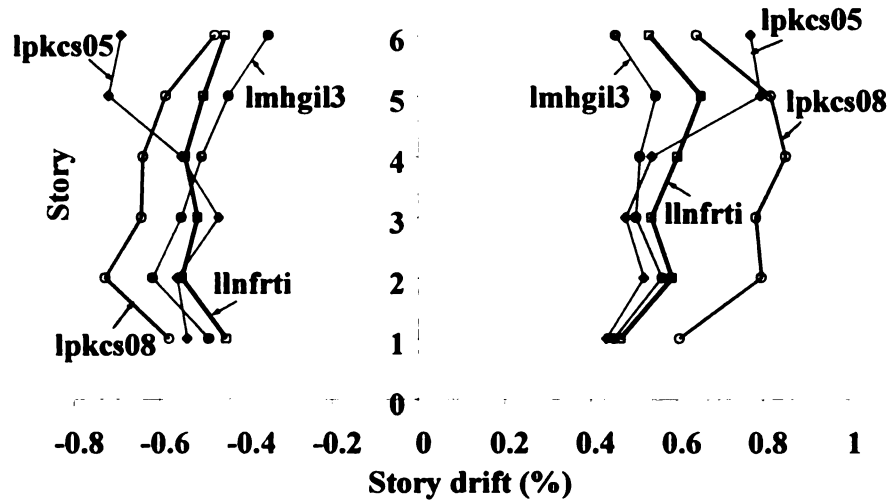


Figure 5.28 Story drift envelop of flexible six-story distributed CFT MRF subjected to SAC 50/50 time-histories: *lmhgil3, llnfrti, lpkcs05* and *lpkcs08*

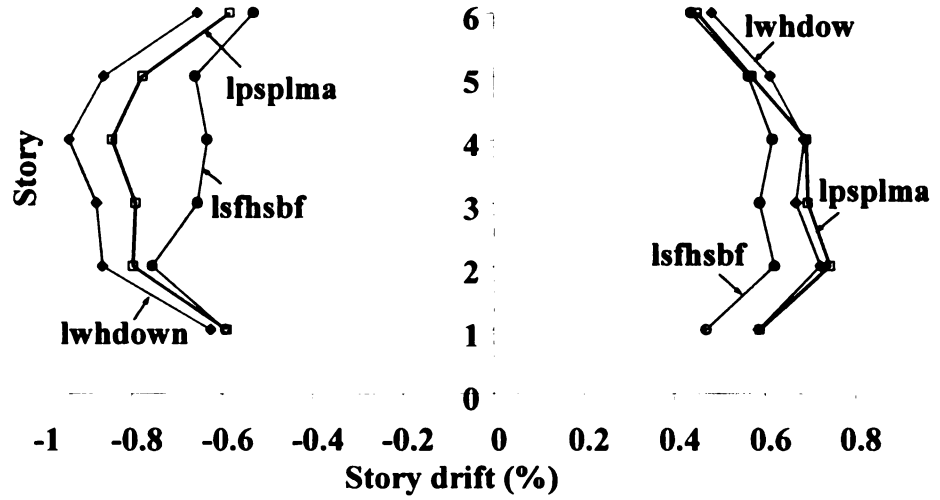


Figure 5.29 Story drift envelop of flexible six-story distributed CFT MRF subjected to SAC 50/50 time-histories: *lpsplma, lsfhsbf* and *lwhdown*

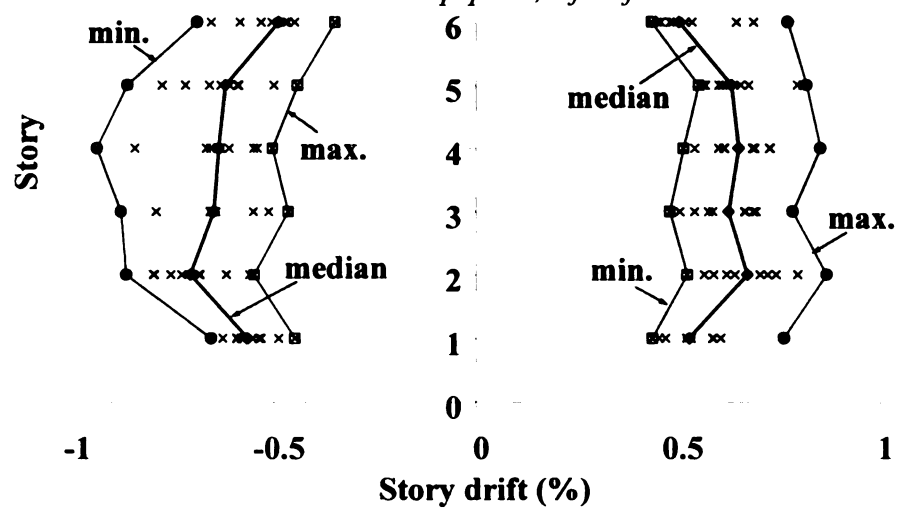


Figure 5.30 Maximum, minimum and median story drift envelop of flexible six-story distributed CFT MRF subjected to SAC 50/50 time-histories

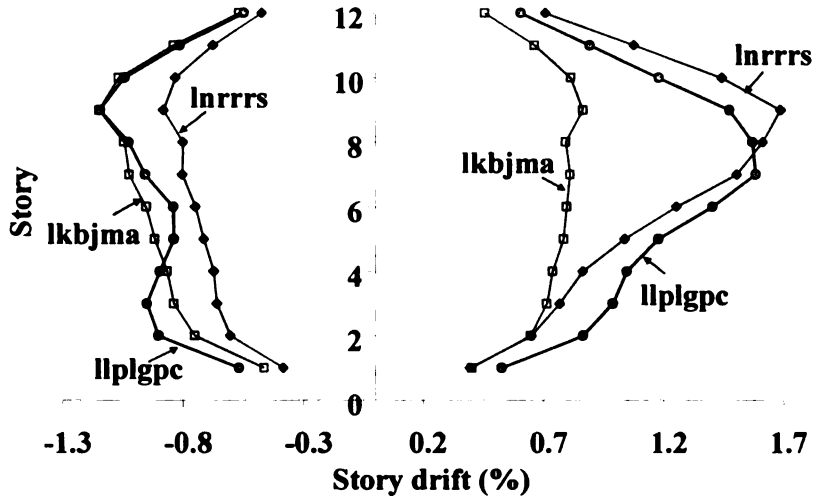


Figure 5.31 Story drift envelop of flexible twelve-story distributed CFT MRF subjected to SAC 2/50 time-histories: *lkbjma, lnrrrs* and *llplgpc*

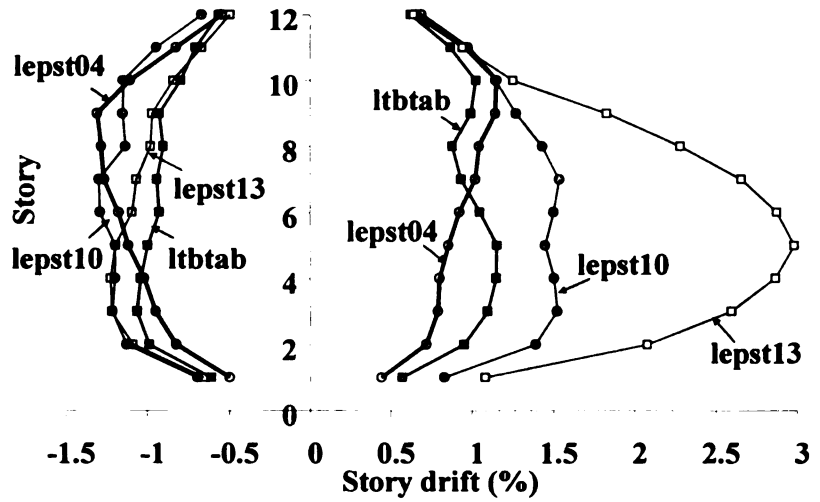


Figure 5.32 Story drift envelop of flexible twelve-story distributed CFT MRF subjected to SAC 2/50 time-histories: *ltbtab, lepst04, lepst10* and *lepst13*

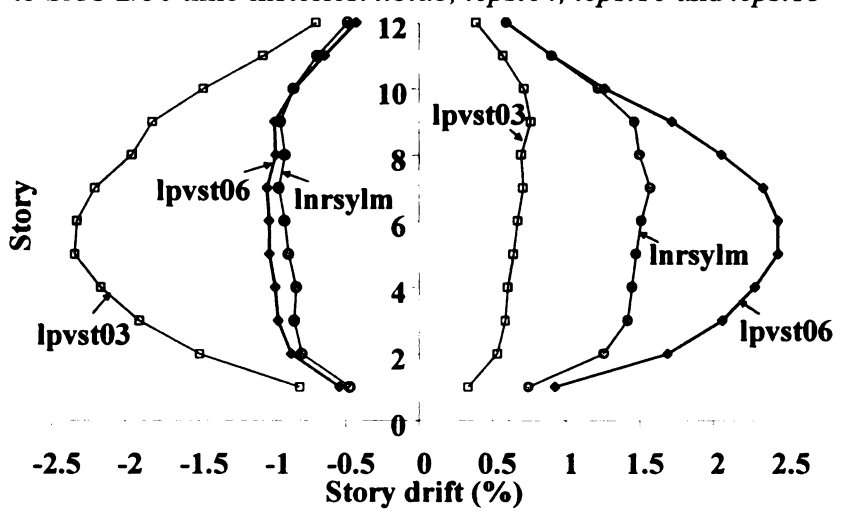


Figure 5.33 Story drift envelop of flexible twelve-story distributed CFT MRF subjected to SAC 2/50 time-histories: *lnrsylm, lpvst03* and *lpvst06*

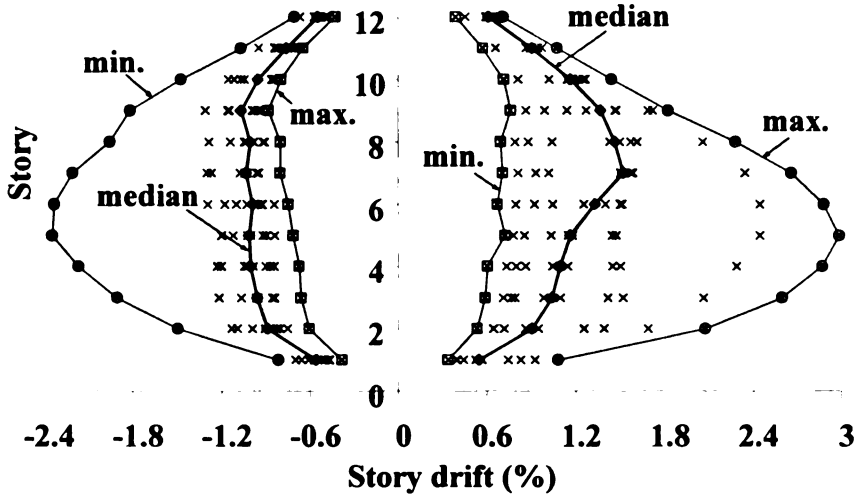


Figure 5.34 Maximum, minimum and median story drift envelop of flexible twelve-story distributed CFT MRF subjected to SAC 2/50 time-histories

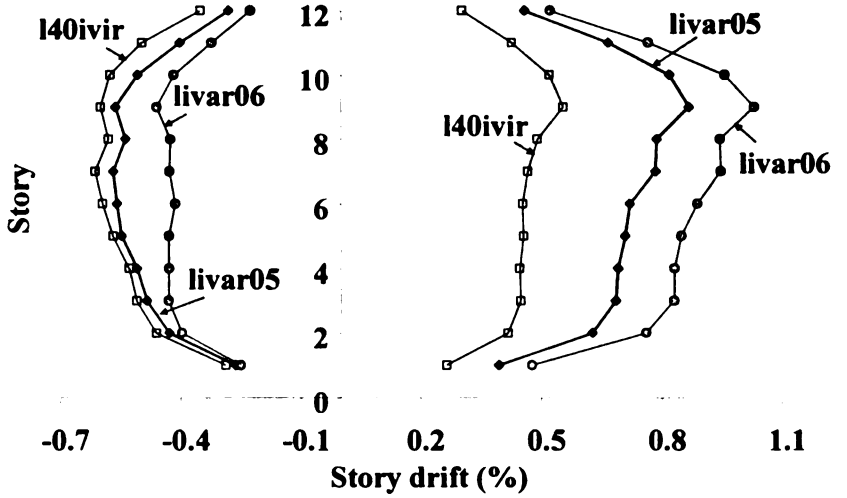


Figure 5.35 Story drift envelop of flexible twelve-story distributed CFT MRF subjected to SAC 10/50 time-histories: *l40ivir, livar05* and *livar06*

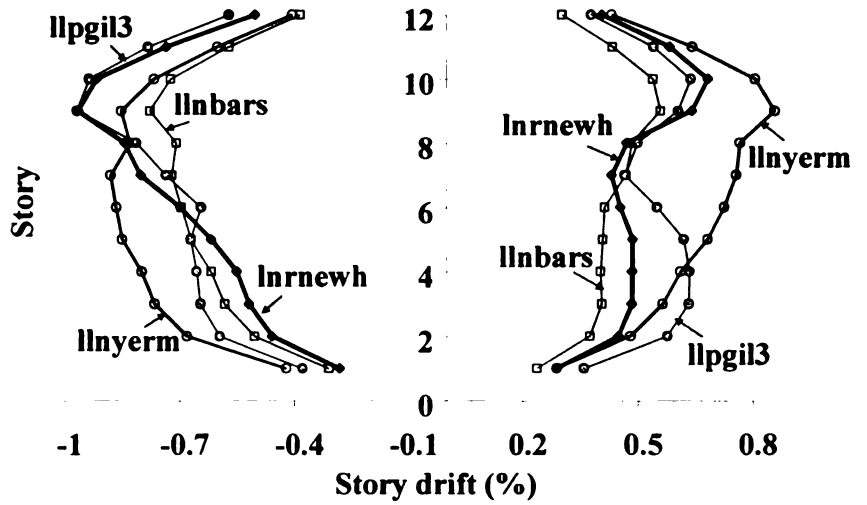


Figure 5.36 Story drift envelop of flexible twelve-story distributed CFT MRF subjected to SAC 10/50 time-histories: *llnbars, llnyerm, llpgil3* and *lnrnewh*

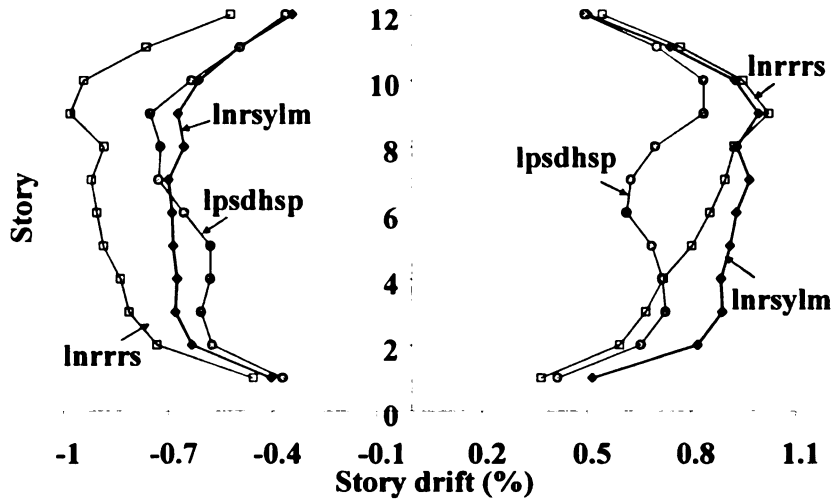


Figure 5.37 Story drift envelop of flexible twelve-story distributed CFT MRF subjected to SAC 10/50 time-histories: *lnrrrs, lnrsylm* and *lpsdhsp*

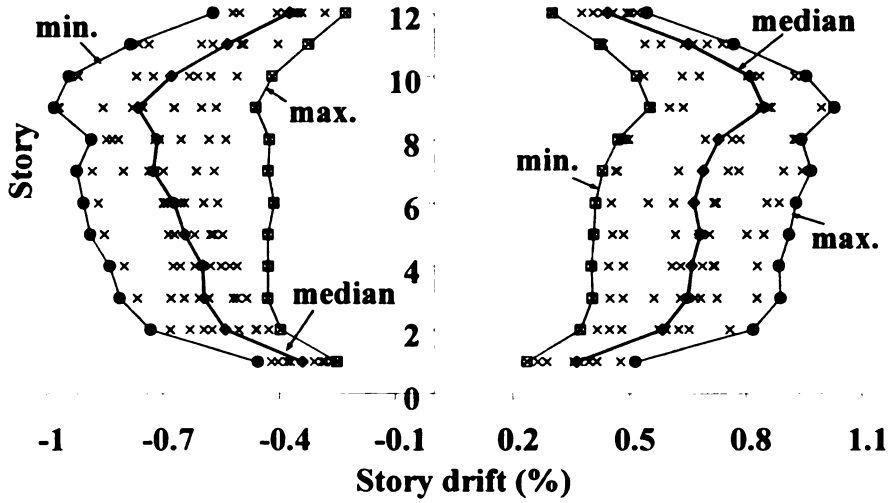


Figure 5.38 Maximum, minimum and median story drift envelop of flexible twelve-story distributed CFT MRF subjected to SAC 10/50 time-histories

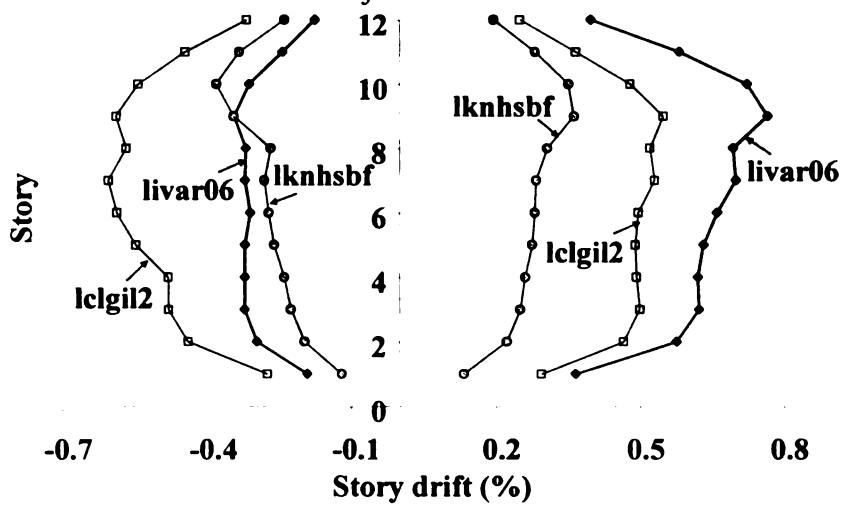


Figure 5.39 Story drift envelop of flexible twelve-story distributed CFT MRF subjected to SAC 50/50 time-histories: *lclgil2, lknhsbf* and *livar06*

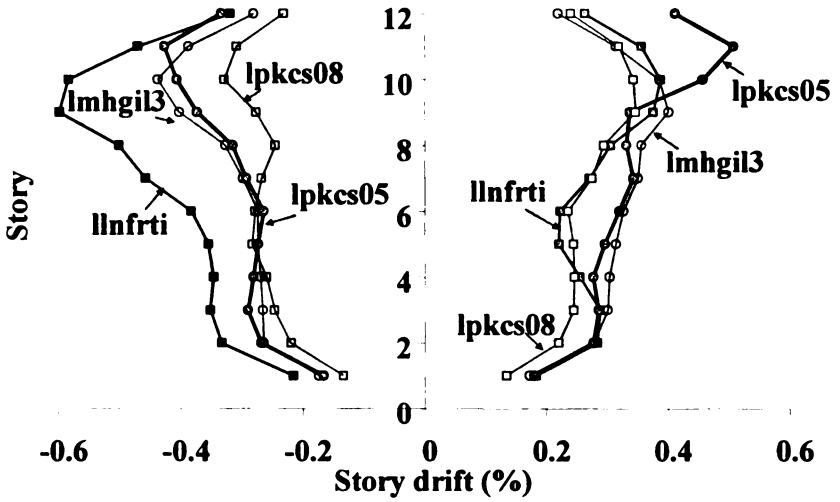


Figure 5.40 Story drift envelop of flexible twelve-story distributed CFT MRF subjected to SAC 50/50 time-histories: *lmhgil3, llnfrti, lpkcs05* and *lpkcs08*

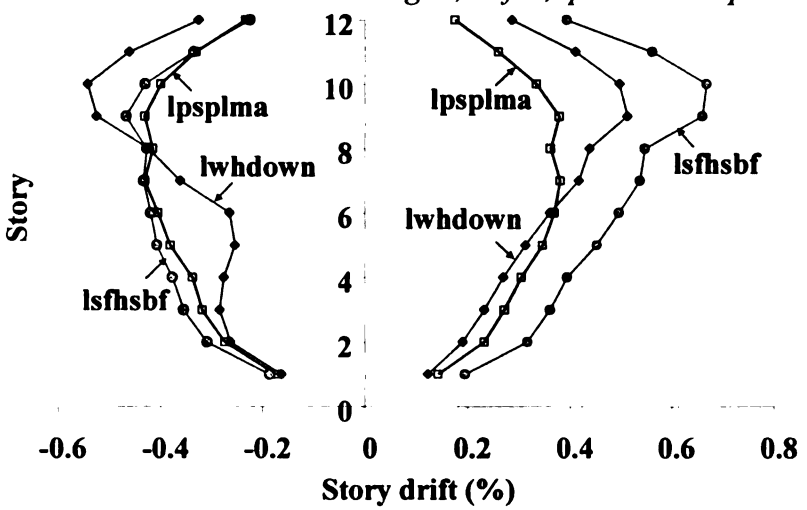


Figure 5.41 Story drift envelop of flexible twelve-story distributed CFT MRF subjected to SAC 50/50 time-histories: *lpsplma, lsfhsbf* and *lwhdown*

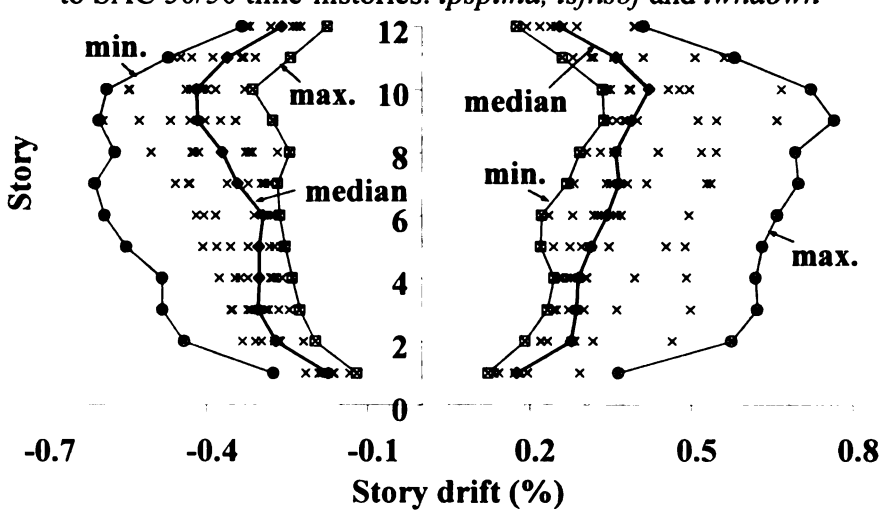


Figure 5.42 Maximum, minimum and median story drift envelop of flexible twelve-story distributed CFT MRF subjected to SAC 50/50 time-histories

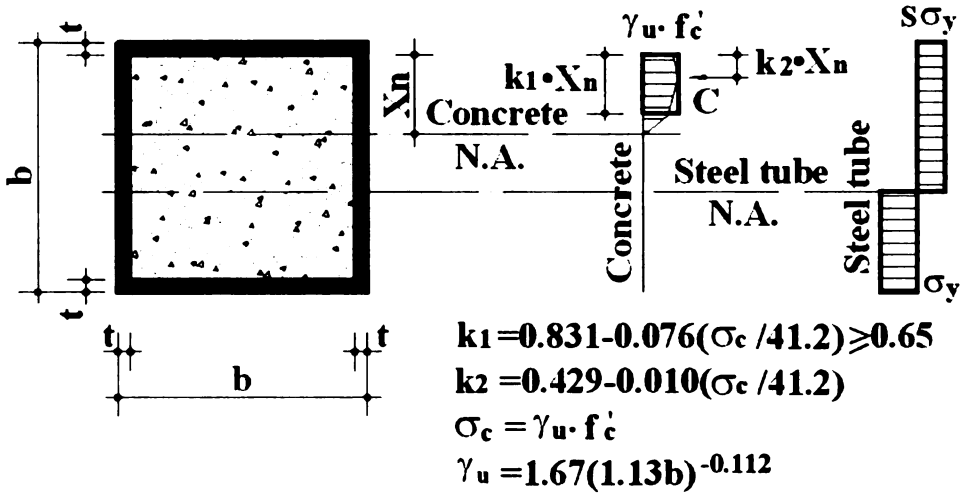


Figure 5.43 Stress block of MAIJ method (Sakino and Nakahara, 2000)

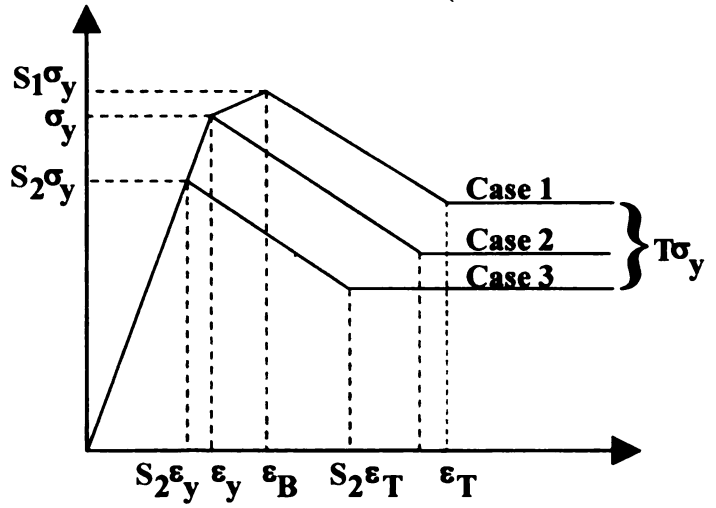


Figure 5.44 Idealized steel stress-strain curves for three different cases of CFT specimens (Nakahara et al., 1998)

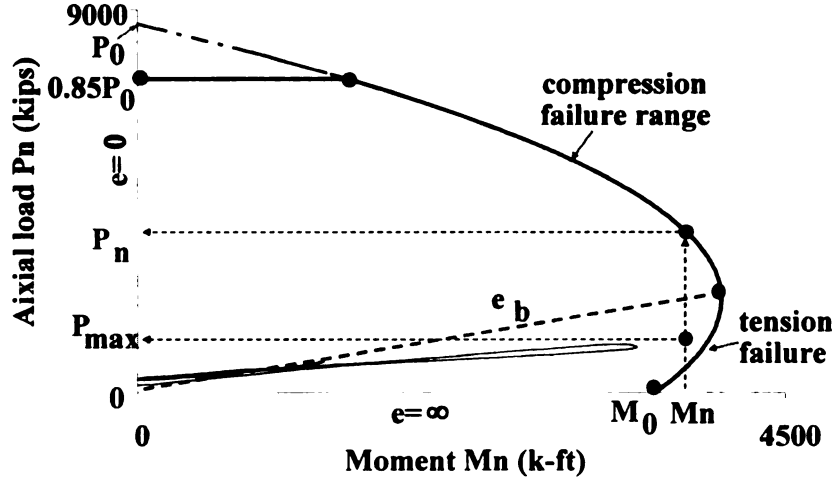


Figure 5.45 Interaction diagram for nominal CFT beam-column strength in combined bending and axial load

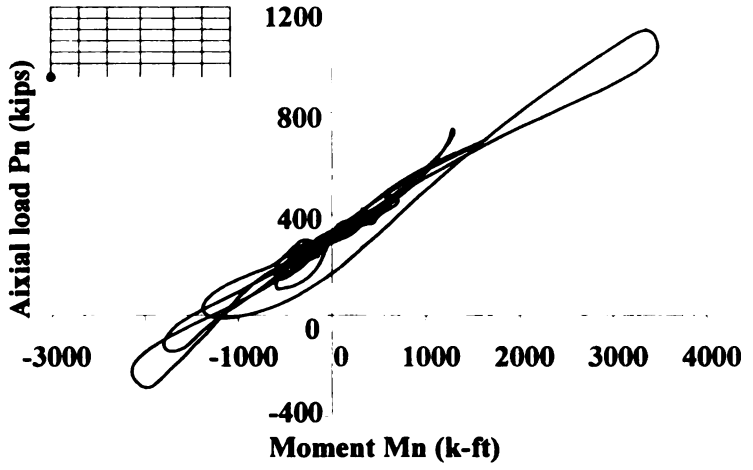


Figure 5.46a Left corner column P-M interaction curve of flexible six-story CFT MRF subjected to SAC 2/50 time-history *lpvst03*

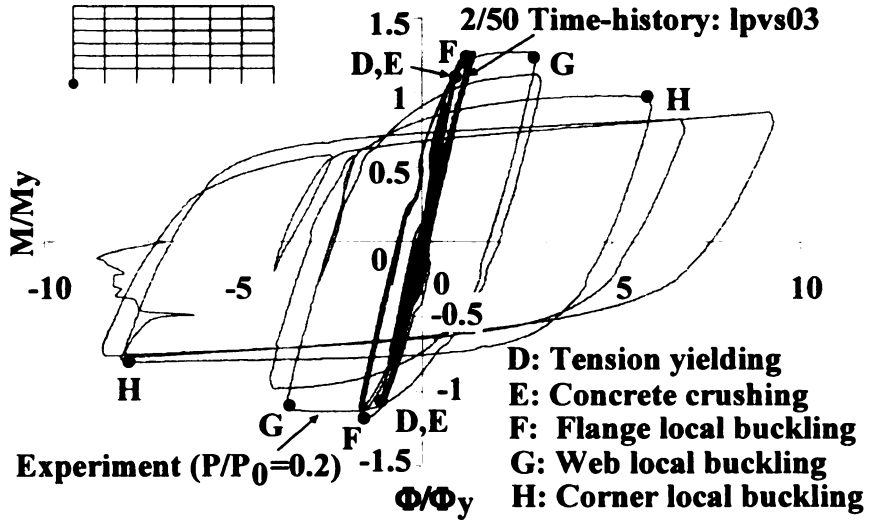


Figure 5.46b Left corner column M-Φ interaction curve of flexible six-story CFT MRF subjected to SAC 2/50 time-history *lpvst03*

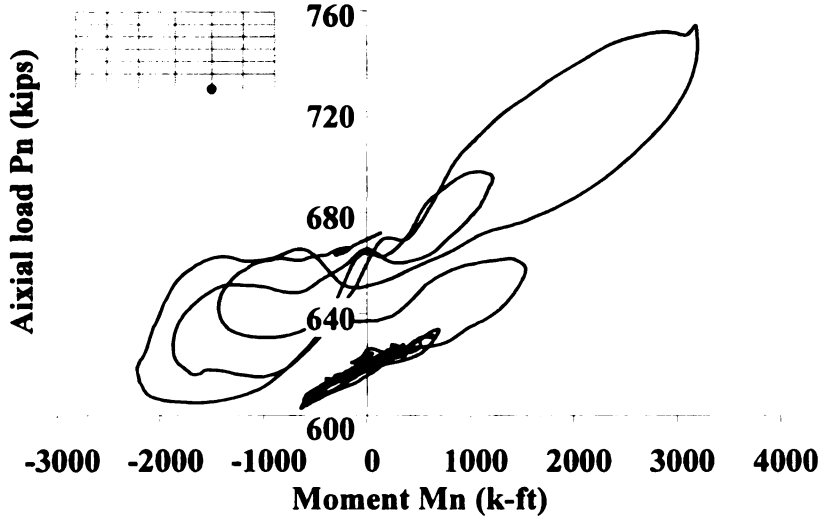


Figure 5.47a Interior column P-M interaction curve of flexible six-story CFT MRF subjected to SAC 2/50 time-history *lpvst03*

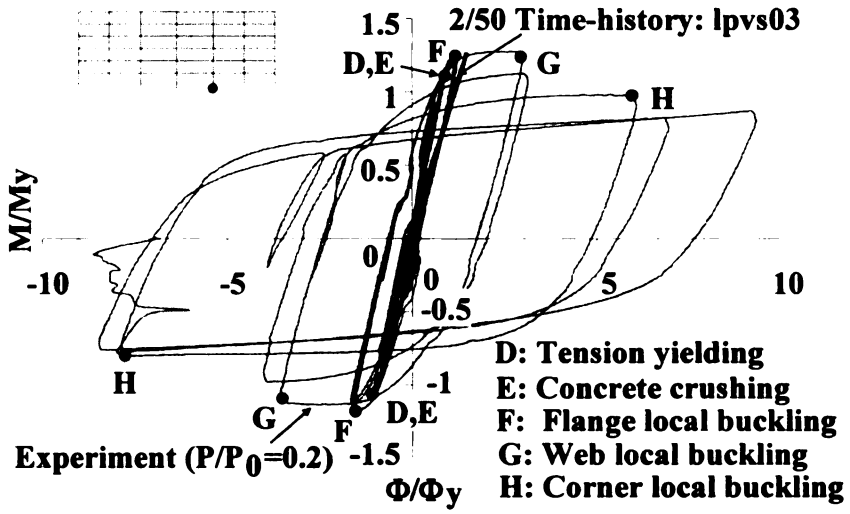


Figure 5.47b Interior column M-Φ interaction curve of flexible six-story CFT MRF subjected to SAC 2/50 time-history *lpvst03*

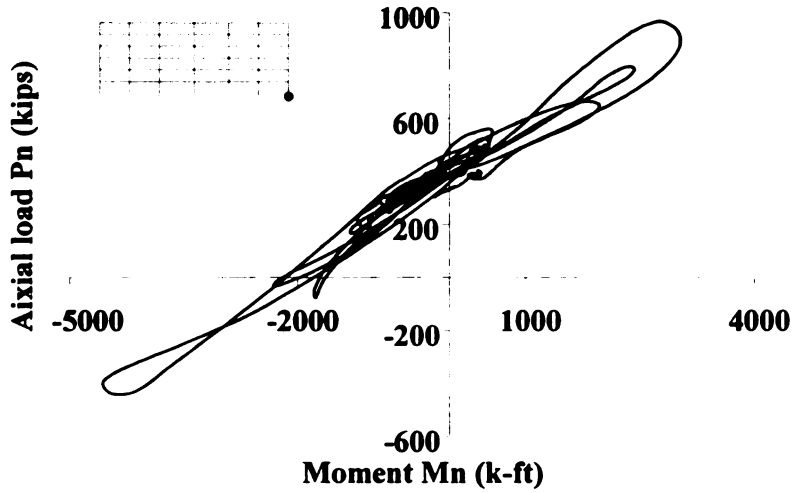


Figure 5.48a Right corner column P-M interaction curve of flexible six-story CFT MRF subjected to SAC 2/50 time-history *lpvst03*

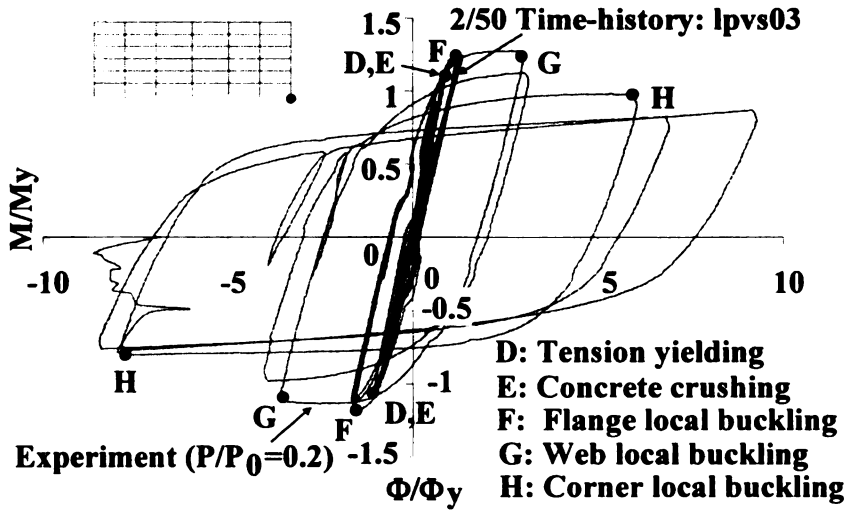


Figure 5.48b Right corner column M-Φ interaction curve of flexible six-story CFT MRF subjected to SAC 2/50 time-history *lpvst03*

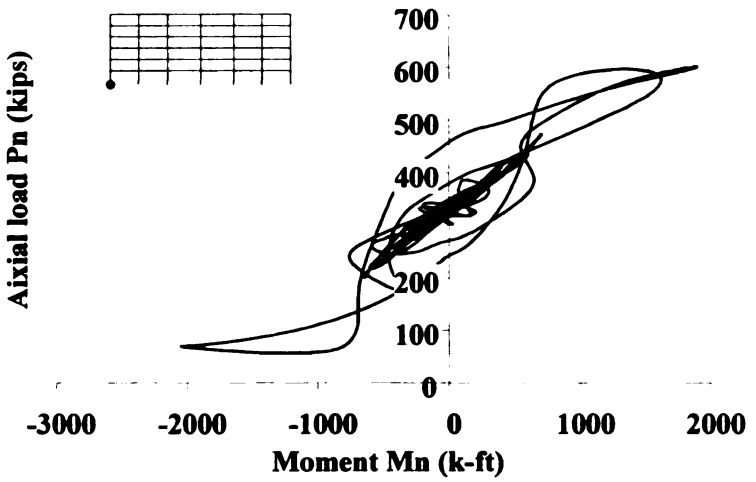


Figure 5.49a Left corner column P-M interaction curve of flexible six-story CFT MRF subjected to SAC 50/50 time-history *lclgil2*

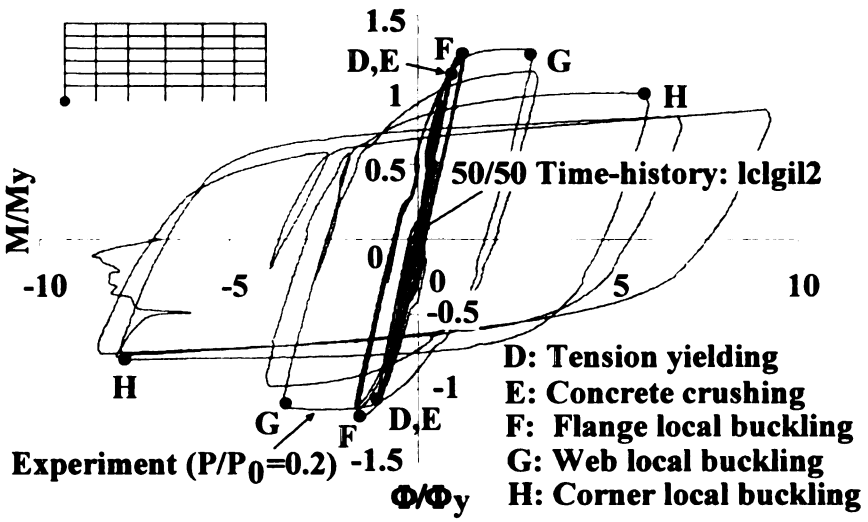


Figure 5.49b Left corner column M-Φ interaction curve of flexible six-story CFT MRF subjected to SAC 50/50 time-history *lclgil2*

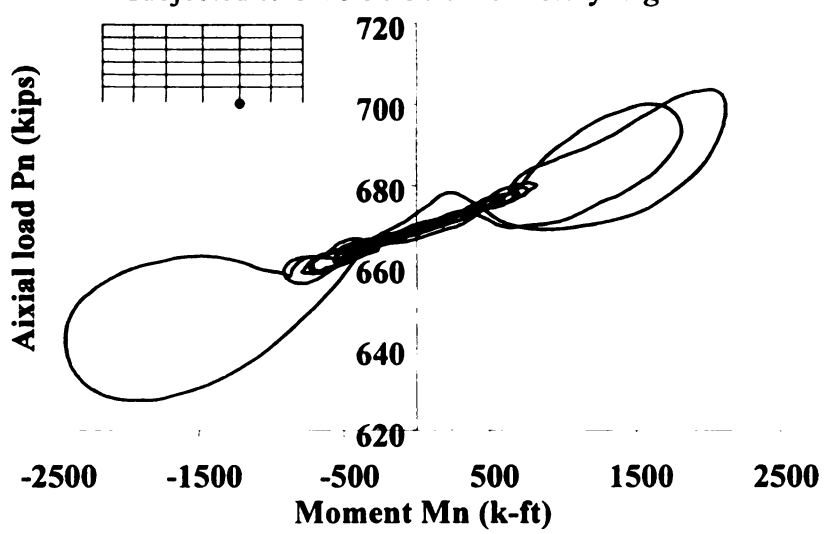


Figure 5.50a Interior column P-M interaction curve of flexible six-story CFT MRF subjected to SAC 50/50 time-history *lclgil2*

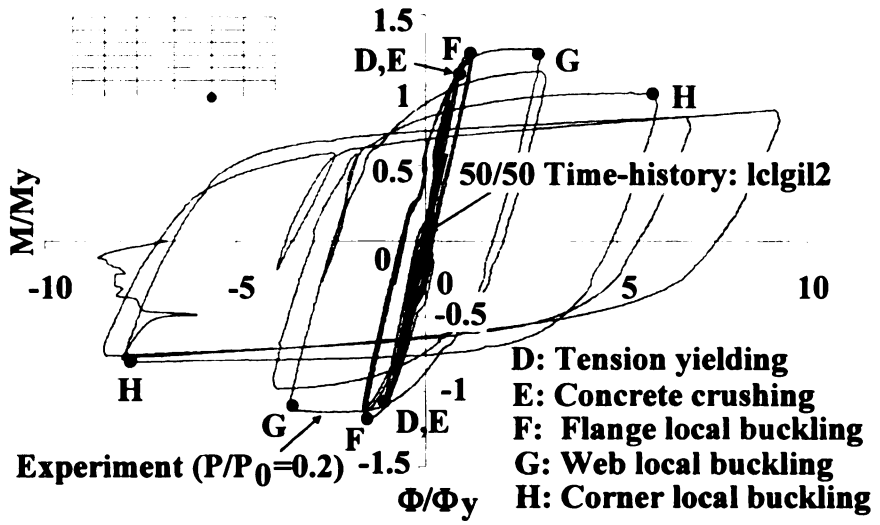


Figure 5.50b Interior column M-Φ interaction curve of flexible six-story CFT MRF subjected to SAC 50/50 time-history *lclgil2*

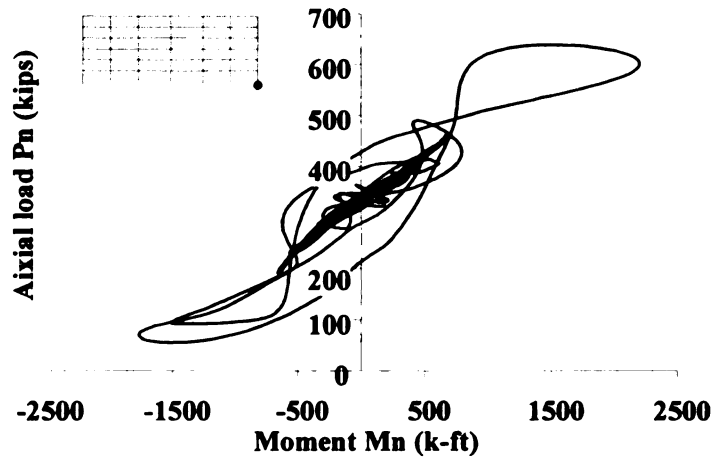


Figure 5.51a Right corner column P-M interaction curve of flexible six-story CFT MRF subjected to SAC 50/50 time-history *lclgil2*

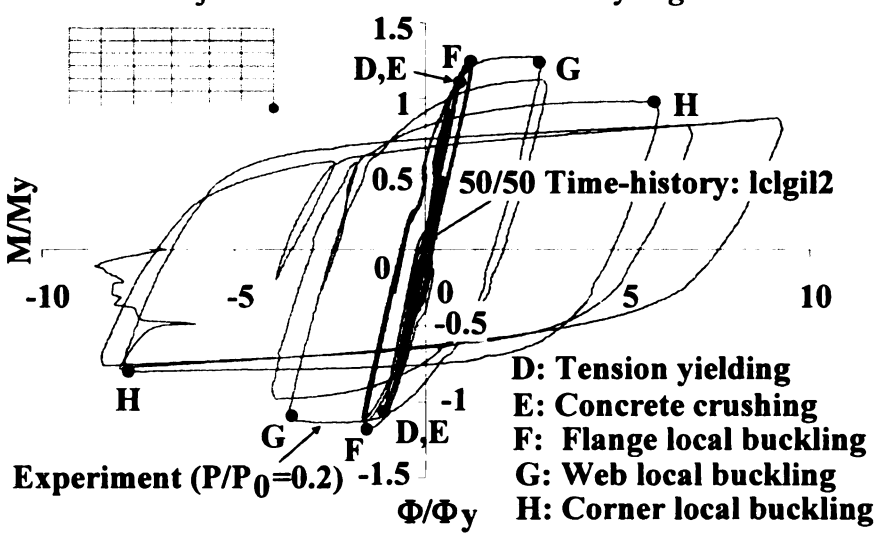


Figure 5.51b Right corner column M-Φ interaction curve of flexible six-story CFT MRF subjected to SAC 50/50 time-history *lclgil2*

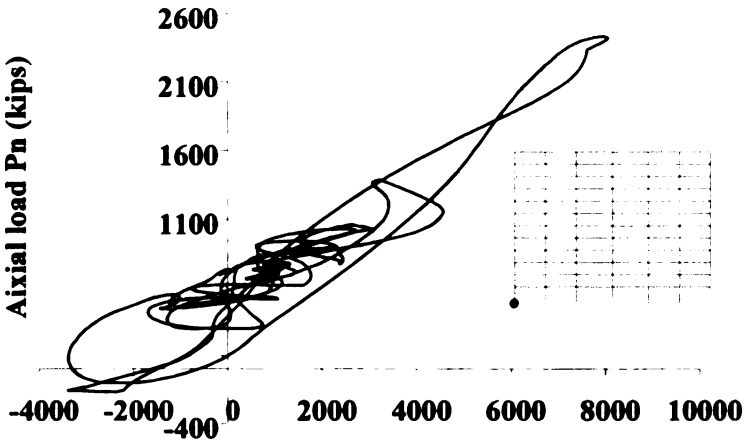


Figure 5.52a Left corner column P-M interaction curve of flexible twelve-story CFT MRF subjected to SAC 2/50 time-history *lpvst03*

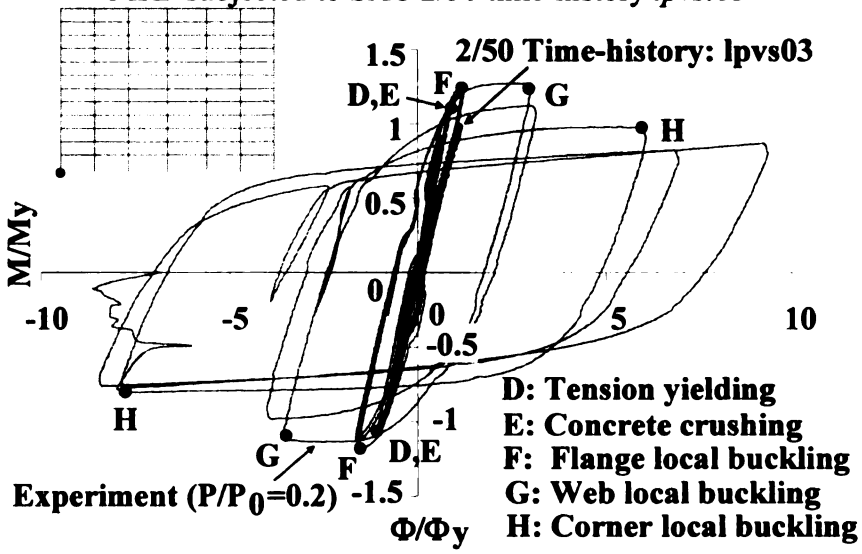


Figure 5.52b Left corner column M-Φ interaction curve of flexible twelve-story CFT MRF subjected to SAC 2/50 time-history *lpvst03*

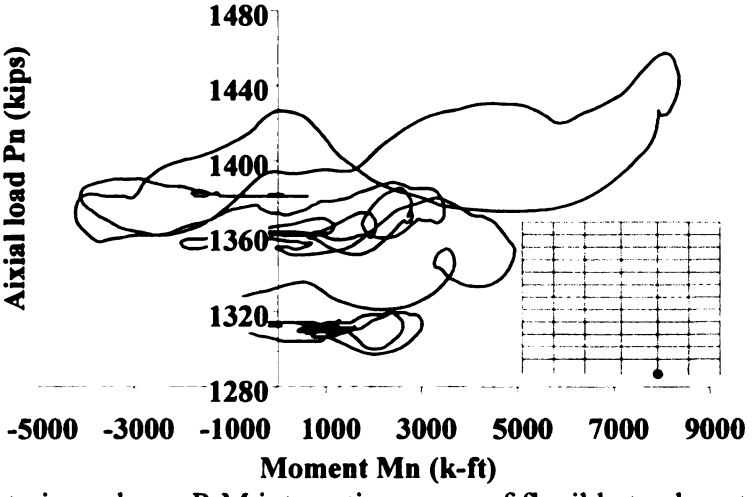


Figure 5.53a Interior column P-M interaction curve of flexible twelve-story CFT MRF subjected to SAC 2/50 time-history *lpvst03*

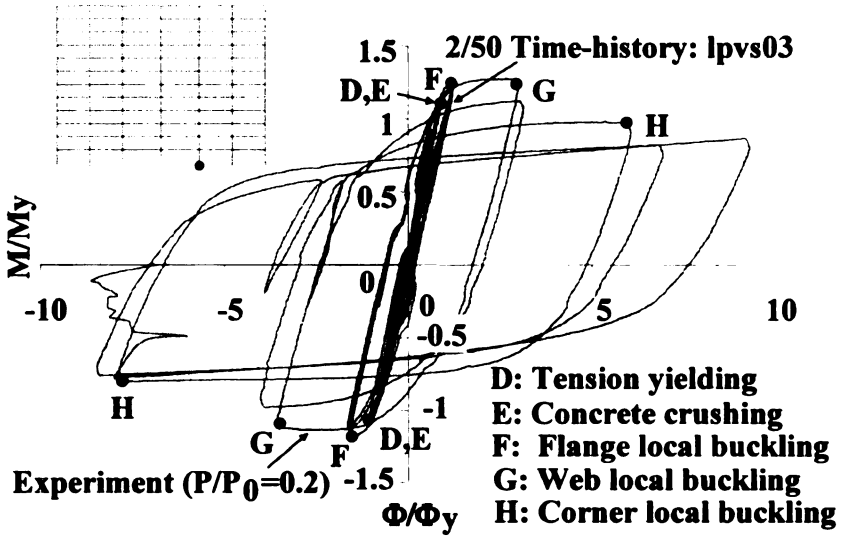


Figure 5.53b Interior column M-Φ interaction curve of flexible twelve-story CFT MRF subjected to SAC 2/50 time-history *lpvst03*

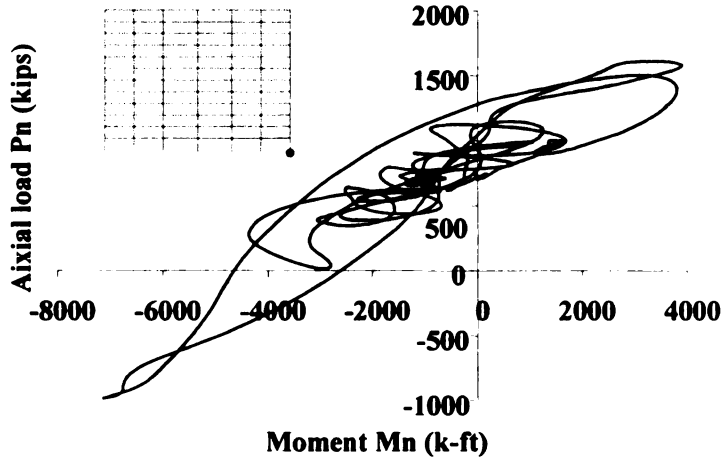


Figure 5.54a Right corner column P-M interaction curve of flexible twelve-story CFT MRF subjected to SAC 2/50 time-history *lpvst03*

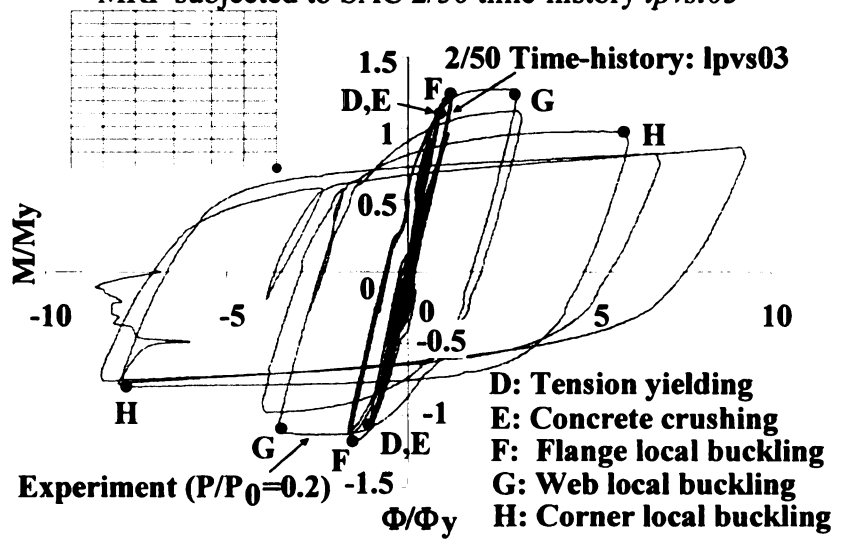


Figure 5.54b Right corner column M-Φ interaction curve of flexible twelve-story CFT MRF subjected to SAC 2/50 time-history *lpvst03*

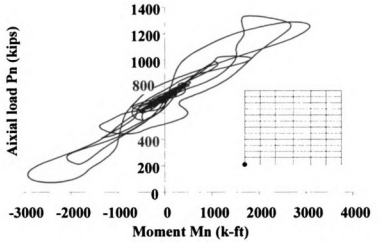


Figure 5.55a Left corner column P-M interaction curve of flexible twelve-story CFT MRF subjected to SAC 50/50 time-history *lclgil2*

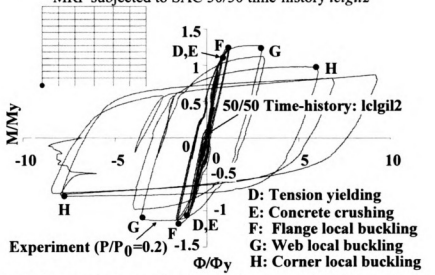


Figure 5.55b Left corner column M-Φ interaction curve of flexible twelve-story CFT MRF subjected to SAC 50/50 time-history *lclgil2*

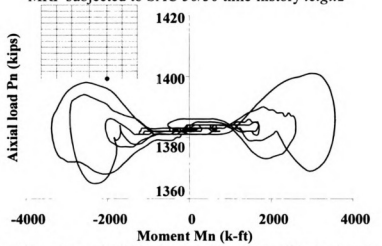


Figure 5.56a Interior column P-M interaction curve of flexible twelve-story CFT MRF subjected to SAC 50/50 time-history *lclgil2*

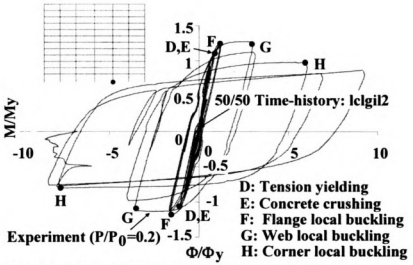


Figure 5.56b Interior column M-Φ interaction curve of flexible twelve-story CFT MRF subjected to SAC 50/50 time-history *lclgil2*

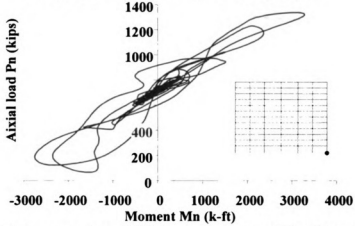


Figure 5.57a Right corner column P-M interaction curve of flexible twelve-story CFT MRF subjected to SAC 50/50 time-history *lclgil2*

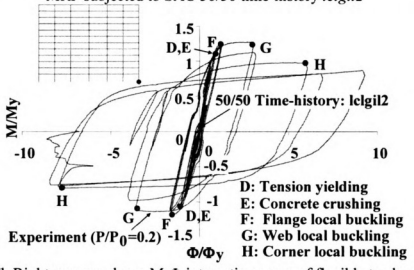


Figure 5.57b Right corner column M-Φ interaction curve of flexible twelve-story CFT MRF subjected to SAC 50/50 time-history *lclgil2*

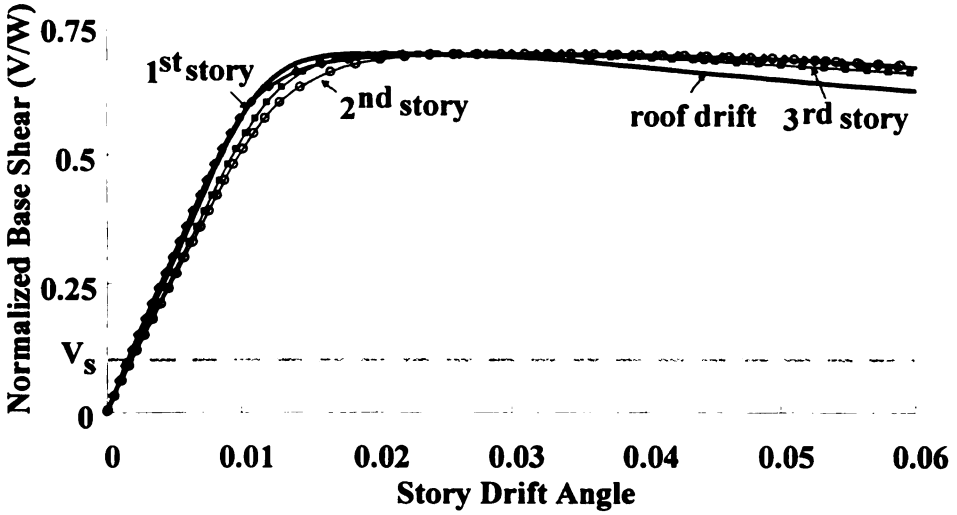


Figure 5.58 Story pushover curves for lower three stories of the flexible six-story distributed CFT MRF

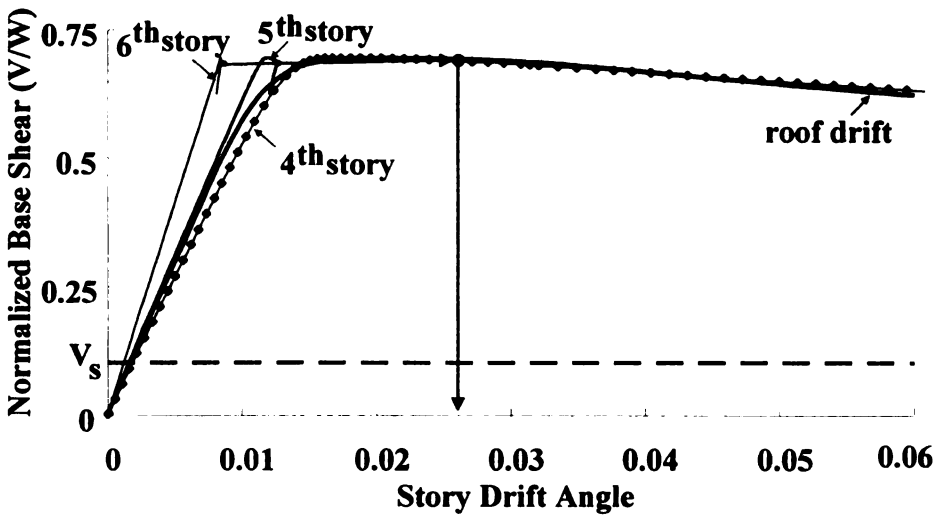


Figure 5.59 Story pushover curves for upper three stories of the flexible six-story distributed CFT MRF

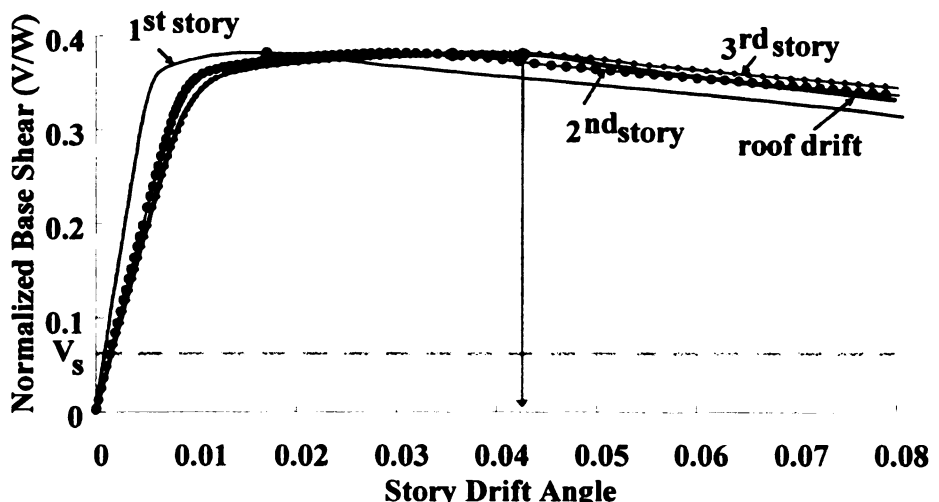


Figure 5.60 Story pushover curves for the 1st to 3rd stories of the flexible twelve-story distributed CFT MRF

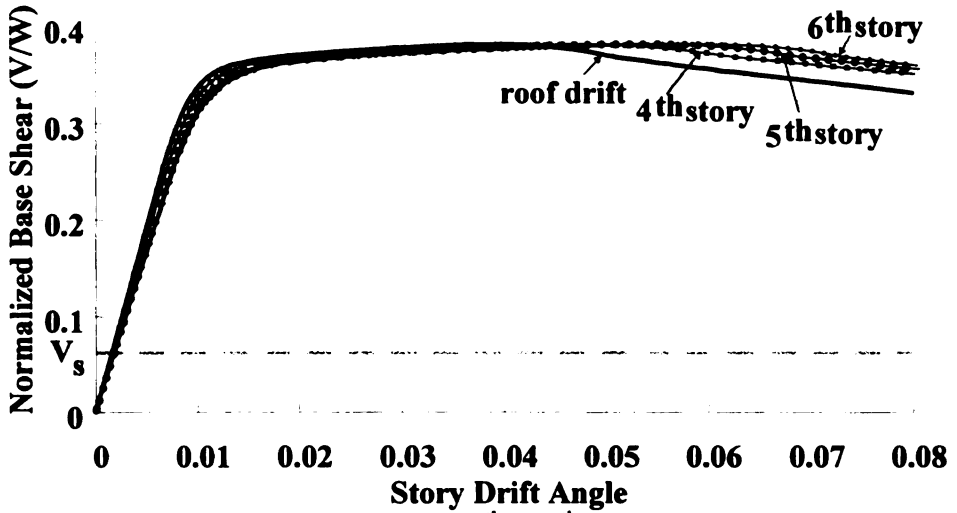


Figure 5.61 Story pushover curves for the 4th to 6th stories of the flexible twelve-story distributed CFT MRF

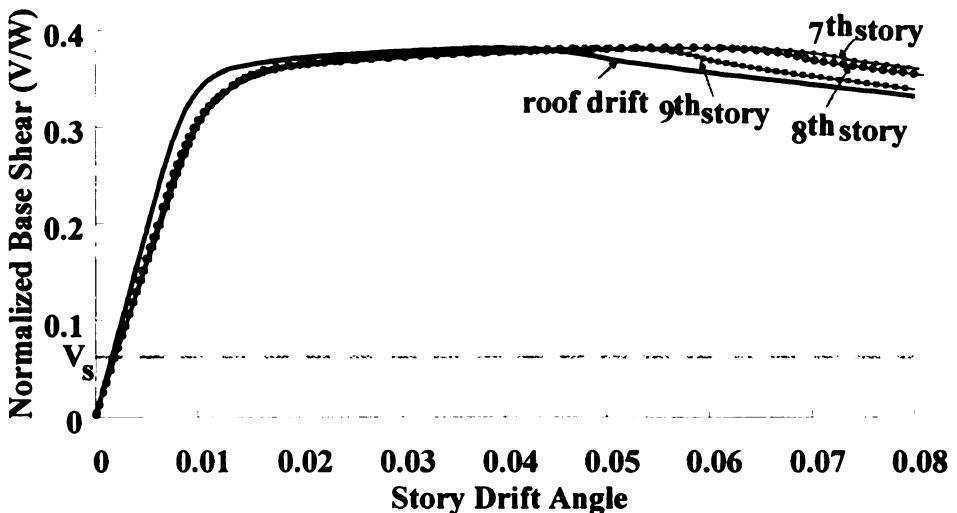


Figure 5.62 Story pushover curves for the 7th to 9th stories of the flexible twelve-story distributed CFT MRF

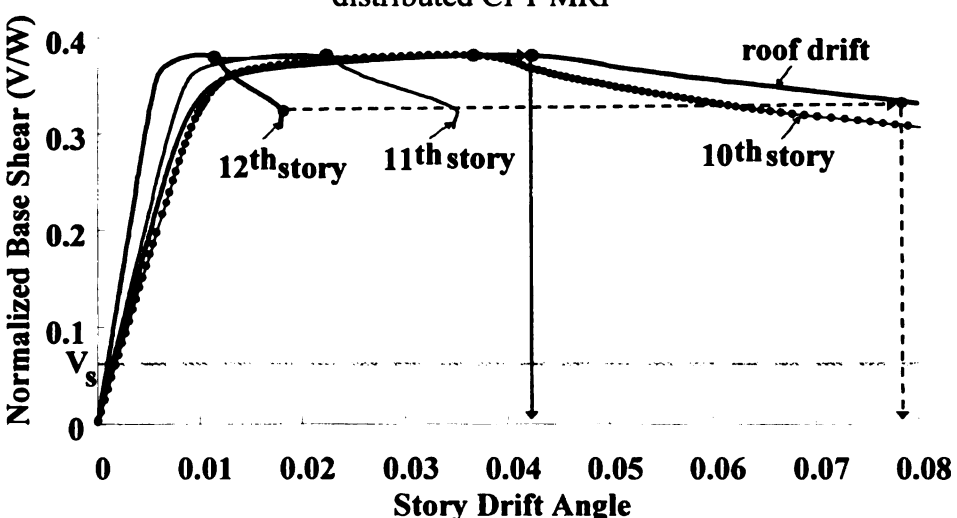


Figure 5.63 Story pushover curves for the 10th to 12th stories of the flexible twelve-story distributed CFT MRF

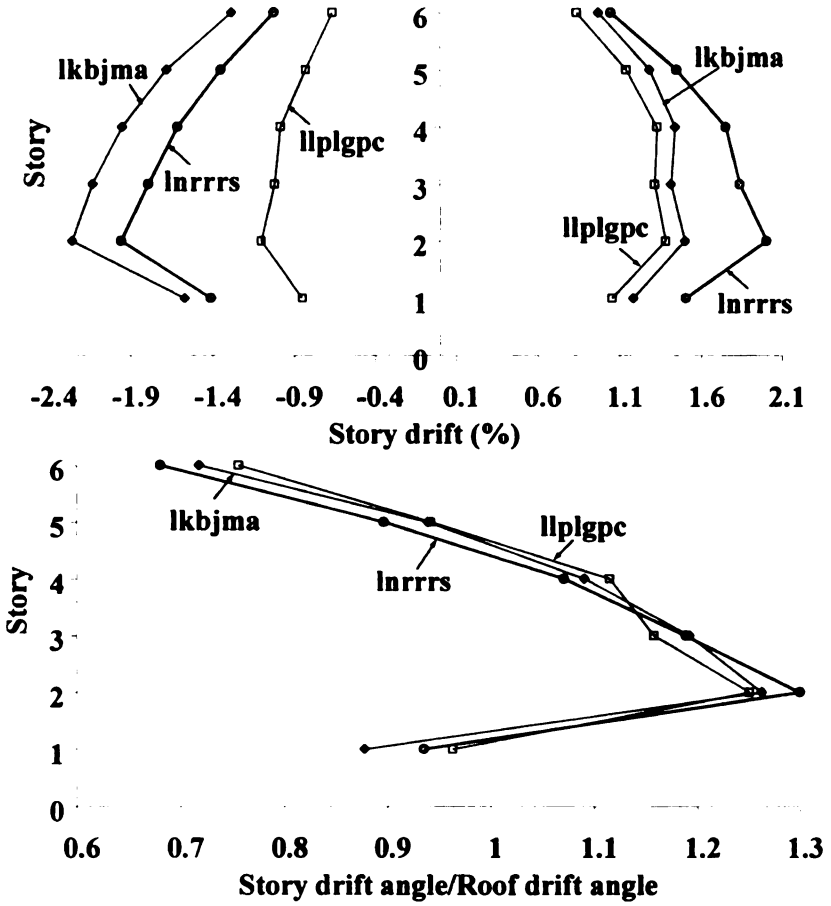


Figure 5.64 Story drift envelop and story drift angle to roof drift angle ratio of flexible six-story distributed CFT MRF subjected to SAC 2/50 time-histories: *lkbjma, lnrrrs* and *llplgpc*

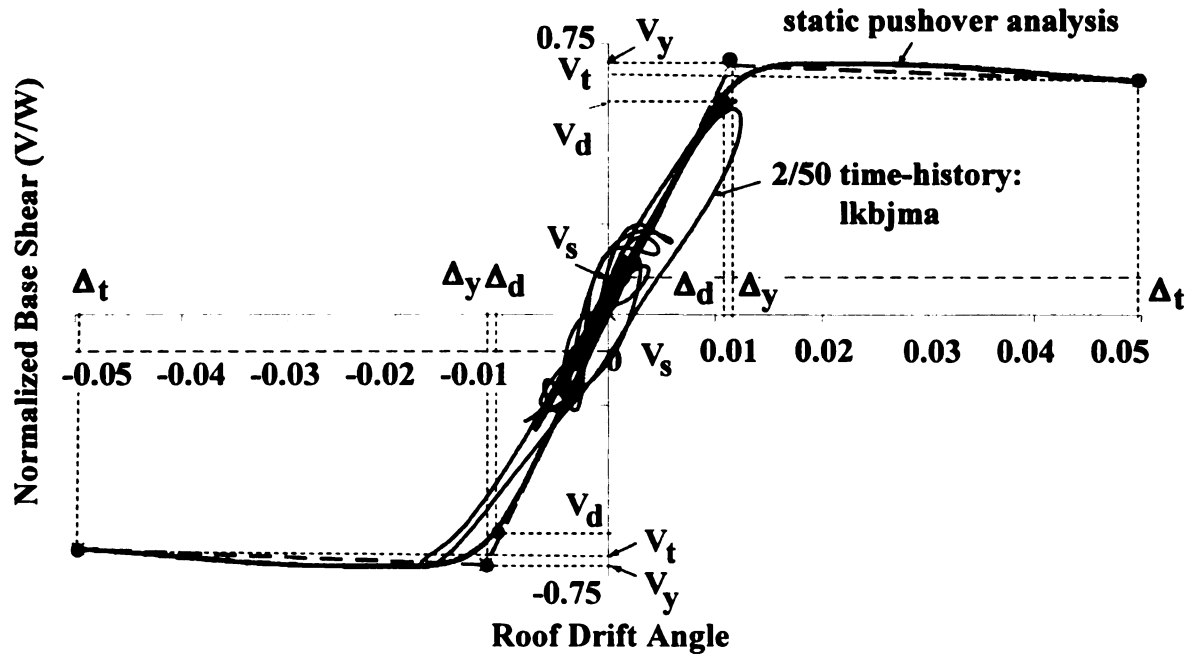


Figure 5.65 Static pushover and time-history analyses (SAC 2/50, *lkbjma*) of flexible six-story distributed CFT MRF

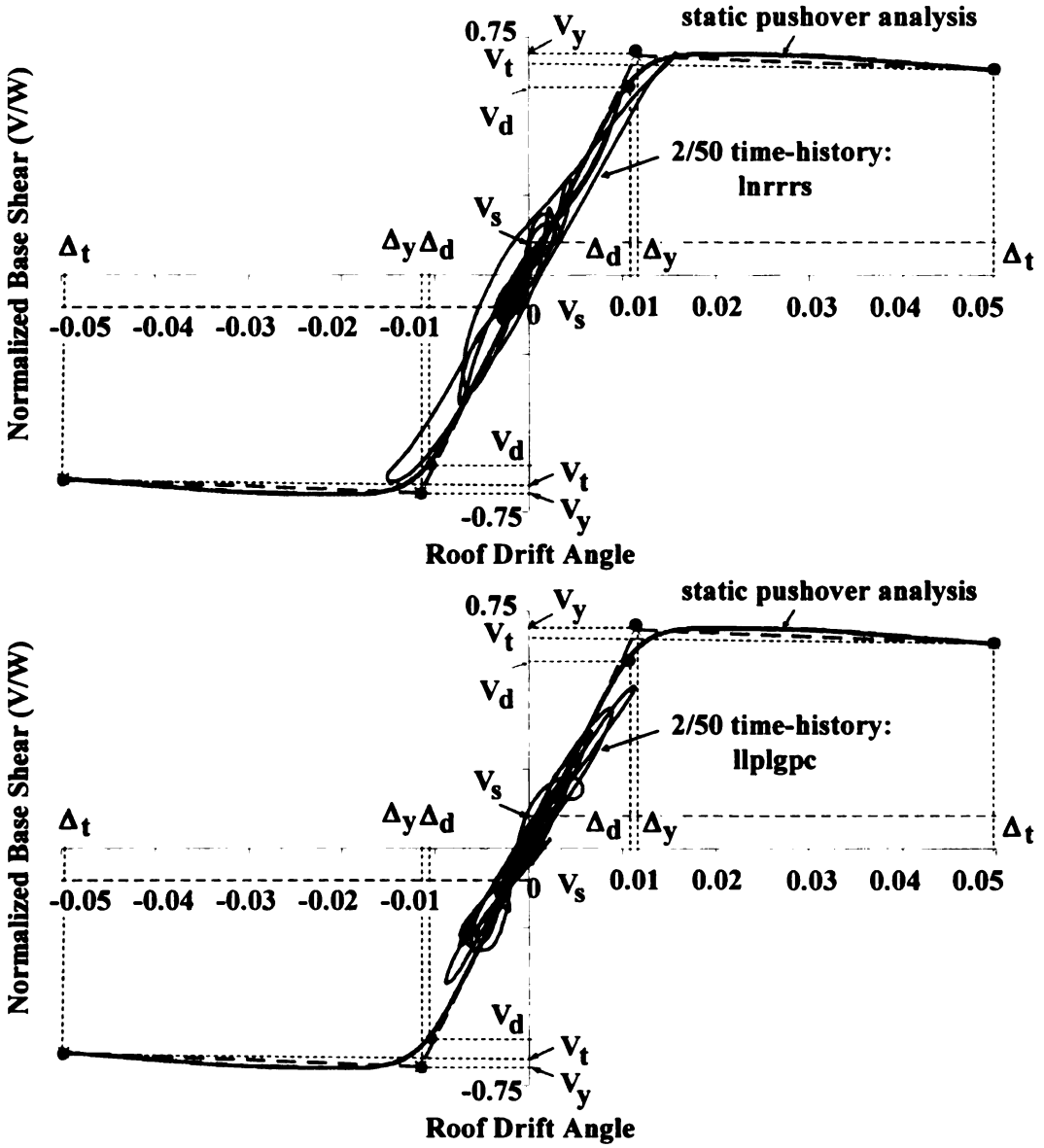


Figure 5.66 Static pushover analysis and time-history analyses (SAC 2/50, *lnrrrs* and *llplgpc*) of flexible six-story distributed CFT MRF

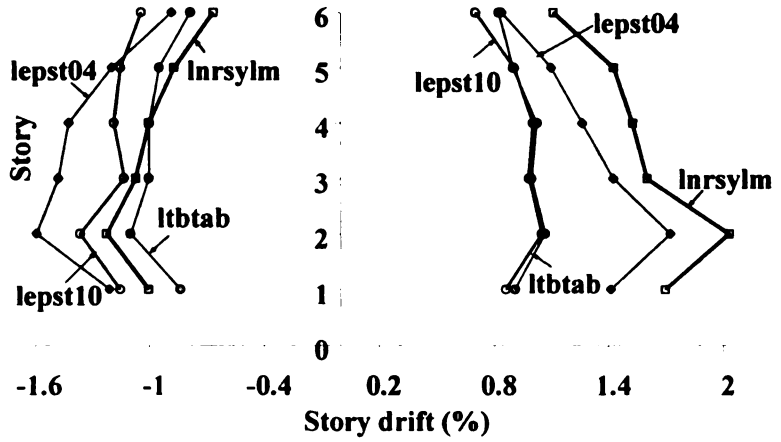


Figure 5.67 Story drift envelope of flexible six-story distributed CFT MRF subjected to SAC 2/50 time-histories: *lnrsylm, ltbtab, lepst04* and *lepst10*

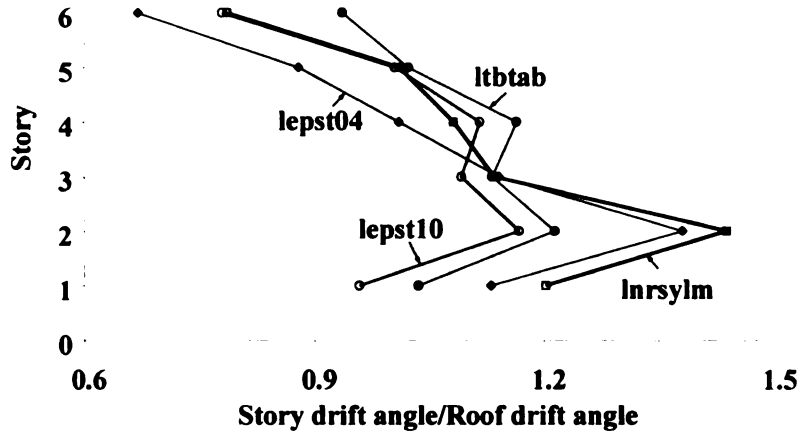


Figure 5.68 Story drift angle to roof drift angle ratio of flexible six-story distributed CFT MRF subjected to SAC 2/50 time-histories: *lnrsylm, ltbtab, lepst04* and *lepst10*

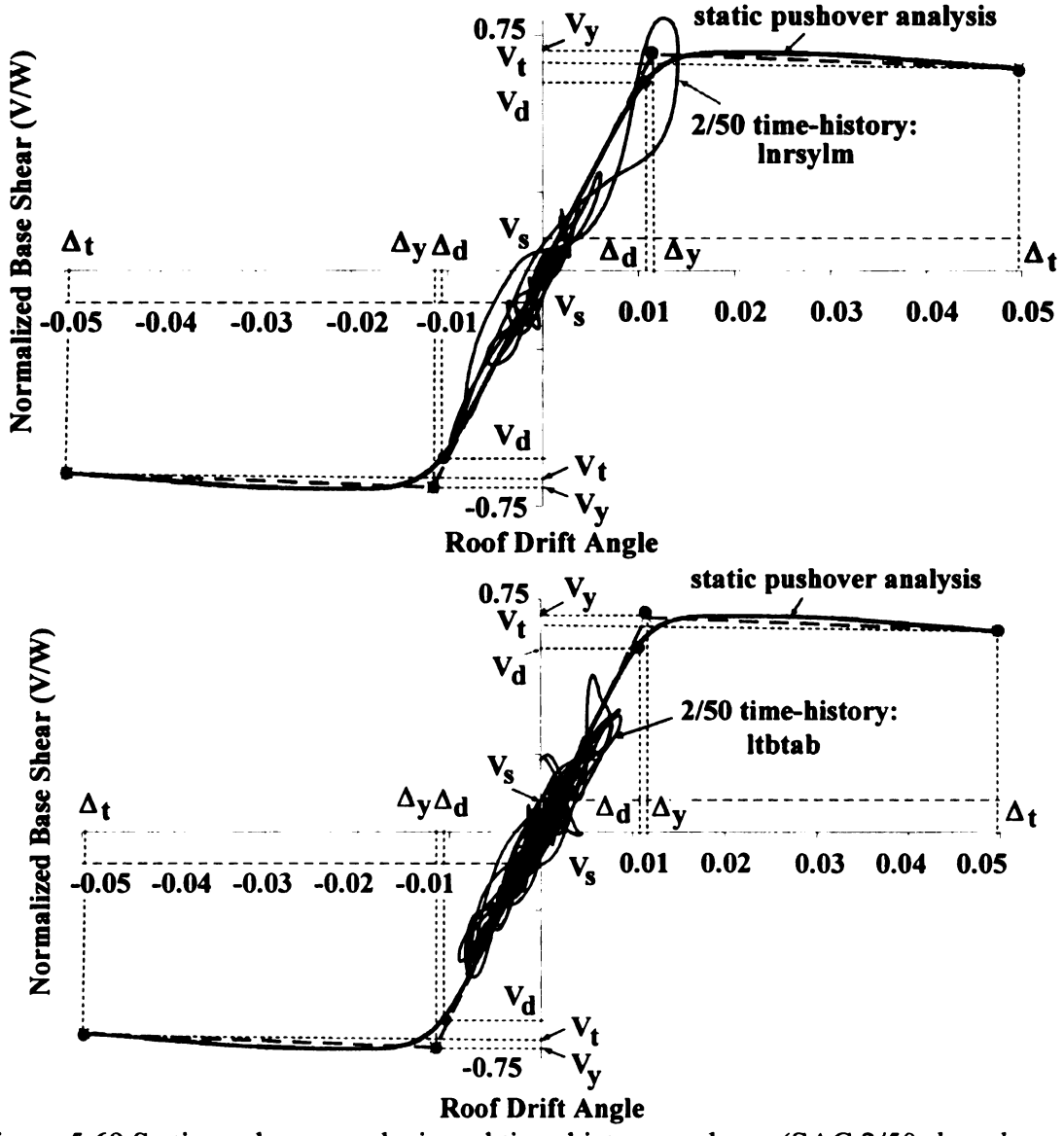


Figure 5.69 Static pushover analysis and time-history analyses (SAC 2/50, *lnrsylm* and *ltbtab*) of flexible six-story distributed CFT MRF

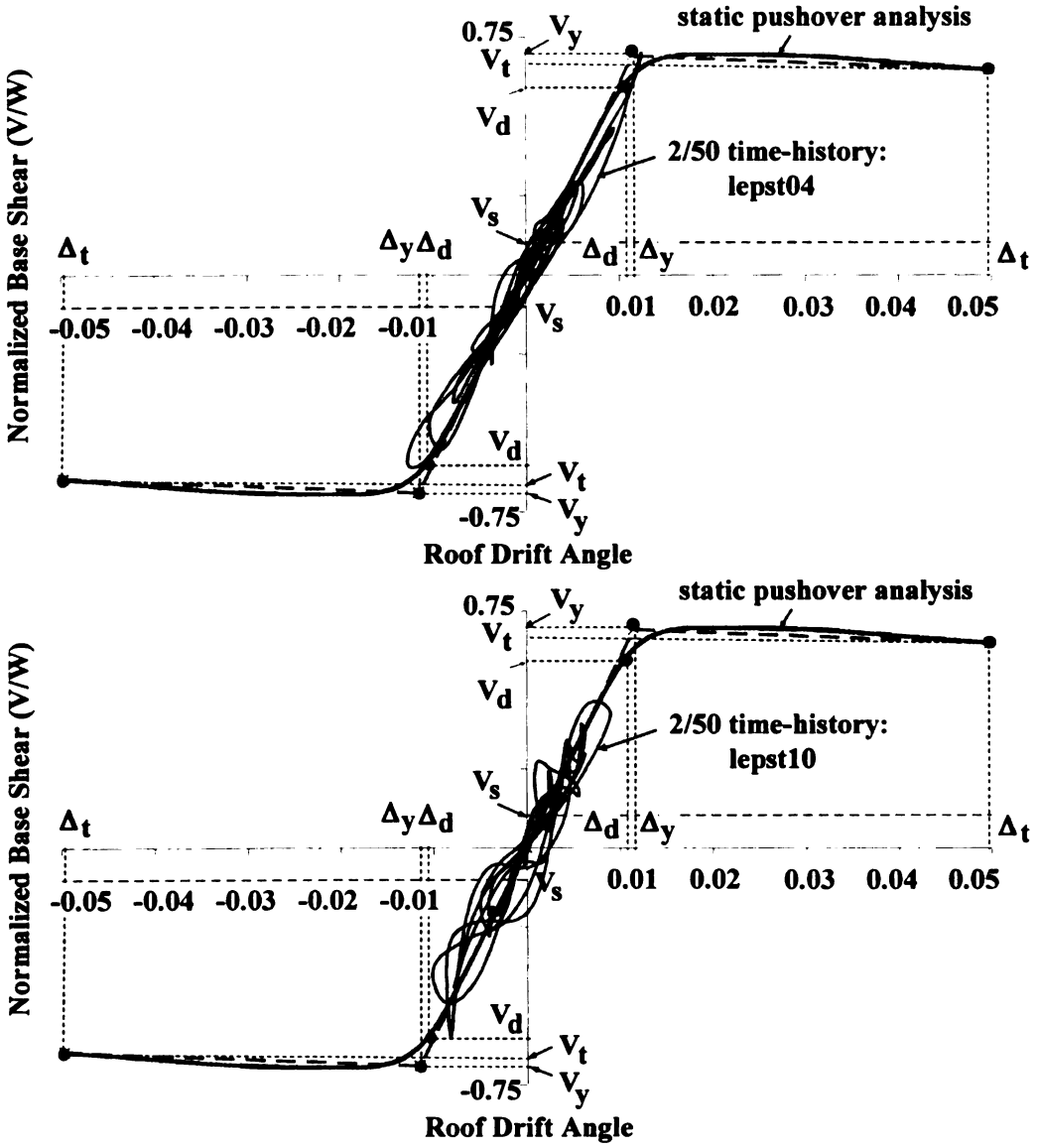


Figure 5.70 Static pushover analysis and time-history analyses (SAC 2/50, *lepst04* and *lepst10*) of flexible six-story distributed CFT MRF

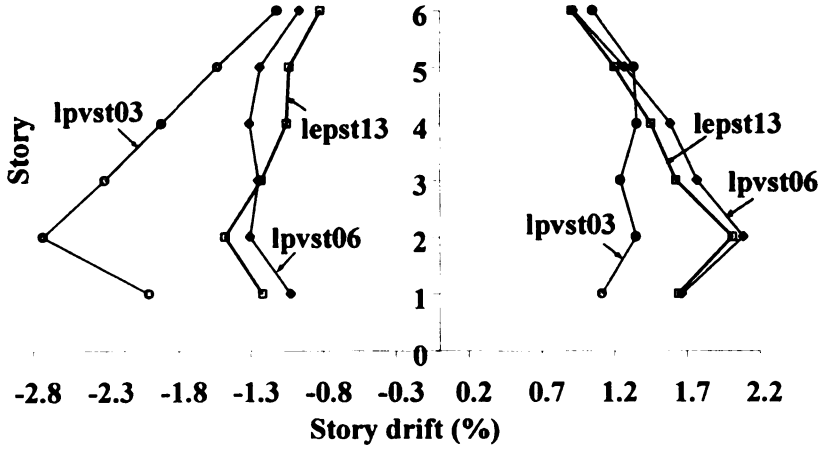


Figure 5.71 Story drift envelop of flexible six-story distributed CFT MRF subjected to SAC 2/50 time-histories: *lepst13, lpvst03* and *lpvst06*

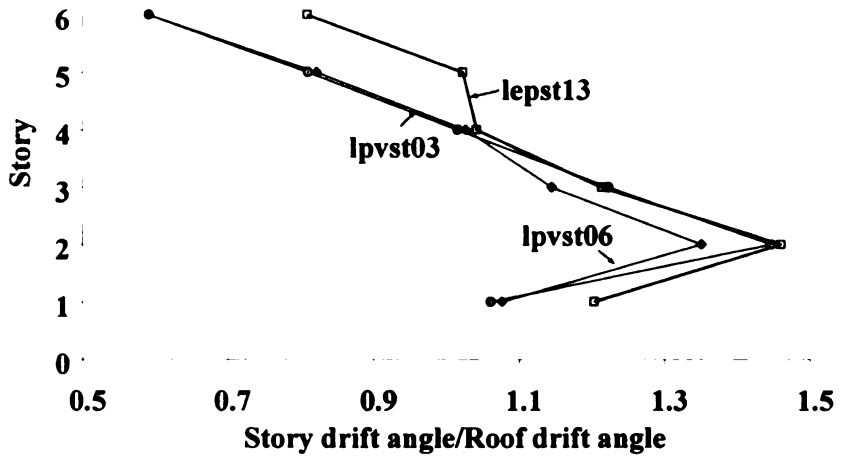


Figure 5.72 Story drift angle to roof drift angle ratio of flexible six-story distributed CFT MRF subjected to SAC 2/50 time-histories: *lepst13, lpvst03* and *lpvst06*

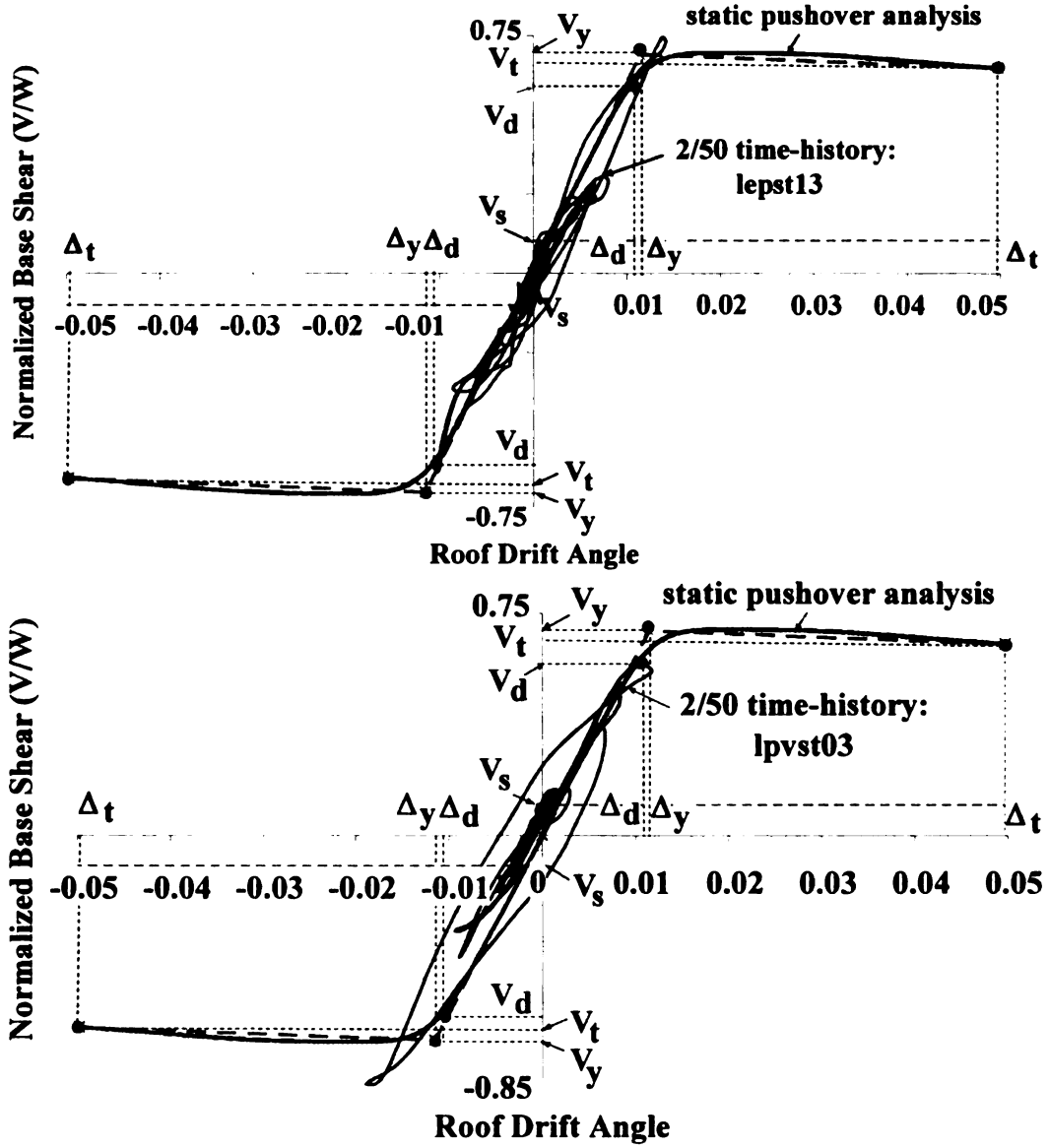


Figure 5.73 Static pushover analysis and time-history analyses (SAC 2/50, *lepst13* and *lpvst03*) of flexible six-story distributed CFT MRF

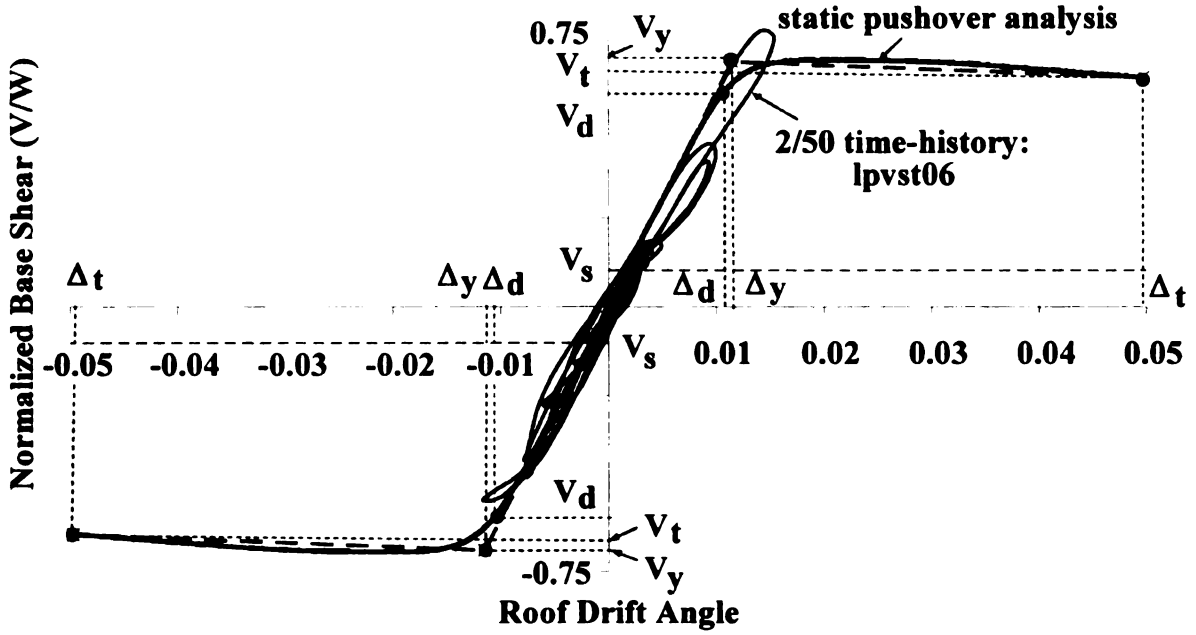


Figure 5.74 Static pushover and time-history analyses (SAC 2/50, *lpvst06*) of flexible six-story distributed CFT MRF

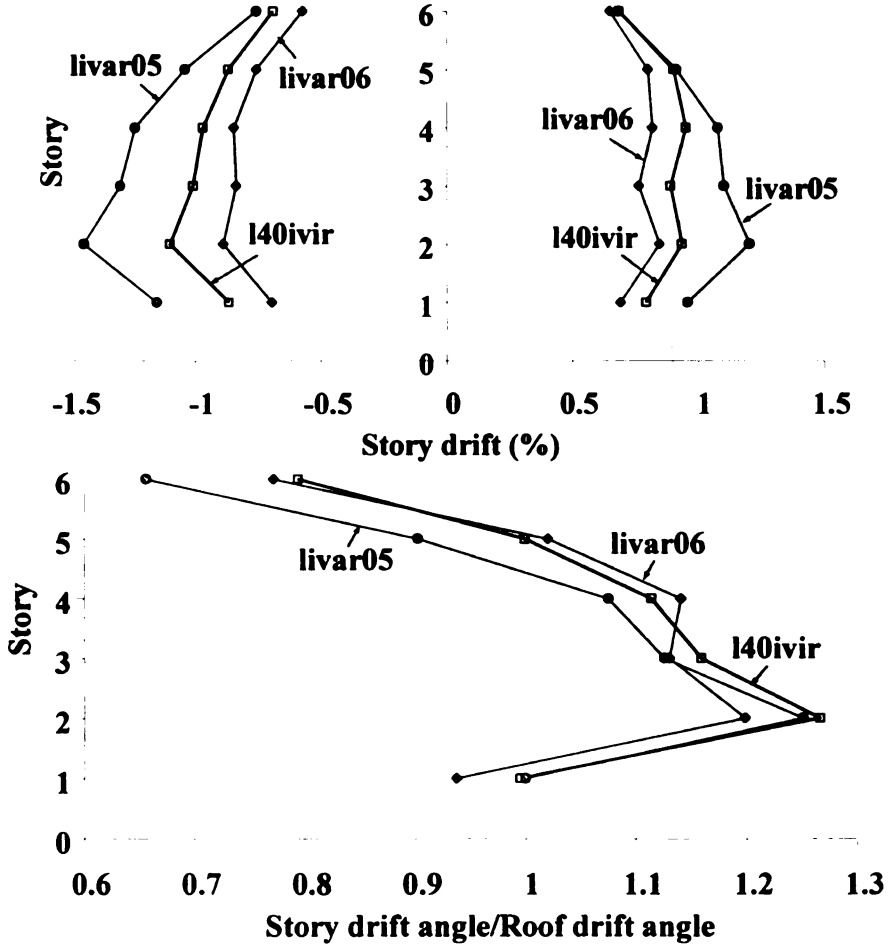


Figure 5.75 Story drift envelope and story drift angle to roof drift angle ratio of flexible six-story distributed CFT MRF subjected to SAC 10/50 time-histories: *l40ivir, livar05* and *livar06*

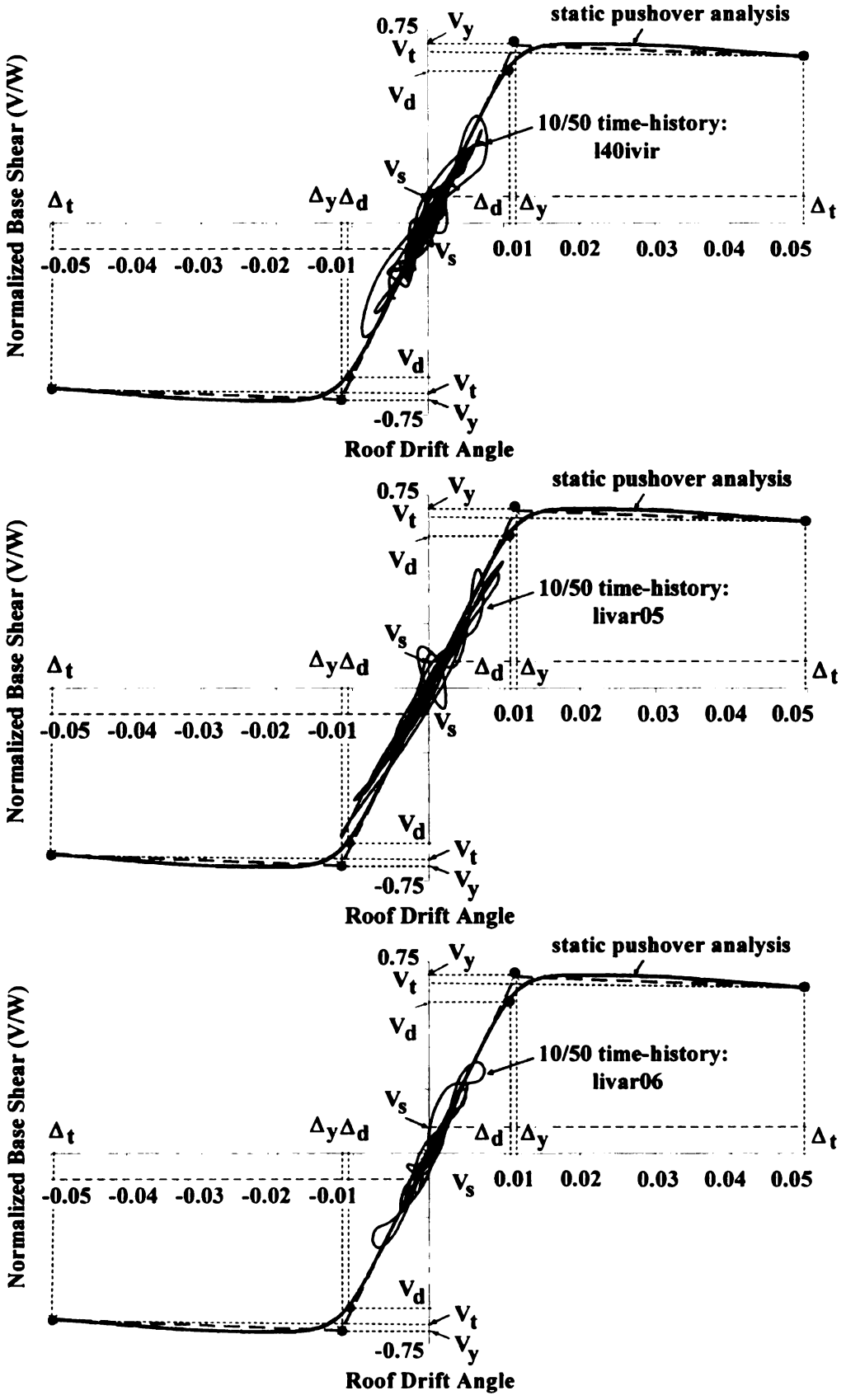


Figure 5.76 Static pushover analysis and time-history analyses (SAC 10/50, *l40ivir*, *livar05* and *livar06*) of flexible six-story distributed CFT MRF

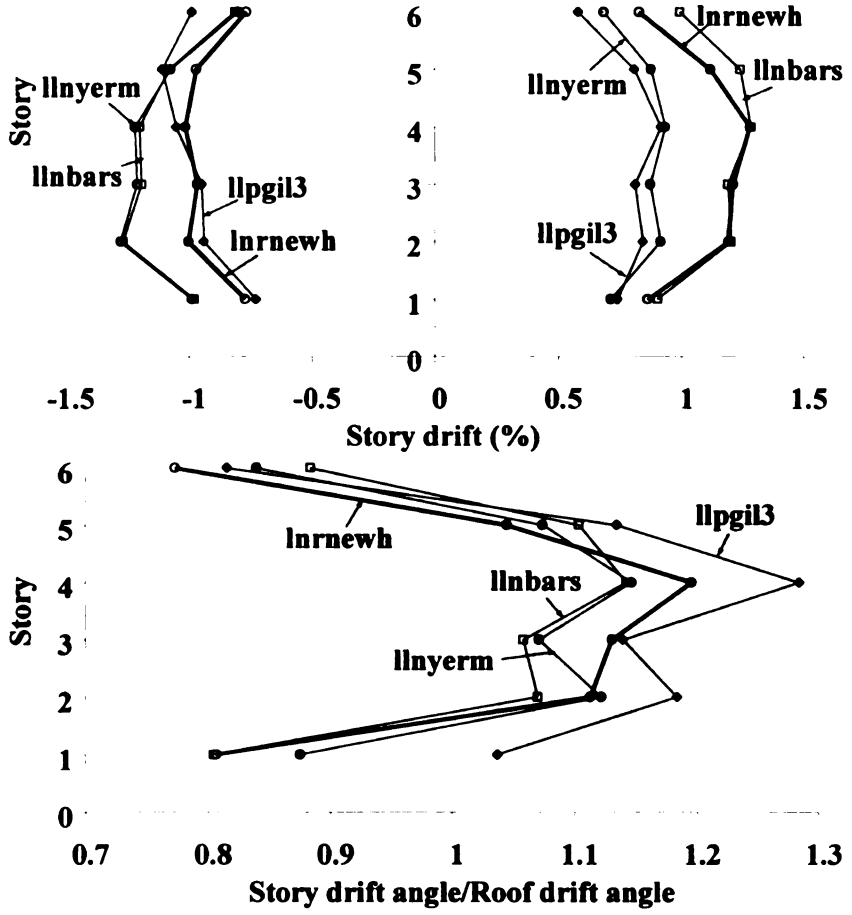


Figure 5.77 Story drift envelope and story drift angle to roof drift angle ratio of flexible six-story distributed CFT MRF subjected to SAC 10/50 time-histories: *llnbars, llnyerm, llpgil3* and *lnrnewh*

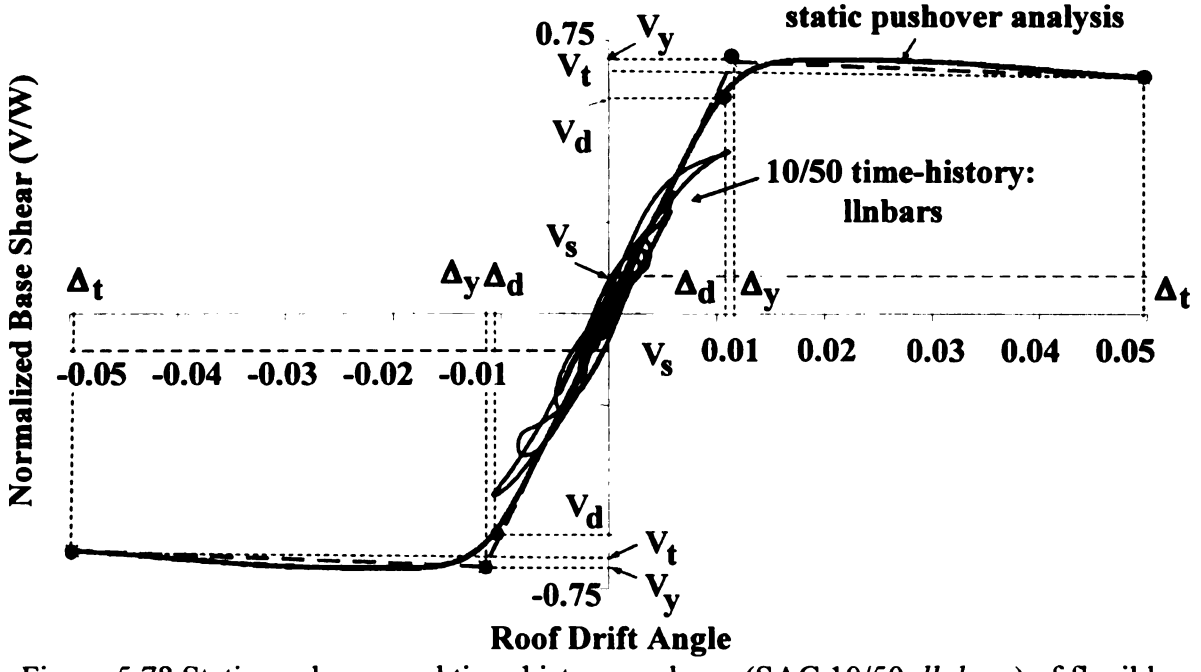


Figure 5.78 Static pushover and time-history analyses (SAC 10/50, *llnbars*) of flexible six-story distributed CFT MRF

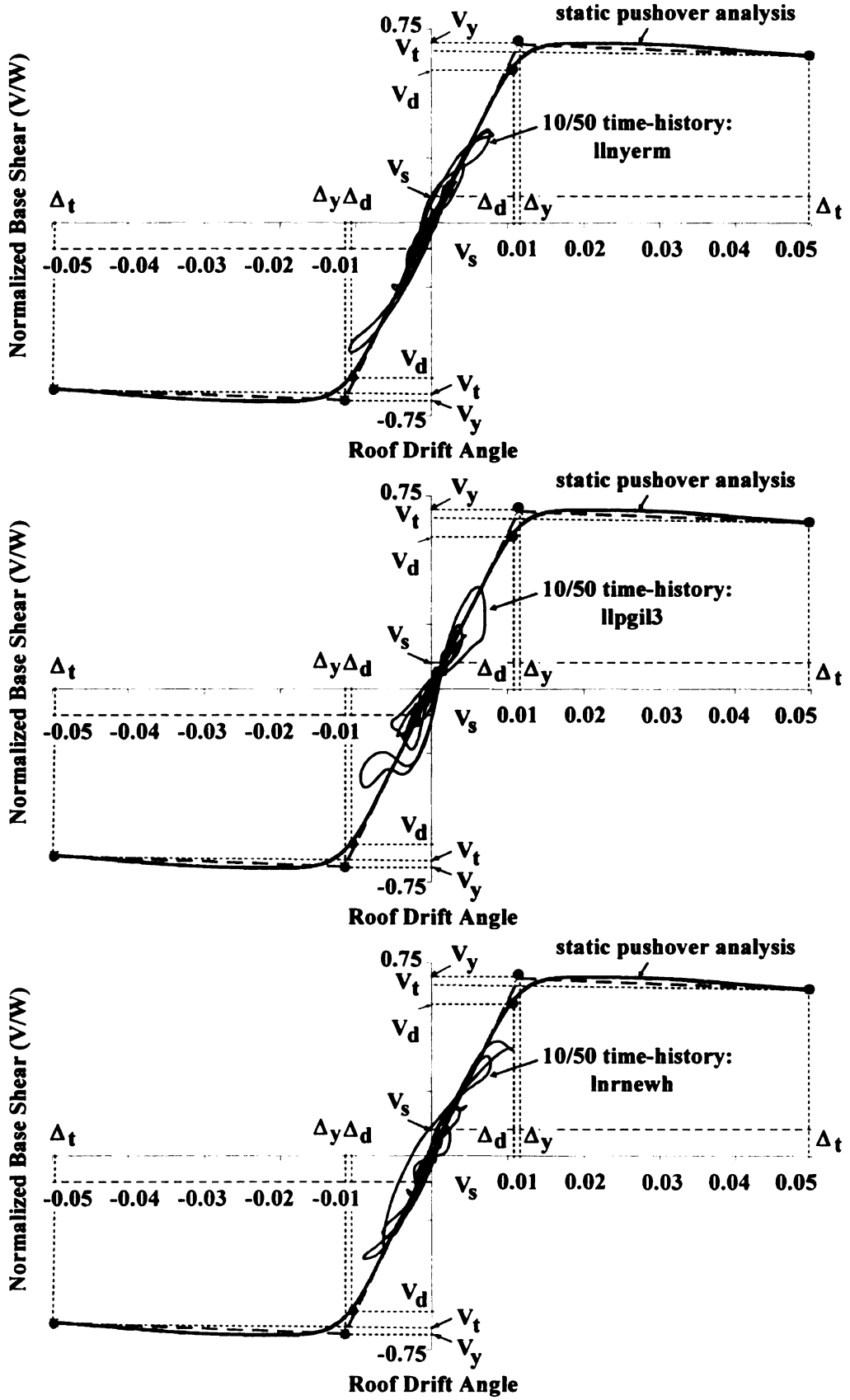


Figure 5.79 Static pushover analysis and time-history analyses (SAC 10/50, *llnyerm, llpgil3* and *lnrnewh*) of flexible six-story distributed CFT MRF

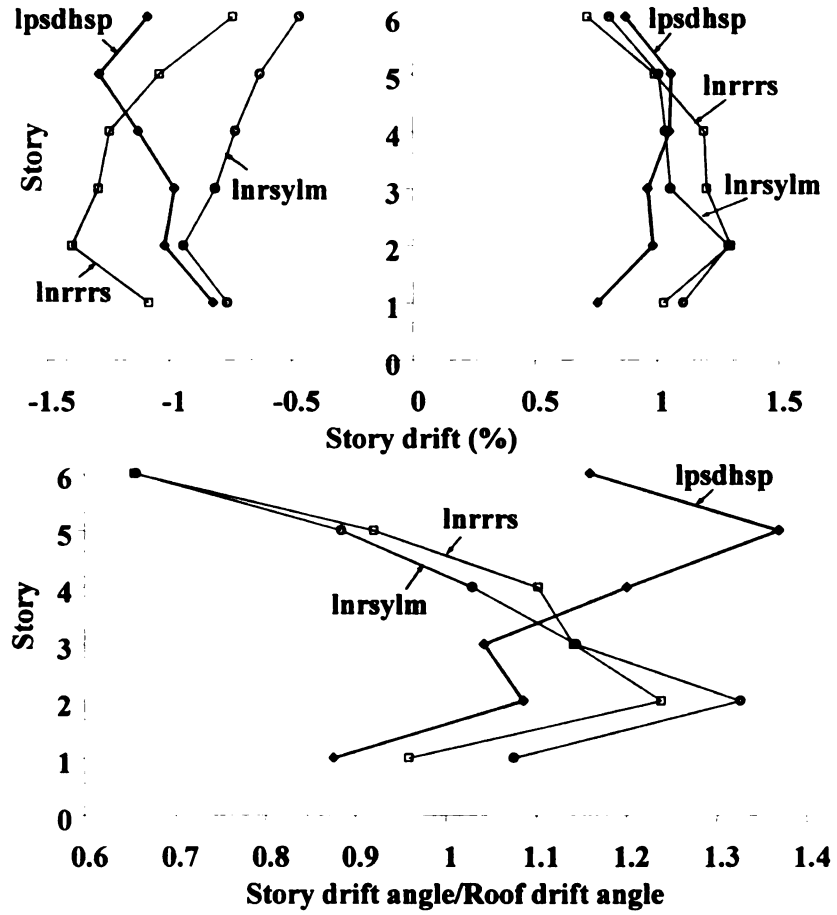


Figure 5.80 Story drift envelope and story drift angle to roof drift angle ratio of flexible six-story distributed CFT MRF subjected to SAC 10/50 time-histories: *lnrrrs, lnrsylm* and *lpsdhsp*

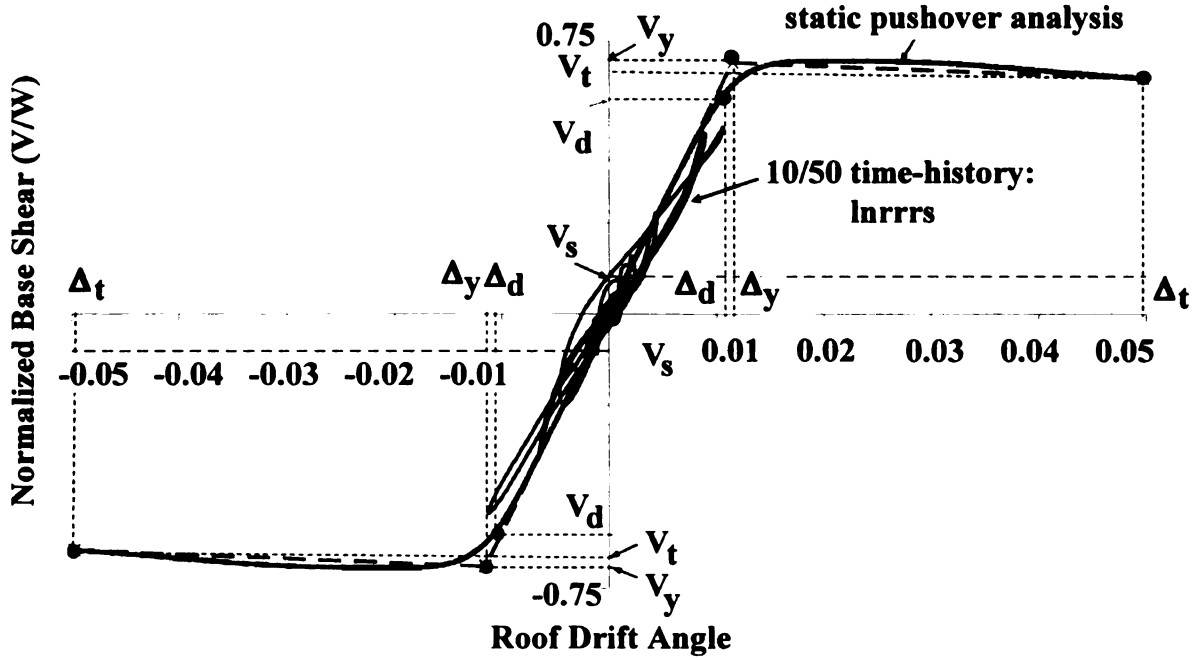


Figure 5.81 Static pushover and time-history analyses (SAC 10/50, *lnrrrs*) of flexible six-story distributed CFT MRF

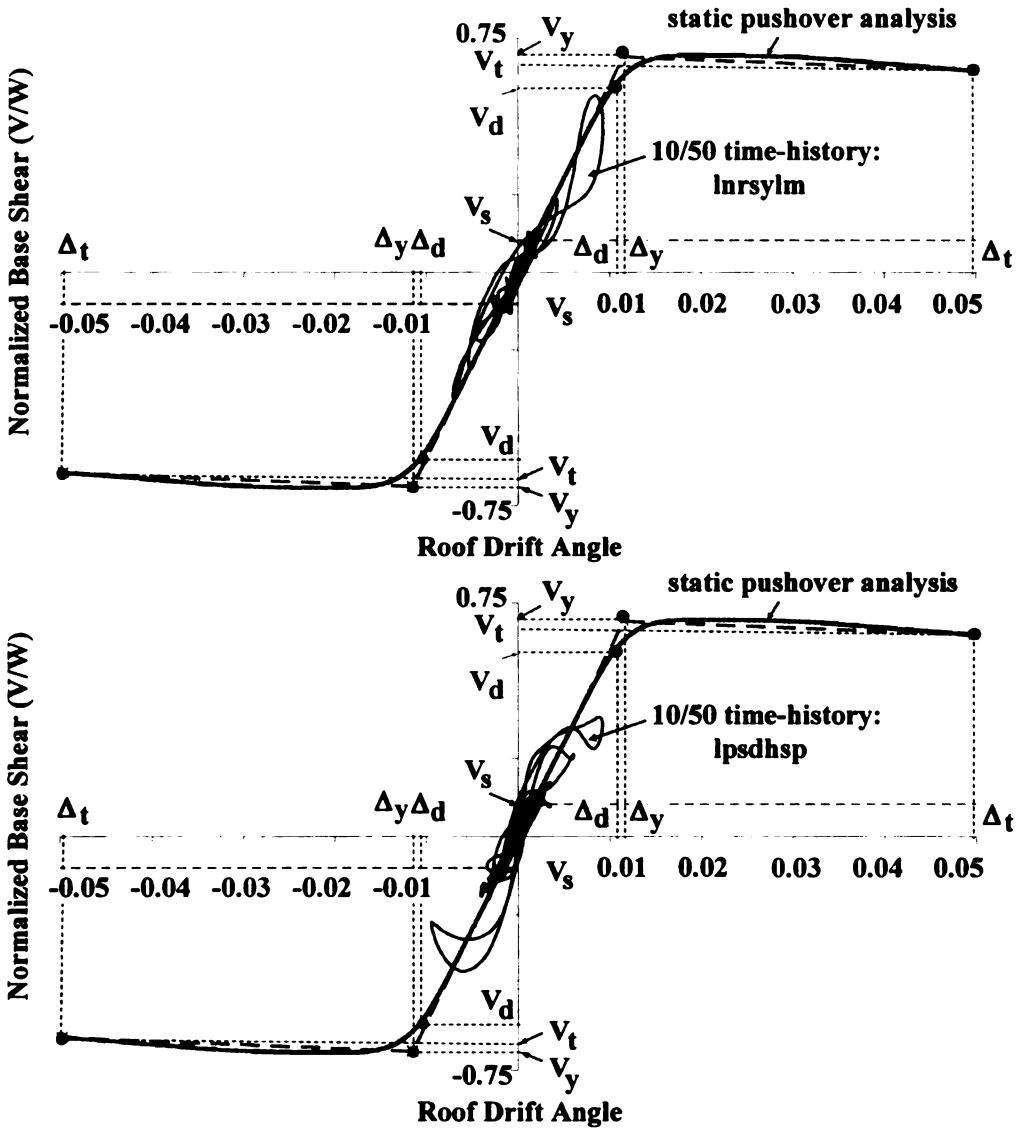


Figure 5.82 Static pushover analysis and time-history analyses (SAC 10/50, *lnrsylm* and *lpsdhsp*) of flexible six-story distributed CFT MRF

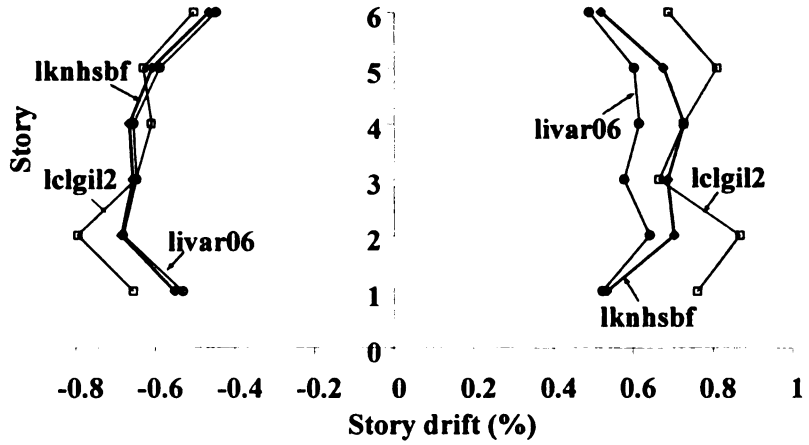


Figure 5.83 Story drift envelope of flexible six-story distributed CFT MRF subjected to SAC 50/50 time-histories: *lnrrrs, lnrsylm* and *lpsdhsp*

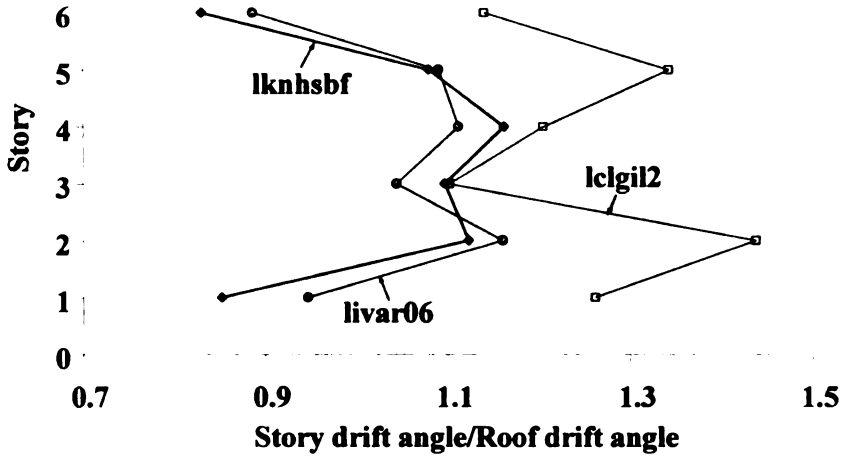


Figure 5.84 Story drift angle to roof drift angle ratio of flexible six-story distributed CFT MRF subjected to SAC 50/50 time-histories: *lnrrrs, lnrsylm* and *lpsdhsp*

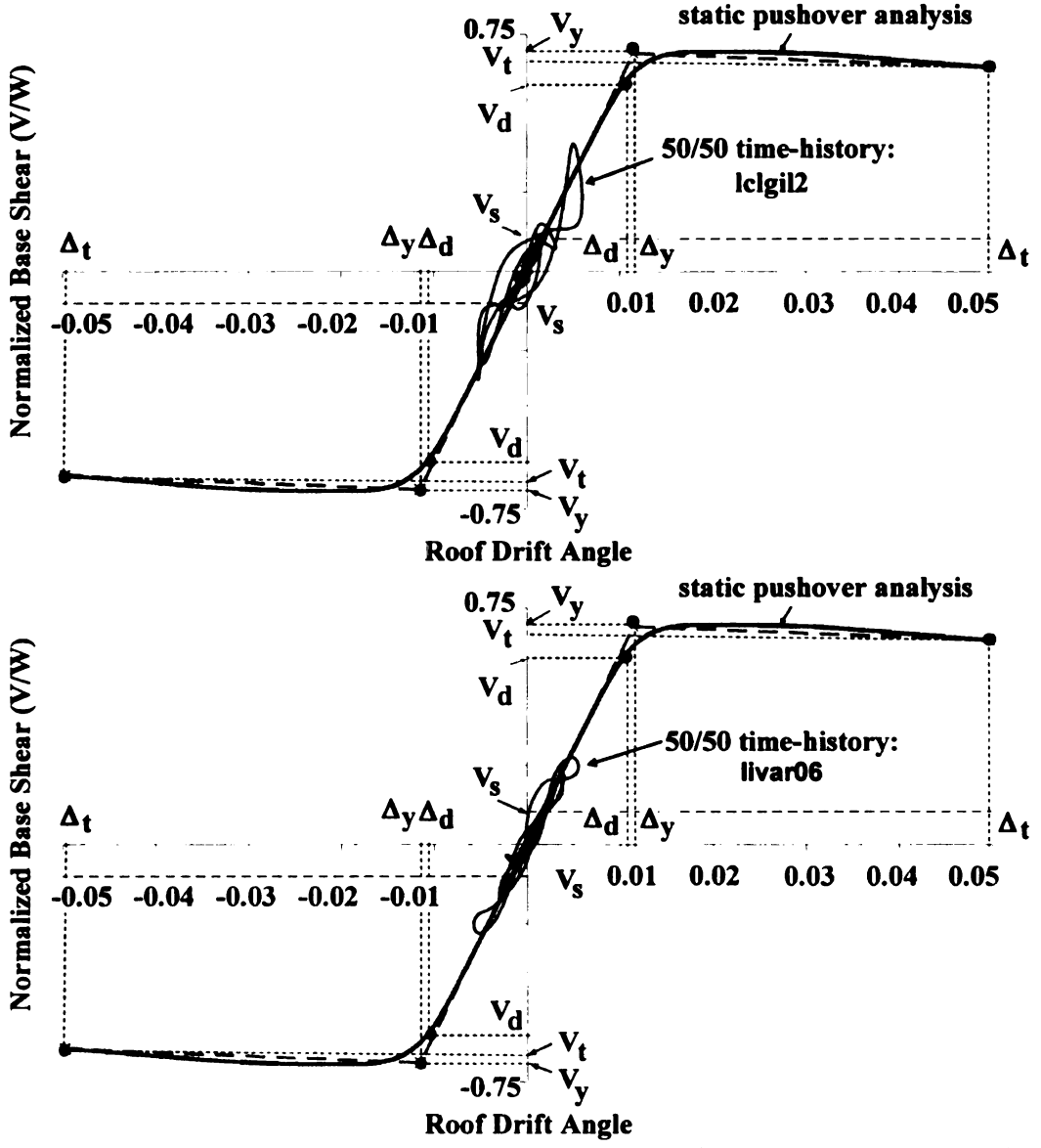


Figure 5.85 Static pushover analysis and time-history analyses (SAC 50/50, *lclgil2* and *livar06*) of flexible six-story distributed CFT MRF

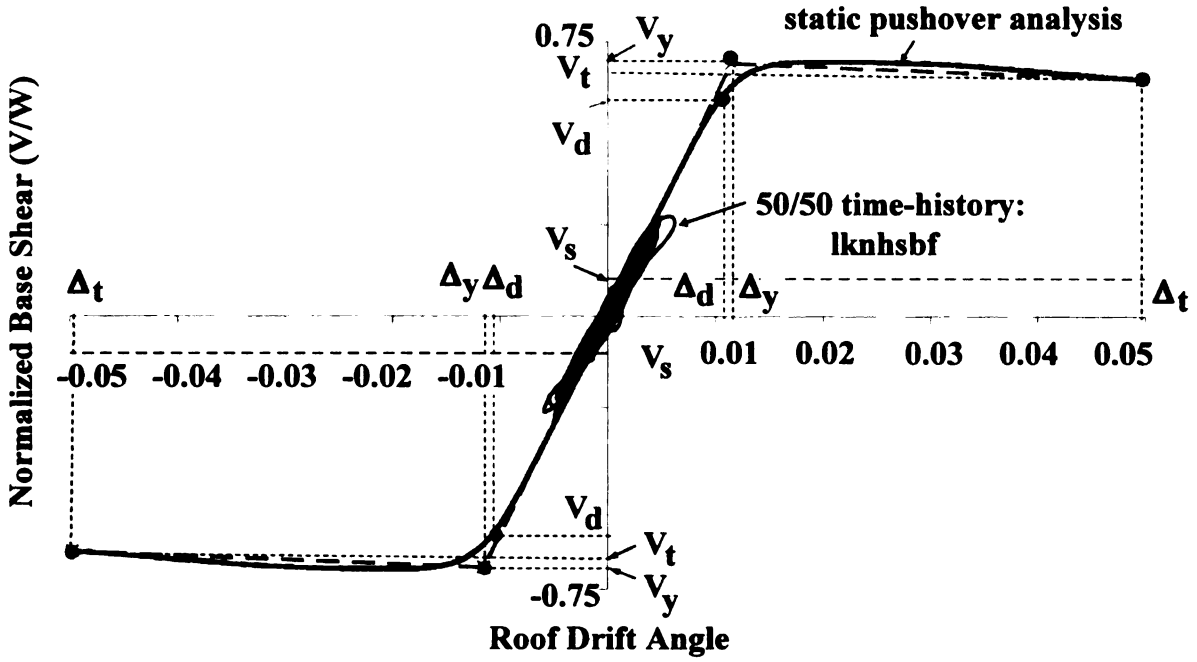


Figure 5.86 Static pushover and time-history analyses (SAC 50/50, *lknhsbf*) of flexible six-story distributed CFT MRF

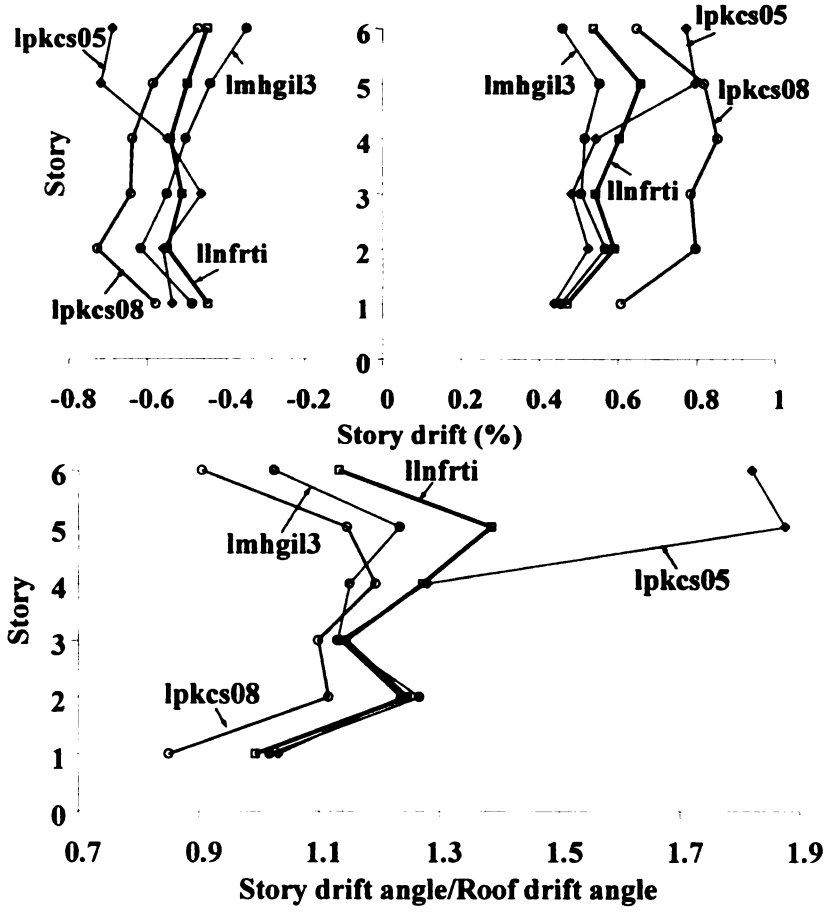


Figure 5.87 Story drift envelope and story drift angle to roof drift angle ratio of flexible six-story distributed CFT MRF subjected to SAC 50/50 time-histories: *lmhgil3, llnfrti, lpkcs05* and *lpkcs08*

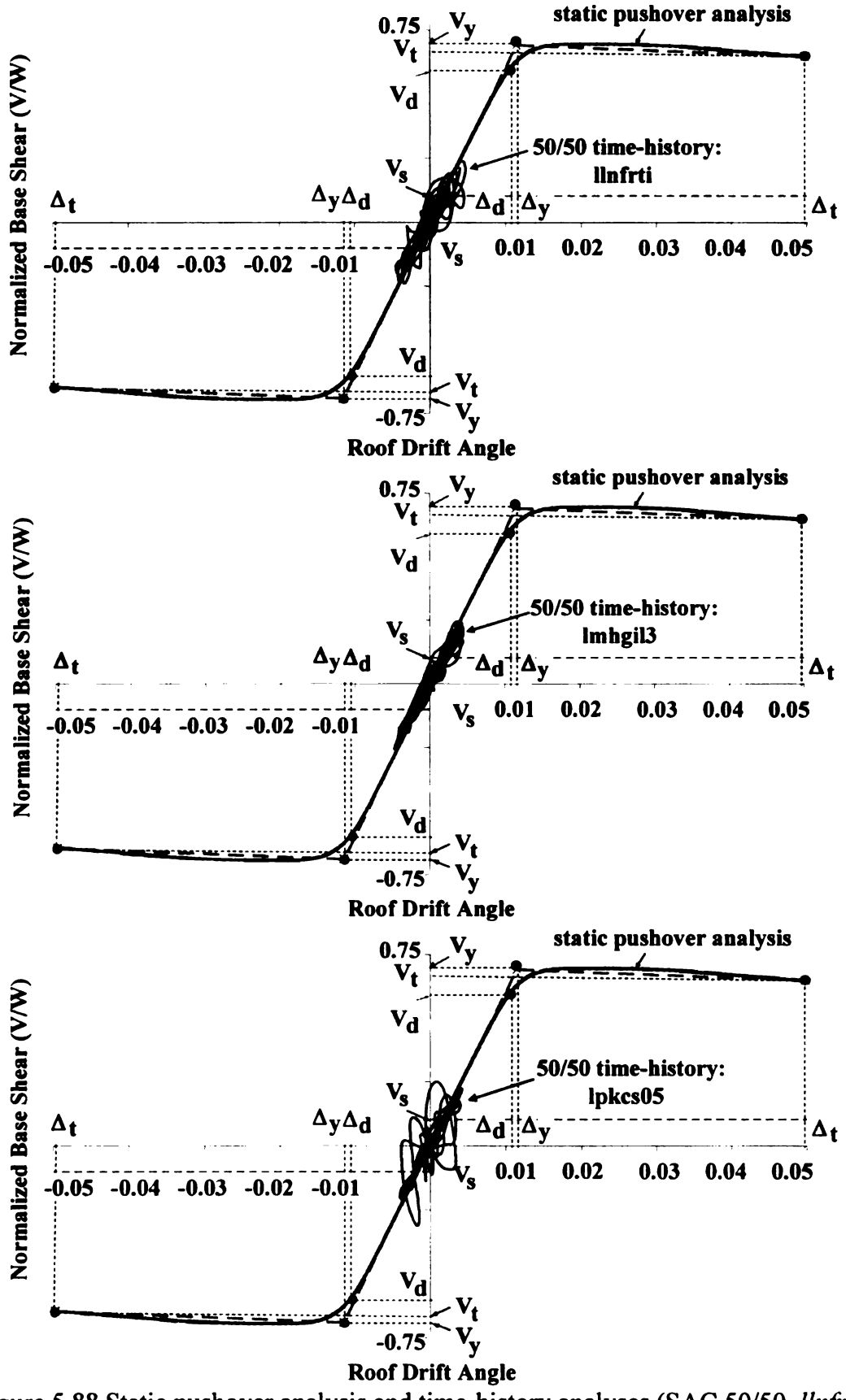


Figure 5.88 Static pushover analysis and time-history analyses (SAC 50/50, *llnfrti*, *lmhgil3* and *lpkcs05*) of flexible six-story distributed CFT MRF

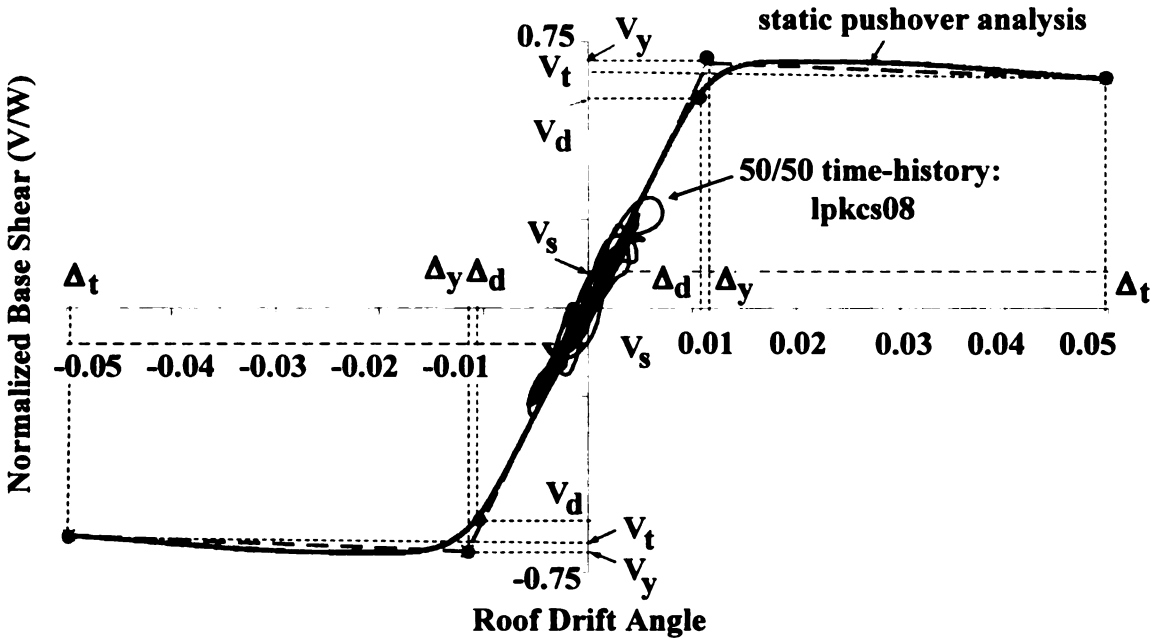


Figure 5.89 Static pushover and time-history analyses (SAC 50/50, *lpkcs08*) of flexible six-story distributed CFT MRF

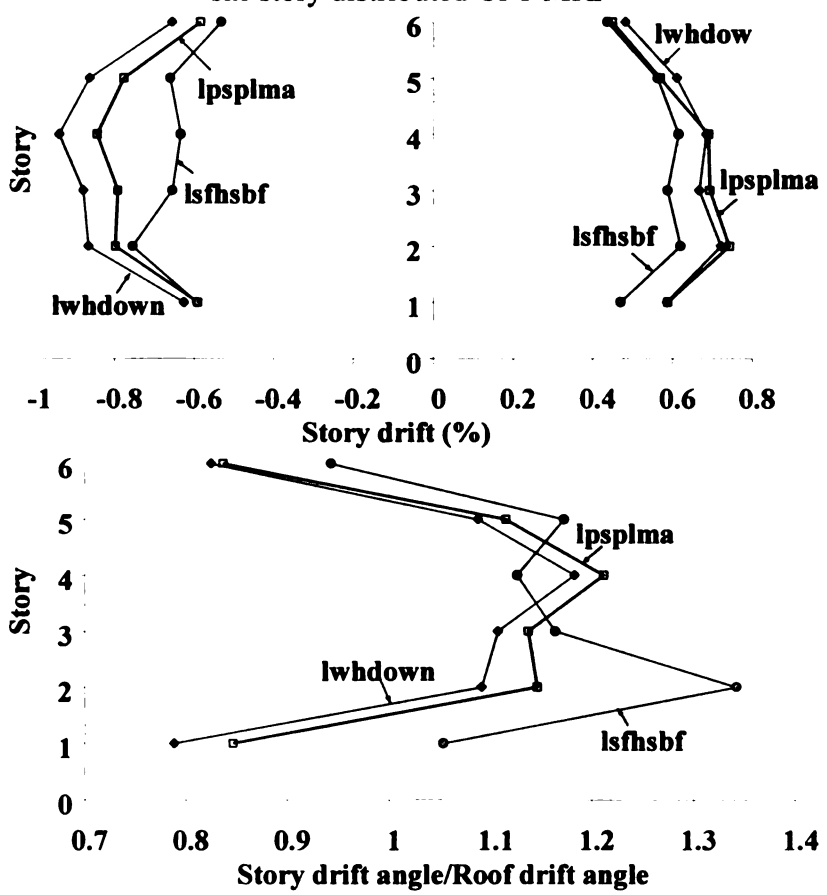


Figure 5.90 Story drift envelope and story drift to roof drift angle ratio of flexible six-story distributed CFT MRF subjected to SAC 50/50 time-histories: *lpsplma, lsfhsbf* and *lwhdown*

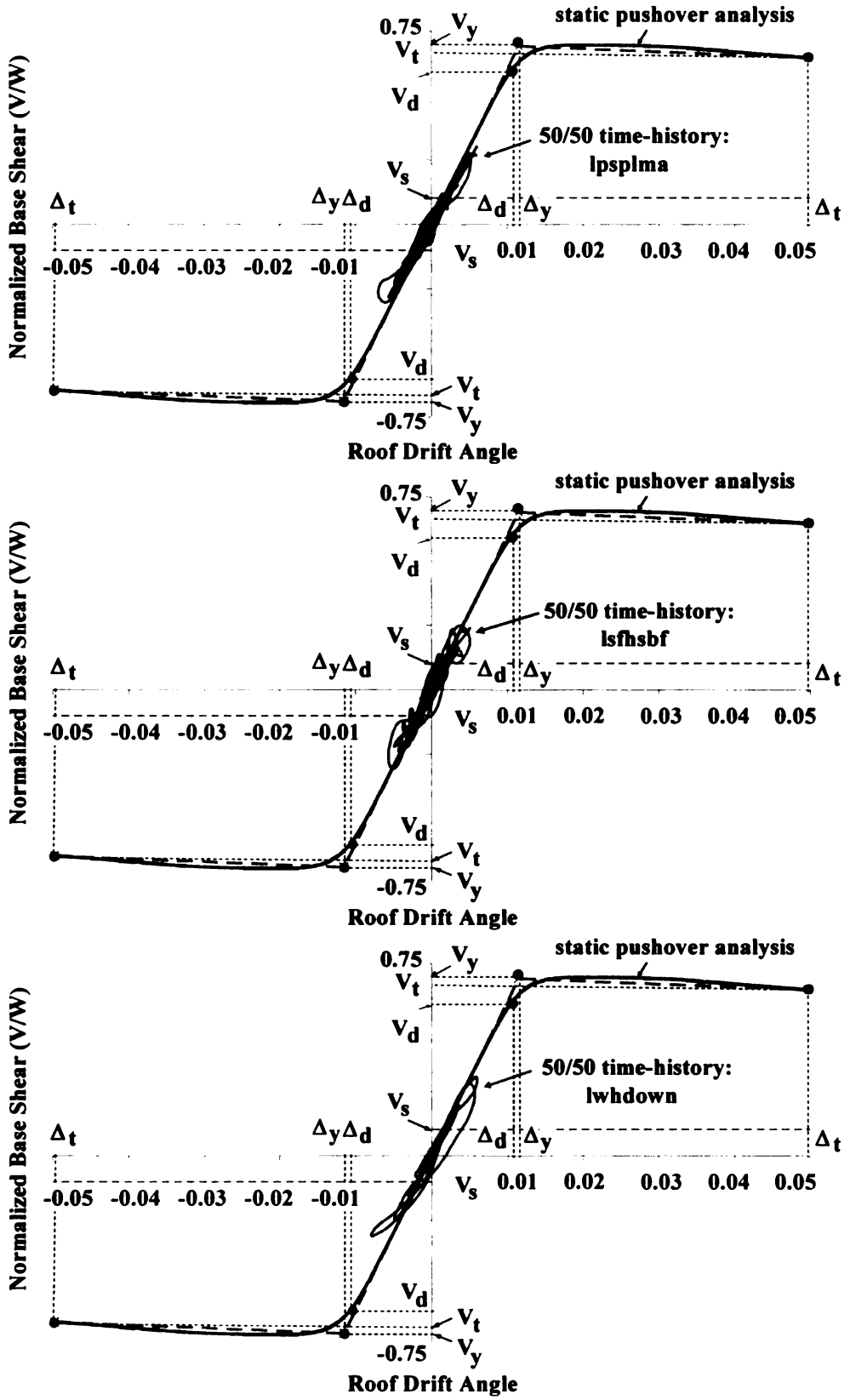


Figure 5.91 Static pushover analysis and time-history analyses (SAC 50/50, *lpsplma*, *lsfhsbf* and *lwhdown*) of flexible six-story distributed CFT MRF

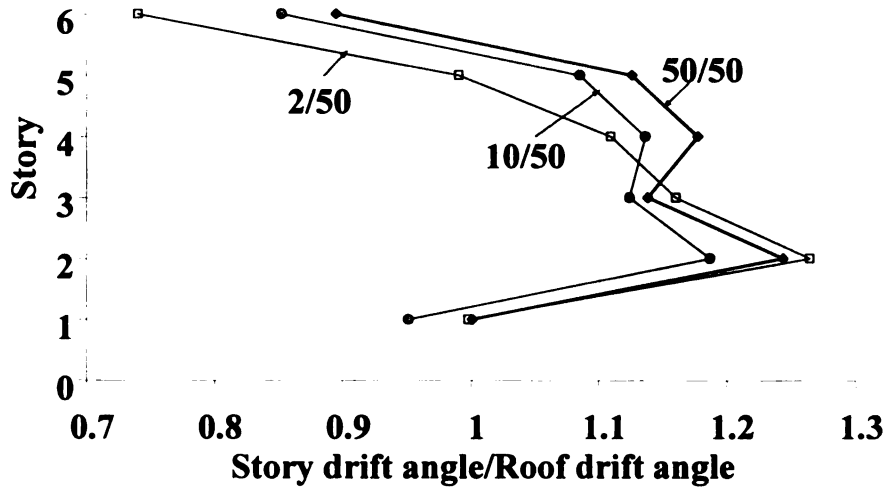


Figure 5.92 Median story drift angle to roof drift angle ratio of flexible six-story distributed CFT MRF subjected to SAC time-histories

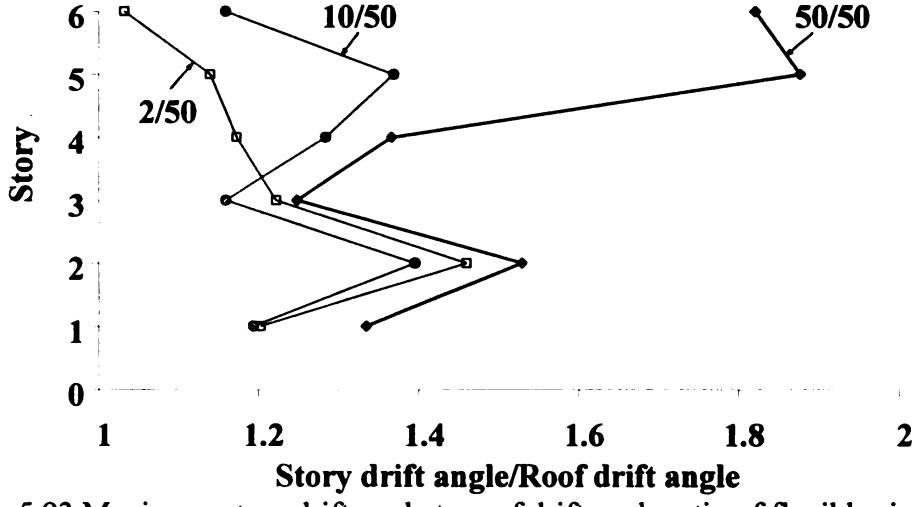


Figure 5.93 Maximum story drift angle to roof drift angle ratio of flexible six-story distributed CFT MRF subjected to SAC time-histories

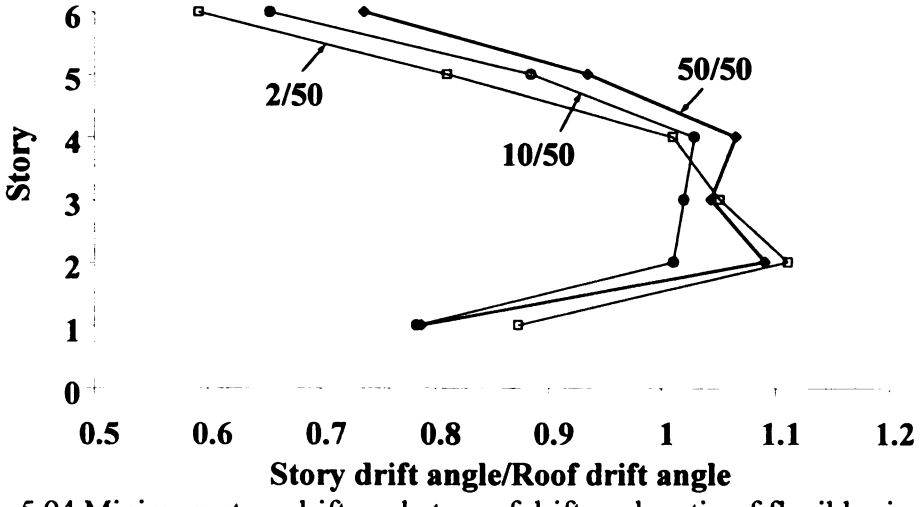


Figure 5.94 Minimum story drift angle to roof drift angle ratio of flexible six-story distributed CFT MRF subjected to SAC time-histories

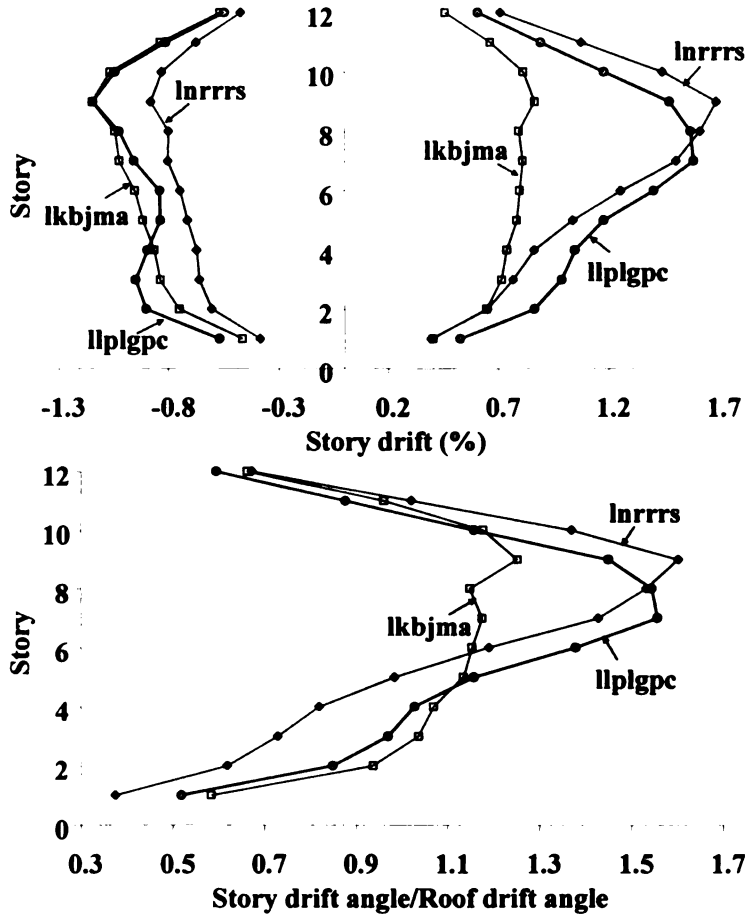


Figure 5.95 Story drift envelope and story drift angle to roof drift angle ratio of flexible twelve-story distributed CFT MRF subjected to SAC 2/50 time-histories: *lkbjma, lnrrrs* and *llplgpc*

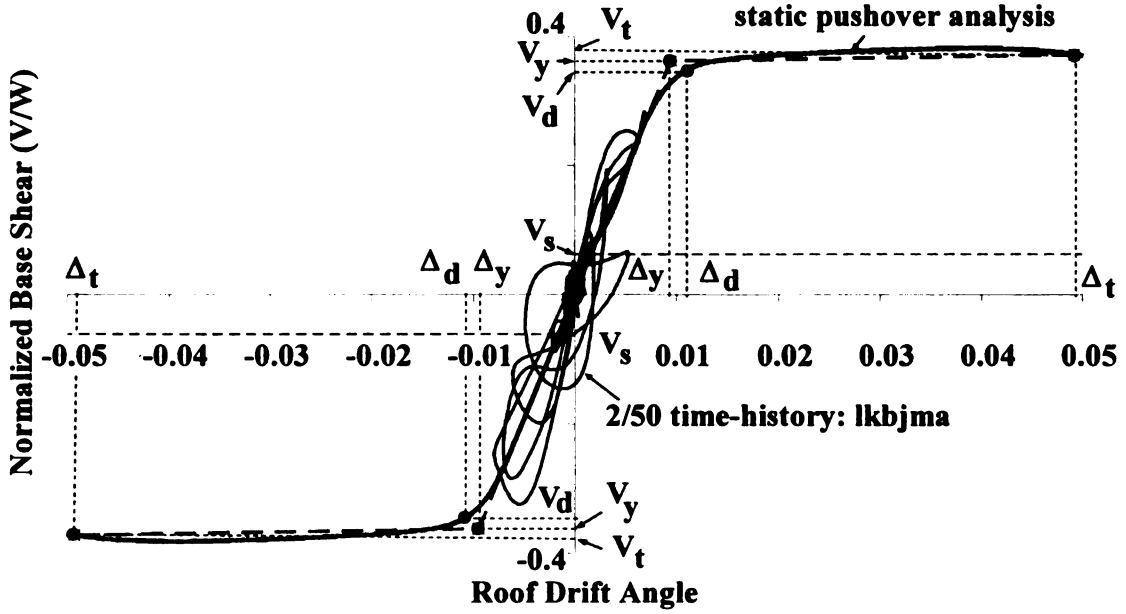


Figure 5.96 Static pushover and time-history analyses (SAC 2/50, *lkbjma*) of flexible twelve-story distributed CFT MRF

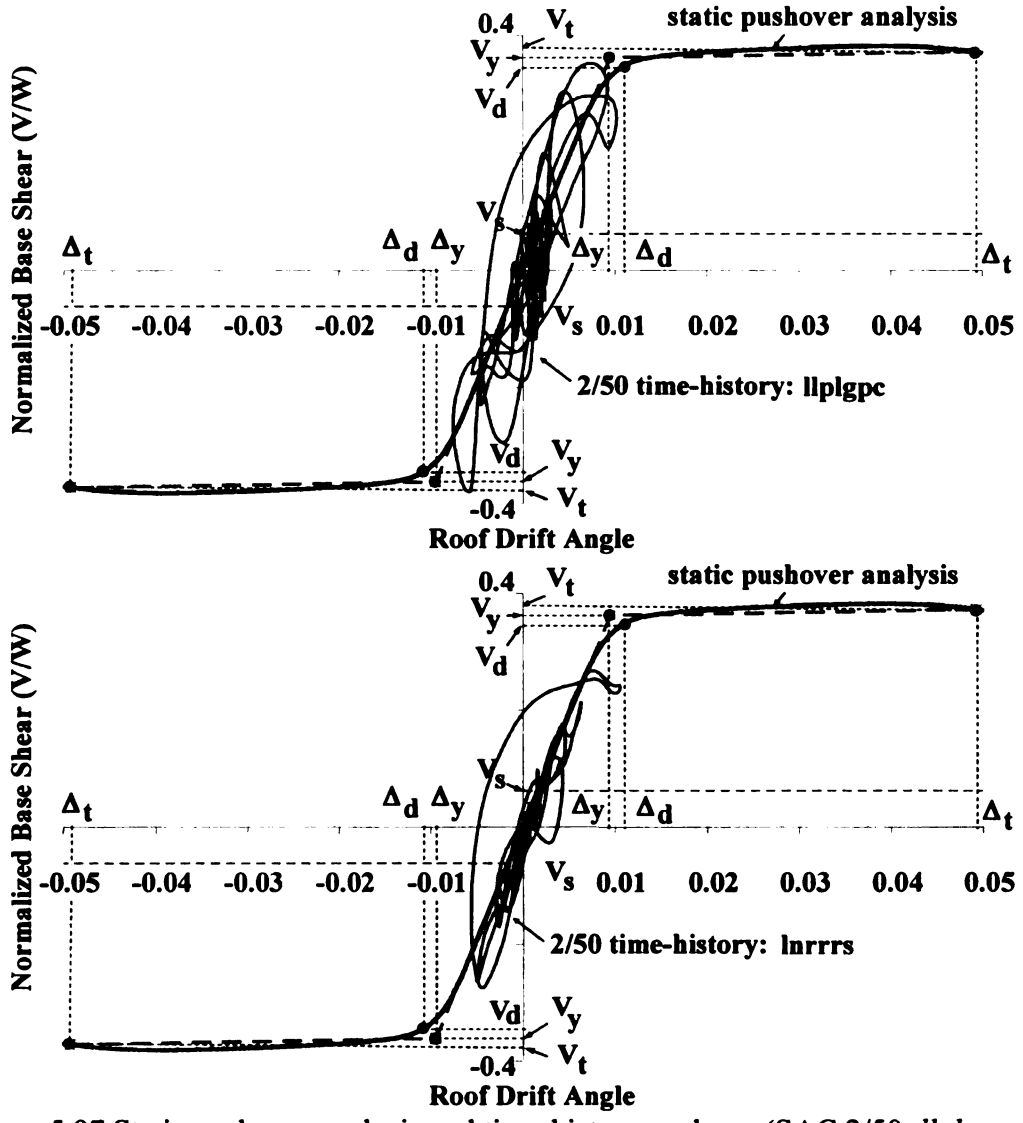


Figure 5.97 Static pushover analysis and time-history analyses (SAC 2/50, *llplgpc* and *lnrrrs*) of flexible twelve-story distributed CFT MRF

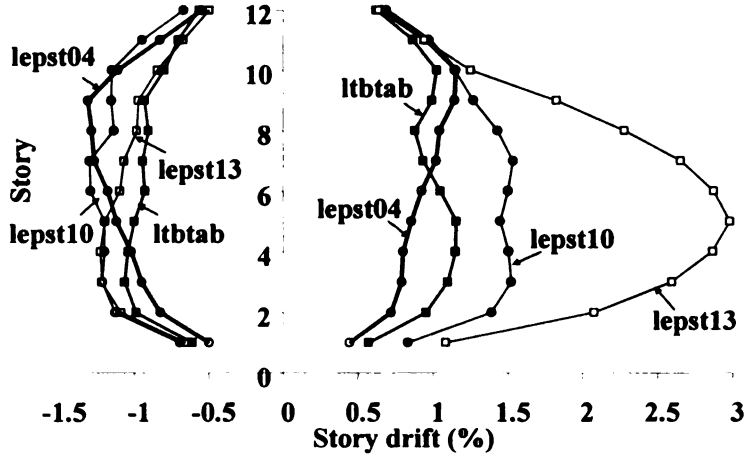


Figure 5.98 Story drift envelope of flexible twelve-story distributed CFT MRF subjected to SAC 2/50 time-histories: *ltbtab, lepst04, lepst10* and *lepst13*

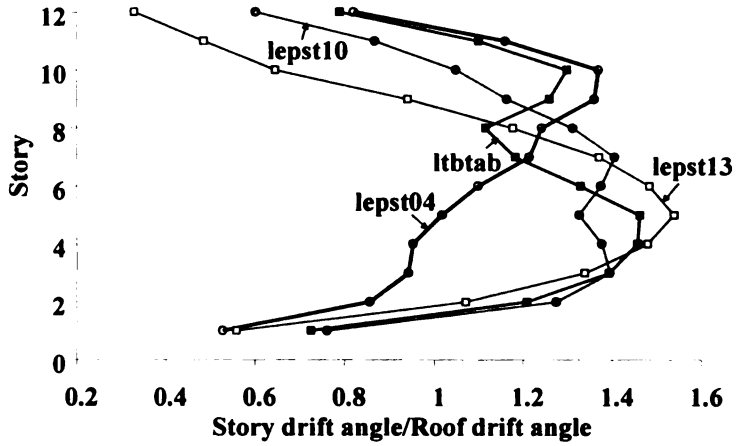


Figure 5.99 Story drift angle to roof drift angle ratio of flexible twelve-story distributed CFT MRF subjected to SAC 2/50 time-histories: *ltbtab, lepst04, lepst10* and *lepst13*

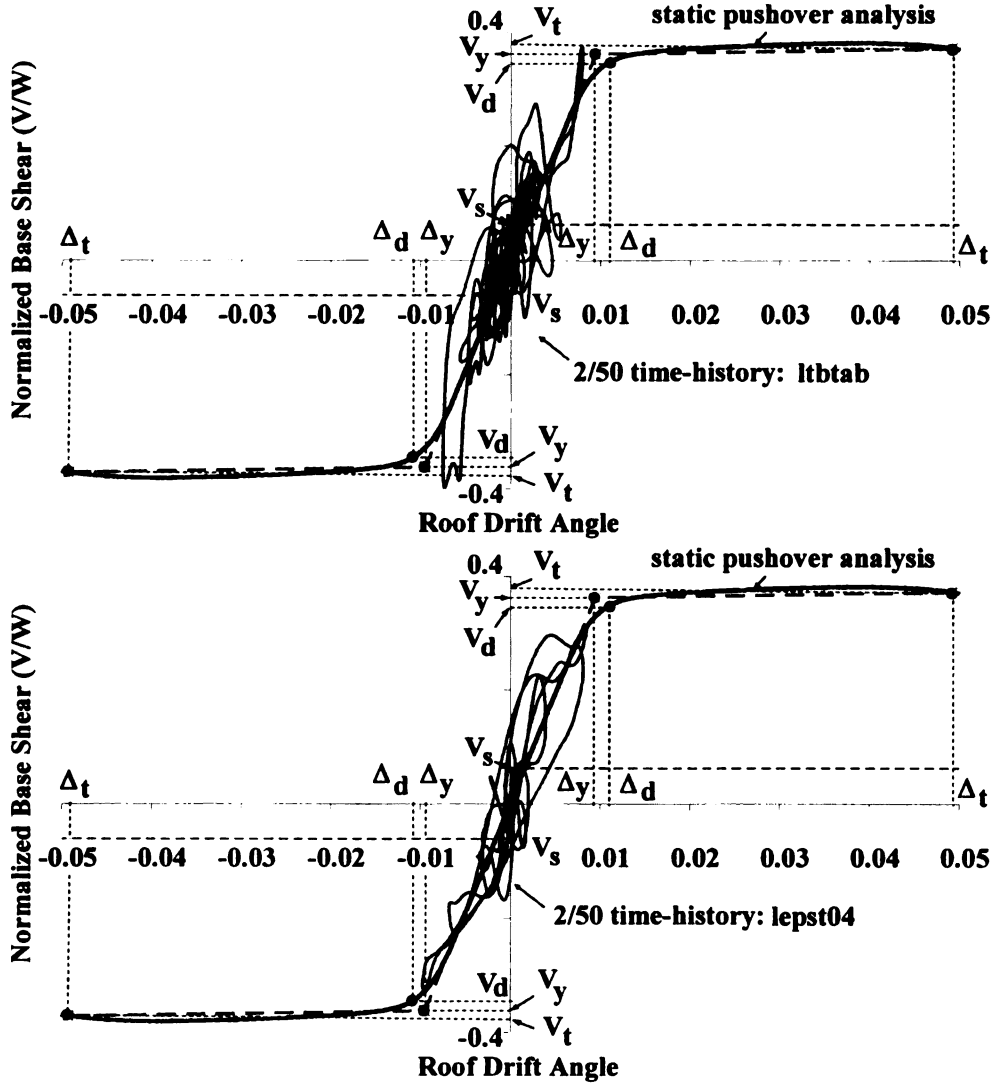


Figure 5.100 Static pushover analysis and time-history analyses (SAC 2/50, *ltbtab* and *lepst04*) of flexible twelve-story distributed CFT MRF

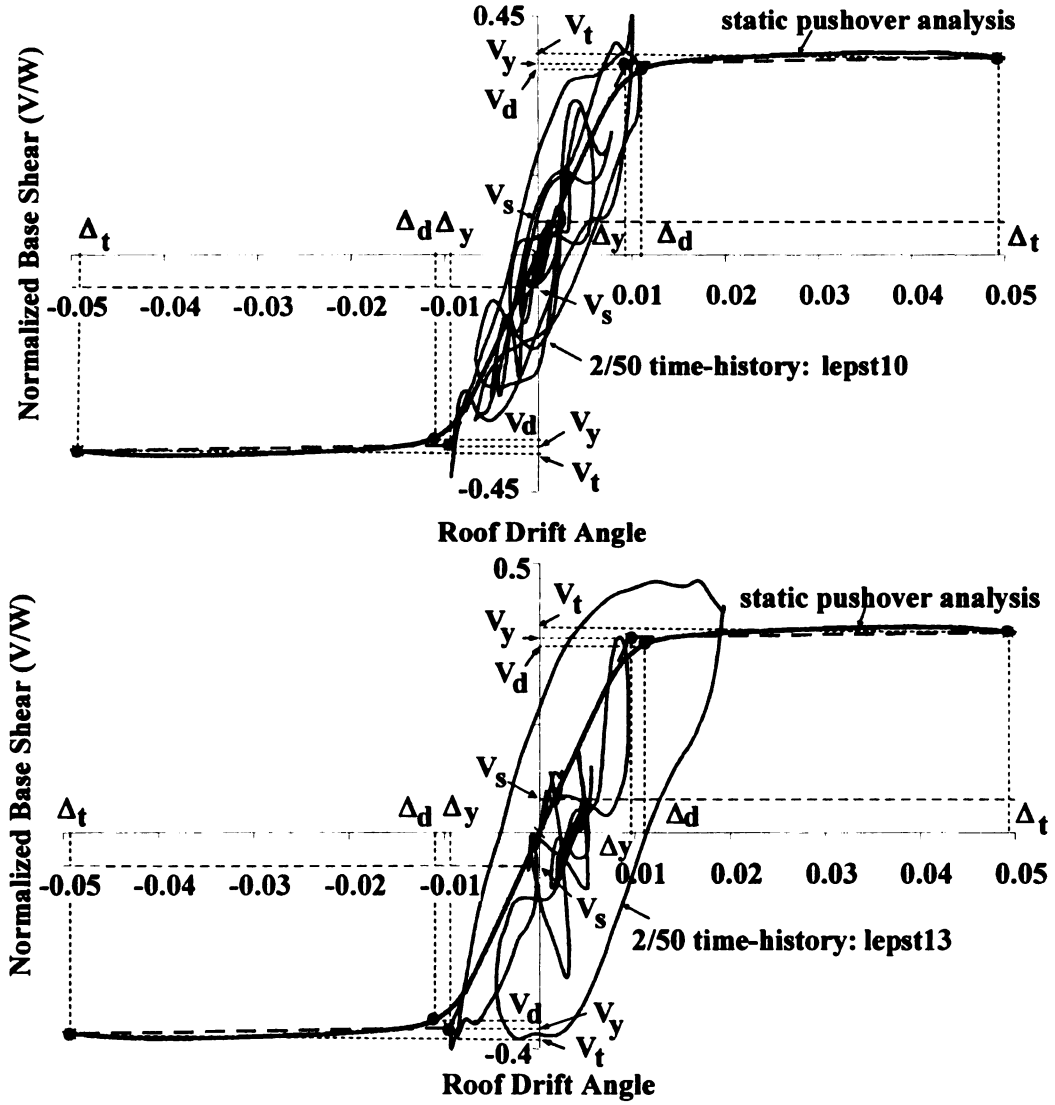


Figure 5.101 Static pushover analysis and time-history analyses (SAC 2/50, *lepst10* and *lepst13*) of flexible twelve-story distributed CFT MRF

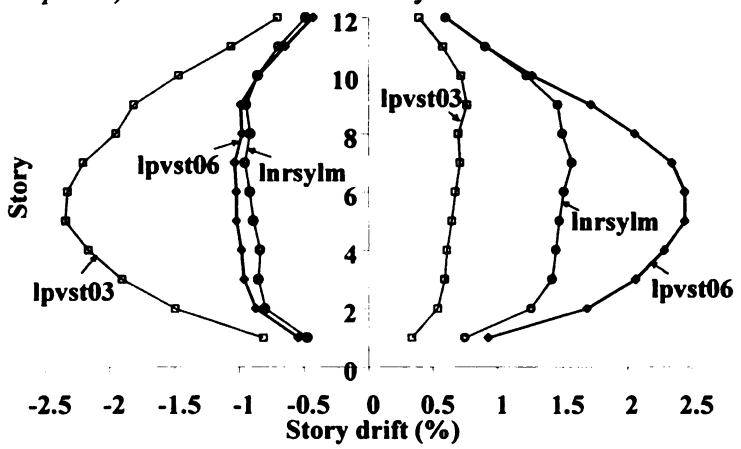


Figure 5.102 Story drift envelope of flexible twelve-story distributed CFT MRF subjected to SAC 2/50 time-histories: *lnrsylm, lpvst03* and *lpvst06*

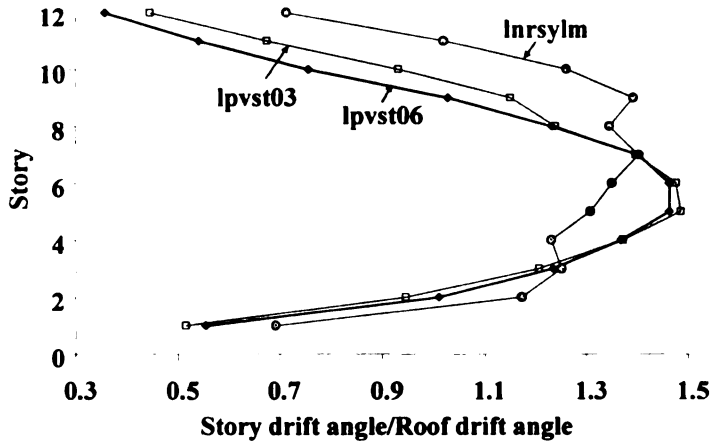


Figure 5.103 Story drift angle to roof drift angle ratio of flexible twelve-story distributed CFT MRF subjected to SAC 2/50 time-histories: *lnrsylm, lpvst03* and *lpvst06*

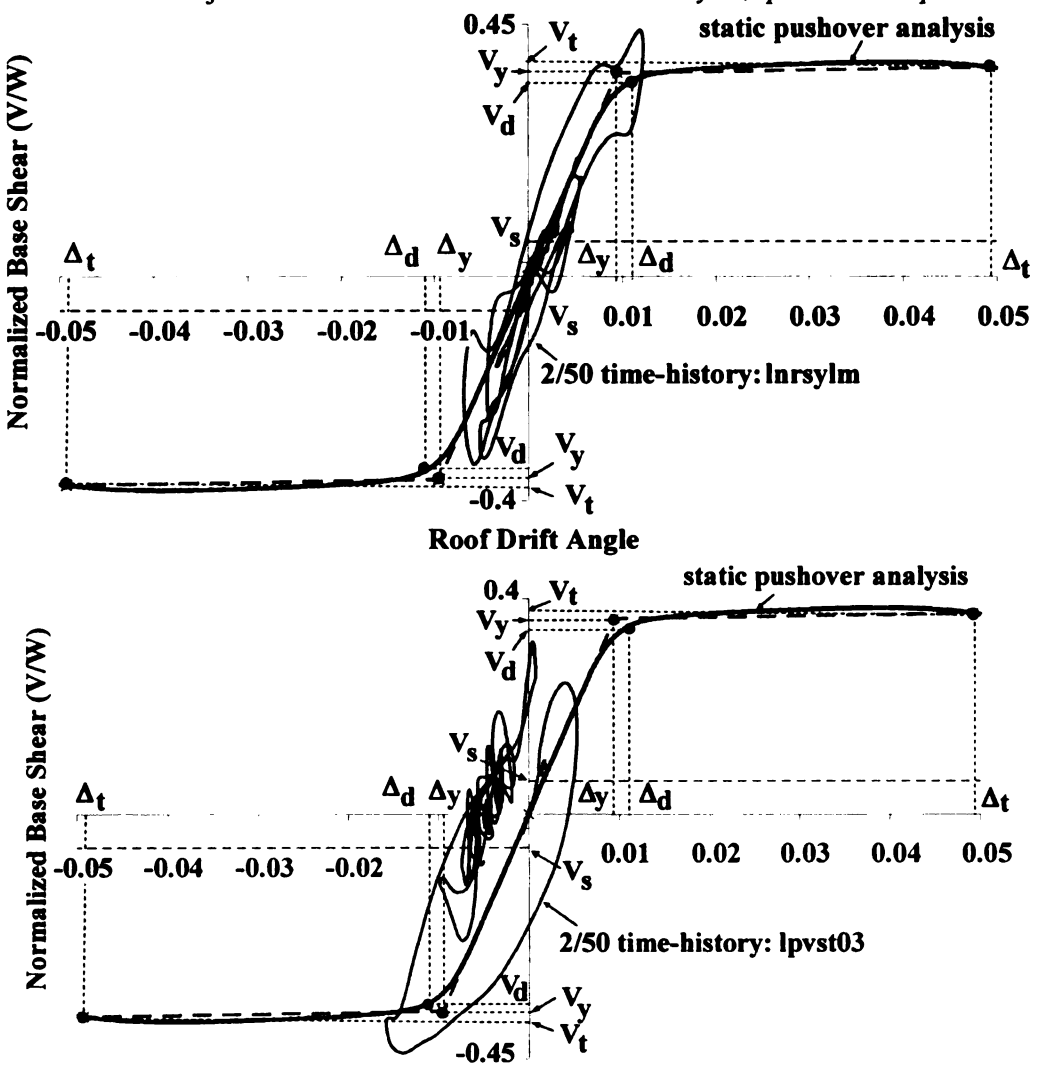


Figure 5.104 Static pushover analysis and time-history analyses (SAC 2/50, *lnrsylm* and *lpvst03*) of flexible twelve-story distributed CFT MRF

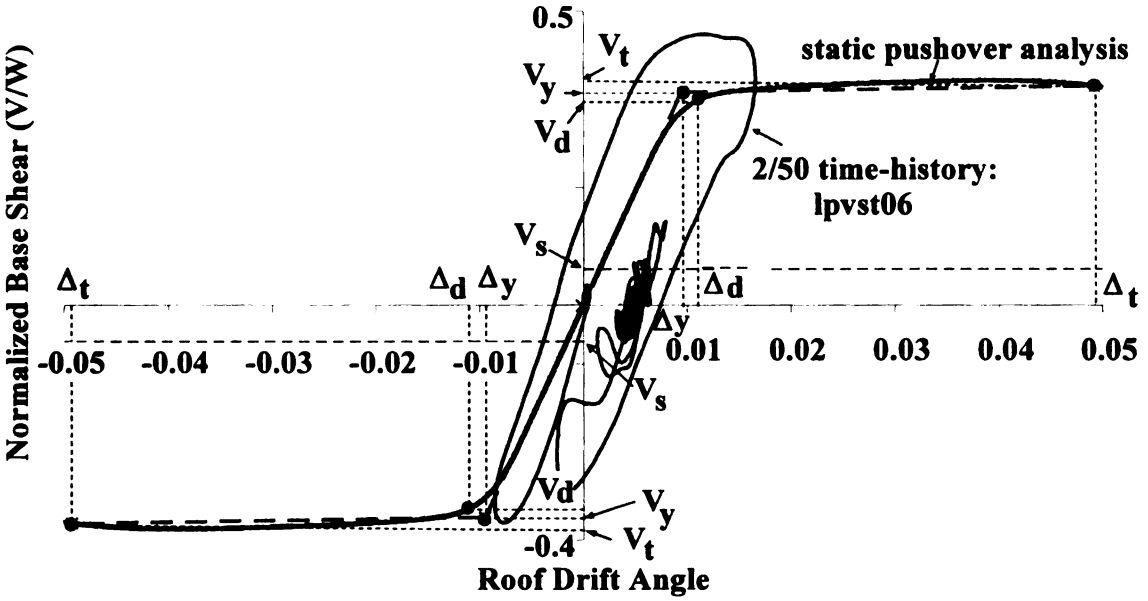


Figure 5.105 Static pushover and time-history analyses (SAC 2/50, *lpvst06*) of flexible twelve-story distributed CFT MRF

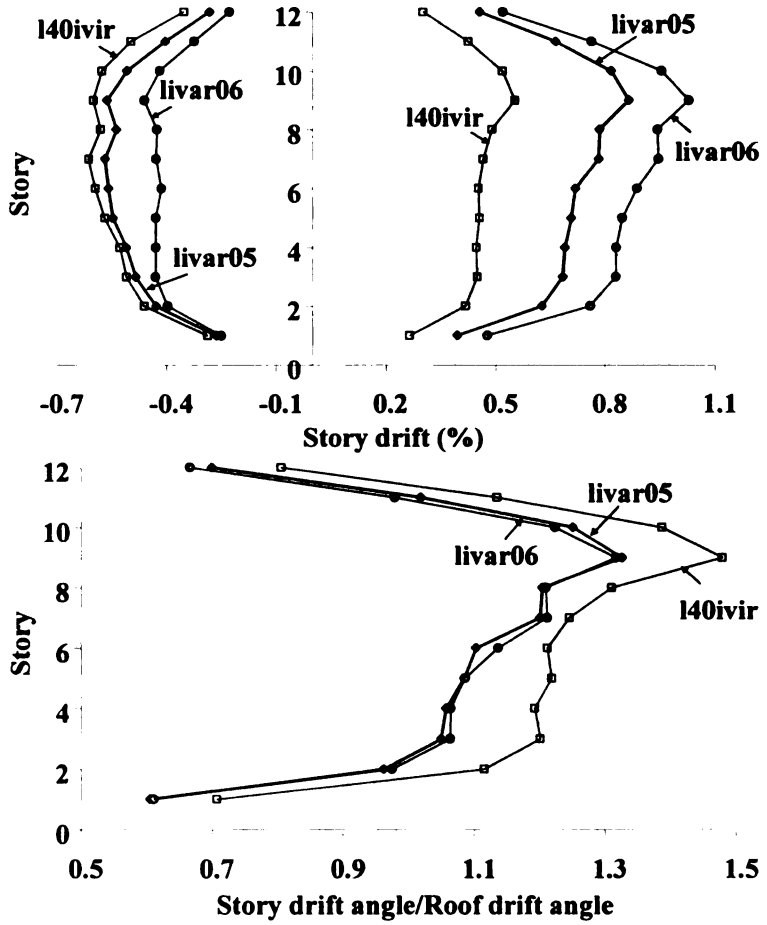


Figure 5.106 Story drift envelope and story drift angle to roof drift angle ratio of flexible twelve-story distributed CFT MRF subjected to SAC 10/50 time-histories: *l40ivir, livar05* and *livar06*

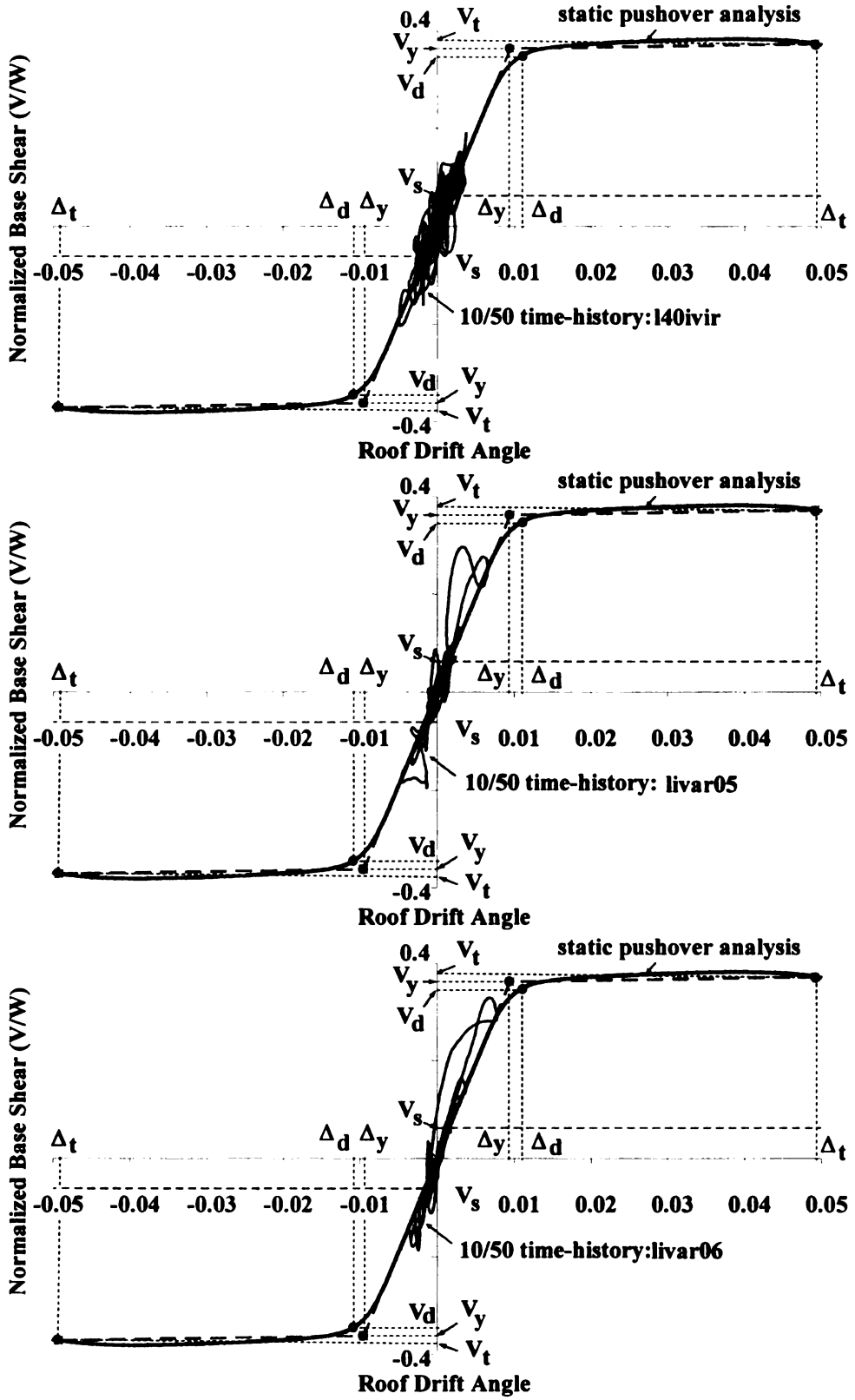


Figure 5.107 Static pushover analysis and time-history analyses (SAC 10/50, *l40ivir, livar05* and *livar06*) of flexible twelve-story distributed CFT MRF

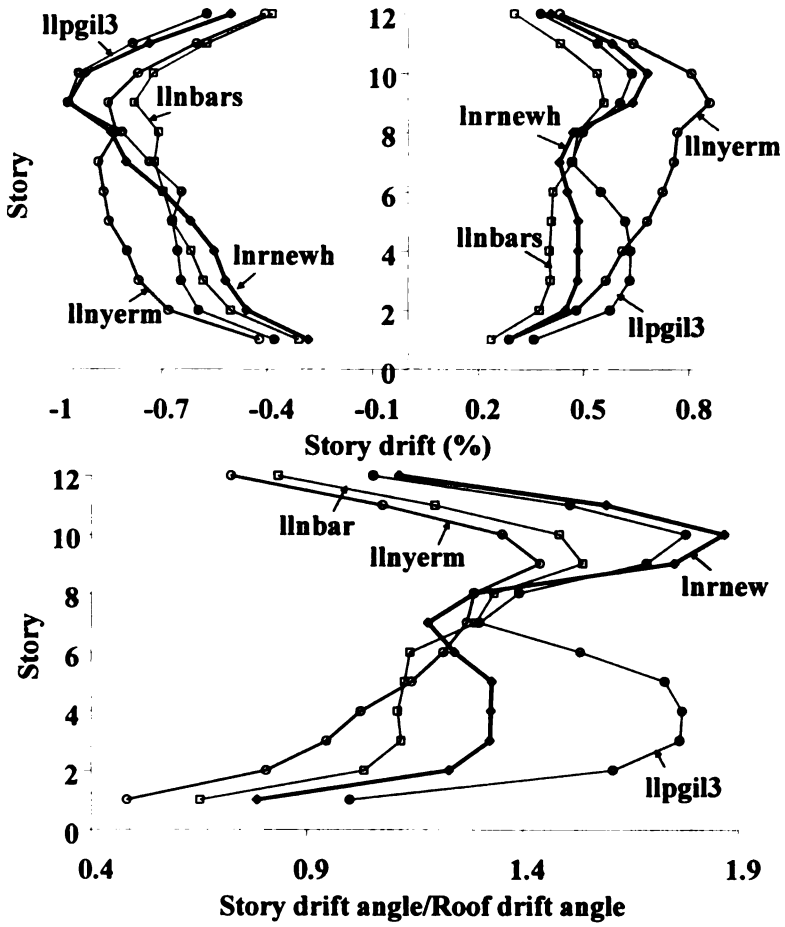


Figure 5.108 Story drift envelope and story drift angle to roof drift angle ratio of flexible twelve-story distributed CFT MRF subjected to SAC 10/50 time-histories: *llnbars, llnyerm, llpgil3* and *lnrnewh*

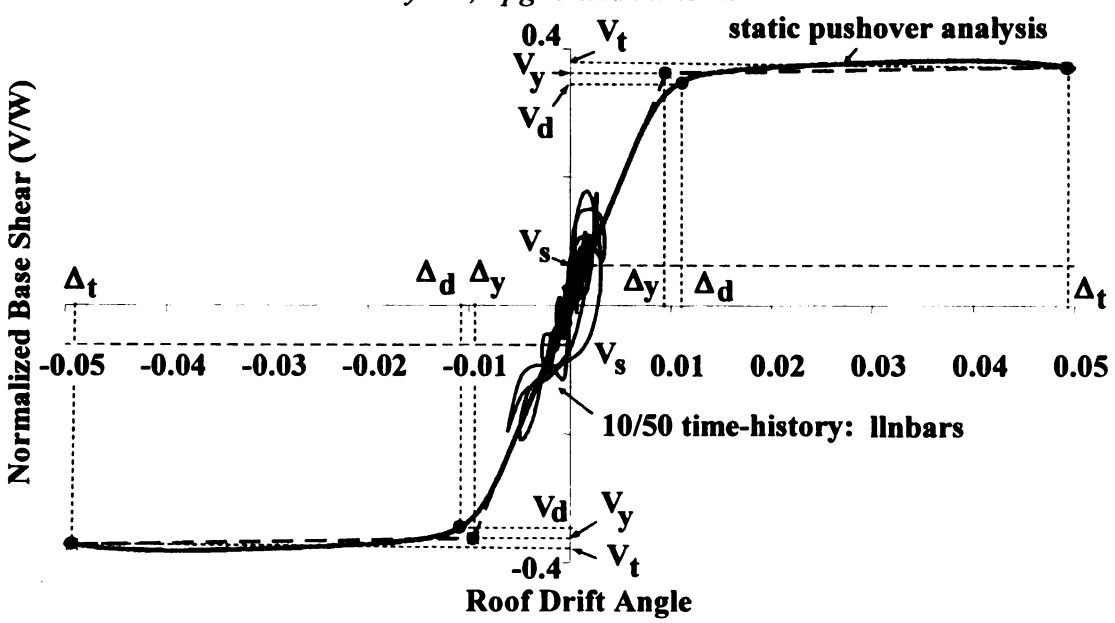


Figure 5.109 Static pushover and time-history analyses (SAC 10/50, *llnbars*) of flexible twelve-story distributed CFT MRF

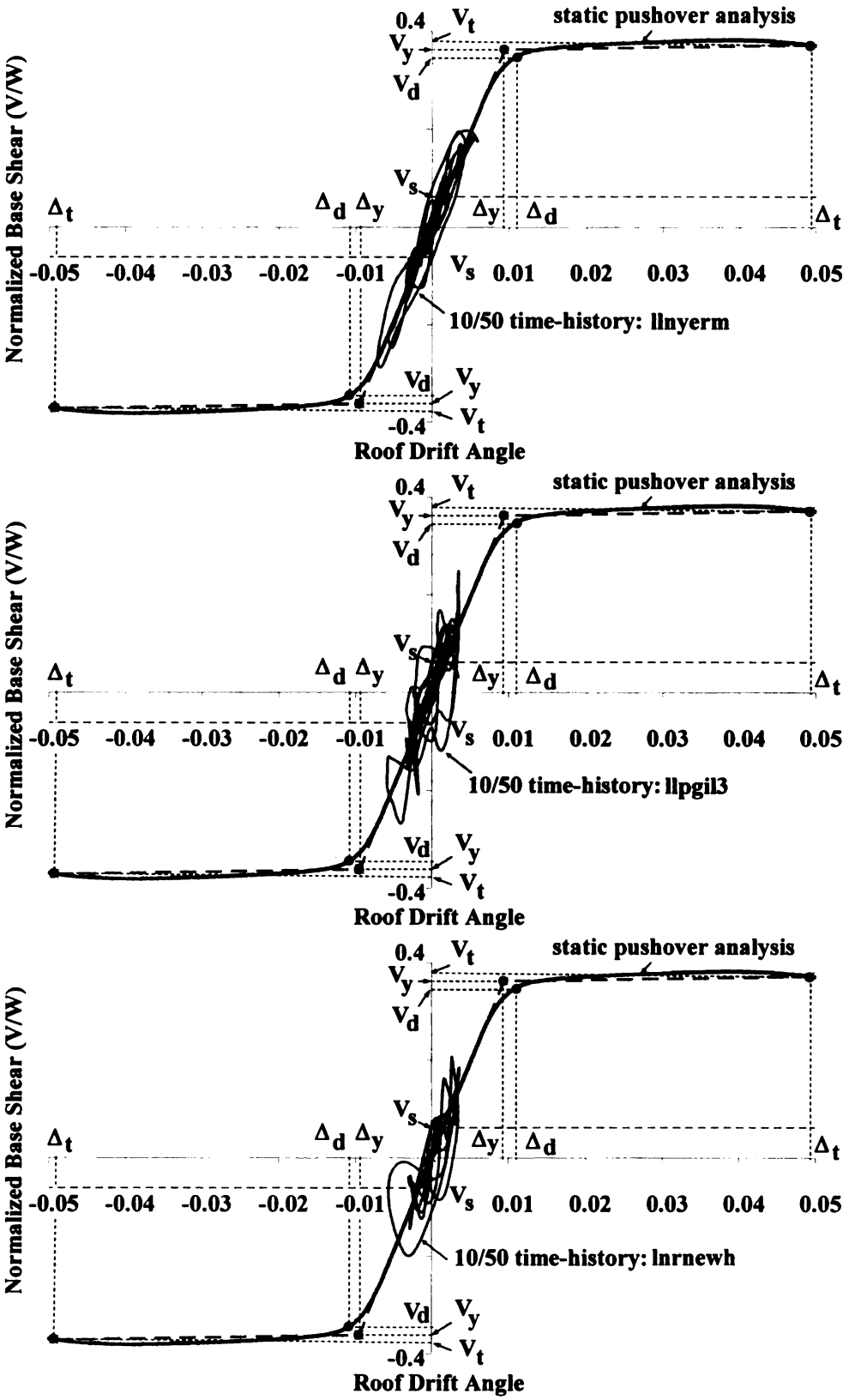


Figure 5.110 Static pushover analysis and time-history analyses (SAC 10/50, *llnyerm, llpgil3* and *lnrnewh*) of flexible twelve-story distributed CFT MRF

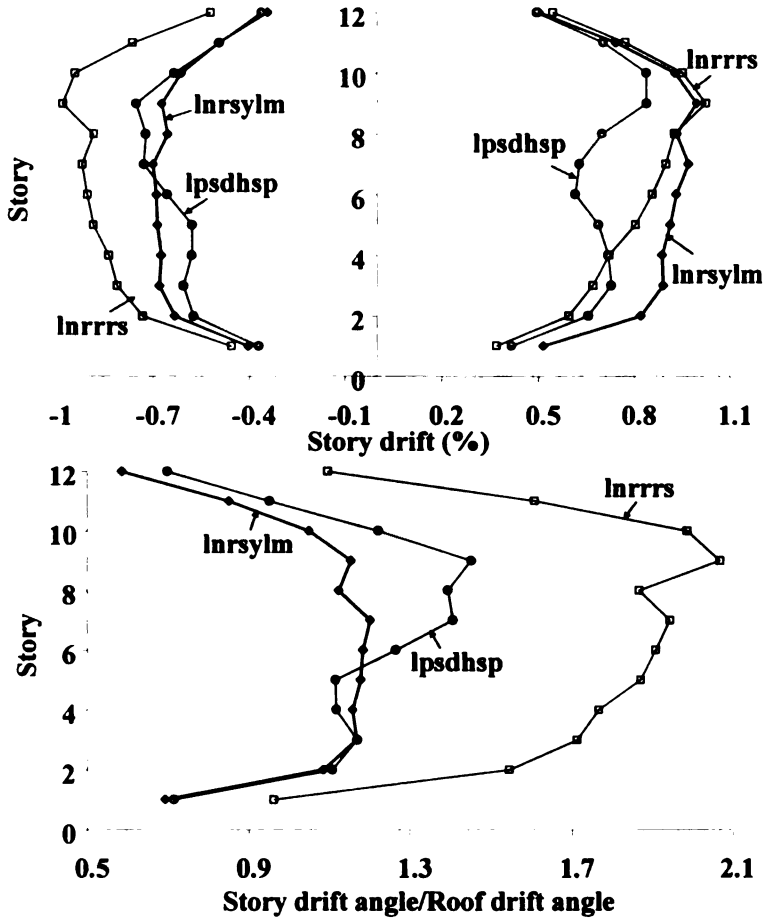


Figure 5.111 Story drift envelope and story drift angle to roof drift angle ratio of flexible twelve-story distributed CFT MRF subjected to SAC 10/50 time-histories: *lnrrrs, lnrsylm* and *lpsdhsp*

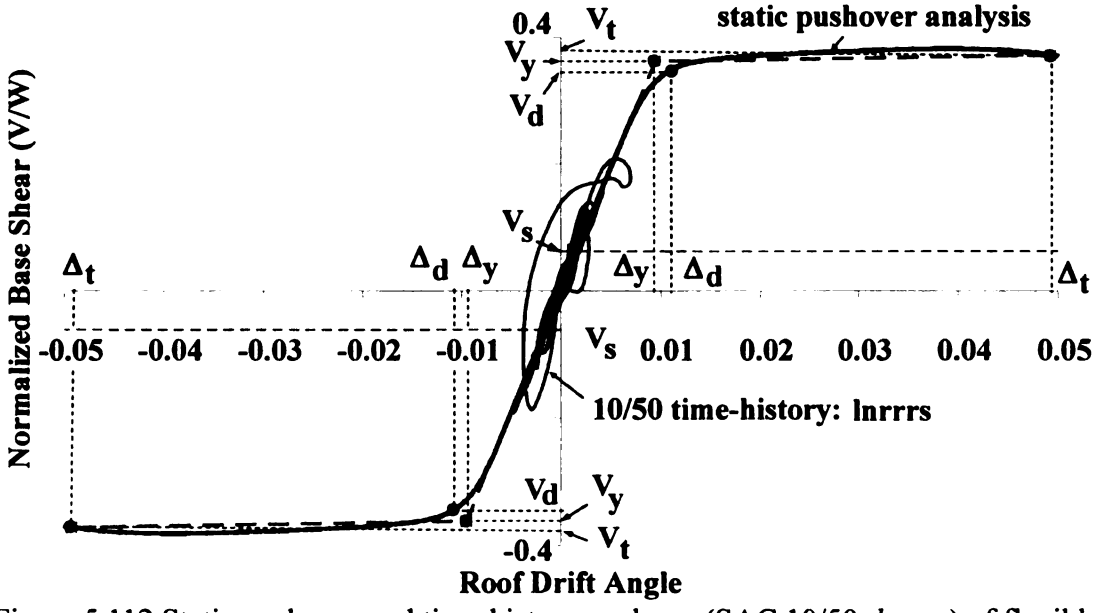


Figure 5.112 Static pushover and time-history analyses (SAC 10/50, *lnrrrs*) of flexible twelve-story distributed CFT MRF

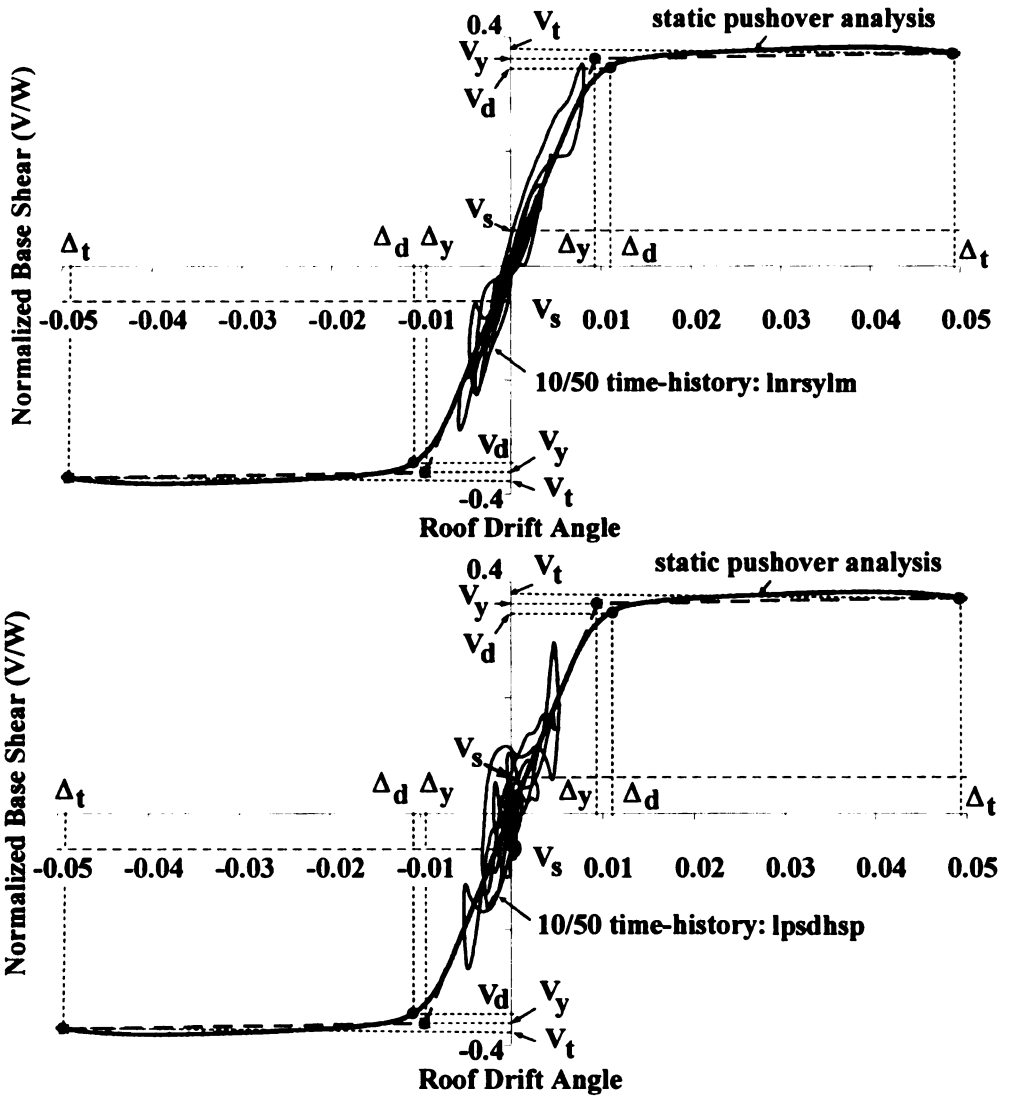


Figure 5.113 Static pushover and time-history analyses (SAC 10/50, *lnrsylm* and *lpsdhsp*) of flexible twelve-story distributed CFT MRF

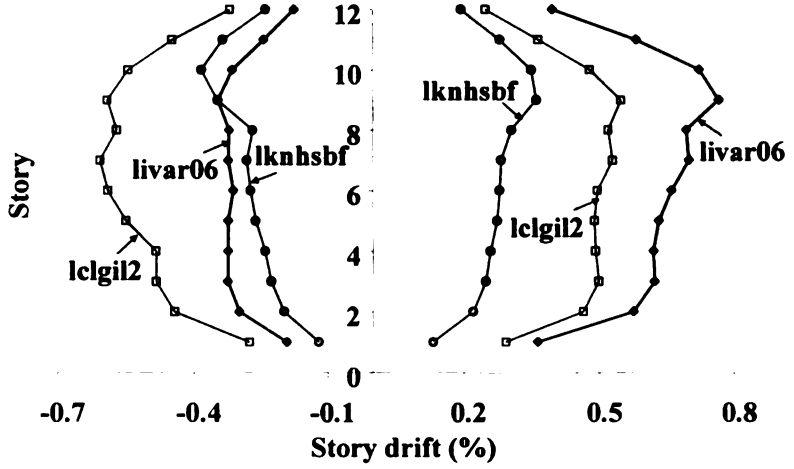


Figure 5.114 Story drift envelope of flexible twelve-story distributed CFT MRF subjected to SAC 50/50 time-histories: *lclgil2, lknhsbf* and *livar06*

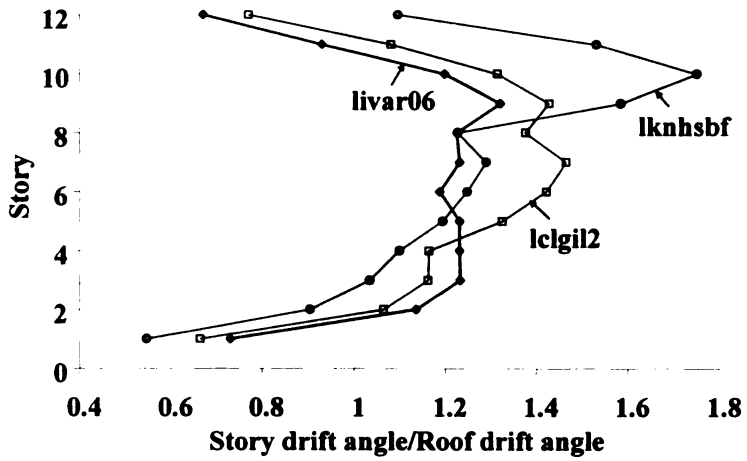


Figure 5.115 Story drift angle to roof drift angle ratio of flexible twelve-story distributed CFT MRF subjected to SAC 50/50 time-histories: *lclgil2, lknhsbf* and *livar06*

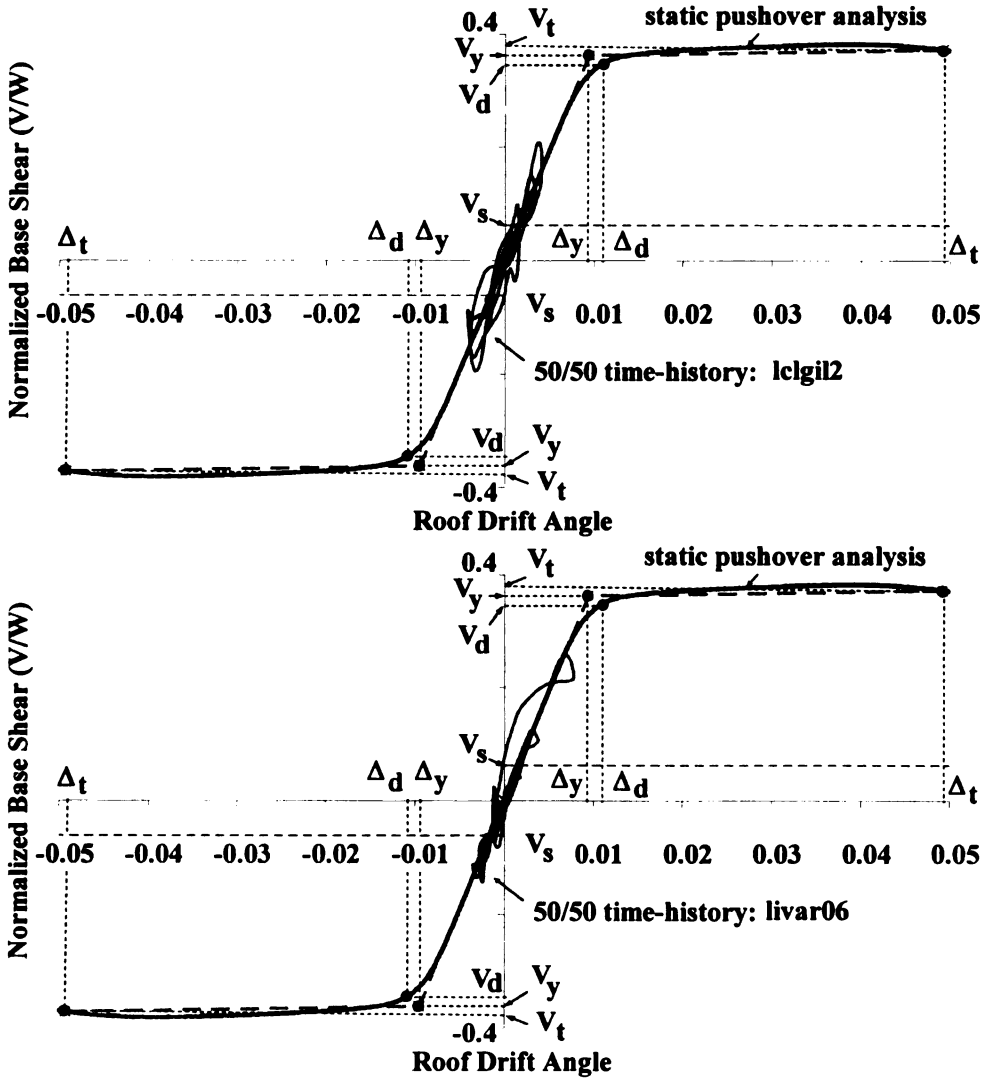


Figure 5.116 Static pushover analysis and time-history analyses (SAC 50/50, *lclgil2* and *livar06*) of flexible twelve-story distributed CFT MRF

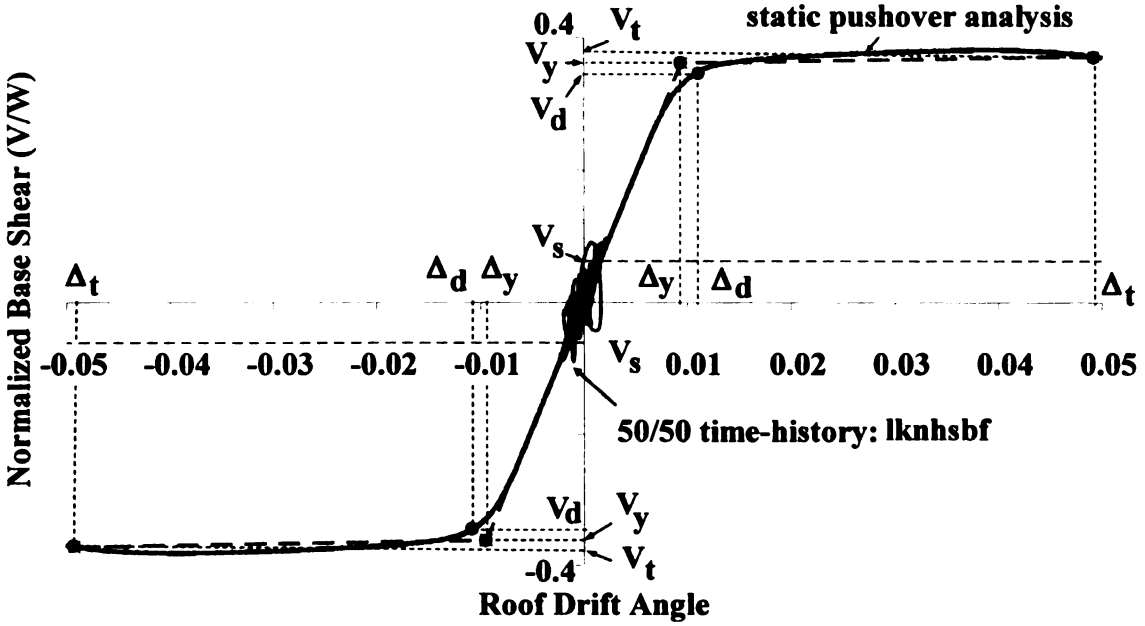


Figure 5.117 Static pushover and time-history analyses (SAC 50/50, *lknhsbf*) of flexible twelve-story distributed CFT MRF

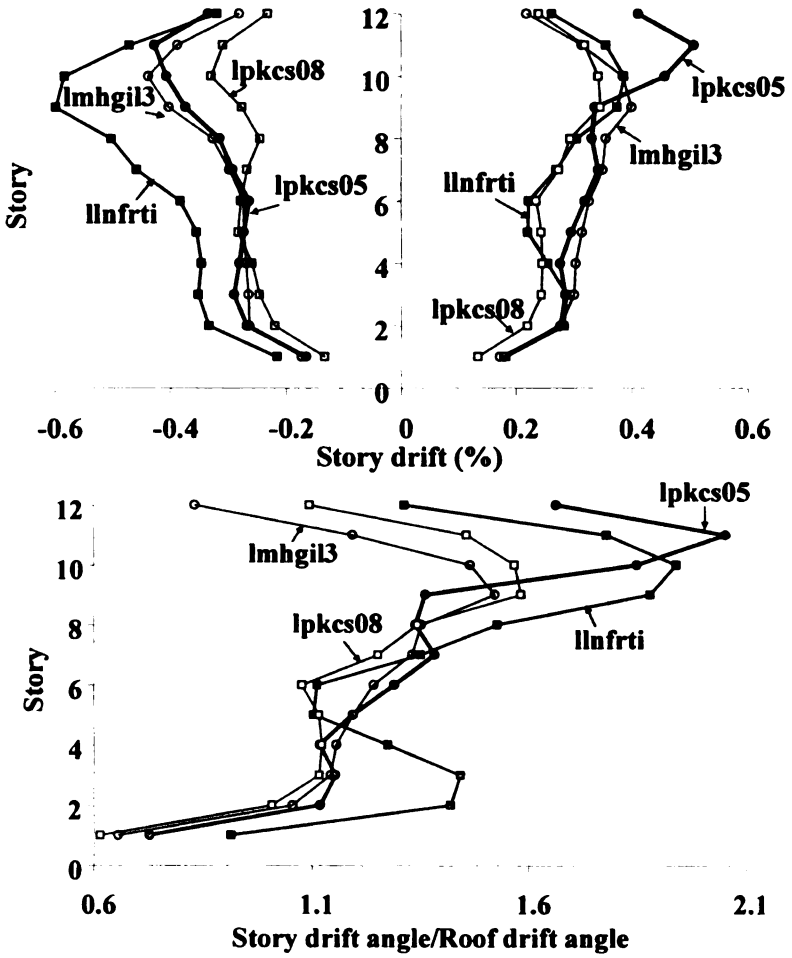


Figure 5.118 Story drift envelope and story drift angle to roof drift angle ratio of flexible twelve-story distributed CFT MRF subjected to SAC 50/50 time-histories: *lmhgil3, llnfrti, lpkcs05* and *lpkcs08*

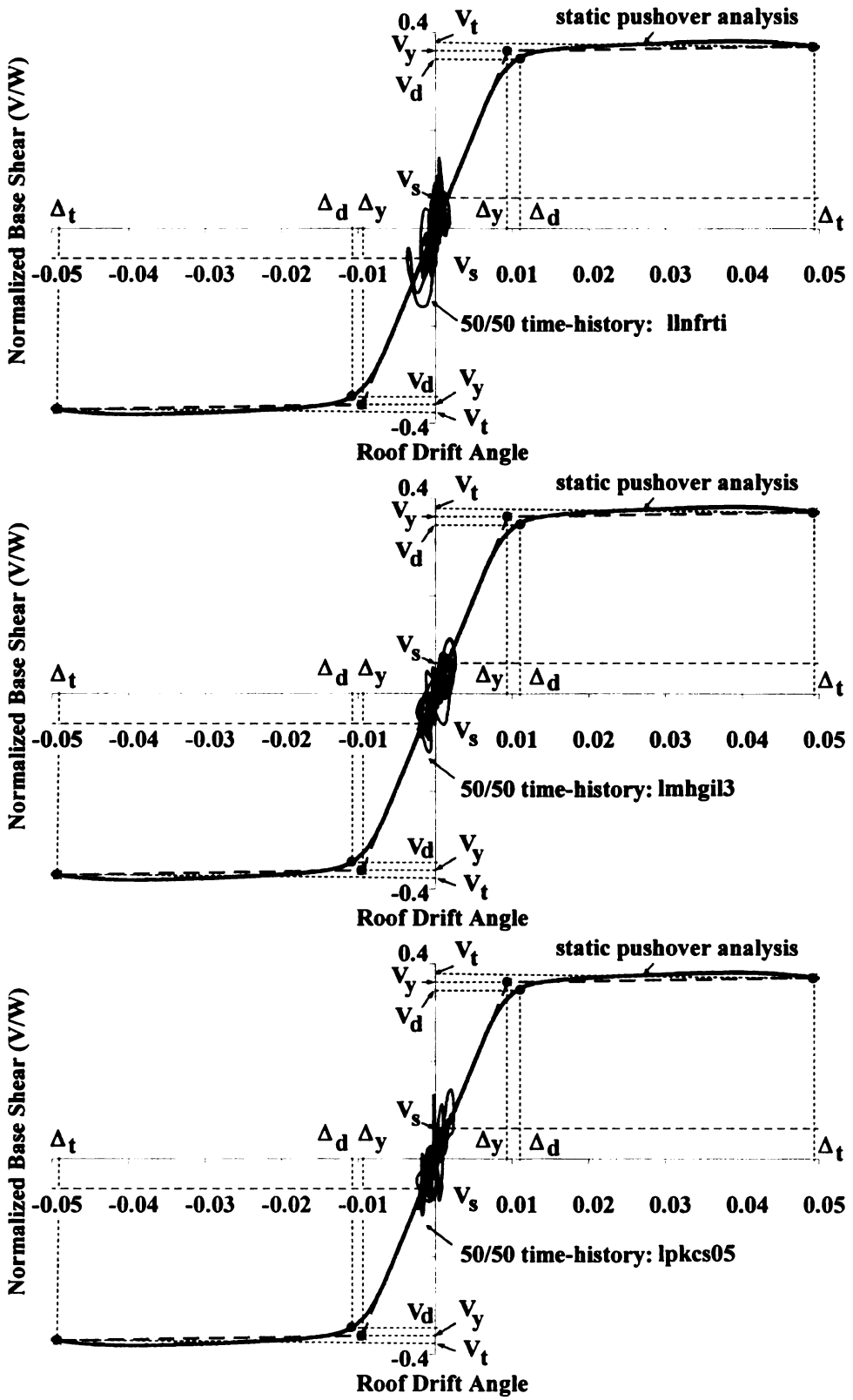


Figure 5.119 Static pushover analysis and time-history analyses (SAC 50/50, *llnfrti, lmhgil3* and *lpkcs05*) of flexible twelve-story distributed CFT MRF

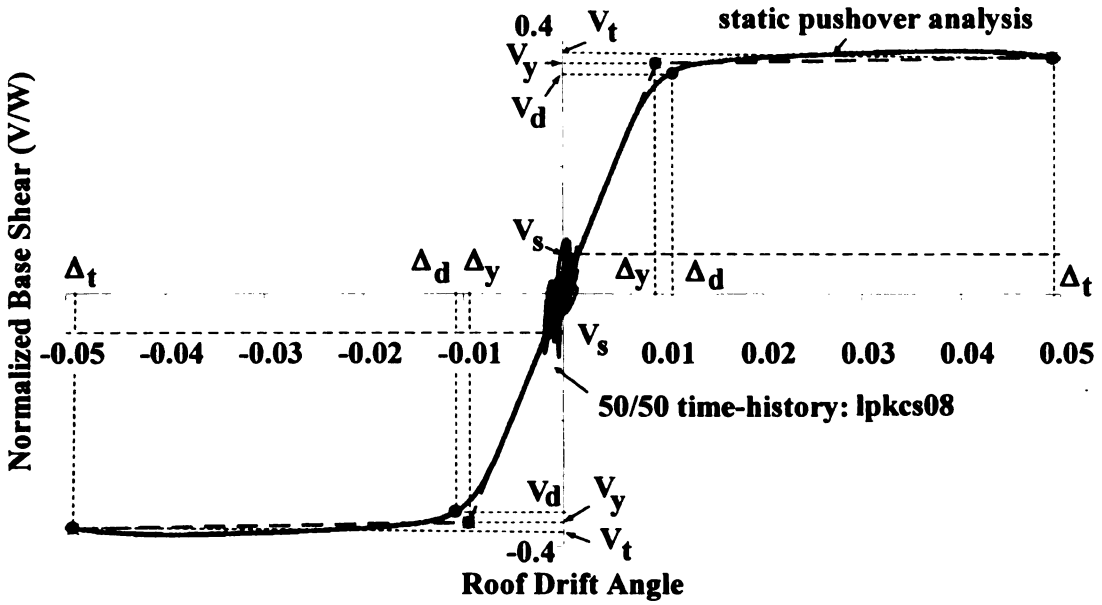


Figure 5.120 Static pushover and time-history analyses (SAC 50/50, *lpkcs08*) of flexible twelve-story distributed CFT MRF

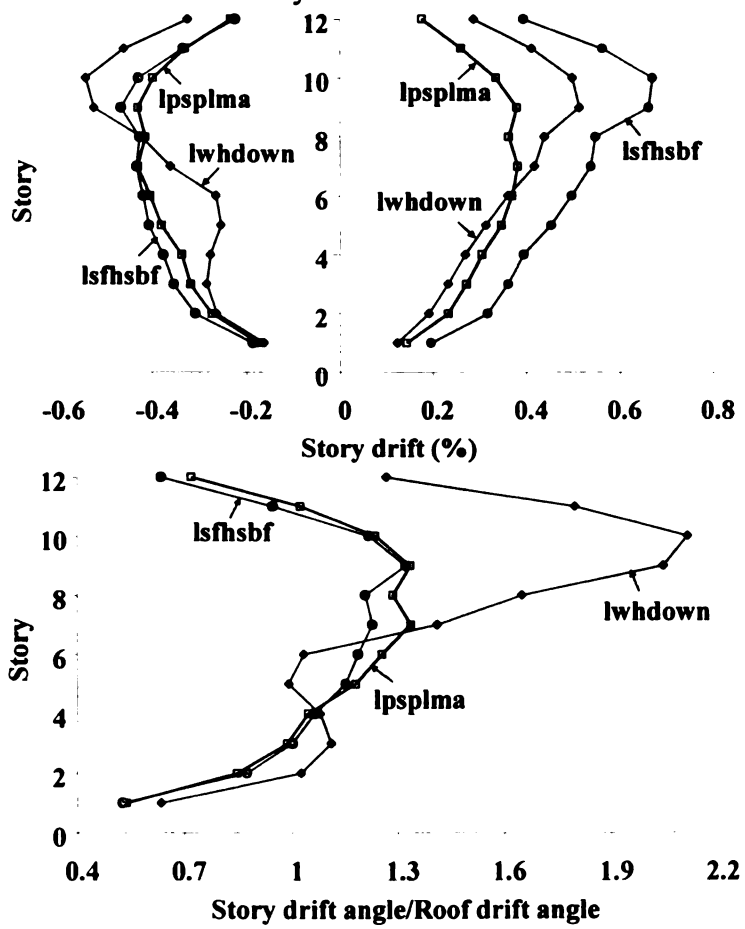


Figure 5.121 Story drift to roof drift angle ratio of flexible twelve-story distributed CFT MRF subjected to SAC 50/50 time-histories: *lpsplma, lsfhsbf* and *lwhdown*

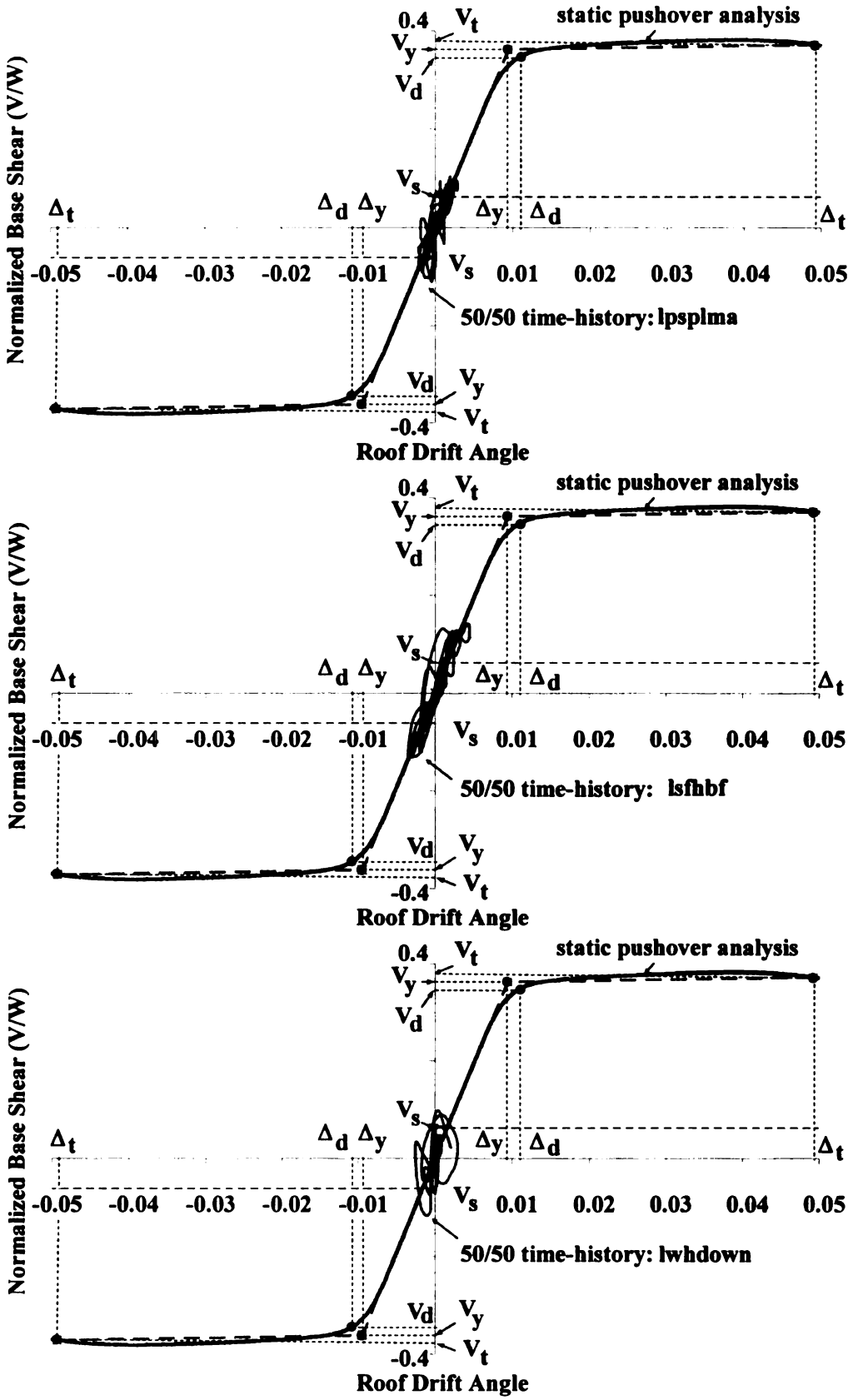


Figure 5.122 Static pushover analysis and SAC 50/50 time-history (*lpsplma, lsfhbf* and *lwhdown*) of flexible twelve-story distributed CFT MRF

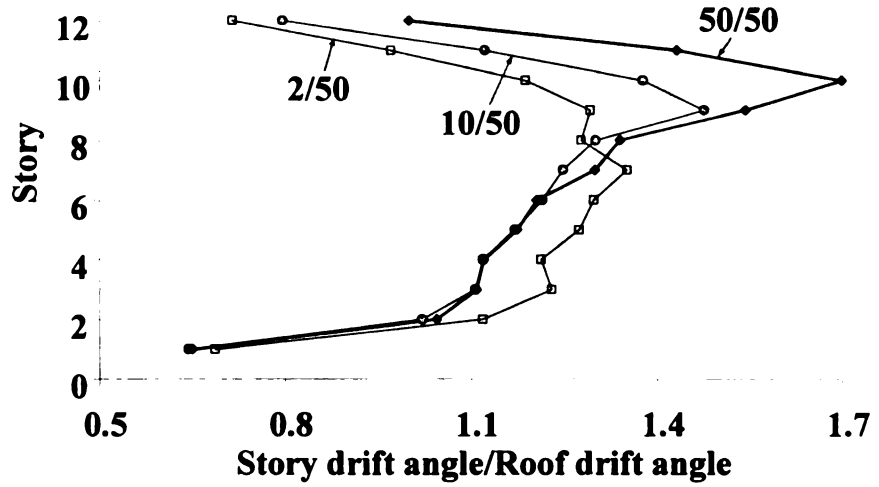


Figure 5.123 Median story drift angle to roof drift angle ratio of flexible twelve-story distributed CFT MRF subjected to SAC time-histories

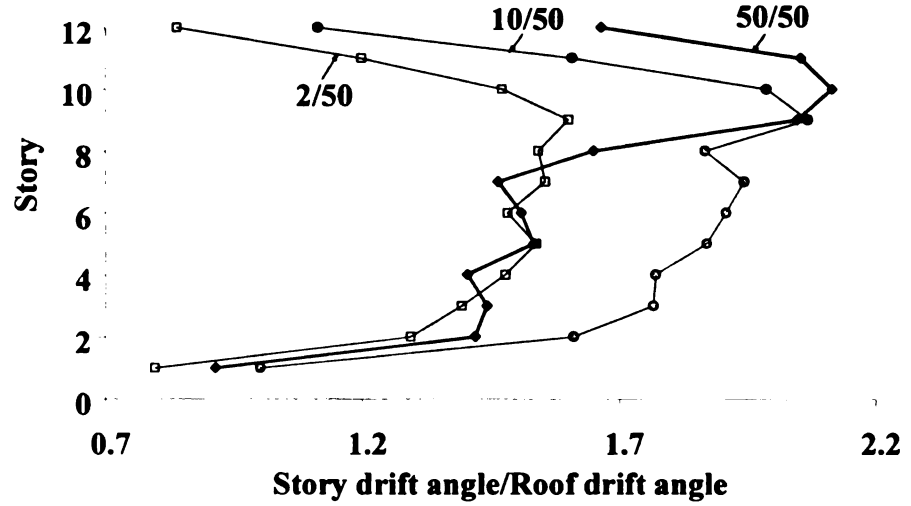


Figure 5.124 Maximum story drift angle to roof drift angle ratio of flexible twelve-story distributed CFT MRF subjected to SAC time-histories

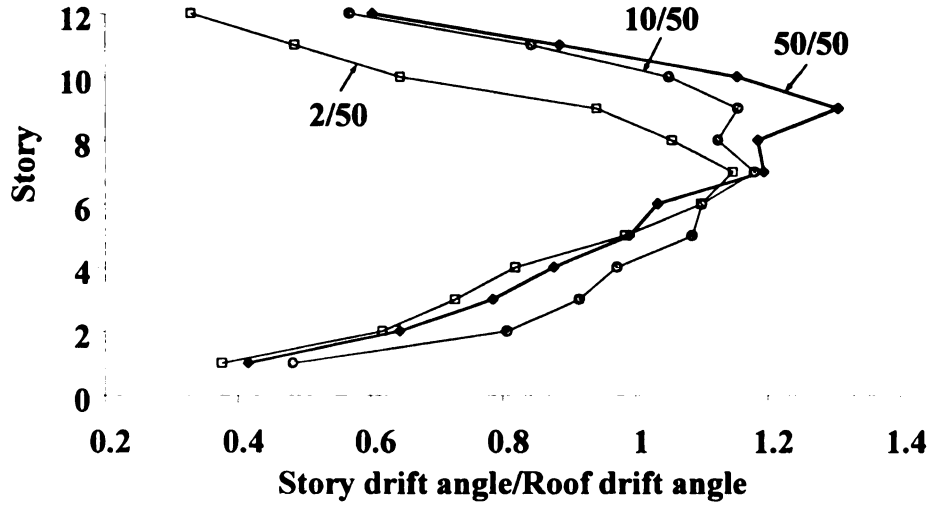


Figure 5.125 Minimum story drift angle to roof drift angle ratio of flexible twelve-story distributed CFT MRF subjected to SAC time-histories

CHAPTER 6 SUMMARY, CONCLUSIONS, AND RECOMMENDATIONS FOR FUTURE WORK

6.1 Summary

The seismic behavior of low and medium rise (six and twelve story) moment resisting frames (MRFs) with high strength square CFT beam-columns was investigated analytically. The modified fiber element implemented by Cordero et al. (2002) in the nonlinear structural analysis program DRAIN-2DX (Prakash et al. 1993) was used to model the CFT beam-columns and steel beams of the high strength CFT MRFs. This fiber element can implicitly account for the various complexities of member behavior including the effects of cyclic local buckling, concrete confinement, and tension crack opening and closing behavior. A versatile connection implemented in DRAIN-2DX was calibrated and used to model the nonlinear inelastic behavior of double split-Tee (DST) moment connections between the steel beams and CFT beam-columns.

Low and medium rise (six and twelve-story) office buildings located in the Los Angeles area, were designed using *high strength* CFT beam-columns, steel beams, and DST moment connections. The six and twelve story high strength CFT MRFs of the office buildings were designed to meet all the requirements of the current seismic design provisions. The seismic behavior of these high strength CFT MRFs were investigated analytically by conducting: (a) nonlinear static pushover analyses according to the FEMA 356 and adaptive pushover analyses procedures, and (b) nonlinear time-history analyses for three sets of earthquake ground motions. The analytical models for the high strength CFT MRFs were developed and analyzed using DRAIN-2DX. The earthquake ground motions for the nonlinear time-history analyses were developed by Somerville et al.

(1997) and included records with 2%, 10%, or 50% probability of exceedance over 50 years.

6.1.1 Analytical Models for CFT MRFs

Chapter 3 presented the development and validation of the analytical models for the structural components of the CFT MRFs, namely, the high strength CFT beam-columns, steel beams, and double split-Tee (DST) moment connections. All the analytical models were developing using finite elements implemented in DRAIN-2DX.

Analytical Model for CFT Beam-Columns

The modified fiber element along with the 'S' and 'C' type fiber σ–ε relationships in DRAIN-2DX (Cordero et al. 2002) was used to model the high strength CFT beam-columns of the CFT MRFs. The governing input parameters for the fiber element models, namely, the σ–ε curves for the steel and concrete fibers modeling the CFT cross-section were developed analytically using the results of 3D finite element analyses of CFT segments subjected to pure axial compressive loading. Thus, the fiber σ–ε curves implicitly accounted for the effects of material inelasticity, tube local buckling, and concrete confinement. The analytical approach for developing the fiber σ–ε curves from the results of 3D finite element analyses was developed by Varma et al. (2005), but validated only for high strength square CFT beam-columns. It was adopted in this research, and extended and validated for CFTs made from both conventional and high strength materials as follows.

3D finite element models were developed for several CFT segments and analyzed for pure axial compression loading using ABAQUS (2003). Thirty-two 3D finite element

models were developed and analyzed for CFTs with concrete strength f'_c=4, 8, 10, or 16 ksi, steel yield stress σ_y=46 or 80 ksi, and tube b/t ratio=24, 32, 48, and 64. The results from the finite element analyses were used to develop steel and concrete fiber σ–ε curves in compression for CFTs with a wide range of material (σ_y and f'_c) and geometric (b/t) parameters.

Specific trends were identified in these steel and concrete fiber σ–ε curves, and idealized steel and concrete fiber σ–ε curves were proposed for CFTs with: (a) σ_y=46 ksi, (b) $f'_c \leq 10$ ksi, (c) σ_y=80 ksi, and (d) $f'_c > 10$ ksi. These proposed steel and concrete fiber σ–ε curves were validated by using them with the modified fiber element to predict the force-deformation behavior of conventional and high strength CFT specimens tested independently in Japan by Fujimoto et al. (2004). The analytical results compared favorably with experimental results and other analytical models developed by Japanese researchers (Sakino et al. 2004, etc.). This validated the modeling approach for the CFT beam-columns.

Analytical Model for Steel Beams

The modified fiber element along with the 'S' type fiber σ–ε relationship implemented in DRAIN-2DX by Cordero et al. (2002) was used to model the steel beams of the CFT MRFs. The governing input parameters for the fiber element models, namely, the σ–ε curves for the steel fibers modeling the beam cross-section were developed analytically using the results of 3D finite element analyses of steel beam segments subjected to pure flexural loading. The analytical approach for developing the fiber σ–ε curves from the results of the 3D finite element analyses was similar to that used for CFT beam-columns. The steel fiber σ–ε curves implicitly accounted for the effects of inelastic

flange and web local buckling. The fiber element model for steel beams was validated by using it to predict the experimental results of Green et al. (2002). The validated fiber element model was used for the steel beams of the CFT MRFs.

Analytical Model for Double Split-Tee (DST) Connections

The zero-length spring elements in DRAIN-2DX (Prakash et al. 1993) were used to model the DST beam-to-column moment connections of the CFT MRFs. The governing input parameters for the connection models, namely, the force-deformation relationships for the spring elements were developed using the results of rigorous 3D finite element analyses of DST connections subjected to tensile or compressive loading. The force-deformation relations for the spring elements implicitly accounted for the effects of bolt pre-tensioning, and contact interaction between the DST connection components. The connection model was validated by using it to predict the experimental results of Swanson et al. (1999). The validated connection model was used for the DST moment connections of the CFT MRFs.

Analytical Model for CFT MRF Subassemblies

The analytical models for CFT beam-columns, steel beams, and DST moment connections were validated further by using them to predict the experimental behavior (lateral force-displacement responses) of full-scale CFT MRF sub-assemblies tested under pseudo-cyclic loading by Peng (2001). The sub-assemblies tested by Peng (2001) consisted of CFT beam-columns, steel beams, and DST beam-to-column connections. Analytical models were developed for the tested sub-assemblies: fiber element models were used for the CFT beam-columns and beams, and connection element models were used for the DST connections. The models were analyzed for the same loading conditions

as the test specimens using DRAIN-2DX. The results from the analyses compared favorably with the experimental results reported by Peng. This further validated the analytical models developed for the components of CFT MRFs, and the approach for combining them to model MRF sub-assemblies.

Analytical Model for CFT MRFs

Analytical models were developed in Chapter 4 for the six and twelve-story CFT MRFs that are the focus of this research. The validated analytical models were used for the components of the CFT MRFs, i.e., validated fiber element models were used for the high strength CFT beam-columns and steel beams, and the validated connection element models were used for the DST moment connections. The validated approach for combining these component models to model the behavior of MRF sub-assemblies was used to develop the complete (overall) analytical model for the CFT MRFs. A dummy column was attached to each story of the CFT MRFs to account for the second-order sway P-Δ effects. Mass proportional damping with a viscous damping ratio $\xi_1=0.05$ was used as the damping for the CFT MRFs.

6.1.2 Seismic Design and Pushover Analyses of CFT MRFs

Seismic Design

Chapter 4 presented the seismic design of the six-story and twelve-story office buildings using MRFs with high strength square CFT beam-columns, steel beams, and DST moment connections, and located in the Los Angeles area. Two structure types were designed for each building story height: (1) consisting of perimeter moment resisting frames and gravity interior frames, and (2) consisting of moment resisting frames in the

long direction and braced frames in the short direction. Both the low (six-story) and medium-rise (twelve-story) CFT MRFs were designed to meet all the requirements of the current seismic design provisions.

Nonlinear Static Pushover Analyses

The seismic behavior of the six-story and twelve-story high strength CFT MRFs were investigated analytically by performing nonlinear static pushover analyses following the FEMA 356 and the adaptive pushover analysis procedures. These nonlinear analyses were conducted using DRAIN-2DX and the analytical models for the CFT MRFs that were developed as described earlier. These analytical models explicitly accounted for the nonlinear inelastic behavior of the CFT MRF components (high strength CFT beam-columns, steel beams, and DST connection) and the complex interactions between them. The results from these analyses indicate that:

- High strength CFT MRFs can be classified as rigid, flexible, and highly flexible depending on the ratio of the first natural period T_1 to T_{max}, i.e., (a) rigid if $0.9 \leq T_1/T_{max} \leq 1$, (b) flexible if $1 < T_1/T_{max} < 1.15$, and highly flexible if $T_1/T_{max} \geq 1.15$
- Upper bound limits were established for the roof drift angles (roof displacement/ building height) of the high strength CFT MRFs. These upper bound limits are 1.5%, 1.5%, and 1.0% for rigid, flexible, and highly flexible CFT MRFs, respectively.
- If the roof drift angle is less than the upper bound limit, then the overall seismic behavior of the high strength CFT MRFs will not influenced by the local inelastic degradation (e.g., inelastic local buckling, concrete crushing, etc.) of the MRF components, namely, the high strength CFT beam-columns and steel beams.

- For the flexible and the rigid CFT MRFs, when the roof drift angle is greater than the upper bound value, then local degradation (flange and web local buckling) of the steel beams controls the post-yield pushover behavior. Local degradation (steel tube local buckling) of high strength CFT beam-columns has smaller influence than the beams.
- For highly flexible CFT MRFs, when the roof drift angle is larger than the upper bound value, then local degradation (steel tube local buckling) of the high CFT beam-columns controls the post-yield pushover behavior of the MRFs. Local degradation (flange and web local buckling) of the steel beams has smaller influence than CFTs.
- Additionally, the adaptive pushover analysis procedures predict smaller displacement ductility ratios (μ) for flexible twelve-story distributed CFT MRFs. These ductility ratios are about 90% of those predicted by FEMA 356 pushover analysis procedures.
- The adaptive pushover analysis procedures also predict larger displacement amplification factors C_d for flexible six-story and twelve-story distributed CFT MRFs, and rigid six-story perimeter CFT MRFs. These C_d values are about 105 % of those predicted by the FEMA 356 pushover analysis procedures.

6.1.3 Nonlinear Time-history Analyses of CFT MRFs

The flexible designs ($1<T_1/T_{max}<1.15$) of the six-story and twelve-story distributed high strength CFT MRFs were subjected to three sets of earthquake ground motions developed for Los Angeles by Somerville et al. (1997). These earthquake ground motions included those with 2%, 10% and 50% probability of exceedance in 50 years. The global and local seismic performances of the six-story and twelve-story high strength CFT MRFs were evaluated following FEMA 350 procedures to determine the level of

confidence in the building's ability to meet the desired performance objectives. Additionally, the global performances limited by inter-story drift for the ***Life Safety*** (LS) performance level were also checked to meet the requirement of FEMA 368.

Ground Motion Ensemble

The flexible designs ($1<T_1/T_{max}<1.15$) of six-story and twelve-story distributed CFT MRFs were subjected to three sets of earthquake ground motion records with 2%, 10% and 50% probability of exceedance in 50 years (return periods of 2,475, 475 and 72 years, respectively). These earthquake ground motions were developed based on the SAC earthquake ground motions developed for Los Angeles by Somerville et al. (1997). The

The SAC earthquake ground motions matched (in the mean) the target response spectra defined in the 1994 NEHRP provisions, i.e., on the average, their spectral values match with a least-square error fit to the USGS mapped values at 0.3, 1.0 and 2.0 s (USGS 1996) and a predicted value at 4.0 s, for the appropriate return period. Somerville et al. (1997) selected these periods (0.3, 1.0, 2.0 and 4.0 s) because they covered the range of interest for flexible steel structures.

These SAC earthquake ground motions were not suitable for the six and twelve-story high strength CFT MRFs, because they have fundamental periods of around 1.0 s to 2.0 s. The SAC earthquake ground motions were rescaled so that their spectral values matched with a least-square error fit to the response spectra at 0.3, 1.0, 1.5 and 2.0 s. The scaling was done following the recommendations of Somerville et al. (1997). The weights used were 0.1, 0.3, 0.3 and 0.3 for periods of 0.3, 1.0, 1.5 and 2.0 seconds, respectively.

Global Seismic Performance

The global seismic performances of the six-story and twelve-story CFT MRFs were evaluated by following FEMA 350 procedures to determine a level of confidence in the building's ability to meet the desired performance objectives, based on the time-history results of the six-story and twelve-story CFT MRF subjected to SAC 2/50 and 50/50 ground motions. The global performance of the flexible ($1<T_1/T_{max}<1.15$) six-story and twelve-story distributed CFT MRF limited by inter-story drift for the *Immediate Occupancy* (IO) and *Collapse Prevention* (CP) performance levels meet the requirements of FEMA 350.

Due to the fact that no factor and confidence levels are recommended by FEMA 350 for the *Life Safety* (LS) level, for CFT MRFs subjected to the 10/50 SAC ground motion time-histories, only the global performance, i.e., the global behavior limited by inter-story drift, was evaluated according to the deflection and drift limits set by FEMA 368. The global performances of the flexible six-story and twelve-story CFT MRF limited by inter-story drift for the *Life Safety* (LS) performance level were found to meet the requirements of FEMA 368.

Local Seismic Performance

The local seismic performances of the six-story and twelve-story CFT MRFs were evaluated by following FEMA 350 procedures to determine a level of confidence in the building's ability to meet the desired performance objectives, based on the time-history results of the six-story and twelve-story CFT MRF subjected to SAC 2/50 and 50/50 ground motions. The local connection performance and the local column compression performance of the flexible ($1<T_1/T_{max}<1.15$) six-story and twelve-story distributed CFT

MRF for the *Immediate Occupancy* (IO) and *Collapse Prevention* (CP) performance levels met the requirements of FEMA 350.

Due to the fact that no factor and confidence levels are recommended by FEMA 350 for the *Life Safety* (LS) level, for CFT MRFs subjected to the 10/50 SAC ground motion time-histories, only the global performance, i.e., the global behavior limited by inter-story drift, was evaluated according to the deflection and drift limits set by FEMA 368. No local behavior of CFT MRFs subjected to the 10/50 SAC ground motion time-histories was evaluated.

Higher Mode and P-Δ Effects

The results from the nonlinear static pushover analyses and the nonlinear time-history analyses of the high strength CFT MRFs included: (a) the story drift envelops, (b) the variation of story drift angle-to-roof drift angle over the height of structure, and (c) the normalized base shear-roof drift angle relationships. These results provide insight into the effects of higher modes and second-order P-Δ effects on the global seismic performance of the high strength CFT MRFs.

The normalized base shear-roof drift angle relationships obtained from the pushover analysis provided good indices to distinguish the influence zones of the higher mode and second-order P-Δ effects. For the cases in which the roof displacements from the time-history analysis are larger than the design drift, Δ_d, the second-order P-Δ effects on the seismic performance of the structure should not be neglected. Especially for the cases in which the global (roof) drift angles have entered the "yield" (constant strength) plateau, the second-order P-Δ effects on the seismic performance becomes significant.

The roof displacements from the time-history analysis of the CFT MRFs subjected to the modified SAC 2/50 ground motions were larger than the design drift, Δ_d, and in some cases have even entered the "yield" (constant strength) plateau. With more than 80% of the total mass participating in the 1st mode, the seismic performance of the six-story CFT MRF subjected to the 2/50 ground motions is controlled by the P-Δ effects. While with less than 80% of the total mass participating in the 1st mode, the seismic performance of the twelve-story CFT MRF subjected to the 2/50 ground motions is controlled by the higher mode effects, yet still influenced by the P-Δ effects.

Since the maximum roof drift angles for the high strength CFT MRFs subjected to the modified SAC 2/50 ground motions were less than the roof drift angle at which the slope of the global pushover curve becomes clearly negative, the second-order P-Δ effects did not fully offset the first-order story shear resistance and dynamic instability was considered an unlikely event. Almost all the roof displacements from the time-history analysis for the six-story and twelve-story CFT MRFs subjected to the modified SAC 10/50 and 50/50 ground motions were less than the design drift, Δ_d.

For a structure with a negative post-yield stiffness for the simplified pushover curve, which was simplified following the FEMA 356 bilinear simplification procedure, it is usually considered to be a structure prone to dynamic instability. One important finding based on the pushover and time-history analyses results is that, the desired global and local performance objectives of such a structure could still be met, providing that the maximum roof drift angle has entered the relatively short "yield" (constant strength) plateau of the actual pushover curve, but is less than the roof drift angle at which the slope of the actual pushover curve clearly becomes negative.

The second-order P-Δ effects have not fully offset the first-order story shear resistance and dynamic instability was considered an unlikely event in this case. For example, the flexible six-story distributed CFT MRF has a negative post-yield stiffness for the simplified pushover curve. It still met all the desired global and local performance objectives since the maximum roof drift angle entered the relatively short "yield" (constant strength) plateau of the actual pushover curve, but it was less than the roof drift angle at which the slope of the actual pushover curve clearly becomes negative.

For the six-story and twelve-story high strength CFT MRFs subjected to the modified SAC 2/50, 10/50 and 50/50 ground motions, the story drift to roof drift ratios were larger than 1.0 for most stories. The sum of the maximum story displacements was always larger than the maximum roof displacement. If pushover analyses are used to capture all maximum story drifts over height of CFT MRFs, the target displacement should be amplified by the median ratios of the sum of maximum story displacements to maximum roof displacement.

Another observation from the story drift-to-roof drift ratios over the building height is that, for a first mode dominated low-rise (6-story) CFT MRF with effective modal masses for the 1st mode larger than 80%, the distribution of the story drift to roof drift ratios over the building height is sensitive to the severity of the records. While for a higher mode effects dominated medium-rise CFT MRF with effective modal masses for the 1st mode less than 80%, the distribution of the story drift-to-roof drift ratios over the building height indicates little sensitivity to the severity of the records. This observation is corroborated by similar observations for 20-story steel structures subjected to the same ground motion records (Gupta and Krawinkler, 2000b).

6.2 Conclusions

The results from the nonlinear static pushover analyses of the high strength CFT MRFs indicate that:

- Upper bound limits can be established for the roof drift angles (roof displacement/ building height) of the high strength CFT MRFs. These upper bound limits are 1.5%, 1.5%, and 1.0% for rigid, flexible, and highly flexible CFT MRFs, respectively.
- If the roof drift angle is less than the upper bound limit, then the overall seismic behavior of the high strength CFT MRFs will not influenced by the local inelastic degradation (e.g., inelastic local buckling, concrete crushing, etc.) of the MRF components, namely, the high strength CFT beam-columns and steel beams.
- For the flexible and the rigid CFT MRFs, when the roof drift angle is greater than the upper bound value, then local degradation (flange and web local buckling) of the steel beams controls the post-yield pushover behavior. Local degradation (steel tube local buckling) of high strength CFT beam-columns has smaller influence than the beams.
- For highly flexible CFT MRFs, when the roof drift angle is larger than the upper bound value, then local degradation (steel tube local buckling) of the high CFT beam-columns controls the post-yield pushover behavior of the MRFs. Local degradation (flange and web local buckling) of the steel beams has smaller influence than CFTs.
- For the flexible twelve-story distributed CFT MRFs, the adaptive pushover analysis procedure predicts smaller displacement ductility ratios (μ), about 90% of those predicted by the static pushover analysis following FEMA 356 procedures.
- Higher mode effects on the seismic behavior of CFT MRFs should not be neglected, and adaptive pushover analysis should be performed in addition to the static pushover

analysis recommended in the FEMA 356 procedures.

The results from the nonlinear time-history analyses of high strength CFT MRFs indicate that:

- The global performance of the flexible six-story and twelve-story distributed CFT MRFs limited by inter-story drift, as well as the local connection performance and the local column compression performance for the *Immediate Occupancy* (IO) and *Collapse Prevention* (CP) performance levels meet the requirements of FEMA 350. In addition, the global performance of the flexible six-story and twelve-story CFT MRF limited by inter-story drift for the *Life Safety* (LS) performance level also meet the requirement of FEMA 368.
- The base shear-roof drift angle relationships obtained from the pushover analysis provide good indices to distinguish the influence zones of the higher mode and second-order P-Δ effects. For the cases in which the roof displacements of the time-history analysis are larger than the design drift, Δ_d, the second-order P-Δ effects on the seismic performance of the structure should not be neglected. Especially for the cases in which the roof drift angles have entered the "yield" (constant strength) plateau, the second-order P-Δ effects on the seismic performance of the structure becomes significant.
- With more than 80% of the total mass participating in the 1st mode, the seismic performance of the six-story CFT MRF subjected to the 2/50 ground motions is controlled by the P-Δ effects.
- With less than 80% of the total mass participating in the 1st mode, the seismic performance of the twelve-story CFT MRF subjected to the 2/50 ground motions is

controlled by the higher mode effects, yet still influenced by the P-Δ effects.

- The maximum roof drift angles of the six-story and twelve-story CFT MRFs subjected to the 2/50 ground motions are all less than the roof drift angle at which the slope of the global push over curve clearly becomes negative. The second-order P-Δ effects have not fully offset the first-order story shear resistance and dynamic instability is considered an unlikely event.
- For a structure with a negative post-yield stiffness in the simplified pushover curve, the desired global and local performance objectives can still be met, provided that the maximum roof drift angle enters the relatively short "yield" (constant strength) plateau of the actual pushover curve, but is less than the roof drift angle at which the slope of the actual pushover curve clearly becomes negative.
- If pushover analysis is used to capture all maximum story drifts over height of CFT MRFs, the target displacement should be amplified by the median ratios of the sum of maximum story displacements to maximum roof displacement.
- For a first mode dominated low-rise CFT MRF with effective modal masses for the 1^{st} mode larger than 80%, the distribution of the story drift to roof drift ratios over the building height is sensitive to the severity of the records.
- For a higher mode effects dominated medium-rise CFT MRF with effective modal masses for the 1^{st} mode less than 80%, the distribution of the story drift to roof drift ratios over the building height indicate little sensitivity to the severity of the records.

The results from the nonlinear static pushover and time-history analyses of high strength CFT MRFs indicate that:

- The current seismic design provisions, e.g., *International Building Code* (2000, abbreviated as *IBC 2000*), *FEMA 350, FEMA 368, AISC-LRFD 1999, ASCE 7-98, ACI 318-99*, etc, can be used to design moment resisting frames consisting of high-strength CFT columns (σ_y>50 ksi, f'_c>10 ksi), as long as the width-to-thickness (b/t) ratio of the CFT is less than or equal to 32.
- For buildings located in regions of high seismicity (Los Angles), the distributed frame configuration consisting of high strength CFT MRFs in the long direction and braced frames in the short direction, is recommend for low-rise and medium-rise office building. The distributed CFT MRFs will have smaller and more useable CFT column sections. Perimeter CFT MRFs will result in impractical CFT sections for the medium-story heights.
- The upper bound limitation on fundamental period, T_{max}, set by IBC-2000 for the purposes of strength check, provides a good index to distinguish relatively rigid and flexible CFT MRFs. The flexible ($1<T_1/T_{max}<1.15$) distributed CFT MRF, which has smaller CFT sections than the rigid ($0.9<T_1/T_{max}<1$) distributed CFT MRF, is recommended for use with the distributed frame system.
- The flexible distributed CFT MRF meets all the global and local performance objectives set by FEMA 350 and FEMA 368, because that the maximum roof drift angle obtained from the time-history analysis for the 2/50 earthquake ground motion, is less than the roof drift angle at which the slope of the actual pushover curve clearly becomes negative.

6.3 Recommendations for Future Work

- The analytical models developed and used in this research should be improved and made more accurate. The analytical models for the steel beams and the moment connections should be more generalized so that other researchers and engineers can develop them more easily.
- The analytical models of the connections must be improved to include the possibilities of brittle fracture due to ultra low cycle fatigue.
- The current research has focused on the seismic behavior of MRFs with square CFT columns only. Additional research should be conducted to investigate the seismic behavior of MRFs with circular CFT columns and corresponding connections.
- The fundamental behavior and collapse susceptibility of CFT MRF structures subjected to realistic compartment fire loading events should be investigated analytically and experimentally.
- Finally, large-scale experimental investigations should be conducted on high strength CFT MRF sub-systems to evaluate their static, cyclic, and pseudo-dynamic behavior under earthquake loading conditions. The results from such experimental investigations will develop further confidence in the use of high strength steel and concrete materials in composite construction, and will be useful for further validating the analytical results from this study.

APPENDIX: DESIGN OF DOUBLE SPLIT-TEE CONNECTIONS

A.1 T-stub Section Selection

A.1.1 Required Shear Strength (Flange Force)

According to *LRFD Seismic Provisions (1997),* Sec. I-9.2c, the required shear strength (required flange force of Tee Stubs), P_{reqd}, is:

$$P_{reqd} = \frac{1.1 F_{ye} Z_x}{d_b} \qquad \text{(A.1)}$$

where:

$F_{ye} = R_y F_y$ (*AISC-97 Seismic Provisions*, I-6.2), the specified minimum yield stress of the yielding element;

$R_y = 1.1$ for rolled shapes of ASTM A992 (*AISC-97 Seismic Provisions*, I-6.2);

F_y= the yield strength of the T-stub;

Z_x= the effective plastic modulus of the section;

d_b= the depth of girder.

Then for $F_y = 50$ *ksi*, the required shear strengths (flange forces) of the sections used in this research are listed in Table A.1.

A.1.2 Selection of Size and Grade for Tension Bolts

According to *LRFD Specification for Structural Joints Using ASTM A325 or A490 Bolts (2000),* Sec. 5.1, the required factored bolt strength must be satisfied (assuming a 30% prying):

$$\phi B_{n,reqd} = \frac{1.30 P_{reqd}}{n_{tb}} \le \phi B_n = 0.75 F_n A_b \qquad \text{(A.2)}$$

where:

n_{tb} = the number of the tension bolts;

B_n = nominal strength of a bolt;

A_b = cross section area of tension bolt;

F_n = nominal strength per union area for the appropriate applied load conditions.

If ASTM 490 tension bolts with ASTM 563 nuts are used for each case, then $F_n = 113\ ksi$ (Applied static tension, *LRFD (2000)*, Table 5.1), one has:

$$n_{tb} \ge \frac{1.30 P_{reqd}}{0.75 F_n A_b} = \frac{1.30 P_{reqd}}{0.75 F_n \times \frac{\pi}{4} d_{bt}^2} \qquad \text{(A.3)}$$

where: d_{bt} = the diameter of the tension bolt.

Using Equation A.3, the required bolt numbers of DST connections used in this research can be obtained and are listed in Table A.2.

A.1.3 T-stub Section Selection

(1) Equilibrium Equations of T-Stub Flange

As shown in Fig. A.1, moment equilibrium of the T-flange between the face of the stem and the bolt line is:

$$(1 + \delta\alpha) M = Tb' \qquad \text{(A.4)}$$

where:

$\delta = 1 - \frac{d_h}{p}$, the ratio of the net section of the flange at the bolt line to the gross section at the face of the stem,

$p = 2W_{T-stub}/n_{tb}$, the tributary width of the T-stub to one pair of bolts,

n_{tb} = the number of tension bolts connecting the T-stub flange,

d_h = the diameter of the bolt holes.

Moment equilibrium of the T-flange between the end of the flange and the bolt line is:

$$\delta\alpha M = Qa' \qquad \text{(A.5)}$$

And the force equilibrium of the entire flange results in:

$$B = \phi B_n = T + Q \qquad \text{(A.6)}$$

From Equations A.4 to A.6, the balanced load for a T-stub flange is:

$$T = \frac{\phi B_n}{1 + \left(\frac{\delta}{1+\delta}\right)\left(\frac{b'}{a'}\right)} \qquad \text{(A.7)}$$

If the design load, $T_{reqd,}$ is set to equal to the balanced load, T, then from Equation A.7, one has:

$$b'_{reqd} = \left(\frac{\phi_f B_n - T_{reqd}}{T_{reqd}}\right)\left(\frac{1+\delta}{\delta}\right)a' \qquad \text{(A.8)}$$

where:

$\phi_f = 0.75$, the resistance factor for the failure mode of net section or block shear fracture.

For a ductile flange, the tension bolts will be located near the edge of the flange. If a minimum edge distance $1.5\ d_{bt}$ is used, then a' can be set equal to $2d_{bt}$. Equation A.8 can be rewritten as:

$$b'_{reqd} = \left(\frac{\phi_f B_n - T_{reqd}}{T_{reqd}} \right) \left(\frac{1+\delta}{\delta} \right) 2d_{bt} \qquad \text{(A.9)}$$

Using Equation A.9, the calculations of the minimum distance from the bolt hole to the k-zone, b'_{reqd} are listed in Table A.3.

(2) Minimum Stem Thickness, t_s

The minimum stem thickness, t_s, must satisfy:

$$\phi R_{n,stem} = \phi_f F_u A_{stem,net} = \phi_f F_u W_{eff} t_s \geq P_{reqd} \qquad \text{(A.10)}$$

where:

F_u = the specified minimum tensile stress of the yielding element;

$W_{eff} = W_{T\text{-}stub}$, the effective width of the T-stem.

Then the minimum stem thickness is:

$$t_s \geq \frac{P_{reqd}}{\phi_f F_u W_{eff}} = \frac{P_{reqd}}{\phi_f F_u W_{T-stub}} \qquad \text{(A.11)}$$

Using Equation A.11, the minimum stem thickness of T-stubs are obtained and listed in Table A.4.

(3) Minimum flange width B_f

Assuming that the effective stem thickness, $t_{s,eff}$, is approximately equal to twice the nominal stem thickness, t_s, then flange width can then be estimated by

$$B_{f,reqd} = 2\left(a' + b'\right) + t_{s,eff} = 2b'_{reqd} + 4d_{bt} + 2t_{s,\min} \qquad \text{(A.12)}$$

Using Equation A.12, the minimum flange widths of T-stubs are obtained and listed in Table A.5.

(4) Minimum and maximum flange thickness t_f

The traditional approach to predict the minimum and maximum flange thickness is based on the experiments of DST connections in which the flanges of the T-stubs are bolted to the flanges of the steel beams. For a ductile flange, the thickness of the flange should not less than that predicted by the intercept of Jaspart's flange capacity prediction, with the combined failure prediction of Kulak et al. The minimum required flange thickness of a DST connection with bolted flanges is determined by:

$$t_{f,reqd-\min} = \sqrt{\frac{T_{reqd}\left[8b'_{reqd} - \left(2d_{bt} + b'_{reqd}\right)\right]}{\phi_{bt} 3.75 p F_y}} \qquad \text{(A.13)}$$

where:

$\phi_{bt} = 0.90$, the resistance factor for failure modes of bending or plastic moment.

In addition, the thickness of the flange should not greater than that predicted by the intercept of Kulak's flange mechanism capacity, with the combined failure capacity. The maximum flange thickness of a DST connection with bolted flanges is determined by:

$$t_{f,reqd-\max} = \sqrt{\frac{4T_{reqd}b'_{reqd}}{\phi_{bt} p F_y (1+\delta)}} \qquad \text{(A.14)}$$

While for the double split Tee connections with the T stem being fillet welded to the beam flange, the maximum required flange thickness predicted by Kulak's flange mechanism capacity, seems to give a relative lower value. Sometime it even it difficult to achieve a balanced failure, i.e., a more desirable stem fracture (ductile failure) will precede a tension bolt fracture (brittle failure). Likewise, the minimum flange thickness predicted by Jaspart's flange capacity prediction, also seems to give a relative lower value.

Proposed Approach for Minimum Flange Thickness Prediction

For a ductile double split Tee connections with the T-stems fillet welded to the beam flanges, flange yielding governed by bolt fracture due to prying is the control failure mode for the flange, which indicate a tension bolt fracture instead of the develop of a plastic flange mechanism. It's important to make sure a ductile failure mode, net stem yielding, precedes a brittle failure, tension bolt fracture. In order to achieve this goal, the design resistance of the flange controlled by the failure mode of net stem yielding must be less than the design resistance of the flange controlled by the failure mode of tension bolt fracture:

$$\phi_y F_y A_{stem,net} = \phi_y F_y W_{T-stub} t_s < \phi R_{n,flange} = n_{tb} \phi T_n \qquad \text{(A.15)}$$

where:

$A_{stem,\,net} = W_{T\text{-}stub}\, t_s$, net cross section area of the T-stem.

And the design strength controlled by tension bolt fracture is:

$$\phi T_n = \phi T_2 = \frac{\phi B_n a'}{a' + b'} + \frac{\phi_{bt} p F_y t_f^2}{4\left(a' + b'\right)} \qquad \text{(A.16)}$$

Based on this observation, the minimum flange thickness can be predicted as:

$$n_{tb}\left[\frac{\phi B_n a'}{a' + b'} + \frac{\phi_{bt} p F_y t_f^2}{4\left(a' + b'\right)}\right] \geq \phi_y F_y t_s W_{T-stub} \qquad \text{(A.17)}$$

i.e.,

$$t_f^2 \geq \left(\frac{\phi_y F_y W_{T-stub} t_s}{n_{tb} \phi B_n} - \frac{a'}{a' + b'}\right) \frac{4\left(a' + b'\right)}{p} \frac{\phi B_n}{\phi_{bt} F_y} \qquad \text{(A.18)}$$

Assume that a minimum edge distance *1.5* d_{bt} is used, a' can be set equal to $2d_{bt}$, then:

$$t_{f,reqd-\min} = \sqrt{\left(\frac{\phi_y F_y W_{T-stub} t_{s,\min}}{n_{tb}\phi B_n} - \frac{2d_{bt}}{b'_{reqd} + 2d_{bt}}\right)\frac{4\left(b'_{reqd} + 2d_{bt}\right)}{p}\frac{\phi B_n}{\phi_{bt} F_y}} \qquad \text{(A.19)}$$

Proposed Approach for Maximum Flange Thickness Prediction

For a ductile double split Tee connections with the T-stems fillet welded to the beam flanges, the flange yielding governed by bolt fracture due to prying is the control failure mode for the flange. In order to preclude brittle failure mode, *Tension bolt fracture without the effects of prying,* the design resistance of the flange controlled by the failure mode of the flange yielding governed by bolt fracture due to prying must be less than the design resistance of the flange controlled by the failure mode of tension bolt fracture without the effects of prying:

$$\phi T_n = \phi T_2 = \frac{\phi B_n a'}{a' + b'} + \frac{\phi_{bt} p F_y t_f^2}{4\left(a' + b'\right)} \le \phi T_3 = \phi B_n \qquad \text{(A.21)}$$

i.e.,

$$t_f^2 \le \left(1 - \frac{a'}{a' + b'}\right)\frac{4\left(a' + b'\right)}{p}\frac{\phi B_n}{\phi_{bt} F_y} = \frac{4b'}{p}\frac{\phi B_n}{\phi_{bt} F_y} \qquad \text{(A.22)}$$

Then the maximum flange thickness can be predicted by:

$$t_{f,reqd-\max} = \sqrt{\frac{4b'}{p}\frac{\phi B_n}{\phi_{bt} F_y}} \qquad \text{(A.23)}$$

Using Equations A.19 and A.23, the minimum and maximum flange thicknesses are obtained and listed in Table A.6.

(5) A trial T-stub section selection

The minimum stem thickness, required flange width and the range of flange thickness are listed in Table A.7. Then the T-stub section can be selected as listed in Table A.8.

A.2 T-stub Capacity Check

A.2.1 Geometry for Prying Forces and Bending of T-section Flanges

To ensure that the flange fails in a ductile mechanism, the distance from the bolt to the edge of the T-stub flange, *a*, and the distance from the bolt line to the face of the T-stem, *b*, must satisfy:

$$a = \frac{1}{2}\left(B_f - g_t\right) \le 1.25b \qquad \text{(A.24)}$$

$$b = \frac{1}{2}\left(g_t - t_{s,eff}\right) \qquad \text{(A.25)}$$

From Equations A.24 and A.25, one has:

$$g_t \ge \left(B_f + 1.25t_{s,eff}\right)/2.25 \qquad \text{(A.26)}$$

where:

$t_{s,eff} = k_1 + \frac{t_s}{2}$, the effective thickness of T-stem.

The geometries for T-stub flanges are listed in Table A.9. And the geometries for prying forces and bending of T-section flanges are listed in Table A.10.

A.2.2 Flange Capacity Check

The design resistance of the flange including tension bolt fracture and prying is

determined by the modified Kulak et al model (Swanson 1999) as follow:

$$\phi R_{n,flange} = n_{tb}\phi T_n \geq P_{reqd} = \frac{1.1F_{ye}Z_x}{d_b} \qquad \text{(A.27)}$$

where:

n_{tb} = the number of tension bolts,

ϕT_n = the minimum design resistance per bolt of the flange.

The minimum design resistance per bolt of the flange, ϕT_n, should be determined by considering three failure modes: (1) plastic flange mechanism, (2) flange yielding governed by bolt fracture due to prying, and (3) tension bolt fracture without the effects of prying. The value of ϕT_n is the lowest of ϕT_1, ϕT_2, and ϕT_3 which are determined by the above three failure modes, respectively.

(1) Plastic flange mechanism

$$\phi T_1 = \frac{\phi_{bt}\left(2a' - \frac{d_{bt}}{4}\right)pF_y t_f^2}{4a'b' - d_{bt}\left(a' + b'\right)} \qquad \text{(A.28)}$$

(2) Flange yielding governed by bolt fracture due to prying

$$\phi T_2 = \frac{\phi B_n a'}{a' + b'} + \frac{\phi_{bt} pF_y t_f^2}{4\left(a' + b'\right)} \qquad \text{(A.29)}$$

(3) Tension bolt fracture without the effects of prying

$$\phi T_3 = \phi B_n \qquad \text{(A.30)}$$

The design resistances per bolt of the flanges controlled by the failure modes of plastic flange mechanism and flange yielding governed by bolt fracture due to prying are listed in Table A.11. The design resistances per bolt of the flanges controlled by the failure mode of tension bolt fracture without the effects of prying are listed in Table A.12. For the three T-stub sections, flange yielding governed by bolt fracture due to prying is the control failure mode, since ϕT_2 is the smallest.

The minimum design resistances of the flanges for T-stubs are listed in Table A.13. As shown in Table A.13, all the minimum design resistances of the flanges are larger than the corresponding required flange forces of DST connections, OK. The actual levels of prying in the flanges of the T-stubs are listed in Table A.14. As listed in Table A.14, all the actual levels of prying in the flanges are less than or close to 30% as previously assumed.

A.2.3 Stem Capacity Check

The design resistance of the stem in net section fracture must satisfy:

$$\phi R_{n,stem} = \phi_f F_u A_{stem,net} = \phi_f F_u W_{T-stub} t_s \geq P_{reqd} \qquad \text{(A.31)}$$

The design resistances of the stems in net section fracture are list in Table A.15. As show in Table A.15, all the design resistances of the stems in net section fracture are larger than the required flange forces of DST connections, OK.

A.2.4 Check $t_{s,max}$ to Ensure a Balanced T-stub Failure

For a ductile T-stub with significant deformation capacity, it's important to design such that the bending capacity of the stem is less than the bending capacity of the flange.

Then a more desirable stem fracture (ductile failure) will precede a tension bolt fracture (brittle failure).

In this design, flange yielding governed by bolt fracture due to prying is the control failure mode for the flange, which indicate a tension bolt fracture instead of the develop of a plastic flange mechanism. It's important to make sure a ductile failure mode, net stem yielding, precedes a brittle failure, tension bolt fracture. This requirement can be expressed as the design resistances controlled by failure mode of net stem yielding is less than the design resistances controlled by failure mode of tension bolt fracture:

$$\phi_y F_y A_{stem,net} = \phi_y F_y W_{T-stub} t_s < \phi R_{n,flange} = n_{tb} \phi T_n \qquad \text{(A.32)}$$

The design resistances of T-stubs controlled by failure modes of net stem yielding and tension bolt fracture are shown in Table A.16. As shown in Table A.16, all the design resistances controlled by failure mode of net stem yielding is less than the corresponding design resistances controlled by failure mode of tension bolt fracture, OK.

A.2.5 Check net Stem Section for Shear Capacity

According to *LRFD Seismic Provisions (1997),* Sec. I-9.2c, the required shear strength of a beam to column connection is:

$$V_{reqd} = \frac{2 \times 1.1 F_{ye} Z_x}{L_{beam}} \qquad \text{(A.33)}$$

where:

$F_{ye} = R_y F_y$ (*AISC-97 Seismic Provisions*, I-6.2), the specified minimum yield stress of the yielding element;

$R_y = 1.1$ for rolled shapes of ASTM A992 (*AISC-97 Seismic Provisions*, I-6.2);

L_{beam} = the length of the beam.

According to *LRFD - F2.2 (AISC, 1999),* the design shear strength of unstiffened webs, with $h/t_w \leq 260$, is:

$$\phi_v V_n = 0.90 \times 0.6 F_{yw} A_w \qquad \text{(A.34)}$$

The required shear strengths of DST connections for $F_y = 50\ ksi$ are listed in Table A.17. The design shear strengths of net stem sections (at k-zone) are listed in A.18. As shown in Table A.18, all the design shear strengths of net stem sections (at k-zone) are larger than the corresponding required shear strengths of DST connections, OK

A.3 Fillet Welds between T-Stem and Beam Flange

Minimum and Maximum Sizes of Fillet Welds

According to *LRFD – Table J2.4* (AISC, 1999), and *LRFD –J2.2b* (AISC, 1999), the minimum, maximum and effective thicknesses of the fillet welds used in the connections between T-stems and beam flanges are listed in Table A.19.

Design Strength of Fillet Welds

According to *LRFD-J2.4* (AISC, 1999), the design strength per unit length of a fillet weld is based on the shear resistance through the throat of the weld:

$$\phi R_{nw} = 0.75 t_e \left(0.60 F_{EXX}\right) \quad \text{fillet weld} \qquad \text{(A.35)}$$

where:

R_{nw} = the nominal strength per unit length of the weld.

but not greater than the shear rupture strength (*LRFD-J4, 1999)* of the adjacent base metal:

$$\phi R_{nw} = 0.75t(0.60F_u) \quad \text{base metal} \qquad (A.36)$$

where:

R_{nw} = the nominal strength per unit length of adjacent base material.

Assume that the welding process is shielded metal arc welding, and E70 electrodes having minimum tensile strength F_{EXX} of *70ksi* are used, then the design strengths per unit length of fillet welds used in DST connections between T-stems and beam flanges are obtained and listed in Table A.20.

Length of fillet welds

The design strengths of the fillet welds used in DST connections between T-stems and beam flanges must equal or exceed the summation of factored loads:

$$\phi R_{nw} \geq R_u \qquad (A.37)$$

where:

R_{nw} = the nominal strength per unit length of the weld, but not exceed the nominal strength per unit length of adjacent base material;

R_u = factor load per unit length of weld.

When the effective length of the fillet weld, *l*, is multiplied to the two sides of Equation A.37, one has

$$\phi R_{nw} l \geq P_{reqd} \qquad (A.38)$$

where:

R_{nw} = the required shear strength (required flange force) of Tee Stub;

l = the effective length of the fillet weld.

Using Equation A.38, the effective length of the fillet weld, *l*, can be determined. The required and actual lengths of fillet welds used in DST connections between T-stems and

beam flanges are listed in Table A.21. Details of the DST connections used in this research are shown in Figs. A.2 to A.4.

A.4 Summary

For the double split Tee connections with the T-stems fillet welded to the beam flanges, the maximum required flange thickness predicted by Kulak's flange mechanism capacity, seems to give a relative lower value. Sometime it even it difficult to achieve a balanced failure, i.e., a more desirable stem fracture (ductile failure) will precede a tension bolt fracture (brittle failure).

For a ductile double split Tee connections with the T-stems fillet welded to the beam flanges, flange yielding governed by bolt fracture due to prying is the control failure mode for the flange, which indicate a tension bolt fracture instead of the develop of a plastic flange mechanism. In order to make sure a ductile failure mode, net stem yielding, precedes a brittle failure, tension bolt fracture, a new approach for minimum flange thickness prediction was proposed.

Likewise, in order to preclude brittle failure mode, *Tension bolt fracture without the effects of prying,* i.e., to make sure that the failure mode of the flange yielding governed by bolt fracture due to prying precedes failure mode of tension bolt fracture without the effects of prying, a new approach for maximum flange thickness prediction was proposed. The DST connections used in this research were designed based on these two propose approaches. The strength check and the results of pushover and time-history analyses prove that these two propose approaches are reliable for minimum and maximum flange thicknesses prediction of DST connections with the T-stems fillet welded to the beam flanges.

Table A.1 Required flange forces of DST connections

Girder Section	d_b (in)	Z_e (in^3)	$P_{reqd} = \frac{1.21F_yZ_x}{d_b}$ (k)
W36x135	35.55	509	866.23
W33x118	32.86	415	764.07
W30x108	29.83	346	701.74
W27x94	26.92	278	624.78
W27x84	26.71	244	552.68
W24x76	23.92	200	505.85
W24x62	23.73	153	390.08

Table A.2 Required bolt numbers of DST connections

Girder Section	P_{reqd} (k)	Bolt size d_{bt} (in)	Bolt number n_{tb}	
			Calculated	Used
W36x135	866.23	1.5	7.5	8
W33x118	764.07		6.6	
W30x108	701.74		6.1	
W27x94	624.78	1.25	7.8	8
W27x84	552.68		6.9	
W24x76	505.85	1.0	7.8	8
W24x62	390.08		6.0	

Table A.3 Minimum distance from the bolt hole to the k-zone

Girder Section	T_{reqd} (k)	p (in)	δ	b'_{reqd} (in)
W36x135	108.28	4.22	0.630	2.98
W33x118	95.51			4.41
W30x108	87.72			5.49
W27x94	78.10	4.22	0.650	2.11
W27x84	69.08			3.21
W24x76	63.23	3.75	0.683	1.84
W24x62	48.76			4.03

Note: 1. $T_{reqd} = P_{reqd}/n_{tb}$, required flange forces for one tension bolt.

2. $p = 2W_{T-stub}/n_{tb}$, the tributary width of the T-stub to one pair of bolts.

3. $\delta = 1 - d_h/p$, the ratio of the net section of the flange at the bolt line to the gross section at the face of the stem.

Table A.4 Minimum stem thickness of T-stubs

Girder Section	P_{reqd} (k)	W_{T-stub} (in)	$t_{s,\min}$ (in)
W36x135	866.23	16.875	1.053
W33x118	764.07		0.929
W30x108	701.74		0.853
W27x94	624.78	16.875	0.854
W27x84	552.68		0.756
W24x76	505.85	15	0.692
W24x62	390.08		0.533

Table A.5 Minimum flange width of T-stubs

Girder Section	b'_{reqd} (in)	$t_{s,\min}$ (in)	d_{bt} (in)	$B_{f,reqd}$ (in)
W36x135	2.98	1.053	1.5	12.39
W33x118	4.41	0.929		13.76
W30x108	5.49	0.853		14.23
W27x94	2.11	0.854	1.25	10.92
W27x84	3.21	0.756		12.93
W24x76	1.84	0.692	1.0	9.57
W24x62	4.03	0.533		12.64

Table A.6 Minimum and maximum flange thickness

Girder Section	b'_{reqd} (in)	T_{reqd} (k)	$t_{f,reqd-\max}$ (in)	$t_{f,reqd-\min}$ (in)
W36x135	2.60	108.28	3.06	0.41
W33x118	3.86	95.51	3.73	0.43
W30x108	4.80	87.72	4.16	0.43
W27x94	1.87	78.10	2.28	0.39
W27x84	2.84	69.08	2.82	0.42
W24x76	1.70	63.23	1.91	0.38
W24x62	3.71	48.76	2.83	0.42

Table A.7 Minimum stem thickness, required flange width and the range of flange thickness of T-stubs

Girder Section	$t_{s,\min}$ *(in)*	$B_{f,reqd}$ *(in)*	$t_{f,reqd-\max}$ *(in)*	$t_{f,reqd-\min}$ *(in)*
W36x135	1.053	12.39	3.06	0.41
W33x118	0.929	13.76	3.73	0.43
W30x108	0.853	14.23	4.16	0.43
W27x94	0.854	10.92	2.28	0.39
W27x84	0.756	12.93	2.82	0.42
W24x76	0.692	9.57	1.91	0.38
W24x62	0.533	12.64	2.83	0.42

Table A.8 Selected T-stub sections

Girder Section	T-stub section	T-stub dimensions		
		t_s *(in)*	B_f *(in)*	t_f *(in)*
W36x135	W27x281	*1.06>1.053*	*14.35>14.23*	*0.43<1.93=3.06*
W33x118				
W30x108				
W27x84	W24x229	*0.96>0.854*	*13.11>10.92*	*0.42<1.73<2.28*
W27x94				
W24x76	W24x176	*0.750>0.692*	*12.89>12.64*	*0.42<1.34<1.92*
W24x62				

Table A.9 Geometries for T-stub flanges

Girder Section	T-stub section	T-stub geometry			
		$t_{s,eff}$ *(in)*	$g_t \geq \frac{B_f + 1.25 t_{s,eff}}{2.25}$ *(in)*	*a (in)*	*b (in)*
W36x135	W27x281	1.75	7.5≥7.35	3.425	2.875
W33x118					
W30x108					
W27x84	W24x229	1.5	7.0≥6.97	3.063	2.75
W27x94					
W24x76	W24x176	1.3125	7.0≥6.45	2.938	2.844
W24x62					

Table A.10 Geometries for prying forces and bending of T-section flanges

Girder Section	T-stub section	d_{bt} *(in)*	*a (in)*	*b (in)*	*a' (in)*	*b' (in)*
W36x135	W27x281	*1.5*	*3.425<1.25b*	*2.875*	4.175	2.125
W33x118						
W30x108						
W27x84	W24x229	*1.25*	*3.063<1.25b*	*2.75*	3.688	2.125
W27x94						
W24x76	W24x176	*1.0*	*2.938<1.25b*	*2.844*	3.5	2.281
W24x62						

Note: 1. $a' = a + d_{bt}/2$, $b' = b - d_{bt}/2$, where d_{bt} is the diameter of tension bolt.

Table A.11 Design resistances per bolt of the flanges controlled by the failure modes of plastic flange mechanism and flange yielding governed by bolt fracture due to prying

Girder Section	T-stub section	t_f *(in)*	a' *(in)*	b' *(in)*	ϕT_1 *(k/bolt)*	ϕT_2 *(k/bolt)*
W36x135	W27x281	1.93	4.175	2.125	240.66	130.43
W33x118						
W30x108						
W27x84	W24x229	1.73	3.688	2.125	148.14	87.70
W27x94						
W24x76	W24x176	1.34	3.5	2.281	80.04	64.10
W24x62						

Table A.12 Design resistances per bolt of the flanges controlled by the failure modes of tension bolt fracture without the effects of prying

Girder Section	T-stub section	d_{bt} *(in)*	ϕT_3 *(k/bolt)*
W36x135	W27x281	*1.5*	149.77
W33x118			
W30x108			
W27x84	W24x229	*1.25*	104.00
W27x94			
W24x76	W24x176	*1.0*	84.24
W24x62			

Table A.13 Minimum design resistances of the flanges for T-stubs

Girder Section	T-stub section	P_{reqd} (k)	n_{tb}	ϕT_2 (k/bolt)	$\phi R_{n,flange} = n_{tb}\phi T_n$ (k)
W36x135	W27x281	866.23	8	130.43	1043.43>866.23, OK
W33x118		764.07	8		
W30x108		701.74	8		
W27x84	W24x229	624.78	8	87.70	701.63>624.78, OK
W27x94		552.68	8		
W24x76	W24x176	505.85	8	64.10	512.83>505.85, OK
W24x62		390.08	8		

Table A.14 Actual levels of prying in the flanges for T-stubs

Girder Section	T-stub section	ϕB_n (k/bolt)	ϕT_2 (k/bolt)	$prying = \frac{\phi B_n - \phi T_2}{\phi T_2}$ (%)
W36x135	W27x281	149.77	130.43	14.8%<30%, OK
W33x118				
W30x108				
W27x84	W24x229	104.00	87.70	18.5%<30%, OK
W27x94				
W24x76	W24x176	84.24	64.10	31.4%≅30%, OK
W24x62				

Table A.15 Design resistances of the stems in net section fracture

Girder Section	T-stub section	P_{reqd} (k)	W_{T-stub} (in)	t_s (in)	$\phi R_{n,stem}$ (k)
W36x135	W27x281	866.23	16.875	1.06	872.02>866.23, OK
W33x118		764.07			
W30x108		701.74			
W27x84	W24x229	624.78	15	0.96	702.00>624.77, OK
W27x94		552.68			
W24x76	W24x176	505.85	15	0.75	548.44>505.85, OK
W24x62		390.08			

Table A.16 Design resistances of T-stubs controlled by failure modes of net stem yielding and tension bolt fracture

Girder Section	T-stub section	$\phi R_{n,flange}$ (k)	$\phi_y F_y A_{stem,net}$ (k)
W36x135	W27x281	1043.43	804.94<1043.43, OK
W33x118			
W30x108			
W27x84	W24x229	701.63	648.00<701.63, OK
W27x94			
W24x76	W24x176	512.83	506.25<512.83, OK
W24x62			

Table A.17 Required shear strengths of DST connections

Girder Section	L_{beam} (in)	Z_e (in^3)	V_{reqd} (k)
W36x135	360	509	171.08
W33x118		415	139.49
W30x108		346	116.29
W27x84	360	278	93.44
W27x94		244	82.01
W24x76	360	200	67.22
W24x62		153	51.43

Table A.18 Design shear strengths of net stem sections (at k-zone)

Girder Section	T-stub section	W_{T-stub} (in)	t_s (in)	V_{reqd} (k)	$\phi_v V_n$ (k)
W36x135	W27x281	16.875	1.06	171.08	347.73>171.08, OK
W33x118				139.49	
W30x108				116.29	
W27x84	W24x229	15	0.96	93.44	279.94>93.44, OK
W27x94				82.01	
W24x76	W24x176	15	0.75	67.22	218.70>67.22, OK
W24x62				51.43	

Table A.19 Maximum, minimum and effective thicknesses of the fillet welds used in DST connections between T-stems and beam flanges

Girder Section	T-stub section	$t_{f,beam}$ (in)	t_s (in)	a_{max} (in)	a_{min} (in)	a (in)	t_e (in)
W36x135	W27x281	13/16	1.06	3/4	5/16	5/8	0.442
W33x118		3/4		11/16	1/4		
W30x108		3/4		11/16	1/4		
W27x84	W24x229	3/4	0.96	11/16	1/4	1/2	0.354
W27x94		5/8		9/16	1/4		
W24x76	W24x176	11/16	0.75	5/8	1/4	1/2	0.354
W24x62		9/16		1/2	1/4		

Note: 1. $a_{max} = t_f - 1/16$, the maximum size of fillet welds of connected parts,

2. $t_e = 0.707a$, effective thickness of fillet welds.

Table A.20 Design strengths per unit length of fillet welds used in DST connections between T-stems and beam flanges

Girder Section	T-stub section	$t_{f,beam}$ (in)	t_s (in)	*fillet weld* ϕR_{nw} (k/in)	*base metal* ϕR_{nw} (k/in)	ϕR_{nw} (k/in)
W36x135	W27x281	13/16	1.06	13.92	23.77	13.92
W33x118		3/4			21.94	
W30x108		3/4			21.94	
W27x84	W24x229	3/4	0.96	11.14	21.94	11.14
W27x94		5/8			21.94	
W24x76	W24x176	11/16	0.75	11.14	18.28	11.14
W24x62		9/16			20.11	

Table A.21 Required and actual lengths of fillet welds used in DST connections between T-stems and beam flanges

Girder Section	T-stub section	P_{reqd} (k)	Design fillet weld strength ϕR_{nw} (k/in)	Required length of fillet welds (in)	Actual length of fillet welds
W36x135	W27x281	866.23	13.92	62.2	64.0>62.2, OK
W33x118		764.07			
W30x108		701.74			
W27x84	W24x229	624.78	11.14	56.1	59.0>56.1, OK
W27x94		552.68			
W24x76	W24x176	505.85	11.14	45.4	53.0>45.4, OK
W24x62		390.08			

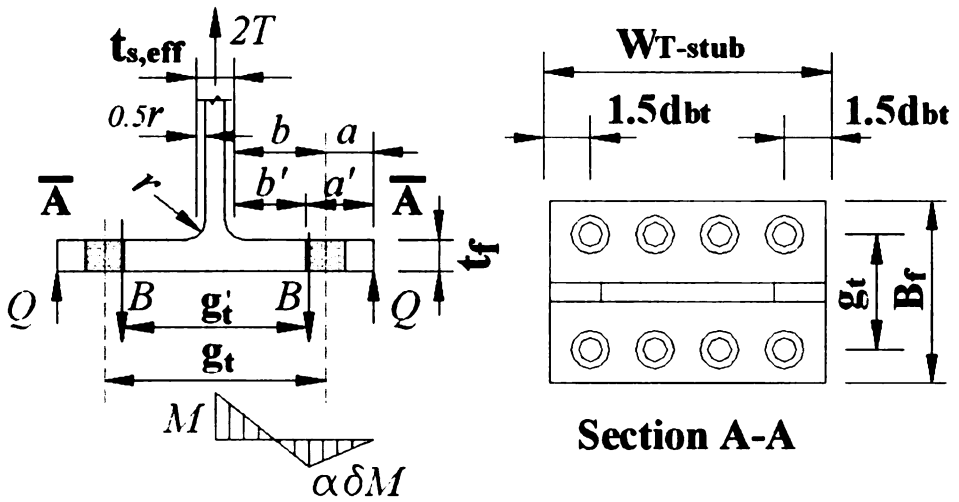


Figure A.1 Geometry for prying forces and bending of T-section flanges

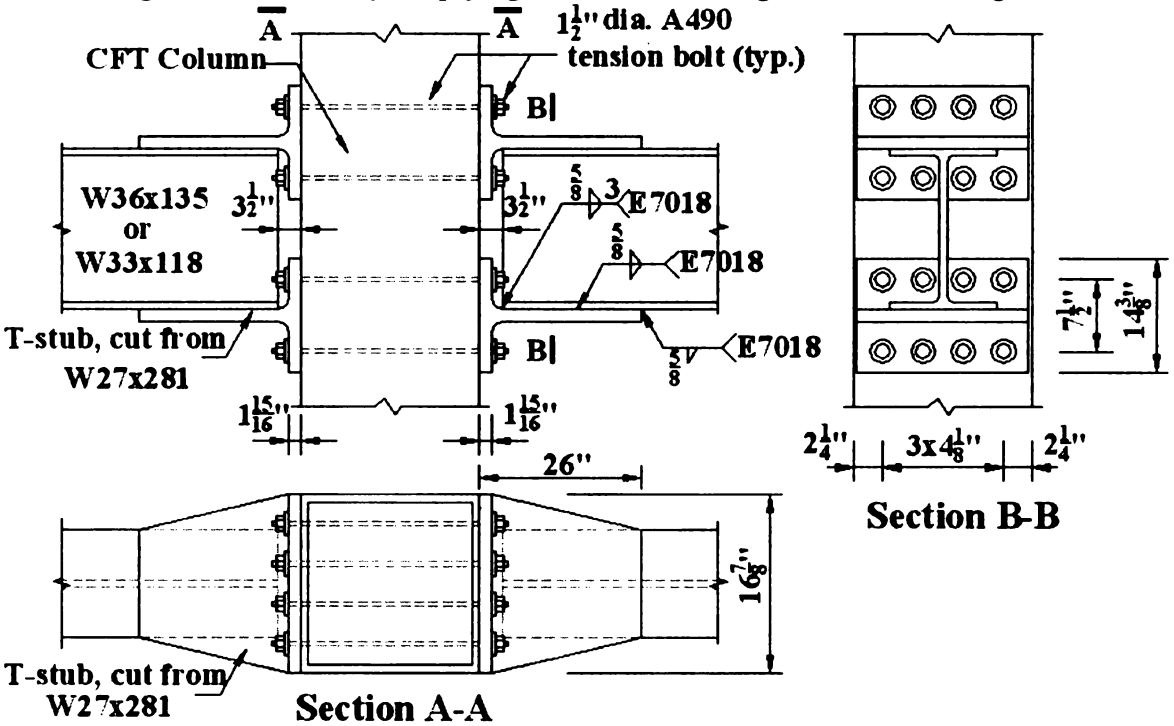


Figure A.2 DST Connection for rolled sections W36x135, W33x118 and W30x108

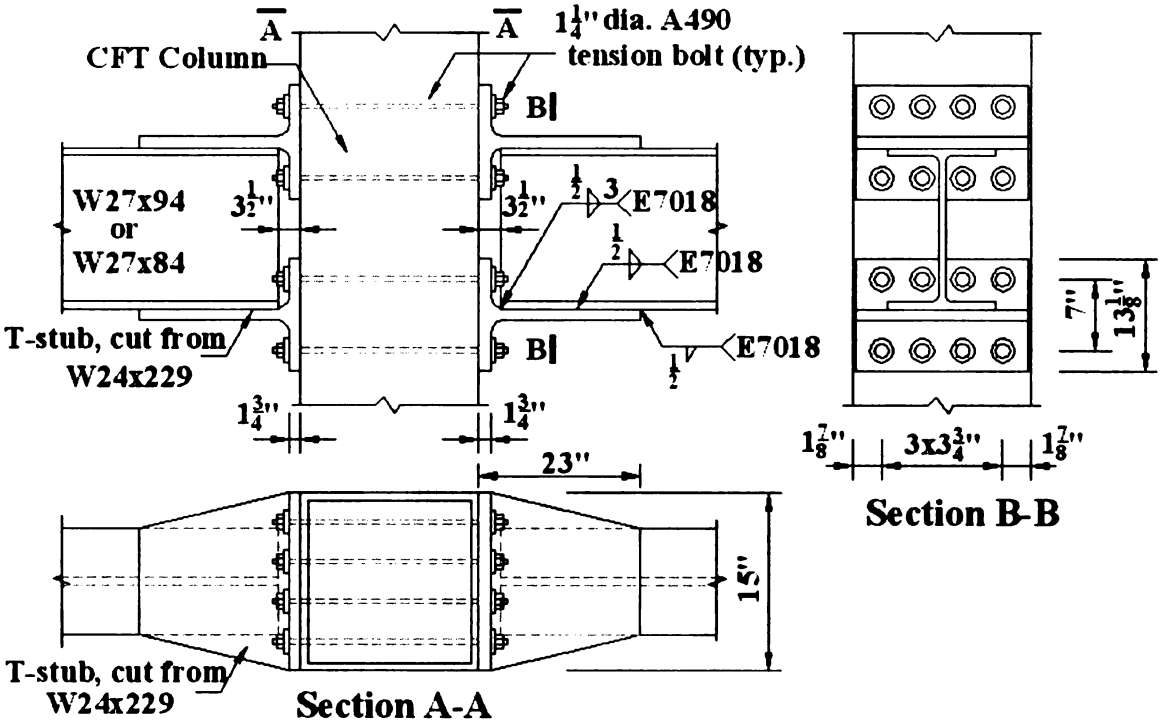


Figure A.3 DST Connection for rolled sections W27x94 and W27x84

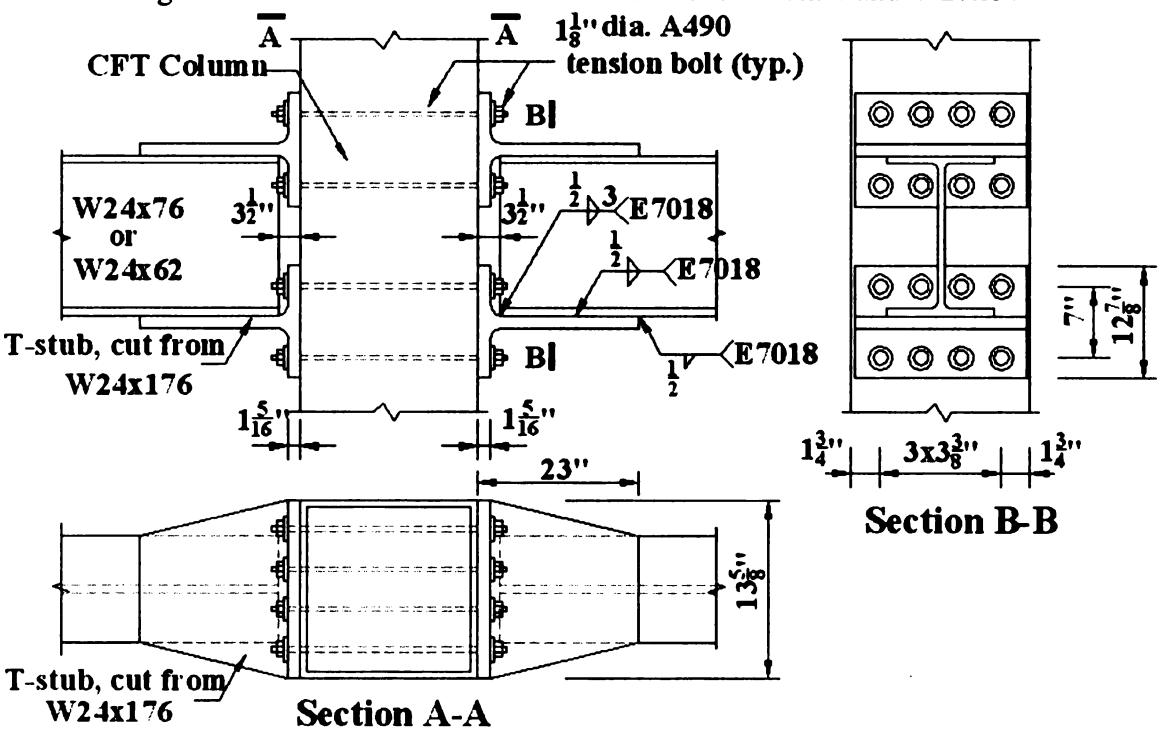


Figure A.4 DST Connection for rolled sections W27x94 and W27x84

REFERENCES

Alostaz, Y. M., and S. P. Schneider. 1996. "Analytical Behavior of Connections to Concrete- Filled Steel Tubes". *Journal of Constructional Steel Research* v40, n2, pp. 95-127.

American Society of Civil Engineers, (2000) "Minimum Design Loads for Buildings and Other Structures, ASCE 7-98". New York, 2000.

American Society of Civil Engineers, (2000) "Prestandard and Commentary for the Seismic Rehabilitation of Buildings, FEMA-356". Federal Emergency Management Agency, Washington, D.C., March 2001.

Building Seismic Safety Council, (2001) "NEHRP Recommended Provisions for Seismic Regulations for New Buildings and Other Structures, FEMA-368 and Commentary FEMA-369". Federal Emergency Management Agency, Washington, D.C., March 2001.

Browning, J., Li, Y. R., Lynn, A., and Moehle, J. P., (2001) "Performance Assessment for a Reinforced Concrete Frame Building", *Earthquake Spectra*, v16, n3, 2000, pp541-555.

Chopra, A. K., (1995) "Dynamics of Structures, Theory and Applications to Earthquake Engineering", Prentice-Hall, Inc., New Jersey, 1995.

Chopra, A. K., Goel, P. K. (2002) "A modal pushover analysis procedure for estimating seismic demands for buildings", *Earthquake Engineering and Structural Dynamic*, 2002; v31, n3, pp561-582.

Cheng, F. Y. (2001) "Matrix Analysis of Structural Dynamics: applications and earthquake engineering", Marcel Dekker, Inc., New York, 2001.

Converse, April M., Brady, Gerald (1992). "BAP: Basic Strong-Motion Accelerogram Processing Software; Version 1.0", United States Department of the Interior Geological Survey, Open File Report 92-296A.

Domenech, A. C. (2002) "Development of a modified fiber-based beam-column element for *DRAIN2DX*", *Master thesis*, Department of Civil and Environmental Engineering, Michigan State University, East Lansing, MI, July 2002.

Elremaily, A. (2000) "Connections between Steel Beam and Concrete-filled Steel Tube

Columns", *Ph.D. dissertation*, Department of Civil Engineering, University of Nebraska-Lincoln, Lincoln, NE, May 2000.

Elremaily, A. and Azizinamini, A. (2001) "Design provisions for connections between steel beams and concrete filled tube columns", *J. Constructional Steel Research*, v57, n9, September, 2001, p 971-995

Foutch, D. A., and Yun, S.-Y., (2002) "Modeling of steel moment frames for seismic loads", *J. Constructional Steel Research*, Vol. 58, 2002, pp.529-564

Fujii, S., Aoyama, H. and Umemura, H. (1973). "Analytical moment-curvature relationship of reinforced concrete section based on material characteristics." *Summary of Technical Papers of Annual Meeting of Architectural Institute of Japan, Structures,* Architectural Institute of Japan, Tokyo, 1261-1262.

Furlong, R.W. (1968), "Design of Steel-Encased Concrete Beam-Columns," ASCE, *Journal of Structural Engineering*, Vol. 94, No. ST1, pp 267-281.

Garlock, M. M., Ricles, J. M., Sause, R., Zhao, C., and Lu, L.-W. (2000) "Seismic Behavior of Post-Tensioned Steel Frames," *Third International Conference on the Behavior of Steel Structures in Seismic Areas*, August 21-24, Montreal, Canada, pp. 593-599

Gasparini, D. A., Vanmarke, E. H. (1976). "SIMQKE – A Program for Artificial Motion Generation," Department of Civil Engineering, Massachusetts Institute of Technology, MA, November, 1976.

Green, P. S., Sause, R. and Ricles, J. M., (2002) "Strength and ductility of HPS flexural members", *J. Constructional Steel Research*, Vol. 58, 2002, pp.907-941

Gupta, A. and Krawinkler H. (2000a) "Dynamic P-Delta Effects for Flexible Inelastic Steel Structures", *J. Structural Engineering*, Vol. 126, No. 1, 2000, pp.145-154

Gupta, A. and Krawinkler H. (2000b) "Estimation of Seismic Drift Demand for Frame Structures", *Earthquake Engineering and Structural Dynamic*, Vol. 29, No. 3, 2000, pp.1287-1305

Gupta, B. and Kunnath S. K. (2000) "Adaptive Spectra-Base Pushover Procedure for Seismic Evaluation of Structures", *Earthquake Spectra*, Vol. 16, No. 2, 2000, pp.367-391

Hajjar, J.F. and Gourley, B.C. (1996), "Representation of Concrete-Filled Steel Tube Cross-Section Strength," *Journal of Structural Engineering*, ASCE, Vol. 122, No. 11,

November 1996, pp. 1327-1336.

Hajjar, J.F. and Gourley, B.C. (1997a), "A Cyclic Nonlinear Model for Concrete-Filled Tubes. I. Formulation," *Journal of Structural Engineering*, ASCE, Vol. 123, No. 6, June 1997, pp. 736-744.

Hajjar, J.F., Gourley, B.C. and Olson, M.C. (1997b), "A Cyclic Nonlinear Model for Concrete-Filled Tubes. II. Verification," *Journal of Structural Engineering*, ASCE, Vol. 123, No. 6, June 1997, pp. 745-754.

Hajjar, J.F., Molodan, A., and Schiller, P.H. (1998a), "A Distributed Plasticity Model for Cyclic Analysis of Concrete-Filled Steel Tube Beam-Columns and Composite Frames," *Engineering Structures*, Vol. 20, Nos. 4-6, April-June 1998, pp. 398-412.

Hajjar, J.F., Schiller, P.H., and Molodan, A. (1998b), "A Distributed Plasticity Model for Concrete-Filled Steel Tube Beam-Columns with Interlayer Slip," *Engineering Structures*, Vol. 20, No. 8, August 1998, pp. 663-676.

HIBBITT, KARLSSON & SORENSEN, INC., (2001) "ABAQUS STANDARD USER'S MANUAL VERSION 6.2"

Huang, Z., Varma, A. H., Harichandran, R. S., and Cordero, A. (2004) "Effects of Inelastic Local Buckling on the Seismic Behavior of Structural Members and Frames", *Proceedings of SSRC 2004 Annual Technical Session and Meeting*, March 24-27, 2004, Long Beach, California, pp. 329-351.

International Code Council, (2000) "International Building Code, IBC-2000", Birmingham, AL, 2000.

Kato, B., Nishiyama, I. (1980). "Local buckling strength and deformation capacity of cold-formed steel rectangular hollow section." *Journal of Structural and Construction Engineering*, Vol. 294, pp. 45-52.

Kim, D. K., and Engelhardt, M. D., (2002) "Monotonic and cyclic loading models for panel zones in steel moment frames", *J. Constructional Steel Research*, Vol. 58, 2002, pp.605-635

Koester, B. D. (2000) "Panel zone behavior of moment connections between rectangular concrete-filled steel tubes and wide flange beams", *Ph.D. dissertation*, Department of Civil and Environmental Engineering, The University of Texas at Austin, Austin, TX, May 2000.

Kowalkowski, K. J. and Varma, A. H. (2003) "Evaluation of Analytical Models for High

Strength CFT Beam-Columns", *Proceedings of SSRC 2003 Annual Technical Session and Meeting*, April 2-5, 2003, Baltimore, Maryland, pp. 539-563.

Kramer, S. L. (1996) "Geotechnical Earthquake Engineering", Prentice-Hall, Inc., New Jersey, 1996.

Krawinkler H. and Seveviratna G. (1998) "Pros and cons of a pushover analysis of seismic performance evaluation", *Engineering Structures*, Vol. 20, No. 4-6, 1998, pp.452-464

Kurama, Y., Pessiki, S. P., Sause, R., Lu, L.-W., and El-Sheikh, M., (1996) "Analytical modeling and lateral load behavior of unbonded post-tensioned precast concrete walls", *Earthquake engineering research report NO. EQ-96-02*, Department of Civil and Environmental Engineering, Lehigh University, Bethlehem, PA

Leon, R. T. and Swanson, J. A., (2000) "Cyclic Modeling of T-stub Bolted Connections", *Third International Conference on the Behavior of Steel Structures in Seismic Areas*, August 21-24, Montreal, Canada, pp. 703-710

Mao, C., Ricles, J. M., Lu, L.-W., and Fisher, J., (2000) "Inelastic Finite Element Studies of Unreinforced Welded Beam-to-Column Moment Connections", *Third International Conference on the Behavior of Steel Structures in Seismic Areas*, August 21-24, Montreal, Canada, pp. 711-717

Mao, C., Ricles, J. M., Lu, L.-W., and Fisher, J., (2001) "Effect of Local Details on Ductility of Welded Moment Connections", *J. Structural Engineering*, Vol. 127, No. 9, 2001, pp. 1036-1044

Nakahara, H., Saikino, K. and Inai, E. (1998) "Analytical model for compressive behavior of concrete filled square steel tubular columns", *Transcation of the Japan Concrete Institute*, V20, 1998, pp.171-177

Nakashima, M., Minami, T. and Mitani, I. (2000) "Moment Redistribution Caused by Beam Fracture in Steel Moment Frames", *J. Structural Engineering*, V126, n1, 2000, pp.137-144

Mehanny, S. S. and Deierlein, G. G. (2001) "Seismic Damage and Collapse Assessment of Composite Moment Frames", *J. Structural Engineering*, V127, n9, 2001, pp.1045-1053

Meng, L., Ohi, K., and Takanashi, K. (1992). "A simplified model of steel structural members with strength deterioration used for earthquake response analysis." *Journal of Structures and Construction Eng.*, AIJ, 437, 115-124.

Peng, S.-W. (2001) "Seismic resistant moment connections for concrete filled tube column-to- WF beam moment resisting frames", *Ph.D. dissertation*, Department of Civil and Environmental Engineering, Lehigh University, Bethlehem, PA, March 2001.

Perdomo, M., Ramirez, A. and Florez-Lopez, J. (1999) "Simulation of damage in RC frames with variable axial forces", *Earthquake Engineering and Structural Dynamics*, Vol. 28, No. 3, 1999, pp.311-328

Prakash, V., Powell, G. H., and Campbell S., (1993) "*DRAIN2DX* base program description and user guide version 1.10".

Ricles, J. M., Lu, L.-W., and Pang, A. K, (1993) "Capacity of high strength thin wall box columns under axial load", *Proceedings SSRC ATS*, Milwaukee, WI, pp.115-139

Ricles, J. M., Lu, L.-W., and Peng, S.-W., (1997) "Split-Tee Seismic Connections for CFT Column-WF Beam MRFs", *Building to Last, Proceedings of Structures Congress XV*, Portland, Oregon, Apr. 13-16, 1997, pp.959-963

Ricles, J. M., Sause, R., Garlock, M. M., and Zhao, C., (2001) "Posttensioned seismic-resistant connections for steel frames", *J. Structural Engineering*, Vol. 127, No. 2, 2001, pp.113-121

Roeder, C. W., (2002) "General issues influencing connection performance", *J. Structural Engineering*, Vol. 128, No. 4, 2002, pp.420-428

SAC Joint Venture, (2000) "Recommended Seismic Design Criteria for New Steel Moment- Frame Buildings, FEMA-350". Federal Emergency Management Agency, Washington, D.C., June 2000.

Shams, M., (1997) "Non-linear Evaluation of Concrete-filled Steel Tubular Columns", *Ph.D. dissertation*, Department of Civil and Environmental Engineering, New Jersey Institute of Technology, Atlanta, NJ, January 1997.

Somerville, P., Smith, N., Punyamurthula, S., and Sun, J. (1997) "Development of Ground Motion Time Histories for Phase 2 of the FEMA/SAC Steel Project", *SAC/BD-97/04*, SAC Joint Venture

Swanson, J. A., (1999) "Characterization of the strength, stiffness and ductility behavior of T-stub connection", *Ph.D. dissertation*, Department of Civil and Environmental Engineering, Georgia Institute of Technology, Atlanta, GA, August 1999.

Swanson, J. A., and Leon, R. T., (2000) "Bolted steel connection: tests on T-stub components", *J. Structural Engineering*, Vol. 126, No. 1, 2000, pp.50-56

Swanson, J. A., and Leon, R. T., (2001) "Stiffness modeling of bolted T-stub connection components", *J. Structural Engineering*, Vol. 127, No. 5, 2001, pp.498-505

Tomii, M. and Sakino, K. (1979a), "Experimental Studies on the Ultimate Moment of Concrete Filled Square Steel Tubular Beam-Columns," *Transactions of the Architectural Institute of Japan*, No. 275, pp. 55-63.

Tomii, M. and Sakino, K. (1979b), "Elasto-Plastic Behavior of Concrete Filled Square Steel Tubular Beam-Columns," *Transactions of the Architectural Institute of Japan*, No. 280, pp. 111-120.

Varma, A. H. (2000) "Seismic Behavior, Analysis, and Design of High Strength Square Concrete Filled Steel Tube (CFT) Columns", *Ph.D. dissertation*, Department of Civil and Environmental Engineering, Lehigh University, Bethlehem, PA., November 2000

Varma, A. H., Ricles, J. M., Sause, R., and Lu, L.-W. (2001) "Seismic Behavior, Analysis, and Design of High Strength Square CFT Beam-Columns", *ATLSS Research Report No. 2001-01*, ATLSS Research Center, Lehigh Univ., Bethlehem, PA.

Varma, A. H., Ricles, J. M., Sause, R., and Lu, L.-W. (2002a) "Seismic behavior and modeling of high-strength composite concrete-filled steel tube (CFT) beam-column", *J. Constructional Steel Research*, Vol. 58, 2002, pp.725-758

Varma, A. H., Ricles, J. M., Sause, R., and Lu, L.-W. (2002b) "Experimental Behavior of High Strength Square Concrete-Filled Steel Tube Beam-Columns", *J. Structural Engineering* , Vol. 128, No. 3, 2002, pp. 309-318

Varma, A. H., Ricles, J. M., and Sause, R. (2002c) "Analysis and Design of High Strength Square CFT Beam-Columns", *Proceedings 2002 Annual Stability Conference*, Structural Stability Research Council, Florida, pp. 219-243.

Varma, A. H., Ricles, J. M., Sause, R., and Lu, L.-W. (2004a) "Seismic Behavior and Design of High-Strength Square Concrete-Filled Steel Tube Beam Columns", *J. Structural Engineering*, Vol. 130, No. 2, 2004, pp. 169-179

Varma, A. H., Sause, R., Ricles, J. M., and Li, Q. (2005) "Development and Validation of Fiber Model fro High-Strength Square Concrete-Filled Steel Tube Beam-Columns", *ACI Structural Journal*, Vol. 102, No. 1, 2005, pp. 89-101

Xu, Y., Kasai, K., and Mao, C., (2000) "Experiment and Analysis of Bolted Semi-Rigid Beam-Column Connections Part II: 3-D Finite Element Analysis of the Connections using Angles", *Third International Conference on the Behavior of Steel Structures in Seismic Areas*, August 21-24, Montreal, Canada, pp. 207-214

Yun, S.-Y., Hamburger, R. O., Cornell, C. A., and Foutch, D. A. (2002) "Seismic Performance Evaluation for Steel Moment Frames", *J. Structural Engineering* , Vol. 128, No. 4, 2002, pp. 534-544

Zhang, H., and Ricles, J. M. (1996) "An analytical study of seismic resistant CFT MRFs", *Fritz Laboratory Research Report*, Department of Civil and Environmental Engineering, Lehigh University, Bethlehem, PA

Zhang, W., and Shahrooz, B.M. (1997), "Analytical and Experimental Studies into Behavior of Concrete-Filled Tubular Columns", *Report No. UC-CII 97/01*, University of Cincinnati, College of Engineering, Cincinnati Infrastructure Institute, Cincinnati, OH.

MICHIGAN STATE UNIVERSITY LIBRARIES
3 1293 02736 0837